frontiers | Research Topics

Innovative approaches for wound treatment

Edited by
Jinlong Ma, Yapei Zhang and Yizhou Zhan

Published in
Frontiers in Pharmacology



FRONTIERS EBOOK COPYRIGHT STATEMENT

The copyright in the text of individual articles in this ebook is the property of their respective authors or their respective institutions or funders. The copyright in graphics and images within each article may be subject to copyright of other parties. In both cases this is subject to a license granted to Frontiers.

The compilation of articles constituting this ebook is the property of Frontiers.

Each article within this ebook, and the ebook itself, are published under the most recent version of the Creative Commons CC-BY licence. The version current at the date of publication of this ebook is CC-BY 4.0. If the CC-BY licence is updated, the licence granted by Frontiers is automatically updated to the new version.

When exercising any right under the CC-BY licence, Frontiers must be attributed as the original publisher of the article or ebook, as applicable.

Authors have the responsibility of ensuring that any graphics or other materials which are the property of others may be included in the CC-BY licence, but this should be checked before relying on the CC-BY licence to reproduce those materials. Any copyright notices relating to those materials must be complied with.

Copyright and source acknowledgement notices may not be removed and must be displayed in any copy, derivative work or partial copy which includes the elements in question.

All copyright, and all rights therein, are protected by national and international copyright laws. The above represents a summary only. For further information please read Frontiers' Conditions for Website Use and Copyright Statement, and the applicable CC-BY licence.

ISSN 1664-8714
ISBN 978-2-8325-7301-3
DOI 10.3389/978-2-8325-7301-3

Generative AI statement
Any alternative text (Alt text) provided alongside figures in the articles in this ebook has been generated by Frontiers with the support of artificial intelligence and reasonable efforts have been made to ensure accuracy, including review by the authors wherever possible. If you identify any issues, please contact us.

About Frontiers

Frontiers is more than just an open access publisher of scholarly articles: it is a pioneering approach to the world of academia, radically improving the way scholarly research is managed. The grand vision of Frontiers is a world where all people have an equal opportunity to seek, share and generate knowledge. Frontiers provides immediate and permanent online open access to all its publications, but this alone is not enough to realize our grand goals.

Frontiers journal series

The Frontiers journal series is a multi-tier and interdisciplinary set of open-access, online journals, promising a paradigm shift from the current review, selection and dissemination processes in academic publishing. All Frontiers journals are driven by researchers for researchers; therefore, they constitute a service to the scholarly community. At the same time, the *Frontiers journal series* operates on a revolutionary invention, the tiered publishing system, initially addressing specific communities of scholars, and gradually climbing up to broader public understanding, thus serving the interests of the lay society, too.

Dedication to quality

Each Frontiers article is a landmark of the highest quality, thanks to genuinely collaborative interactions between authors and review editors, who include some of the world's best academicians. Research must be certified by peers before entering a stream of knowledge that may eventually reach the public - and shape society; therefore, Frontiers only applies the most rigorous and unbiased reviews. Frontiers revolutionizes research publishing by freely delivering the most outstanding research, evaluated with no bias from both the academic and social point of view. By applying the most advanced information technologies, Frontiers is catapulting scholarly publishing into a new generation.

What are Frontiers Research Topics?

Frontiers Research Topics are very popular trademarks of the *Frontiers journals series*: they are collections of at least ten articles, all centered on a particular subject. With their unique mix of varied contributions from Original Research to Review Articles, Frontiers Research Topics unify the most influential researchers, the latest key findings and historical advances in a hot research area.

Find out more on how to host your own Frontiers Research Topic or contribute to one as an author by contacting the Frontiers editorial office: frontiersin.org/about/contact

Innovative approaches for wound treatment

Topic editors

Jinlong Ma — Shandong Second Medical University, China

Yapei Zhang — Michigan State University, United States

Yizhou Zhan — Dongguan University of Technology, China

Citation

Ma, J., Zhang, Y., Zhan, Y., eds. (2026). *Innovative approaches for wound treatment*. Lausanne: Frontiers Media SA. doi: 10.3389/978-2-8325-7301-3

Table of contents

05 Editorial: Innovative approaches for wound treatment
Junxiao Zhang, Shenglin Geng, Guojuan Fan and Jinlong Ma

08 Nervonic acid as novel therapeutics initiates both neurogenesis and angiogenesis for comprehensive wound repair and healing
Yu-Da Liu, Xiao Peng, Hao-Ran Chen, Xue-Song Liu and Li-Hua Peng

19 Phytochemicals, promising strategies combating *Cutibacterium acnes*
Cuilian Sun, Yuhang Na, Ziyu Wang, Tingting Zhu and Xiaojuan Liu

29 Compliant immune response of silk-based biomaterials broadens application in wound treatment
Zhiqiang Tian, Hong Chen and Ping Zhao

49 Exploration the therapeutic effects of sodium houttuyfonate combined with penicillin G on methicillin resistant *staphylococcus aureus* infected wounds
Yujie Li, Shunjie You, Sheng Li, Si Li, Aimin Jia, Xiaoyan Xiang, Shi Shen and Yan Cai

70 The inherent defects of cold atmospheric plasma for the treatment of burns
Yingying Li, Hong Guan, Guojuan Fan and Jinlong Ma

73 Rapid *in situ* formation of a double cross-linked network hydrogels for wound healing promotion
Yifan Liu, Ye Zhang, Qianqian Jia, Xiaoyun Liang and Kejin Xu

85 Thymoquinone alleviates the accumulation of ROS and pyroptosis and promotes perforator skin flap survival through SIRT1/NF-κB pathway
Jianxin Yang, Haojie Zhang, Libin Ni and Jun He

100 Silk fibroin–collagen hydrogel loaded with IGF1-CESCs attenuates intervertebral disk degeneration by accelerating annulus fibrosus healing in rats
Zhiqiang Tian, Zigang Shen, Hong Chen and Ping Zhao

114 LL37 promotes angiogenesis: a potential therapeutic strategy for lower limb ischemic diseases
Yingying Yang, Gang Wu, Yini Wang, Qiancheng Mao, Dongxu Zhang and Jitao Wu

125 Multifunctional PdH-hydride MOFs for synergistic hydrogen and photothermal antibacterial therapy in accelerated wound healing
Qing Wang, Daixing Zhang, Yining Qi, Changbao Huang, Dejun Ding and Chuanliang Liu

141 BaDuShengJi hydrogel accelerates diabetic wounds healing and regeneration of deep burn injury by anti-bacteria, anti-inflammation and promoting epithelialization
Yuxiang Zhang, Yuanyuan Yu, Lien Yu, Fang Wang, Fuwei Yang, Shiyu Liang, Wen Xu, Mengying Ji, Yinuo Geng, Jingwei Xue, Chunmao Han, Zhongtao Zhang and Yilin Zhang

159 Narirutin treatment accelerates the process of diabetic wound repair by regulating phenotype switching of macrophages through affecting metabolic reprogramming
Liang Liu, Han Wang, Juan Zhou, Jing Lu, Yan Zhang, Haiyan Liu and Li Lu

frontiers | Frontiers in Pharmacology

TYPE Editorial
PUBLISHED 09 December 2025
DOI 10.3389/fphar.2025.1738213

Check for updates

OPEN ACCESS

EDITED AND REVIEWED BY
Albino Martins,
Universidade do Minho Instituto de Investigacao em Biomateriais Biodegradaveis e Biomimeticos, Portugal

*CORRESPONDENCE
Guojuan Fan,
shantianri@163.com
Jinlong Ma,
majinlong99@hotmail.com

†These authors have contributed equally to this work

RECEIVED 03 November 2025
REVISED 26 November 2025
ACCEPTED 26 November 2025
PUBLISHED 09 December 2025

CITATION
Zhang J, Geng S, Fan G and Ma J (2025) Editorial: Innovative approaches for wound treatment.
Front. Pharmacol. 16:1738213.
doi: 10.3389/fphar.2025.1738213

COPYRIGHT
© 2025 Zhang, Geng, Fan and Ma. This is an open-access article distributed under the terms of the Creative Commons Attribution License (CC BY). The use, distribution or reproduction in other forums is permitted, provided the original author(s) and the copyright owner(s) are credited and that the original publication in this journal is cited, in accordance with accepted academic practice. No use, distribution or reproduction is permitted which does not comply with these terms.

Editorial: Innovative approaches for wound treatment

Junxiao Zhang[1†], Shenglin Geng[1†], Guojuan Fan[2*] and Jinlong Ma[1,3*]

[1]School of Pharmacy, Shandong Second Medical University, Weifang, Shandong, China, [2]Dermatology, Weifang Hospital of Traditional Chinese Medicine, Shandong Second Medical University, Weifang, Shandong, China, [3]Shandong Engineering Research Center for Smart Materials and Regenerative Medicine, Shandong Second Medical University, Weifang, Shandong, China

KEYWORDS

wound healing, wound management, foundational research, therapeutic design, antibacterial strategy

Editorial on the Research Topic
Innovative approaches for wound treatment

Wound healing constitutes a sophisticated biological cascade involving inflammation resolution, tissue regeneration, and extracellular matrix remodeling. Yet it remains a pressing clinical challenge—particularly in refractory cases such as diabetic ulcers, severe burns, and drug-resistant infected wounds (Wang et al., 2023a; Wang et al., 2023b). Against the backdrop of a growing global burden of diabetes, age-related wounds, and traumatic injuries, the development of innovative and translatable wound management strategies has never been more urgent (Wang et al., 2024). This Research Topic brings together 12 selected contributions—comprising 9 original research articles, 2 comprehensive reviews, and 1 thought-provoking opinion piece—each tackling critical unresolved Research Topic in wound care through cutting-edge advances in biomaterial engineering, bioactive compound development, and mechanism-driven therapeutic design.

Two review articles provide foundational frameworks for key research domains in this Research Topic. The first addresses the emerging threat of antibiotic-resistant Cutibacterium acnes by systematically evaluating phytochemicals as promising therapeutic alternatives. It highlights compounds such as resveratrol—a polyphenolic antioxidant derived from plants like Smilax, peanuts, and berries—and punicalagin, detailing antibacterial mechanisms including membrane disruption, lipase inhibition, and redox homeostasis regulation, which collectively offer effective antimicrobial action with reduced adverse effects (Sun et al.). The second review underscores the unique biological properties of silk proteins, sericin and fibroin, which exhibit high biocompatibility, low immunogenicity, and significant immunomodulatory capacities—such as promoting macrophage M2 polarization and modulating cytokine release—thereby supporting their broad applicability in advanced wound dressings and tissue regeneration (Tian et al.).

Complementing these reviews, an opinion piece highlights the broad biomedical potential of cold atmospheric pressure plasma in areas such as sterilization, wound care, and even cancer therapy, attributing its bioactivity to a rich mixture of reactive species, charged particles, and ultraviolet radiation (Li et al.). However, the article also notes a critical limitation in burn wound treatment: the desiccating effect of high gas flow rates

and the emission of harmful UV radiation contradict the established principles of moist wound healing, thereby restricting its therapeutic utility.

The Research Topic further presents nine original research articles that introduce innovative, mechanism-driven solutions for wound repair. In the realm of biomaterial engineering, one study reports a novel double-cross-linked PDGA hydrogel (comprising polyacrylamide, dopamine-grafted sodium alginate, glycidyl methacrylate-grafted gelatin, and Angelica sinensis polysaccharide), which rapidly forms *in situ*, acts as a protective barrier, and accelerates healing through rapid hemostasis, enhanced cell proliferation, collagen deposition, and angiogenesis (Liu et al.). Another study combines biomaterials with stem cell-derived exosomes by constructing rIGF1-enriched exosomes delivered via a silk fibroin–collagen hydrogel, effectively promoting annulus fibrosus wound repair and attenuating intervertebral disc degeneration in rats by stimulating cell proliferation and migration (Tian et al.).

To address bacterial infection-related impairments, a multifunctional nanoplatform (P(H)ZPAg) was developed by embedding palladium hydride into a ZIF-8 framework, modifying its surface with polydopamine, and generating silver nanoparticles *in situ*. This system enables synergistic antibacterial action through controlled hydrogen release, photothermal conversion, and Ag^+ activity, collectively accelerating wound healing in infected models (Wang et al.). Separately, a traditional herbal formula (BaDuShengJi San) was reformulated into a stable carbomer-based hydrogel, which significantly enhanced its antibacterial efficacy (MIC 64 μg/mL), accelerated diabetic wound re-epithelialization by 40%, and reduced its inherent renal toxicity (Zhang et al.).

Beyond biomaterial innovations, several studies focus on bioactive compounds and peptides. Nervonic acid, a key component of myelin and nerve cell membranes, was shown to uniquely synchronize neurogenesis and angiogenesis, enabling holistic repair of both neural and vascular tissues (Liu et al.). Thymoquinone, a natural quinone, enhanced skin flap survival by 44% through dual regulation of SIRT1/NF-κB-mediated pyroptosis and pro-angiogenic activity, providing a synergistic countermeasure to ischemia-reperfusion injury (Yang et al.). The human antimicrobial peptide LL37, the sole cathelicidin-derived peptide in humans, not only exerts broad-spectrum microbicidal and immunomodulatory effects but also acts as a potent angiogenic agent by activating the VEGFA-PI3K/AKT/mTOR pathway, suggesting new translational avenues from antimicrobial to ischemic wound therapy (Yang et al.). Another investigation revealed that narirutin, a citrus-derived flavonoid, accelerates diabetic wound healing by reprogramming macrophage metabolism via the AMPK/Mfn2 axis, shifting energy metabolism from glycolysis to oxidative phosphorylation, promoting M1-to-M2 polarization, and resulting in a 58% improvement in wound closure (Liu et al.).

In preclinical therapeutic development, the combination of sodium houttuyfonate with penicillin G demonstrated strong synergy against MRSA-infected wounds, reducing bacterial load by 91% and lowering key inflammatory cytokines (IL-6, TNF-α) by 50% in rat models, offering a viable alternative for combating drug-resistant infections (Li et al.).

Collectively, this Research Topic offers a holistic perspective on current advances in wound management. The two review articles establish essential background, the opinion piece provides a critical outlook on antibacterial technology, and the nine original research papers deliver actionable, mechanism-based solutions. We extend our gratitude to all contributing authors for their rigorous work and to the editorial team for their dedicated efforts. It is our hope that this Research Topic will foster cross-disciplinary collaboration, accelerate the translation of novel strategies into clinical practice, and, ultimately, improve outcomes for patients suffering from refractory wounds.

Author contributions

JZ: Writing – original draft. SG: Writing – original draft. GF: Writing – review and editing. JM: Writing – review and editing.

Funding

The authors declare that financial support was received for the research and/or publication of this article. This work was supported by the National Natural Science Foundation of China (Grant No. 82302840), the Shandong Provincial Natural Science Foundation (Grant Nos. ZR2023QH038 and ZR2023MH037), Shandong Provincial Traditional Chinese Medicine Science and Technology Project (Grant Nos. Q-2023047 and M-2023084).

Conflict of interest

The authors declare that the research was conducted in the absence of any commercial or financial relationships that could be construed as a potential conflict of interest.

Generative AI statement

The authors declare that Generative AI was used in the creation of this manuscript. The author(s) verify and take full responsibility for the use of generative AI in the preparation of this manuscript.

Any alternative text (alt text) provided alongside figures in this article has been generated by Frontiers with the support of artificial intelligence and reasonable efforts have been made to ensure accuracy, including review by the authors wherever possible. If you identify any issues, please contact us.

Publisher's note

All claims expressed in this article are solely those of the authors and do not necessarily represent those of their affiliated organizations, or those of the publisher, the editors and the reviewers. Any product that may be evaluated in this article, or claim that may be made by its manufacturer, is not guaranteed or endorsed by the publisher.

References

Wang, X., Yang, H., Fan, G., Sun, A., Qin, J., Zhao, J., et al. (2023a). A ROS balance system with medication and photothermal therapy ability for burn treatment. *J. Sci. Adv. Mater. Devices* 8 (2), 100534. doi:10.1016/j.jsamd.2023.100534

Wang, X., Liu, Z., Zhao, L., Yang, H., Qin, J., Zhang, J., et al. (2023b). Synergetic burns treatment by self-adaption release system combined with cold atmospheric plasma. *Sci. China Technol. Sci.* 66, 2808–2823. doi:10.1007/s11431-022-2258-x

Wang, L., Fan, G., Zhu, L., Zhang, Y., Wang, X., Qin, J., et al. (2024). A lipoic acid supramolecular polymer-based hydrogel with self-regulating ROS, reduced blood sugar, and antibacterial ability for improved diabetic wound healing. *J. Sci. Adv. Mater. Devices* 9 (2), 100677. doi:10.1016/j.jsamd.2024.100677

frontiers | Frontiers in Pharmacology

TYPE Original Research
PUBLISHED 22 October 2024
DOI 10.3389/fphar.2024.1487183

Check for updates

OPEN ACCESS

EDITED BY
Chong Li,
Southwest University, China

REVIEWED BY
Jianhui Liu,
Chongqing University of Technology, China
Christian Kweku Adokoh,
University of Cape Coast, Ghana

*CORRESPONDENCE
Li-Hua Peng,
lhpeng@zju.edu.cn

RECEIVED 27 August 2024
ACCEPTED 10 October 2024
PUBLISHED 22 October 2024

CITATION
Liu Y-D, Peng X, Chen H-R, Liu X-S and Peng L-H (2024) Nervonic acid as novel therapeutics initiates both neurogenesis and angiogenesis for comprehensive wound repair and healing.
Front. Pharmacol. 15:1487183.
doi: 10.3389/fphar.2024.1487183

COPYRIGHT
© 2024 Liu, Peng, Chen, Liu and Peng. This is an open-access article distributed under the terms of the Creative Commons Attribution License (CC BY). The use, distribution or reproduction in other forums is permitted, provided the original author(s) and the copyright owner(s) are credited and that the original publication in this journal is cited, in accordance with accepted academic practice. No use, distribution or reproduction is permitted which does not comply with these terms.

Nervonic acid as novel therapeutics initiates both neurogenesis and angiogenesis for comprehensive wound repair and healing

Yu-Da Liu[1], Xiao Peng[2], Hao-Ran Chen[1], Xue-Song Liu[1,2] and Li-Hua Peng[1,2]*

[1]College of Pharmaceutical Sciences, Zhejiang University, Hangzhou, China, [2]Jinhua Institute, Zhejiang University, Jinhua, Zhejiang, China

Rapid tissue reconstruction in acute and chronic injuries are challengeable, the inefficient repair mainly due to the difficulty in simultaneous promoting the regeneration of peripheral nerves and vascular, which are closely related. Main clinical medication strategy of tissue repair depends on different cytokines to achieve nerves, blood vessels or granulation tissue regeneration, respectively. However, their effect is still limited to single aspect with biorisk exists upon long-time use. Herein, for the first time, we have demonstrated that NA isolated from *Malania oleifera* has potential to simultaneously promote both neurogenesis and angiogenesis *in vitro* and *in vivo*. First, NA was identified by NMR and FTIR structural characterization analysis. In a model of oxidative stress in neural cells induced by hydrogen peroxide, the cells viability of RSC96 and PC12 were protected from oxidative stress injury by NA. Similarly, based on the rat wound healing model, effective blood vessel formation and wound healing can be observed in tissue staining under NA treatment. In addition, according to the identification of nerve and vascular related markers in the wound tissue, the mechanism of NA promoting nerve regeneration lies in the upregulation of the secretion NGF, NF-200 and S100 protein, and NA treatment was also able to up-regulate VEGF and CD31 to directly promote angiogenesis during wound healing. This study provides an important candidate drug molecules for acute or chronic wound healing and nerve vascular synchronous regeneration.

KEYWORDS

nervonic acid, natural product, neural regeneration, angiogenesis, wound repair

1 Introduction

The therapy process of wound includes continuous and complex phases and suffering from a variety of adverse factors, particularly chronic wound such as non-healing diabetic ulcer present one of the most difficult therapeutic challenges in the clinical practice, which is due to excessive oxidative stress, multiple infections, poor neuropathy, and angiopathy (Brazil et al., 2019). Emerging evidence suggests that therapeutic strategies for the promotion of neurogenesis in wound can beneficially accelerate wound healing. However, neurogenesis is not an independent event, and it is tightly mediated by both complicated molecular mechanisms from surrounding neural and non-neural cells. The

cellular crosstalk between neural cells and vascular endothelial cells (ECs) plays a key role in neurogenesis (Marrella et al., 2018; Gilbert-Honick and Grayson, 2020). ECs can promote neurogenesis by supporting the high metabolic demands of neural cells, and the bioactive molecules released by the neuroepithelium can also drive the growth and maturation of blood vessels (Marenzana and Arnett, 2013; Chen et al., 2015; Das et al., 2020; Guo et al., 2020; Mi et al., 2021). Both neural cells and ECs constitute a "neurovascular niche" that enhances cell function and accelerates wound healing. Previous studies have confirmed that insufficient vascularization and innervation can lead to delayed tissue regeneration (Fan et al., 2023). Therefore, therapeutics with efficacy in both promoting nerve and angiogenesis might be an important and new key to the rapid tissues and organs regeneration.

However, current tissue regeneration drugs are insufficient in promoting the combination of neurovascular networks to induce vascularization and innervation. In addition to debridement and maintaining a wound environment conducive to healing, various strategies including growth factor and gene delivery as well as cell therapy have been used to enhance the healing of non-healing wounds (Kim et al., 2019). Tissue repair drugs such as vascular endothelial growth factor (VEGF) or nerve growth factor (NGF) delivery approaches in regenerative medicine have a short half-life in the body (Levy et al., 1998), because they are rapidly degraded by proteases and subsequently inactive (Huang et al., 2007), they are quickly eliminated when used alone, and high concentrations can have significant side effects on the human body (Tayalia and Mooney, 2009; Simón-Yarza et al., 2012). As a result, few drugs can specifically promote nerve regeneration and angiogenesis and have significant therapeutic effects on both.

Nervonic acid (NA) has been found to be clinically critical in nerve development and regeneration. It is the fundamental component of the white matter, myelin and cell membranes of nerve fibers, supplementing the glial cell differentiation and myelin regeneration. By combining with sphingoside to form sphingolipid, NA plays the indispensable roles in maintaining the development of nerve cells (Amminger et al., 2012; Kageyama et al., 2018; Lewkowicz et al., 2019; Song et al., 2022) and promoting the repair and regeneration of nerve fibers in damaged tissues (Dhobale et al., 2011; Li et al., 2019). Increasing researches have shown that NA are associated with many neurological diseases such as demyelinating diseases, multiple sclerosis (Lewkowicz et al., 2019; Terluk et al., 2022), Alzheimer's disease (Astarita et al., 2011), Parkinson's disease (Amminger et al., 2012; Vozella et al., 2017), cognition (Song et al., 2022), mood symptoms (Kageyama et al., 2018; Kageyama et al., 2021), cardiovascular death (Delgado et al., 2017) and even obesity (Keppley et al., 2020). Various nerve damages cause the NA biosynthesis defects that further induce myelin synthesis disorders, thus leading to abnormal nerve regeneration and impaired axon signal transduction (Love, 2006; Alizadeh et al., 2015; Phung et al., 2023). Accordingly, the administration of external NA has the potential in accelerating the nerve repair and regeneration in wound by promoting the repair of myelin and axons (Gerstl et al., 1972; Ledeen et al., 1973; Nave, 2010; Plemel et al., 2017; Kremer et al., 2019). Although the regeneration of blood vessels is closely related to the recovery of nerve function, direct evidence on the effect of neurotropic drugs such as neuronic acid on angiogenesis is still insufficient. It is hypothesized that neuronic acid could first reconstruct the vascular network by repairing the nerve, and investigated its direct promotion effect on vascular regeneration, confirming its prospect of realizing the promotion of wound repair and healing.

Currently, NA can be purified from plant, while its therapeutic efficacy and application prospect are urgent to be identified. However, the scientific evidence for their effectiveness in wound repair, the peripheral nerve repair and angiogenesis is still very limited.

Herein, we have demonstrated for the first time that NA from *Malania oleifera* has potential to simultaneous promote both neurogenesis and angiogenesis *in vitro* and *in vivo* (Figure 1), and location of its physiological mechanism has been investigated. It is expected to provide the scientific evidence for the therapeutic use of NA, as well as identify new effective drug candidate for initiating both nerve and blood vessels regeneration for the complete repair of injured tissues or organs.

2 Materials and methods

2.1 Materials

NA (cis-15-Tetracosenoic acid, purity ≥ 99%, CAS No: 506-37-6) was obtained from Yunnan Beimu Biotechnology Co., LTD. Major extraction method: the *M. oleifera* kernels are dried, crushed and sieved before being put into a Soxhlet extractor. Then the petroleum ether was added and extracted in a 75°C constant temperature water bath for 7 h. After filtration, the filtrate was distilled. The obtained garlic kernel oil was saponified for 8 h in cold storage, and the pH was adjusted to 2 to obtain the mixed crude solution of neural acid. The concentrated crude neurotic acid was added to absolute ethanol, heated and stirred to fully dissolve, and the purified neurotic acid was obtained by fast dry column chromatography.

Normal saline (0.9%, sterile, CAS No: 7647-14-5) and dimethyl sulfoxide (DMSO, purity ≥ 99.9%, CAS No: 67-68-5) were acquired from Beijing Solarbio Technology Co., Ltd. (Beijing, China). Dulbecco's modified Eagle's medium (DMEM), fetal bovine serum (FBS), penicillin, streptomycin, and trypsin were obtained from Gibco BRL (Gaithersburg, MD). H&E staining and Masson's trichrome staining kit were purchased from Wuhan BiochiDu Biotechnology Co., Ltd. NGF anti-mouse antibody and buffered paraformaldehyde were purchased from Sigma, Inc. (MO, United States). NF-200 (18934-1-AP) and S100 (15146-1-AP) anti-mouse antibody and buffered paraformaldehyde were purchased from Proteintech Group, Inc. (Wuhan, China). CD31 (ab182981) anti-mouse antibody and buffered paraformaldehyde were purchased from Abcam, Inc. (Wuhan, China). VEGF (BA0407) and TGF-β (BA0290) anti-mouse antibody and buffered paraformaldehyde were purchased from Boster, Inc. (Wuhan, China). Horseradish peroxidase (HRP)-labeled (5220-0364) goat anti-mouse antibody and buffered paraformaldehyde were purchased from SeraCare, Inc. (Beijing, China). Hydrogen peroxide solution (500 mL, 3%) was purchased from Sinopharm Chemical Reagent Co., Ltd. and stored at room temperature. All other reagents were of analytical grade.

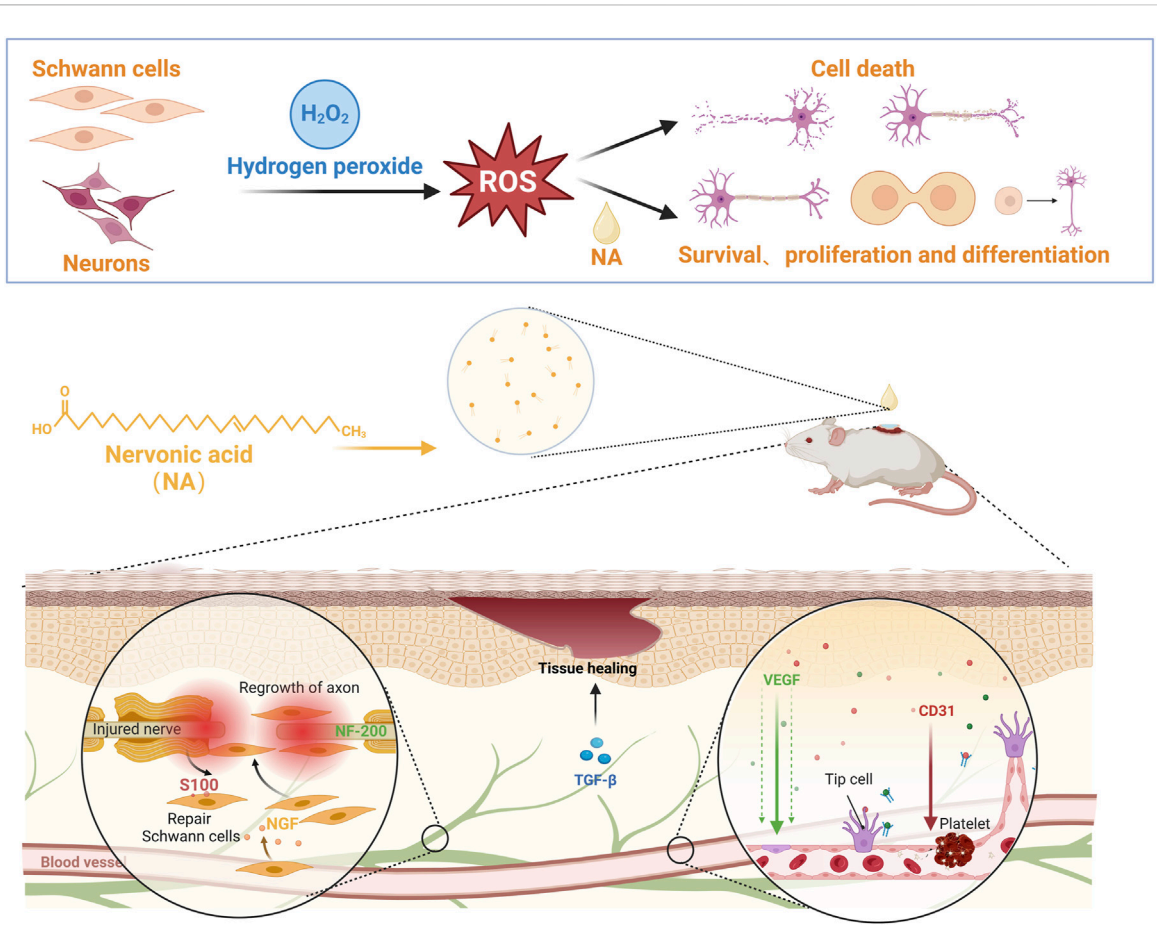


FIGURE 1
NA accelerate the repair of nerve injury by promoting schwann cells proliferation and nerve growth factor secretion, and stimulate new blood vessels formation by up-regulating the angiogenesis related growth factors levels.

2.2 Methods

2.2.1 Cell culture

Human neuroblastoma cells PC12 (as a neuronal model, were obtained from the Cell Resource Center of Shanghai Institute of Biological Science, Chinese Academy of Science) and rat Schwann cells RSC96 (as a Schwann cell model, were obtained from the Cell Resource Center of Shanghai Institute of Biological Science, Chinese Academy of Science) were cultured in Dulbecco's modified Eagle's medium (DMEM). Both cell culture media were supplemented with 10% fetal bovine serum (FBS). Cells were maintained in the cell standard incubator at 37°C in a humidified atmosphere of 5% CO_2.

2.2.2 Cell viability and proliferation tests

Cell viability was evaluated by using cell counting kit-8 (CCK-8) (AR1160-500, Boster, Wuhan, China) according to the manufacturer's instructions. About 5,000 cells of PC12 and RSC96 cells were seeded in a 96-well plate per cell and cultured for 24 h. NA of different concentrations (0, 25, 50, 75, 100, 125, 150, 175, 200 μM) were added into each well in pentaplicate. 12 μM and 15 μM of H_2O_2 or NA of different concentrations (0, 10, 20, 40, 60, 80, 100, 125, 150, 175, 200 μM) were added into each well in pentaplicate. After incubation for 24 h, the cells were washed by PBS (pH = 7.4) and the culture medium was replaced with 100 μL fresh medium containing 10 μL CCK-8 solution, and incubated at 37°C for 1 h. Finally, the OD value was measured at 450 nm by a microplate reader (Multiskan FC, Thermo Fisher instruments Co., Ltd., United States) and the relative cell viability was presented as percentage of control.

2.2.3 Skin nerve injury in animal model

All animal-related procedures were reviewed and approved by the Animal Advisory Committee at Zhejiang University (ZJU20170733). Sprague–Dawley rats (8 weeks old) were supplied by Zhejiang University Experimental Animal Center, China. 6 rats were included in each investigational group, prior to wound modeling, each rat was assigned a unique identifier, and the hairs on the back of the rats were shaved and removed. The rats were anesthetized by intraperitoneal injection of 30 mg/kg pentobarbital sodium and the dorsal back skin was sterilized by topical application of 10% w/w povidone-iodine solution, followed by washing three times with sterile water. Skin excisions (20 mm × 20 mm) were made by excising the skin within the confines of the square down to the level of subcutaneous panniculus carnosus. Following surgery, rats were monitored during recovery daily to record wound closure. In the experiment, the rat wounds were treated by: 1) 0.2 mL PBS in 10% DMSO, 2) 0.2 mL NA suspension at a concentration of 5 mg/mL in 10% DMSO, 3) 0.2 mL NA

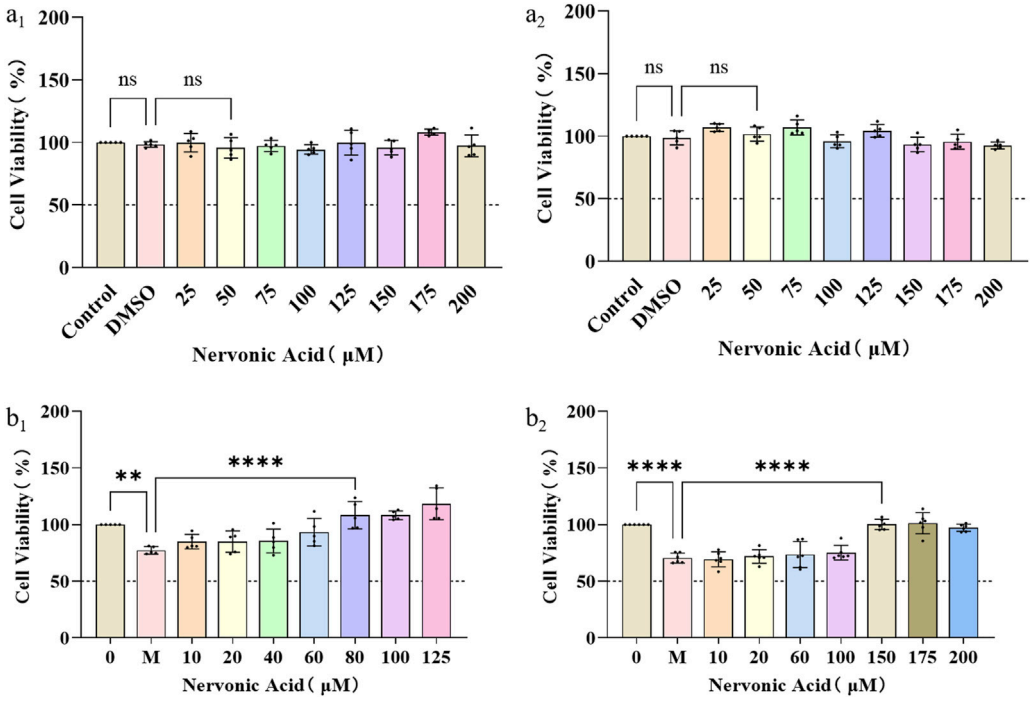


FIGURE 2
The protection and anti-oxidative stress effects of NA in PC12 and RSC96. **(A_1,A_2)** The influence of NA on the cell viability of PC12 (a_1) and RSC96 (a_2). **(B_1,B_2)** The influence of NA on oxidative stress of PC12 (b_1) and RSC96 (b_2) damage caused by hydrogen peroxide. Statistical significance is indicated as $^{ns}p > 0.05$, $^{**}p < 0.01$, $^{***}p < 0.001$, $^{****}p < 0.0001$ versus the DMSO group and the hydrogen peroxide group (M).

suspension at a concentration of 25 mg/mL in 10% DMSO. The rats were given the drug every other day for 18 days and their weight changes were continuously recorded.

2.2.4 Immunofluorescence staining

Paraffin sections (5 μm) were deparaffinized in xylol and then rehydrated in a graded alcohol series. Endogenous peroxidase was inhibited using 3% H_2O_2 in methanol for 10 min. The sections were washed with distilled water and then soaked in 0.01 M citrate buffer for epitope retrieval. The sections were washed three times with PBS and incubated with 5% bovine serum albumin at room temperature for 20 min. The samples were subsequently incubated with FITC-conjugated secondary antibodies for 2 h, followed by incubation with DAPI solution (3 μg/mL) for nucleic staining. For immunofluorescence staining, primary antibodies against S100 (1: 200, PROTEINTECH GROUP, 15146-1-AP), NF-200 (1:200, PROTEINTECH GROUP, 18934-1-AP), NGF (1:500, Sigma, MO, United States), CD31 (1:1,000, Abcam, ab182981), VEGF (1: 200, Boster, BA0407) and TGF-β (1:200, Boster, BA0290), and HRP-labeled anti-rabbit secondary antibodies (1:200, SeraCare, 5220-0364) were used. The cells were observed and photographed under a fluorescence microscope (Olympus BX61) by using Olympus Soft Imaging Solution software (analysis Caseviewer-3DHISTECH Ltd.).

2.2.5 H&E staining

After dewaxing, sections were washed, followed by the addition of hematoxylin (Wuhan BiochiDu Biotechnology Co., Ltd.) for staining for 5 min, hydrochloric acid aqueous solution for 2 s and ammonia aqueous differentiation solution (Wuhan BiochiDu Biotechnology Co., Ltd., B1004) for 15–30 s, and then washed. The slices were dehydrated with 95% alcohol and then stained with eosin solution (Wuhan BiochiDu Biotechnology Co., Ltd.) for 5–8 s. After dehydration and sealing, the slices were observed under microscope.

2.2.6 Masson's trichrome staining

The reconstituted skin samples, which include full-thickness skin layers, were fixed in 4% paraformaldehyde and processed according to standard procedures for routine light microscopy. The processed tissues were embedded in paraffin. Then, 5 μm sections were stained with Masson's trichrome stain according to the protocol and were examined and photographed by the Leica image analysis system (Leica, Germany).

2.2.7 Wound healing rate

The wound area was measured on days 0,3, 7, 11, 15 and 19 after the trauma by tracing the wound margin and was calculated using an image analysis program (ImageJ, NIH, MD, United States). The date of complete wound closure was recorded and the wound healing time (WHT) was calculated accordingly.

2.2.8 Structural characterization of NA

The solvent used for NMR analysis is DMSO-d_6 ((CD3)2S = O). A range of 20–25 mg of the sample was dissolved in this solvent and analyzed on a Bruker 600 MHz NMR spectrometer using five different modes: ^{1}H experiment, ^{13}C experiment with decoupling, ^{1}H-^{1}H COSY ex-periment, ^{1}H-^{13}C multiplicity edited HSQC with gradient selection BF1 ≤600 MHz, and ^{1}H-^{13}C HMBC with gradient

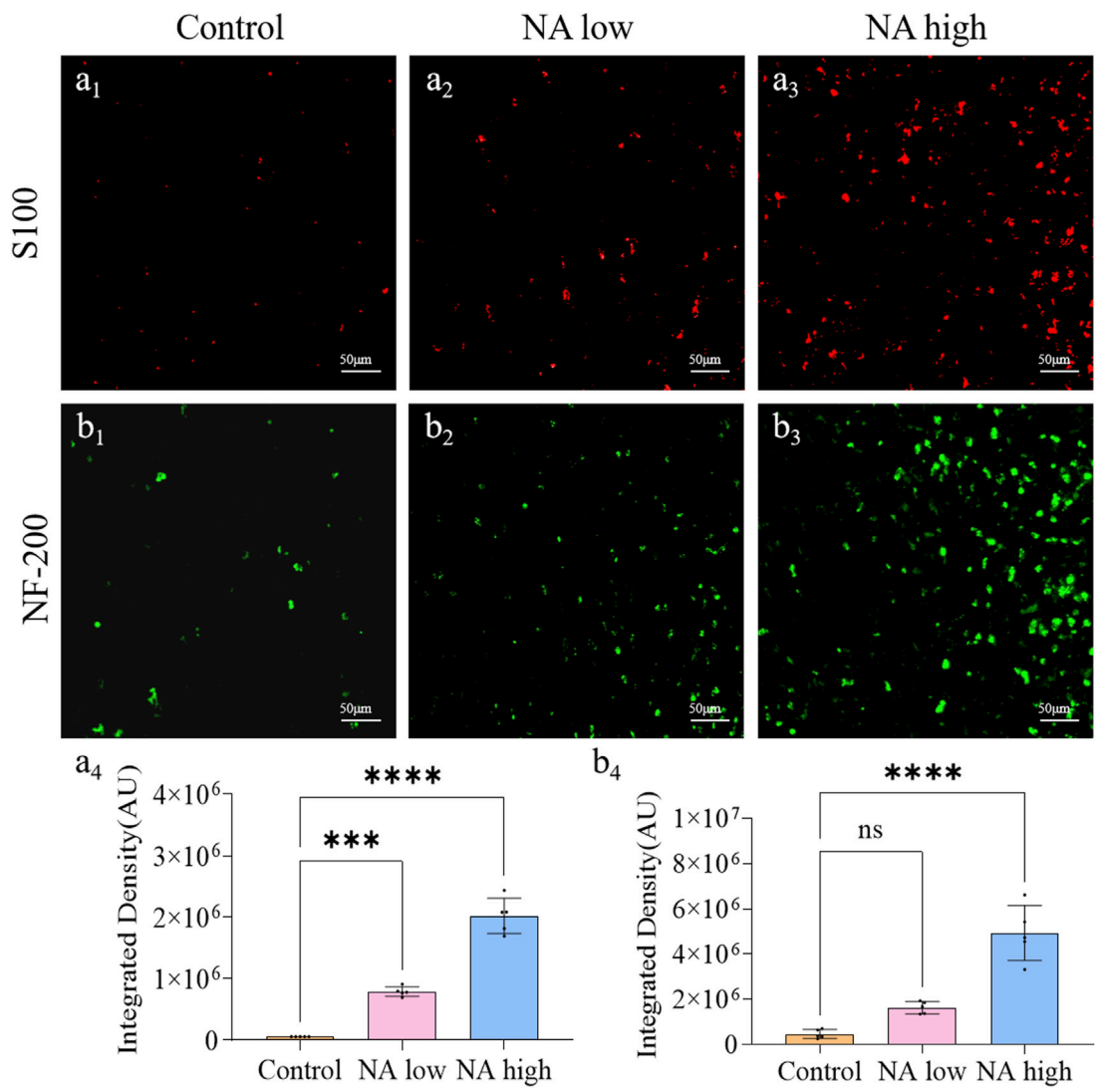


FIGURE 3
The promotion of NA for the expression of NF-200/S100 *in vivo*. **(A_1–A_3)** Immunofluorescence staining indicating the S100 expression in the healed skins on 11 days post-treatment. **(A_4)** The semi-quantification of S100 *in vivo* on day 11. **(B_1–B_3)** Immunofluorescence staining indicating the NF-200 expression in the healed skins on 11 days post-treatment. **(B_4)** The semi-quantification of NF-200 *in vivo* on day 11. Statistical significance is indicated as $^{ns}p > 0.05$, $^{***}p < 0.001$, $^{****}p < 0.0001$ versus the Control group.

selection, and these five modes were scanned and tested. A Nicolet infrared spectrometer (iS 50 FTIR; Nicolet, Glendale, WI, United States) was used to acquire FTIR spectra of NA. A droplet of oil sample was applied onto the Platinum ATR at a temperature of 25°C. Wavenumber ranged from 4,000 to 400 cm^{-1} for 16 scans.

2.2.9 Statistical analysis

Statistical analyses were performed with GraphPad Prism 10.1 (GraphPad Software Inc., CA). All data were reported as the mean ± SEM. Student's t test was used to compare two groups. Two-way analysis of variance (ANOVA) with Tukey's multiple comparisons test was performed for multiple comparisons. Value $p < 0.05$ was considered as differences. $^{*}p < 0.05$, $^{**}p < 0.01$, $^{***}p < 0.001$, $^{****}p < 0.0001$. ImageJ software was used for quantification of images.

3 Results

3.1 The structural characterization of NA from *Malania oleifera*

To identify the NA which were isolated and purified from the *M. oleifera*, ^{1}H and ^{13}C NMR analysis was first performed. ^{1}H-NMR of the NA sample (Supplementary Figure S1) reveals a peak at 11.92 ppm, which corresponds to the carboxyl protons of various fatty acid compounds. The peaks at 5.26 ppm are attributed to the NA. In the spectrum, the signal at 3.42 ppm is from solvent water, while the peak at 2.51 ppm corresponds to protons in the solvent DMSO. The high field range of 0.81–2.13 ppm displays several peaks associated with different saturated alkyl C-H protons of fatty acids. Specifically, the relatively high field signals at 2.13 and 1.94 ppm are attributed to alkyl protons near the carboxyl group, while the

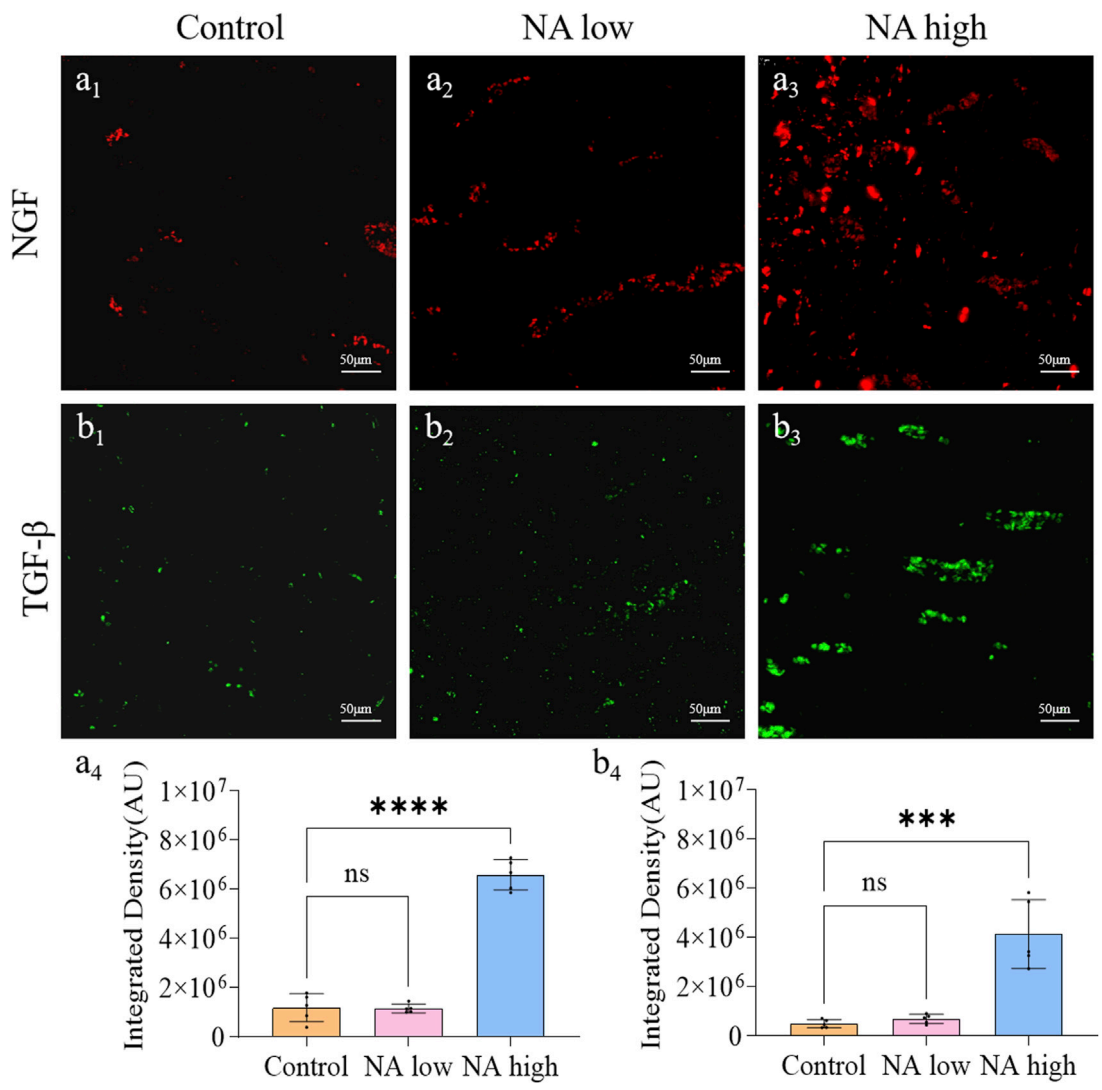


FIGURE 4
The promotion of NA for the expression of NGF and TGF-β *in vivo*. **(A_1–A_3)** Immunofluorescence staining indicating the NGF expression in the healed skins on 11 days post-treatment. **(A_4)** The semi-quantification of NGF *in vivo* on day 11. **(B_1–B_3)** Immunofluorescence staining indicating the TGF-β expression in the healed skins on 11 days post-treatment. **(B_4)** The semi-quantification of TGF-β *in vivo* on day 11. Statistical significance is indicated as $^{ns}p > 0.05$, $^{***}p < 0.001$, $^{****}p < 0.0001$ versus the Control group.

-CH_3 proton signal appears at 0.81 ppm. The majority of remaining alkyl protons are represented by a strong signal at 1.20 ppm ^{13}C-NMR of the NA compound (Supplementary Figure S2) reveals a peak at 174.72 ppm, attributed to the carboxyl carbons of NA. Multiple peaks near 129.77 ppm correspond to the olefin carbon signals of NA. The peak at 40.21 ppm represents the carbon signal from DMSO. In the high field range of 14–35 ppm, several peaks correspond to saturated alkyl carbon signals, reflecting the saturated carbons in different long-chain fatty acids. The signals at 34.10 and 31.87 ppm are attributed to alkyl carbons near the carboxyl and olefin groups, while the carbon signal for -CH_3 appears at 14.16 ppm. A significant number of alkyl carbons are concentrated in the 20–30 ppm range, consistent with the characteristic features of NA ^{13}C-NMR. Consequently, the NMR spectra provide reliable structural information confirming the presence of NA.

In addition, the FTIR analysis was performed to obtain structural evidence and information about functional groups and to determine if there was NA. The FTIR spectrum of the combined treatment samples in the region of 4,000-500 cm^{-1} are shown in Supplementary Figure S3. The peaks observed at 2,918 cm^{-1} correspond to functional group hydrogen bond stretching. Specifically, they are indicative of -OH stretching vibrations found in saturated carbon and the symmetric stretching vibrations of the aliphatic CH_2 groups present in NA. The carbonyl stretching vibration of the carboxylic acid in NA produces a distinct peak at 1,690 cm^{-1}. The peak observed at 1,473 cm^{-1} is associated with the -C=C- double bond in NA. The -OH of carboxylic acid has two relatively strong and wide bending vibration absorption peaks at 1,400 cm^{-1} and 936 cm^{-1}, which can be used as further evidence to determine the existence of carboxylic acid structure. The peak at 717 cm^{-1} was attributed to the vibration

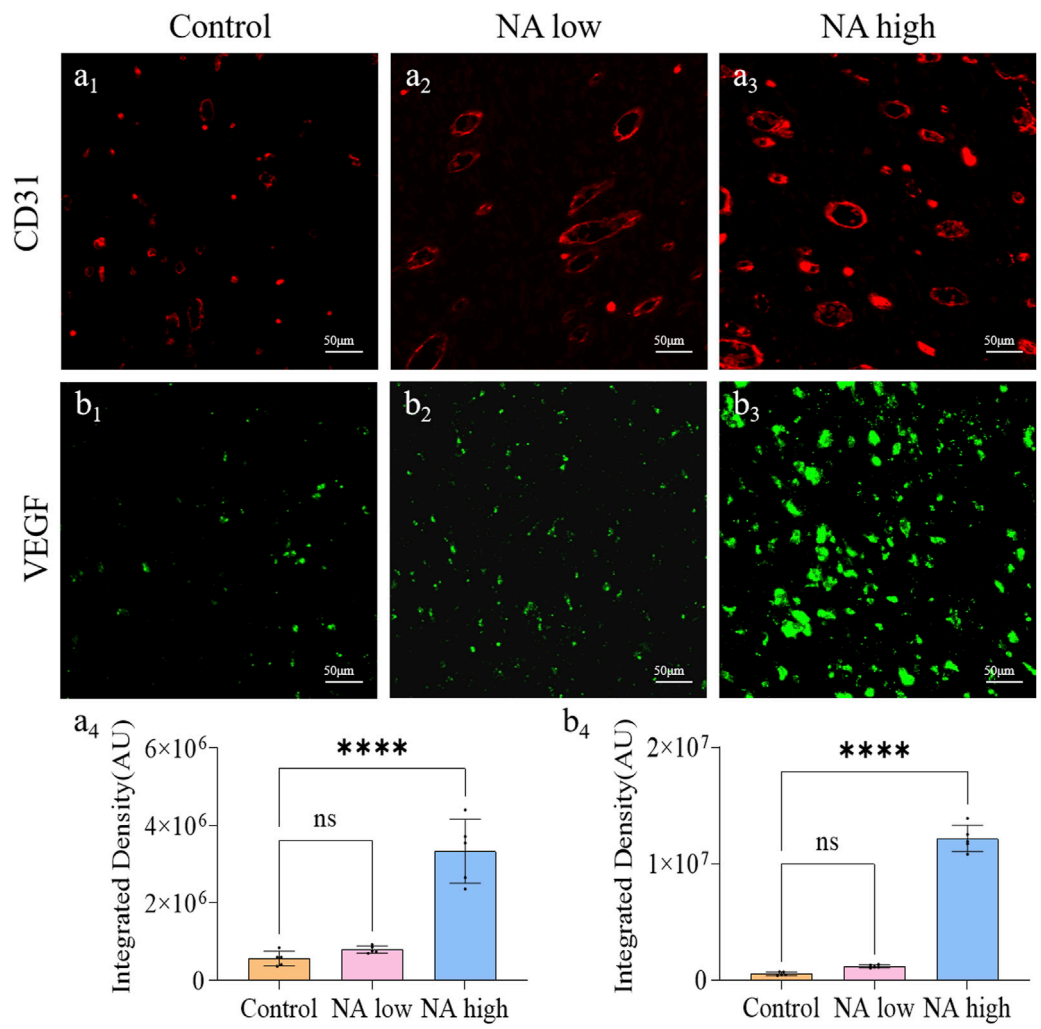


FIGURE 5
The promotion of NA for the expression of CD31 and VEGF *in vivo*. **(A_1–A_3)** Immunofluorescence staining indicating the CD31 expression in the healed skins on 11 days post-treatment. **(A_4)** The semi-quantification of CD31 *in vivo* on day 11. **(B_1–B_3)** Immunofluorescence staining indicating the VEGF expression in the healed skins on 11 days post-treatment. **(B_4)** The semi-quantification of VEGF *in vivo* on day 11. Statistical significance is indicated as $^{ns}p > 0.05$, $^{****}p < 0.0001$ versus the Control group.

of the disubstituted olefins cis-HC = CH, which overlapped with the vibration of CH_2. This structural information is similar to molecular data by FTIR, previously reported in other study (Gao et al., 2024). In-dept comparison of these signals indicated that the extracts match the chemical structures present of NA.

3.2 The promotion of NA on nerve regeneration

3.2.1 The protection and anti-oxidative stress effects of NA in nerve cells *in vitro*

SCs are glial cells that have been extensively investigated in the context of nerve repair and are recognized as the typical targets for nerve injury therapy. Maintaining the physiological function of neurons and SCs is particularly important in the process of wound nerve repair. The biocompatibility of NA on nerve cells at different concentrations was first investigated by measuring the cell viability of PC12 and RSC9 under normal culture conditions. It can be seen that NA was not cytotoxic to PC12 (Figure $2A_1$) and RSC96 (Figure $2A_2$) cells at concentrations of 0–200 μM.

Furthermore, in order to study the protective effect of NA on nerve cells and SCs under oxidative stress, the PC12 and RSC96 were treated with H_2O_2 at concentration of 0–35 μM for 24 h, respectively, to initially construct a H_2O_2-induced injury mode. According to the cell viability by CCK8 method, NA was found to show protective effects on PC12 under 80–125 μM H_2O_2 (Figure $2B_1$) and RSC96 at 150–200 μM H_2O_2 (Figure $2B_2$), which indicated that NA can avoid the damage of nerve cells from oxidative stress caused by hydrogen peroxide.

3.2.2 The activation and repair effect of NA on nerve cells *in vivo*

Neurofilament protein NF-200 is a cytoskeleton protein of nerve cells, which can completely display the morphology and distribution of the entire nerve cells, including the nucleosome, nerve dendrites

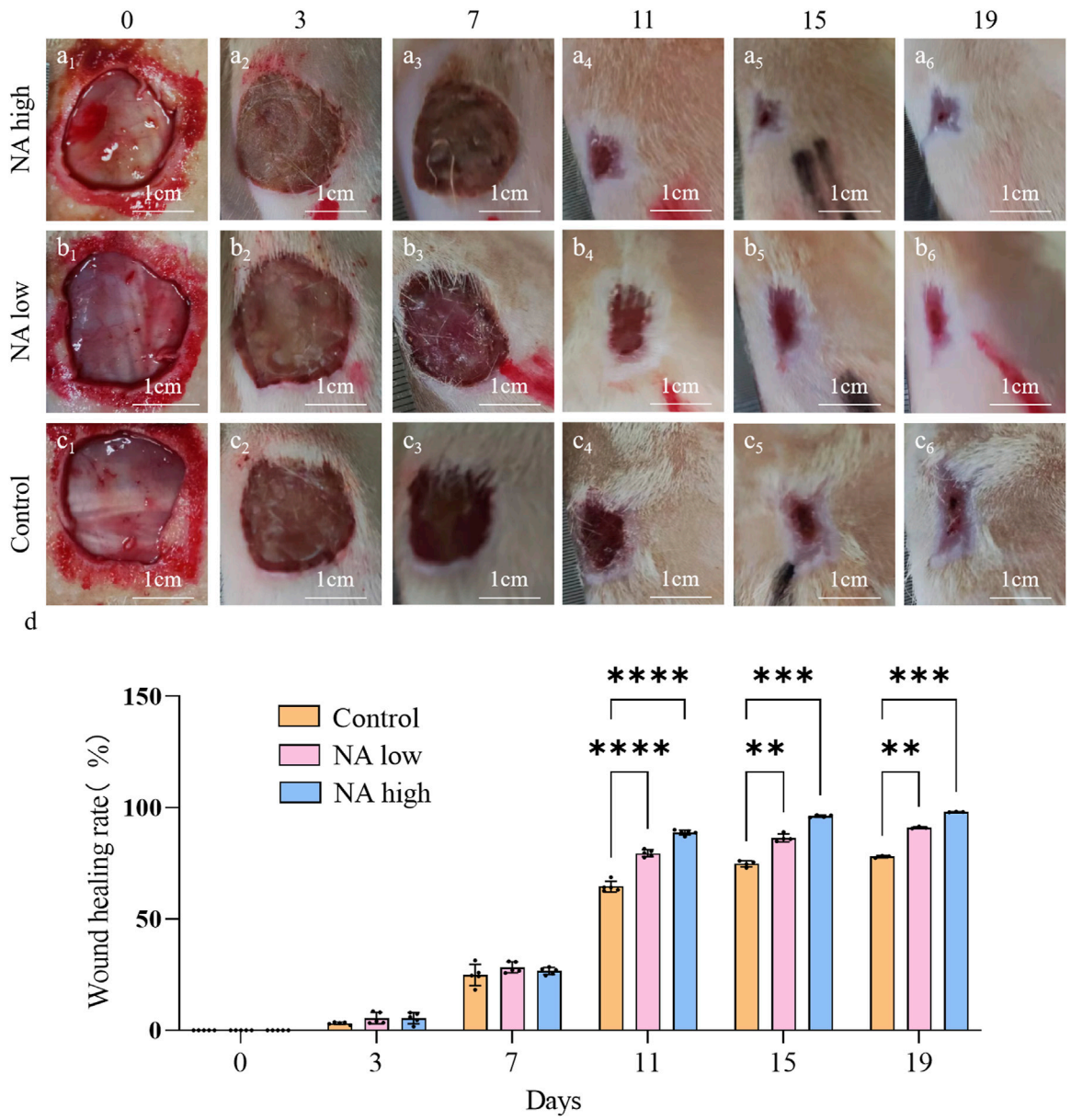


FIGURE 6
Wound closure under different treatment *in vivo*. **(A_1–A_6)** Representative images of skin wound healing of NA high on 0, 3, 7, 11, 15, 19 days. **(B_1–B_6)** NA low on 0, 3, 7, 11, 15, 19 days. **(C_1–C_6)** Control on 0, 3, 7, 11, 15, 19 days. **(D)** Wound healing rates at different time points of Control, NA low and NA high groups. Statistical significance is indicated as $^{**}p < 0.01$, $^{***}p < 0.001$, $^{****}p < 0.0001$ versus the Control group.

and axons of neurons. S100 is a specific protein of the nervous system that reflects the activity and damage of glial cells. Therefore, the expression level of NF-200 and S100 around the wound were characterized to show the degree of Schwann cell activation and the neuronal cell repair effect. On the 11th day, the integrated density of NF-200 (Figures $3B_1$–B_3) of the NA high group ($p < 0.001$) group (Figure $3B_4$) were significantly higher than the control group. Meanwhile, the integrated density of S100 (Figures $3A_1$–A_3) of both the NA low group ($p < 0.001$) and NA high group ($p < 0.0001$) group (Figure $3A_4$) were significantly higher than the control group. NA has the ability to promote the activation of SCs in the early stage of wound repair, and promote the repair process of neurons in a certain dose dependent manner.

3.2.3 The promotion of NA for the expression of NGF and TGF-β *in vivo*

The application of neurotrophic factors was considered to be an effective therapy for the wound peripheral nerve injuries, as they support the regeneration of axons and formation of new myelin sheaths. NGF is the prototype for the neurotrophin family of polypeptides, which are essential for the development and survival of certain sympathetic and sensory neurons in both the central and peripheral nervous systems. The TGF-β was shown to stimulate angiogenesis, fibroblast proliferation, myofibroblast differentiation, and matrix deposition. Experimentally, on the 11th day, the integrated density of NGF (Figure $4A_1$) and TGF-β (Figure $4B_1$) in control group maintained at a low level, which

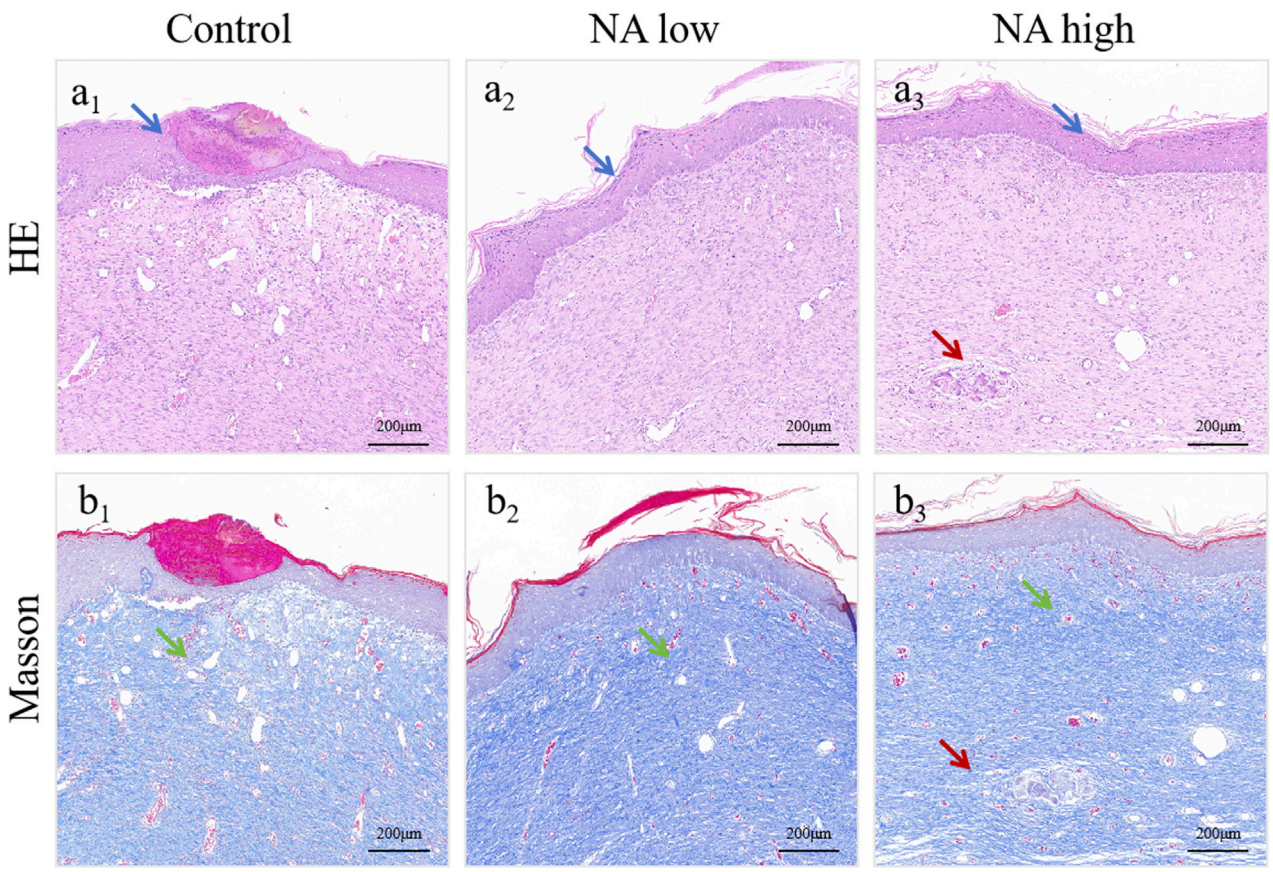


FIGURE 7
H&E **(A_1–A_3)** and Masson **(B_1–B_3)** staining of healed skin on day 19 post-treatment. The green arrows indicate the blood vessel, the blue arrows indicate the epidermis and the red arrows indicate the skin appendages.

indicate the natural expression of NGF was prevented by the wound. By contrast, both the integrated density of NGF (Figures 4A_3, A_4) and TGF-β (Figures 4B_3, B_4) in high NA group were significantly higher than the control group. Therefore, NA increased the expression of NGF and TGF-β in the early stage of wound, these results present evidence for the promotion of NA in the accelerated regeneration of neural cells.

3.3 The promotion of NA for the expression of CD31 and VEGF *in vivo*

The formation of new capillaries in the original blood vessel network is a key process of wound healing. CD31 is a marker of angiogenesis and can reflect the remodeling of neovascularization, and VEGF has the ability to induce the regeneration of existing blood vessels or the growth of new blood vessels. Therefore, the CD31 and VEGF expression were detected through immunohistochemical staining. As shown in Figure 5, the integrated density of CD31 in NA low group was up-regulated, and the level in NA high group was significantly higher than the NA low and control group (Figures 5A_1-A_4). Similarly, the integrated density of VEGF in both NA low group and high group were significantly higher than the control group (Figures 5B_1-B_4). There results indicate that NA also has the ability to increase the expression of CD31 and VEGF in wound healing, thereby promoting skin angiogenesis.

3.4 The promotion of NA on angiogenesis and tissue repair *in vivo*

No postoperative adverse effects, such as infection, pyogenesis, or body fluid effusion were observed in the animals during the experiment. The wound closure rates on days 0d, 3d, 7d, 11d, 15d and 19d were determined by the percentage of wound surface covered by healed skin and are shown (Figures 6A-D). Briefly, all wounds demonstrated gradual healing, but notably, both the NA low and high group obtained a significantly smaller wound area than the control group from day 11, which indicate that NA has the ability to accelerated the wound closure.

In addition, the wounds and surrounding skin of rats were collected at 11th and 19th days. The results of H&E staining (Figure 7A_1–A_3) and Masson staining (Figure 7B_1–B_3) for 19d indicated that the distribution of angiogenesis in the skin of rats in NA low group was significantly increased, and the level of angiogenesis was higher than that in the control group. At the same time, angiogenesis increased significantly with the increase of NA dose, and it was found that the NA high group had better cuticle repair than the other two groups.

4 Discussion

Acute and chronic wounds undergo multiple stages of healing, especially chronic and refractory wounds such as diabetic ulcers, which are often challenged by excessive oxidative stress, inflammation, and infection, leading to adverse neuropathy and vascular damage, delaying the efficiency of healing. The "neurovascular niche" is a novel theory to guide the treatment of acute and chronic wounds, and the cellular crosstalk between nerve cells and vascular endothelial cells may represent a complex physiological mechanism that needs further study to elucidate. In this study, based on individual nerve cell protection experiments, NA has been proven its unique effect in protecting nerve cells against oxidative stress and maintain nerve cell homeostasis, promoting SCs activation and nerve fiber repair, which is consistent with the reported functions of NA (Guo et al., 2022). The mechanism is closely related to growth factors such as NGF, TGF-β and they are really upregulated owing to the NA treatment. Correspondingly, the expression of neurofilament protein, a marker of nerve fibers, also increased significantly, and there was a high colocalization phenomenon with S100 expression (Qian et al., 2023), indicating that the presence of NA also increased the activity of SCs in the peripheral nervous system, which promotes myelin repair and axon regeneration at skin wounds. At the same time, in the rat wound healing model, angiogenesis was indeed promoted by NA which is regard as a neuro-promoting drug. Based on previous studies that mentioned in section "introduction," the bioactive molecules released by the neuroepithelium can also drive the growth and maturation of blood vessels, the secretions such as NGF following the reconstruction of nerve function are promising to help angiogenesis. The important role and mechanism of NA in promoting angiogenesis was shown for the first time. It is worth noting that both VEGF and CD31 were found to be significantly increased in parallel with neural-related markers in wounds, suggesting that NA has the potential to directly promote angiogenesis in acute and chronic wounds, and the angiogenesis is not caused by bioactive molecules after nerve reconstruction. Owing to the promotion of NA in constituting "neurovascular niche," NA also showed a significant promoting effect on the comprehensive wound repair. These results further prove and suggest the great potential of NA in initiating the complete repair of organs and tissues by promoting the regeneration of both blood vessels and nerves, and provides a promising new drug candidate for tissue/organ comprehensive repair and functional reconstruction.

Data availability statement

The original contributions presented in the study are included in the article/Supplementary Material, further inquiries can be directed to the corresponding author.

Ethics statement

The animal study was approved by Animal Advisory Committee at Zhejiang University. The study was conducted in accordance with the local legislation and institutional requirements.

Author contributions

Y-DL: Data curation, Formal Analysis, Visualization, Writing–original draft, Writing–review and editing. XP: Data curation, Formal Analysis, Methodology, Visualization, Writing–original draft. H-RC: Data curation, Writing–review and editing. X-SL: Supervision, Writing–review and editing. L-HP: Conceptualization, Funding acquisition, Project administration, Supervision, Visualization, Writing–review and editing.

Funding

The author(s) declare that financial support was received for the research, authorship, and/or publication of this article. The study was supported by the National Natural Science Foundation and National Key Research and Development Program of China (Grant no. 82374043, U23A20505, 2022YFC3501904), Zhejiang Province Commonweal Projects (Grant no. LGF22H280001).

Conflict of interest

The authors declare that the research was conducted in the absence of any commercial or financial relationships that could be construed as a potential conflict of interest.

Publisher's note

All claims expressed in this article are solely those of the authors and do not necessarily represent those of their affiliated organizations, or those of the publisher, the editors and the reviewers. Any product that may be evaluated in this article, or claim that may be made by its manufacturer, is not guaranteed or endorsed by the publisher.

Supplementary material

The Supplementary Material for this article can be found online at: https://www.frontiersin.org/articles/10.3389/fphar.2024.1487183/full#supplementary-material

References

Alizadeh, A., Dyck, S. M., and Karimi-Abdolrezaee, S. (2015). Myelin damage and repair in pathologic CNS: challenges and prospects. *Front. Mol. Neurosci.* 8, 35. doi:10.3389/fnmol.2015.00035

Amminger, G. P., Schäfer, M. R., Klier, C. M., Slavik, J. M., Holzer, I., Holub, M., et al. (2012). Decreased nervonic acid levels in erythrocyte membranes predict psychosis in help-seeking ultra-high-risk individuals. *Mol. Psychiatry* 17 (12), 1150–1152. doi:10.1038/mp.2011.167

Astarita, G., Jung, K.-M., Vasilevko, V., Dipatrizio, N. V., Martin, S. K., Cribbs, D. H., et al. (2011). Elevated stearoyl-CoA desaturase in brains of patients with Alzheimer's disease. *PloS One* 6 (10), e24777. doi:10.1371/journal.pone.0024777

Brazil, J. C., Quiros, M., Nusrat, A., and Parkos, C. A. (2019). Innate immune cell-epithelial crosstalk during wound repair. *J. Clin. Invest* 129 (8), 2983–2993. doi:10.1172/jci124618

Chen, W.-H., Mao, C.-Q., Zhuo, L.-L., and Ong, J. L. (2015). Beta-nerve growth factor promotes neurogenesis and angiogenesis during the repair of bone defects. *Neural Regen. Res.* 10 (7), 1159–1165. doi:10.4103/1673-5374.160114

Das, S., Gordián-Vélez, W. J., Ledebur, H. C., Mourkioti, F., Rompolas, P., Chen, H. I., et al. (2020). Innervation: the missing link for biofabricated tissues and organs. *NPJ Regen. Med.* 5, 11. doi:10.1038/s41536-020-0096-1

Delgado, G. E., Krämer, B. K., Lorkowski, S., März, W., von Schacky, C., and Kleber, M. E. (2017). Individual omega-9 monounsaturated fatty acids and mortality-the ludwigshafen risk and cardiovascular health study. *J. Clin. Lipidol.* 11 (1), 126–135. doi:10.1016/j.jacl.2016.10.015

Dhobale, M. V., Wadhwani, N., Mehendale, S. S., Pisal, H. R., and Joshi, S. R. (2011). Reduced levels of placental long chain polyunsaturated fatty acids in preterm deliveries. *Prostagl. Leukot. Essent. Fat. Acids* 85 (3–4), 149–153. doi:10.1016/j.plefa.2011.06.003

Fan, X., Wang, Y., Li, X., Zhong, T., Cheng, C., and Zhang, Y. (2023). Scutellarin alleviates liver injury in type 2 diabetic mellitus by suppressing hepatocyte apoptosis *in vitro* and *in vivo*. *Chin. Herb. Med.* 15 (4), 542–548. doi:10.1016/j.chmed.2023.03.007

Gao, H., Sun, J., Guo, X., Zhang, Z., Liu, H., Zhang, Z., et al. (2024). Study on the extraction of nervonic acid from the oil of xanthoceras sorbifolium bunge seeds. *Foods* 13 (17), 2757. doi:10.3390/foods13172757

Gerstl, B., Tavaststjerna, M. G., Eng, L. F., and Smith, J. K. (1972). Sphingolipids and their precursors in human brain (normal and MS). *Z Neurol.* 202 (2), 104–120. doi:10.1007/bf00316160

Gilbert-Honick, J., and Grayson, W. (2020). Vascularized and innervated skeletal muscle tissue engineering. *Adv. Healthc. Mater.* 9 (1), e1900626. doi:10.1002/adhm.201900626

Guo, J., Peng, J., Han, J., Wang, K., Si, R., Shan, H., et al. (2022). Extracts of Portulaca oleracea promote wound healing by enhancing angiology regeneration and inhibiting iron accumulation in mice. *Chin. Herb. Med.* 14 (2), 263–272. doi:10.1016/j.chmed.2021.09.014

Guo, Y., Chen, H., Jiang, Y., Yuan, Y., Zhang, Q., Guo, Q., et al. (2020). CGRP regulates the dysfunction of peri-implant angiogenesis and osseointegration in streptozotocin-induced diabetic rats. *Bone* 139, 115464. doi:10.1016/j.bone.2020.115464

Huang, M., Vitharana, S. N., Peek, L. J., Coop, T., and Berkland, C. (2007). Polyelectrolyte complexes stabilize and controllably release vascular endothelial growth factor. *Biomacromolecules* 8 (5), 1607–1614. doi:10.1021/bm061211k

Kageyama, Y., Deguchi, Y., Hattori, K., Yoshida, S., Goto, Y.-I., Inoue, K., et al. (2021). Nervonic acid level in cerebrospinal fluid is a candidate biomarker for depressive and manic symptoms: a pilot study. *Brain Behav.* 11 (4), e02075. doi:10.1002/brb3.2075

Kageyama, Y., Kasahara, T., Nakamura, T., Hattori, K., Deguchi, Y., Tani, M., et al. (2018). Plasma nervonic acid is a potential biomarker for major depressive disorder: a pilot study. *Int. J. Neuropsychopharmacol.* 21 (3), 207–215. doi:10.1093/ijnp/pyx089

Keppley, L. J. W., Walker, S. J., Gademsey, A. N., Smith, J. P., Keller, S. R., Kester, M., et al. (2020). Nervonic acid limits weight gain in a mouse model of diet-induced obesity. *FASEB J.* 34 (11), 15314–15326. doi:10.1096/fj.202000525R

Kim, H. S., Sun, X., Lee, J. H., Kim, H. W., Fu, X., and Leong, K. W. (2019). Advanced drug delivery systems and artificial skin grafts for skin wound healing. *Adv. Drug Deliv. Rev.* 146, 209–239. doi:10.1016/j.addr.2018.12.014

Kremer, D., Akkermann, R., Küry, P., and Dutta, R. (2019). Current advancements in promoting remyelination in multiple sclerosis. *Mult. Scler.* 25 (1), 7–14. doi:10.1177/1352458518800827

Ledeen, R. W., Yu, R. K., and Eng, L. F. (1973). Gangliosides of human myelin: sialosylgalactosylceramide (G7) as a major component. *J. Neurochem.* 21 (4), 829–839. doi:10.1111/j.1471-4159.1973.tb07527.x

Levy, N. S., Chung, S., Furneaux, H., and Levy, A. P. (1998). Hypoxic stabilization of vascular endothelial growth factor mRNA by the RNA-binding protein HuR. *J. Biol. Chem.* 273 (11), 6417–6423. doi:10.1074/jbc.273.11.6417

Lewkowicz, N., Piątek, P., Namiecińska, M., Domowicz, M., Bonikowski, R., Szemraj, J., et al. (2019). Naturally occurring nervonic acid ester improves myelin synthesis by human oligodendrocytes. *Cells* 8 (8), 786. doi:10.3390/cells8080786

Li, Q., Chen, J., Yu, X., and Gao, J.-M. (2019). A mini review of nervonic acid: source, production, and biological functions. *Food Chem.* 301, 125286. doi:10.1016/j.foodchem.2019.125286

Love, S. (2006). Demyelinating diseases. *J. Clin. Pathol.* 59 (11), 1151–1159. doi:10.1136/jcp.2005.031195

Marenzana, M., and Arnett, T. R. (2013). The key role of the blood supply to bone. *Bone Res.* 1 (3), 203–215. doi:10.4248/BR201303001

Marrella, A., Lee, T. Y., Lee, D. H., Karuthedom, S., Syla, D., Chawla, A., et al. (2018). Engineering vascularized and innervated bone biomaterials for improved skeletal tissue regeneration. *Mater. TodayKidlingt. Engl.* 21 (4), 362–376. doi:10.1016/j.mattod.2017.10.005

Mi, J., Xu, J., Yao, H., Li, X., Tong, W., Li, Y., et al. (2021). Calcitonin gene-related peptide enhances distraction osteogenesis by increasing angiogenesis. *Tissue Eng. Part A* 27 (1-2), 87–102. doi:10.1089/ten.TEA.2020.0009

Nave, K. A. (2010). Myelination and the trophic support of long axons. *Nat. Rev. Neurosci.* 11 (4), 275–283. doi:10.1038/nrn2797

Phung, N. V., Rong, F., Xia, W. Y., Fan, Y., Li, X. Y., Wang, S. A., et al. (2023). Nervonic acid and its sphingolipids: biological functions and potential food applications. *Crit. Rev. Food Sci. Nutr.* 64, 8766–8785. doi:10.1080/10408398.2023.2203753

Plemel, J. R., Liu, W. Q., and Yong, V. W. (2017). Remyelination therapies: a new direction and challenge in multiple sclerosis. *Nat. Rev. Drug Discov.* 16 (9), 617–634. doi:10.1038/nrd.2017.115

Qian, A., Zhou, L., Shi, D., Pang, Z., and Lu, B. (2023). Portulaca oleracea alleviates CCl4-induced acute liver injury by regulating hepatic S100A8 and S100A9. *Chin. Herb. Med.* 15 (1), 110–116. doi:10.1016/j.chmed.2022.05.004

Simón-Yarza, T., Formiga, F. R., Tamayo, E., Pelacho, B., Prosper, F., and Blanco-Prieto, M. J. (2012). Vascular endothelial growth factor-delivery systems for cardiac repair: an overview. *Theranostics* 2 (6), 541–552. doi:10.7150/thno.3682

Song, W., Zhang, K., Xue, T., Han, J., Peng, F., Ding, C., et al. (2022). Cognitive improvement effect of nervonic acid and essential fatty acids on rats ingesting Acer truncatum Bunge seed oil revealed by lipidomics approach. *Food Funct.* 13 (5), 2475–2490. doi:10.1039/d1fo03671h

Tayalia, P., and Mooney, D. J. (2009). Controlled growth factor delivery for tissue engineering. *Adv. Mater* 21 (32–33), 3269–3285. doi:10.1002/adma.200900241

Terluk, M. R., Tieu, J., Sahasrabudhe, S. A., Moser, A., Watkins, P. A., Raymond, G. V., et al. (2022). Nervonic acid attenuates accumulation of very long-chain fatty acids and is a potential therapy for adrenoleukodystrophy. *Neurother.* 19 (3), 1007–1017. doi:10.1007/s13311-022-01226-7

Vozella, V., Basit, A., Misto, A., and Piomelli, D. (2017). Age-dependent changes in nervonic acid-containing sphingolipids in mouse hippocampus. *Biochim. Biophys. Acta Mol. Cell Biol. Lipids* 1862 (12), 1502–1511. doi:10.1016/j.bbalip.2017.08.008

frontiers | Frontiers in Pharmacology

TYPE Review
PUBLISHED 09 December 2024
DOI 10.3389/fphar.2024.1476670

Check for updates

OPEN ACCESS

EDITED BY
Luigi Milella,
University of Basilicata, Italy

REVIEWED BY
Juan Moisés De La Serna,
International University of La Rioja, Spain
Gerald Mboowa,
Makerere University, Uganda

*CORRESPONDENCE
Tingting Zhu,
zhutt29@163.com
Xiaojuan Liu,
lxj@ntu.edu.cn

†These authors have contributed equally to this work

RECEIVED 06 August 2024
ACCEPTED 25 November 2024
PUBLISHED 09 December 2024

CITATION
Sun C, Na Y, Wang Z, Zhu T and Liu X (2024) Phytochemicals, promising strategies combating *Cutibacterium acnes*. *Front. Pharmacol.* 15:1476670. doi: 10.3389/fphar.2024.1476670

COPYRIGHT
© 2024 Sun, Na, Wang, Zhu and Liu. This is an open-access article distributed under the terms of the Creative Commons Attribution License (CC BY). The use, distribution or reproduction in other forums is permitted, provided the original author(s) and the copyright owner(s) are credited and that the original publication in this journal is cited, in accordance with accepted academic practice. No use, distribution or reproduction is permitted which does not comply with these terms.

Phytochemicals, promising strategies combating *Cutibacterium acnes*

Cuilian Sun[1†], Yuhang Na[1†], Ziyu Wang[2], Tingting Zhu[3*] and Xiaojuan Liu[1*]

[1]Department of Pathogen Biology, Medical College, Nantong University, Nantong, Jiangsu, China, [2]Medical College, Nantong University, Nantong, Jiangsu, China, [3]Department of Dermatology, The First Affiliated Hospital of Soochow University, Suzhou, China

The excessive proliferation of *Cutibacterium acnes (C. acnes)* is an important reason for the occurrence of acne vulgaris, and genetic detection ratio of *C. acnes* in acne is as high as 60.5%. Until now, the treatment of *C. acnes* is mainly limited to antibiotics, but some strains of *C. acnes* produce antimicrobial resistances, making it difficult for clinical treatment. Additionally, antibiotics can cause severe adverse effects. Therefore, more and more people are paying attention to phytochemicals. It is well known that plants can synthesize a range of secondary metabolites, named phytochemicals, part of which have antibacterial properties. Additionally, the main advantages of phytochemicals are that they have good efficacies and less side effects, so they are suitable choices for medical treatment. This review mainly discusses the effects and mechanisms of phytochemicals against *C. acnes*.

KEYWORDS

***Cutibacterium acnes*, acne vulgaris, phytochemicals, plant composition, antibiosis**

1 Introduction

Acne vulgaris (AV) is a chronic inflammatory disease of the pilosebaceous unit. The 2010 Global Burden of Disease Study found that AV ranked eighth in the common disease sequelae, with a global prevalence of 9.38% (Vos et al., 2012). Based on a systematic review and meta analysis about relevant studies published between 1 January 1996 and 30 September 2016, the overall pooled prevalence rates of acne in Mainland China were 39.2% (Li et al., 2017). AV is common in adolescents and can be identified by their facial lesion (Silverberg and Silverberg, 2014). It is mainly manifested as a series of clinical signs related to swelling, inflammation or scarring of sebaceous gland units (Ayer and Burrows, 2006), which can be divided into noninflammatory skin lesions (comedones) and inflammatory skin lesions. Noninflammatory lesions include open comedones (blackheads) and closed comedones (whiteheads). Inflammatory lesions can range from papules or pustules to nodules or cysts, and finally scar formation, which is the result of inflammation of the acne dermis, and these processes tend to occur on the face, neck, chest, and back of AV patients (Titus and Hodge, 2012). There are four primary factors in the pathogenesis of acne, which interact with each other to produce acne lesions, including inflammatory mediators released into the skin; alteration of the keratinisation process leading to comedones; sebum production by the sebaceous gland; and colonization by *C. acnes* (Thiboutot et al., 2009). The occurrence of acne may not cause serious harm physically, but it will cause psychological trauma to teenagers, causing low self-esteem, anxiety, social inhibition and depression (Williams et al., 2012).

Cutibacterium acnes is closely related to the occurrence of acne. The facial acne lesions of 375 acne patients were collected and 227 acne patients were isolated from *C. acnes*. The positive ratio of *C. acnes* was 60.5% (Zhu et al., 2019). *Cutibacterium acnes* is a lipophilic Gram-positive facultative anaerobic bacterium, possessing a typical appearance of corynebacterium, coarse and irregular short branched structure under microscope (Ahle et al., 2023). Excessive proliferation of *C. acnes*-induced Toll-like receptor (TLR)-2 and protease-activated receptors expressed in keratinocytes activate innate immunity, inducing the production of inflammatory factors and matrix metalloproteinases in early and advanced acne lesions (Williams et al., 2012). *Cutibacterium acnes* also stimulates increased sebum secretion, increased free fatty acids and abnormal keratinization of sebaceous ducts (Tucker et al., 1980). At the same time, the sebaceous glands of acne lesions provide an anaerobic and fat-rich environment for *C. acnes* to multiply within the sebum glands. In addition, *C. acnes* produces protease, lipase and hyaluronidase, which increases free fatty acids in acne lesions, stimulates excessive keratinization of sebaceous duct, resulting in poor sebum excretion, aggravates acne inflammation, and thus forms a vicious cycle to deteriorate acne (Adler et al., 2017). Moreover, besides acne, *C. acnes* causes severe infections at various body sites, resulting in endophthalmitis (Meisler and Mandelbaum, 1989), endocarditis (Banzon et al., 2017), central nervous system infections (Richards et al., 1989), arthroplastic and osteosynthetic infections (Lutz et al., 2005). Therefore, anti-*C. acnes* therapies are important in clinical practice tackling *C. acnes* associated diseases.

The common clinical approach to combat *C. acnes* is the use of topical or oral antibiotics, such as tetracyclines and macrolides. However, the long-term use of antibiotics can cause a dramatic increase in antimicrobial resistances (AMRs) (Habeshian and Cohen, 2020). Thus, it is not recommended the monotherapy of topical and oral antibiotics, which is replaced by antibiotics combined with benzoyl peroxide (BP). BP is an antibacterial agent that kills *C. acnes* through the release of free oxygen radicals, but BP therapy is limited by staining and bleaching of fabric, concentration-dependent irritation, dryness, erythema and uncommon contact allergy (Reynolds et al., 2024).

The phytochemicals have been used to ameliorate and cure diseases since ancient times, including the treatments of bacterial infectious diseases (Liang et al., 2022). Discovery of novel drugs can be accomplished with the use of the phytochemicals, which are the broad-spectrum secondary metabolites. The phytochemicals can effectively prevent and ease the toxicity induced by other toxins or drugs (Bhatia et al., 2021). Many studies have shown that some phytochemicals have anti-*C. acnes* efficacies (Sinha et al., 2014). These phytochemicals are classified as quinones, saponins, tannins, terpenoids, alkaloids, volatile oils, organic acids, phenols, and flavonoids according to the main active components. This review will summarize the ingredients efficiencies, and mechanisms of the phytochemicals that have anti-*C. acnes* effects.

2 The emerging threat of antibiotic therapy for *Cutibacterium acnes*

Currently, both topical and oral antibiotics are used to treat acne. Erythromycin and clindamycin, belonging to the antibiotic family of macrolides, are the two most commonly used topical antibiotics, and they can slow bacterial growth (Walsh et al., 2016). However, we have to face the problem of AMRs caused by the overuse and abuse of antimicrobial drugs. Many countries have reported that over 50% of *C. acnes* strains are AMRs (Walsh et al., 2016), and the incidence of *C. acnes* AMRs increased from 20% in 1978 to 62% in 1996 (Walsh et al., 2016). Approximately 50% of patients with acne develop resistance after oral or topical therapy, and 1 in 4 *C. acnes* strains are currently resistant to macrolides (Zhang et al., 2022). Although not specific to *C. acnes*, recent publications have highlighted the dangers of antibiotic resistance, the first comprehensive assessment on the global health impact of antimicrobial resistances (AMRs) in 2022 estimated that 4.95 million deaths in 2019 were associated with AMRs (Antimicrobial Resistance, 2022). The consequences of AMRs to *C. acnes* may include failure of acne treatment, skin microbiome disturbances, emergence of multidrug-resistant bacteria, and the spread of resistant strains to healthcare workers and the general population.

3 Possible alternatives to classical antibiotics

3.1 Bacteriophage therapy

Given the growing burden of AMRs worldwide, bacteriophage therapy is one of the promising solutions for AMRs (Strathdee et al., 2023). Phages are bacterial viruses widely distributed in environments. They attach to the surfaces of bacteria and inject their genomes into the bacterial cells, then manipulate the bacterial metabolic machinery to produce viral proteins and copy the viral genome. Finally, viral proteins and genes assemble to form new viral particles and the bacterial cells are lysed, releasing numerous new phages (Torres-Barceló, 2018). Many studies have shown that the use of phage can indeed reduce the number of *C. acnes* (Han et al., 2023; Rimon et al., 2023; Xuan G. et al., 2023), but bacteriophage therapy needs to face greater scrutiny in terms of safety and lack of efficacy data from clinical trials, and the low phage variability and phage resistance in *C. acnes* (Aslan Kayiran et al., 2020).

3.2 Antimicrobial peptides therapy

Antimicrobial peptides (AMPs) are positively charged amphiphilic molecules. Being electrostatically adsorbed on the surface of bacterial membranes, AMPs can easily penetrate and destroy the membrane structures of the bacteria, resulting in bacterial death (Xuan J. et al., 2023). Therefore, most AMPs exhibit a broad spectrum of antimicrobial activity. The effect of AMPs on *C. acnes* has been widely reported by far. Bombinin-like peptide 7 (BLP-7) has antibacterial activity with a minimum inhibitory concentration (MIC) of 5 μM, which was extracted from *Bombina orientalis* (Wu et al., 2020). Two novel AMPs WSKK11 and WSRR11 also provide great potentials to kill *C. acnes* (Theansungnoen et al., 2022). However, AMPs therapy still has shortcomings, including cause systemic and local toxicity, decreased sensitivity to salt, serum, and pH, sensitization and allergy after repeated application, confounding biological

TABLE 1 Summary of phytochemicals with anti-*C. acnes* s activity.

Phytochemicals	Classification	Botanical source	Botanical Family	Plant part used	Bacterial Strain	MIC/MBC (μg/mL)	References
Resveratrol	Polyphenols	Smilax china L.	Liliaceae	Root	KCTC 3314	125/125	Joo et al. (2022)
Quercetin	Flavonoid	Smilax china L.	Liliaceae	Root	KCTC 3314	31.25/31.25	Joo et al. (2022)
Kaempferol	Flavonoid	Impatiens balsamina	Balsaminaceae	Whole plant	ATCC 6919	≤32/≤128	Lim et al. (2007)
Thymol	Phenols	Origanum vulgare L.	Labiatae	Whole plant	ATCC 6919	700/1,400	Taleb et al. (2018)
Honokiol	Biphenols	Magnolia sp.	Magnoliaceae	Stem bark	ATCC 6919	3–4/20	Park et al. (2004)
Magnolol	Biphenols	Magnolia sp.	Magnoliaceae	Stem bark	ATCC 6919	9/45	Park et al. (2004)
Rhodomyrtone	Phenols	Rhodomyrtus tomentosa (Aiton) Hassk	Myrtaceae Juss.	Leaves	Acne lesions from human volunteers	0.12–0.5/0.12–1	Saising et al. (2012)
Acidic polysaccharide CS-F2	Polysaccharie	Camellia sinensis	Theaceae	Whole plant	ATCC 6919	50/-	Lee et al. (2006)
Sapindoside A	Triterpenes	S. mukorossi	Arboricaceae	Whole plant	ATCC 6919	6.3/-	Wei et al. (2022)
Sapindoside B	Triterpenes	S. mukorossi	Arboricaceae	Whole plant	ATCC 6919	13/-	Wei et al. (2022)
Punicalagin	Tannins	Punica granatum Linne	Punicaceae	Pericarp	BCRC10723	6.25/12.5	Lee et al. (2017)
Punicalin	Tannins	Punica granatum Linne	Punicaceae	Pericarp	BCRC10723	6.25/12.5	Lee et al. (2017)
Strictinin A	Tannins	Punica granatum Linne	Punicaceae	Pericarp	BCRC10723	12.5/25	Lee et al. (2017)
Granatin B	Tannins	Punica granatum Linne	Punicaceae	Pericarp	BCRC10723	100/-	Lee et al. (2017)
Lauric acids	Saturated fatty acid	Coconut	Palmae	Oil	ATCC 6919	–/–	Darren Yang et al. (2009)
Myrtucommulone A	Phloroglucino-ls	Myrtus communis L.	Myrtaceae	Leaves	EryR (EryS)	1.2 (1.2)/-	Feuillolay et al. (2016), Fiorini-Puybaret et al. (2011)
Myrtucommulone B	Phloroglucino-ls	Myrtus communis L.	Myrtaceae	Leaves	EryR (EryS)	0.3 (0.6)/-	Fiorini-Puybaret et al. (2011)
Humulones	Hop alpha acid	Humulus lupulus Linn.	Moraceae	Flowers	ATCC 6919	10/30	Yamaguchi et al. (2009)
Lupulones	Hop beta acid	Humulus lupulus Linn.	Moraceae	Flowers	ATCC 6919	0.1/0.3	Yamaguchi et al. (2009)
Xanthohumol	Flavonoid	Humulus lupulus Linn.	Moraceae	Flowers	ATCC 6919	3/3	Yamaguchi et al. (2009)
Icariin	Flavonol	Epimedium brevicornum	Berberidaceae	Whole plant	LMG 16711	25/-	Coenye et al. (2012)
Alpha-kosin	Long chain fatty alcohols	Leucosidea sericea	Rosaceae	Leaves	—	1.9/-	Sharma et al. (2014)
Artocarpin	Flavonoid	Artocarpus integer	Moraceae	Root	DMST 14916	2/32	Dej-adisai et al. (2013)
Cudraflavone C	Flavonol	Artocarpus integer	Moraceae	Root	DMST 14916	2/32	Dej-adisai et al. (2013)
Artocarpanone	Flavonoid	Artocarpus integer	Moraceae	Root	DMST 14916	32/64	Dej-adisai et al. (2013)

(Continued on following page)

TABLE 1 (*Continued*) Summary of phytochemicals with anti-*C. acnes* s activity.

Phytochemicals	Classification	Botanical source	Botanical Family	Plant part used	Bacterial Strain	MIC/ MBC (μg/mL)	References
5,7-dimethoxyflavo-ne	Flavonoid	Kaempferia parviflora Wall. ex Baker	Zingiberace-ae	Rhizome	DIMST 14916	–/–	Sitthichai et al. (2022)
Pulsaquinone	Quinone-type compound	Pulsatilla koreana	Ranunculac-eae	Rhizomes	KCTC 3314	2/-	Cho et al. (2009)
Farnesol	Sesquiterpene alcohol	Magnolia flower, loquat leaves and other plants	—	Flowers, leaves, stems, etc	—	0.14 mM[a]/-	Wu et al. (2021)
Dumoside	C22-steroidal lactone glycosides	Paris polyphylla var. yunnanensis	Trilili aceae	Stems and leaves	—	3.9/-	Qin et al. (2013)
15-nor-14-oxolabda-8 (17),12E-diene-18-oic acid	Diterpene aldehyde	Pinus densiflora	Pinaceae	Cones	—	64/-	Sultan et al. (2008)
Phloretin	Flavonoid	Apples and other plants	—	Branches, leaves, etc	ATCC 11827	500/-	Kum et al. (2016)

[a]The MIC of Farnesol was 0.14 mM, and the concentration unit was not μg/mL (Wu et al., 2021).

functions (e.g., angiogenesis) and high manufacturing costs (Gupta et al., 2018).

3.3 Phytochemicals therapy

The therapies bacteriophage and antimicrobial peptides bear high production costs and display low safety performance, easily causing local or systemic toxicity. Therefore, it is crucial to find a new therapeutic strategy that is easy to implement with little side effects. Phytochemicals have been studied as an alternative therapy to antibiotics. Traditional medicine has used plants to fight diseases for thousands of years, and according to World Health Organization (WHO), 80 percent of the global populations rely on the plant-based medicines for their basic healthcare needs (Kifle et al., 2021). In fact, many reports have pointed to the possibility of antimicrobial use of medicinal plant active ingredients. For example, Ginger essential oil (GEO) inhibits and kills *Escherichia coli* (*E.coli*) and *Staphylococcus aureus* (*S. aureus*) (Wang et al., 2020). These important bioactive compounds have broad application prospects in the field of biomedical development.

Now the inhibitory effects of phytochemicals, such as phloretin (Cheon et al., 2019), and rhodomyrtone (Saising and Voravuthikunchai, 2012), on *C. acnes* have been widely studied. Phytochemicals are readily available, effective, and with small numbers of side effects, and are expected to be widely used. Therefore, it is necessary to study the inhibitory effects and underlying mechanisms of phytochemicals on *C. acnes*.

4 Phytochemicals that have an inhibitory effect on *Cutibacterium acnes*

Considerable efforts have been made to find plant-derived antimicrobials against C. acnes. Table 1 summarizes 31 phytochemicals with anti-C. acnes activity, showing their classification, botanical source, MIC, minimum bactericidal concentration (MBC), and tested C. acnes strains. These phytochemicals with anti-C. acnes activities were either isolated from plants or commercially purchased as standard reagents. In view of the antibacterial activity parameters (Kuete, 2010), including significant (MIC ≤ 10 μg/mL), moderate (MIC ≤ 100 μg/mL) and low or negligible (MIC ≤ 100 μg/mL), 17 phytochemicals have significant inhibitory effects, and the hop extract Lupulones has the strongest anti-C. acnes ability.

In the following section, the inhibitory effects of phytochemicals on C. acnes and their mechanisms will be described in detail according to the classification of plant active ingredients, including phenols, flavonoids, Polyols, essential oils, tannins, saponins, fatty acids and Quinone compounds.

4.1 Phenols and their derivatives, polyols and flavonoids

Phenols, Polyols and flavonoids are widely distributed in the plant kingdom, which have antioxidant, anti-inflammatory, antibacterial and antiviral activities. Antibacterial mechanisms of flavonoids including inhibition of nucleic acid synthesis, cytoplasmic membrane function and energy metabolism (Cushnie and Lamb, 2005).

Resveratrol (RSL) is a polyphenolic compound derived from the Smilax plant, peanuts, blueberries and cranberries, and it is an antioxidant with a variety of biological effects, including antibacterial properties. Studies have shown the beneficial effects of RSL in fighting C. acnes (Docherty et al., 2007; Taylor et al., 2014). After RSL treatment, C. acnes shows changes in bacterial morphology under electron microscope, represented by intracellular edema and destruction of intracellular structural integrity (Taylor et al., 2014). As a membrane permeable compound, RSL may be able to alter the bacterial membrane

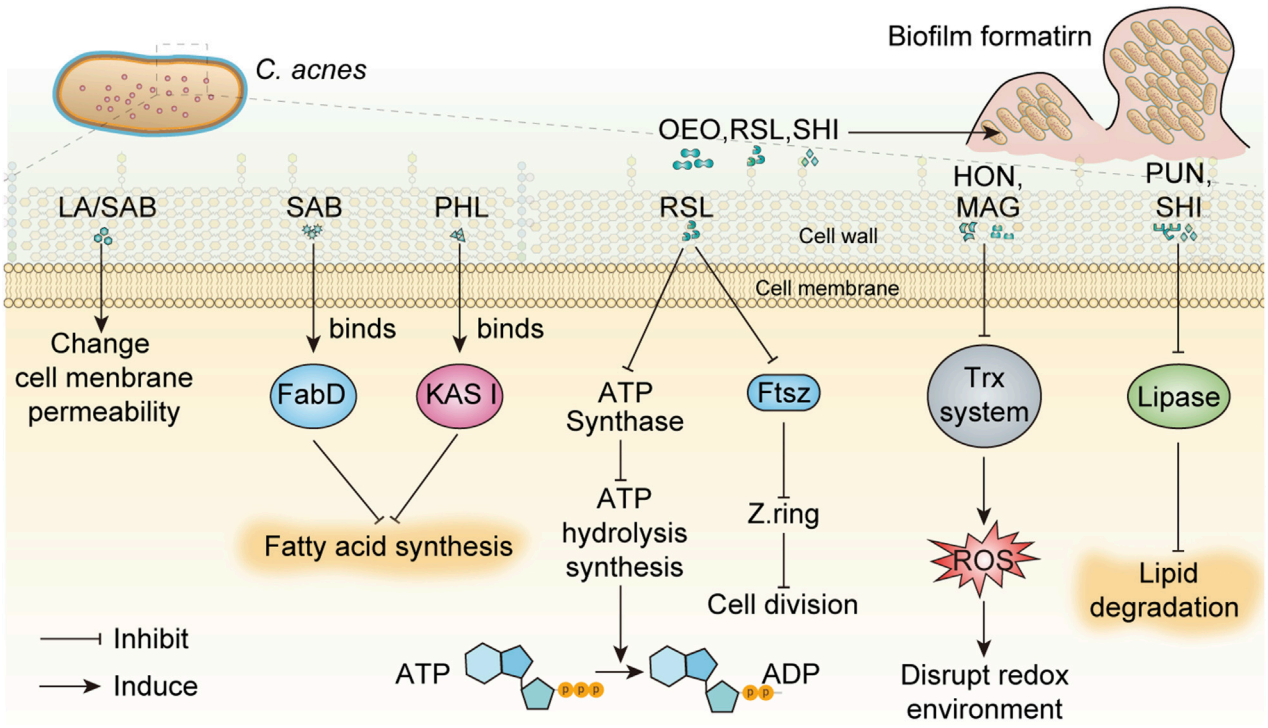


FIGURE 1
The mechanisms of phytochemicals against *C. acnes* were summarized. In this figure, the inhibition of ATP synthase and Ftsz protein by RSL on *C. acnes* was speculated by the inhibition mechanism of RSL on *E. coli*, which has not been confirmed by relevant studies. Oregano essential oil has broad-spectrum anti-biofilm activity, but its anti-*C. acnes* biofilm effect is only speculated and has not been confirmed. Abbreviations in the Figure: ADP, adenosine diphosphate; ATP, adenosine triphosphate; FabD, Malonyl-CoA-acyl carrier protein transacylase; FtsZ, filamentous temperature sensitive protein; HON, honokiol; KAS III, β-ketoacyl acyl carrier protein synthase III; MAG, magnolol; resveratrol, RSL; SAB, saponins A and B; SHI, shikonin; Trx, thioredoxin; LA, Lauric acid; OEO, oregano essential oil; PHL, Phloretin; PUN, punicalagin.

structure of C. acnes and disrupt intracellular machinery (Taylor et al., 2014). At present, the specific mechanism of resveratrol inhibiting *C. acnes* is not clear, but studies have shown that RSL can bind to *E. coli* adenosine triphosphate (ATP) synthase and inhibit ATP hydrolysis and synthesis (Dadi et al., 2009). Filamentous temperature sensitive protein (FtsZ, a GTP-dependent prokaryotic cell division protein) is a key protein in septum formation during cell division, and it is responsible for cell division by forming a dynamic Z ring in the middle of the cell. In *E. coli*, RSL can inhibit FtsZ-mediated Z ring formation and inhibit cell division (Hwang and Lim, 2015; Ma et al., 2018). Furthermore, RSL can also alter the expression of bacterial virulence characteristics, thereby reducing toxin production, inhibiting biofilm formation, reducing motility, and interfering with quorum sensing (Vestergaard andIngmer, 2019). These might be the mechanisms for anti-*C. acnes* activities of RSL.

Honokiol (HON) and magnolol (MAG) are two major phenolic constituents of Magnoliaceae, which have anti-*C. acnes* activities (Park et al., 2004). In addition, they have anti-inflammatory effects and can be used as acne-mitigating candidates for topical application (Park et al., 2004). HON and MAG have effective antibacterial effects against Gram-positive bacteria, showing inhibitory effects on the bacterial thioredoxin (Trx) system (the main thiol-dependent disulfide reductase system in bacteria) (Ouyang et al., 2023). Most Gram-positive bacteria have a Trx system but lack a glutathione (GSH)/glutaredoxin (Grx) system, so in these Gram-positive bacteria, the Trx system plays irreplaceable roles in DNA synthesis and repair, cell proliferation and antioxidant defense. The inhibition of Trx by HON and MAG can disrupt the intracellular redox environment of bacteria. HON and MAG lead to dysregulation of cellular redox environment homeostasis and increase intracellular ROS levels, eventually contribute to their bactericidal efficacies (Ouyang et al., 2023).

Phloretin (PHL) is a flavonoid found in free form and glycoside form in apples and strawberries, with antioxidant, anti-inflammatory and antibacterial activities. H. Kum et al. demonstrate that PHL has inhibitory effects on *C. acnes*, *propionibacterium granulosum* and *Staphylococcus epidermidis (S. epidermidis)* (Kum et al., 2016). Fatty acids are essential for bacterial survival, hence molecules involved in fatty acid synthesis can be targeted by antimicrobial agents (Cheon et al., 2019). β-ketoacyl acyl carrier protein synthase III (KAS III) is one of the important enzymes in bacterial fatty acid synthesis. PHL can bind to the active site of *C. acnes* KAS III, block the extension reaction between *C. acnes* KAS III and its substrate, and finally inhibit the synthesis of fatty acids in *C. acnes* to obtain antibacterial effect (Cheon et al., 2019; Lee et al., 2009).

Erythritol is a kind of sugar alcohol compound, belonging to the polyalcohol sweetener, which is widely found in fruits such as melons, grapes and various fermented foods. Erythritol acts as an antioxidant *in vivo* and may prevent blood vessel damage caused by hyperglycemia (den Hartog et al., 2010). It also has an antibacterial effect, including *Streptococcus gordonii* (Hashino et al., 2013),

Corynebacterium minutissimum, *Corynebacterium striatum*, and *S. epidermidis* (Fujii et al., 2022a). Fujii T et al. demonstrated that erythritol contributed to the growth of *C. acnes* ribotype 2 (RT2) and RT6 associated with healthy skin, inhibiting RT4 and RT5 associated with the progression of acne (Tadashi Fujii et al., 2022b). Glycerol 3-phosphate dehydrogenase encoded by g3pD is one of the key enzymes in erythritol metabolism. Due to the low expression level of g3pD in RT5, phosphorylated erythritol might accumulate intracellularly in the presence of erythritol in the environment, thereby directly inhibiting the activity of glycolytic enzymes (Tadashi Fujii et al., 2022a). Xylitol is a sugar alcohol compound with one more carbon atom than erythritol. L Trahan reveals that the antibacterial effect of xylitol is mainly through direct inhibition of the phosphoenolpyruvate phosphotransferase system (PEP-PTS), which causes the accumulation of xylitol-derived xylitol 5-phosphate inside bacterial cells, thus inhibiting the activity of glycolytic enzyme (Tadashi Fujii et al., 2022b; Trahan, 1995). Erythritol may have a growth inhibiting effect on C. acnes similar to xylitol (Tadashi Fujii et al., 2022a).

4.2 Volatile oil

Volatile oil, also known as essential oil, is a general term for an oily liquid that can be volatilized at room temperature and can be distilled with steam. The basic compositions of volatile oil include aliphatic compounds, aromatic compounds and terpenoids. In addition, it also contains other compounds, such as ligustilide, a phenol component in Angelica. Volatile oil is an important active ingredient, which can be directly used in the clinical application of crude drugs mainly containing volatile oil (Vora et al., 2024).

Oregano essential oil (OEO) contains thymol, carvacrol and ursolic acid, which is a kind of Volatile oil. OEO plays a spectral antibacterial activity, especially on *C. acnes* (Taleb et al., 2018). After OEO treatment, the bacteria mainly show protrusions on the cell surface without typical bacterial morphology, and the number of bacteria decreases (Scandorieiro et al., 2022). Though the specific antibacterial mechanisms of OEO against *C. acnes* are occult, OEO can inhibit the production and activity of lipase and coagulase of *S. aureus*, thus down-regulating the growth of bacteria (Soltani et al., 2021). In addition, OEO, as an anti-biofilm agent, has broad-spectrum anti-biofilm activity, which can inhibit and destroy the formation of *Streptococcus pyogenes* and *Enterococcus faecalis* biofilms (biofilm is composed of bacterial clusters and extracellular polymer matrix, ensuring the survival environment of bacteria) (Ogawa et al., 2011; Sirati et al., 2024; Wijesundara and Rupasinghe, 2018; Zhan et al., 2022). Ultee A et al. reveal that in *Bacillus cereus*, thymol and carvacrol, as ingredients of OEO, can damage cellular membranes and reduce the pH gradient in the cellular membranes, resulting in proton motive force, reduced ATP pools, and cell death (Ultee et al., 2002). Therefore, it is speculated that OEO may play its anti-C. acnes role via the above mechanisms.

4.3 Tannins

Tannins are a kind of polyphenolic compounds with complex structure in plants, which can be divided into hydrolyzable tannins and condensed tannins according to their chemical structures. Many tannins have pharmacological activities. The tannins contained in Cyrtomium fortunei have strong inhibitory effect on a variety of influenza viruses, the tannins contained in Castanea sativa mill leaf are effective substances in the treatment of acne (Piazza et al., 2024), and some tannins also can be used as effective antibacterial agents for *C. acnes*.

Punicalagin (PUN) is a tannin compound isolated from Punica granatum Linne (Lee et al., 2017). It is a low polymeric compound of 2-3 ellagic acids and can be degraded to produce ellagic acid. PUN has anti-inflammatory, antioxidant and antibacterial properties (Lee et al., 2017). Studies have revealed that PUN can destroy the cell structures of *C. acnes*. The bacterial surface exhibits obvious shrinkage and the surrounding environment is damaged under the electron microscope after 12 h treatment with PUN (Lee et al., 2017). In addition, PUN also has the effect of inhibiting lipase, which is an enzyme that hydrolyzes lipids. Many bacteria, such as *C. acnes*, can secrete lipase to decompose lipids and promote the absorption of lipid-related nutrients from external media, thus benefiting the growth of bacteria itself. The fluorescence determination of the lipase treated by PUN shows that PUN can inhibit the lipase activity of *C. acnes* (Lee et al., 2017). Moreover, Bakkiyaraj D et al. show that ellagic acid, a degradation product of PUN, has anti-biofilm potential against a large number of pathogenic bacteria (Bakkiyaraj et al., 2013).

4.4 Saponins

Saponins are a special class of glycosides existing in the plant kingdom. According to the structure produced by hydrolysis, saponins are divided into two categories, including triterpenoid saponins and steroid saponins. Saponins have anti-inflammatory, antibacterial and anti-tumor effects, having pharmacological activities in clinical practice (Passos et al., 2022).

Sapindus saponins are a group of Saponins, which extracted from Sapindus mukorossi Gaertn (S. mukorossi). S. mukorossi is a wide distributed medicinal plant. The Compendium of Materia Medica reports that S. mukorossi extract traditionally can be used to treat cough, excess salivation and whitening skin (M. P. Wei et al., 2021). Sapindus saponins have antibacterial (Alberice et al., 2012), antifungal (Hu et al., 2018), antitumor (Kuo et al., 2005) biological activities. Wei MP et al. point out that Sapindus saponins have anti-*C. acnes* activity (Wei et al., 2021). They mainly investigate the synergistic antibacterial mechanism of two saponins [saponins A and B (SAB)] against *C. acnes* 6919. The compositions of fatty acids in the cell membrane of *C. acnes* are changed with the treatment of SAB. 12-methyl-tetraalkanoic acid and octadecanoic acid decreases and increases, respectively. Meanwhile, the genes related to fatty acid biosynthesis are significantly downregulated. The changes of fatty acid composition in the membrane of *C. acnes* increase the hydrophobicity of the cell surface and decrease the fluidity of the membrane (Wei et al., 2021). In addition, molecular docking calculations show that SAB interacts with Malonyl-CoA-acyl carrier protein transacylase (FabD; an essential enzyme for bacterial type II fatty acid synthesis), through hydrogen bonding and hydrophobic interactions, thus SAB have a competitive inhibitory effect on fatty acid biosynthesis (Wei et al., 2021). In

summary, SAB alter the fatty acid composition of *C. acnes* and further disrupt cell membrane properties, suggesting that Sapindus saponins may be natural additives against *C. acnes*.

P. polyphylla saponins, the mixture of saponins extracted from Paris polyphylla, have spectral antibacterial activity and have been shown to inhibit *C. acnes*, *S. aureus* and *S. epidermidis* (Thapa et al., 2022). The MIC of P. polyphylla saponins against *C. acnes* NCTC737L and *C. acnes* ATCC6919 are 97.5 μg/mL and 48.7 μg/mL, MBC are 198 μg/mL and 97.5 μg/mL, respectively (Li et al., 2024). Among the known saponins extracted from P. polyphylla, including PP I, PP II, PP VI, PP H and PP VII, PP I has the strongest antibacterial effect, while PP H has a relatively weak antibacterial effect (Li et al., 2024). However, the mechanism of P. polyphylla saponins against *C. acnes* need to be further explored.

4.5 Fatty acid

Fatty acids are divided into essential fatty acids and non-essential fatty acids according to whether they can be synthesized by the body. Non-essential fatty acids are fatty acids that can be synthesized by the body without relying on the food supply, and they include saturated fatty acids and some monounsaturated fatty acids. Essential fatty acids are essential for human health and life, but the body can't synthesize it itself and must rely on the food supply, they are unsaturated fatty acids. Fatty acids are closely related to growth and development, intellectual development, memory and physiological functions (Yashodhara et al., 2009). Such as linoleic acid and arachidonic acid can promote the transport of cholesterol in the blood and reduce its deposition on the blood vessel wall (Demetz et al., 2014). Besides, some fatty acids can inhibit the growth of bacteria (Lamas et al., 2019).

Lauric acid (LA), a natural free fatty acid, which is the main acidic compound in coconut oil, has anti-*C. acnes* activity and can completely kill *C. acnes* at 80 μg/mL (Yang et al., 2009). LA may kill bacteria by breaking down the cell membrane of Gram-positive bacteria while the cell wall of the bacteria is intact, leading to the disintegration of the bacterial cytoplasm (Bergsson et al., 2001). LA is difficult to be dissolved in water. Therefore, to dissolve LA into creams and gels for better application, Darren Yang loads LA into liposomes and prepares LipoLA (Yang et al., 2009). LipoLA also has anti-*C. acnes* activity similar to that of LA. LipoLA was labeled by FRET chromophobe, and the change of FRET signal when LipoLA mixed with bacteria under different conditions was monitored to detect the bacteriostatic mechanism. The data suggest that LipoLA fuses with the membrane of *C. acnes* and releases the carried LA into the bacterial membrane, which is consistent with the bacteriostatic mechanism of LA (Yang et al., 2009).

4.6 Quinone compound

Quinones are mainly divided into four types, benzoquinone, naphthoquinone, phenanthrene quinone and anthraquinone, which usually have anti-cancer, anti-bacterial and anti-reactive oxygen activities.

Shikonin (SHI) is a naphthoquinone compound extracted from the root of Lithospermum erythrorhizon Siebold and Zucc, which has been widely used in Asia, and is currently believed to have less obvious side effects, and has anti-tumor (Wang et al., 2024), anti-viral (Borde et al., 2023), antioxidant (Gautam et al., 2024) and antibacterial (Watson et al., 2023) effects. A recent study explores the effects of SHI on *C. acnes* strains ATCC 6919 and KCCM 42791. SHI inhibits the growth and biofilm formation of *C. acnes* in a dose-dependent manner (Kim et al., 2024). The study also shows that SHI reduces biofilm formation by decreasing the production of extracellular polymeric substances (EPS) and increasing the production of porphyrin in *C. acnes* (Kim et al., 2024). In addition, quantitative real-time PCR (qRT-PCR) displays that the expression of 11 genes related to biofilm and virulence in *C. acnes* is changed after the application of SHI. For example, the mRNA levels of adhesin, lipase, hyaluronate lyase and virulence related genes is downregulated (Kim et al., 2024). ATP production is essential for bacterial survival and related functions, and inhibition of ATP synthase destroys cellular energy and leads to bacterial death. Zulfiqar Ahmad et al. propose that SHI inhibit the ATP synthase of *E. coli*, thus inhibiting the activity of *E. coli*, which may also be one of the reasons why SHI play antibacterial roles, including against *C. acnes* (Watson et al., 2023).

5 Combination therapy

Many phytochemicals have shown good anti-*C. acnes* ability, but some studies have shown that the combination of some phytochemicals with other substances will have better bactericidal properties. Lim et al. studied the efficacy of quercetin and kaempferol combined with two commonly used antibiotics (erythromycin and clindamycin) against *C. acnes* and found that the bactericidal activity of quercetin or kaempferol was significantly increased when combined with clindamycin (Lim et al., 2007). Taylor et al. evaluated the effect of resveratrol in combination with BP on C. acnes. Resveratrol showed sustained antibacterial activity against C. acnes, while BP showed a short-term bactericidal response. The combination of resveratrol and BP showed high initial antibacterial activity and sustained bacterial growth inhibition, with better antibacterial activity (Taylor et al., 2014).

6 Conclusion and prospect

Overgrowth of *C. acnes* produces extracellular enzymes and specific inflammatory factors that break down triglycerides in sebum into free fatty acids and glycerol, leading to worsening of acne. A large number of studies have suggested that phytochemicals, including phenolic compounds, flavonoids, Polyols, essential oils, tannins, saponins, fatty acids and Quinone compounds, have inhibitory effects on *C. acnes*. The mechanisms of these components against *C. acnes* mainly include changing membrane permeability, inhibiting protein and nucleic acid synthesis, inhibiting enzyme activity, controlling pathogenic bacteria and preventing biofilm formation (Figure 1). However, current studies lack detailed investigation or demonstration of these mechanisms, which may reduce the depth of scientific analysis. Among the phytochemicals discussed in this review, myrtucommulone B and lupulones show extraordinary activity with MIC of 0.3 μg/mL and 0.1 μg/mL, followed by rhodomyrtone with MIC of 0.12–0.5 μg/mL.

In addition to the phytochemicals mentioned above, there may be numerous phytochemicals in nature that have better inhibitory activity against *C. acnes*, which have not been discovered until now. For example, cannabinoids have inhibitory activities against a variety of Gram-positive bacteria, including *Listeria monocytogenes*, *S. aureus* and so on (Saleemi et al., 2022). Cannabinoids can act on the membrane of bacterial cells, change the membrane permeability, and block the release of bacterial vesicles (Saleemi et al., 2022). We hypothesize whether cannabinoids may also have inhibitory effects on C. acnes, which needs further exploration.

Some phytochemicals have anti-*C. acnes* activity due to their phytoactive ingredients. These ingredients can be used as alternative candidates for drug development to alleviate AMRs and adverse drug reactions.

However, most current research relies on vitro experiments to demonstrate the efficacy of phytochemicals against *C. acnes*. *In vivo*, the studies mainly prove the anti-inflammatory and anti-lipid effects of phytochemicals, lacking phytochemicals anti-*C. acnes* experiment validation. In other words, their antibacterial effects haven't been authenticated *in vivo*, and their therapeutic potential hasn't been validated using clinical trials yet. Therefore, further investigation is needed in this field. In addition, in the practical application of anti-*C. acnes*, the stability and bioavailability of phytochemical in the acne treatment formula are key factors to achieve the therapeutic effect. pH value, temperature, light, metal ions, and co-pigments can directly affect the stability of phytochemicals (Kumar et al., 2023). Through studying the stability and bioavailability of these ingredients, more effective and safer acne treatment formulations can be developed. For example, the scientists package and deliver phytochemicals using nanoparticle drug delivery systems, leading to enhanced stability and bioavailability of phytochemicals (Melim et al., 2022).

Author contributions

CS: Investigation, Writing–original draft. YN: Writing–original draft, Data curation. ZW: Writing–original draft. TZ: Writing–review and editing, Data curation. XL: Funding acquisition, Writing–review and editing, Investigation, Supervision.

Funding

The author(s) declare that financial support was received for the research, authorship, and/or publication of this article. The work was supported by the College Student Innovation Program of Nantong University (No. 2023103041070).

Conflict of interest

The authors declare that the research was conducted in the absence of any commercial or financial relationships that could be construed as a potential conflict of interest.

Publisher's note

All claims expressed in this article are solely those of the authors and do not necessarily represent those of their affiliated organizations, or those of the publisher, the editors and the reviewers. Any product that may be evaluated in this article, or claim that may be made by its manufacturer, is not guaranteed or endorsed by the publisher.

References

Adler, B. L., Kornmehl, H., and Armstrong, A. W. (2017). Antibiotic resistance in acne treatment. *JAMA Dermatol* 153 (8), 810–811. doi:10.1001/jamadermatol.2017.1297

Ahle, C. M., Feidenhansl, C., and Brüggemann, H. (2023). Cutibacterium acnes. *Trends Microbiol.* 31 (4), 419–420. doi:10.1016/j.tim.2022.10.006

Alberice, J. V., Funes-Huacca, M. E., Guterres, S. B., and Carrilho, E. (2012). Inactivation of Alicyclobacillus acidoterrestris in orange juice by saponin extracts combined with heat-treatment. *Int. J. Food Microbiol.* 159 (2), 130–135. doi:10.1016/j.ijfoodmicro.2012.08.004

Antimicrobial Resistance, C. (2022). Global burden of bacterial antimicrobial resistance in 2019: a systematic analysis. *Lancet* 399 (10325), 629–655. doi:10.1016/S0140-6736(21)02724-0

Aslan Kayiran, M., Karadag, A. S., Al-Khuzaei, S., Chen, W., and Parish, L. C. (2020). Antibiotic resistance in acne: mechanisms, complications and management. *Am. J. Clin. Dermatol* 21 (6), 813–819. doi:10.1007/s40257-020-00556-6

Ayer, J., and Burrows, N. (2006). Acne: more than skin deep. *Postgrad. Med. J.* 82 (970), 500–506. doi:10.1136/pgmj.2006.045377

Bakkiyaraj, D., Nandhini, J. R., Malathy, B., and Pandian, S. K. (2013). The anti-biofilm potential of pomegranate (Punica granatum L.) extract against human bacterial and fungal pathogens. *Biofouling* 29 (8), 929–937. doi:10.1080/08927014.2013.820825

Banzon, J. M., Rehm, S. J., Gordon, S. M., Hussain, S. T., Pettersson, G. B., and Shrestha, N. K. (2017). Propionibacterium acnes endocarditis: a case series. *Clin. Microbiol. Infect.* 23 (6), 396–399. doi:10.1016/j.cmi.2016.12.026

Bergsson, G., Arnfinnsson, J., Steingrímsson, O., and Thormar, H. (2001). Killing of Gram-positive cocci by fatty acids and monoglycerides. *Apmis* 109 (10), 670–678. doi:10.1034/j.1600-0463.2001.d01-131.x

Bhatia, P., Sharma, A., George, A. J., Anvitha, D., Kumar, P., Dwivedi, V. P., et al. (2021). Antibacterial activity of medicinal plants against ESKAPE: an update. *Heliyon* 7 (2), e06310. doi:10.1016/j.heliyon.2021.e06310

Borde, C., Escargueil, A. E., and Maréchal, V. (2023). Shikonin, an inhibitor of inflammasomes, inhibits Epstein-Barr virus reactivation. *Antivir. Res.* 217, 105699. doi:10.1016/j.antiviral.2023.105699

Cheon, D., Kim, J., Jeon, D., Shin, H. C., and Kim, Y. (2019). Target proteins of phloretin for its anti-inflammatory and antibacterial activities against propionibacterium acnes-induced skin infection. *Molecules* 24 (7), 1319. doi:10.3390/molecules24071319

Cho, S.-C., Sultan, M. Z., and Moon, S.-S. (2009). Anti-acne activities of pulsaquinone, hydropulsaquinone, and structurally related 1, 4-quinone derivatives. *Archives Pharmacal Res.* 32 (4), 489–494. doi:10.1007/s12272-009-1402-z

Coenye, T., Brackman, G., Rigole, P., De Witte, E., Honraet, K., Rossel, B., et al. (2012). Eradication of Propionibacterium acnes biofilms by plant extracts and putative identification of icariin, resveratrol and salidroside as active compounds. *Phytomedicine* 19 (5), 409–412. doi:10.1016/j.phymed.2011.10.005

Cushnie, T. P. T., and Lamb, A. J. (2005). Antimicrobial activity of flavonoids. *Int. J. Antimicrob. Agents* 26 (5), 343–356. doi:10.1016/j.ijantimicag.2005.09.002

Dadi, P. K., Ahmad, M., and Ahmad, Z. (2009). Inhibition of ATPase activity of *Escherichia coli* ATP synthase by polyphenols. *Int. J. Biol. Macromol.* 45 (1), 72–79. doi:10.1016/j.ijbiomac.2009.04.004

Dej-adisai, S., Meechai, I., Puripattanavong, J., and Kummee, S. (2013). Antityrosinase and antimicrobial activities from Thai medicinal plants. *Archives Pharmacal Res.* 37 (4), 473–483. doi:10.1007/s12272-013-0198-z

Demetz, E., Schroll, A., Auer, K., Heim, C., Patsch, J. R., Eller, P., et al. (2014). The arachidonic acid metabolome serves as a conserved regulator of cholesterol metabolism. *Cell Metab.* 20 (5), 787–798. doi:10.1016/j.cmet.2014.09.004

den Hartog, G. J., Boots, A. W., Adam-Perrot, A., Brouns, F., Verkooijen, I. W., Weseler, A. R., et al. (2010). Erythritol is a sweet antioxidant. *Nutrition* 26 (4), 449–458. doi:10.1016/j.nut.2009.05.004

Docherty, J. J., McEwen, H. A., Sweet, T. J., Bailey, E., and Booth, T. D. (2007). Resveratrol inhibition of Propionibacterium acnes. *J. Antimicrob. Chemother.* 59 (6), 1182–1184. doi:10.1093/jac/dkm099

Feuillolay, C., Pecastaings, S., Gac, C. L., Fiorini-Puybaret, C., Luc, J., Joulia, P., et al. (2016). A Myrtus communis extract enriched in myrtucummulones and ursolic acid reduces resistance of Propionibacterium acnes biofilms to antibiotics used in acne vulgaris. *Phytomedicine* 23 (3), 307–315. doi:10.1016/j.phymed.2015.11.016

Fiorini-Puybaret, C., Aries, M.-F., Fabre, B., Mamatas, S., Luc, J., Degouy, A., et al. (2011). Pharmacological properties of Myrtacine® and its potential value in acne treatment. *Planta Med.* 77 (14), 1582–1589. doi:10.1055/s-0030-1270955

Fujii, T., Inoue, S., Kawai, Y., Tochio, T., and Takahashi, K. (2022a). Suppression of axillary odor and control of axillary bacterial flora by erythritol. *J. Cosmet. Dermatol* 21 (3), 1224–1233. doi:10.1111/jocd.14201

Fujii, T., Tochio, T., and Endo, A. (2022b). Ribotype-dependent growth inhibition and promotion by erythritol in Cutibacterium acnes. *J. Cosmet. Dermatology* 21 (10), 5049–5057. doi:10.1111/jocd.14958

Gautam, S., Lapčík, L., and Lapčíková, B. (2024). Pharmacological significance of boraginaceae with special insights into shikonin and its potential in the food industry. *Foods* 13 (9), 1350. doi:10.3390/foods13091350

Gupta, S., Bhatia, G., Sharma, A., and Saxena, S. (2018). Host defense peptides: an insight into the antimicrobial world. *J. Oral Maxillofac. Pathol.* 22 (2), 239–244. doi:10.4103/jomfp.JOMFP_113_16

Habeshian, K. A., and Cohen, B. A. (2020). Current issues in the treatment of acne vulgaris. *Pediatrics* 145 (Suppl. ment_2), S225–S230. doi:10.1542/peds.2019-2056L

Han, M. H., Khan, S. A., and Moon, G. S. (2023). Cutibacterium acnes KCTC 3314 growth reduction with the combined use of bacteriophage PAP 1-1 and nisin. *Antibiot. (Basel)* 12 (6), 1035. doi:10.3390/antibiotics12061035

Hashino, E., Kuboniwa, M., Alghamdi, S. A., Yamaguchi, M., Yamamoto, R., Cho, H., et al. (2013). Erythritol alters microstructure and metabolomic profiles of biofilm composed of Streptococcus gordonii and Porphyromonas gingivalis. *Mol. Oral Microbiol.* 28 (6), 435–451. doi:10.1111/omi.12037

Hu, Q., Chen, Y. Y., Jiao, Q. Y., Khan, A., Li, F., Han, D. F., et al. (2018). Triterpenoid saponins from the pulp of Sapindus mukorossi and their antifungal activities. *Phytochemistry* 147, 1–8. doi:10.1016/j.phytochem.2017.12.004

Hwang, D., and Lim, Y. H. (2015). Resveratrol antibacterial activity against *Escherichia coli* is mediated by Z-ring formation inhibition via suppression of FtsZ expression. *Sci. Rep.* 5, 10029. doi:10.1038/srep10029

Joo, J.-H., Han, M.-H., Kim, J.-I., Kim, J.-E., Jung, K.-H., Oh, H. S., et al. (2022). Antimicrobial activity of Smilax China L. Root extracts against the acne-causing bacterium, Cutibacterium acnes, and its active compounds. *Molecules* 27 (23), 8331. doi:10.3390/molecules27238331

Kifle, Z. D., Bayleyegn, B., Yimer Tadesse, T., and Woldeyohanins, A. E. (2021). Prevalence and associated factors of herbal medicine use among adult diabetes mellitus patients at government hospital, Ethiopia: an institutional-based cross-sectional study. *Metabol. Open* 11, 100120. doi:10.1016/j.metop.2021.100120

Kim, Y. G., Lee, J. H., Kim, S. H., Park, S. Y., Kim, Y. J., Ryu, C. M., et al. (2024). Inhibition of biofilm formation in Cutibacterium acnes, *Staphylococcus aureus*, and Candida albicans by the phytopigment shikonin. *Int. J. Mol. Sci.* 25 (4), 2426. doi:10.3390/ijms25042426

Kuete, V. (2010). Potential of Cameroonian plants and derived products against microbial infections: a review. *Planta Med.* 76 (14), 1479–1491. doi:10.1055/s-0030-1250027

Kum, H., Roh, K. B., Shin, S., Jung, K., Park, D., and Jung, E. (2016). Evaluation of anti-acne properties of phloretin *in vitro* and *in vivo*. *Int. J. Cosmet. Sci.* 38 (1), 85–92. doi:10.1111/ics.12263

Kumar, A., P, N., Kumar, M., Jose, A., Tomer, V., Oz, E., et al. (2023). Major phytochemicals: recent advances in health benefits and extraction method. *Molecules* 28 (2), 887. doi:10.3390/molecules28020887

Kuo, Y. H., Huang, H. C., Yang Kuo, L. M., Hsu, Y. W., Lee, K. H., Chang, F. R., et al. (2005). New dammarane-type saponins from the galls of Sapindus mukorossi. *J. Agric. Food Chem.* 53 (12), 4722–4727. doi:10.1021/jf047963s

Lamas, A., Regal, P., Vázquez, B., Cepeda, A., and Franco, C. M. (2019). Short chain fatty acids commonly produced by gut microbiota influence *Salmonella enterica* motility, biofilm formation, and gene expression. *Antibiot. (Basel)* 8 (4), 265. doi:10.3390/antibiotics8040265

Lee, C.-J., Chen, L.-G., Liang, W.-L., and Wang, C.-C. (2017). Multiple activities of Punica granatum Linne against acne vulgaris. *Int. J. Mol. Sci.* 18 (1), 141. doi:10.3390/ijms18010141

Lee, J. H., Shim, J. S., Lee, J. S., Kim, J. K., Yang, I. S., Chung, M. S., et al. (2006). Inhibition of pathogenic bacterial adhesion by acidic polysaccharide from green tea (Camellia sinensis). *J. Agric. Food Chem.* 54 (23), 8717–8723. doi:10.1021/jf061603i

Lee, J. Y., Jeong, K. W., Shin, S., Lee, J. U., and Kim, Y. (2009). Antimicrobial natural products as beta-ketoacyl-acyl carrier protein synthase III inhibitors. *Bioorg Med. Chem.* 17 (15), 5408–5413. doi:10.1016/j.bmc.2009.06.059

Li, D., Chen, Q., Liu, Y., Liu, T., Tang, W., and Li, S. (2017). The prevalence of acne in Mainland China: a systematic review and meta-analysis. *BMJ Open* 7 (4), e015354. doi:10.1136/bmjopen-2016-015354

Li, L., Zhang, J., Cheng, W., Di, F., Wang, C., and An, Q. (2024). Saponins of Paris polyphylla for the improvement of acne: anti-inflammatory, antibacterial, antioxidant and immunomodulatory effects. *Molecules* 29 (8), 1793. doi:10.3390/molecules29081793

Liang, M., Ge, X., Xua, H., Ma, K., Zhang, W., Zan, Y., et al. (2022). Phytochemicals with activity against methicillin-resistant *Staphylococcus aureus*. *Phytomedicine* 100, 154073. doi:10.1016/j.phymed.2022.154073

Lim, Y. H., Kim, I. H., and Seo, J. J. (2007). *In vitro* activity of kaempferol isolated from the Impatiens balsamina alone and in combination with erythromycin or clindamycin against Propionibacterium acnes. *J. Microbiol.* 45 (5), 473–477.

Lutz, M. F., Berthelot, P., Fresard, A., Cazorla, C., Carricajo, A., Vautrin, A. C., et al. (2005). Arthroplastic and osteosynthetic infections due to Propionibacterium acnes: a retrospective study of 52 cases, 1995-2002. *Eur. J. Clin. Microbiol. Infect. Dis.* 24 (11), 739–744. doi:10.1007/s10096-005-0040-8

Ma, D. S. L., Tan, L. T., Chan, K. G., Yap, W. H., Pusparajah, P., Chuah, L. H., et al. (2018). Resveratrol-potential antibacterial agent against foodborne pathogens. *Front. Pharmacol.* 9, 102. doi:10.3389/fphar.2018.00102

Meisler, D. M., and Mandelbaum, S. (1989). Propionibacterium-associated endophthalmitis after extracapsular cataract extraction. Review of reported cases. *Ophthalmology* 96 (1), 54–61. doi:10.1016/s0161-6420(89)32939-3

Melim, C., Magalhães, M., Santos, A. C., Campos, E. J., and Cabral, C. (2022). Nanoparticles as phytochemical carriers for cancer treatment: news of the last decade. *Expert Opin. Drug Deliv.* 19 (2), 179–197. doi:10.1080/17425247.2022.2041599

Ogawa, T., Terao, Y., Okuni, H., Ninomiya, K., Sakata, H., Ikebe, K., et al. (2011). Biofilm formation or internalization into epithelial cells enable Streptococcus pyogenes to evade antibiotic eradication in patients with pharyngitis. *Microb. Pathog.* 51 (1-2), 58–68. doi:10.1016/j.micpath.2011.03.009

Ouyang, Y., Tang, X., Zhao, Y., Zuo, X., Ren, X., Wang, J., et al. (2023). Disruption of bacterial thiol-dependent redox homeostasis by magnolol and honokiol as an antibacterial strategy. *Antioxidants* 12 (6), 1180. doi:10.3390/antiox12061180

Park, J., Lee, J., Jung, E., Park, Y., Kim, K., Park, B., et al. (2004). *In vitro* antibacterial and anti-inflammatory effects of honokiol and magnolol against Propionibacterium sp. *Eur. J. Pharmacol.* 496 (1-3), 189–195. doi:10.1016/j.ejphar.2004.05.047

Passos, F. R. S., Araújo-Filho, H. G., Monteiro, B. S., Shanmugam, S., Araújo, A. A. S., Almeida, J., et al. (2022). Anti-inflammatory and modulatory effects of steroidal saponins and sapogenins on cytokines: a review of pre-clinical research. *Phytomedicine* 96, 153842. doi:10.1016/j.phymed.2021.153842

Piazza, S., Martinelli, G., Maranta, N., Pozzoli, C., Fumagalli, M., Nicolaci, V., et al. (2024). Investigation into the anti-acne effects of Castanea sativa mill leaf and its pure ellagitannin castalagin in HaCaT cells infected with Cutibacterium acnes. *Int. J. Mol. Sci.* 25 (9), 4764. doi:10.3390/ijms25094764

Qin, X.-J., Chen, C.-X., Ni, W., Yan, H., and Liu, H.-Y. (2013). C22-steroidal lactone glycosides from stems and leaves of Paris polyphylla var. yunnanensis. *Fitoterapia* 84, 248–251. doi:10.1016/j.fitote.2012.12.007

Reynolds, R. V., Yeung, H., Cheng, C. E., Cook-Bolden, F., Desai, S. R., Druby, K. M., et al. (2024). Guidelines of care for the management of acne vulgaris. *J. Am. Acad. Dermatol* 90 (5), 1006.e1–1006.e30. doi:10.1016/j.jaad.2023.12.017

Richards, J., Ingham, H. R., Hickman, J., Crawford, P. J., Sengupta, R. P., and Mendelow, A. D. (1989). Focal infections of the central nervous system due to Propionibacterium acnes. *J. Infect.* 18 (3), 279–282. doi:10.1016/s0163-4453(89)80064-7

Rimon, A., Rakov, C., Lerer, V., Sheffer-Levi, S., Oren, S. A., Shlomov, T., et al. (2023). Topical phage therapy in a mouse model of Cutibacterium acnes-induced acne-like lesions. *Nat. Commun.* 14 (1), 1005. doi:10.1038/s41467-023-36694-8

Saising, J., and Voravuthikunchai, S. P. (2012). Anti Propionibacterium acnes activity of rhodomyrtone, an effective compound from Rhodomyrtus tomentosa (Aiton) Hassk. leaves. *Anaerobe* 18 (4), 400–404. doi:10.1016/j.anaerobe.2012.05.003

Saleemi, M. A., Yahaya, N., Zain, N. N. M., Raoov, M., Yong, Y. K., Noor, N. S., et al. (2022). Antimicrobial and cytotoxic effects of cannabinoids: an updated review with future perspectives and current challenges. *Pharm. (Basel)* 15 (10), 1228. doi:10.3390/ph15101228

Scandorieiro, S., Rodrigues, B. C. D., Nishio, E. K., Panagio, L. A., de Oliveira, A. G., Durán, N., et al. (2022). Biogenic silver nanoparticles strategically combined with origanum vulgare derivatives: antibacterial mechanism of action and effect on multidrug-resistant strains. *Front. Microbiol.* 13, 842600. doi:10.3389/fmicb.2022.842600

Sharma, R., Kishore, N., Hussein, A., and Lall, N. (2014). The potential of Leucosidea sericea against Propionibacterium acnes. *Phytochem. Lett.* 7, 124–129. doi:10.1016/j.phytol.2013.11.005

Silverberg, J. I., and Silverberg, N. B. (2014). Epidemiology and extracutaneous comorbidities of severe acne in adolescence: a U.S. population-based study. *Br. J. Dermatology* 170 (5), 1136–1142. doi:10.1111/bjd.12912

Sinha, P., Srivastava, S., Mishra, N., and Yadav, N. P. (2014). New perspectives on antiacne plant drugs: contribution to modern therapeutics. *BioMed Res. Int.* 2014, 301304–301319. doi:10.1155/2014/301304

Sirati, R., Khajehrahimi, A. E., Kazempoor, R., Kakoolaki, S., and Ghorbanzadeh, A. (2024). Development, physicochemical characterization, and antimicrobial evaluation of niosome-loaded oregano essential oil against fish-borne pathogens. *Heliyon* 10 (5), e26486. doi:10.1016/j.heliyon.2024.e26486

Sitthichai, P., Chanpirom, S., Maneerat, T., Charoensup, R., Tree-Udom, T., Pintathong, P., et al. (2022). Kaempferia parviflora rhizome extract as potential anti-acne ingredient. *Molecules* 27 (14), 4401. doi:10.3390/molecules27144401

Soltani, S., Shakeri, A., Iranshahi, M., and Boozari, M. (2021). A review of the phytochemistry and antimicrobial properties of origanum vulgare L. And subspecies. *Iran. J. Pharm. Res.* 20 (2), 268–285. doi:10.22037/ijpr.2020.113874.14539

Strathdee, S. A., Hatfull, G. F., Mutalik, V. K., and Schooley, R. T. (2023). Phage therapy: from biological mechanisms to future directions. *Cell* 186 (1), 17–31. doi:10.1016/j.cell.2022.11.017

Sultan, M. Z., Jeon, Y. M., and Moon, S. S. (2008). Labdane-type diterpenes active against acne from pine cones (Pinus densiflora). *Planta Med.* 74 (4), 449–452. doi:10.1055/s-2008-1034321

Taleb, M., Abdeltawab, N., Shamma, R., Abdelgayed, S., Mohamed, S., Farag, M., et al. (2018). Origanum vulgare L. Essential oil as a potential anti-acne topical nanoemulsion—*in vitro* and *in vivo* study. *Molecules* 23 (9), 2164. doi:10.3390/molecules23092164

Taylor, E. J., Yu, Y., Champer, J., and Kim, J. (2014). Resveratrol demonstrates antimicrobial effects against propionibacterium acnes *in vitro*. *Dermatol Ther. (Heidelb)* 4 (2), 249–257. doi:10.1007/s13555-014-0063-0

Thapa, C. B., Paudel, M. R., Bhattarai, H. D., Pant, K. K., Devkota, H. P., Adhikari, Y. P., et al. (2022). Bioactive secondary metabolites in Paris polyphylla Sm. and their biological activities: a review. *Heliyon* 8 (2), e08982. doi:10.1016/j.heliyon.2022.e08982

Theansungnoen, T., Phosri, S., Bumrungthai, S., Daduang, J., Klaynongsruang, S., and Daduang, S. (2022). Nov*el non*-cytotoxic antimicrobial peptides WSKK11 and WSRR11 with potent activity against Cutibacterium acnes. *J. Antimicrob. Chemother.* 77 (4), 1012–1019. doi:10.1093/jac/dkac014

Thiboutot, D., Gollnick, H., Bettoli, V., Dréno, B., Kang, S., Leyden, J. J., et al. (2009). New insights into the management of acne: an update from the global alliance to improve outcomes in acne group. *J. Am. Acad. Dermatology* 60 (5), S1–S50. doi:10.1016/j.jaad.2009.01.019

Titus, S., and Hodge, J. (2012). Diagnosis and treatment of acne. *Am. Fam. Physician* 86 (8), 734–740.

Torres-Barceló, C. (2018). The disparate effects of bacteriophages on antibiotic-resistant bacteria. *Emerg. Microbes Infect.* 7 (1), 168. doi:10.1038/s41426-018-0169-z

Trahan, L. (1995). Xylitol: a review of its action on mutans streptococci and dental plaque--its clinical significance. *Int. Dent. J.* 45 (1 Suppl. 1), 77–92.

Tucker, S. B., Rogers, R. S., Winkelmann, R. K., Privett, O. S., and Jordon, R. E. (1980). Inflammation in acne vulgaris: leukocyte attraction and cytotoxicity by comedonal material. *J. Invest Dermatol* 74 (1), 21–25. doi:10.1111/1523-1747.ep12514573

Ultee, A., Bennik, M. H., and Moezelaar, R. (2002). The phenolic hydroxyl group of carvacrol is essential for action against the food-borne pathogen Bacillus cereus. *Appl. Environ. Microbiol.* 68 (4), 1561–1568. doi:10.1128/aem.68.4.1561-1568.2002

Vestergaard, M., and Ingmer, H. (2019). Antibacterial and antifungal properties of resveratrol. *Int. J. Antimicrob. Agents* 53 (6), 716–723. doi:10.1016/j.ijantimicag.2019.02.015

Vora, L. K., Gholap, A. D., Hatvate, N. T., Naren, P., Khan, S., Chavda, V. P., et al. (2024). Essential oils for clinical aromatherapy: a comprehensive review. *J. Ethnopharmacol.* 330, 118180. doi:10.1016/j.jep.2024.118180

Vos, T., Flaxman, A. D., Naghavi, M., Lozano, R., Michaud, C., Ezzati, M., et al. (2012). Years lived with disability (YLDs) for 1160 sequelae of 289 diseases and injuries 1990–2010: a systematic analysis for the Global Burden of Disease Study 2010. *Lancet* 380 (9859), 2163–2196. doi:10.1016/s0140-6736(12)61729-2

Walsh, T. R., Efthimiou, J., and Dréno, B. (2016). Systematic review of antibiotic resistance in acne: an increasing topical and oral threat. *Lancet Infect. Dis.* 16 (3), e23–e33. doi:10.1016/s1473-3099(15)00527-7

Wang, M., Sun, Y., Gu, R., Tang, Y., Han, G., and Zhao, S. (2024). Shikonin reduces M2 macrophage population in ovarian cancer by repressing exosome production and the exosomal galectin 3-mediated β-catenin activation. *J. Ovarian Res.* 17 (1), 101. doi:10.1186/s13048-024-01430-3

Wang, X., Shen, Y., Thakur, K., Han, J., Zhang, J. G., Hu, F., et al. (2020). Antibacterial activity and mechanism of ginger essential oil against *Escherichia coli* and *Staphylococcus aureus*. *Molecules* 25 (17), 3955. doi:10.3390/molecules25173955

Watson, M., Saitis, T., Shareef, R., Harb, C., Lakhani, M., and Ahmad, Z. (2023). Shikonin and Alkannin inhibit ATP synthase and impede the cell growth in *Escherichia coli*. *Int. J. Biol. Macromol.* 253 (Pt 4), 127049. doi:10.1016/j.ijbiomac.2023.127049

Wei, M. P., Qiu, J. D., Li, L., Xie, Y. F., Yu, H., Guo, Y. H., et al. (2021). Saponin fraction from Sapindus mukorossi Gaertn as a novel cosmetic additive: extraction, biological evaluation, analysis of anti-acne mechanism and toxicity prediction. *J. Ethnopharmacol.* 268, 113552. doi:10.1016/j.jep.2020.113552

Wei, M.-p., Yu, H., Guo, Y.-h., Cheng, Y.-l., Xie, Y.-f., and Yao, W.-r. (2022). Synergistic antibacterial combination of Sapindoside A and B changes the fatty acid compositions and membrane properties of Cutibacterium acnes. *Microbiol. Res.* 255, 126924. doi:10.1016/j.micres.2021.126924

Wijesundara, N. M., and Rupasinghe, H. P. V. (2018). Essential oils from Origanum vulgare and Salvia officinalis exhibit antibacterial and anti-biofilm activities against Streptococcus pyogenes. *Microb. Pathog.* 117, 118–127. doi:10.1016/j.micpath.2018.02.026

Williams, H. C., Dellavalle, R. P., and Garner, S. (2012). Acne vulgaris. *Lancet* 379 (9813), 361–372. doi:10.1016/s0140-6736(11)60321-8

Wu, G.-X., Wang, Y.-W., Wu, C.-S., Lin, Y.-H., Hung, C.-H., Huang, H.-H., et al. (2021). Therapeutic efficacy of sesquiterpene Farnesol in treatment of Cutibacterium acnes-induced dermal disorders. *Molecules* 26 (18), 5723. doi:10.3390/molecules26185723

Wu, Y., Qiang, Y., Cao, K., Zhang, W., and Zhang, G. (2020). Inhibitory effect of the antimicrobial peptide BLP-7 against Propionibacterium acnes and its anti-inflammatory effect on acne vulgaris. *Toxicon* 184, 109–115. doi:10.1016/j.toxicon.2020.06.006

Xuan, G., Wang, Y., Wang, Y., Lin, H., Wang, C., and Wang, J. (2023). Characterization of the newly isolated phage Y3Z against multi-drug resistant Cutibacterium acnes. *Microb. Pathog.* 180, 106111. doi:10.1016/j.micpath.2023.106111

Xuan, J., Feng, W., Wang, J., Wang, R., Zhang, B., Bo, L., et al. (2023). Antimicrobial peptides for combating drug-resistant bacterial infections. *Drug Resist Updat* 68, 100954. doi:10.1016/j.drup.2023.100954

Yamaguchi, N., Satoh-Yamaguchi, K., and Ono, M. (2009). *In vitro* evaluation of antibacterial, anticollagenase, and antioxidant activities of hop components (Humulus lupulus) addressing acne vulgaris. *Phytomedicine* 16 (4), 369–376. doi:10.1016/j.phymed.2008.12.021

Yang, D., Pornpattananangkul, D., Nakatsuji, T., Chan, M., Carson, D., Huang, C.-M., et al. (2009). The antimicrobial activity of liposomal lauric acids against Propionibacterium acnes. *Biomaterials* 30 (30), 6035–6040. doi:10.1016/j.biomaterials.2009.07.033

Yashodhara, B. M., Umakanth, S., Pappachan, J. M., Bhat, S. K., Kamath, R., and Choo, B. H. (2009). Omega-3 fatty acids: a comprehensive review of their role in health and disease. *Postgrad. Med. J.* 85 (1000), 84–90. doi:10.1136/pgmj.2008.073338

Zhan, X., Tan, Y., Lv, Y., Fang, J., Zhou, Y., Gao, X., et al. (2022). The antimicrobial and antibiofilm activity of oregano essential oil against *Enterococcus faecalis* and its application in chicken breast. *Foods* 11 (15), 2296. doi:10.3390/foods11152296

Zhang, J., Yu, F., Fu, K., Ma, X., Han, Y., Ali, C. C., et al. (2022). C. Acnes qPCR-based antibiotics resistance assay (ACQUIRE) reveals widespread macrolide resistance in acne patients and can eliminate macrolide misuse in acne treatment. *Front. Public Health* 10, 787299. doi:10.3389/fpubh.2022.787299

Zhu, T., Zhu, W., Wang, Q., He, L., Wu, W., Liu, J., et al. (2019). Antibiotic susceptibility of Propionibacterium acnes isolated from patients with acne in a public hospital in Southwest China: prospective cross-sectional study. *BMJ Open* 9 (2), e022938. doi:10.1136/bmjopen-2018-022938

frontiers | Frontiers in Pharmacology

TYPE Review
PUBLISHED 12 February 2025
DOI 10.3389/fphar.2025.1548837

Check for updates

OPEN ACCESS

EDITED BY
Jinlong Ma,
Shandong Second Medical University, China

REVIEWED BY
Jatuporn Ngoenkam,
Naresuan University, Thailand
Yun He,
Southwest Medical University, China

*CORRESPONDENCE
Ping Zhao,
zhaop@swu.edu.cn

†These authors have contributed equally to this work

RECEIVED 20 December 2024
ACCEPTED 23 January 2025
PUBLISHED 12 February 2025

CITATION
Tian Z, Chen H and Zhao P (2025) Compliant immune response of silk-based biomaterials broadens application in wound treatment. *Front. Pharmacol.* 16:1548837. doi: 10.3389/fphar.2025.1548837

COPYRIGHT
© 2025 Tian, Chen and Zhao. This is an open-access article distributed under the terms of the Creative Commons Attribution License (CC BY). The use, distribution or reproduction in other forums is permitted, provided the original author(s) and the copyright owner(s) are credited and that the original publication in this journal is cited, in accordance with accepted academic practice. No use, distribution or reproduction is permitted which does not comply with these terms.

Compliant immune response of silk-based biomaterials broadens application in wound treatment

Zhiqiang Tian[1†], Hong Chen[2†] and Ping Zhao[1*]

[1]Biological Science Research Center, Integrative Science Center of Germplasm Creation in Western China (CHONGQING) Science City, Southwest University, Chongqing, China, [2]Department of Orthopedics, 903 Hospital of Joint Logistic Support Force of The People's Liberation Army, Hangzhou, China

The unique properties of sericin and silk fibroin (SF) favor their widespread application in biopharmaceuticals, particularly in wound treatment and bone repair. The immune response directly influences wound healing cycle, and the extensive immunomodulatory functions of silk-based nanoparticles and hydrogels have attracted wide attention. However, different silk-processing methods may trigger intense immune system resistance after implantation into the body. In this review, we elaborate on the inflammation and immune responses caused by the implantation of sericin and SF and also explore their anti-inflammatory properties and immune regulatory functions. More importantly, we describe the latest research progress in enhancing the immunotherapeutic and anti-inflammatory effects of composite materials prepared from silk from a mechanistic perspective. This review will provide a useful reference for using the correct processes to exploit silk-based biomaterials in different wound treatments.

KEYWORDS

biopharmaceuticals, nanomedicine, sericin, silk fibroin (SF), wound treatment

1 Introduction

Silk is a natural fiber with a long history. It is formed by the solidification of the silk liquid secreted by the mature silkworm during the cocoon phase. Silk is mainly composed of hydrophobic silk fibroin (SF), which forms the core fiber, and hydrophilic sericin, a globular protein that binds to SF (Johari et al., 2022; Silva et al., 2022). SF is rich in glycine, alanine and serine, while sericin mainly contains serine and threonine (Silva et al., 2022; Takahashi et al., 1999).

Initially, sericin was often discarded in large quantities as textile waste, resulting in environmental pollution and wastage of natural resources (Aramwit et al., 2012). With the rapid development of biomaterials, the use of sericin in medicines has received increasing attention. Sericin possesses outstanding antioxidant, anti-inflammatory, antibacterial, antiviral, and biological characteristics that promote tissue regeneration, making it important in curing diseases such as hypertension, cancer, and diabetes (Hu et al., 2022). In addition, sericin biomaterials exhibit good biocompatibility and low immunogenicity, and have been engineered

Abbreviations: CH, chitosan; SF, silk fibroin; SS1, sericin; HBsAg, hepatitis B surface antigen; IL-1/5/8/12/16/23, interleukin-1/5/8/12/16/23; TNF-α, tumor necrosis factor alpha; iNOS, inducible nitric oxide synthase; COX-2, Cyclooxygenase-2; LMW, low molecular weight; MMP, metalloproteinases; M1, classical activated macrophages; M2, Alternatively activated macrophages; BMP, morphogenetic protein; UC, ulcerative colitis; RA, rheumatoid arthritis; NF-κB, nuclear factor kappa-B; MAPK, mitogen-activated protein kinase; BM, *Bombyx mori*; PEG, polyethylene glycol; SCI, spinal cord injury.

into various biomaterials, including films, hydrogels, scaffolds, fiber pads, particles, coatings, conduits, and nanoparticles for tissue repair, regeneration, and disease cure (Qi et al., 2018; Shah et al., 2019; Li et al., 2020; Wang et al., 2021; Xu et al., 2022; Deng Y. et al., 2022; Ghensi et al., 2019; Fu et al., 2022). Over the past decade, sericin-based biomaterials have developed rapidly in drug-delivery and tissue engineering.

SF has superior biocompatibility, marked mechanical properties, controlled biodegradation rates, and ideal cellular-SF interactions (Gholipourmalekabadi et al., 2020; Wani et al., 2022; Wang et al., 2008). The application of silk in the textile industry has a long history and the preparation technology for silk is very mature; therefore, the source of SF is rich (Huang W. et al., 2018). These characteristics have made SF emerge among biomaterial applications in recent years. SF can be transformed into scaffolds, hydrogels, films, microspheres, and nanoparticles alone or in combination with other materials for tissue engineering such as nerves, bone and muscles, and can also be used in drug delivery systems for skin wound treatment, tumor immunotherapy, and other medical treatments (Cui et al., 2020; Wang D. et al., 2022; Wenhao et al., 2020; Del Bianco et al., 2022; Cai et al., 2023; Hassan et al., 2024).

The body possesses intricate and precise protective mechanisms. When silk is used as a medical material, the immune system often faces challenges. Silk medical materials require different processing techniques before implantation into the body, which can cause significantly alteration of the protein structure of the original silk, resulting in varying levels of immune system activation. This difference may be due to surface chemistry, protein conformation, and polymer formation with other proteins in the treated silk-based materials (Majumder et al., 2024). This has expanded the application of silk in the medical field and has extended the proinflammatory effects to anti-tumor, antibacterial, and vaccine adjuvant fields, although a low immune response contributes to bone, skin, and vascular repair. In this review, we aimed to provide profound discussion of the activation of a wide range of immune responses *in vivo* using silk-based biomaterials and describe the rigorous and accurate processing methods required for different clinical applications in subsequent research.

2 Immune responses induced by silk material in mammals

One of the most important characteristics of biomaterials is their biocompatibility, the initiation of the innate immune cells is the decisive factor in the biocompatibility of biomaterials. This process usually causes an inflammatory response, and the degree of the response resides mainly on the properties of the biomaterial (Ekdahl et al., 2011). In this section, we summarize and discuss the biosafety, immunogenicity and immunomodulatory properties of sericin and SF.

2.1 Sericin

2.1.1 Favorable biocompatibility and low immunogenicity

The biosafety of sericin has long been controversial. Studies have confirmed that sericin has good biocompatibility from the three standpoints of inflammation, allergy, and immunogenicity: (i) sericin only causes low response of inflammatory cells *in vivo* (macrophages and neutrophils) (Jiao et al., 2017; Li et al., 2015) (Figures 1A, B); (ii) neglected allergens (Jiao et al., 2017) and (iii) sericin only causes mild innate and adaptive immune responses (Jiao et al., 2017; Zhang et al., 2006; Zhang Y. et al., 2021; Panilaitis et al., 2003). Furthermore, the addition of sericin to a mixture of chitosan and silver nanoparticles (AgNPs) can reduce their immunogenicity (Nayak et al., 2021). Various forms of materials such as nanoparticles, hydrogels, scaffolds, sponges and films prepared from sericin have also not been found to cause marked immune responses or inflammatory reactions (such as mast cell degranulation) (Hassan et al., 2024; Ampawong and Aramwit, 2016). An important reason for the low immunogenicity of serine is that it is rich in hydrophilic amino acids. Inspired by this, poly-β-homoserineand poly-DL-serine materials can substantially reduce foreign body reactions and are expected to replace polyethylene glycol as an ideal implantable biological material (Zhang et al., 2020; Zhang D. et al., 2021) (Table 1).

2.1.2 Anti-inflammatory properties

Inflammation is the body's defense response to injury or infection and involves a variety of cellular and molecular mechanisms. In the process of tissue healing, inflammatory cells such as macrophages and neutrophils are first recruited to the injury site and release pro-inflammatory factors such as interleukin-1 beta (IL-1β), IL-6, tumor necrosis factor α (TNF-α), etc. These factors promote vascular dilation and increased permeability, attracting more immune cells to participate in the inflammatory response. It also activates the degradation and remodeling of extracellular matrix. Subsequently, anti-inflammatory factors such as IL-4 and IL-10 begin to play a role, inhibiting the production of pro-inflammatory factors, reducing the activity of inflammatory cells, and promoting tissue repair and regeneration (Eming et al., 2017). The balance of inflammation and inflammatory factors is crucial for tissue healing. Excessive inflammatory response may lead to increased tissue damage, while insufficient anti-inflammatory factors may delay the healing process.

Sericin preparations have found application in skin repair, blood sugar reduction, and treatment of acute myocardial infarction (Wang D. et al., 2022; Aramwit et al., 2013; Tuentam et al., 2022; Song et al., 2016) (Figure 1C). There are three main mechanisms through which sericin inhibits the inflammatory response: (i) inhibits infiltration and proliferation of inflammatory cells (Zhaorigetu et al., 2003; Chlapanidas et al., 2013); (ii) inhibits expression of IL-1β, IL-6, IL-23, etc (Song et al., 2016; Chlapanidas et al., 2013; Deenonpoe et al., 2019; Kumar J. P. et al., 2018; Dong et al., 2020; Farajdokht et al., 2021); and (iii) increases the expression of IL-4 andIL-10, etc (Seyedaghamiri et al., 2021; Aramwit et al., 2018) (Figures 1D, E). Notably, Sun et al. revealed the mechanism of sericin inhibiting lipopolysaccharide (LPS) induced inflammation by multi omics integration: (i) sericin inhibits LPS-activated PRRs, Toll-like receptors and NOD-like receptors pathways; (ii) sericin significantly downregulates the expression of the *MyD88* and *NOD1*; (iii) sericin decreases the expression of IL-1β, IL-6, INOS, etc (Sun et al., 2022). Interestingly, I-sericin is induced by γ-irradiation of sericin, and exhibits potent anti-inflammatory activities as the

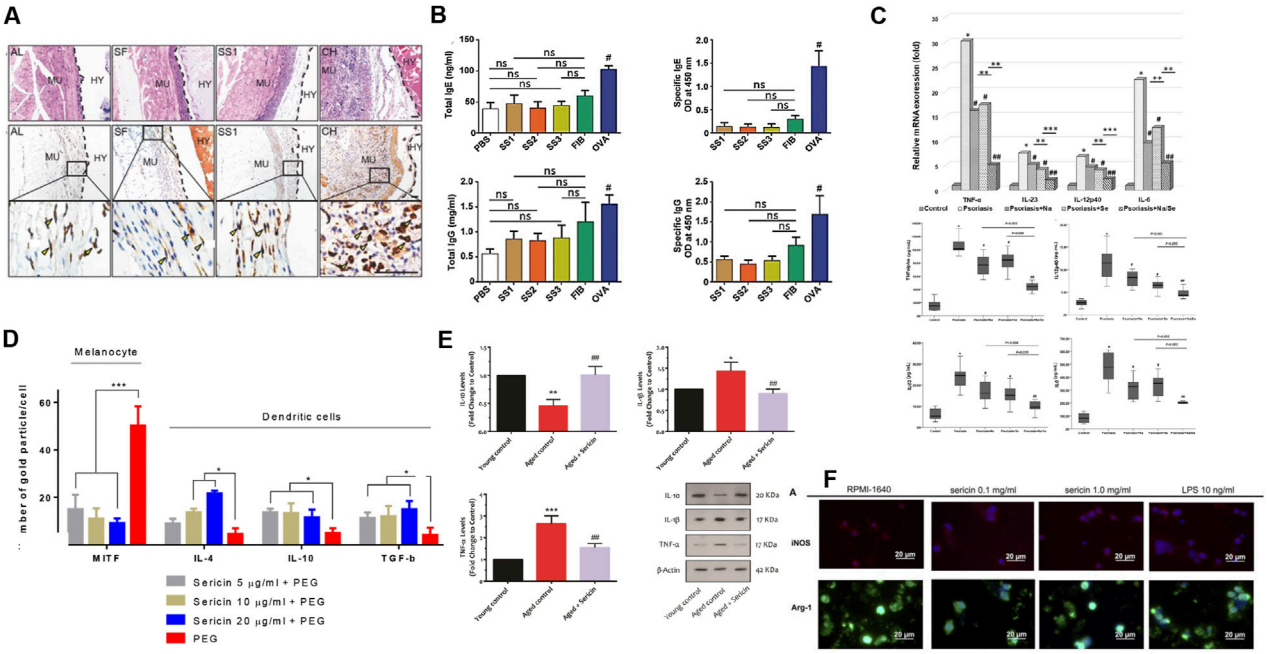


FIGURE 1
Sericin presents characteristics of good biocompatibility, low immunogenicity, inhibition of inflammatory responses, and good immune regulatory function. **(A)** Hematoxylin and eosin (H&E) staining following 10 days of implantation of AL, SF, SS1 and CH. AL, alginate; SF, silk fibroin; SS, sericin; CH, chitosan; MU, mouse muscles; HY, hydrogel-implanted sites. **(B)** ELISA results measuring total IgE, allergen-specific IgE, IgG (total) and induced by sericin, fibrinogen, PBS, and ovalbumin (OVA). Reprinted with permission from (Jiao et al., 2017). Copyright (2017) Wiley-VCH. **(C)** mRNA expression and cytokine production of proinflammatory factor in hPBMC from the psoriasis patients, who exposure to naringin (20 μg/mL), sericin (100 μg/mL), or sericin/naringin. Reprinted with permission from (Deenonpoe et al., 2019). Copyright (2019) BMC. **(D)** Expression of microphthalmia-associated transcription factor (MITF) and IL-4, IL-10, and TGF-β on melanocytes and DC 48 h after allergy induction treated with PEG or sericin (5, 10 and 20 μg/mL) + PEG. Reprinted with permission from (Aramwit et al., 2018). Copyright (2018) BMC. **(E)** Western blotting results of IL-10, IL-1β, and TNF-α in the young mice, adult mice, and older adult mice + oral sericin treatment groups (250 mg/kg, 21 days). Reprinted with permission from (Seyedaghamiri et al., 2021). Copyright (2021) Springer nature. **(F)** Arg-1 and iNOS immunofluorescence staining of macrophage treated with 0.1 mg/mL, 1 mg/mL LMW-sericin (<10 kDa) and 10 ng/mL lipopolysaccharide (LPS). Reprinted with permission from (Cherng et al., 2022).Copyright (2022) Frontiers.

parent molecule, including reduction of oxidative stress-induced inflammatory cytokines cyclooxygenase-2 (COX-2), inducible nitric oxide synthase (iNOS), TNF-α, IL-1β and alleviation of LPS-induced inflammation (Choi et al., 2023; Song et al., 2020).

2.1.3 Good immune regulatory function

Sericin reportedly modulates epidermal immune responses in patients with psoriasis by reducing cytokine production by Th17 cells, upregulating galectin-3 (Lgals3) and down-regulating sphingosine-1-phospholyase 1 (Sgpl1) (Rujimongkon et al., 2021). As recently shown, low molecular weight (LMW) sericin (<10 kDa) enhances immune regulation *in vitro*: LMW-sericin (0.1 mg/mL) can upregulate the expression of CXCL9, IL-12A, BMP-7, and IL-10 in macrophages; balance Th1 and Th2 levels; and induce M2 polarization of macrophages. Sericin regulates macrophage proliferation to achieve immune regulation (Cherng et al., 2022) (Figure 1F). In addition, I-sericin has immune-enhancing effects, manifested as a significant increase in lymphocyte proliferation and activation of NK cells (Song et al., 2020). In addition, biosynthetic sericin 1-like protein can induce tolerant dendritic cells (DCs), which have excellent immunomodulatory capabilities. The purity of sericin 1- like protein is positively correlated with the anti-inflammatory effect of sericin; therefore, it is expected to be developed as an immune modulator (Song et al., 2020; Ritprajak et al., 2021).

In summary, the good biocompatibility and low immunogenicity of sericin are now widely recognized, making it a new avenue for drug delivery and tissue engineering (Wang C. et al., 2022; Sapru et al., 2021). Moreover, the anti-inflammatory properties and good immune regulatory functions of sericin will greatly expand its clinical applications.

2.2 Silk fibroin (SF)

SF exhibits good biocompatibility and low immunogenicity; therefore, it is favored for application in biological materials. Many studies have explored inflammatory processes *in vitro* or *in vivo* of SF-based biomaterials in the form of hydrogels, scaffolds, films, and nanoparticles (Table 2).

2.2.1 SF hydrogel induce only a mild inflammatory response

SF can achieve solution-gel transition by altering the pH, temperature, and solvation state, or by increasing biopolymer dynamics (Matsumoto et al., 2006). Studies on the biocompatibility and low immunogenicity of hydrogels are often based on the histological evaluation of tissue reactions, with the main focus of observing changes in inflammatory markers, such as

TABLE 1 Application of sericin in the pharmaceutical field and induced immune responses.

Biomaterial	Bio-medical field	Immune cellular response	Effect	Reference
Nanomicelles	Tumor immunotherapy	Promote T cell recruiting; induce DC maturation	Induce anti-tumor immunity	Guo et al. (2022)
Hydrogels	Cancer chemotherapy	Enhance the phagocytic capacity of liver macrophages and promote the proliferation of splenic lymphocytes	Alleviate chemotherapy-induced immunosuppression	Xu et al. (2021)
Microparticles	Psoriasis	Increase the level of TNF-α secreted by LPS-induced human peripheral blood mononuclear cells (hPBMC)	Treat middle-stage psoriasis	Chlapanidas et al. (2014)
Scaffolds	Periodontitis	Downregulate the MMP-9 and MMP-3, upregulate the IL-10 in LPS-stimulated macrophages	Stable anti-inflammatory effect on periodontal disease treatment	Chachlioutaki et al. (2022)
Scaffolds	Chronic nerve compression	Downregulate TNF-α and IL-1β mRNA levels in macrophages	Achieve significant nerve functional recovery in a preclinical CNC animal mode	Zhang et al. (2017)
Hydrogels	Wound repair	Reduce inflammation and TNF-α secretion by macrophages	Promote wound healing	Jiang et al. (2021a)
Nanoparticles	Carrageenan-induced paw edema	Significantly decrease the infiltration of polymorphonuclear cells	Inhibit inflammation induced by carrageenan	Khampieng et al. (2015)
Nanocarriers	Ulcerative colitis	Reduce the infiltration of inflammatory cells in the liver and kidneys	Relieve symptoms of DSS induced UC	Wang et al. (2022b)
Hydrogels	Diabetic wounds	Reduce the infiltration of inflammatory cells at the wound site	Promote the healing of diabetic wounds	El-Samad et al. (2022)
Nanospheres	Ulcerative colitis	Inhibite the LPS-induced inflammatory response of the macrophage cells	Achieve effective therapeutic effects on ulcerative colitis	Xu et al. (2022)
Hydrogels	Ulcerative colitis	Inhibit IL-6 and IL-12 secreted by macrophages	Alleviate UC via wound healing, inhibit inflammation, and inhibit oxidation pathway	Ma et al. (2019)

neutrophils, eosinophils, and macrophages, in the SF hydrogel and the surrounding tissues (Fu et al., 2022; Etienne et al., 2009; Maity et al., 2022) (Figure 2A). However, these methods are not sufficiently precise to determine the biocompatibility and low immunogenicity of SF hydrogels. Therefore, advanced equipment and technical means are required to explore the inflammatory reaction caused by SF hydrogels in detail. Recently, using noninvasive bioluminescence imaging, Gorenkova et al. demonstrated that SF hydrogels elicited an acute but mild local inflammatory response *in vivo*, which elicited an innate immune response similar to that elicited by polyethylene glycol (PEG) hydrogels (Gorenkova et al., 2021) (Figure 2B). The Forster/fluorescence resonance energy transfer (FRET)-based sensor experiment developed by Kambe et al. first exposed the initial immune response of SF hydrogels. SF hydrogels are surrounded or invaded by matrix metalloproteinases (MMP) within 24 h after implantation and undergo biodegradation within 3 h after implantation, which may favor immune cells (macrophages, foreign body giant cells) to achieve major degradation of the hydrogel over a period of weeks (Kambe and Yamaoka, 2021; Janani et al., 2022) (Figure 2C).

2.2.2 SF scaffolds have low immunogenicity

The surface morphology, physical structure, and chemical structure of the scaffold play a decisive role in the reaction with immune cells, and these features also regulate macrophage polarization at the host tissue implant interface (Antmen et al., 2021). The SF scaffold reportedly has good biocompatibility and low immunogenicity through histological and immunofluorescence staining analysis (Fu et al., 2022; Wang et al., 2008; Guan et al., 2013; Yang et al., 2021; Ge et al., 2012; Suzuki et al., 2019; Singh et al., 2018). Recent studies have revealed the effects of SF scaffolds on macrophages. SF scaffold implants can inhibit classical activated macrophages (M1) and stimulate alternatively activated macrophages (M2) to regulate local inflammatory responses (Janani et al., 2022; Yang et al., 2021). Mast cells, an important type of immune cells, can be activated by biomaterials, which can trigger inflammation by releasing histamine, cytokines and other mediators, promote recruitment and activation of macrophages and other immune cells, and affect the immune microenvironment at the transplant site of biomaterials. Garg K et al. found that SF scaffolds were not conducive to mast cell adhesion and proliferation, suggesting that they were largely immune inert (Garg et al., 2011). The origin, protein conformation, amino acid sequence, fiber thickness, and porosity of SF play important roles in determining the macrophage phenotype, monocyte responsiveness, and T-cell activity (Janani et al., 2022; Yang et al., 2021; Bhattacharjee et al., 2013). Therefore, it is necessary to consider factors that affect the immune response when designing SF scaffolds.

2.2.3 SF nanoparticles/nanofilaments have anti-inflammatory properties and low immunogenicity

Evaluation of the innate and adaptive immunity of SF nanoparticles (SFNPs) *in vivo* demonstrate low immunogenicity and anti-inflammatory properties (Zhang Y. et al., 2021). SFNPs play an anti-inflammatory role and immunomodulatory properties in intestine of trinitrophenyl sulfonic acid-induced experimental colitis in rats, which is specifically manifested as reducing

TABLE 2 Application of SF in the pharmaceutical field and induced immune response.

Biomaterial	Bio-medical field	Immune cellular response	Effect	Reference
Nanoreactors	Cancer	Initiate M1 activation; therapy-triggered ICD	Beneficial for systemic tumor clearance	Yu et al. (2023)
Nanomotors	Cancer	Mature dendritic cells, enhance immune cell infiltration, polarize macrophages from M2 to M1, and inhibit Tregs	Causing changes in immunosuppressive TME and activating tumor suppressive immunity	Zhang et al. (2022a)
Nanocomposites	Cancer	Polarize macrophages towards M1, alter immunosuppressive TME	Promote immunotherapy for PD1/PD-L1 checkpoint	Tan et al. (2020)
Nanomotors	Cancer	Reduce the percentage of immunosuppressive Treg cells, activate and recruit tumor-infiltrating lymphocytes	Inhibit the proliferation and growth of primary and metastatic tumor cells	Cao et al. (2022)
Nanofibrous mats	Transcutaneous immunization	Induce effective Th1 and Th2 cellular and humoral immune response	Activation response to OVA	Yang et al. (2020)
Nanofibrous patches	Transcutaneous immunization	Promote the infiltration of T cells	Promote the apoptosis of tumor cells	Hong et al. (2021)
Hydrogels	Diabetes	Promote anti-inflammatory M2 macrophage polarization	Locally regulate the inflammatory response *in vivo*	Kumar et al. (2018b)
Microneedles	Vaccine	Increase B cell responses	Greatly enhanced the humoral immune response of subunit vaccines	Boopathy et al. (2019)
Microneedles	Vaccine	Generate stronger antigen-specific cellular immune responses	Improve protection against lethal influenza challenge in mice	Stinson et al. (2021)
Microneedles	Vaccine	Promote the proliferation of antigen-specific T cells and increase the level of antigen-specific CD8 T cells	Generate stronger cellular and humoral immunity than the initial vaccine	DeMuth et al. (2014)
Nano-adjuvants	Vaccine	Trigger Th1 and Th2 immune responses	Efficient protect to bladder and kidneys	Hasanzadeh et al. (2020)
Nano-adjuvants	Vaccine	Promote the proliferation and differentiation of CD4 TRM cells	Enhance the local immunity of the stomach	Xu et al. (2019)
Hydrogels	Vaccine	Promote the expansion of $CD4^{+}$TRM cell distribution within the gastric epithelium	Enhanced immune response against *Helicobacter felis*	Hu et al. (2020)
Nanoparticles	Immunotherapeutic agents	Enhance the capacity of macrophages to secrete immune cytokines	Notably improve CpG ODN delivery	Zhang et al. (2019)
Hydrogels	Rheumatoid arthritis	Reduce the capacity of THP-1 cells differentiated with Phorbol 12-myristate 13-acetate (PMA) and stimulated with LPS to secrete immune cytokines	Improve rheumatoid arthritis more effectively	Oliveira et al. (2020)
Hydrogels	Skin wounds	Promote M2 macrophage polarization	Accelerate wound healing	Chouhan et al. (2018), Pang et al. (2021), Mei et al. (2022), Qian et al. (2022b), Chen et al. (2023a)
Nanoparticles	Bone regeneration and repair	Promote M2 macrophage polarization	Promote osteoporotic fracture repair	Wang et al. (2022a)
Scaffolds	Bone regeneration and repair	Promote M2 macrophage polarization	Enhance bone regeneration	Xiang et al. (2021), Patel et al. (2022)
Nanoparticles	Ulcerative colitis	Promote M2 macrophage polarization	Alleviate immune response, retard progression and treat UC	Liu et al. (2022)
Nanoparticles	Ulcerative colitis	Increase the CD8 T and B cells, promote M2 macrophage polarization	Regulating innate immune response and enhancing the therapeutic effect of acute colitis	Du et al. (2022)
Nanoparticles	Ulcerative colitis	Promote M2 macrophage polarization	Substantially relieve UC symptoms	Ma et al. (2022)
Nanoparticles	Ulcerative colitis	Promote the secretion of proinflammatory cytokine in macrophages	Significant relief of symptoms of UC disease	Gou et al. (2019)

(Continued on following page)

TABLE 2 (*Continued*) Application of SF in the pharmaceutical field and induced immune response.

Biomaterial	Bio-medical field	Immune cellular response	Effect	Reference
Nano-micro fibrous woven scaffolds	Tendon tissue engineering	Regulating macrophage polarization towards M2	Notably facilitated Achilles tendon regeneration	Cai et al. (2023)
Scaffolds	Tendon adhesion	Promote M2 polarization of macrophages	Greatly mitigate tendon adhesion	Dong et al. (2021)
Engineering meshes	Pelvic organ prolapse	Promote M2 polarization of macrophages	Enhance tissue repair	Wu et al. (2022)
Hydrogels	Skin wounds	Reduce inflammatory cells	Promote skin appendage formation	Yin et al. (2022)
Scaffolds	Spinal cord injury	Reduce the macrophage/microglia (CD68 positive cells)	Facilitate regeneration of injured spinal cord	Li et al. (2016b)

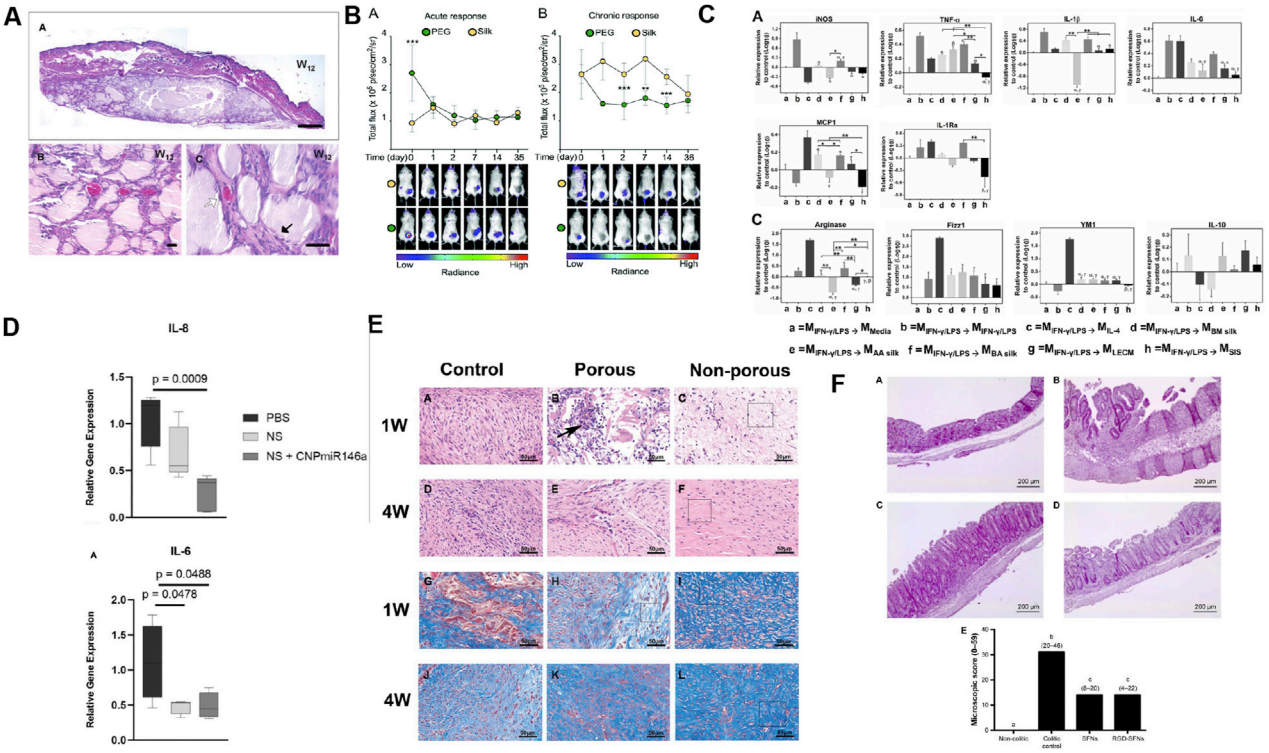


FIGURE 2
Biomaterials constructed with SF causes a modest inflammatory response and has low immunogenicity and anti-inflammatory properties. **(A)** The H&E staining of skin tissue from the backs of mice subcutaneously transplanted with SF after 12 weeks. Reprinted with permission from (Etienne et al., 2009). Copyright (2009) Wiley-VCH. **(B)** Non-invasive imaging of the acute and chronic inflammatory response towards implanted SF and PEG hydrogels. Reprinted with permission from (Gorenkova et al., 2021). Copyright (2021) the ROYAL SOCIETY of CHEMISTRY. **(C)** Relative expression of proinflammatory and pro-remodeling genes after exposure to degradation products of silk (*Bombyx mori* (BM) silk; *Antheraea assamensi* (AA) silk, and BA silk and ECM (liver ECM (LECM) and small intestinal submucosa ECM (SIS)) bioscaffolds on proinflammatory activated macrophages. Reprinted with permission from (Janani et al., 2022). Copyright (2022) Elsevier. **(D)** H&E staining of colon in non-colitic, colitic control, SFNs and RGD-SFNs group. Reprinted with permission from (Rodriguez-Nogales et al., 2016) Copyright (2016) Dovepress. **(E)** Proinflammatory gene expression of diabetic wounds treated with PBS, nanosilk (made from SF), and nanosilk + cerium oxide nanoparticle-microRNA146a (CNP-miR146a) after 7 days. Reprinted with permission from (Niemiec et al., 2020). Copyright (2020) Frontiers. **(F)** H&E and Masson trichrome staining were performed on the control group, porous SF membrane group, and non porous SF membrane group at 1 and 4 weeks postoperatively. Reprinted with permission from (Yao et al., 2019). Copyright (2019) Wiley-VCH.

neutrophil infiltration, decreasing the expression of IL-1β and promoting the expression of IL-10, while functionalization of arginine–glycine–aspartic acid (RGD) peptide can significantly improve its anti-inflammatory properties (Rodriguez-Nogales et al., 2016) (Figure 2D). In addition, a SF nanosilk solution reportedly reduces gene expression of the proinflammatory factor IL-6 accompanied by a tendency to reduce inflammatory cell infiltration early in the healing process (Niemiec et al., 2020) (Figure 2E).

SF films are also biocompatible, have low immunogenicity, and can reduce the infiltration of inflammatory cells. SF films are mainly used in wound healing and tissue repair (Ge et al., 2012; Arthe et al.,

2020; Yao et al., 2019) (Figure 2F). In addition, the transparent artificial dura made from SF effectively reduces the expression of IL-1β, IL-6, and TNF-α (Kim et al., 2011).

Notably, peptides produced by SF hydrolysis exhibit anti-inflammatory potential. SF peptide alone inhibits TPA-induced increase in COX-2, IL-6, IL-1β, and TNF-α levels, and significantly enhances the anti-inflammatory activity of Tat-SOD and PEP-1-FK506 binding proteins (Kim et al., 2011; Kim et al., 2012). γ-irradiated SF significantly enhances various aspects of the immune systems by activating NK cells, T-cell proliferation, NO production, and increasing cytokine levels (Byun et al., 2010). The anti-inflammatory potential of the SF hydrolysate and irradiation products suggests that further processing and treatment of SF will be a new strategy to explore its value.

3 Strategies to reduce the immunogenicity and foreign body reaction (FBR) of sericin-based and SF-based biomaterials

Compared with the current artificial materials, such as polylactic acid, PEG, etc., the degradation products of sericin and SF are small molecular amino acids, and possess lower inflammatory response and better biocompatibility, while the degradation products of artificial materials such as polylactic acid will produce obvious inflammatory response by reducing the pH value of the environment (Ma et al., 2024). Chemical crosslinking is an important strategy to reduce the immunogenicity of biomaterials. Based on the active groups on various amino acid residues in sericin and SF, it can be chemically modified to meet the needs of different applications. For instance, by introducing methacrylic acid group into the amino acid side chain of SF protein, the water solubility of SF protein can be improved, thus reducing the immunogenicity (Kim et al., 2021). Reducing the antigenic epitopes exposed by material surface modification is another important strategy to reduce the immunogenicity. For example, the introduction of specific bioactive molecules, such as PEG, on the surface of fibroin proteins can reduce the immunogenicity of SF (Wei et al., 2020).

Biomaterials implanted in the body will cause FBR, including local aseptic inflammatory responses, such as inflammatory cell infiltration, including macrophages, lymphocytes, neutrophils, etc. Over time, foreign-body giant cell form and eventually lead to fibrosis (Cai et al., 2024). In order to overcome the FBR, it is necessary to pay attention to the following characteristics when preparing sericin-based and SF-based biomaterials. Firstly, the mechanical properties of the hydrogels should be suitable for the implant site, and the lower stiffness helps to mitigate FBR (Blakney et al., 2012). Secondly, preventing protein adsorption by binding hydrogels with PEG or other novel anti-fouling biomaterials (such as zwitterionic or hydroxyl-rich polypeptides) is another attractive option (Zhou et al., 2024). Another method to mitigate FBR is to use biomimetic materials (such as decellularized extracellular matrix and mucins) mimic the extracellular matrix (ECM) of native tissues (Bhunia et al., 2023; Werlang et al., 2024). In regard to nanoparticles, surface functionalized by different chemical groups can affect the intensity of the FBR (Huang Y. J. et al., 2018; Huang et al., 2015). It is noteworthy that the membrane encapsulation to reduce the FBR of the nanoparticle has become another novel way (Fan et al., 2018).

Finally, the composition and MW of sericin and SF also play a key role in its immunogenicity. SF is a fibrous protein consisting of a heavy chain (H chain) (390 kDa), a light chain (L chain) (26 kDa), and a glycoprotein P25 (30 kDa), which are assembled in a ratio of 6: 6:1 (Inoue et al., 2000). Sericin is also a macromolecular protein, with MW ranges from about 10 kDa to over 300 kDa (Zhang, 2002). The MW of them is greatly affected by the extraction conditions. LMW-sericin (below 10 kDa) not only displays good biocompatibility, but also owns good anti-inflammatory ability to regulate macrophage polarization towards the M2 phenotype (Cherng et al., 2022). Therefore, it is another way to reduce the immunogenicity of sericin-based and SF-based biomaterials by optimizing the extraction and purification process to obtain the appropriate MW of sericin and SF.

4 Application of sericin biomaterial in medicine

Due to the good biocompatibility, low immunogenicity and outstanding immunomodulatory properties, sericin is highly favored in the biomedical field. Sericin-based biomaterials have shown excellent effects in improving immunotherapy and anti-inflammatory.

4.1 Improving immunotherapy

Immunotherapy is mainly a method of treating diseases by artificially enhancing or inhibiting the body's immune function. It is suitable for treating various diseases, including cancer and autoimmune diseases. Currently, the drug delivery system using sericin as a biological material for immune agents become a very promising method for immunotherapy.

4.1.1 Enhance anti-tumor immunotherapy

Small interfering RNA (siRNA) is essential for the effective inhibition of tumorigenesis, targeting of tumor metastasis, and activation of tumor-associated immune cells via silencing the specific gene (such as p65 and PD-L1) responsible for different cancer hallmarks (Ngamcherdtrakul and Yantasee, 2019). Using an effective delivery system, siRNAs can be selectively targeted to tumor microenvironment (TME), sent to regulatory T cells (Tregs), macrophages, myeloid-derived suppressor cells, and other cells to "silence" immunosuppressive cells, and enhance therapeutic immunotherapy (Deng K. et al., 2022; Qian H. et al., 2022; Li S. Y. et al., 2016; Hossain et al., 2015). Currently, sericin as a biological material has been designed as a delivery system for targeted delivery of siRNA. For example, a system consisting of superparamagnetic iron oxide nanoparticles (SPIONs) modified with sericin can target triple-negative breast cancer, accelerate tumor necrosis, and inhibit tumor proliferative growth (Shirangi et al., 2022). Furthermore, hyaluronic acid/poly-L-lysine-siRNA/albumin-sericin (2:1) nanoparticles can be used as siRNA delivery system for laryngeal cancer treatment (Yalcin et al., 2019). Therefore, it is expected that, in the future, serine will be

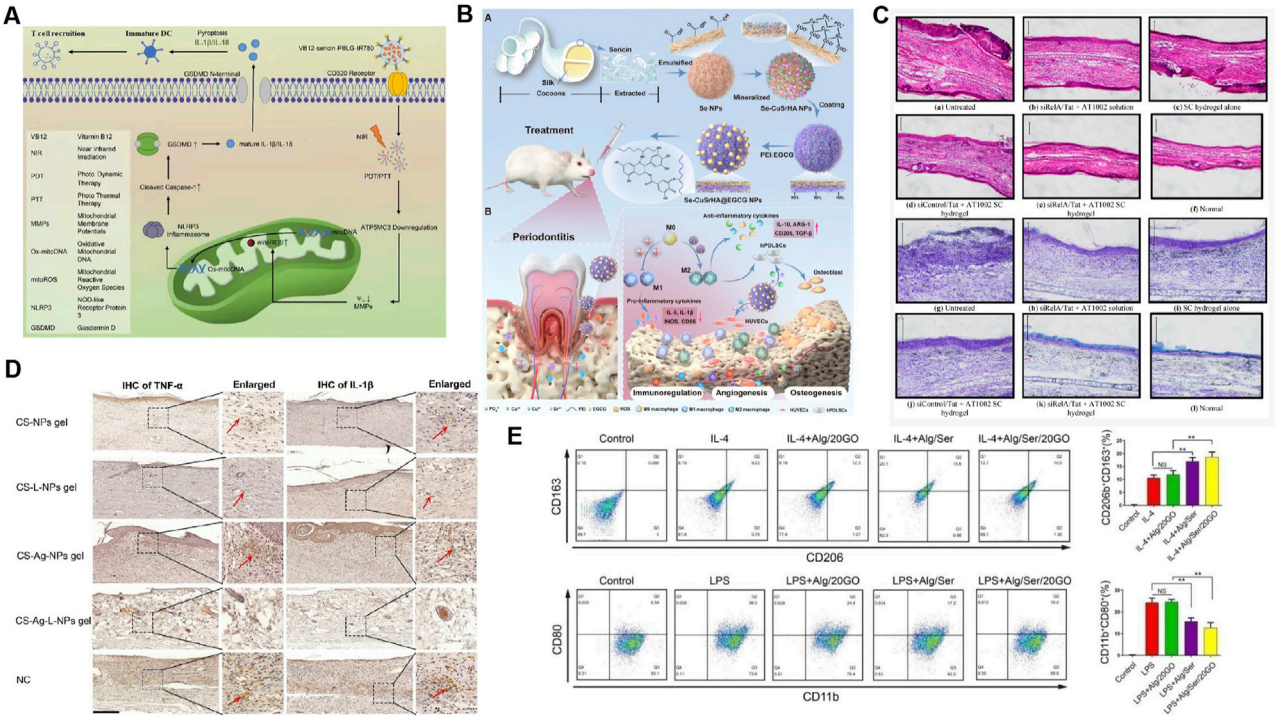


FIGURE 3
Application of sericin-based biomedical composites in immune regulation. **(A)** The preparation process and mechanism of VB12-sericin-PBLG-IR780 nanomicelles mediated pyroptosis are related to DC maturation, T cell recruitment, and tumor inhibition efficiency. Reprinted with permission from (Guo et al., 2022). Copyright (2022) ACS. **(B)** Treatment of atopic dermatitis in mice with siRelA sericin (SC) hydrogel. Observation of ear swelling (HE staining) and mast cell infiltration (TB staining) in tissue sections through optical microscopy. Reprinted with permission from (Kanazawa et al., 2015). Copyright (2015) MDPI. **(C)** Se-CuSrHA@EGCG Preparation and functional model diagram of nanoplatforms, including clearance of ROS, regulation of immune response, angiogenesis, and bone formation. Reprinted with permission from (Ming et al., 2025). Copyright (2025) Elsevier. **(D)** Chitosan (CS) - NPs gel, CS Lupeol (L) - NPs gel, CS Ag NPs gel and CS Ag L-NPs gel were used to treat skin wounds. The expression of TNF - α and IL-1 β in tissues was detected by immunohistochemistry. Reprinted with permission from (Chu et al., 2023). Copyright (2023) Elsevier. **(E)** Treated with IL-4 and alginate/sericin/graphene oxide (Alg/Ser/GO) hydrogel, the frequency of $CD206^+CD163^+$and $CD11b^+CD80^+$cells was analyzed by flow cytometry. Reprinted with permission from (Jiang et al., 2021a). Copyright (2021) Elsevier.

increasingly used as a biological material to design a drug delivery system to target siRNA to immunosuppressive cells in the TME, which will be a potential new direction for enhancing immunotherapy.

Photothermal therapy (PTT) and photodynamic therapy (PDT) are two novel cancer treatments. Their anti-tumor efficacy can be improved by inducing non-invasive pyroptosis of cancer cells and stimulating anti-tumor immune responses. For example, recently prepared VB12-Sericin-PBLG-IR780 nanomicelles not only trigger programmed pyroptosis in cancer cells but also activate DC maturation, initiate T-cell recruitment, and play a key role in anti-tumor processes (Guo et al., 2022) (Figure 3A).

In addition, during the treatment for tumors, although the use of chemotherapy drugs inhibits tumor formation and development, it can also have a negative impact on the immune system. Lactoferrin (LF), a common iron-binding glycoprotein, not only has the function of regulating iron metabolism, but also plays a crucial role in antibacterial, antiviral, anti-tumor and immune regulation (Jańczuk et al., 2022). A sericin hydrogel system for the delivery of recombinant human LF (SSH-rhLF) can prolong the bioactivity and bioavailability of rhLF and may have a therapeutic effect on the cyclophosphamide (CTX) induced immunosuppression mice by enhancing the function of liver macrophages, promoting the expression of immunoregulatory factors (IL-2, IL-21, IL-18, and CD-3), and promoting the proliferation of splenic lymphocytes (Xu et al., 2021). This provides a new strategy for enhancing immunity in patients undergoing cancer chemotherapy.

4.1.2 Involvement in immune regulation of autoimmune diseases

Atopic dermatitis (AD) is a common chronic inflammatory disease, for which immunotherapy is an important treatment (Li and Man, 2022). Sericin prepared in emulsion gel and hydrogel forms is very effective in correcting the abnormal immune response caused by AD by loading levocetirizine (an antihistamine), anti-RelA siRNA, and functional peptides (Pal et al., 2019; Kanazawa et al., 2015) (Figure 3B). Intra-articular injection of sericin hydrogel preparations containing anti-RelA siRNA also has great therapeutic potential for the treatment of rheumatoid arthritis (RA) (Kanazawa et al., 2017). Moreover, sericin-based microspheres loaded with racemic flavanone naringenin (a TNF-α blocker) helped to suppress LPS-induced serum TNF-α levels, which mediate immune disorders in psoriasis, and thus are expected to be a new modality for psoriasis immunotherapy (Chlapanidas et al., 2014).

4.2 Role in anti-inflammatory activity

Sericin has good adhesion and hydrophilicity, which helps to regulate the mechanical properties of biomaterials, enhance their degradation ability, promote cell adhesion and proliferation, and facilitate the sustained release of anti-inflammatory drugs, thereby enhancing their anti-inflammatory effects. From a mechanistic perspective, the drug delivery system and composite biomaterials involved in sericin play an anti-inflammatory role, mainly by promoting the M2 polarization of macrophages, inhibiting the proliferation and infiltration of inflammatory cells, and regulating the secretion of inflammatory mediators.

4.2.1 Inhibition of inflammation by promoting M2 polarization of macrophages

Macrophages are among the first cells to arrive at and interact with implanted materials and involved in regulating the resolution of inflammation, promoting tissue repair and regeneration. Mature macrophages are polarized into M1 or M2 subtypes. Classically activated M1 induced by IFN-γ, exhibit a proinflammatory phenotype. Activated M2 induced by IL-4 or IL-13 exhibit an anti-inflammatory phenotype (Kumar et al., 2016). During tissue repair, excessive and prolonged activation of proinflammatory M1 macrophages in the early stages of inflammation can lead to increased inflammation, thereby impairing tissue repair and regeneration (Martin and García, 2021; Bessa-Gonçalves et al., 2023). Therefore, accelerating the change in the macrophage from M1 to M2 is an important strategy in both biomaterial development and tissue repair/regeneration.

The polarization response of macrophages to biomaterials is currently being explored in three main approaches: (i) immunofluorescence staining using M1 surface markers (such as chemokine receptors 7, CCR7) and M2 surface markers (such as CD206) and observing results (Wang et al., 2020); (ii) determining cytokine secretion profiles of macrophages, which indirectly reflect macrophage phenotype (Wang et al., 2020; Chachlioutaki et al., 2022); (iii) examining the expression of M1 and M2 genes (Wang et al., 2020; Zhang et al., 2017; Jiang et al., 2021a). Sericin composite biomaterials in the form of scaffolds, films, hydrogels, and other treatments combined with drugs such as ketoprofen (an anti-inflammatory agent), nerve growth factor, and exosomes inhibit inflammatory responses by promoting macrophage M2/M1 conversion, which is exploited for tissue and peripheral nerve repair (Chachlioutaki et al., 2022; Zhang et al., 2017; Jiang et al., 2021a). Recently, the bone immune microenvironment, in which macrophages play a key role in reprogramming of the bone regeneration and immune microenvironment, has attracted increasing attention. Sericin released in an injectable alginate/serin/graphene oxide (Alg/Ser/GO) hydrogel promotes M2 polarization and migration through nuclear factor kappa-B (NF-κB) and mitogen-activated protein kinase (MAPK) signaling, inducing osteogenic differentiation and bone regeneration (Jiang et al., 2021a). Se-CuSrHA@ (epigallocatechin -3- gallate) EGCG (Figure 3C), a sericin-based nanoplatform, increases mRNA level of *Arg-1* and *CD206*, increases the secretion of anti-inflammatory cytokines, inhibit M1 while promoting the polarization of M2, balanced immune homeostasis, and accelerating bone regeneration (Ming et al., 2025). In another study, serine incorporated into a gelatin sponge polarizes M1 macrophages and promotes bone morphogenetic protein 2(BMP-2) secretion to enhance osteogenesis (Jo et al., 2021). Therefore, the factors through which sericin materials determine macrophage phenotypes may be complex and require further exploration.

4.2.2 Inhibition of the infiltration and proliferation of inflammatory cells

Sericin-composite biomaterials can also inhibit inflammatory cell proliferation and infiltration in the treatment of inflammatory diseases. Sericin-loaded alginate nanoparticles significantly reduce polymorphonuclear cell (PMN) infiltration and inhibit carrageenan-induced paw edema (Khampieng et al., 2015). The sericin/proanthocyanidin (PAC) composite reverses histological damage, including inflammatory cell infiltration and goblet cell loss, slowing disease progression and is a promising alternative therapeutic strategy for dextran sulfate sodium (DSS) -induced ulcerative colitis (UC) (Wang C. et al., 2022). In addition, the reduction of inflammatory cells in the surrounding tissues was observed at the initial stages of implantation of the alginate/sericin/graphene oxide (Alg/Ser/GO) hydrogel, which is conducive to bone regeneration (Jiang et al., 2021a). Sericin can promote chondrocyte differentiation and growth by activating the Smad2/3/TGF-β pathway and regulate local proinflammatory responses (Fongsodsri et al., 2024).

4.2.3 Regulate the release of inflammatory factors

In terms of wound treatment, carboxymethyl cellulose/sericin-based hydrogel dressing can downregulate the IL-1β, IL-6, and TNF-α to improve the pro-inflammatory response at the diabetic wound site (El-Samad et al., 2022; Bai et al., 2023). Hydrogels made of fibroin and sericin are excellent at promoting wound healing and reducing inflammation (Zhang D. et al., 2024; Ashraaf et al., 2023). Using sericin as a biological template, CuS@Ser NPs stimulate angiogenesis and inhibited inflammation, thereby facilitating rapid wound healing (Guo et al., 2023).

Another bacterial cellulose wound dressing made from sericin/polyhexamethylene biguanide has a strong ability to promote tissue secretion of IL-4 and TGF- β, thereby achieving a more efficient regulatory ability to promote wound treatment (Napavichayanun et al., 2018). In terms of psoriasis treatment, the combination of naringin and sericin in equal proportions significantly reduced the production IL-6, TNF-α and IL-23 in patients (Deenonpoe et al., 2019). Sericin-based poly (vinyl) alcohol (SS/PVA) hydrogel alleviates the development of psoriasis symptoms by up-regulating nuclear factor erythroid 2 related factor 2 (Nrf2), IL-10, and down-regulating TNF-α and IL-20 (Tuentam et al., 2022). In terms of colitis treatment, sericin composite biomaterials can alleviate UC by reducing the levels of proinflammatory cytokines TNF-α, IL2, IL-6, IL-17, and IL-12 and upregulating the levels of the anti-inflammatory cytokine IL-10 (Xu et al., 2022; Fongsodsri et al., 2024; Ma et al., 2019). The mixture of sericin and curcumin can inhibit carrageenan-induced foot edema in mice by suppressing the release of IL-1 β, promoting the secretion of IL-4 and IL-10 (Ashraaf et al., 2023).

The sericin composite biomaterials loaded with drugs can be used to treat inflammatory diseases by reducing the release of proinflammatory mediators, upregulating anti-inflammatory cytokines and macrophage polarization (Jiang et al., 2021a; Chu

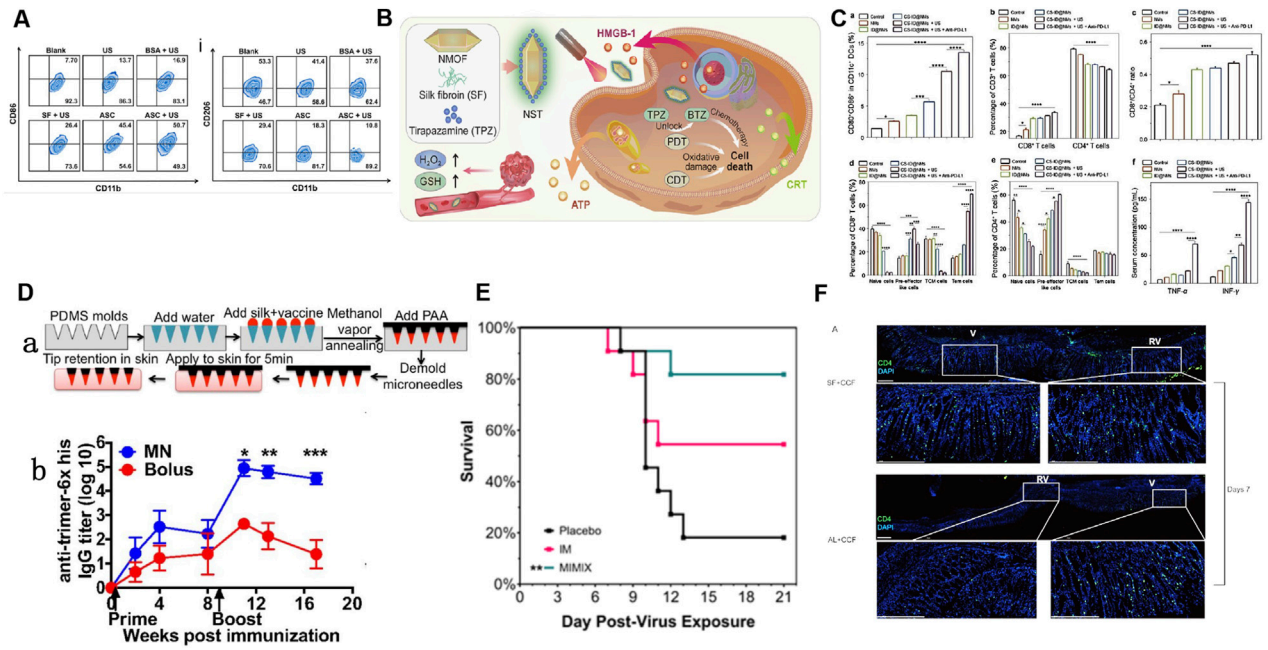


FIGURE 4
Application of SF-based biomedical composites in anti-tumor immune response and enhancing the immune response to vaccines. **(A)** Flow cytometry analysis showing the frequency of M1 and M2 macrophages after various treatments: ultrasound (US), bovine serum albumin (BSA)+US, SF + US, Au/SF@Cu2-xS nanoreactor (ASC), and ASC + US. Reprinted with permission from (Yu et al., 2022). Copyright (2023) Elsevier. **(B)** Schematic illustration of the synthetic route of NST NPs (metal-organic framework nanosystem (NMOF)+SF + tirapazamine (TPZ)) and the mechanism of synergistic induction of strong immune response by deoxygenation driven chemotherapy in the treatment of tumor specific redox imbalance. Reprinted with permission from (Yu et al., 2022a). **(C)** Impact of different types of oral nanomotors (NMs)-embedded hydrogel plus anti-PD-L1 on DC maturation, the ratio of $CD8^+/CD4^+$ T cells and changes, central memory cells (TCM), effector memory T cells in the mouse spleen and variations in cytokine levels (e.g., TNF-α and IFN-γ) in the mice serum. Reprinted with permission from (Cao et al., 2022). Copyright (2022) Wiley-VCH. **(D)** (a) Schematic of the fabrication and application to skin of SF/poly (acrylic acid) (PAA) composite microneedles. (b) ELISA analyses of anti-trimer-His serum IgG responses over time. Reprinted with permission from (Boopathy et al., 2019). Copyright (2018) PNAS. **(E)** Kaplan–Meier survival curves showing that MIMIX (SF-based microneedle patch) reduced mortality relative to control, whereas bolus vaccination vaccines did not significantly improve survival rates. Reprinted with permission from (Stinson et al., 2021). Copyright (2022) Elsevier. **(F)** Immunofluorescence staining in acute or steady-state conditions: Adding SF to vaccines can induce stronger immune responses and increase the distribution of $CD4^+$T cells in the gastric mucosa. Reprinted with permission from (Hu et al., 2020). Copyright (2020) Taylor and Francis.

et al., 2023) (Figures 3D, E). Sericin base biomaterial is a new and gradually emerging therapeutic strategy for wound treatment.

5 Application of SF in medicine

Compared with sericin, SF is more widely used in the field of tissue engineering and regenerative medicine attributed to its better mechanical properties and versatile processing capabilities. SF-based biomaterials have also played an outstanding role in enhancing immunotherapy and anti-inflammatory.

5.1 Improving immunotherapy

5.1.1 Enhanced anti-tumor immune response

SF has biocompatibility, controlled-release characteristics, and excellent mechanical and biological properties, such as immunomodulatory and anti-inflammatory properties, making it an excellent choice for the construction of composite biomaterials for tumor immunotherapy. Surface-engineered SF nanocomposites not only exhibit excellent anti-tumor functions but can also be combined with different types of tumor therapies to enhance tumor immunotherapy. The related mechanisms mainly include: (i) reversal of the immunosuppressive TME, including inducing the transformation of tumor-associated macrophages from M2 to M1 and reducing the number of Tregs (Zhang X. et al., 2022; Yu et al., 2022a; Tan et al., 2020; Yu et al., 2023) (Figures 4A, B); (ii) induction of immunogenic cell death (ICD) to stimulate anti-tumor immunity (Zhang X. et al., 2022; Yu et al., 2022a; Tan et al., 2020; Yu et al., 2023; Tkach et al., 2017); and (iii) promotion of the maturation of DCs, the formation of effector T cells and effector memory T cells to improve immune activation and promote immune memory (Zhang X. et al., 2022; Yu et al., 2022a; Tan et al., 2020; Tkach et al., 2017; Cao et al., 2022) (Figures 4A–C).

Transcutaneous immunization (TCI) enhances tumor immunotherapy by delivering antigens to DCs through skin. Compared to traditional oral or injection vaccinations, it has the advantages of excellent immunogenicity, avoidance of the liver first-pass effect, good compliance, safety, high efficiency, non-invasiveness, and ease of use (Karande and Mitragotri, 2010). However, the presence of a cuticular barrier leads to a low transdermal delivery efficiency of TCI, thereby limiting its large-scale clinical application. SF has good biocompatibility, air

permeability, and skin affinity, and can mimic the extracellular matrix, making it a good biological material for constructing transdermal drug delivery systems. Composite biomaterials constructed using SF can Stimulate cellular and humoral immune responses and induce systemic anti-tumor response by improving the transdermal properties of transdermal carriers, targeting, and inducing DCs maturation (Yang et al., 2020; Song et al., 2022). According to recent researches, the combination of SF-constructed percutaneous tumor immune materials and immune checkpoint blockers, such as programmed cell death protein 1 monoclonal antibody (aPD-1) which can enhance T-cell responses and mediate preclinical antitumor activity by blocking the binding of PD-1 on T cell with PD-L1 on cancer cells, may be a new strategy for effectively enhancing tumor immunotherapy. The involved mechanisms include: (i) promotion of the infiltration of CD4 and CD8 T cells into the tumor tissue, and (ii) promotion of the expression of IL-12, IFN-γ, and TNF-α (Song et al., 2022; Hong et al., 2021).

It is also of interest that SF has been used as a vaccine carrier for cancer immunotherapy. For example, Lei et al. recently developed an injectable SF microsphere loaded with an antigen and an immune adjuvant. Its macroporous structure is conducive for the recruitment of immune cells and can promote the activation of DCs to forms a favorable immune microenvironment. In turn, strong humoral and cellular immunity is induced. In addition, an enhanced vaccine modified by adsorbing antigens on SF microspheres effectively inhibits tumor growth by improving the cytotoxic T lymphocyte (CTL) response (Lei et al., 2022), properties that encourage a new approach for the future development of tumor immunotherapy vaccines.

5.1.2 Enhanced immune response to vaccines

Antigen delivery dynamics can influence the immune response to vaccines. For example, vaccine antigens can induce sustained humoral immunity after they are delivered to the lymph nodes to trigger naïve B cell response, whereas traditionally injected immunization can rapidly eliminate antigens, which is not conducive to the establishment of humoral and cellular immunity. Improving the immunogenicity of vaccine antigens and maintaining their slow release are new strategies for enhancing vaccine efficacy. The ability of the SF matrix to enclose and release intact and bioactive immunologically active materials has attracted much attention in the construction of slow-release novel vaccines (Reeves et al., 2015; Guziewicz et al., 2011; Kumar M. et al., 2018) (Figure 4D). The microneedle patch combined with the SF matrix can achieve the continuous release of vaccine antigens, enhance the immunogenicity of the vaccine, and thereby significantly enhance the degree, duration, and breadth of the humoral and cellular immune responses caused by the vaccine. Therefore, this represents a promising vaccine delivery strategy at present (Boopathy et al., 2019; Stinson et al., 2021; DeMuth et al., 2014) (Figure 4E).

SFNPs can enhance antigen target delivery, immunogenicity, and stability and can release antigens slowly and continuously, making them a promising new vaccine preparation. SFNPs was used as nanoadjuvants to deliver recombinant hepatitis B surface antigen (HBsAg) and FimH-IutA antigen, with the resulting vaccine significantly increasing the content of specific antibody IgG and promoting humoral and cellular immune responses (Rezaei et al., 2021; Hasanzadeh et al., 2020). Similarly, SF, which presents the advantages of sustained release, absorption, and *in situ* gelation in various tissues, has been used as a mucosal vaccine carrier. This vaccine carrier not only alleviates gastric injury but also leads to significant infiltration and generation of CD4 tissue-resident memory T (TRM) cellsin gastric epithelial tissues, which are the key mediators of anti-infection immunity in various tissues and have recently been shown to boost local stomach immunity (Schenkel et al., 2014; Xu et al., 2019; Hu et al., 2020) (Figure 4F).

5.1.3 Enhanced efficacy of immunotherapy drugs

CpG oligodeoxynucleotides (CpG ODNs) are short single-stranded synthetic DNA molecules which are designed to mimic bacterial DNA. These molecules are recognized by Toll-like receptor 9 (TLR9), which is expressed in certain immune cells such as myeloid cells, thus possess potent immune-stimulatory properties (Hekmatshoar et al., 2019). SFNPs have been used as effective carriers of CpG ODNs, which can significantly improve the delivery of CpG ODNs, as shown by the significantly enhanced cellular uptake and significantly increased levels of cytokines and nitric oxide produced following CpG ODN stimulation (Zhang et al., 2019).

SF has particularly excellent biocompatibility and can slowly degrade *in vivo*, has an excellent mechanical strength, and increases cell adhesion. Injectable hydrogels prepared by combining SF with other materials achieve controlled biodegradation and low mass loss and can be loaded with immunosuppressive agents such as methylprednisolone and betamethasone for cartilage regeneration and the treatment of rheumatoid arthritis (Phan et al., 2022; Oliveira et al., 2020).

Human bone marrow mesenchymal stem cells (hBMSC) are widely used in cell therapy because of their powerful proliferative and immune-regulatory abilities. SF films reportedly preserve not only the immunosuppressive effects of hBMSCs on T-cell proliferation and cytokine release, but also IL-6 secretion, and the immunophenotypes of hBMSCs (Luan et al., 2009).

5.2 Anti-inflammatory properties

5.2.1 Inhibition of inflammation via promotion of M2 polarization of macrophages

M2 macrophage polarization is an important immune regulatory event that reduces inflammation during wound repair, bone regeneration and repair, and colitis repair. Many composite biomaterials targeting this key event have been developed based on the excellent mechanical properties, biocompatibility, and bioactivity of SF. For example, Silk-6/ε-PL@Exo (constructed from SF/poly-L-lysine hydrogel) controls inflammation, inhibits glycolysis and lactic acid accumulation by targeting M1 macrophages, and promotes the polarization of macrophages from M1 to M2 (Jin et al., 2024). The inflammatory response induced by SF is not fixed: SF/nano-hydroxyapatite scaffolds trigger a proinflammatory response by M1 macrophages on the first day, whereas SF degradation products induce an anti-inflammatory response by M2 macrophages on the day 24 of treatment (Wong et al., 2024). Lv et al. found that SF treated

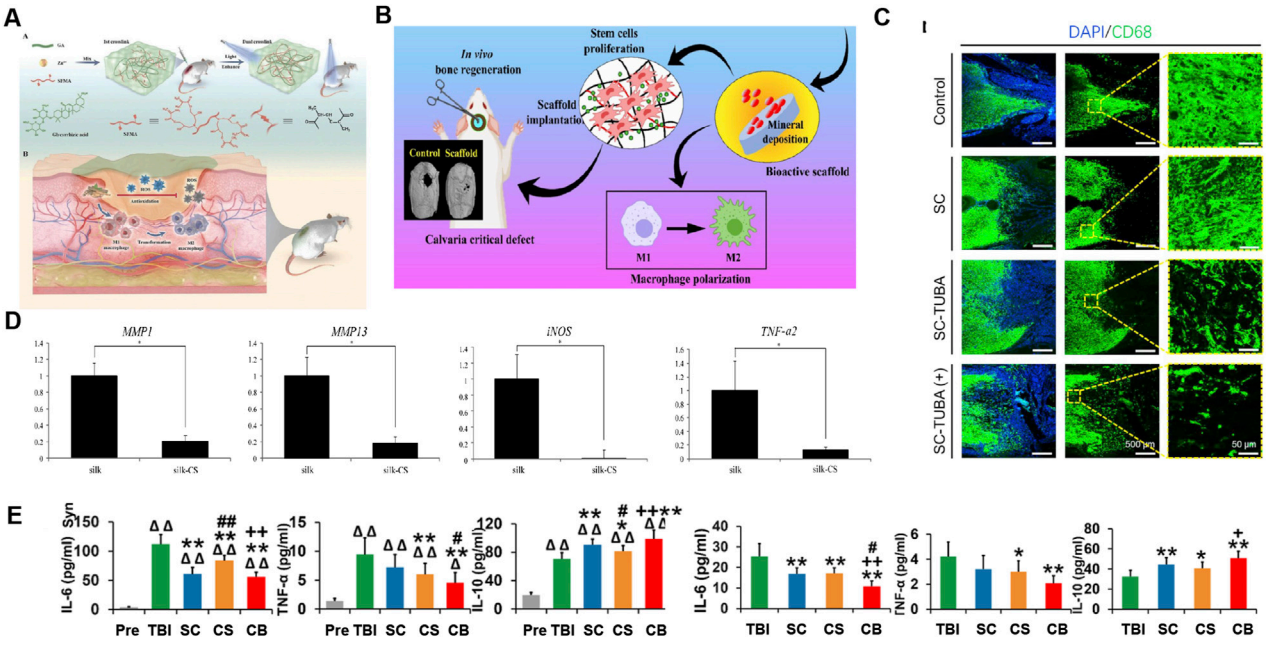


FIGURE 5
Application of SF-based biomedical composites in inhibiting inflammation. **(A)** Preparation of SF/GA/Zn hybrid hydrogel and its immunomodulatory mechanism in wound treatment of diabetes. Reprinted with permission from (Qian Y. et al., 2022). Copyright (2022) Wiley-VCH. **(B)** Schematic of the osteo-immunomodulatory effects of three-dimensional-printed biodegradable cellulose nanoparticles-reinforced chitosan/silk fibroin (CS/SF/CNPs) scaffolds. Reprinted with permission from (Patel et al., 2022). Copyright (2022) Elsevier. **(C)** The CD68 antibody fluorescence staining image confirmed the inhibitory effect of the hybrid poly (glycolide-co-ε-caprolactone) (PGCL)/SF-Tubasatin A (TUBA) multi-channel bioactive filament nanofiber catheters on inflammation after SCI. Reprinted with permission from (Liao et al., 2022). Copyright (2022) Elsevier. **(D)** RT-PCR displays the expression levels of genes *MMP-1, MMP-13, iNOS*, and *TNF-α2* activated by IL-1β, were dramatically lower in the silk-chondroitin sulfate (CS) scaffolds compared with the silk scaffold. Reprinted with permission from (Zhou et al., 2017). Copyright (2017) Elsevier. **(E)** The expression of IL-6, TNF-α, and IL-10 showed that the implantation of collagen/SF scaffold combined with human umbilical cord mesenchymal stem cells (hUCMSCs) regulated systemic inflammatory factor levels in the acute and chronic stages of traumatic brain injury. Reprinted with permission from (Jiang J. et al., 2021). Copyright (2021) Theranostics.

with reagents such as acetic acid and sodium hydroxide increased the expression of proinflammatory cytokines in rats and accelerated their degradation *in vivo*. Overall, most studies suggest that SF has good biocompatibility and anti-inflammatory properties.

Owing to the dissolution of the scaffold by protease K in the body, the secondary/tertiary structure of SF is altered, leading to significantly different immune responses. Maintaining the stability of SF in the body is of great clinical value, and bioactive gold cluster sutures (clusters assembled on the SF surface) ensure the structural stability of SF for 15 months without degradation *in vivo* (Tian et al., 2024).

5.2.1.1 Wound treatment and macrophage polarization

Wound treatment promotes M2 polarization of macrophages to establish anti-inflammatory niche required for tissue healing, which is critical for skin wound treatment. SF hydrogels can significantly increase the expression of the anti-inflammatory marker CD163 in M2 macrophages in the early stage, accelerating the transition from inflammation to the proliferation stage of wound repair (Chouhan et al., 2018). Considering that the SF hydrogel system has a controlled drug delivery capacity, good mechanical properties, skin tissue adhesion, and bioactivity, the combination of other biomaterials and therapeutic drugs will not only be beneficial for promoting angiogenesis in the wound area but will also induce M2 polarization in the wound area to create a pro-healing anti-inflammatory microenvironment. For example, after *in situ* photocuring, methacrylonyloxylated SF hydrogel showed good adhesion and sealing properties. Currently, two methacryloxylated SF hydrogel systems loaded with borosilicate and metformin have been prepared, both of which can regulate inflammation by inducing macrophage polarization towards the anti-inflammatory phenotype M2 and support diabetic wound treatment (Pang et al., 2021; Mei et al., 2022; Wu et al., 2021; Wang et al., 2023; Li et al., 2023). In addition, novel glycyrrhizic acid and inorganic zinc in the immunoregulatory SF/novel glycyrrhizic acid/inorganic $Zn2^{+}$ (SF/GA/Zn) hydrogels synergistically reduce the activation of M1-type macrophages, induced an M2 phenotype shift, and accelerate the three stages of diabetic wound repair (Qian Y. et al., 2022) (Figure 5A).

SF can co-self-assemble with VEGF-mimicking peptides to construct an immunoregulatory hydrogel, QK-SF, which supports tissue repair and wound healing by regulating macrophage polarization and promoting angiogenesis (Chen Z. et al., 2023). Similarly, gelatin methacrylate/silk fibroin glycidyl methacrylate/mesoporous silica NP-resveratrol/platelet-derived extracellular vesicles (GelMA/SFMA/MSN-RES/PDEVs) hydrogels have appropriate mechanical properties and swelling ratios, which allow sustainable release of MS-RES and PDEVs to regulate macrophage to M2 phenotype conversion, promote angiogenesis, and accelerate the diabetic wound treatment process (Zhu et al., 2022).

5.2.1.2 Bone regeneration and repair

During the process of fracture healing, the first stage is acute inflammation, followed by a transition to repair and regeneration. Therefore, the development of bone immunoregulatory biomaterials that favor polarization of the M2-phenotype macrophages is a novel strategy for bone regeneration and repair (Hu et al., 2018). SFNPs improve the bioavailability of hydrophobic anti-inflammatory drugs. Ti-MAO/Sr/LBL_{WNP} prepared according to this strategy can continuously release wogonin, which can transform M1 macrophages into M2 macrophages, regulate the ratio of M1/M2 macrophages, and promote osteoblast differentiation (Wang D. et al., 2022). SF also has the ability to release cytokines locally and can be used for the local release of sitagliptin to induce macrophages to polarize to the M2 phenotype and effectively recruit M2 macrophages to the titanium implant site to support bone regeneration (Xiang et al., 2021). In addition, the addition of SF/cellulose nanofibrils (CNFs) makes three-dimensional printing of chitosan/SF/cellulose nanoparticle scaffolds, and on activation of the M2 phenotype, macrophage polarization and immune regulation contribute to bone regeneration (Patel et al., 2022) (Figure 5B). A composite hydrogel composed of photoresponsive methacrylate SF, laponite nanocomposite, and tannic acid has the ability to resist oxidation and inflammation and induce bone formation (Wang et al., 2024). SF/black phosphorus/lycrhizic acid nanocomposite hydrogels can weaken the damage caused by oxygen free radicals, promote macrophage polarization towards M2, inhibit proinflammatory effects, and enhance the repair of damaged bone marrow (Zhang B. et al., 2024). Multilayered regenerated SF (RSF) on the surface of PET artificial ligaments regulates the inflammatory response and promotes the maturation of intra-articular grafts (Chen N. et al., 2023).

5.2.1.3 Colitis

Oral nanoparticles have been used to treat ulcerative (UC) as they can deliver drugs directly to the colonic region and are more convenient, achieving high patient compliance and safety (Zu et al., 2021). Therapeutic strategies for the treatment of UC include enhancing inflammation resolution, alleviating oxidative stress, promoting colonic mucosal repair, and regulating the intestinal flora. Macrophage M2 polarization is conducive to resolving inflammation and promoting mucosal healing, and has recently been shown to involved in the treatment of inflammatory bowel disease (IBD) (Koelink et al., 2020; Sun et al., 2020). At present, improving the targeting and co-treatment of UC from multiple aspects is the most recent strategy for preparing UC therapeutic drug delivery systems. Specific ideas include (i) modifying oral nanoparticles with ligands that specifically target colonic epithelial cells or macrophages (Li et al., 2022) and (ii) using drugs with multiple therapeutic functions (Zu et al., 2021). In line with this strategy, SFNPs have been designed as oral nanodrug delivery systems to exert multiple therapeutic effects (such as promoting macrophage M2 polarization) by the targeted delivery of therapeutic agents to the colonic mucosa and to significantly alleviate UC symptoms (Liu et al., 2022; Du et al., 2022; Ma et al., 2022; Gou et al., 2019).

In addition, the prepared SF composite biomaterials with immune regulatory functions can regulate macrophage M2 polarization, which is used to promote tendon repair, prevent tendon adhesion, and promote pelvic floor tissue repair (Cai et al., 2023; Dong et al., 2021; Yin et al., 2022).

5.2.2 Inhibition the infiltration and proliferation of inflammatory immune cells

Composite biomaterial systems in the form of hydrogels, scaffolds, and nanoparticles prepared using SF can be loaded with anti-inflammatory drugs, endowing them with anti-inflammatory activity by inhibiting the infiltration and proliferation of inflammatory immune cells. For example, SF hydrogels loaded with EGCG, rhein, and glycyrrhizic acid can effectively reduce the infiltration and proliferation of inflammatory cells (Qian Y. et al., 2022; Yin et al., 2022; Lee et al., 2022; Zhang F. et al., 2022). For the scaffold system, a gelatin sponge scaffold modified with neurotrophin-3 (NT-3)/SF can achieve a controlled-artificial release system with significant inflammatory inhibitory activity in the rat spinal cord injury (SCI) model, as shown by a significant reduction in the number of IBA-1 positive and CD68 positive macrophages/microglia (Li et al., 2018; Li G. et al., 2016). SF NP drug delivery systems loaded with bromelain and ZnO NPs, EGCG and Tubasatin A is effective in reducing the massive infiltration and proliferation of inflammatory cells (Liu et al., 2022; Hasannasab et al., 2021; Xie et al., 2022; Liao et al., 2022) (Figure 5C).

In particular, it is worth noting that SFNPs have anti-inflammatory properties, which can inhibit the infiltration and proliferation of inflammatory immune cells and can cooperate with anti-inflammatory drugs to exert anti-inflammatory effects. Therefore, SFNPs are a suitable choice for the preparation of anti-inflammatory composite biomaterials.

5.2.3 Repair of immune homeostasis by modulating the release of inflammatory factors

5.2.3.1 Wound treatment and induction of inflammatory factors

SF exhibits excellent biocompatibility, very low immunogenicity, great modification potential, and can regulate wound treatment process through the NF-κB signaling pathway, and thus, it has attracted much attention (Chouhan and Mandal, 2020). However, SF materials are brittle and have rapid enzymatic biodegradability, which limits their application in wound healing. Therefore, they are usually complemented with other polymers to optimize their effects for wound treatment (Shen et al., 2022). SF hydrogels, scaffolds, and nanofibrous membrane systems have been developed to promote wound treatment by loading anti-inflammatory drugs and regulating the release of inflammatory factors to repair immune homeostasis. The SF hydrogel system can reduce the expression of IL-1, IL-6, IL-8 and TNF-α, and can increase the expression of IL-10, TGF-β, and Arg-1 by loading resveratrol, novel glycyrrhiza, CNP-miR146a, and borosilicate (BS). Inhibition of inflammation in the wound microenvironment accelerates the transition from the inflammatory to proliferative phase, thereby accelerating diabetic wound treatment (Niemiec et al., 2020; Pang et al., 2021; Qian Y. et al., 2022; Zhu et al., 2022; Yang et al., 2024). In addition, SF composite biomaterials loaded with rhein and puerarin promote the inflammatory stage of the wound by reducing the levels of IL-6, Inos, COX-2 and TNF-α, and correspondingly increasing the levels of IL-10, thereby

promoting wound treatment process (Liu et al., 2022; Yin et al., 2022).

5.2.3.2 Articular cartilage repair

IL-1β is a proinflammatory factor, which induces inflammation and hinders articular cartilage repair (Wojdasiewicz et al., 2014). Therefore, it is an effective therapeutic strategy to use SF composite biomaterials system to deliver anti-inflammatory drugs to inhibit IL-1β and create an anti-inflammatory microenvironment to promote the repair of articular cartilage. At present, ginsenoside Rb1/TGF-β1-loaded biodegradable SF-gelatin scaffolds, SF-chondroitin sulfate scaffolds and injectable SF hydrogels containing articular chondrocytes (ACs) and hypoxic preconditioned exosomes (H-Exos) (SF/ACs/H-Exos) have been developed, all of which can reduce the inflammatory response of chondrocytes induced by IL-1β and support cartilage regeneration (Shen et al., 2022; Zhou et al., 2017; Wu et al., 2020) (Figure 5D).

5.2.3.3 Colitis and delivery of anti-inflammatory drugs

As a non-toxic drug carrier with good biocompatibility, immunogenicity, and low biodegradability, SF can effectively treat colitis by preparing a NP system to deliver anti-inflammatory drugs to the inflamed parts of the colon. It is reported that SFNPs system loaded with pluronic F127 (PF127) -modified resveratrol (RSV), EGCG, patchouli alcohol (PA), and curcumin (CUR) can downregulate proinflammatory cytokines such as IL-1β, IL-6, IL-12, and TNF-α, upregulate anti-inflammatory cytokines such as IL-10, thus effectively alleviating the inflammatory response (Liu et al., 2022; Du et al., 2022; Gou et al., 2019; Xie et al., 2022).

5.2.3.4 Nerve regeneration

Stem cell transplantation and biological scaffold implantation are considered effective methods for nerve regeneration. Safety and biocompatibility are two key factors in material selection for nerve regeneration research. SF is an excellent carrier for cell and growth factor delivery, a natural material with good biocompatibility, good mechanical properties, and biodegradability, and is reportedly a favorable choice for the repair of SCI and traumatic brain injury (Xu et al., 2016; Jiang et al., 2020). The inflammatory response in the injured area of the nervous system will inhibit nerve regeneration; thus, SF scaffolds with anti-inflammatory effects have also been developed, mainly by reducing the proinflammatory cytokines IL-6 and TNF-α, and increasing the anti-inflammatory cytokines IL-10 to inhibit inflammation and promote nerve regeneration (Li G. et al., 2016; Jiang J. et al., 2021) (Figure 5E).

SF hydrogel significantly improves skin penetration and the anti-keratinization ability of curcumin-loaded NPs (CUR-NPs), and can prolong the release of curcumin-loaded NPs; thus, inhibition of inflammatory cytokines (TNF-αand IL-6) is achieved to a greater extent with improvements in the therapeutic efficacy of curcumin on psoriasis mouse model (Mao et al., 2017). In addition, neutrophil membrane-coated SF-NPs can enhance the bioavailability and solubility of ferulic acid (FA), improve its pharmacological characteristics and targeted delivery, thereby significantly reducing proinflammatory cytokines IL-6, IL-1β and TNF-α (Hassanzadeh et al., 2021). Similarly, liquid SF along with the RES-SFN treatment achieved better results than each of these treatments used separately, and showed a more significant reduction in the proinflammatory cytokines IL-1β and TGF-β (Giménez-Siurana et al., 2020).

6 Conclusion

SF and sericin have been widely used in wound treatment, tissue engineering, and other fields in the form of hydrogels, scaffolds, films, and nanoparticles in recent decades. These different

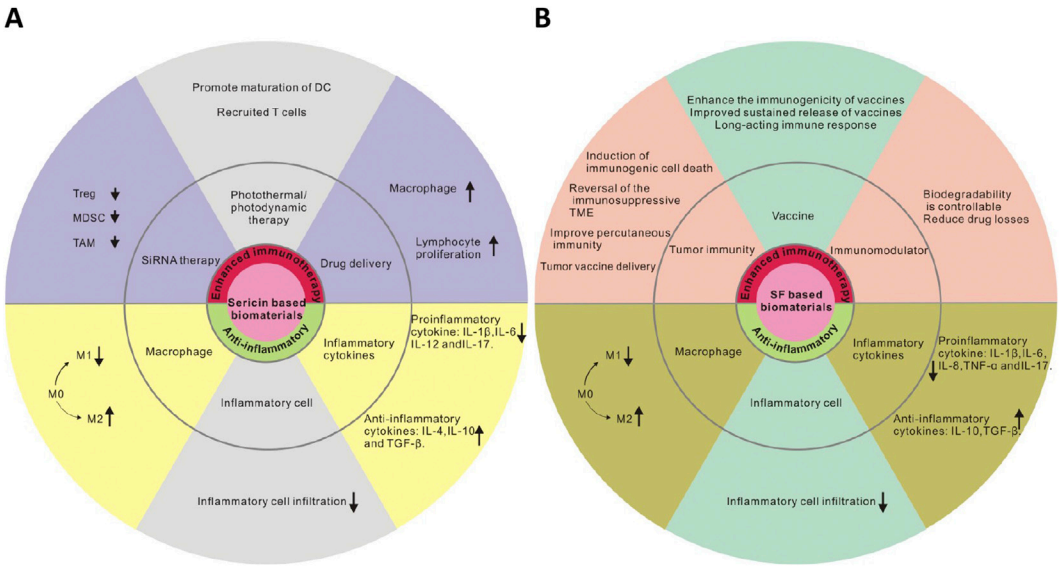


FIGURE 6
Immune response induced by **(A)** sericin/**(B)** SF-based biomaterials *in vivo* and their application.

processing methods enable them to play different roles in the wound treatment process (proinflammatory and antibacterial stage or anti-inflammatory and healing promoting stage).

Our review focused on the anti-inflammatory and immunoregulatory effects of SF and sericin as biomaterials, particularly in the field of wound treatment. SF and sericin have been shown to be safe, biocompatible, and to exhibit low immunogenicity, and can elicit appropriate and acceptable immune responses *in vivo*, including innate and adaptive immune responses, when used alone or prepared in various forms of biomaterials. The anti-inflammatory and immune regulatory properties of sericin and SF make them widely used in skin wound treatment, UC, articular cartilage repair, and psoriasis. In addition to individual applications, they can also be combined with other materials to make composite materials using their modifiability, controllable biodegradability, and good mechanical properties, which can not only be used to improve the properties of single anti-inflammatory drugs, but also give full play to their own immune regulation and anti-inflammatory ability. These composites can improve existing immunotherapy methods, such as delivery of siRNA, enhancement of cellular immunity, and can be exploited as vaccine carriers to exert immune regulation. SF and sericin composites can also exert anti-inflammatory effects by promoting M2 polarization of macrophages, inhibiting the proliferation and infiltration of inflammatory cells, and regulating the release of inflammatory factors (Figure 6).

There are still many challenges to be faced regarding the application of sericin-based and SF-based biomaterials in the field of medical biomedicine. For instance, due to the lack of standardized methods for assessing immune responses, it is difficult to make a comprehensive assessment of implant-induced immune responses (Kaprin et al., 2022). Additionally, it has also been well-known that epithelial cells and other types of immune cells (such as mast cells) equally play a significant role in the direct immune responses. However, there are few researches have explored their inflammatory response to sericin-based and SF-based biomaterials. Last but not least, there are some limitations of sericin-based and SF-based biomaterials in wound applications: (i) The extraction and purification process of SF and sericin is complicated, and other substances are easy to remain, which affects the purity and properties of the biomaterials; (ii) Compared to sericin, SF lacks antibacterial and antioxidant properties, so it is not effective in preventing wound infection.

In conclusion, SF and sericin exhibit good biocompatibility, low immunogenicity, controllable biodegradability, good mechanical properties, and excellent anti-inflammatory and immunomodulatory properties. A profound understanding of the different ways in which SF/sericin acts as a biomaterial and induces either proinflammatory or hypoinflammatory responses in the body will greatly improve utilization rate of silk biomaterials, especially in the field of wound treatment.

Author contributions

ZT: Writing–original draft, Writing–review and editing. HC: Writing–original draft. PZ: Conceptualization, Data curation, Writing–review and editing.

Funding

The author(s) declare that financial support was received for the research, authorship, and/or publication of this article. The National Natural Science Foundation of China (No. 32172798), The Natural Science Foundation of Chongqing (No. CSTB2024NSCQ-MSX0517) and Medical and Health Science and Technology Program of Zhejiang (No. 2025KY1192) provided support for this work.

Acknowledgments

We would like to thank Editage (www.editage.cn) for English language editing.

Conflict of interest

The authors declare that the research was conducted in the absence of any commercial or financial relationships that could be construed as a potential conflict of interest.

Generative AI statement

The author(s) declare that no Generative AI was used in the creation of this manuscript.

Publisher's note

All claims expressed in this article are solely those of the authors and do not necessarily represent those of their affiliated organizations, or those of the publisher, the editors and the reviewers. Any product that may be evaluated in this article, or claim that may be made by its manufacturer, is not guaranteed or endorsed by the publisher.

References

Ampawong, S., and Aramwit, P. (2016). Tolerogenic responses of CD206+, CD83+, FOXP3+, and CTLA-4 to sericin/polyvinyl alcohol/glycerin scaffolds relevant to IL-33 and HSP60 activity. *Histol. Histopathol.* 31 (9), 1011–1027. doi:10.14670/hh-11-733

Antmen, E., Vrana, N. E., and Hasirci, V. (2021). The role of biomaterials and scaffolds in immune responses in regenerative medicine: macrophage phenotype modulation by biomaterial properties and scaffold architectures. *Biomater. Sci.* 9 (24), 8090–8110. doi:10.1039/d1bm00840d

Aramwit, P., Luplertlop, N., Kanjanapruthipong, T., and Ampawong, S. (2018). Effect of urea-extracted sericin on melanogenesis: potential applications in post-inflammatory hyperpigmentation. *Biol. Res.* 51 (1), 54. doi:10.1186/s40659-018-0204-5

Aramwit, P., Siritientong, T., and Srichana, T. (2012). Potential applications of silk sericin, a natural protein from textile industry by-products. *Waste Manag. Res.* 30 (3), 217–224. doi:10.1177/0734242x11404733

Aramwit, P., Towiwat, P., and Srichana, T. (2013). Anti-inflammatory potential of silk sericin. *Nat. Prod. Commun.* 8 (4), 501–504. doi:10.1177/1934578x1300800424

Arthe, R., Arivuoli, D., and Ravi, V. (2020). Preparation and characterization of bioactive silk fibroin/paramylon blend films for chronic wound healing. *Int. J. Biol. Macromol.* 154, 1324–1331. doi:10.1016/j.ijbiomac.2019.11.010

Ashraaf, S., Tahir, H. M., Raza, C., Awad, E. M., Ali, S., Khan, S. Y., et al. (2023). Synergistic effect of silk sericin and curcumin to treat an inflammatory condition. *J. Burn Care Res.* 44 (1), 106–113. doi:10.1093/jbcr/irac157

Bai, L., Zhang, X., Li, X., Wang, S., Zhang, Y., and Xu, G. (2023). Impact of a novel hydrogel with injectable platelet-rich fibrin in diabetic wound healing. *J. Diabetes Res.* 2023, 7532637. doi:10.1155/2023/7532637

Bessa-Gonçalves, M., Ribeiro-Machado, C., Costa, M., Ribeiro, C. C., Barbosa, J. N., Barbosa, M. A., et al. (2023). Magnesium incorporation in fibrinogen scaffolds promotes macrophage polarization towards M2 phenotype. *Acta Biomater.* 155, 667–683. doi:10.1016/j.actbio.2022.10.046

Bhattacharjee, M., Schultz-Thater, E., Trella, E., Miot, S., Das, S., Loparic, M., et al. (2013). The role of 3D structure and protein conformation on the innate and adaptive immune responses to silk-based biomaterials. *Biomaterials* 34 (33), 8161–8171. doi:10.1016/j.biomaterials.2013.07.018

Bhunia, B. K., Bandyopadhyay, A., Dey, S., and Mandal, B. B. (2023). Silk-hydrogel functionalized with human decellularized Wharton's jelly extracellular matrix as a minimally invasive injectable hydrogel system for potential nucleus pulposus tissue replacement therapy. *Int. J. Biol. Macromol.* 254, 127686. doi:10.1016/j.ijbiomac.2023.127686

Blakney, A. K., Swartzlander, M. D., and Bryant, S. J. (2012). The effects of substrate stiffness on the *in vitro* activation of macrophages and *in vivo* host response to poly(ethylene glycol)-based hydrogels. *J. Biomed. Mater Res. A* 100 (6), 1375–1386. doi:10.1002/jbm.a.34104

Boopathy, A. V., Mandal, A., Kulp, D. W., Menis, S., Bennett, N. R., Watkins, H. C., et al. (2019). Enhancing humoral immunity via sustained-release implantable microneedle patch vaccination. *Proc. Natl. Acad. Sci. U. S. A.* 116 (33), 16473–16478. doi:10.1073/pnas.1902179116

Byun, E. B., Sung, N. Y., Kim, J. H., Choi, J. I., Matsui, T., Byun, M. W., et al. (2010). Enhancement of anti-tumor activity of gamma-irradiated silk fibroin via immunomodulatory effects. *Chem. Biol. Interact.* 186 (1), 90–95. doi:10.1016/j.cbi.2010.03.032

Cai, F., Jiang, B., and He, F. (2024). Formation and biological activities of foreign body giant cells in response to biomaterials. *Acta Biomater.* 188, 1–26. doi:10.1016/j.actbio.2024.08.034

Cai, J., Liu, J., Xu, J., Li, Y., Zheng, T., Zhang, T., et al. (2023). Constructing high-strength nano-micro fibrous woven scaffolds with native-like anisotropic structure and immunoregulatory function for tendon repair and regeneration. *Biofabrication* 15, 025002. doi:10.1088/1758-5090/acb106

Cao, Y., Liu, S., Ma, Y., Ma, L., Zu, M., Sun, J., et al. (2022). Oral nanomotor-enabled mucus traverse and tumor penetration for targeted chemo-sono-immunotherapy against colon cancer. *Small* 18 (42), e2203466. doi:10.1002/smll.202203466

Chachlioutaki, K., Karavasili, C., Adamoudi, E., Bouropoulos, N., Tzetzis, D., Bakopoulou, A., et al. (2022). Silk sericin/PLGA electrospun scaffolds with anti-inflammatory drug-eluting properties for periodontal tissue engineering. *Biomater. Adv.* 133, 112723. doi:10.1016/j.msec.2022.112723

Chen, N., Jin, W., Gao, H., Hong, J., Sun, L., Yao, J., et al. (2023b). Sequential intervention of anti-inflammatory and osteogenesis with silk fibroin coated polyethylene terephthalate artificial ligaments for anterior cruciate ligament reconstruction. *J. Mater Chem. B* 11 (34), 8281–8290. doi:10.1039/d3tb00911d

Chen, Z., Wang, L., Guo, C., Qiu, M., Cheng, L., Chen, K., et al. (2023a). Vascularized polypeptide hydrogel modulates macrophage polarization for wound healing. *Acta Biomater.* 155, 218–234. doi:10.1016/j.actbio.2022.11.002

Cherng, J. H., Chang, S. J., Chiu, Y. K., Chiu, Y. H., Fang, T. J., and Chen, H. C. (2022). Low molecular weight sericin enhances the *in vitro* of immunological modulation and cell migration. *Front. Bioeng. Biotechnol.* 10, 925197. doi:10.3389/fbioe.2022.925197

Chlapanidas, T., Faragò, S., Lucconi, G., Perteghella, S., Galuzzi, M., Mantelli, M., et al. (2013). Sericins exhibit ROS-scavenging, anti-tyrosinase, anti-elastase, and *in vitro* immunomodulatory activities. *Int. J. Biol. Macromol.* 58, 47–56. doi:10.1016/j.ijbiomac.2013.03.054

Chlapanidas, T., Perteghella, S., Leoni, F., Faragò, S., Marazzi, M., Rossi, D., et al. (2014). TNF-α blocker effect of naringenin-loaded sericin microparticles that are potentially useful in the treatment of psoriasis. *Int. J. Mol. Sci.* 15 (8), 13624–13636. doi:10.3390/ijms150813624

Choi, J. H., Lee, S., Han, H. J., and Kwon, J. (2023). Antioxidation and anti-inflammatory effects of gamma-irradiated silk sericin and fibroin in H2O2-induced HaCaT Cell. *Korean J. Physiol. Pharmacol.* 27 (1), 105–112. doi:10.4196/kjpp.2023.27.1.105

Chouhan, D., Lohe, T. U., Samudrala, P. K., and Mandal, B. B. (2018). *In situ* forming injectable silk fibroin hydrogel promotes skin regeneration in full thickness burn wounds. *Adv. Healthc. Mater* 7 (24), e1801092. doi:10.1002/adhm.201801092

Chouhan, D., and Mandal, B. B. (2020). Silk biomaterials in wound healing and skin regeneration therapeutics: from bench to bedside. *Acta Biomater.* 103, 24–51. doi:10.1016/j.actbio.2019.11.050

Chu, W., Wang, P., Ma, Z., Peng, L., Guo, C., Fu, Y., et al. (2023). Lupeol-loaded chitosan-Ag(+) nanoparticle/sericin hydrogel accelerates wound healing and effectively inhibits bacterial infection. *Int. J. Biol. Macromol.* 243, 125310. doi:10.1016/j.ijbiomac.2023.125310

Cui, T., Yu, J., Li, Q., Wang, C. F., Chen, S., Li, W., et al. (2020). Large-scale fabrication of robust artificial skins from a biodegradable sealant-loaded nanofiber scaffold to skin tissue via microfluidic blow-spinning. *Adv. Mater* 32 (32), e2000982. doi:10.1002/adma.202000982

Deenonpoe, R., Prayong, P., Thippamom, N., Meephansan, J., and Na-Bangchang, K. (2019). Anti-inflammatory effect of naringin and sericin combination on human peripheral blood mononuclear cells (hPBMCs) from patient with psoriasis. *BMC Complement. Altern. Med.* 19 (1), 168. doi:10.1186/s12906-019-2535-3

Del Bianco, L., Spizzo, F., Yang, Y., Greco, G., Gatto, M. L., Barucca, G., et al. (2022). Silk fibroin films with embedded magnetic nanoparticles: evaluation of the magneto-mechanical stimulation effect on osteogenic differentiation of stem cells. *Nanoscale* 14 (39), 14558–14574. doi:10.1039/d2nr03167a

DeMuth, P. C., Min, Y., Irvine, D. J., and Hammond, P. T. (2014). Implantable silk composite microneedles for programmable vaccine release kinetics and enhanced immunogenicity in transcutaneous immunization. *Adv. Healthc. Mater* 3 (1), 47–58. doi:10.1002/adhm.201300139

Deng, K., Yang, D., and Zhou, Y. (2022b). Nanotechnology-based siRNA delivery systems to overcome tumor immune evasion in cancer immunotherapy. *Pharmaceutics* 14 (7), 1344. doi:10.3390/pharmaceutics14071344

Deng, Y., Yang, C., Zhu, Y., Liu, W., Li, H., Wang, L., et al. (2022a). Lamprey-teeth-Inspired oriented antibacterial sericin microneedles for infected wound healing improvement. *Nano Lett.* 22 (7), 2702–2711. doi:10.1021/acs.nanolett.1c04573

Dong, L., Li, L., Song, Y., Fang, Y., Liu, J., Chen, P., et al. (2021). MSC-derived immunomodulatory extracellular matrix functionalized electrospun fibers for mitigating foreign-body reaction and tendon adhesion. *Acta Biomater.* 133, 280–296. doi:10.1016/j.actbio.2021.04.035

Dong, X., Zhao, S. X., Yin, X. L., Wang, H. Y., Wei, Z. G., and Zhang, Y. Q. (2020). Silk sericin has significantly hypoglycaemic effect in type 2 diabetic mice via anti-oxidation and anti-inflammation. *Int. J. Biol. Macromol.* 150, 1061–1071. doi:10.1016/j.ijbiomac.2019.10.111

Du, Y., Shi, J., Duan, R., Tsim, K. W. K., Shen, L., Zhang, N., et al. (2022). cRGD peptide incorporated with patchouli alcohol loaded silk fibroin nanoparticles for enhanced targeting of inflammatory sites in colitis. *Biomater. Adv.* 140, 213069. doi:10.1016/j.bioadv.2022.213069

Ekdahl, K. N., Lambris, J. D., Elwing, H., Ricklin, D., Nilsson, P. H., Teramura, Y., et al. (2011). Innate immunity activation on biomaterial surfaces: a mechanistic model and coping strategies. *Adv. Drug Deliv. Rev.* 63 (12), 1042–1050. doi:10.1016/j.addr.2011.06.012

El-Samad, L. M., Hassan, M. A., Basha, A. A., El-Ashram, S., Radwan, E. H., Abdul Aziz, K. K., et al. (2022). Carboxymethyl cellulose/sericin-based hydrogels with intrinsic antibacterial, antioxidant, and anti-inflammatory properties promote re-epithelization of diabetic wounds in rats. *Int. J. Pharm.* 629, 122328. doi:10.1016/j.ijpharm.2022.122328

Eming, S. A., Wynn, T. A., and Martin, P. (2017). Inflammation and metabolism in tissue repair and regeneration. *Science* 356 (6342), 1026–1030. doi:10.1126/science.aam7928

Etienne, O., Schneider, A., Kluge, J. A., Bellemin-Laponnaz, C., Polidori, C., Leisk, G. G., et al. (2009). Soft tissue augmentation using silk gels: an *in vitro* and *in vivo* study. *J. Periodontol.* 80 (11), 1852–1858. doi:10.1902/jop.2009.090231

Fan, Z., Li, P. Y., Deng, J., Bady, S. C., and Cheng, H. (2018). Cell membrane coating for reducing nanoparticle-induced inflammatory responses to scaffold constructs. *Nano Res.* 11 (10), 5573–5583. doi:10.1007/s12274-018-2084-y

Farajdokht, F., Vatandoust, S. M., Hosseini, L., Fekri, K., Rahigh Aghsan, S., Majdi, A., et al. (2021). Sericin protects against acute sleep deprivation-induced memory impairment via enhancement of hippocampal synaptic protein levels and inhibition of oxidative stress and neuroinflammation in mice. *Brain Res. Bull.* 174, 203–211. doi:10.1016/j.brainresbull.2021.06.013

Fongsodsri, K., Tiyasatkulkovit, W., Chaisri, U., Reamtong, O., Adisakwattana, P., Supasai, S., et al. (2024). Sericin promotes chondrogenic proliferation and differentiation via glycolysis and Smad2/3 TGF-β signaling inductions and alleviates inflammation in three-dimensional models. *Sci. Rep.* 14 (1), 11553. doi:10.1038/s41598-024-62516-y

Fu, Z., Li, W., Wei, J., Yao, K., Wang, Y., Yang, P., et al. (2022). Construction and biocompatibility evaluation of fibroin/sericin-based scaffolds. *ACS Biomater. Sci. Eng.* 8 (4), 1494–1505. doi:10.1021/acsbiomaterials.1c01426

Garg, K., Ryan, J. J., and Bowlin, G. L. (2011). Modulation of mast cell adhesion, proliferation, and cytokine secretion on electrospun bioresorbable vascular grafts. *J. Biomed. Mater Res. A* 97 (4), 405–413. doi:10.1002/jbm.a.33073

Ge, Z., Yang, Q., Xiang, X., and Liu, K. Z. (2012). Assessment of silk fibroin for the repair of buccal mucosa in a rat model. *Int. J. Oral Maxillofac. Surg.* 41 (5), 673–680. doi:10.1016/j.ijom.2011.11.016

Ghensi, P., Bettio, E., Maniglio, D., Bonomi, E., Piccoli, F., Gross, S., et al. (2019). Dental implants with anti-biofilm properties: a pilot study for developing a new sericin-based coating. *Mater. (Basel)* 12 (15), 2429. doi:10.3390/ma12152429

Gholipourmalekabadi, M., Sapru, S., Samadikuchaksaraei, A., Reis, R. L., Kaplan, D. L., and Kundu, S. C. (2020). Silk fibroin for skin injury repair: where do things stand? *Adv. Drug Deliv. Rev.* 153, 28–53. doi:10.1016/j.addr.2019.09.003

Giménez-Siurana, A., Gómez García, F., Pagan Bernabeu, A., Lozano-Pérez, A. A., Aznar-Cervantes, S. D., Cenis, J. L., et al. (2020). Chemoprevention of experimental periodontitis in diabetic rats with silk fibroin nanoparticles loaded with resveratrol. *Antioxidants (Basel)* 9 (1), 85. doi:10.3390/antiox9010085

Gorenkova, N., Maitz, M. F., Böhme, G., Alhadrami, H. A., Jiffri, E. H., Totten, J. D., et al. (2021). The innate immune response of self-assembling silk fibroin hydrogels. *Biomater. Sci.* 9 (21), 7194–7204. doi:10.1039/d1bm00936b

Gou, S., Huang, Y., Wan, Y., Ma, Y., Zhou, X., Tong, X., et al. (2019). Multi-bioresponsive silk fibroin-based nanoparticles with on-demand cytoplasmic drug release capacity for CD44-targeted alleviation of ulcerative colitis. *Biomaterials* 212, 39–54. doi:10.1016/j.biomaterials.2019.05.012

Guan, L., Ge, H., Tang, X., Su, S., Tian, P., Xiao, N., et al. (2013). Use of a silk fibroin-chitosan scaffold to construct a tissue-engineered corneal stroma. *Cells Tissues Organs* 198 (3), 190–197. doi:10.1159/000355944

Guo, W., Li, Z., Huang, H., Xu, Z., Chen, Z., Shen, G., et al. (2022). VB12-Sericin-PBLG-IR780 nanomicelles for programming cell pyroptosis via photothermal (PTT)/Photodynamic (PDT) effect-induced mitochondrial DNA (mitoDNA) oxidative damage. *ACS Appl. Mater Interfaces* 14 (15), 17008–17021. doi:10.1021/acsami.1c22804

Guo, Y., Xie, B., Jiang, M., Yuan, L., Jiang, X., Li, S., et al. (2023). Facile and eco-friendly fabrication of biocompatible hydrogel containing CuS@Ser NPs with mechanical flexibility and photothermal antibacterial activity to promote infected wound healing. *J. Nanobiotechnology* 21 (1), 266. doi:10.1186/s12951-023-02035-6

Guziewicz, N., Best, A., Perez-Ramirez, B., and Kaplan, D. L. (2011). Lyophilized silk fibroin hydrogels for the sustained local delivery of therapeutic monoclonal antibodies. *Biomaterials* 32 (10), 2642–2650. doi:10.1016/j.biomaterials.2010.12.023

Hasannasab, M., Nourmohammadi, J., Dehghan, M. M., and Ghaee, A. (2021). Immobilization of bromelain and ZnO nanoparticles on silk fibroin nanofibers as an antibacterial and anti-inflammatory burn dressing. *Int. J. Pharm.* 610, 121227. doi:10.1016/j.ijpharm.2021.121227

Hasanzadeh, S., Farokhi, M., Habibi, M., Shokrgozar, M. A., Ahangari Cohan, R., Rezaei, F., et al. (2020). Silk fibroin nanoadjuvant as a promising vaccine carrier to deliver the FimH-IutA antigen for urinary tract infection. *ACS Biomater. Sci. Eng.* 6 (8), 4573–4582. doi:10.1021/acsbiomaterials.0c00736

Hassan, M. A., Basha, A. A., Eraky, M., Abbas, E., and El-Samad, L. M. (2024). Advancements in silk fibroin and silk sericin-based biomaterial applications for cancer therapy and wound dressing formulation: a comprehensive review. *Int. J. Pharm.* 662, 124494. doi:10.1016/j.ijpharm.2024.124494

Hassanzadeh, P., Arbabi, E., and Rostami, F. (2021). Coating of ferulic acid-loaded silk fibroin nanoparticles with neutrophil membranes: a promising strategy against the acute pancreatitis. *Life Sci.* 270, 119128. doi:10.1016/j.lfs.2021.119128

Hekmatshoar, Y., Rahbar Saadat, Y., Hosseiniyan Khatibi, S. M., Ozkan, T., Zununi Vahed, F., Nariman-Saleh-Fam, Z., et al. (2019). The impact of tumor and gut microbiotas on cancer therapy: beneficial or detrimental? *Life Sci.* 233, 116680. doi:10.1016/j.lfs.2019.116680

Hong, H., Wang, X., Song, X., Fawal, G. E., Wang, K., Jiang, D., et al. (2021). Yp, Zw and Hw: transdermal delivery of interleukin-12 gene targeting dendritic cells enhances the anti-tumour effect of programmed cell death protein 1 monoclonal antibody. *Biomater. Transl.* 2 (2), 151–164. doi:10.12336/biomatertransl.2021.02.005

Hossain, D. M., Pal, S. K., Moreira, D., Duttagupta, P., Zhang, Q., Won, H., et al. (2015). TLR9-Targeted STAT3 silencing abrogates immunosuppressive activity of myeloid-derived suppressor cells from prostate cancer patients. *Clin. Cancer Res.* 21 (16), 3771–3782. doi:10.1158/1078-0432.Ccr-14-3145

Hu, C., Liu, W., Xu, N., Huang, A., Zhang, Z., Fan, M., et al. (2020). Silk fibroin hydrogel as mucosal vaccine carrier: induction of gastric CD4+TRM cells mediated by inflammatory response induces optimal immune protection against Helicobacter felis. *Emerg. Microbes Infect.* 9 (1), 2289–2302. doi:10.1080/22221751.2020.1830719

Hu, D., Li, T., Liang, W., Wang, Y., Feng, M., and Sun, J. (2022). Silk sericin as building blocks of bioactive materials for advanced therapeutics. *J. Control Release* 353, 303–316. doi:10.1016/j.jconrel.2022.11.019

Hu, Z., Ma, C., Rong, X., Zou, S., and Liu, X. (2018). Immunomodulatory ECM-like microspheres for accelerated bone regeneration in diabetes mellitus. *ACS Appl. Mater Interfaces* 10 (3), 2377–2390. doi:10.1021/acsami.7b18458

Huang, W., Ling, S., Li, C., Omenetto, F. G., and Kaplan, D. L. (2018a). Silkworm silk-based materials and devices generated using bio-nanotechnology. *Chem. Soc. Rev.* 47 (17), 6486–6504. doi:10.1039/c8cs00187a

Huang, Y. J., Hung, K. C., Hsieh, F. Y., and Hsu, S. H. (2015). Carboxyl-functionalized polyurethane nanoparticles with immunosuppressive properties as a new type of anti-inflammatory platform. *Nanoscale* 7 (48), 20352–20364. doi:10.1039/c5nr06379e

Huang, Y. J., Hung, K. C., Hung, H. S., and Hsu, S. H. (2018b). Modulation of macrophage phenotype by biodegradable polyurethane nanoparticles: possible relation between macrophage polarization and immune response of nanoparticles. *ACS Appl. Mater Interfaces* 10 (23), 19436–19448. doi:10.1021/acsami.8b04718

Inoue, S., Tanaka, K., Arisaka, F., Kimura, S., Ohtomo, K., and Mizuno, S. (2000). Silk fibroin of *Bombyx mori* is secreted, assembling a high molecular mass elementary unit consisting of H-chain, L-chain, and P25, with a 6:6:1 molar ratio. *J. Biol. Chem.* 275 (51), 40517–40528. doi:10.1074/jbc.M006897200

Janani, G., Zhang, L., Badylak, S. F., and Mandal, B. B. (2022). Silk fibroin bioscaffold from *Bombyx mori* and Antheraea assamensis elicits a distinct host response and macrophage activation paradigm *in vivo* and *in vitro*. *Biomater. Adv.* 145, 213223. doi:10.1016/j.bioadv.2022.213223

Jańczuk, A., Brodziak, A., Czernecki, T., and Król, J. (2022). Lactoferrin-the health-promoting properties and contemporary application with genetic aspects. *Foods* 12 (1), 70. doi:10.3390/foods12010070

Jiang, J., Dai, C., Liu, X., Dai, L., Li, R., Ma, K., et al. (2021b). Implantation of regenerative complexes in traumatic brain injury canine models enhances the reconstruction of neural networks and motor function recovery. *Theranostics* 11 (2), 768–788. doi:10.7150/thno.50540

Jiang, J. P., Liu, X. Y., Zhao, F., Zhu, X., Li, X. Y., Niu, X. G., et al. (2020). Three-dimensional bioprinting collagen/silk fibroin scaffold combined with neural stem cells promotes nerve regeneration after spinal cord injury. *Neural Regen. Res.* 15 (5), 959–968. doi:10.4103/1673-5374.268974

Jiang, L.-B., Ding, S.-L., Ding, W., Su, D.-H., Zhang, F.-X., Zhang, T.-W., et al. (2021a). Injectable sericin based nanocomposite hydrogel for multi-modal imaging-guided immunomodulatory bone regeneration. *Chem. Eng. J.* 418, 129323. doi:10.1016/j.cej.2021.129323

Jiao, Z., Song, Y., Jin, Y., Zhang, C., Peng, D., Chen, Z., et al. (2017). *In vivo* characterizations of the immune properties of sericin: an ancient material with emerging value in biomedical applications. *Macromol. Biosci.* 17 (12). doi:10.1002/mabi.201700229

Jin, J., Yang, Y., Yang, J., Sun, Z., Wang, D., Qin, Y., et al. (2024). Macrophage metabolic reprogramming-based diabetic infected bone defect/bone reconstruction though multi-function silk hydrogel with exosome release. *Int. J. Biol. Macromol.* 278 (Pt 4), 134830. doi:10.1016/j.ijbiomac.2024.134830

Jo, Y. Y., Kweon, H., Kim, D. W., Baek, K., Chae, W. S., Kang, Y. J., et al. (2021). Silk sericin application increases bone morphogenic protein-2/4 expression via a toll-like receptor-mediated pathway. *Int. J. Biol. Macromol.* 190, 607–617. doi:10.1016/j.ijbiomac.2021.09.021

Johari, N., Khodaei, A., Samadikuchaksaraei, A., Reis, R. L., Kundu, S. C., and Moroni, L. (2022). Ancient fibrous biomaterials from silkworm protein fibroin and spider silk blends: biomechanical patterns. *Acta Biomater.* 153, 38–67. doi:10.1016/j.actbio.2022.09.030

Kambe, Y., and Yamaoka, T. (2021). Initial immune response to a FRET-based MMP sensor-immobilized silk fibroin hydrogel *in vivo*. *Acta Biomater.* 130, 199–210. doi:10.1016/j.actbio.2021.05.030

Kanazawa, T., Shizawa, Y., Takeuchi, M., Tamano, K., Ibaraki, H., Seta, Y., et al. (2015). Topical anti-nuclear factor-kappa B small interfering RNA with functional peptides containing sericin-based hydrogel for atopic dermatitis. *Pharmaceutics* 7 (3), 294–304. doi:10.3390/pharmaceutics7030294

Kanazawa, T., Tamano, K., Sogabe, K., Endo, T., Ibaraki, H., Takashima, Y., et al. (2017). Intra-articular retention and anti-arthritic effects in collagen-induced arthritis model mice by injectable small interfering RNA containing hydrogel. *Biol. Pharm. Bull.* 40 (11), 1929–1933. doi:10.1248/bpb.b17-00481

Kaprin, A. D., Shegay, P. V., Krasilnikova, M., Baranovskii, D. S., Klabukov, I. D., and Shestakova, V. A. (2022). Assessment of immunological responses - a novel challenge in tissue engineering and regenerative medicine. *Biomed. Res. Ther.* 9 (11), 5384–5386. doi:10.15419/bmrat.v9i11.776

Karande, P., and Mitragotri, S. (2010). Transcutaneous immunization: an overview of advantages, disease targets, vaccines, and delivery technologies. *Annu. Rev. Chem. Biomol. Eng.* 1, 175–201. doi:10.1146/annurev-chembioeng-073009-100948

Khampieng, T., Aramwit, P., and Supaphol, P. (2015). Silk sericin loaded alginate nanoparticles: preparation and anti-inflammatory efficacy. *Int. J. Biol. Macromol.* 80, 636–643. doi:10.1016/j.ijbiomac.2015.07.018

Kim, D. W., Eum, W. S., Jang, S. H., Park, J., Heo, D. H., Sheen, S. H., et al. (2011). A transparent artificial dura mater made of silk fibroin as an inhibitor of inflammation in craniotomized rats. *J. Neurosurg.* 114 (2), 485–490. doi:10.3171/2010.9.Jns091764

Kim, D. W., Hwang, H. S., Kim, D. S., Sheen, S. H., Heo, D. H., Hwang, G., et al. (2012). Enhancement of anti-inflammatory activity of PEP-1-FK506 binding protein by silk fibroin peptide. *J. Microbiol. Biotechnol.* 22 (4), 494–500. doi:10.4014/jmb.1111.11024

Kim, S. H., Hong, H., Ajiteru, O., Sultan, M. T., Lee, Y. J., Lee, J. S., et al. (2021). 3D bioprinted silk fibroin hydrogels for tissue engineering. *Nat. Protoc.* 16 (12), 5484–5532. doi:10.1038/s41596-021-00622-1

Koelink, P. J., Bloemendaal, F. M., Li, B., Westera, L., Vogels, E. W. M., van Roest, M., et al. (2020). Anti-TNF therapy in IBD exerts its therapeutic effect through macrophage IL-10 signalling. *Gut* 69 (6), 1053–1063. doi:10.1136/gutjnl-2019-318264

Kumar, J. P., Alam, S., Jain, A. K., Ansari, K. M., and Mandal, B. B. (2018a). Protective activity of silk sericin against UV radiation-induced skin damage by downregulating oxidative stress. *ACS Appl. Bio Mater* 1 (6), 2120–2132. doi:10.1021/acsabm.8b00558

Kumar, M., Coburn, J., Kaplan, D. L., and Mandal, B. B. (2016). Immuno-informed 3D silk biomaterials for tailoring biological responses. *ACS Appl. Mater Interfaces* 8 (43), 29310–29322. doi:10.1021/acsami.6b09937

Kumar, M., Gupta, P., Bhattacharjee, S., Nandi, S. K., and Mandal, B. B. (2018b). Immunomodulatory injectable silk hydrogels maintaining functional islets and promoting anti-inflammatory M2 macrophage polarization. *Biomaterials* 187, 1–17. doi:10.1016/j.biomaterials.2018.09.037

Lee, G., Ko, Y. G., Bae, K. H., Kurisawa, M., Kwon, O. K., and Kwon, O. H. (2022). Green tea catechin-grafted silk fibroin hydrogels with reactive oxygen species scavenging activity for wound healing applications. *Biomater. Res.* 26 (1), 62. doi:10.1186/s40824-022-00304-3

Lei, F., Cai, J., Lyu, R., Shen, H., Xu, Y., Wang, J., et al. (2022). Efficient tumor immunotherapy through a single injection of injectable antigen/adjuvant-loaded macroporous silk fibroin microspheres. *ACS Appl. Mater Interfaces* 14 (38), 42950–42962. doi:10.1021/acsami.2c11286

Li, D. F., Yang, M. F., Xu, H. M., Zhu, M. Z., Zhang, Y., Tian, C. M., et al. (2022). Nanoparticles for oral delivery: targeted therapy for inflammatory bowel disease. *J. Mater Chem. B* 10 (31), 5853–5872. doi:10.1039/d2tb01190e

Li, G., Che, M. T., Zeng, X., Qiu, X. C., Feng, B., Lai, B. Q., et al. (2018). Neurotrophin-3 released from implant of tissue-engineered fibroin scaffolds inhibits inflammation, enhances nerve fiber regeneration, and improves motor function in canine spinal cord injury. *J. Biomed. Mater Res. A* 106 (8), 2158–2170. doi:10.1002/jbm.a.36414

Li, G., Che, M. T., Zhang, K., Qin, L. N., Zhang, Y. T., Chen, R. Q., et al. (2016b). Graft of the NT-3 persistent delivery gelatin sponge scaffold promotes axon regeneration, attenuates inflammation, and induces cell migration in rat and canine with spinal cord injury. *Biomaterials* 83, 233–248. doi:10.1016/j.biomaterials.2015.11.059

Li, L., Qian, Y., Lin, C., Li, H., Jiang, C., Lv, Y., et al. (2015). The effect of silk gland sericin protein incorporation into electrospun polycaprolactone nanofibers on *in vitro* and *in vivo* characteristics. *J. Mater Chem. B* 3 (5), 859–870. doi:10.1039/c4tb00653d

Li, Q., Hu, W., Huang, Q., Yang, J., Li, B., Ma, K., et al. (2023). MiR146a-loaded engineered exosomes released from silk fibroin patch promote diabetic wound healing by targeting IRAK1. *Signal Transduct. Target Ther.* 8 (1), 62. doi:10.1038/s41392-022-01263-w

Li, S. Y., Liu, Y., Xu, C. F., Shen, S., Sun, R., Du, X. J., et al. (2016a). Restoring anti-tumor functions of T cells via nanoparticle-mediated immune checkpoint modulation. *J. Control Release* 231, 17–28. doi:10.1016/j.jconrel.2016.01.044

Li, W., and Man, X. Y. (2022). Immunotherapy in atopic dermatitis. *Immunotherapy* 14 (14), 1149–1164. doi:10.2217/imt-2022-0054

Li, X., Yang, W., Xie, H., Wang, J., Zhang, L., Wang, Z., et al. (2020). CNT/Sericin conductive nerve guidance conduit promotes functional recovery of transected peripheral nerve injury in a rat model. *ACS Appl. Mater Interfaces* 12 (33), 36860–36872. doi:10.1021/acsami.0c08457

Liao, S., Liu, Y., Kong, Y., Shi, H., Xu, B., Tang, B., et al. (2022). A bionic multichannel nanofiber conduit carrying Tubastatin A for repairing injured spinal cord. *Mater Today Bio* 17, 100454. doi:10.1016/j.mtbio.2022.100454

Liu, S., Cao, Y., Ma, L., Sun, J., Ramos-Mucci, L., Ma, Y., et al. (2022). Oral antimicrobial peptide-EGCG nanomedicines for synergistic treatment of ulcerative colitis. *J. Control Release* 347, 544–560. doi:10.1016/j.jconrel.2022.05.025

Luan, X. Y., Huo, G. H., Li, M. Z., Lu, S. Z., and Zhang, X. G. (2009). *Antheraea pernyi* silk fibroin maintains the immunosupressive properties of human bone marrow mesenchymal stem cells. *Cell Biol. Int.* 33 (11), 1127–1134. doi:10.1016/j.cellbi.2009.07.005

Ma, T., Wu, J., Chen, S., Bian, J., Gao, G., and Nong, L. (2024). pH-Responsive modified HAMA microspheres regulate the inflammatory microenvironment of intervertebral discs. *ACS Appl. Mater Interfaces* 16 (46), 63295–63305. doi:10.1021/acsami.4c14475

Ma, Y., Duan, L., Sun, J., Gou, S., Chen, F., Liang, Y., et al. (2022). Oral nanotherapeutics based on *Antheraea pernyi* silk fibroin for synergistic treatment of ulcerative colitis. *Biomaterials* 282, 121410. doi:10.1016/j.biomaterials.2022.121410

Ma, Y., Tong, X., Huang, Y., Zhou, X., Yang, C., Chen, J., et al. (2019). Oral administration of hydrogel-embedding silk sericin alleviates ulcerative colitis through wound healing, anti-inflammation, and anti-oxidation. *ACS Biomater. Sci. Eng.* 5 (11), 6231–6242. doi:10.1021/acsbiomaterials.9b00862

Maity, B., Alam, S., Samanta, S., Prakash, R. G., and Govindaraju, T. (2022). Antioxidant silk fibroin composite hydrogel for rapid healing of diabetic wound. *Macromol. Biosci.* 22 (9), e2200097. doi:10.1002/mabi.202200097

Majumder, N., Bhattacharjee, M., Spagnoli, G. C., and Ghosh, S. (2024). Immune response profiles induced by silk-based biomaterials: a journey from 'immunogenicity' towards 'immuno-compatibility. *J. Of Mater. Chem. B* 12 (38), 9508–9523. doi:10.1039/d4tb01231c

Mao, K. L., Fan, Z. L., Yuan, J. D., Chen, P. P., Yang, J. J., Xu, J., et al. (2017). Skin-penetrating polymeric nanoparticles incorporated in silk fibroin hydrogel for topical delivery of curcumin to improve its therapeutic effect on psoriasis mouse model. *Colloids Surf. B Biointerfaces* 160, 704–714. doi:10.1016/j.colsurfb.2017.10.029

Martin, K. E., and García, A. J. (2021). Macrophage phenotypes in tissue repair and the foreign body response: implications for biomaterial-based regenerative medicine strategies. *Acta Biomater.* 133, 4–16. doi:10.1016/j.actbio.2021.03.038

Matsumoto, A., Chen, J., Collette, A. L., Kim, U. J., Altman, G. H., Cebe, P., et al. (2006). Mechanisms of silk fibroin sol-gel transitions. *J. Phys. Chem. B* 110 (43), 21630–21638. doi:10.1021/jp056350v

Mei, J., Zhou, J., Kong, L., Dai, Y., Zhang, X., Song, W., et al. (2022). An injectable photo-cross-linking silk hydrogel system augments diabetic wound healing in orthopaedic surgery through spatiotemporal immunomodulation. *J. Nanobiotechnology* 20 (1), 232. doi:10.1186/s12951-022-01414-9

Ming, P., Li, B., Li, Q., Yuan, L., Jiang, X., Liu, Y., et al. (2025). Multifunctional sericin-based biomineralized nanoplatforms with immunomodulatory and angio/osteo-genic activity for accelerated bone regeneration in periodontitis. *Biomaterials* 314, 122885. doi:10.1016/j.biomaterials.2024.122885

Napavichayanun, S., Ampawong, S., Harnsilpong, T., Angspatt, A., and Aramwit, P. (2018). Inflammatory reaction, clinical efficacy, and safety of bacterial cellulose wound dressing containing silk sericin and polyhexamethylene biguanide for wound treatment. *Arch. Dermatol Res.* 310 (10), 795–805. doi:10.1007/s00403-018-1871-3

Nayak, D., Thathapudi, N. C., Ashe, S., and Nayak, B. (2021). Bioengineered ethosomes encapsulating AgNPs and Tasar silk sericin proteins for non melanoma skin carcinoma (NMSC) as an alternative therapeutics. *Int. J. Pharm.* 596, 120265. doi:10.1016/j.ijpharm.2021.120265

Ngamcherdtrakul, W., and Yantasee, W. (2019). siRNA therapeutics for breast cancer: recent efforts in targeting metastasis, drug resistance, and immune evasion. *Transl. Res.* 214, 105–120. doi:10.1016/j.trsl.2019.08.005

Niemiec, S. M., Louiselle, A. E., Hilton, S. A., Dewberry, L. C., Zhang, L., Azeltine, M., et al. (2020). Nanosilk increases the strength of diabetic skin and delivers CNP-miR146a to improve wound healing. *Front. Immunol.* 11, 590285. doi:10.3389/fimmu.2020.590285

Oliveira, I. M., Gonçalves, C., Shin, M. E., Lee, S., Reis, R. L., Khang, G., et al. (2020). Anti-inflammatory properties of injectable betamethasone-loaded tyramine-modified gellan gum/silk fibroin hydrogels. *Biomolecules* 10 (10), 1456. doi:10.3390/biom10101456

Pal, R. R., Parashar, P., Singh, I., and Saraf, S. A. (2019). Tamanu oil potentiated novel sericin emulgel of levocetirizine: repurposing for topical delivery against DNCB-induced atopic dermatitis, QbD based development and *in vivo* evaluation. *J. Microencapsul.* 36 (5), 432–446. doi:10.1080/02652048.2019.1637474

Pang, L., Tian, P., Cui, X., Wu, X., Zhao, X., Wang, H., et al. (2021). *In situ* photo-cross-linking hydrogel accelerates diabetic wound healing through restored hypoxia-inducible factor 1-alpha pathway and regulated inflammation. *ACS Appl. Mater Interfaces* 13 (25), 29363–29379. doi:10.1021/acsami.1c07103

Panilaitis, B., Altman, G. H., Chen, J., Jin, H. J., Karageorgiou, V., and Kaplan, D. L. (2003). Macrophage responses to silk. *Biomaterials* 24 (18), 3079–3085. doi:10.1016/s0142-9612(03)00158-3

Patel, D. K., Dutta, S. D., Hexiu, J., Ganguly, K., and Lim, K. T. (2022). 3D-printable chitosan/silk fibroin/cellulose nanoparticle scaffolds for bone regeneration via M2 macrophage polarization. *Carbohydr. Polym.* 281, 119077. doi:10.1016/j.carbpol.2021.119077

Phan, V. H. G., Murugesan, M., Nguyen, P. P. T., Luu, C. H., Le, N. H., Nguyen, H. T., et al. (2022). Biomimetic injectable hydrogel based on silk fibroin/hyaluronic acid embedded with methylprednisolone for cartilage regeneration. *Colloids Surf. B Biointerfaces* 219, 112859. doi:10.1016/j.colsurfb.2022.112859

Qi, C., Liu, J., Jin, Y., Xu, L., Wang, G., Wang, Z., et al. (2018). Photo-crosslinkable, injectable sericin hydrogel as 3D biomimetic extracellular matrix for minimally invasive repairing cartilage. *Biomaterials* 163, 89–104. doi:10.1016/j.biomaterials.2018.02.016

Qian, H., Zhou, T., Fu, Y., Guo, M., Yang, W., Zhang, D., et al. (2022a). Self-assembled tetrahedral framework nucleic acid mediates tumor-associated macrophage reprogramming and restores antitumor immunity. *Mol. Ther. Nucleic Acids* 27, 763–773. doi:10.1016/j.omtn.2021.12.036

Qian, Y., Zheng, Y., Jin, J., Wu, X., Xu, K., Dai, M., et al. (2022b). Immunoregulation in diabetic wound repair with a photoenhanced glycyrrhizic acid hydrogel scaffold. *Adv. Mater* 34 (29), e2200521. doi:10.1002/adma.202200521

Reeves, A. R., Spiller, K. L., Freytes, D. O., Vunjak-Novakovic, G., and Kaplan, D. L. (2015). Controlled release of cytokines using silk-biomaterials for macrophage polarization. *Biomaterials* 73, 272–283. doi:10.1016/j.biomaterials.2015.09.027

Rezaei, F., Keshvari, H., Shokrgozar, M. A., Doroud, D., Gholami, E., Khabiri, A., et al. (2021). Nano-adjuvant based on silk fibroin for the delivery of recombinant hepatitis B surface antigen. *Biomater. Sci.* 9 (7), 2679–2695. doi:10.1039/d0bm01518k

Ritprajak, P., Sirithanakorn, C., Nguyen, T. N., Sereemaspun, A., and Aramwit, P. (2021). Biosynthetic sericin 1-like protein skews dendritic cells to tolerogenic-like phenotype. *Biotechnol. Appl. Biochem.* 68 (6), 1508–1517. doi:10.1002/bab.2072

Rodriguez-Nogales, A., Algieri, F., De Matteis, L., Lozano-Perez, A. A., Garrido-Mesa, J., Vezza, T., et al. (2016). Intestinal anti-inflammatory effects of RGD-functionalized silk fibroin nanoparticles in trinitrobenzenesulfonic acid-induced experimental colitis in rats. *Int. J. Nanomedicine* 11, 5945–5958. doi:10.2147/ijn.S116479

Rujimongkon, K., Ampawong, S., Reamtong, O., Buaban, T., and Aramwit, P. (2021). The therapeutic effects of *Bombyx mori* sericin on rat skin psoriasis through modulated epidermal immunity and attenuated cell proliferation. *J. Tradit. Complement. Med.* 11 (6), 587–597. doi:10.1016/j.jtcme.2021.06.007

Sapru, S., Das, S., Mandal, M., Ghosh, A. K., and Kundu, S. C. (2021). Sericin-chitosan-glycosaminoglycans hydrogels incorporated with growth factors for *in vitro* and *in vivo* skin repair. *Carbohydr. Polym.* 258, 117717. doi:10.1016/j.carbpol.2021.117717

Schenkel, J. M., Fraser, K. A., Beura, L. K., Pauken, K. E., Vezys, V., and Masopust, D. (2014). T cell memory. Resident memory CD8 T cells trigger protective innate and adaptive immune responses. *Science* 346 (6205), 98–101. doi:10.1126/science.1254536

Seyedaghamiri, F., Farajdokht, F., Vatandoust, S. M., Mahmoudi, J., Khabbaz, A., and Sadigh-Eteghad, S. (2021). Sericin modulates learning and memory behaviors by tuning of antioxidant, inflammatory, and apoptotic markers in the hippocampus of aged mice. *Mol. Biol. Rep.* 48 (2), 1371–1382. doi:10.1007/s11033-021-06195-2

Shah, A., Ali Buabeid, M., Arafa, E. A., Hussain, I., Li, L., and Murtaza, G. (2019). The wound healing and antibacterial potential of triple-component nanocomposite (chitosan-silver-sericin) films loaded with moxifloxacin. *Int. J. Pharm.* 564, 22–38. doi:10.1016/j.ijpharm.2019.04.046

Shen, K., Duan, A., Cheng, J., Yuan, T., Zhou, J., Song, H., et al. (2022). Exosomes derived from hypoxia preconditioned mesenchymal stem cells laden in a silk hydrogel promote cartilage regeneration via the miR-205-5p/PTEN/AKT pathway. *Acta Biomater.* 143, 173–188. doi:10.1016/j.actbio.2022.02.026

Shirangi, A., Mottaghitalab, F., Dinarvand, S., and Atyabi, F. (2022). Theranostic silk sericin/SPION nanoparticles for targeted delivery of ROR1 siRNA: synthesis, characterization, diagnosis and anticancer effect on triple-negative breast cancer. *Int. J. Biol. Macromol.* 221, 604–612. doi:10.1016/j.ijbiomac.2022.09.020

Silva, A. S., Costa, E. C., Reis, S., Spencer, C., Calhelha, R. C., Miguel, S. P., et al. (2022). Silk sericin: a promising sustainable biomaterial for biomedical and pharmaceutical applications. *Polym. (Basel)* 14 (22), 4931. doi:10.3390/polym14224931

Singh, Y. P., Moses, J. C., Bhunia, B. K., Nandi, S. K., and Mandal, B. B. (2018). Hierarchically structured seamless silk scaffolds for osteochondral interface tissue engineering. *J. Mater Chem. B* 6 (36), 5671–5688. doi:10.1039/c8tb01344f

Song, I. B., Han, H. J., and Kwon, J. (2020). Immune-enhancing effects of gamma-irradiated sericin. *Food Sci. Biotechnol.* 29 (7), 969–976. doi:10.1007/s10068-020-00734-6

Song, X., Jiang, Y., Zhang, W., Elfawal, G., Wang, K., Jiang, D., et al. (2022). Transcutaneous tumor vaccination combined with anti-programmed death-1 monoclonal antibody treatment produces a synergistic antitumor effect. *Acta Biomater.* 140, 247–260. doi:10.1016/j.actbio.2021.11.033

Song, Y., Zhang, C., Zhang, J., Sun, N., Huang, K., Li, H., et al. (2016). An injectable silk sericin hydrogel promotes cardiac functional recovery after ischemic myocardial infarction. *Acta Biomater.* 41, 210–223. doi:10.1016/j.actbio.2016.05.039

Stinson, J. A., Boopathy, A. V., Cieslewicz, B. M., Zhang, Y., Hartman, N. W., Miller, D. P., et al. (2021). Enhancing influenza vaccine immunogenicity and efficacy through infection mimicry using silk microneedles. *Vaccine* 39 (38), 5410–5421. doi:10.1016/j.vaccine.2021.07.064

Sun, T., Kwong, C. H. T., Gao, C., Wei, J., Yue, L., Zhang, J., et al. (2020). Amelioration of ulcerative colitis via inflammatory regulation by macrophage-biomimetic nanomedicine. *Theranostics* 10 (22), 10106–10119. doi:10.7150/thno.48448

Sun, Y., Shi, W., Zhang, Q., Guo, H., Dong, Z., Zhao, P., et al. (2022). Multi-omics integration to reveal the mechanism of sericin inhibiting LPS-induced inflammation. *Int. J. Mol. Sci.* 24 (1), 259. doi:10.3390/ijms24010259

Suzuki, S., Shadforth, A. M. A., McLenachan, S., Zhang, D., Chen, S. C., Walshe, J., et al. (2019). Optimization of silk fibroin membranes for retinal implantation. *Mater Sci. Eng. C Mater Biol. Appl.* 105, 110131. doi:10.1016/j.msec.2019.110131

Takahashi, Y., Gehoh, M., and Yuzuriha, K. (1999). Structure refinement and diffuse streak scattering of silk (*Bombyx mori*). *Int. J. Biol. Macromol.* 24 (2-3), 127–138. doi:10.1016/s0141-8130(98)00080-4

Tan, M., Chen, Y., Guo, Y., Yang, C., Liu, M., Guo, D., et al. (2020). A low-intensity focused ultrasound-assisted nanocomposite for advanced triple cancer therapy: local chemotherapy, therapeutic extracellular vesicles and combined immunotherapy. *Biomater. Sci.* 8 (23), 6703–6717. doi:10.1039/d0bm00804d

Tian, F., Zhang, S., Wang, M., Yan, Y., Cao, Y., Wang, Y., et al. (2024). Clinical grade fibroin sutures with bioactive gold clusters enhance surgical wound healing via inflammation modulation. *ACS Appl. Mater Interfaces*. doi:10.1021/acsami.4c10451

Tkach, M., Kowal, J., Zucchetti, A. E., Enserink, L., Jouve, M., Lankar, D., et al. (2017). Qualitative differences in T-cell activation by dendritic cell-derived extracellular vesicle subtypes. *Embo J.* 36 (20), 3012–3028. doi:10.15252/embj.201696003

Tuentam, K., Aramwit, P., Reamtong, O., Supasai, S., Chaisri, U., Fongsodsri, K., et al. (2022). Sericin-based poly(vinyl) alcohol relieves plaque and epidermal lesions in psoriasis; a chance for dressing development in a specific area. *Int. J. Mol. Sci.* 24 (1), 145. doi:10.3390/ijms24010145

Wang, C., Li, J., Han, X., Liu, S., Gao, X., Guo, C., et al. (2022b). Silk sericin stabilized proanthocyanidins for synergetic alleviation of ulcerative colitis. *Int. J. Biol. Macromol.* 220, 1021–1030. doi:10.1016/j.ijbiomac.2022.08.134

Wang, D., Chen, M. W., Wei, Y. J., Geng, W. B., Hu, Y., Luo, Z., et al. (2022a). Construction of wogonin nanoparticle-containing strontium-doped nanoporous structure on titanium surface to promote osteoporosis fracture repair. *Adv. Healthc. Mater* 11 (21), e2201405. doi:10.1002/adhm.202201405

Wang, J., Li, X., Song, Y., Su, Q., Xiaohalati, X., Yang, W., et al. (2021). Injectable silk sericin scaffolds with programmable shape-memory property and neuro-differentiation-promoting activity for individualized brain repair of severe ischemic stroke. *Bioact. Mater* 6 (7), 1988–1999. doi:10.1016/j.bioactmat.2020.12.017

Wang, R., He, X., Su, S., Bai, J., Liu, H., and Zhou, F. (2024). Multifunctional tannic acid-based nanocomposite methacrylated silk fibroin hydrogel with the ability to scavenge reactive oxygen species and reduce inflammation for bone regeneration. *Int. J. Biol. Macromol.* 266 (Pt 2), 131357. doi:10.1016/j.ijbiomac.2024.131357

Wang, S., Zhang, Y., Shi, Y., He, Q., Tan, Q., Peng, Z., et al. (2023). Rhubarb charcoal-crosslinked chitosan/silk fibroin sponge scaffold with efficient hemostasis, inflammation, and angiogenesis for promoting diabetic wound healing. *Int. J. Biol. Macromol.* 253 (Pt 2), 126796. doi:10.1016/j.ijbiomac.2023.126796

Wang, Y., Rudym, D. D., Walsh, A., Abrahamsen, L., Kim, H. J., Kim, H. S., et al. (2008). *In vivo* degradation of three-dimensional silk fibroin scaffolds. *Biomaterials* 29 (24-25), 3415–3428. doi:10.1016/j.biomaterials.2008.05.002

Wang, Y., Yao, D., Li, L., Qian, Z., He, W., Ding, R., et al. (2020). Effect of electrospun silk fibroin-silk sericin films on macrophage polarization and vascularization. *ACS Biomater. Sci. Eng.* 6 (6), 3502–3512. doi:10.1021/acsbiomaterials.0c00175

Wani, S. U. D., Zargar, M. I., Masoodi, M. H., Alshehri, S., Alam, P., Ghoneim, M. M., et al. (2022). Silk fibroin as an efficient biomaterial for drug delivery, gene therapy, and wound healing. *Int. J. Mol. Sci.* 23 (22), 14421. doi:10.3390/ijms232214421

Wei, W., Liu, J., Peng, Z., Liang, M., Wang, Y., and Wang, X. (2020). Gellable silk fibroin-polyethylene sponge for hemostasis. *Artif. Cells Nanomed Biotechnol.* 48 (1), 28–36. doi:10.1080/21691401.2019.1699805

Wenhao, Z., Zhang, T., Yan, J., Li, Q., Xiong, P., Li, Y., et al. (2020). *In vitro* and *in vivo* evaluation of structurally-controlled silk fibroin coatings for orthopedic infection and *in-situ* osteogenesis. *Acta Biomater.* 116, 223–245. doi:10.1016/j.actbio.2020.08.040

Werlang, C. A., Sahoo, J. K., Cárcarmo-Oyarce, G., Stevens, C., Uzun, D., Putnik, R., et al. (2024). Selective biofilm inhibition through mucin-inspired engineering of silk glycopolymers. *J. Am. Chem. Soc.* 146 (50), 34661–34668. doi:10.1021/jacs.4c12945

Wojdasiewicz, P., Poniatowski, A., Ł, and Szukiewicz, D. (2014). The role of inflammatory and anti-inflammatory cytokines in the pathogenesis of osteoarthritis. *Mediat. Inflamm.* 2014, 561459. doi:10.1155/2014/561459

Wong, K., Tan, X. H., Li, J., Hui, J. H. P., and Goh, J. C. H. (2024). An *in vitro* macrophage response study of silk fibroin and silk fibroin/nano-hydroxyapatite scaffolds for tissue regeneration application. *ACS Biomater. Sci. Eng.* 10 (11), 7073–7085. doi:10.1021/acsbiomaterials.4c00976

Wu, T., Chen, Y., Liu, W., Tong, K. L., Suen, C. W., Huang, S., et al. (2020). Ginsenoside Rb1/TGF-β1 loaded biodegradable silk fibroin-gelatin porous scaffolds for inflammation inhibition and cartilage regeneration. *Mater Sci. Eng. C Mater Biol. Appl.* 111, 110757. doi:10.1016/j.msec.2020.110757

Wu, X., Guo, H., Jia, Y., Wang, Q., Wang, J., Sun, X., et al. (2022). Adipose mesenchymal stem cell-based tissue engineering mesh with sustained bFGF release to enhance tissue repair. *Biomater. Sci.* 10 (12), 3110–3121. doi:10.1039/d1bm01893k

Wu, X., Zhou, M., Jiang, F., Yin, S., Lin, S., Yang, G., et al. (2021). Marginal sealing around integral bilayer scaffolds for repairing osteochondral defects based on photocurable silk hydrogels. *Bioact. Mater* 6 (11), 3976–3986. doi:10.1016/j.bioactmat.2021.04.005

Xiang, G., Liu, K., Wang, T., Hu, X., Wang, J., Gao, Z., et al. (2021). *In situ* regulation of macrophage polarization to enhance osseointegration under diabetic conditions using injectable silk/sitagliptin gel scaffolds. *Adv. Sci. (Weinh)* 8 (3), 2002328. doi:10.1002/advs.202002328

Xie, D., Zhou, X., Xiao, B., Duan, L., and Zhu, Z. (2022). Mucus-Penetrating silk fibroin-based nanotherapeutics for efficient treatment of ulcerative colitis. *Biomolecules* 12 (9), 1263. doi:10.3390/biom12091263

Xu, N., Ruan, G., Liu, W., Hu, C., Huang, A., Zeng, Z., et al. (2019). Vaccine-induced gastric CD4(+) tissue-resident memory T cells proliferate *in situ* to amplify immune response against *Helicobacter pylori* insult. *Helicobacter* 24 (5), e12652. doi:10.1111/hel.12652

Xu, S., Tan, H., Yang, Q., Wang, R., Tian, C., Ji, Y., et al. (2021). Fabrication of a silk sericin hydrogel system delivering human lactoferrin using genetically engineered silk with improved bioavailability to alleviate chemotherapy-induced immunosuppression. *ACS Appl. Mater Interfaces* 13 (38), 45175–45190. doi:10.1021/acsami.1c08409

Xu, S., Yang, Q., Wang, R., Tian, C., Ji, Y., Tan, H., et al. (2022). Genetically engineered pH-responsive silk sericin nanospheres with efficient therapeutic effect on ulcerative colitis. *Acta Biomater.* 144, 81–95. doi:10.1016/j.actbio.2022.03.012

Xu, Y., Zhang, Z., Chen, X., Li, R., Li, D., and Feng, S. (2016). A silk fibroin/collagen nerve scaffold seeded with a Co-culture of schwann cells and adipose-derived stem cells for sciatic nerve regeneration. *PLoS One* 11 (1), e0147184. doi:10.1371/journal.pone.0147184

Yalcin, E., Kara, G., Celik, E., Pinarli, F. A., Saylam, G., Sucularli, C., et al. (2019). Preparation and characterization of novel albumin-sericin nanoparticles as siRNA delivery vehicle for laryngeal cancer treatment. *Prep. Biochem. Biotechnol.* 49 (7), 659–670. doi:10.1080/10826068.2019.1599395

Yang, H., Xu, H., Lv, D., Li, S., Rong, Y., Wang, Z., et al. (2024). The naringin/carboxymethyl chitosan/sodium hyaluronate/silk fibroin scaffold facilitates the healing of diabetic wounds by restoring the ROS-related dysfunction of vascularization and macrophage polarization. *Int. J. Biol. Macromol.* 260 (Pt 1), 129348. doi:10.1016/j.ijbiomac.2024.129348

Yang, N., Moore, M. J., Michael, P. L., Santos, M., Lam, Y. T., Bao, S., et al. (2021). Silk fibroin scaffold architecture regulates inflammatory responses and engraftment of bone marrow-mononuclear cells. *Adv. Healthc. Mater* 10 (16), e2100615. doi:10.1002/adhm.202100615

Yang, X., Wang, X., Hong, H., Elfawal, G., Lin, S., Wu, J., et al. (2020). Galactosylated chitosan-modified ethosomes combined with silk fibroin nanofibers is useful in transcutaneous immunization. *J. Control Release* 327, 88–99. doi:10.1016/j.jconrel.2020.07.047

Yao, S., Xie, Y., Xiao, L., Cai, L., and Ma, Z. (2019). Porous and nonporous silk fibroin (SF) membranes wrapping for Achilles tendon (AT) repair: which one is a better choice? *J. Biomed. Mater Res. B Appl. Biomater.* 107 (3), 733–740. doi:10.1002/jbm.b.34167

Yin, C., Han, X., Lu, Q., Qi, X., Guo, C., and Wu, X. (2022). Rhein incorporated silk fibroin hydrogels with antibacterial and anti-inflammatory efficacy to promote healing of bacteria-infected burn wounds. *Int. J. Biol. Macromol.* 201, 14–19. doi:10.1016/j.ijbiomac.2021.12.156

Yu, H., He, M., Li, Y., Liu, Y., Xu, Z., Zhang, L., et al. (2023). A robust Au@Cu(2-x)S nanoreactor assembled by silk fibroin for enhanced intratumoral glucose depletion and redox dyshomeostasis. *Biomaterials* 293, 121970. doi:10.1016/j.biomaterials.2022.121970

Yu, H., Li, Y., Zhang, Z., Ren, J., Zhang, L., Xu, Z., et al. (2022). Silk fibroin-capped metal-organic framework for tumor-specific redox dyshomeostasis treatment synergized by deoxygenation-driven chemotherapy. *Acta Biomater.* 138, 545–560. doi:10.1016/j.actbio.2021.11.009

Zhang, B., Wang, W., Gao, P., Li, X., Chen, L., Lin, Z., et al. (2024b). Injectable, electroconductive, free radical scavenging silk fibroin/black phosphorus/glycyrrhizic acid nanocomposite hydrogel for enhancing spinal cord repair. *Adv. Healthc. Mater* 13 (18), e2304300. doi:10.1002/adhm.202304300

Zhang, D., Chen, Q., Bi, Y., Zhang, H., Chen, M., Wan, J., et al. (2021b). Bio-inspired poly-DL-serine materials resist the foreign-body response. *Nat. Commun.* 12 (1), 5327. doi:10.1038/s41467-021-25581-9

Zhang, D., Chen, Q., Zhang, W., Liu, H., Wan, J., Qian, Y., et al. (2020). Silk-Inspired β-peptide materials resist fouling and the foreign-body response. *Angew. Chem. Int. Ed. Engl.* 59 (24), 9586–9593. doi:10.1002/anie.202000416

Zhang, D., Zhao, L., Cui, X., Li, X., Qian, Z., Zhou, X., et al. (2024a). Silkworm cocoon bionic design in wound dressings: a novel hydrogel with self-healing and antimicrobial properties. *Int. J. Biol. Macromol.* 280 (Pt 4), 136114. doi:10.1016/j.ijbiomac.2024.136114

Zhang, F., Yin, C., Qi, X., Guo, C., and Wu, X. (2022b). Silk fibroin crosslinked glycyrrhizic acid and silver hydrogels for accelerated bacteria-infected wound healing. *Macromol. Biosci.* 22 (4), e2100407. doi:10.1002/mabi.202100407

Zhang, H., Lai, L., Wang, Y., Ye, B., Deng, S., Ding, A., et al. (2019). Silk fibroin for CpG oligodeoxynucleotide delivery. *ACS Biomater. Sci. Eng.* 5 (11), 6082–6088. doi:10.1021/acsbiomaterials.9b01413

Zhang, L., Yang, W., Tao, K., Song, Y., Xie, H., Wang, J., et al. (2017). Sustained local release of NGF from a chitosan-sericin composite scaffold for treating chronic nerve compression. *ACS Appl. Mater Interfaces* 9 (4), 3432–3444. doi:10.1021/acsami.6b14691

Zhang, X., He, Q., Sun, J., Gong, H., Cao, Y., Duan, L., et al. (2022a). Near-infrared-enpowered nanomotor-mediated targeted chemotherapy and mitochondrial phototherapy to boost systematic antitumor immunity. *Adv. Healthc. Mater* 11 (14), e2200255. doi:10.1002/adhm.202200255

Zhang, Y., Shi, N., He, L., Wang, S., Li, X., Lu, S., et al. (2021a). Silk sericin activates mild immune response and increases antibody production. *J. Biomed. Nanotechnol.* 17 (12), 2433–2443. doi:10.1166/jbn.2021.3206

Zhang, Y. Q. (2002). Applications of natural silk protein sericin in biomaterials. *Biotechnol. Adv.* 20 (2), 91–100. doi:10.1016/s0734-9750(02)00003-4

Zhang, Y. Q., Ma, Y., Xia, Y. Y., Shen, W. D., Mao, J. P., and Xue, R. Y. (2006). Silk sericin-insulin bioconjugates: synthesis, characterization and biological activity. *J. Control Release* 115 (3), 307–315. doi:10.1016/j.jconrel.2006.08.019

Zhaorigetu, S., Yanaka, N., Sasaki, M., Watanabe, H., and Kato, N. (2003). Silk protein, sericin, suppresses DMBA-TPA-induced mouse skin tumorigenesis by reducing oxidative stress, inflammatory responses and endogenous tumor promoter TNF-alpha. *Oncol. Rep.* 10 (3), 537–543. doi:10.3892/or.10.3.537

Zhou, F., Zhang, X., Cai, D., Li, J., Mu, Q., Zhang, W., et al. (2017). Silk fibroin-chondroitin sulfate scaffold with immuno-inhibition property for articular cartilage repair. *Acta Biomater.* 63, 64–75. doi:10.1016/j.actbio.2017.09.005

Zhou, X., Wang, Y., Ji, J., and Zhang, P. (2024). Materials strategies to overcome the foreign body response. *Adv. Healthc. Mater* 13 (18), e2304478. doi:10.1002/adhm.202304478

Zhu, W., Dong, Y., Xu, P., Pan, Q., Jia, K., Jin, P., et al. (2022). A composite hydrogel containing resveratrol-laden nanoparticles and platelet-derived extracellular vesicles promotes wound healing in diabetic mice. *Acta Biomater.* 154, 212–230. doi:10.1016/j.actbio.2022.10.038

Zu, M., Ma, Y., Cannup, B., Xie, D., Jung, Y., Zhang, J., et al. (2021). Oral delivery of natural active small molecules by polymeric nanoparticles for the treatment of inflammatory bowel diseases. *Adv. Drug Deliv. Rev.* 176, 113887. doi:10.1016/j.addr.2021.113887

frontiers | Frontiers in Pharmacology

TYPE Original Research
PUBLISHED 21 February 2025
DOI 10.3389/fphar.2025.1530217

Check for updates

OPEN ACCESS

EDITED BY
Jinlong Ma,
Shandong Second Medical University, China

REVIEWED BY
Qi Liu,
Anhui Medical University, China
Yijie Cheng,
Michigan State University, United States, in collaboration with reviewer QL
Mukesh Kumar Meher,
Michigan State University, United States

*CORRESPONDENCE
Yan Cai,
caiyandd@163.com
Shi Shen,
583493289@qq.com
Xiaoyan Xiang,
1399041661@qq.com

†These authors share first authorship

RECEIVED 18 November 2024
ACCEPTED 24 January 2025
PUBLISHED 21 February 2025

CITATION
Li Y, You S, Li S, Li S, Jia A, Xiang X, Shen S and Cai Y (2025) Exploration the therapeutic effects of sodium houttuyfonate combined with penicillin G on methicillin resistant *staphylococcus aureus* infected wounds. *Front. Pharmacol.* 16:1530217. doi: 10.3389/fphar.2025.1530217

COPYRIGHT
© 2025 Li, You, Li, Li, Jia, Xiang, Shen and Cai. This is an open-access article distributed under the terms of the Creative Commons Attribution License (CC BY). The use, distribution or reproduction in other forums is permitted, provided the original author(s) and the copyright owner(s) are credited and that the original publication in this journal is cited, in accordance with accepted academic practice. No use, distribution or reproduction is permitted which does not comply with these terms.

Exploration the therapeutic effects of sodium houttuyfonate combined with penicillin G on methicillin resistant *staphylococcus aureus* infected wounds

Yujie Li[1,2†], Shunjie You[3†], Sheng Li[3], Si Li[4], Aimin Jia[4], Xiaoyan Xiang[4*], Shi Shen[5*] and Yan Cai[1*]

[1]Genetic and Prenatal Diagnosis Center, Affiliated Hospital of North Sichuan Medical College, Nanchong, China, [2]Department of Orthopedics, The Leshan People's Hospital, Leshan, China, [3]Burn and Plastic Surgery Department of Ziyang Central Hospital, Ziyang, China, [4]Affiliated Hospital, North Sichuan Medical College, Nanchong, China, [5]Department of Orthopedics, The Affiliated Hospital, Southwest Medical University, Luzhou, China

Background: Methicillin resistant *Staphylococcus aureus* (MRSA) is a Gram-positive bacterium that can cause local or systemic infectious diseases, and treatment for MRSA has become a major global health issue. Sodium houttuyfonate (SH) is a natural extract of Houttuynia cordata, which has antibacterial and anti-inflammatory effects. The aim of this study is to evaluate the antibacterial effect of SH combined with penicillin G (PNC) against MRSA and its potential beneficial effects in a rat model of MRSA wound infection, and to investigate its possible mechanism in combination with network pharmacology.

Methods: Evaluating the antibacterial effect of drugs through *in vitro* antibacterial experiments. Construct a MRSA infected wound model in SD rats and determine the optimal drug ratio based on the degree of wound healing. Hematoxylin & Eosin (H&E) staining was used to determine inflammatory cell infiltration, Masson staining was used to observe collagen fiber proliferation in the wound, Elisa method was used to detect inflammatory cytokine content in retrobulbar venous blood, and network pharmacology methods were used to elucidate possible molecular mechanisms.

Result: The MIC of SH and PNC are 60–80 μg/mL and 40–70 U/mL, respectively. The FICI of the combined group is 0.375–0.5625, and the optimal drug ratio is SH20 μg/mL + PNC15u/mL. The number of central granulocytes infiltrated in the combined group was less than that in other groups, and the levels of IL-6 and TNF-α were significantly reduced. In addition, the collagen fibers in the wound were significantly increased. Thirteen target genes were predicted through network pharmacology, among which the core targets were IL1B, IL6, MMP9, IFNG, and TNF. SH and PNG have shown good binding potential with various targets in molecular docking. Among the 83 potential pathways of action, IL-17 signaling pathway is considered a key pathway for promoting wound healing.

Conclusion: Sodium houttuyfonate combined with penicillin G can inhibit bacterial growth in MRSA infected wounds in rats, reduce neutrophil infiltration, promote collagen fiber generation in wounds, and decrease the

expression levels of inflammatory factors IL-6 and TNF-α in the blood of rats after MRSA infection. It promotes wound healing through multiple targets and pathways, and preliminarily reveals the drug's targets and molecular mechanisms.

KEYWORDS

MRSA, sodium houttuyfonate, penicillin G, network pharmacology, wound healing

1 Introduction

Staphylococcus aureus, which can encode penicillin binding protein 2a (PBP2a) and cannot be inactivated by β-lactam antibiotics, is called methicillin-resistant *Staphylococcus aureus* (MRSA) (Peacock and Paterson, 2015). Since its first discovery in the United Kingdom in 1961, MRSA has spread to various parts of the world and has become one of the leading pathogens causing community-acquired and healthcare related infections (Gurieva et al., 2012), it has a fast transmission speed, strong pathogenicity, and exhibits multiple drug resistance with high mortality rate (Oliveira et al., 2018). MRSA is resistant to a variety of antibiotics, such as β-lactams, fluoroquinolones, macrolides, aminoglycosides, tetracyclines, rifampicin and fusidic acid. Its drug resistance mechanism is complex, mainly including the production of β-lactamase (Lee and Park, 2016) and PBP2a (Miyachiro et al., 2019), the reduction of the permeability of antibiotics to cell membranes, the change of drug targets, the activation of drug efflux in bacteria, the inhibition of enzyme expression, the transfer of drug-resistant plasmids and the formation of bacterial biofilms (Roberts et al., 2012). Glycopeptide antibiotics are currently the "last line of defense" for the treatment of MRSA infection, but there have been intermediates between vancomycin resistant *Staphylococcus aureus* (visa) and vancomycin resistant *Staphylococcus aureus* (VRSA) (Spagnolo et al., 2014), At present, MRSA has become a major problem in clinical anti infection treatment, which requires further research on the resistance mechanism of MRSA and the development of new antibacterial treatment strategies.

The development of new antibacterial drugs faces two major challenges, namely, high costs and lengthy clinical validation time. This means that not only does it require massive financial support, but it also takes a long time to ensure the safety and effectiveness of new drugs, and the combination of multiple antibiotics may also lead to high bacterial resistance. In recent years, the therapeutic effects of traditional Chinese medicine and its active ingredients have been increasingly recognized. Traditional Chinese medicine has minimal toxic side effects, and its combination with antibiotics can reduce drug toxicity and effective dosage, reduce bacterial resistance, and provide a new approach for the clinical treatment of MRSA. Houttuynia cordata, a traditional Chinese medicine, has good anti-inflammatory activity, and is often used in clinical treatment of respiratory infections, urinary tract inflammation, acute and chronic rhinitis, conjunctivitis and other diseases (Liu et al., 2021),Its extract sodium houttuyfonate has antibacterial, antiviral, antiallergic, immune enhancing, tumor proliferation inhibiting and other effects (Zhuang et al., 2022),Numerous studies have shown that SH has a clear therapeutic effect on bacterial infections such as *Staphylococcus aureus*, *Pseudomonas aeruginosa*, *Haemophilus* influenzae, and *Streptococcus* pneumoniae (Chen et al., 2014; Wang et al., 2019), and studies have proved that a certain concentration of SH can inhibit the formation of biofilm of *Staphylococcus aureus* (Liu et al., 2011). However, its mechanism of action is not fully understood and further research is needed to elucidate its potential mechanism of action in combating infections.

Network pharmacology is an important method for exploring the potential target and molecular mechanisms of drugs, and is an emerging field of pharmacological research that integrates traditional pharmacology, bioinformatics, cheminformatics, and network biology (Liu et al., 2024; Zhu et al., 2021). By constructing a drug-disease interaction network to evaluate the molecular mechanism of drugs, we can further study the biological effects of various small molecules (Zhou et al., 2022a; Shang et al., 2023). Molecular docking technology can deeply analyze the interaction between molecules, and intuitively explain the mechanism of action between receptors and ligands in 3D graphics. Therefore, combining molecular simulation validation with network pharmacology analysis is an effective method for studying the mechanism of drug action in drug research (Wang et al., 2024).

This study aims to investigate the antibacterial effect of sodium houttuyfonate combined with the clinically common antibiotic penicillin G, and observe its efficacy in a rat MRSA wound model. At the same time, network pharmacology and molecular docking techniques are used to predict the potential targets and action pathways of the drug, providing experimental evidence for SH to become a potential drug or antibacterial sensitizer for anti-MRSA infection in the future. The general workflow is shown in Figure 1A.

2 Materials and methods

2.1 Experimental strains and animals

Collect 20 strains of MRSA isolated from the microbiology laboratory of the Affiliated Hospital of North Sichuan Medical College from September 2020 to November 2020, with specimen types of sputum and pus. The strain was identified by VITEK GP identification card and VITEK AST-GP67 drug susceptibility card of French bioMerieux company. The quality control strain is *Staphylococcus aureus* (ATCC 25923) provided by the Microbiology Laboratory of the Affiliated Hospital of North Sichuan Medical College. The experimental animals were 55 female SD rats weighing 150–200 g each, provided by the Animal Experimental Center of North Sichuan Medical College. The ethics of animal experiments were approved by the Ethics Committee of North Sichuan Medical College (NSMC2023071).

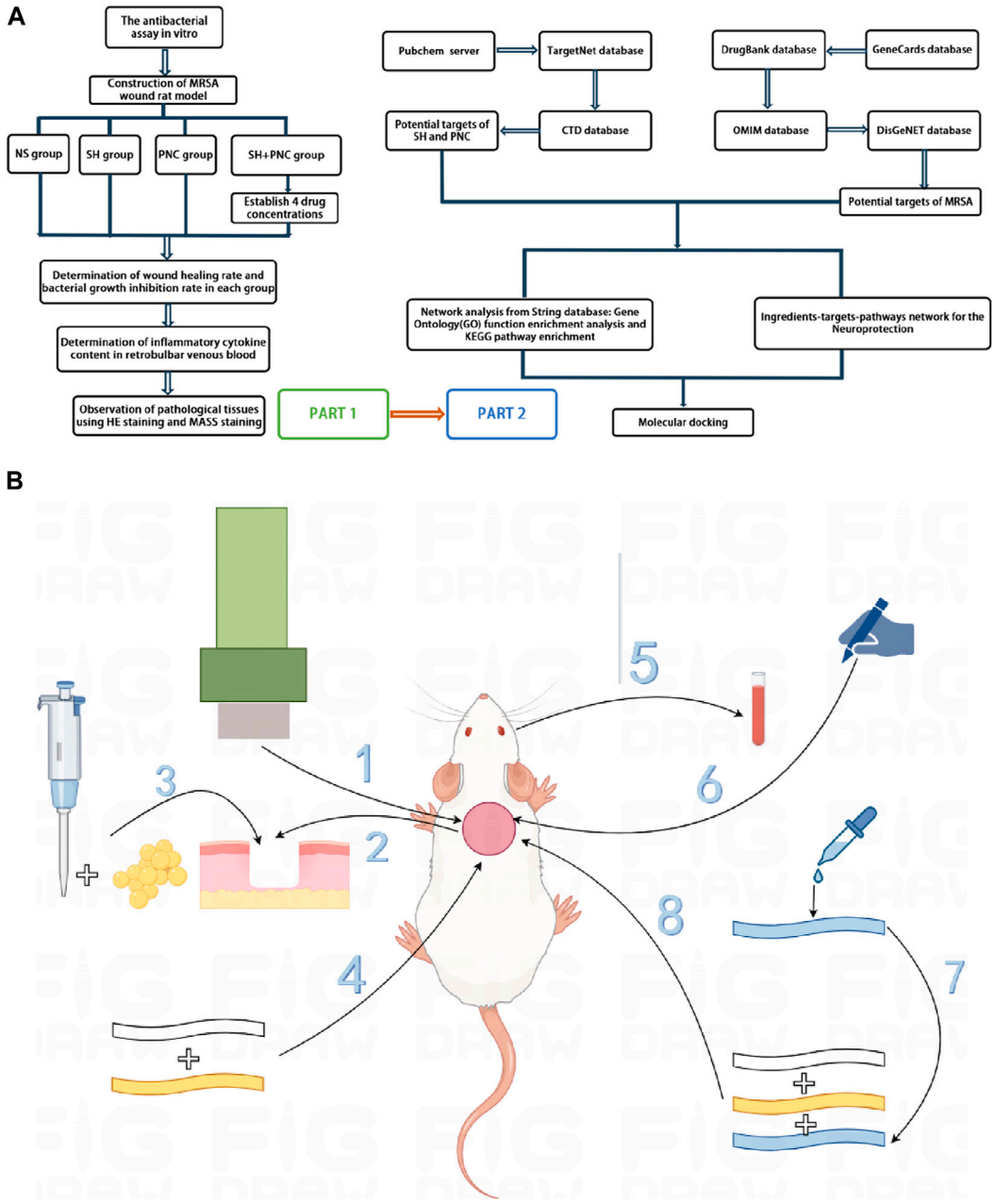


FIGURE 1
Overall workflow of SH + PNC treatment for methicillin resistant *staphylococcus aureus* infected wounds (**(A)**, Part 1 is workflow of network pharmacology; Part 2 is workflow of animal experiments). Schematic diagram of the flow of animal experiments (**(B)**, 1. Using a skin picker to create a wound on the back of the rat; 2. The wound is transverse and deep to the fascia layer.; 3. Inoculating the bacterial solution onto the back wound; 4. Wraping with vaseline gauze and sterile gauze in turn; 5. Collecting the blood from the retrobulbar vein of the rat; 6. Using a sterile transparent film to outline the wound surface; 7. Preparing drug gauze by impregnating it with drug solution; 8. Apply drug gauze, vaseline gauze, and sterile gauze to bind up the wound in order).

2.2 Experimental drugs

Sodium houttuyfonate (purity≥99%) (Xi'an Kailai Biological Engineering Co., Ltd.); Penicillin G for injection (Shandong Lukang Pharmaceutical Co., Ltd.); Tetrazolium salt (MTT, Guangzhou Saiguo Biotechnology Co., Ltd.); dimethyl sulfoxide (DMSO, Chengdu Kelong Chemicals Co., Ltd.).

2.3 Strain identification

2.3.1 Preparation of strain plate and bacterial solution

Prepare MH broth medium and MH agar medium and store them in a refrigerator at 4°C for future use. Thaw the standard strain of *Staphylococcus aureus* ATCC 25923 and a MRSA strain.

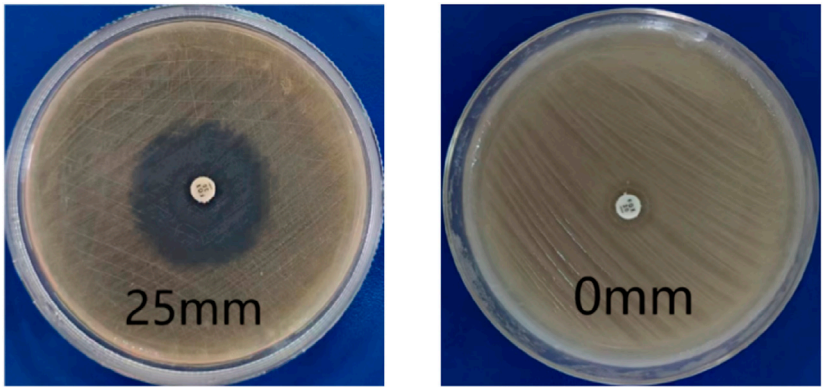


FIGURE 2
Drug sensitivity test results. **(A)** is MSSA (the diameters of bacterial inhibition zone≥22 mm). **(B)** is MRSA (the diameters of bacterial inhibition zone <21 mm).

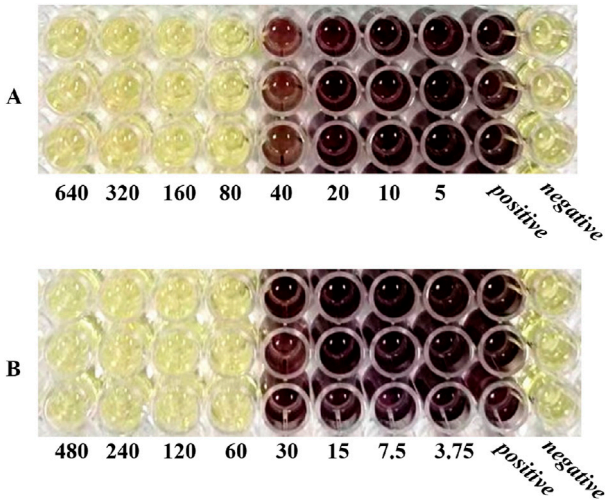


FIGURE 3
Microbroth dilution method was used to determine the MIC of drugs. **(A)** is SH(μg/mL). **(B)** is PNC(u/mL).

Pipette 2 μL of bacterial solution into 1 mL of MH broth culture medium, place it in a constant temperature shaker at 37°C and 120r/min for 12 h of shaking culture. Use a loop to dip a small amount of bacterial solution and inoculate it onto the MH agar plate using a continuous serpentine curve streaking method. After 24 h of cultivation, freeze it and pick a single colony from the plate with the inoculated strain into 1 mL of MH broth culture medium. Centrifuge the cultured bacterial solution at 8000r/min for 3 min, and then add 1 mL of normal saline to resuspend it. Use physiological saline as a blank control, detect the OD600 nm value of the bacterial solution using a nucleic acid protein analyzer, dilute the OD value of the bacterial solution with physiological saline to 1.0 (1OD600 = 1.5 × 108 cfu/mL), and finally dilute the bacterial solution with MH broth medium to 1 × 105 cfu/mL for use.

2.3.2 MRSA identification

Adjust the concentration of the bacterial solution to 0.5 McFarland concentration using a turbidimeter, dip a sterile cotton swab into the bacterial suspension, then evenly spread it onto the MH agar plate, and finally attach a cefoxitin (FOX) drug susceptibility disk (30 μg/disk). Incubate for 24 h in a 37°C incubator. The results were interpreted in accordance with the Clinical and Laboratory Standards Institute (CLSI) standards. The quality control strain is *Staphylococcus aureus* ATCC 25923.

2.4 *In vitro* antibacterial experiment

2.4.1 Drug preparation

Add sodium houttuyfonate powder and penicillin G powder to the MH broth culture solution, shake and mix well, and prepare according to the two-fold dilution method. The concentration gradients are 1,600, 800, 400, 200, 100, 50, 25, 12.5 μg/mL and 1,200, 600, 300, 150, 75, 37.5, 18.75, 9.375 μg/mL. Weigh 250 mg of MTT powder and dissolve it in 50 mL of PBS solution that has been sterilized under high pressure. Prepare a MTT solution with a concentration of 5 mg/mL, filter it through a 0.25 μm bacterial filter, and store it in a refrigerator at 4°C away from light.

2.4.2 Determination of minimum inhibitory concentration (MIC)

Take a sterile 96-well plates, set up 3 replicates for each drug concentration, and do not add samples to the edge wells of the 96-well plates. Add the diluted drugs in the order from high concentration to low concentration, except for the negative control, and add bacterial solution (concentration of 1 × 105 cfu/mL) to each well. Use MH broth culture solution to make up to 100ul, and the final concentrations of SH solution are 640, 320, 160, 80, 40, 20, 10, 5 μg/mL, and PNC is 480, 240, 120, 60, 30, 15, 7.5, 3.75u/mL. The positive control group consists of MRSA bacteria without drug intervention, while the negative

TABLE 1 MIC and FICI values of various drugs *in vitro* antibacterial experiments.

Strain number	SH alone MIC(μg/mL)	PNC alone MIC(u/mL)	SH MIC(μg/mL) /PNC MIC(u/mL)	FICI
1	80	60	20/15	0.5
2	70	60	4.375/30	0.5625
3	80	70	10/17.5	0.375
4	60	70	3.75/35	0.5625
5	80	60	10/15	0.375
6	60	60	3.75/30	0.5625
7	60	60	15/15	0.5
8	60	60	15/15	0.5
9	70	70	4.375/35	0.5625
10	70	70	17.5/17.5	0.5
11	60	60	3.75/30	0.5625
12	60	60	15/15	0.5
13	60	40	7.5/10	0.375
14	60	40	7.5/10	0.375
15	60	40	7.5/10	0.375
16	60	40	15/10	0.5
17	60	40	7.5/10	0.375
18	60	40	3.75/20	0.5625
19	60	40	15/10	0.5
20	60	40	15/10	0.5

control group consists of pure MH broth medium. The remaining unsampled edge holes were filled with physiological saline. Place it in a 37°C incubator for 15 h, then add 10 μL of MTT solution to each well and shake it for 1 h at 37°C on a shaker (120r/min). The minimum drug concentration corresponding to the absence of bacterial growth in the visual inspection is the MIC of the bacteria. Finally, add DMSO to each well, and use a microplate reader to measure the absorbance value at a wavelength of 490 nm, thereby calculating the inhibition rate of each concentration of the two drugs.

2.4.3 Combined antibacterial effect of drugs

According to the above MIC results, the final concentrations of the two drugs after sample addition were 2MIC, 1MIC, 1/2MIC, 1/4MIC, 1/8MIC, 1/16MIC, and 1/32MIC. Using the chessboard dilution method, add 40ul of each drug and 20ul of bacterial solution to each well, and make up to 100ul with MH broth culture medium. Add 100ul of normal saline to the hole without sample on the edge。Use the same method as above and calculate the MIC and fractional inhibitory concentration index (FICI). Standard: FICI ≤ 0.5 indicates synergistic effect; 0.5 < FICI ≤ 1 is additive effect; 1 < FICI ≤ 2 is an unrelated effect; FICI > 2 is antagonistic.

2.5 Animal experiments

2.5.1 Establishment of rat model of MRSA infection wound

SD rats were injected with 3% sodium pentobarbital solution intraperitoneally at a dose of 0.3 mL/100 g. After complete anesthesia, shave the back hair, with an area of 3 × 3 cm^2. Create a circular wound with a diameter of 15 mm using a skin punch, reaching the fascia. Then, use a pipette to inject 15 μL of bacterial solution with a concentration of 1.5 × 10^8 cfu/mL into the back wound of an SD rat. Once the bacterial solution is fully absorbed, sequentially apply a single layer of sterile vaseline gauze for moisturizing and cover it with four layers of sterile gauze (Figure 1B). Breding in the animal experimental center of Southwest Medical University, with the ambient temperature of 22°C–24°C and the relative humidity of 60%–80% manually controlled.

2.5.2 Identification of wound secretion

On the third day after surgery, the wound secretion was taken with a cotton swab and transferred to a methicillin-resistant *Staphylococcus aureus* color medium, which was evenly applied and incubated for 24 h in a 37°C incubator. The results were

10.3389/fphar.2025.1530217

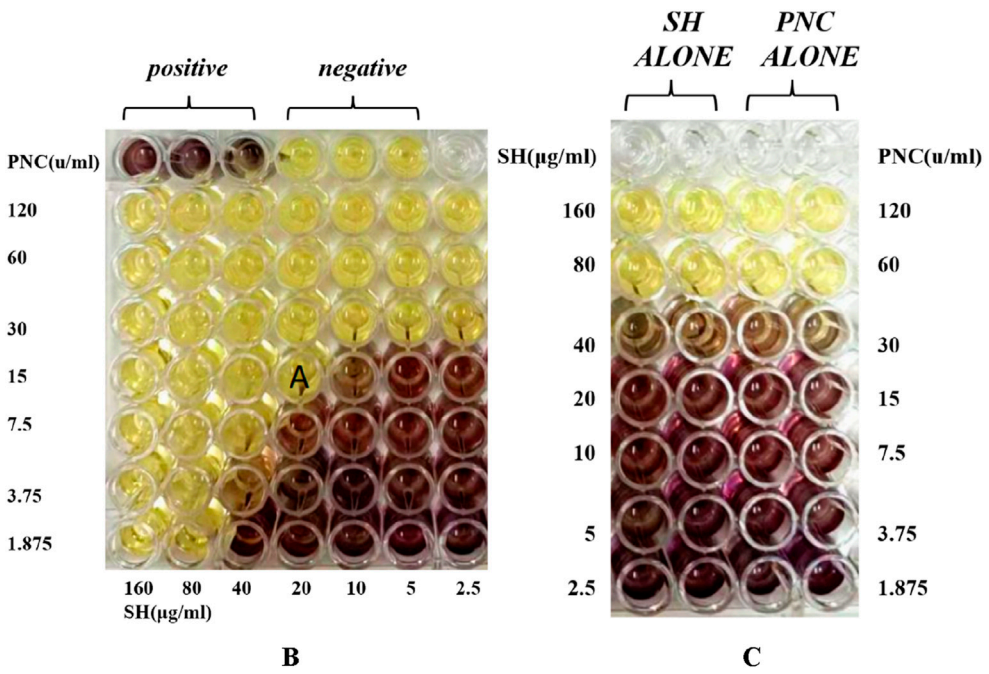


FIGURE 4
Drug sensitivity results of Sodium houttuyfonate combined with Penicilin G detected by microbroth dilution method (**(B)**, Combined drug sensitivity results of strain No. 1). The first row of 1-3 holes are the positive control group, and the 4-6 holes are the negative control group. The MIC of SH alone in the figure is 80 μg/mL, and the MIC of PNC alone is 60u/mL. The best bacteriostatic concentration combination (SH 20 μg/mL + PNC15u/mL) is shown in the hole **(A)** in the figure where no bacterial growth is observed, with FICI = 20/80 + 15/60 = 0.5. Determination of MIC values for SH and PNC of isolated strain No. 1 **(C)**.

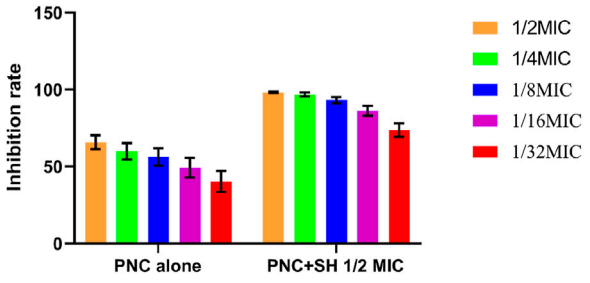


FIGURE 5
Changes in average inhibition rate of Penicilin G alone and combination with Sodium houttuyfonate (1/2 MIC).

identified according to the instructions of the colorimetric medium for methicillin-resistant *Staphylococcus aureus*.

2.5.3 Animal grouping and preparation of drug gauze

Prepare the drug solution according to the results of the *in vitro* antibacterial test, take a sterile double-layer gauze measuring 2 × 2 cm^2, and soak it with the drug solution. SD rats were divided into five groups, with three rats in each group. Four of the groups were treated with different concentrations of SH + PNC, while one group was treated with normal saline as a blank control group.

2.5.4 Measurement of wound healing rate

The rats were subjected to dressing changes on postoperative days 3, 5, and 7, and were sacrificed on day 9. On the 3rd and 9th day, sterile transparent film was placed on the wound surface, and then the wound surface was outlined and scanned using a gel imaging system. The image was analyzed using ImageJ software to calculate the wound area and wound healing rate. The wound healing rate (%) = (area before treatment - area after treatment)/ area before treatment X100%.

2.5.5 HE staining and MASSON staining

On the ninth day, SD rats were sacrificed and skin tissue was removed using a 15 mm diameter skin-removing device aligned with the center of the wound, which reached deep into the fascia. Soak the skin tissue in the fixative for 24 h, and embed the tissue in paraffin. Then, the tissue was stained with HE and MASSON, and the number of neutrophils in a random field of view was observed and recorded under a 200x light microscope. The percentage of collagen fibers in the image was determined using ImageJ software.

2.5.6 Inflammatory factor determination

On the 3rd and 9th day, anesthetize rats with 3% sodium pentobarbital intraperitoneally, insert the capillary glass tube from the inner canthus, slide it to the retrobulbar vein, rotate the glass tube until blood drips out, collect 1 mL, then pull out the glass tube, place the whole blood sample at room

TABLE 2 Comparison of average inhibition rates of Penicilin G alone and combined with Sodium houttuyfonate (1/2 MIC) ($\bar{x} \pm s$, %).

PNC	Inhibition rate (PNC)	Inhibition rate (PNC + SH)	t
1/2MIC	65.74 ± 4.58	98.23 ± 0.48	31.55
1/4MIC	59.89 ± 5.27	96.80 ± 1.26	30.46
1/8MIC	56.18 ± 5.63	93.16 ± 1.98	27.71
1/16MIC	49.20 ± 6.40	86.19 ± 3.21	23.10
1/32MIC	40.35 ± 6.82	73.64 ± 4.33	18.42

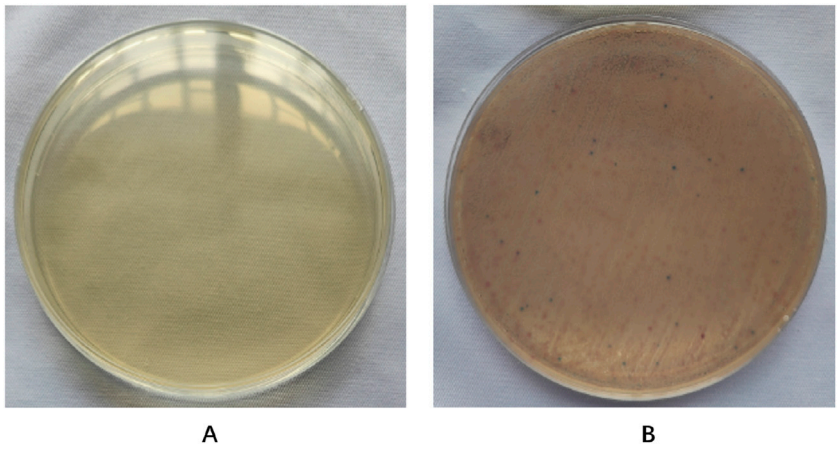


FIGURE 6
Results of MRSA chromoculture plate experiments. The color of the uninoculated MRSA coloration culture plate is light yellow **(A)**. A large number of pink MRSA colonies grow on the plate, scattered among other blue **(B)** colonies.

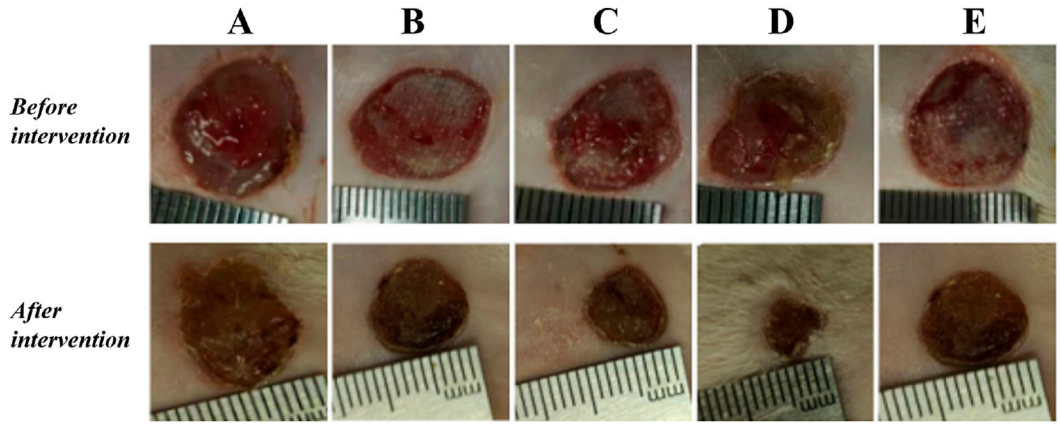


FIGURE 7
The healing status of MRSA wounds under different medication regimens of SH + PNC. **(A)** SH5 μg/mL + PNC15u/mL, **(B)** SH5 μg/mL + PNC30u/mL, **(C)** SH20 μg/mL + PNC15u/mL, **(D)** SH20 μg/mL + PNC30u/mL, **(E)** Normal saline (NS) was used as the blank control group.

temperature for 2 h, take the supernatant, freeze it and store it in a −80°C refrigerator for future use. Use the corresponding ELISA kit instructions, and finally measure the optical density (OD450 nm) value and calculate the sample concentration.

2.6 Network pharmacology

2.6.1 Target acquisition

The chemical structures of SH and PNC were obtained on Pubchem database (https://pubchem.ncbi.nlm.nih.gov/) (Kim,

TABLE 3 The healing rate of MRSA wounds under different medication regimens of SH + NPC.

Group (n = 15)	Healing rate (%)	*F*	*P*
A	28.37 ± 8.63	46.64	<0.0001
B	29.67 ± 8.57		
C	90.78 ± 8.93		
D	91.98 ± 9.77		
E (NS)	28.64 ± 8.21		

TABLE 4 Comparison of MRSA wound healing rate within the SH + PNC therapy group.

Group (n = 15)	Healing rate (%)	*P*
A	28.37 ± 8.63	0.98
B	29.67 ± 8.57	0.96
C	90.78 ± 8.93	<0.0001
D	91.98 ± 9.77	<0.0001

2016). Upload SH and PNC to the TargetNet database (http://targetnet.scbdd.com/) (Zhi-Jiang et al., 2016) and CTD database (Comparative Toxicogenomics Database, https://ctdbase.org/) (Tumayhi et al., 2023) to obtain the target sites of action, load the obtained targets into the UniProtKB database (https://www.uniprot.org/) (Zaru et al., 2020) to obtain standard target names, and set the search criteria to "*Homo Sapiens*". Search for 'methicillin-resistant *Staphylococcus aureus* infection' in the GeneCards database (https://www.genecards.org/) (Stelzer et al., 2016), Drug Bank database (https://go.drugbank.com/) (Svensson et al., 2018), DisGeNET database (https://disgenet.com/) (Piñero et al., 2017), and OMIM database (https://www.omim.org/) (Amberger et al., 2019) to obtain disease-related genes. Integrate data, remove duplicate values, and cross-reference the above targets using R software (Version 4.4.1, The R Project for Statistical Computing) (Sepulveda, 2020; Bota and Fodor, 2019) to obtain potential therapeutic targets.

2.6.2 Network construction

Import the cross targets into the STRING database (Version 12.0, https://cn.string-db.org/) (Szklarczyk et al., 2023) to construct a protein–protein interaction (PPI) network, with the condition set to *Homo sapiens*, minimum required high confidence (0.700) and hide disconnected nodes in the network. Further analysis of the PPI network was conducted through the Cytoscape software (Version 3.10.2) (Doncheva et al., 2019) to identify core targets.

2.6.3 Functional enrichment analyses and compound-target-pathways (CTP) network

Go analysis and KEGG pathway analysis of SH and PNC targets were performed by using DAVID database (https://david.ncifcrf.gov/home.jsp) (Xie et al., 2022) to predict the biological functions, action pathways and potential relationships of SH and PNC. Based on these core targets and pathways, CTP network were constructed to intuitively clarify the therapeutic mechanism of SH + PNC on methicillin resistant *staphylococcus aureus* infected wounds.

2.6.4 Molecular docking

Paymol software (Version 3.0) (Hancock et al., 2022) was used to remove water molecules and small molecule ligands from the protein structure, and then imported into AutoDock Vina (Version 1.1.2) (Forli et al., 2016) for hydrotreating. The receptor and ligand were docked in AutoDock Vina software to analyze their binding activities. Paymol was used to visualize the results of molecular docking simulation validation.

2.7 Statistical methods

SPSS27.0 statistical software was used for analysis. Data were expressed as $\bar{x} \pm s$, and data that conformed to normal distribution and homogeneity of variance were analyzed using one-way analysis of variance and independent sample t-test. LSD-t test was used for inter-group comparison Sample data that do not conform to the normal distribution are represented by the median (interquartile range), and Kruskal–Wallis H tests are used for overall comparisons and pairwise comparisons between sample groups. $P < 0.05$ indicates a statistically significant difference.

3 Result

3.1 Identification of MRSA strains

According to CLSI standards, when the diameter of the inhibition zone is ≤ 21 mm, it can be determined as MRSA; When the diameter of the bacteriostatic zone is ≥ 22 mm, it can be diagnosed as methicillin-sensitive *Staphylococcus aureus* (MSSA). The inhibition zone test was performed on the quality control strain ATCC 25923, and the inhibition zone diameter was 25 mm (Figure 2A), which meets the MSSA standard. The diameter of the inhibition zone for the clinical strains was less than 21 mm (Figure 2B), thus confirming them as MRSA.

3.2 Antibacterial testing *in vitro*

The MIC values of SH and PNC against the standard strain of *Staphylococcus aureus* ATCC 25923 were 60 μg/mL and <1u/mL, respectively. The MIC values for clinical isolates of MRSA ranged from 60 to 80 μg/mL and 40 to 70u/mL (Figure 3, Table 1). The FICI of SH + PNC was 0.375–0.5625, and 14 strains showed synergistic antibacterial effects, while 6 strains showed additive antibacterial effects (Figure 4, Table 1). The OD value of the 96-well plates at a wavelength of 490 nm was measured using a microplate reader, and the average inhibition rate was calculated. The results showed that the inhibition rate of sodium houttuyfonate at a drug concentration of 1/2MIC combined with different concentrations of penicillin G was significantly higher than that of penicillin G alone ($P < 0.05$), indicating that SH can significantly increase the antibacterial effect of PNC(Figure 5, Table 2).

10.3389/fphar.2025.1530217

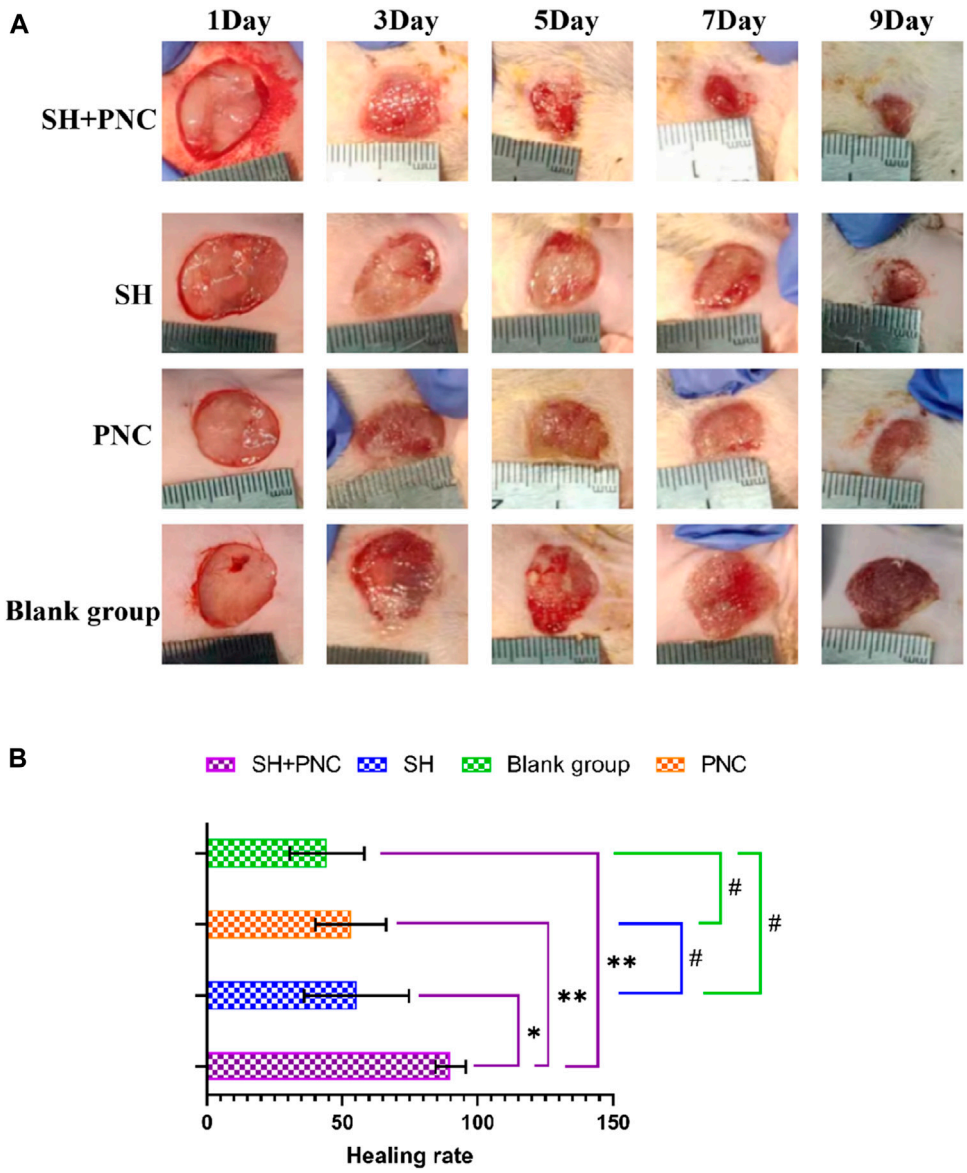


FIGURE 8
Contrast of infected wounds in MRSA ((**A**), Photography equipment: SONY IMAX799 ISO:500 WB:6,000 Shutter:1/30 *1). Comparison of wound healing rates between the groups ((**B**), *p < 0.05, **p < 0.01, #p > 0.05, p < 0.05 indicates statistical significance, while a p < 0.01 indicates a significant difference).

3.3 Identification of wound secretion

According to the instructions for the color medium for methicillin-resistant *Staphylococcus aureus* (MRSA) from the French company Comag, MRSA colonies are pink to light purple; Other bacterial colonies are blue. The results showed that the colonies of bacteria cultured from the wound secretions in each group were almost pink MRSA, with occasional blue colonies of other bacteria (Figure 6).

3.4 Drug proportioning scheme

The results showed that there was redness and swelling around the wound surface in all groups before intervention, accompanied by a large amount of purulent exudation, and all groups had obvious bacterial mats. After intervention, the wound surface area in experimental group C and experimental group D was smaller than that in the control group, and no secretions or bacterial mats were observed (Figure 7). The healing rate of each group is shown in Table 3. The Dunnett-t test showed that the wound healing rate in experimental groups C and D was significantly higher than that in the control group ($P < 0.05$) (Table 4). Group C had a concentration of 90.78 ± 8.93 (%), while the group D had a concentration of 91.98 ± 9.77 (%). There was no significant difference between the two groups, and both were significantly higher than the other three groups. At the same time, the drug concentration of penicillin G in group C was lower than that in group D, which allowed group C to reduce the amount of antibiotic

TABLE 5 Comparison of wound healing rates between the groups.

Group (n = 20)	Healing rate (%)	*F*	*P*
SH + PNC	90.08 ± 5.64	46.65	<0.001
SH	55.35 ± 19.39		
PNC	53.19 ± 13.05		
Blank group	44.38 ± 13.73		

TABLE 6 Comparison of IL-6 and TNF- α in blood between the groups.

Group (n = 40)	TNF-α (ng/L)	IL-6 (ng/L)	
SH + PNC	444.13 ± 6.69	122.80 ± 18.37	Before intervention
SH	443.83 ± 2.86	138.03 ± 24.54	
PNC	443.83 ± 3.12	127.77 ± 10.45	
Blank group	439.19 ± 7.11	145.75 ± 31.20	
F	1.99	2.1	
P	0.13	0.12	
SH + PNC	397.49 ± 41.35	102.13 ± 3.31	After intervention
SH	433.62 ± 22.52	147.39 ± 5.87	
PNC	423.71 ± 10.11	120.75 ± 8.64	
Blank group	442.82 ± 16.18	121.55 ± 2.48	
F	5.94	109.668	
P	0.012	0.009	

TABLE 7 Comparison of neutrophil numbers in MRSA infected wounds.

Group (n = 40)	Piece	F	P
SH + PNC	82.40 ± 16.59	43.793	<0.001
SH	143.50 ± 25.97		
PNC	165.20 ± 28.70		
Blank group	207.50 ± 26.58		

usage while achieving similar wound healing rates. Therefore, the drug concentration of experimental group C (SH20 μg/mL + PNC15u/mL) was selected for subsequent experiments.

3.5 Wound healing rate

Compared with other groups, the SH + PNC group showed a significant reduction in wound area on day 5, with less purulent secretion and no bacterial mats observed. The wound area in the SH group significantly decreased on day 9. The wound area in the PNC group decreased on day 7, but there was no significant change in purulent secretion compared with the blank control group. It can be seen that the healing time of MRSA infected wounds in the combined medication group is faster and the healing effect is better (Figure 8A).

ImageJ software was used to process the images, and the wound area of each group was measured, and the wound healing rate of each group was calculated (Figure 8B, Table 5). The LSD-t test showed that the wound healing rate in the SH + PNC group was significantly higher than that in the other groups ($P < 0.05$), while there was no significant difference in wound healing rate between the SH, PNC, and blank groups ($P > 0.05$).

3.6 Inflammatory factor assay

There were no significant differences in the levels of IL-6, INOS, and TNF-α in the blood of each group before intervention, while there were significant differences in the levels of IL-6 and TNF-α in the blood of each group after intervention ($P < 0.05$) (Table 6; Figure 9).

Using the LSD-t test, it was found that the levels of IL-6 and TNF-α in the blood of the combined medication group were significantly lower than those of the other groups after intervention ($P < 0.05$). The IL-6 content in the SH group was lower than that in the PNC group and the blank control group ($P < 0.05$). There was no significant difference in the levels of IL-6 and TNF-α in the blood between the PNC group and the control group.

3.7 HE staining

Under 100x light microscope, neutrophils were clearly identified based on their microscopic characteristics (Figure 10). Record the average value of the number of neutrophils under random vision (Table 7). The LSD-t test was used to compare the groups, showing that the number of neutrophils in the combined medication group was significantly lower ($P < 0.05$). There was no significant difference in the number of neutrophils between the SH group and the PNC group.

3.8 Masson staining

As shown in Figure 11, blue represents collagen fibers. Randomly record the image of the field of view, use the ImageJ software to determine the percentage of collagen fibers in the image, and take the average value (Table 8). The Kruskal–Wallis H test was used for intra-group comparison, and the percentage of collagen fibers in the combination group was the highest ($P < 0.05$). There was no significant difference in the percentage of collagen fibers between the SH group and the PNC group.

3.9 Network pharmacology

3.9.1 The targets information of SH and PNC

Using PubChem database, we obtained the 3D structure and smiles chemical formula of SH and PNC. By searching the database separately for keywords' sodium houttuyfonate "and" penicillin G ′, we obtained 83 and 325 relevant targets, respectively. Upload the

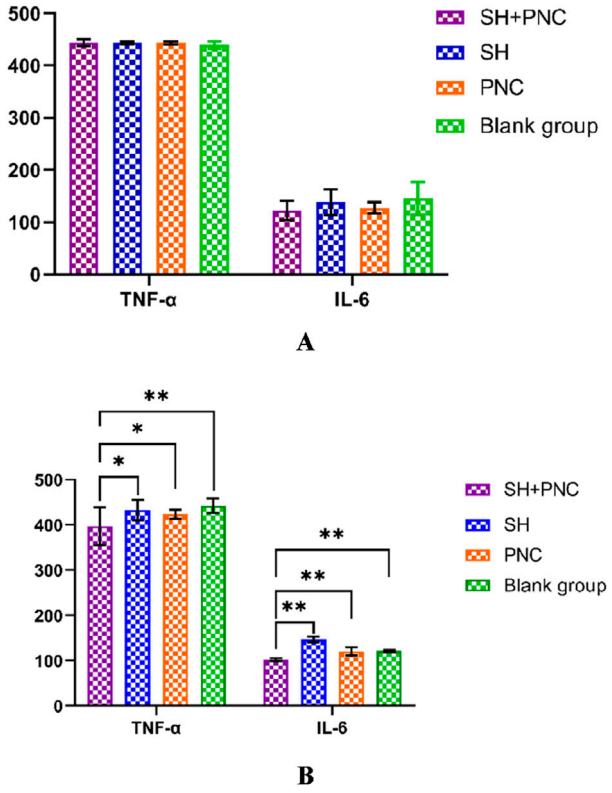


FIGURE 9
Comparison of IL-6, and TNF- α in blood between the groups before intervention **(A)**. Comparison of IL-6, and TNF- α in blood between the groups after intervention **(B)** (*p < 0.05, **p < 0.01, p < 0.05 indicates statistical significance, while a p < 0.01 indicates a significant difference).

above targets to UniProtKB database to get the target standard target names.

3.9.2 Network construction

2,362 disease-related targets were obtained by using GeneCards database, Drug Bank database, OMIM database and DisGeNET database. This indirectly reflects the complex molecular pathways and related mechanisms involved in nerve injury. Using Cytoscape software, we interacted SH and PNC targets with disease targets and obtained Venn diagram (Figure 12A).

We used STRING database to connect 126 potential therapeutic targets and obtained a PPI network consisting of 86 nodes and 502 edges (Figure 12B) to clarify the potential mechanism of SH combined with PNC on MRSA infected wounds. Then the target protein interaction data were imported into Cytoscape software, and the topological parameters of the network were calculated and analyzed by using the plug-in CytoNCA. The key nodes in the network are screened according to Betweenness (BC), Closeness (CC), Degree (DC), Eigenvector (EC), Local Average Connectivity-based method (LAC), Network (NC) as shown in Figure 12C.

3.9.3 Functional enrichment analyses and compound-target-pathways (CTP) network

DAVID database was used to conduct GO enrichment analysis and KEGG pathway enrichment analysis on the core targets to study the biological mechanism, and the biological process, cellular component and molecular function were elaborated.

As shown in Figure 13, the biological processes of the top five are positive regulation of nitric oxide biosynthetic process, positive regulation of gene expression, positive regulation of smooth muscle cell proliferation, cellular response to lipopolysaccharide and inflammatory response, while cellular components are extracellular space, extracellular region, phagocytic cup, external side of plasma membrane and cell surface. The mechanisms of molecular function are cytokine activity, identical protein binding, protein binding, peptidase activity, protease binding.

The target related pathways were obtained by KEGG enrichment analysis. Meanwhile, we selected the top 20 representative pathways for visualization analysis based on gene count, enrichment and P-value (Figure 14A). The analysis results showed that IL-17 signaling pathway play an important role through cell proliferation and differentiation, apoptosis, regulation of immune inflammation, cytokine synthesis/inhibition. At the same time, the targets in the IL-7 pathway are the same as those in other pathways, and can act on multiple molecular pathways through the same target (Figures 14B, C).

To comprehensively elucidate the mechanism of the therapeutic effect, we constructed compound-target-molecular pathways through Cytoscape software, as shown in the Figure 14D. The CTP network of core targets has 174 nodes and 775 edges, and 155 related molecular pathways. CTP network intuitively shows the possible mechanism of treating nerve injury through the interaction between targets and different targets acting on the same pathway. By analyzing the above targets, we found that some of them are related

10.3389/fphar.2025.1530217

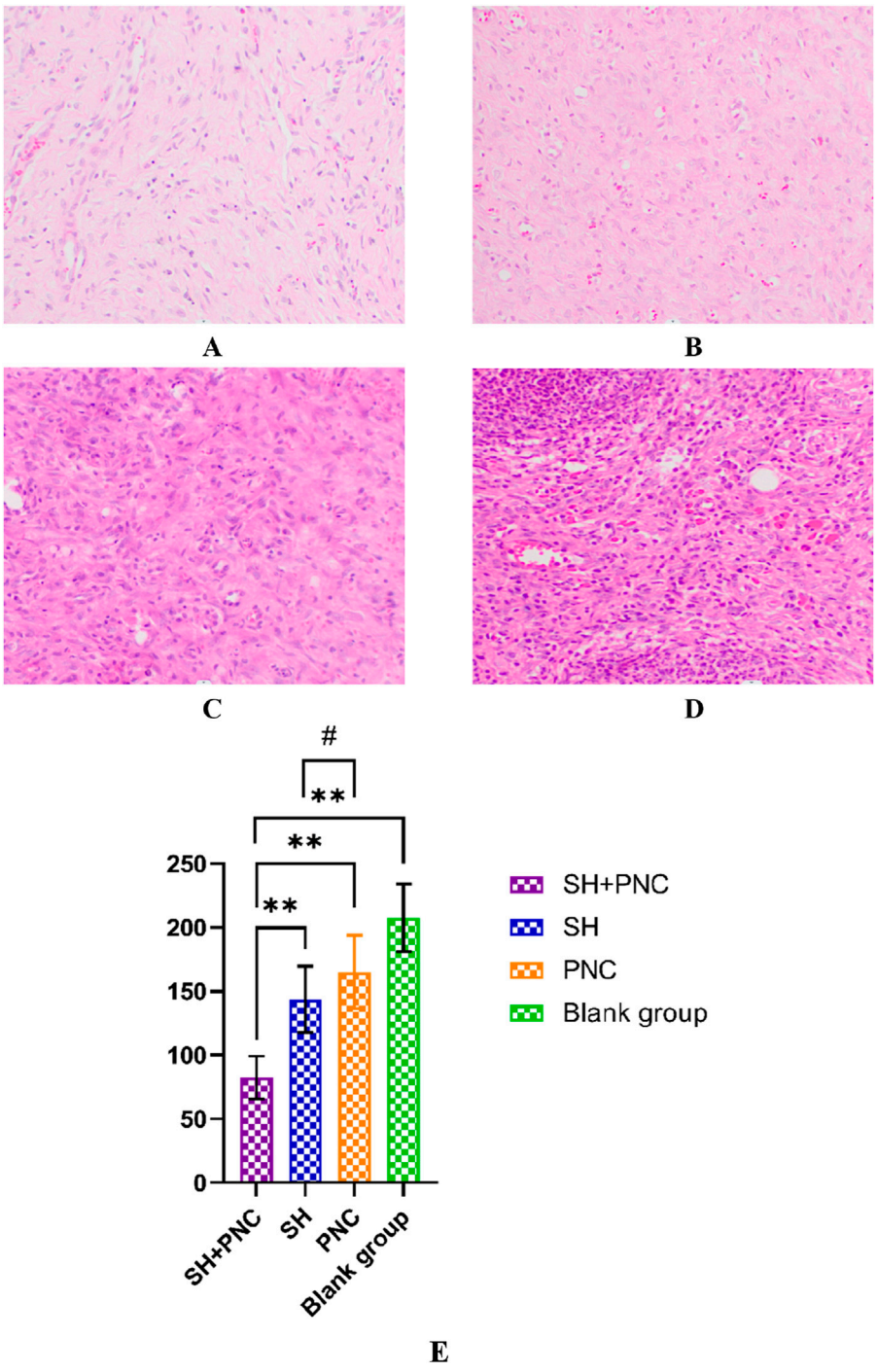


FIGURE 10
HE stained wound tissue pathology sections from MRSA. **(A)** SH + PNC, **(B)** SH, **(C)** PNC, **(D)** Blank group (x100). Comparison of neutrophil numbers in MRSA infected wounds (**(E)**, **p < 0.01, p < 0.05 indicates statistical significance, while a p < 0.01 indicates a significant difference).

to regulating mechanisms such as cell apoptosis, differentiation, and immune inflammation.

3.9.4 Molecular docking

By using CytoNCA software to reprocess the targets in the IL-17 signaling pathway, we obtained the targets IL1B, IL6, MMP9, IFNG, and TNF. Retrieve the molecular structure of the corresponding protein from the PDB database (https://www.rcsb.org/) (Konc and Janežič, 2022), and import it into AutoDock Vina to calculate the optimal binding site and binding energy (Figures 15A–E). The lower the binding energy, the higher the affinity. The binding energies of SH with IFNG, IL1B, IL6, MMP9 and TNF are −5.5, −5, −4.4, −5 and −7 kcal/mol, respectively. The PNCs are −6.8, −6.3, −7.5, −7.9 and −7.3 kcal/mol, respectively (Figure 15F).

10.3389/fphar.2025.1530217

TABLE 8 Comparison of percent collagen fibers of infected wounds in MRSA.

Group (n = 40)	Percentage of collagen fibers (%)	H	P
SH + PNC	71.2 ± 9.69	23.57	<0.001
SH	63.4 ± 5.65		
PNC	61.7 ± 9.90		
Blank group	50.7 ± 16.57		

4 Discussion

Staphylococcus aureus (S.aureus) is one of the most common opportunistic pathogens in humans, which can cause skin and soft tissue infection, intravascular infection, pneumonia, infectious arthritis, endocarditis, osteomyelitis, sepsis and other diseases (Ahmad-Mansour et al., 2021). Due to the emergence of drug-resistant strains, especially the widespread presence of MRSA, S. aureus is one of the main pathogens causing high incidence and mortality rates worldwide (Lee et al., 2018). According to the China

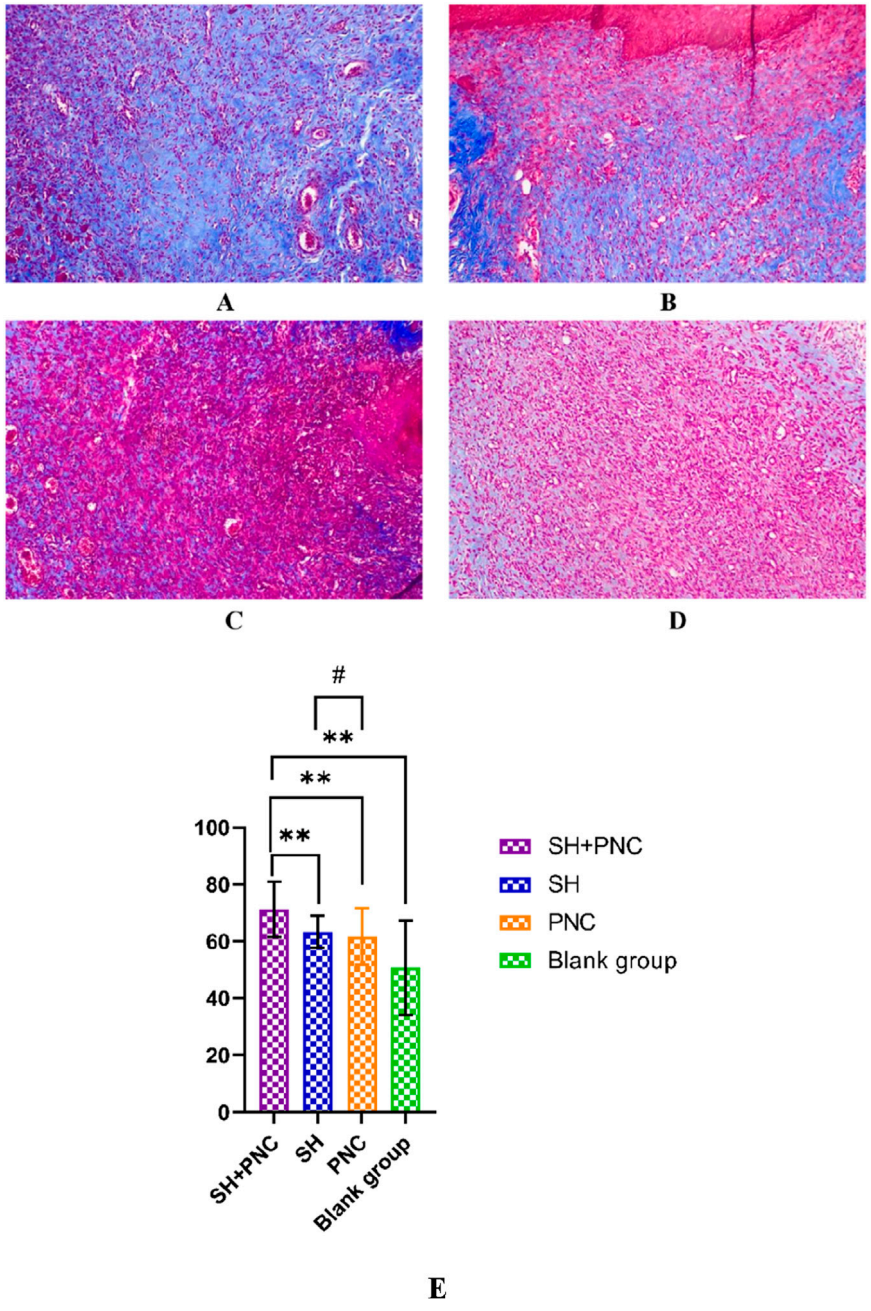


FIGURE 11
Masson-stained wound tissue pathology sections from MRSA. **(A)** SH + PNC, **(B)** SH, **(C)** PNC, **(D)** Blank group (x100). Comparison of percent collagen fibers of infected wounds in MRSA (**(E)**, **p < 0.01, p < 0.05 indicates statistical significance, while a p < 0.01 indicates a significant difference).

TABLE 9 Comparison of percent collagen fibers of infected wounds in MRSA.

Group (n = 40)	Percentage of collagen fibers (%)	H	P
SH + PNC	71.2 ± 9.69	23.57	<0.001
SH	63.4 ± 5.65		
PNC	61.7 ± 9.90		
Blank group	50.7 ± 16.57		

Antimicrobial Surveillance Network report (CHINET), the isolation rate of S. aureus in China in 2020–2021 ranked first among Gram-positive bacteria, and the detection rate of MRSA was around 30%. It is one of the main infectious pathogenic microorganisms in Chinese hospitals (Yun et al., 2023).

MRSA is characterized by rapid transmission, strong pathogenicity, high mortality, and resistance to various antibiotics such as β - lactams, tetracyclines, aminoglycosides, macrolides, etc (Lakhundi and Zhang, 2018; Turner et al., 2019). It is widely believed in clinical practice that vancomycin is an effective treatment for MRSA, but it is concerning that intermediate vancomycin resistant *Staphylococcus aureus* (VISA) and vancomycin resistant *Staphylococcus aureus* (VRSA) have emerged (Hernández-Aristizábal and Ocampo-Ibáñez, 2021; Appelbaum, 2006). Therefore, it is necessary to further study the mechanism of MRSA resistance and develop new treatment plans.

Traditional Chinese medicine has a wide range of sources and multiple targets, making it difficult for bacteria to develop resistance to it. It can be used as a treatment option for drug-resistant bacteria. At present, there are many herbal extracts that can inhibit the production of bacterial biofilm or inhibit the active efflux system to reverse the antibiotic resistance of MRSA (Liu et al., 2022; Li et al., 2022). Houttuynia cordata, belongs to the family of the genus Houttuynia cordata, has the functions of clearing heat and detoxifying, eliminating carbuncles and discharging pus, diuretic and relieving stranguria, and is used for lung carbuncle, phlegm-heat asthma, hot dysentery, hot stranguria, carbuncle and sore poison. Studies shows that its extract Sodium Houttuyfonate has anti-inflammatory and antibacterial effects. At present, studies have shown that Sodium Houttuyfonate has inhibitory effects on a variety of bacteria, such as *Pseudomonas aeruginosa*, *Candida* albicans, *Acinetobacter* baumannii (Ma et al., 2021; Zhou et al., 2022b).

This article tested the antibacterial efficacy of SH *in vitro* using the micro-broth dilution method, and the results showed that SH had a certain inhibitory effect on MRSA *in vitro*. Penicillin G is one of the most commonly used antibiotics in clinical practice, with the characteristics of economy and low toxicity. Experiments have shown that the combination of SH and PNC can increase their bacterial inhibition rate, decrease the MIC of PNC, and significantly enhance the antibacterial effect of PNC.

In the MRSA-infected wound model of SD rats, it was found that the SH + PNC group could significantly reduce the bacterial

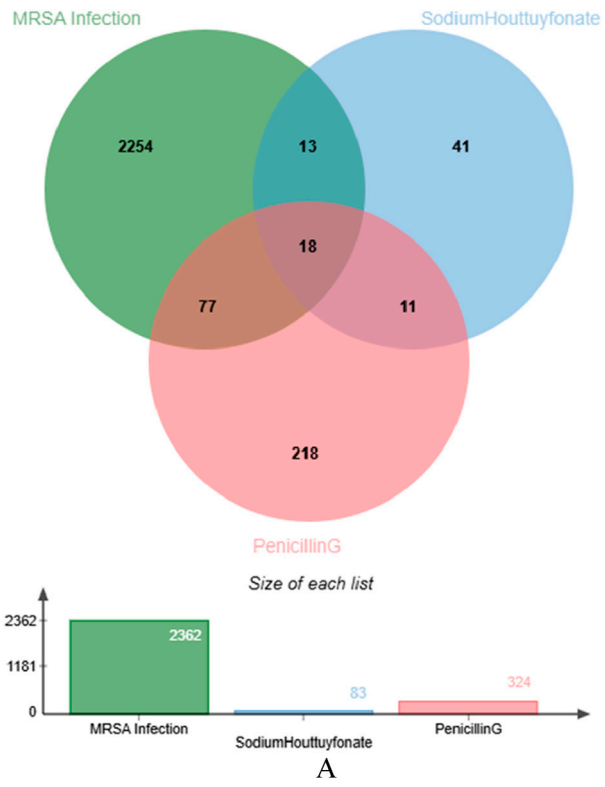


FIGURE 12
(Continued).

10.3389/fphar.2025.1530217

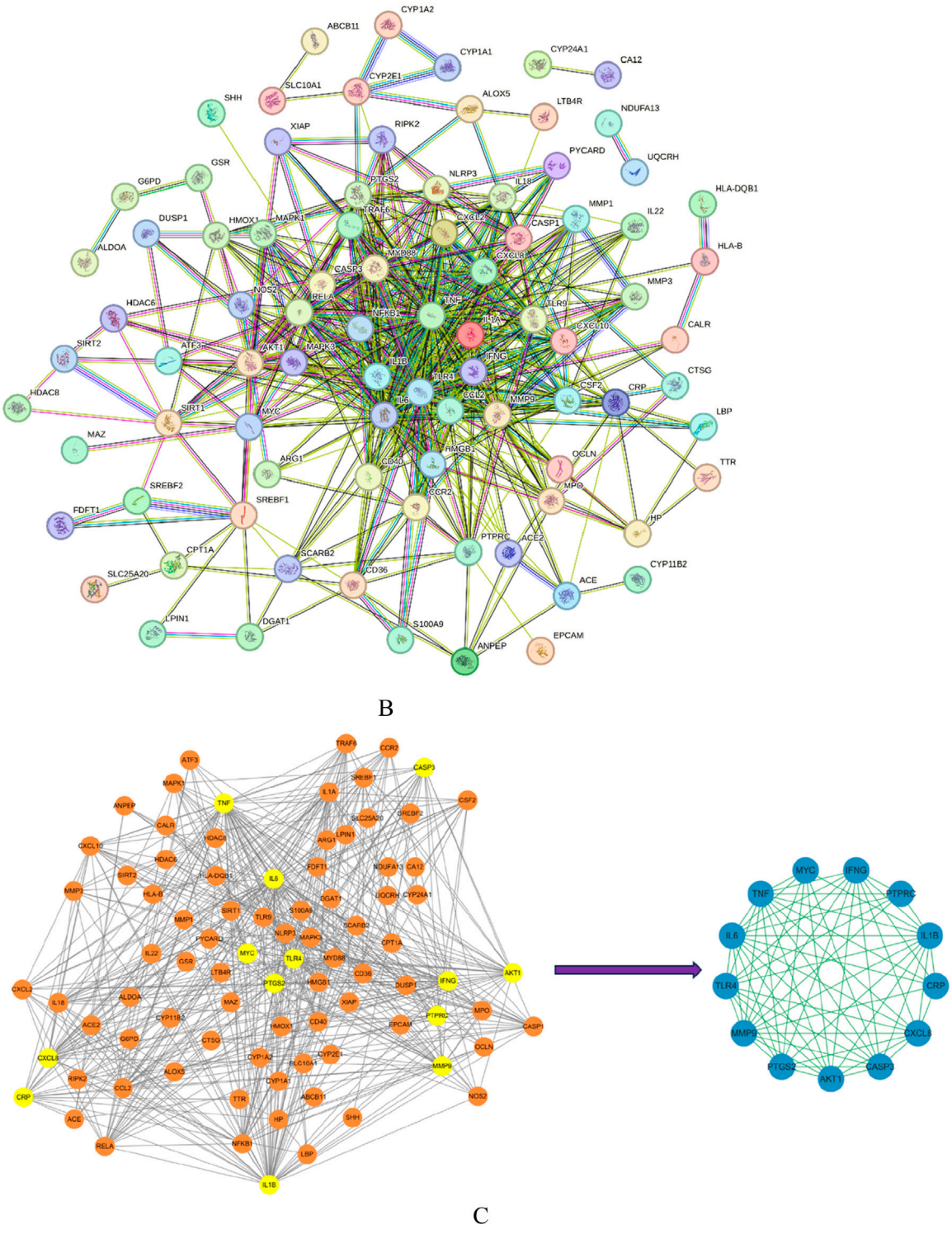


FIGURE 12
(Continued). Venn diagram of Sodium houttuyfonate and penicillin G **(A)**. PPI network of potential therapeutic targets **(B)**. Import PPI network data into Cytoscape to obtain protein interaction network, the key target protein interaction network obtained after filtering by CytoNCA analysis **(C)**.

count in the MRSA wound and promote the healing of the MRSA-infected wound compared with other intervention measures. The combined group can effectively reduce the content of some inflammatory factors in the blood. Pathological examination results showed that the number of neutrophils in the combined group decreased significantly and more collagen fibers were produced, suggesting that SH + PNC can regulate inflammation and promote the secretion of extracellular matrix, thereby generating granulation tissue to accelerate wound healing.

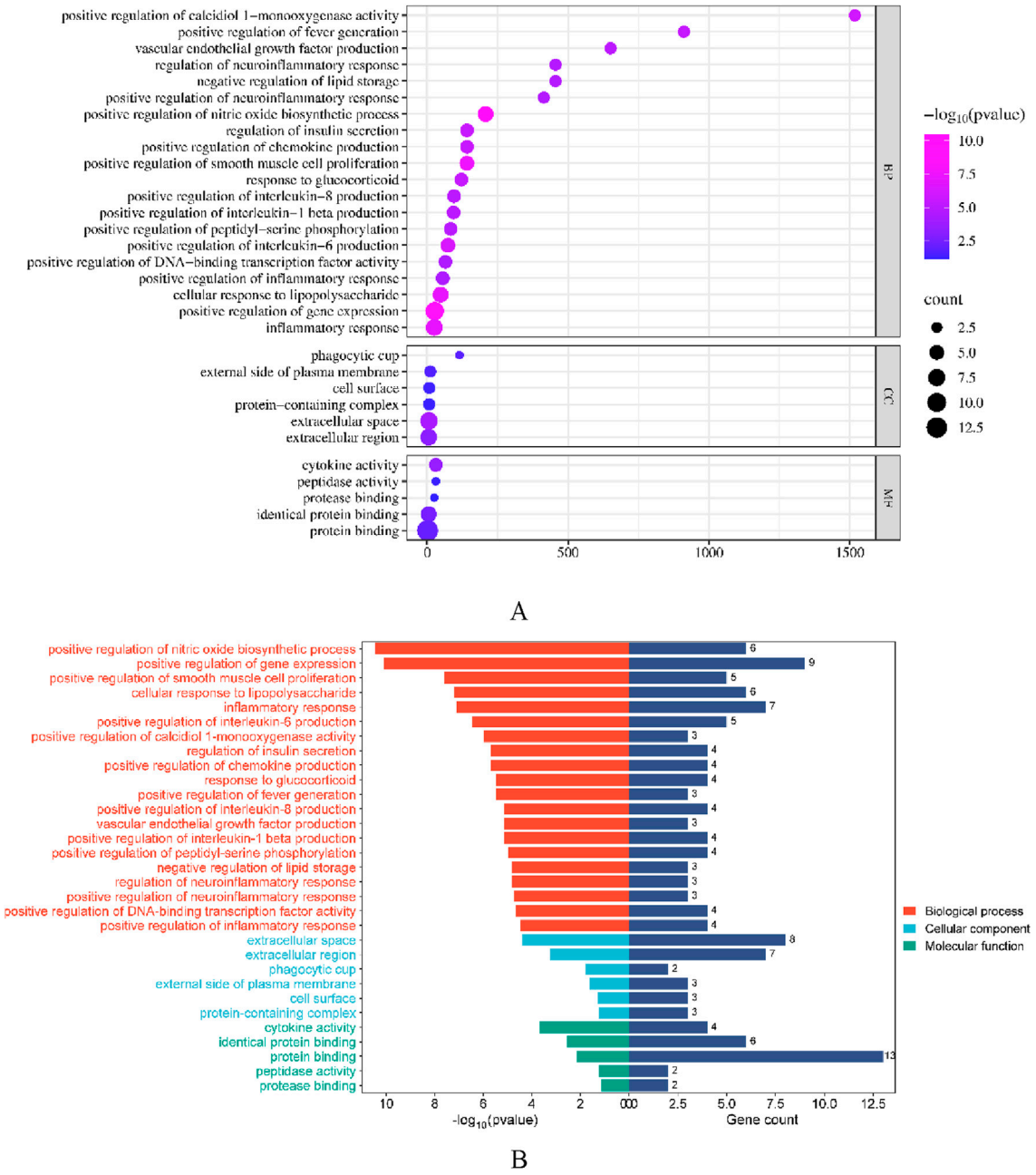
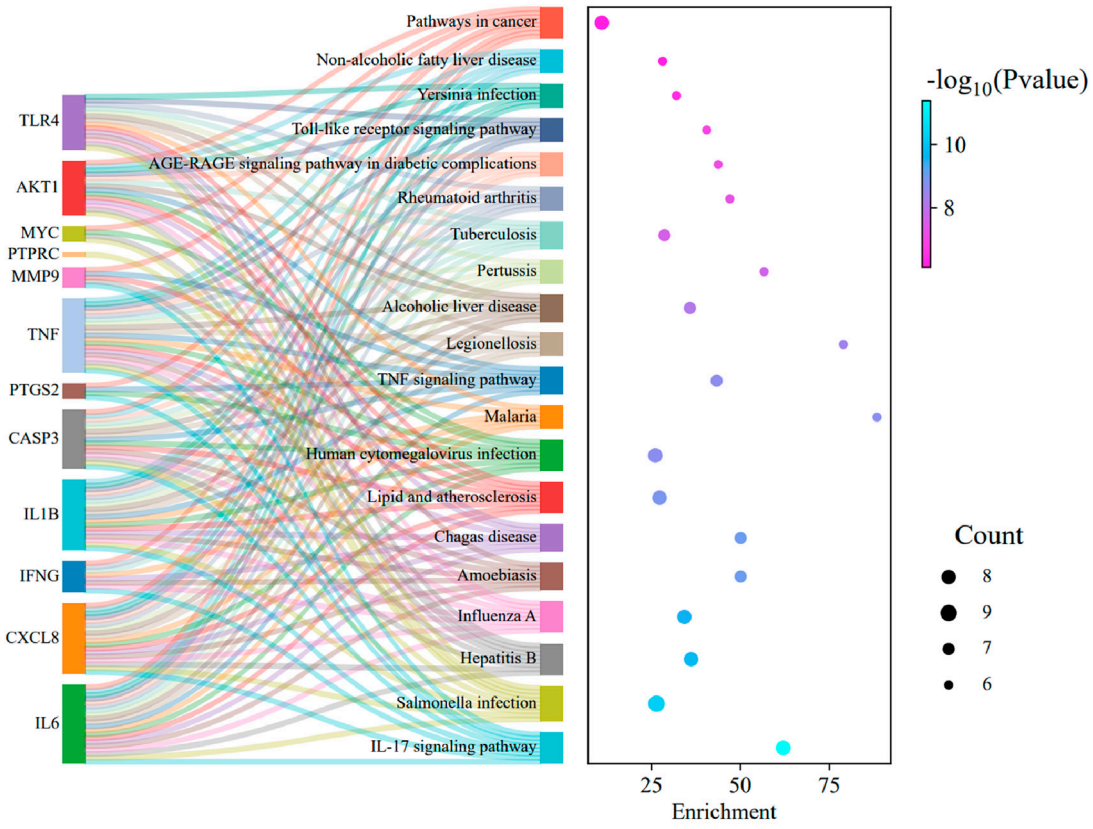


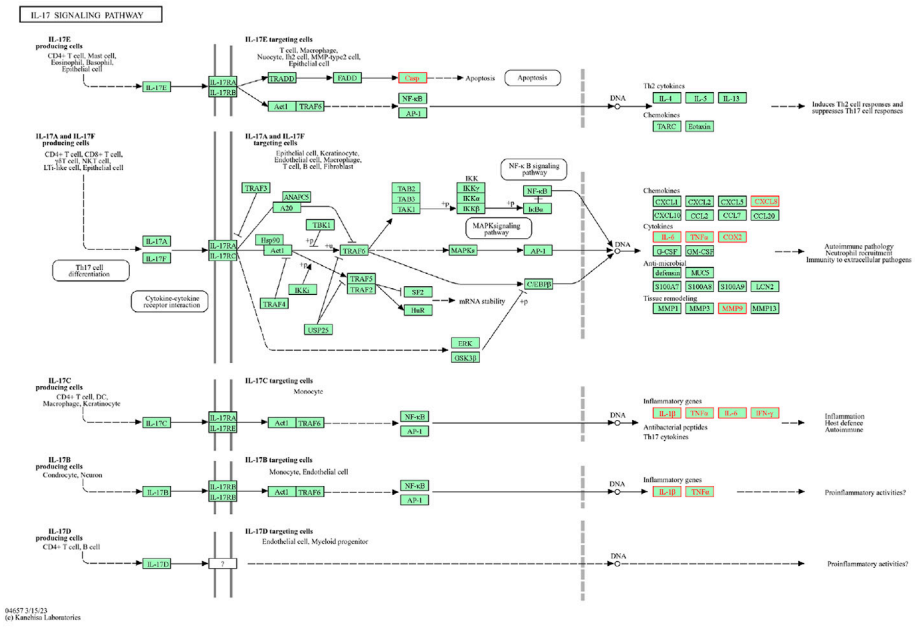
FIGURE 13
GO enrichment analysis bar chart of compounds ((**A**) is GO bubble Chart, **(B)** is bilateral bar chart).

The results of network pharmacology suggest that the mechanism of SH + PNC in treating MRSA-infected wounds is complex, with the IL-17 signaling pathway believed to play an important role. The core targets of this pathway include IL1B, IL6, MMP9, IFNG, and TNF. MMP9 belongs to the matrix metalloprotein family, and its main function is to degrade and reshape the dynamic balance of extracellular matrix. The main components of extracellular matrix and vascular basement membrane are collagen and laminin (Hallmann et al., 2020; Kumar et al., 2022). As an important inflammatory cytokine, TNF-α participates in the inflammatory regulation process, which can indirectly or directly activate the expression of target genes such as NF-κB, IL-6 and IL-1β, aggravate microvascular injury and induce the production of VEGFA, and trigger more severe inflammatory reactions (Tian et al., 2024). IFNG plays a key role in driving innate and acquired defense against infectious pathogens, and Gram-positive bacteria can stimulate the expression of IFNγ, TNF-α, and IL-1β more strongly than Gram-negative bacteria (Leng et al., 2016). IFNG overexpression can also activate macrophages, neutrophils, endothelial cells, platelets, as well as the complement and coagulation systems, thereby inducing the release of bioactive substances such as tumor necrosis factor-α, histamine, serotonin,

10.3389/fphar.2025.1530217



A



B

FIGURE 14
(Continued).

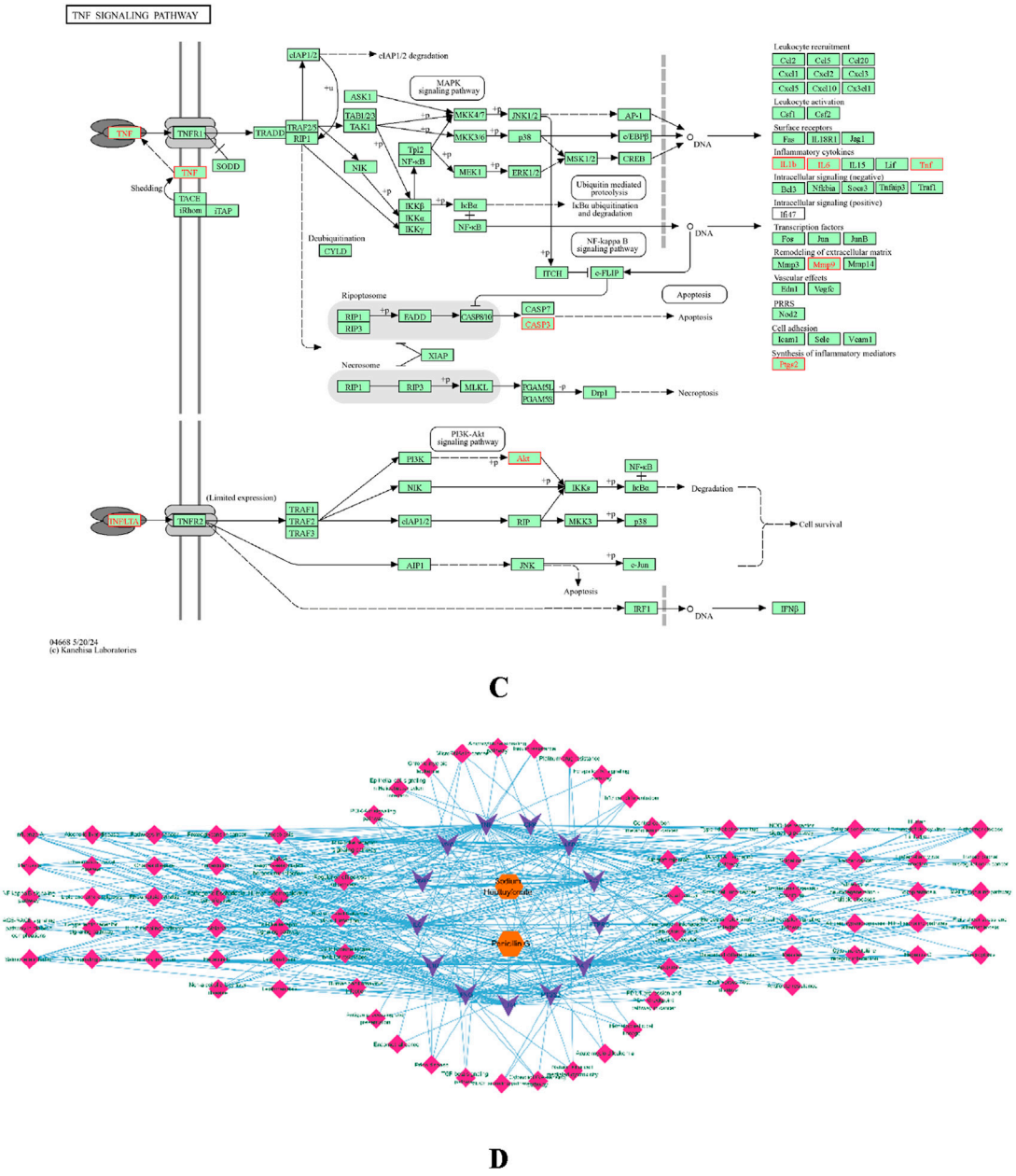


FIGURE 14
(Continued). KEGG pathway Analysis Sankey + dot plot of SH + PNC **(A)** (The X-axis is the enrichment, the Y-axis is the pathway name, and the color represents the size of the p value. The smaller the p value, the redder the color, and the more significant the enrichment. The size of the sphere represents the number of targets). Molecular pathways and specific targets of action. **(B)** is IL-17 signaling pathway. **(C)** is TNF signaling pathway. **(B, C)** shows that there are common targets in both pathways. Compound-target-molecular pathways (**(D)**, Orange nodes are SH and PNC, purple nodes are targets, and pink nodes are molecular pathway).

prostaglandins, and kinins (Higgs et al., 2017). Interleukin 6 (IL-6) is a pleiotropic cytokine that plays a role in immunity, tissue regeneration, and metabolism. The rapid production of IL-6 contributes to host defense during infection and tissue injury, but excessive synthesis of IL-6 and dysregulation of IL-6 receptor signaling are associated with disease pathology. Excessive IL-6 production can induce VEGF to directly or indirectly act on blood vessels, leading to increased angiogenesis activity and vascular permeability. At the same time, an increase in the Th17/Treg ratio can lead to the disruption of immune tolerance (Kang et al., 2019). As a proprotein, IL1B is produced by activated macrophages and participates in signaling pathways mainly including the NF-κB signaling pathway and the MAPK signaling pathway. It binds to its receptor IL-1RI to initiate downstream signaling, leading to the expression of inflammatory factors and acute-phase proteins (Rong et al., 2020). Molecular docking experiments showed that SH and PNC could participate in inflammatory immune regulation, apoptosis, cytokine secretion, and other processes by binding to the above targets, thereby achieving the therapeutic effect of promoting wound healing.

Although it was observed in this experiment that sodium houttuyfonate combined with penicillin G can effectively inhibit

10.3389/fphar.2025.1530217

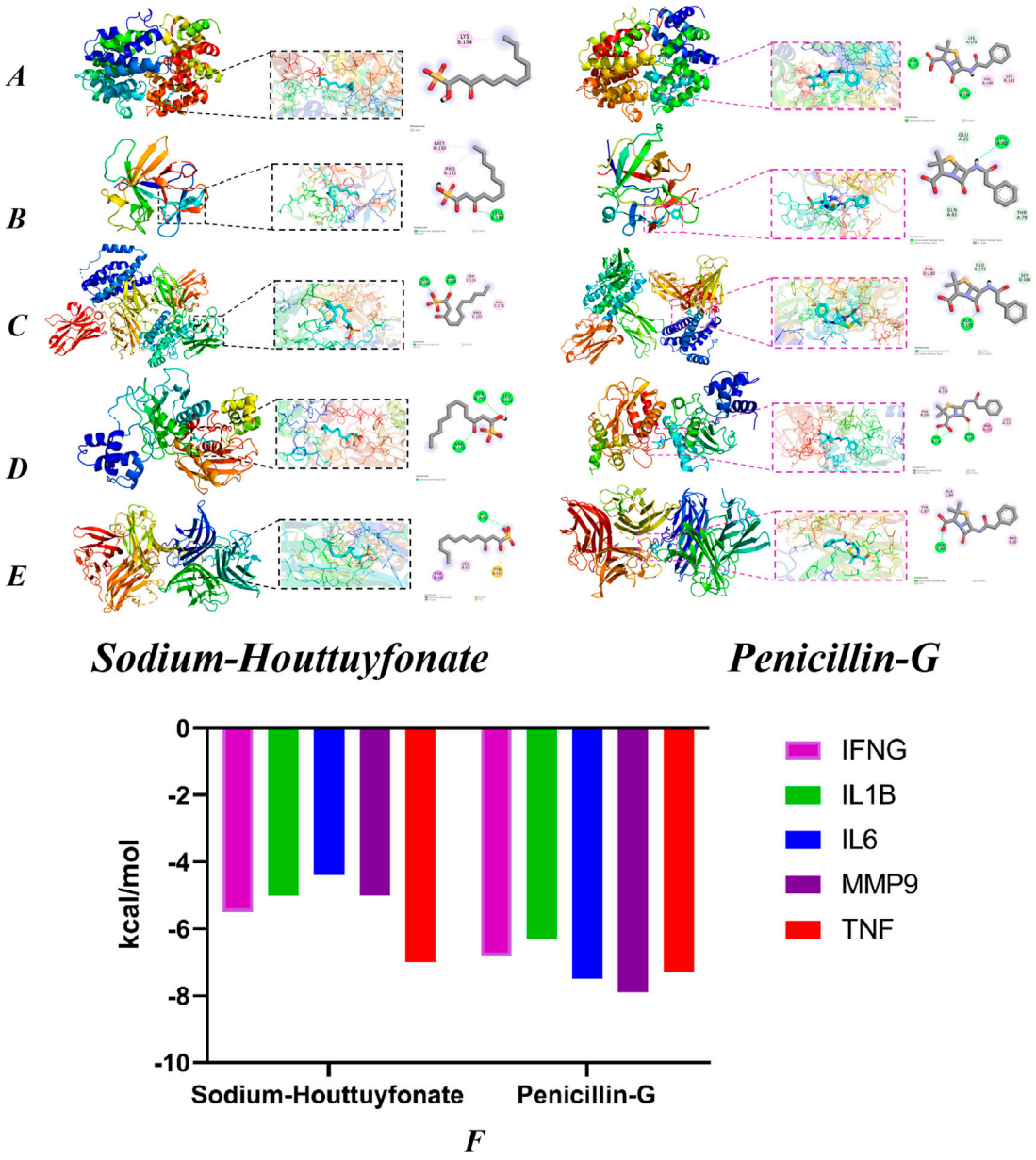


FIGURE 15
Molecular docking models of OA with possible core anti-obesity targets. IFNG **(A, B)** (IL1B), **(C)** (IL6), **(D)** (MMP9) and **(E)** (TNF). The Binding affinity of SH and PNC with various targets **(F)**.

the growth of MRSA in rat models and promote the healing of MRSA-infected wounds in rats, the mechanism by which sodium houttuyfonate reverses MRSA resistance to penicillin G is still unclear. At the same time, follow-up experiments need to supplement single-cell experiments to verify the actual molecular expression and support the analysis results.

5 Conclusion

This study demonstrates that sodium houttuyfonate has an inhibitory effect on the growth of MRSA *in vitro* and can increase the antibacterial effect of penicillin G. It inhibits the growth of bacteria in rat MRSA infected wounds, reduces neutrophil infiltration, promotes local collagen fiber production, reduces the expression of inflammatory factors IL-6 and TNF-α, regulates local inflammatory response, and thus promotes wound healing. The IL-17 signaling pathway may play a key role in wound healing, with core targets including IL1B, IL6, MMP9, IFNG, and TNF, involving inflammatory immune regulation, apoptosis, cytokine secretion, and so on. This study provides a theoretical basis for the clinical treatment of MRSA infection with SH and subsequent related research.

Data availability statement

The original contributions presented in the study are included in the article/supplementary material, further inquiries can be directed to the corresponding authors.

Ethics statement

The animal study was approved by Institutional Animal Care and Use Committee of North Sichuan Medical College. The study was conducted in accordance with the local legislation and institutional requirements.

Author contributions

YL: Writing–original draft. SY: Writing–original draft. ShL: Writing–review and editing. SiL: Writing–review and editing. AJ: Writing–review and editing. XX: Writing–review and editing. SS: Writing–original draft, Writing–review and editing. YC: Writing–original draft, Writing–review and editing.

Funding

The author(s) declare that financial support was received for the research, authorship, and/or publication of this article. This study was sponsored by Sichuan Provincial Health Commission scientific research project (20PJ145), the School-level Scientific Research Development Fund of North Sichuan Medical College (CBY23-QNA58) and the Sichuan Provincial Medical Association Wound Disease (Taige) Special Research Fund (2022TG05).

Acknowledgments

We thank Corp for editing and proofreading drafts of this manuscript.

Conflict of interest

The authors declare that the research was conducted in the absence of any commercial or financial relationships that could be construed as a potential conflict of interest.

Generative AI statement

The author(s) declare that no Generative AI was used in the creation of this manuscript.

Publisher's note

All claims expressed in this article are solely those of the authors and do not necessarily represent those of their affiliated organizations, or those of the publisher, the editors and the reviewers. Any product that may be evaluated in this article, or claim that may be made by its manufacturer, is not guaranteed or endorsed by the publisher.

References

Ahmad-Mansour, N., Loubet, P., Pouget, C., Dunyach-Remy, C., Sotto, A., Lavigne, J. P., et al. (2021). *Staphylococcus aureus* toxins: an update on their pathogenic properties and potential treatments. *Toxins (Basel).* 13 (10), 677. doi:10.3390/toxins13100677

Amberger, J. S., Bocchini, C. A., Scott, A. F., and Hamosh, A. (2019). OMIM.org: leveraging knowledge across phenotype-gene relationships. *Nucleic Acids Res.* 47 (D1), D1038-D1043–D1043. doi:10.1093/nar/gky1151

Appelbaum, P. C. (2006). The emergence of vancomycin-intermediate and vancomycin-resistant *Staphylococcus aureus*. *Clin. Microbiol. Infect.* 12 (Suppl. 1), 16–23. doi:10.1111/j.1469-0691.2006.01344.x

Bota, O., and Fodor, L. (2019). The influence of drugs on peripheral nerve regeneration. *Drug Metab. Rev.* 51 (3), 266–292. doi:10.1080/03602532.2019.1632885

Chen, J., Wang, W., Shi, C., and Fang, J. (2014). A comparative study of sodium houttuyfonate and 2-undecanone for their *in vitro* and *in vivo* anti-inflammatory activities and stabilities. *Int. J. Mol. Sci.* 15 (12), 22978–22994. doi:10.3390/ijms151222978

Doncheva, N. T., Morris, J. H., Gorodkin, J., and Jensen, L. J. (2019). Cytoscape StringApp: network analysis and visualization of proteomics data. *J. Proteome Res.* 18 (2), 623–632. doi:10.1021/acs.jproteome.8b00702

Forli, S., Huey, R., Pique, M. E., Sanner, M. F., Goodsell, D. S., and Olson, A. J. (2016). Computational protein-ligand docking and virtual drug screening with the AutoDock suite. *Nat. Protoc.* 11 (5), 905–919. doi:10.1038/nprot.2016.051

Gurieva, T. V., Bootsma, M. C., and Bonten, M. J. (2012). Decolonization of patients and health care workers to control nosocomial spread of methicillin-resistant *Staphylococcus aureus*: a simulation study. *BMC Infect. Dis.* 12, 302. doi:10.1186/1471-2334-12-302

Hallmann, R., Hannocks, M. J., Song, J., Zhang, X., Di Russo, J., Luik, A. L., et al. (2020). The role of basement membrane laminins in vascular function. *Int. J. Biochem. Cell. Biol.* 127, 105823. doi:10.1016/j.biocel.2020.105823

Hancock, M., Peulen, T. O., Webb, B., Poon, B., Fraser, J. S., Adams, P., et al. (2022). Integration of software tools for integrative modeling of biomolecular systems. *J. Struct. Biol.* 214 (1), 107841. doi:10.1016/j.jsb.2022.107841

Hernández-Aristizábal, I., and Ocampo-Ibáñez, I. D. (2021). Antimicrobial peptides with antibacterial activity against vancomycin-resistant *Staphylococcus aureus* strains: classification, structures, and mechanisms of action. *Int. J. Mol. Sci.* 22 (15), 7927. doi:10.3390/ijms22157927

Higgs, B., Morehouse, C., Streicher, K., Brohawn, P. Z., Steele, K., Rebelatto, M., et al. (2017). Abstract 1773: a baseline IFNG gene expression signature correlates with clinical outcomes in durvalumab-treated advanced NSCLC cancer patients. *CANCER Res.* 77 (13_Suppl. e), 1773. doi:10.1158/1538-7445.am2017-1773

Kang, S., Tanaka, T., Narazaki, M., and Kishimoto, T. (2019). Targeting interleukin-6 signaling in clinic. *Immunity* 50 (4), 1007–1023. doi:10.1016/j.immuni.2019.03.026

Kim, S. (2016). Getting the most out of PubChem for virtual screening. *Expert Opin. Drug Discov.* 11 (9), 843–855. doi:10.1080/17460441.2016.1216967

Konc, J., and Janežič, D. (2022). ProBiS-fold approach for annotation of human structures from the AlphaFold database with No corresponding structure in the PDB to discover new druggable binding sites. *J. Chem. Inf. Model.* 62 (22), 5821–5829. doi:10.1021/acs.jcim.2c00947

Kumar, A. A., Yeo, N., Whittaker, M., Attra, P., Barrick, T. R., Bridges, L. R., et al. (2022). Vascular collagen type-IV in hypertension and cerebral small vessel disease. *Stroke* 53 (12), 3696–3705. doi:10.1161/STROKEAHA.122.037761

Lakhundi, S., and Zhang, K. (2018). Methicillin-resistant *Staphylococcus aureus*: molecular characterization, evolution, and epidemiology. *Clin. Microbiol. Rev.* 31 (4), 000200-18–e118. doi:10.1128/CMR.00020-18

Lee, A. S., de Lencastre, H., Garau, J., Kluytmans, J., Malhotra-Kumar, S., Peschel, A., et al. (2018). Methicillin-resistant *Staphylococcus aureus*. *Nat. Rev. Dis. Prim.* 4, 18033. doi:10.1038/nrdp.2018.33

Lee, Y. D., and Park, J. H. (2016). Phage conversion for β-lactam antibiotic resistance of *Staphylococcus aureus* from foods. *J. Microbiol. Biotechnol.* 26 (2), 263–269. doi:10.4014/jmb.1508.08042

Leng, R. X., Pan, H. F., Liu, J., Yang, X. K., Zhang, C., Tao, S. S., et al. (2016). Evidence for genetic association of TBX21 and IFNG with systemic lupus erythematosus in a Chinese Han population. *Sci. Rep.* 6, 22081. doi:10.1038/srep22081

Li, J., Feng, S., Liu, X., Jia, X., Qiao, F., Guo, J., et al. (2022). Effects of traditional Chinese medicine and its active ingredients on drug-resistant bacteria. *Front. Pharmacol.* 13, 837907. doi:10.3389/fphar.2022.837907

Liu, B. G., Xie, M., Dong, Y., Wu, H., He, D. D., Hu, G. Z., et al. (2022). Antimicrobial mechanisms of traditional Chinese medicine and reversal of drug resistance: a narrative review. *Eur. Rev. Med. Pharmacol. Sci.* 26 (15), 5553–5561. doi:10.26355/eurrev_202208_29426

Liu, G., Xiang, H., Tang, X., Zhang, K., Wu, X., Wang, X., et al. (2011). Transcriptional and functional analysis shows sodium houttuyfonate-mediated inhibition of autolysis in *Staphylococcus aureus*. *Molecules* 16 (10), 8848–8865. doi:10.3390/molecules16108848

Liu, T., Wang, J., Tong, Y., Wu, L., Xie, Y., He, P., et al. (2024). Integrating network pharmacology and animal experimental validation to investigate the action mechanism of oleanolic acid in obesity. *J. Transl. Med.* 22 (1), 86. doi:10.1186/s12967-023-04840-x

Liu, X., Zhong, L., Xie, J., Sui, Y., Li, G., Ma, Z., et al. (2021). Sodium houttuyfonate: a review of its antimicrobial, anti-inflammatory and cardiovascular protective effects. *Eur. J. Pharmacol.* 902, 174110. doi:10.1016/j.ejphar.2021.174110

Ma, K., Chen, M., Liu, J., Ge, Y., Wang, T., Wu, D., et al. (2021). Sodium houttuyfonate attenuates dextran sulfate sodium associated colitis precolonized with Candida albicans through inducing β-glucan exposure. *J. Leukoc. Biol.* 110 (5), 927–937. doi:10.1002/JLB.4AB0221-324RRRR

Miyachiro, M. M., Contreras-Martel, C., and Dessen, A. (2019). Penicillin-binding proteins (PBPs) and bacterial cell wall elongation complexes. *Subcell. Biochem.* 93, 273–289. doi:10.1007/978-3-030-28151-9_8

Oliveira, D., Borges, A., and Simões, M. (2018). *Staphylococcus aureus* toxins and their molecular activity in infectious diseases. *Toxins* 10 (6), 252. doi:10.3390/toxins10060252

Peacock, S. J., and Paterson, G. K. (2015). Mechanisms of methicillin resistance in *Staphylococcus aureus*. *Annu. Rev. Biochem.* 84, 577–601. doi:10.1146/annurev-biochem-060614-034516

Piñero, J., Bravo, À., Queralt-Rosinach, N., Gutiérrez-Sacristán, A., Deu-Pons, J., Centeno, E., et al. (2017). DisGeNET: a comprehensive platform integrating information on human disease-associated genes and variants. *Nucleic Acids Res.* 45 (D1), D833-D839–D839. doi:10.1093/nar/gkw943

Roberts, M. C., Schwarz, S., and Aarts, H. J. (2012). Erratum: acquired antibiotic resistance genes: an overview. *Front. Microbiol.* 3, 384. doi:10.3389/fmicb.2012.00384

Rong, H., He, X., Wang, L., Bai, M., Jin, T., Wang, Y., et al. (2020). Association between IL1B polymorphisms and the risk of rheumatoid arthritis. *Int. Immunopharmacol.* 83, 106401. doi:10.1016/j.intimp.2020.106401

Sepulveda, J. L. (2020). Using R and bioconductor in clinical genomics and transcriptomics. *J. Mol. Diagn* 22 (1), 3–20. doi:10.1016/j.jmoldx.2019.08.006

Shang, L., Wang, Y., Li, J., Zhou, F., Xiao, K., Liu, Y., et al. (2023). Mechanism of Sijunzi Decoction in the treatment of colorectal cancer based on network pharmacology and experimental validation. *J. Ethnopharmacol.* 302 (Pt A), 115876. doi:10.1016/j.jep.2022.115876

Spagnolo, A. M., Orlando, P., Panatto, D., Amicizia, D., Perdelli, F., and Cristina, M. L. (2014). *Staphylococcus aureus* with reduced susceptibility to vancomycin in healthcare settings. *J. Prev. Med. Hyg.* 55 (4), 137–144.

Stelzer, G., Rosen, N., Plaschkes, I., Zimmerman, S., Twik, M., Fishilevich, S., et al. (2016). The GeneCards suite: from gene data mining to disease genome sequence analyses. *Curr. Protoc. Bioinforma.* 54, 1. doi:10.1002/cpbi.5

Svensson, F., Westerman, B., Würdinger, T., and Bailey, D. (2018). GBM Drug Bank-a new resource for glioblastoma drug discovery and informatics research. *Neuro Oncol.* 20 (12), 1680–1681. doi:10.1093/neuonc/noy122

Szklarczyk, D., Kirsch, R., Koutrouli, M., Nastou, K., Mehryary, F., Hachilif, R., et al. (2023). The STRING database in 2023: protein-protein association networks and functional enrichment analyses for any sequenced genome of interest. *Nucleic Acids Res.* 51 (D1), D638–D646. doi:10.1093/nar/gkac1000

Tian, L., Yang, M., Tu, S., Chang, K., Jiang, H., Jiang, Y., et al. (2024). Xiaoke Bitong capsule alleviates inflammatory impairment via inhibition of the TNF signaling pathway to against diabetic peripheral neuropathy. *Phytomedicine* 132, 155867. doi:10.1016/j.phymed.2024.155867

Tumayhi, M., Banji, D., Khardali, I., Banji, O. J. F., Alshahrani, S., Alqahtani, S. S., et al. (2023). Amphetamine-related fatalities and altered brain chemicals: a preliminary investigation using the comparative toxicogenomic database. *Molecules* 28 (12), 4787. doi:10.3390/molecules28124787

Turner, N. A., Sharma-Kuinkel, B. K., Maskarinec, S. A., Eichenberger, E. M., Shah, P. P., Carugati, M., et al. (2019). Methicillin-resistant *Staphylococcus aureus*: an overview of basic and clinical research. *Nat. Rev. Microbiol.* 17 (4), 203–218. doi:10.1038/s41579-018-0147-4

Wang, S., Xing, Y., Wang, R., and Jin, Z. (2024). Jianpi Huayu Decoction suppresses cellular senescence in colorectal cancer via p53-p21-Rb pathway: network pharmacology and *in vivo* validation. *J. Ethnopharmacol.* 319 (Pt 3), 117347. doi:10.1016/j.jep.2023.117347

Wang, T., Huang, W., Duan, Q., Wang, J., Cheng, H., Shao, J., et al. (2019). Sodium houttuyfonate *in vitro* inhibits biofilm dispersion and expression of bdlA in *Pseudomonas aeruginosa*. *Mol. Biol. Rep.* 46 (1), 471–477. doi:10.1007/s11033-018-4497-9

Xie, R., Li, B., Jia, L., and Li, Y. (2022). Identification of core genes and pathways in melanoma metastasis via bioinformatics analysis. *Int. J. Mol. Sci.* 23 (2), 794. doi:10.3390/ijms23020794

Yun, L. I., Zheng, Bo, Feng, X. U. E., et al. (2023). Antimicrobial susceptibility of Gram-positive organisms: results from China antimicrobial resistance surveillance trial (CARST) program, 2021-2022. *Chin. J. Clin. Pharmacol.* 39 (23), 3509–3524.

Zaru, R., Magrane, M., Orchard, S., and Consortium, U. P. (2020). Challenges in the annotation of pseudoenzymes in databases: the UniProtKB approach. *FEBS J.* 287 (19), 4114–4127. doi:10.1111/febs.15100

Zhi-Jiang, Y., Dong, J., Che, Y.-J., Zhu, M.-F., Wen, M., Wang, N.-N., et al. (2016). TargetNet: a web service for predicting potential drug-target interaction profiling via multi-target SAR models. *J. Computer-Aided Mol. Des.* 30, 413–424. doi:10.1007/s10822-016-9915-2

Zhou, W., Zhang, H., Wang, X., Kang, J., Guo, W., Zhou, L., et al. (2022a). Network pharmacology to unveil the mechanism of Moluodan in the treatment of chronic atrophic gastritis. *Phytomedicine* 95, 153837. doi:10.1016/j.phymed.2021.153837

Zhou, M., Jianmei, M. A. O., and Yan, C. A. I. (2022b). Antibacterial effects of sodium houttuyfonate combined with imipenem cilastatin sodium against carbapenem-resistant Acinetobacter baumannii *in vitro*. *Chongqing Med. J.*, 51(07):1122–1126+1130.

Zhu, D. W., Yu, Q., Sun, J. J., and Shen, Y. H. (2021). Evaluating the therapeutic mechanisms of selected active compounds in Houttuynia cordata thunb. In pulmonary fibrosis via network pharmacology analysis. *Front. Pharmacol.* 12, 733618. doi:10.3389/fphar.2021.733618

Zhuang, T., Hu, M., Wang, J., Mei, L., Zhu, X., Zhang, H., et al. (2022). Sodium houttuyfonate effectively treats acute pulmonary infection of *Pseudomonas aeruginosa* by affecting immunity and intestinal flora in mice. *Front. Cell. Infect. Microbiol.* 12, 1022511. doi:10.3389/fcimb.2022.1022511

frontiers | Frontiers in Pharmacology

TYPE Opinion
PUBLISHED 25 February 2025
DOI 10.3389/fphar.2025.1540704

Check for updates

OPEN ACCESS

EDITED BY
Heike Wulff,
University of California, Davis, United States

REVIEWED BY
Xiaoliang Qi,
Wenzhou Medical University, China
Christian Opländer,
Witten Herdecke University, Germany

*CORRESPONDENCE
Guojuan Fan,
shantianri@163.com
Jinlong Ma,
majinlong99@hotmail.com

†These authors have contributed equally to this work and share first authorship

RECEIVED 06 December 2024
ACCEPTED 12 February 2025
PUBLISHED 25 February 2025

CITATION
Li Y, Guan H, Fan G and Ma J (2025) The inherent defects of cold atmospheric plasma for the treatment of burns.
Front. Pharmacol. 16:1540704.
doi: 10.3389/fphar.2025.1540704

COPYRIGHT
© 2025 Li, Guan, Fan and Ma. This is an open-access article distributed under the terms of the Creative Commons Attribution License (CC BY). The use, distribution or reproduction in other forums is permitted, provided the original author(s) and the copyright owner(s) are credited and that the original publication in this journal is cited, in accordance with accepted academic practice. No use, distribution or reproduction is permitted which does not comply with these terms.

The inherent defects of cold atmospheric plasma for the treatment of burns

Yingying Li[1†], Hong Guan[2†], Guojuan Fan[3*] and Jinlong Ma[4*]

[1]Hebei Chemical and Pharmaceutical College, Shijiazhuang, Hebei, China, [2]School of Agriculture and Forestry Technology, Weifang Vocational College, Weifang, Shandong, China, [3]Dermatology, Weifang Hospital of Traditional Chinese Medicine, Shandong Second Medical University, Weifang, Shandong, China, [4]School of Pharmacy, Shandong Second Medical University, Weifang, Shandong, China

KEYWORDS

cold atmospheric plasma, burns treatment, inherent defects, UV radiation, high flow rate gas

Introduction

The skin system constitutes the human body's largest organ, acting as a robust shield against various harmful invaders, including microbes and ultraviolet (UV) rays (Ling et al., 2021; Cheng et al., 2022). When the skin is burned, its barrier function is compromised, making the affected areas susceptible to microbial influence, which can lead to a series of pathological changes in the body. The process of wound recovery from burns can be categorized into three distinct phases: the inflammatory response, tissue proliferation, and the tissue remodeling of the affected area (Qi et al., 2024). A multitude of bacteria multiply rapidly in the compromised area, during the inflammatory phase (1–2 days after burn), which in turn slows down the wound's recovery due to the formation of ulcers (Iacob et al., 2020). During the tissue proliferation phase, which typically occurs 1–2 weeks post-burn, the wound site is marked by the influx and activation of fibroblasts, as well as the development of new blood vessels, which are crucial for the healing process (Wietecha et al., 2020). The tissue remodeling phase initiates approximately 2 weeks following skin injury and continues for a number of weeks, aimed at restoring the skin's physiological functionality (Wang et al., 2022). This stage is primarily characterized by the metamorphosis of granulation tissue into a more advanced connective tissue. However, an overproduction of collagen during this phase can readily result in the formation of scars. Therefore, the development of a burn treatment system that possesses antibacterial properties, promotes skin repair, and inhibits scar formation is of great significance.

Over the past few years, there has been a growing interest in the versatile potential of cold atmospheric plasma (CAP) across various fields, such as sterilization and disinfection, dental cleaning, cosmetology, and the treatment of skin diseases, trauma, and cancer, attracting widespread attention in the biomedical field (Chen et al., 2021; Lunov et al., 2016; Qin et al., 2022). This is mainly due to its rich content of physiologically active components, such as reactive free radicals (ROS and RNS, etc.), charged particles (positive and negative), electrons, and ultraviolet light (Chen et al., 2021; Szili et al., 2021). Research has found that CAP not only has antibacterial effects but also can accelerate the healing process of wounds through the stimulation of fibroblast proliferation and angiogenesis, making it a potential ideal method for treating burns (Dijksteel et al., 2020; Boekema et al., 2021; Oliver et al., 2024; Bagheri et al., 2023; Plattfaut et al., 2021; Duchesne et al., 2019; Nastuta et al., 2011; Bhartiya et al., 2021; Frescaline et al., 2020). The applicant's previous work in combining CAP with nanomedicine for the treatment of third-degree burns has also proven that CAP has the functions of antibacterial activity and skin repair (Wang et al., 2023).

As a new type of treatment, most of the CAP devices currently used are self-built in laboratories, with significant differences in parameters and operations between different

devices, resulting in inconsistent dosage and frequency of treatment. In contrast, in our research, we found that CAP has other inherent defects that severely limit its application in burn treatment.

UV radiation

Although some research reports indicate that the risks are minimal under specific conditions (Lotfi et al., 2024), there is also literature suggesting that long-term treatment can trigger cytotoxic effects and reduce cell viability (Sremački et al., 2021). In the absence of a protective medium, vacuum ultraviolet/ultraviolet radiation significantly contributes to plasma - induced DNA damage and cytotoxicity (accounting for 70%). While normal skin can mitigate the harm of UV light through the stratum corneum, burned areas lack this protective barrier (Shimizu et al., 2010). The damage caused by UV radiation to the skin is mainly manifested as: (1) UV light can impair the physiological functions of macromolecules within cells (proteins, lipids, and nucleic acids, etc.), inducing cellular damage (Gu et al., 2020); (2) It also destroys collagen and elastic fibers, accelerating skin aging and slowing down wound healing (Xiao et al., 2022); (3) By forming pyrimidine dimers and other DNA damages, it leads to skin cancer (Saha et al., 2020; Douki et al., 2024). These hazards of UV radiation limit the drug dosage and administration frequency of CAP treatment, thereby affecting the speed of wound recovery. Although existing literature has noted the hazards of UV light in CAP and improved CAP devices to suppress the generation of UV light, it has also significantly weakened the intensity of its active free radicals (Shimizu et al., 2010). Therefore, how to effectively filter out UV light while retaining the active free radicals of CAP remains a challenge.

There are two potential approaches to address this issue. The first method involves utilizing an instrument that leverages the linear propagation characteristics of light to filter out the majority of UV light. However, this approach may, to some extent, diminish the quantity of active ions that reach the target site. The second idea is to develop an adjuvant drug capable of absorbing UV light, akin to a sunscreen. It is crucial to ensure that the selected sunscreen does not react with ROS or RNS, as such reactions could compromise the overall activity of CAP.

High flow rate gas

A high flow rate gas of CAP can make the wound area extremely dry (Dejonckheere et al., 2024; Shaitelman et al., 2015), which contradicts the theory of moist wound healing and hinders wound healing, preventing it from fully exerting its functions of promoting wound healing and inhibiting scarring. A moist wound environment facilitates the natural process of autolytic debridement, alleviates pain, minimizes scarring, stimulates collagen production, and encourages the migration of keratinocytes across the wound bed, thus collectively contributing to an enhanced wound healing process (Nuutila and Eriksson, 2021). On the other hand, a dry wound environment has at least four disadvantages: (1) Excessive dryness of the wound can dehydrate the traumatized tissue, leading to further tissue damage and the formation of unfavorable eschar, making it difficult for new epithelial cells to move, and prolonging the wound healing time (Breuing et al., 1992); (2) The wound is more susceptible to infection (Daly et al., 2016); (3) Larger scars are produced (Junker et al., 2013); (4) It intensifies the patient's pain (Bechert and Abraham, 2009). Therefore, when using CAP for burn treatment, another issue that needs to be addressed is the dryness brought about by the high flow rate of gas.

Certainly, it is feasible to strike a balance between the efficacy of CAP and the minimization of dryness by fine-tuning the gas flow rate threshold. Nevertheless, this equilibrium merely replicates the wound environment akin to that of exposure therapy and falls considerably short of attaining the optimal state of wet wound healing. In light of this, a question emerges: could we integrate hydrogel, hydrosol, and other relevant materials with CAP to actualize a dual benefit of wet wound healing and combined CAP treatment?

Discussion

In this Opinion, we have summarized the inherent defects that severely limit CAP application in burn treatment. Most of the studies reported self-built in laboratories, with significant differences in parameters and operations between different devices, resulting in inconsistent dosage and frequency of treatment, but ultraviolet light and high-speed gas flow are rarely performed. Therefore, how to effectively address the issues of UV and high-speed gas flow in CAP is a fundamental problem that needs to be solved for the use of CAP in burn treatment.

In view of the challenges associated with UV radiation, innovative instruments could be devised to effectively filter out ultraviolet rays. Additionally, CAP adjuvant drugs might be developed, leveraging the linear propagation traits of light to absorb ultraviolet radiation. When it comes to the drying issue resulting from high-flow-rate gas, the design and application of hydrogels, hydrosols, and other related substances could be explored to facilitate wet wound healing. This Opinion piece offers a novel research vantage point for the utilization of CAP in burn treatments, carrying significant theoretical and practical implications for the exploration of new therapeutic approaches in the field of burns.

Author contributions

YL: Writing–review and editing. HG: Writing–review and editing. GF: Writing–review and editing. JM: Writing–original draft, Writing–review and editing.

Funding

The author(s) declare that financial support was received for the research, authorship, and/or publication of this article. This work was supported by the National Natural Science Foundation of China (No. 82302840), the Shandong Provincial Natural Science Foundation (No. ZR2023QH038, ZR2023MH037), the Shandong Provincial Traditional Chinese Medicine Science and Technology Project (No. M-2023084, Q-2023047).

Conflict of interest

The authors declare that the research was conducted in the absence of any commercial or financial relationships that could be construed as a potential conflict of interest.

The author(s) declared that they were an editorial board member of Frontiers, at the time of submission.

This had no impact on the peer review process and the final decision.

Generative AI statement

The authors declare that no Generative AI was used in the creation of this manuscript.

Publisher's note

All claims expressed in this article are solely those of the authors and do not necessarily represent those of their affiliated organizations, or those of the publisher, the editors and the reviewers. Any product that may be evaluated in this article, or claim that may be made by its manufacturer, is not guaranteed or endorsed by the publisher.

References

Bagheri, M., von Kohout, M., Zoric, A., Fuchs, P. C., Schiefer, J. L., and Opländer, C. (2023). Can cold atmospheric plasma Be used for infection control in burns? A preclinical evaluation. *Biomedicines* 11 (5), 1239. doi:10.3390/biomedicines11051239

Bechert, K., and Abraham, S. E. (2009). Pain management and wound care. *J. Am. Coll. Certif. Wound Specialists* 1 (2), 65–71. doi:10.1016/j.jcws.2008.12.001

Bhartiya, P., Masur, K., Shome, D., Kaushik, N., Nguyen, L. N., Kaushik, N. K., et al. (2021). Influence of redox stress on crosstalk between fibroblasts and keratinocytes. *Biology* 10 (12), 1338. doi:10.3390/biology10121338

Boekema, B., Stoop, M., Vlig, M., van Liempt, J., Sobota, A., Ulrich, M., et al. (2021). Antibacterial and safety tests of a flexible cold atmospheric plasma device for the stimulation of wound healing. *Appl. Microbiol. Biotechnol.* 105 (5), 2057–2070. doi:10.1007/s00253-021-11166-5

Breuing, K., Eriksson, E., Liu, P., and Miller, D. R. (1992). Healing of partial thickness porcine skin wounds in a liquid environment. *J. Surg. Res.* 52 (1), 50–58. doi:10.1016/0022-4804(92)90278-8

Chen, G., Chen, Z., Wang, Z., Obenchain, R., Wen, D., Li, H., et al. (2021). Portable air-fed cold atmospheric plasma device for postsurgical cancer treatment. *Sci. Adv.* 7 (36), eabg5686. doi:10.1126/sciadv.abg5686

Cheng, S., Wang, H., Pan, X., Zhang, C., Zhang, K., Chen, Z., et al. (2022). Dendritic hydrogels with robust inherent antibacterial properties for promoting bacteria-infected wound healing. *ACS Appl. Mater. and Interfaces* 14 (9), 11144–11155. doi:10.1021/acsami.1c25014

Daly, L. T., Tsai, D. M., Singh, M., Nuutila, K., Minasian, R. A., Lee, C. C. Y., et al. (2016). Topical minocycline effectively decontaminates and reduces inflammation in infected porcine wounds. *Plastic Reconstr. Surg.* 138 (5), 856e–868e. doi:10.1097/PRS.0000000000002633

Dejonckheere, C. S., Layer, J. P., Nour, Y., Layer, K., Glasmacher, A., Wiegreffe, S., et al. (2024). Non-invasive physical plasma for preventing radiation dermatitis in breast cancer: results from an intrapatient-randomised double-blind placebo-controlled trial. *Clin. Transl. Radiat. Oncol.* 44, 100699. doi:10.1016/j.ctro.2023.100699

Dijksteel, G. S., Ulrich, M. M. W., Vlig, M., Sobota, A., Middelkoop, E., and Boekema, B. K. H. L. (2020). Safety and bactericidal efficacy of cold atmospheric plasma generated by a flexible surface Dielectric Barrier Discharge device against *Pseudomonas aeruginosa in vitro* and *in vivo*. *Ann. Clin. Microbiol. Antimicrob.* 19 (1), 37. doi:10.1186/s12941-020-00381-z

Douki, T., Bacqueville, D., Jacques, C., Geniès, C., Roullet, N., Bessou-Touya, S., et al. (2024). Blue light impairs the repair of UVB-induced pyrimidine dimers in a human skin model. *Photochem. Photobiol.* 100 (5), 1359–1364. doi:10.1111/php.13921

Duchesne, C., Banzet, S., Lataillade, J. J., Rousseau, A., and Frescaline, N. (2019). Cold atmospheric plasma modulates endothelial nitric oxide synthase signalling and enhances burn wound neovascularisation. *J. Pathology* 249 (3), 368–380. doi:10.1002/path.5323

Frescaline, N., Duchesne, C., Favier, M., Onifarasoaniaina, R., Guilbert, T., Uzan, G., et al. (2020). Physical plasma therapy accelerates wound re-epithelialisation and enhances extracellular matrix formation in cutaneous skin grafts. *J. Pathology* 252 (4), 451–464. doi:10.1002/path.5546

Gu, Y., Han, J., Jiang, C., and Zhang, Y. (2020). Biomarkers, oxidative stress and autophagy in skin aging. *Ageing Res. Rev.* 59, 101036. doi:10.1016/j.arr.2020.101036

Iacob, A. T., Drăgan, M., Ionescu, O. M., Profire, L., Ficai, A., Andronescu, E., et al. (2020). An overview of biopolymeric electrospun nanofibers based on polysaccharides for wound healing management. *Pharmaceutics* 12 (10), 983–1049. doi:10.3390/pharmaceutics12100983

Junker, J. P. E., Kamel, R. A., Caterson, E. J., and Eriksson, E. (2013). Clinical impact upon wound healing and inflammation in moist, wet, and dry environments. *Adv. Wound Care* 2 (7), 348–356. doi:10.1089/wound.2012.0412

Ling, Z., Chen, Z., Deng, J., Wang, Y., Yuan, B., Yang, X., et al. (2021). A novel self-healing polydopamine-functionalized chitosan-arginine hydrogel with enhanced angiogenic and antibacterial activities for accelerating skin wound healing. *Chem. Eng. J.* 420, 130302. doi:10.1016/j.cej.2021.130302

Lotfi, M. R., Tehrani, P. A., Khani, M., Razaghiha, E., Ghasemi, E., and Shokri, B. (2024). Physical and chemical diagnostics of cold atmospheric pressure argon plasma jet. *Plasma Process. Polym.* 21. doi:10.1002/ppap.202400077

Lunov, O., Zablotskii, V., Churpita, O., Jäger, A., Polívka, L., Syková, E., et al. (2016). The interplay between biological and physical scenarios of bacterial death induced by non-thermal plasma. *Biomaterials* 82, 71–83. doi:10.1016/j.biomaterials.2015.12.027

Nastuta, A. V., Topala, I., Grigoras, C., Pohoata, V., and Popa, G. (2011). Stimulation of wound healing by helium atmospheric pressure plasma treatment. *J. Phys. D Appl. Phys.* 44 (10), 105204. doi:10.1088/0022-3727/44/10/105204

Nuutila, K., and Eriksson, E. (2021). Moist wound healing with commonly available dressings. *Adv. Wound Care* 10 (12), 685–698. doi:10.1089/wound.2020.1232

Oliver, M. A., Hussein, L. K., Molina, E. A., Keyloun, J. W., McKnight, S. M., Jimenez, L. M., et al. (2024). Cold atmospheric plasma is bactericidal to wound-relevant pathogens and is compatible with burn wound healing. *Burns* 50 (5), 1192–1212. doi:10.1016/j.burns.2023.12.012

Plattfaut, I., Besser, M., Severing, A. L., Stürmer, E. K., and Opländer, C. (2021). Plasma medicine and wound management: evaluation of the antibacterial efficacy of a medically certified cold atmospheric argon plasma jet. *Int. J. Antimicrob. Agents* 57 (5), 106319. doi:10.1016/j.ijantimicag.2021.106319

Qi, X., Ge, X., Chen, X., Cai, E., Xiang, Y., Xu, H., et al. (2024). An immunoregulation hydrogel with controlled hyperthermia-augmented oxygenation and ROS scavenging for treating diabetic foot ulcers. *Adv. Funct. Mater.* 34 (33). doi:10.1002/adfm.202400489

Qin, J., Zhang, J., Fan, G., Wang, X., Zhang, Y., Wang, L., et al. (2022). Cold atmospheric plasma activates selective photothermal therapy of cancer. *Molecules* 27 (18), 5941. doi:10.3390/molecules27185941

Saha, L. K., Wakasugi, M., Akter, S., Prasad, R., Wilson, S. H., Shimizu, N., et al. (2020). Topoisomerase I-driven repair of UV-induced damage in NER-deficient cells. *Proc. Natl. Acad. Sci. U. S. A.* 117 (25), 14412–14420. doi:10.1073/pnas.1920165117

Shaitelman, S. F., Schlembach, P. J., Arzu, I., Ballo, M., Bloom, E. S., Buchholz, D., et al. (2015). Acute and short-term toxic effects of conventionally fractionated vs hypofractionated whole-breast irradiation: a randomized clinical trial. *JAMA Oncol.* 1 (7), 931–941. doi:10.1001/jamaoncol.2015.2666

Shimizu, T., Nosenko, T., Morfill, G. E., Sato, T., Schmidt, H., and Urayama, T. (2010). Characterization of low-temperature microwave plasma treatment with and without UV light for disinfection. *Plasma Process. Polym.* 7 (3-4), 288–293. doi:10.1002/ppap.200900085

Sremački, I., Kos, Š., Bošnjak, M., Jurov, A., Serša, G., Modic, M., et al. (2021). Plasma damage control: from biomolecules to cells and skin. *ACS Appl. Mater. Interfaces* 13 (39), 46303–46316. doi:10.1021/acsami.1c12232

Szili, E. J., Ghimire, B., Patenall, B. L., Rohaim, M., Mistry, D., Fellows, A., et al. (2021). On-demand cold plasma activation of acetyl donors for bacteria and virus decontamination. *Appl. Phys. Lett.* 119 (5), 054104. doi:10.1063/5.0062787

Wang, X., Fan, G., Guan, Q., Zhao, L., Sun, F., Yang, H., et al. (2022). Hyaluronic acid-modified ZIF-8 nano-vehicle for self-adaption release of curcumin for the treatment of burns. *ACS Appl. Nano Mater.* 5 (11), 16094–16107. doi:10.1021/acsanm.2c02706

Wang, X., Liu, Z., Zhao, L., Yang, H., Qin, J., Zhang, J., et al. (2023). Synergetic burns treatment by self-adaption release system combined with cold atmospheric plasma. *Sci. China Technol. Sci.* 66, 2808–2823.

Wietecha, M. S., Pensalfini, M., Cangkrama, M., Müller, B., Jin, J., Brinckmann, J., et al. (2020). Activin-mediated alterations of the fibroblast transcriptome and matrisome control the biomechanical properties of skin wounds. *Nat. Commun.* 11 (1), 2604. doi:10.1038/s41467-020-16409-z

Xiao, Z., Yang, S., Liu, Y., Zhou, C., Hong, P., Sun, S., et al. (2022). A novel glyceroglycolipid from brown algae Ishige okamurae improve photoaging and counteract inflammation in UVB-induced HaCaT cells. *Chemico-Biological Interact.* 351, 109737. doi:10.1016/j.cbi.2021.109737

frontiers | Frontiers in Pharmacology

TYPE Original Research
PUBLISHED 18 March 2025
DOI 10.3389/fphar.2025.1562264

Check for updates

OPEN ACCESS

EDITED BY
Jinlong Ma,
Shandong Second Medical University, China

REVIEWED BY
Ilya D. Klabukov,
National Medical Research Radiological Center, Russia
Yu Han,
Shanghai Jiao Tong University, China

*CORRESPONDENCE
Kejin Xu,
xukj@ccucm.edu.cn

†These authors have contributed equally to this work and share first authorship

RECEIVED 17 January 2025
ACCEPTED 03 March 2025
PUBLISHED 18 March 2025

CITATION
Liu Y, Zhang Y, Jia Q, Liang X and Xu K (2025) Rapid *in situ* formation of a double cross-linked network hydrogels for wound healing promotion.
Front. Pharmacol. 16:1562264.
doi: 10.3389/fphar.2025.1562264

COPYRIGHT
© 2025 Liu, Zhang, Jia, Liang and Xu. This is an open-access article distributed under the terms of the Creative Commons Attribution License (CC BY). The use, distribution or reproduction in other forums is permitted, provided the original author(s) and the copyright owner(s) are credited and that the original publication in this journal is cited, in accordance with accepted academic practice. No use, distribution or reproduction is permitted which does not comply with these terms.

Rapid *in situ* formation of a double cross-linked network hydrogels for wound healing promotion

Yifan Liu[1†], Ye Zhang[2†], Qianqian Jia[1], Xiaoyun Liang[1] and Kejin Xu[1*]

[1]College of pharmacy, Changchun University of Chinese Medicine, Changchun, Jilin, China, [2]Key Laboratory of Colloid and Interface Chemistry of State Education Ministry, Shandong University, Jinan, Shandong, China

The persistent challenge lies in accelerating wound healing. Bioactive hydrogels with *in situ* formation properties ensure that the dressing completely adheres to the wound and isolates it from external bacteria and microorganisms in order to meet the needs of damaged skin tissue for rapid hemostasis and wound healing. In this paper, hydrogel dressing that Polyacrylamide/Sodium alginate grafted with dopamine/Gelatin grafted with glycidyl methacrylate doped with Angelica sinensis polysaccharide was prepared (PDGA). Chemical cross-linking of PAAM by adding cross-linking agent to initiate free radical polymerization and photocross-linking by free radical polymerization of GMA-GEL under UV light irradiation are two cross-linking modes to construct dual-cross-linking network of PDGA hydrogel dressing. The hydrogel remains fluid when placed in a sealed syringe and solidify rapidly by photocross-linking when placed on the wound. Furthermore, the hydrogel demonstrated excellent biocompatibility and hematological safety. The interaction between angelica polysaccharides and integrins on the platelet surface facilitated an augmentation in platelet adhesion, activation, and aggregation, ultimately inducing rapid coagulation of the blood within 130 s in a mouse tail vein hemorrhage model. ASP can promote tissue healing by promoting cell proliferation around wounds and accelerating the formation of new blood vessels. In a mouse skin defect model, collagen deposition, blood vessel formation, hair follicle regeneration, and granulation tissue formation were observed due to the presence of angelica polysaccharides, showing significantly superior wound healing properties when compared to Tegaderm™ film. In addition, the expression of CD31 in skin wounds treated with PDGA was significantly upregulated. Consequently, PDGA multifunctional dressings exhibit considerable potential for *in vitro* hemostasis and skin wound repair applications.

KEYWORDS

hydrogel dressing, wound healing, angelica sinensis polysaccharide, wound management, material sciences

1 Introduction

As the main barrier between the human body and the external environment, the skin plays a crucial protective role. However, it is also vulnerable to various external factors. These factors may include physical friction, high or low temperature exposure, chemical and corrosive material exposure, and biological microbial infections. These damages can often lead to different types of skin lesions, such as cuts, abrasions, burns, etc. These injuries

can not only bring pain and discomfort to the patient, but also may affect their daily life and work ability, and in severe cases, they may even cause infections and other complications (Tottoli et al., 2020; Tavakoli and Klar, 2021; Ding et al., 2023). After the skin was damaged, the natural healing process is frequently constrained by diverse factors. Without taking timely therapeutic measures, the healing of wounds may be hindered or the process may be prolonged (Jones and Hampton, 2021; Li et al., 2022; Kowalski et al., 2024). Recently, numerous researchers have focused on exploring new materials capable of effectively enhancing wound healing, among which hydrogels have garnered significant attention owing to their ability to keep wounds moist and block external contaminants, among other multiple advantages (Zhang et al., 2023). Hydrogels are mainly derived from a variety of natural or synthetic hydrophilic polymeric materials each of which aims to optimize the specific properties of the hydrogel to meet the varying needs of wound healing (Kamoun et al., 2017; Francesko et al., 2018; Tavakoli and Klar, 2020; Ciolacu et al., 2023). Among these, the *in situ*-forming hydrogel offers distinct advantages, as it rapidly forms a tightly adherent protective layer at the wound site, effectively shielding it from external contaminants and pathogens. It can be used as a drug delivery system, by loading the drug and realizing controlled release and improve the stability of drugs (Agarwal et al., 2022; Feng et al., 2023; Feng et al., 2024; Villa et al., 2024). Current studies have shown that hydrogels formed *in situ* have weak mechanical properties, which may result in their inability to maintain structural stability for long periods of time, and the gelling time is often long, which may delay treatment in medical emergencies.

Polyacrylamide has been widely used in medical fields such as drug delivery, medical materials and surgical aids (Wang L. et al., 2022; Tirey et al., 2024). These applications mainly utilize the biocompatibility, degradability and a certain degree of stability. However, the application of polyacrylamide in wound dressings been limited. This is mainly because polyacrylamide its swelling properties do not meet the requirements of medical dressings, and the molecular structure of polyacrylamide is relatively simple and lacks the specific functional groups or chemical groups required for cell adhesion (Reinhards-Hervás et al., 2024). Researchers improve polyacrylamide defects by combining different materials. Gelatin has been shown to enhance the biocompatibility of acrylamide and promotes cell growth and differentiation capacity (Wang Y. et al., 2022; Chen et al., 2023). Sodium alginate possesses robust water-absorbing capabilities, enabling it to absorb exudate from the wound surface and maintain wound moisture. After the combination of polyacrylamide and sodium alginate, the water-absorbing and moisturizing performance of hydrogel is further improved, which helps to maintain the moist state of the wound and promote the proliferation and differentiation of cells (Hasani-Sadrabadi et al., 2020).

Angelica sinensis polysaccharide (ASP) is the active compound extracted from Angelica sinensis (Tian et al., 2024), with a content of up to 15% in the plant. Studies have demonstrated that angelica polysaccharides exhibit notable advantages in tissue healing, manifesting primarily in their bioactivities. ASP promotes the proliferation and differentiation of pluripotent hematopoietic stem cells and hematopoietic progenitor cells, leading to an increase in the number of peripheral blood cells, leukocytes, hemoglobin, and bone marrow nucleated cells, which ultimately accelerates the tissue healing process. Moreover, ASP serves as an immunomodulatory agent, capable of modulating the activity of complement receptors on the lymphocyte membrane and augmenting the immune response of lymphocytes, thereby exerting a positive effect on the immune function of the body. This contributes to reducing the risk of infection and facilitates wound healing (Wang et al., 2017; Bi et al., 2021; Brumberg et al., 2021; Nai et al., 2021). Despite the numerous benefits associated with angelica polysaccharides, their direct application is constrained by several factors, namely, stability issues, challenges in controlling release rates, and excessively high local concentrations. Utilizing hydrogel as a carrier for angelica polysaccharides can overcome the limitations associated with direct application and offer the following advantages: hydrogel can provide a stable microenvironment that shields angelica polysaccharides from external factors, thereby enhancing their stability. Furthermore, precise control over the release rate and concentration of angelica polysaccharides can be achieved by adjusting the composition and structure of the hydrogel, thereby enabling stable and predictable therapeutic outcomes. The hydrogel ensures that the concentration of angelica polysaccharides in local tissues remains moderate, neither excessively high to elicit adverse reactions nor too low to compromise the therapeutic efficacy.

The central question of this study is: can hydrogels of specific composition and properties accelerate the wound healing process by modulating the wound microenvironment? To answer this question, we propose the following hypothesis: hydrogels containing specific bioactive components can significantly improve the speed and quality of wound healing by promoting cell proliferation, platelet adhesion and aggregation as well as collagen deposition, and vascularization and hair follicle generation. In this study presents the preparation of possessing in *in situ* formation properties a hydrogel dressing (PDGA). The hydrogel's double cross-linked network was induced through the chemical cross-linking of PAAM and the of GMA-GEL. Subsequently, the mechanical properties of the hydrogels were characterized. Furthermore, the biocompatibility of the PDGA hydrogel was assessed through blood compatibility and cytocompatibility tests. Lastly, the PDGA hydrogel was evaluated in a full-thickness skin defect model in mice for its ability to promote vascular and hair follicle regeneration, thereby facilitating wound healing. The results indicated that the PDGA hydrogel exhibited significant hemostatic and wound-healing effects on skin tissue defects (Figure 1). It allows rapid control of bleeding situations, which is particularly important in urgent hemostasis scenarios because of the urgent need for rapid, effective and safe wound treatment strategies in the operating room environment (Chou et al., 2017; Krasilnikova et al., 2022).

2 Materials and methods

2.1 Materials

Acrylamide (AAm): Purchased from Sigma-Aldrich, purity≥99%. Ammonium Persulfate (APS): Obtained from Aladin Reagent (Shanghai, China), purity≥98%. N,N,N′,N′-Tetramethylethylenediamine (TEMED): Supplied by Aladin Reagent (Shanghai, China). N,N′-Methylenebis(acrylamide) (BIS): Procured

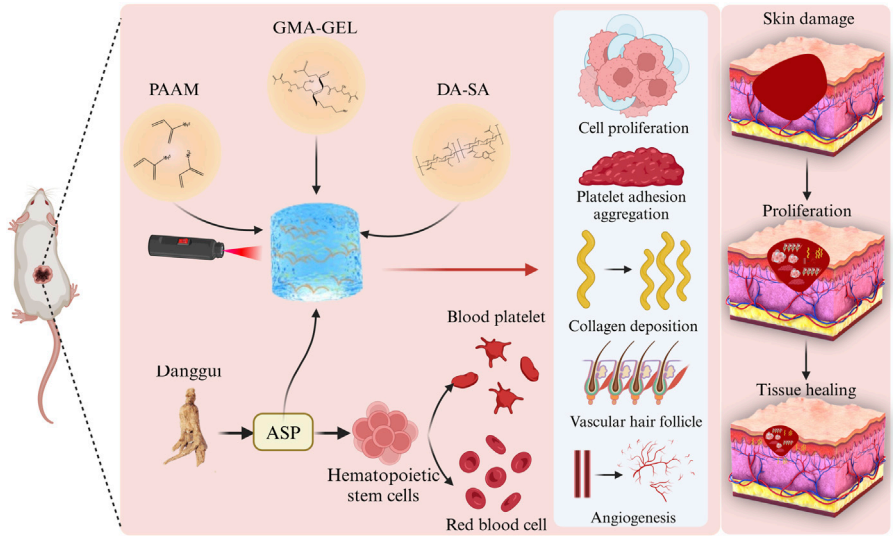


FIGURE 1
Schematic of PDGA hydrogel dressing promotion of wound healing. PDGA remodels tissues by promoting cell proliferation, platelet adhesion and aggregation, collagen deposition, angiogenesis and hair follicle generation.

from Sigma-Aldrich, purity≥99%. 1-Ethyl-3-(3-dimethylaminopropyl) carbodiimide hydrochloride (EDC·HCl): Purchased from Aladin Reagent (Shanghai, China). N-Hydroxysuccinimide (NHS): Obtained from Aladin Reagent (Shanghai, China), purity≥98%. Dopamine hydrochloride (DA·HCl): Supplied by Sigma-Aldrich. Ammonium alginate: Purchased from Aladin Reagent (Shanghai, China). Gelatin: Obtained from BD Biosciences (Franklin Lakes, NJ, United States), type A, from bovine skin. Glycidyl methacrylate (GMA): Procured from Tokyo Chemical Industry Co, Ltd. (Tokyo, Japan), purity≥97%. Angelica sinensis polysaccharide (ASP): Supplied by Shanghai Yuanye Bio-Technology Co, Ltd. (Shanghai, China), Biological Reagent 60%. Lithium Phenyl-2,4,6-trimethylbenzoylphosphinate (LAP): Purchased from Sigma-Aldrich, purity≥98%.All solutions were prepared using ultrapure water (Milli-Q system, MilliporeSigma, Burlington, MA, United States) to ensure the highest purity and minimize contamination.

2.2 Methods

2.2.1 Synthesis of GMA-GEL and DA-SA

GMA-GEL was first synthesized by modifying the previously reported method (Sk et al., 2021). The carboxyl and -OH groups were depleted in the condition of pH = 3.5, and the GMA molecule reacted with the carboxyl group in gelatin. The details were described in the Supplementary Material. DA-SA was synthesized by facilitating the reaction between the carboxyl group of sodium alginate and the amino group of DA. The specific process is shown in the Supplementary Material.

2.2.2 Preparation of PAAM/DA-SA/GMA-GEL hydrogel

First, the acrylamide of 14 wt%, the DA-SA of 2.8 wt%, the GMA-GEL of 10 wt%, and the ASP of 5 wt% were dissolved in 10 mL deionized water under light-shielded conditions. Subsequently, 0.09 mg of MBAA and 0.36 μL of Ammonium Persulfate (APS) were added to the AM/DA-SA/GMA-GEL solution. Prior to mixing, the photo-initiator LAP was introduced into the preparatory solution to obtain the precursor solution. Next, 0.4 mL of TEMED was added to the precursor solution, which was then transferred into a glass mold. Lastly, the hydrogel pre-polymer was exposed to ultraviolet light (365 nm) for 20 s. Over a period of 3 days, the PBS solution was replaced every 6 h to eliminate unreacted monomers and initiators.

2.2.3 Characterizations

The preparation of GMA-GEL and DA-SA was confirmed by nuclear magnetic resonance (^{1}H NMR) and Fourier transform infrared spectroscopy (FT-IR) analyses. The swelling behavior, biodegradability and microstructure of PAAM/DA-SA/GMA-GEL hydrogels were characterized through swelling experiments, degradation experiments and scanning electron microscopy (SEM) observations. For a detailed procedure, please refer to the Supplementary Material.

2.2.4 Mechanical properties of hydrogel

The modulus of these hydrogels was measured using a TA rheometer (DHR-2) and documented as a function of time (Del Giudice, 2020). Compressive stress-strain curves of PAAM/DA-SA/GMA-GEL hydrogels were obtained and analyzed (Fang et al., 2019). The ability of hydrogels to slow drug release at different pH was analyzed. For detailed procedures, please refer to the Supplementary Material.

2.2.5 Hemolytic test of hydrogels

A predetermined amount of hydrogel was combined with erythrocytes and incubated for 1 hour at 37 °C. Subsequently, the absorbance at 540 nm was recorded to evaluate hemolysis (Zhao et al., 2023). For a detailed procedure, please refer to the Supplementary Material.

2.2.6 *In vitro* whole blood-clotting performance

The *in vitro* whole blood-clotting test was conducted following the previously established method (Zhang et al., 2024). For a detailed protocol, please refer to the Supplementary Material.

2.2.7 Hemostasis performance of hydrogels

Based on previous research, the hemostatic efficacy of the PAAM/DA-SA/GMA-GEL hydrogel was assessed using a mouse-tail amputation model (female Kunming mice, weighing 28–32 g). A method of tagging experimental animals with non-invasive ear tags was used by us (Klabukov et al., 2023). For detailed experimental procedures, please refer to the Supplementary Material.

2.2.8 Cytocompatibility test of hydrogels

The cytocompatibility test was performed using the leaching solution method as described in Zangeneh et al. (2019). The detailed procedure is provided in the Supplementary Material.

2.2.9 Evaluation of wound healing sites with a dorsal skin defect model in mice

To further evaluate the therapeutic effect of PDGA hydrogel on wound healing, a mouse back skin defect model was establishedused. A method of tagging experimental animals with non-invasive ear tags was used by us. Hematoxylin-eosin (H&E) staining was used to qualitatively assess the histomorphology of tissue regeneration at various time points, with a particular focus on fibroblasts and epidermal regeneration within the traumatized area. The percentage of collagen deposition was assessed by Masson staining, as described in the Supplementary Material, to gauge the extent of tissue repair. All animal experiments were conducted in accordance with the approval of the Institutional Animal Care and Use Committee of Changchun University of Traditional Chinese Medicine.

2.2.10 Immunofluorescence staining

Immunofluorescence staining was performed to assess vascular regeneration during wound healing, using CD31 as a marker. The detailed procedure is provided in the Supplementary Material.

2.2.11 Statistical analysis

The results were presented as mean values of replicate experiments, and statistical analysis was performed using GraphPad Prism and Origin. Data represent the mean ± SD of at least three replicates. *P < 0.05, **P < 0.01, ***P < 0.001, and ****P < 0.0001 were regarded as statistically significant. In addition, “ns” denoted no significant difference.

3 Results

3.1 Preparation of GMA-GEL and DA-SA

Principles of GMA and GEL reactions as shown in Figure 2A. Figure 2B showed the ^{1}H NMR spectra of GEL and GMA-GEL compounds. The ^{1}H NMR spectra of GMA-GEL revealing the GMA grafting onto gelatin. In this spectrum, the signals observed at 5.4 and 5.8 ppm are attributed to the methacrylate vinyl proton C=C bond vibrations. The FT-IR spectra of GMA-GEL and GEL were showed in Figure 2C. Compared with the FT-IR spectrum of unmodified gelatin, the product GMA-GEL showed enhanced characteristic peaks at 1,211 cm^{-1}, indicating that GMA was successfully grafted. The FT-IR spectra indicated that the stretching vibration peak of the -OH group was observed at 3,305 cm^{-1}; the peak at 2,941 cm^{-1} was attributed to C-H stretching vibration; and the peak at 1,211 cm^{-1} was attributed to the ester bond formed by GMA grafting. The ^{1}H NMR spectrum and FT-IR spectrum collectively demonstrated that GMA had been successfully grafted into the gelatin molecular chain.

Principles of DA and SA reactions as shown in Figure 2D. Figure 2E showed the ^{1}H NMR spectra of DA, SA, and DA-SA. The ^{1}H NMR spectra of DA-SA revealed that the peak at 6.6 ppm specifically corresponded to the proton -CH on the catechol ring, and the -NH group near the catechol ring was observed around 2.77 ppm, thus confirming the successful grafting of the catechol motif. Figure 2F showed the FT-IR spectra of DA, SA, and DA-SA. In the FT-IR spectrum of DA-SA, two characteristic peaks were observed at 1,287 and 1,529 cm^{-1}, which were attributed to the amide III band (C-N stretching vibration) and amide II band (N-H bending vibration), respectively. Additionally, the amide I band was observed at 1,736 cm^{-1}. The presence of the amide group (-CONH-) at 3,100 cm^{-1} indicated the successful grafting of DA. Both ^{1}H NMR spectra and FT-IR spectra were consistent in showing that DA was successfully grafted into the SA molecular chain.

3.2 Preparation and characterization of PDGA hydrogel

In the process of soaking PAAM/DA-SA/GMA-GEL, PAAM, PAAM/DA-SA, PAAM/GMA-GEL, DA-SA, GMA-GEL, and DA-SA/GMA-GEL in deionized water for 3 days to remove unreacted monomers and initiators.

The gelation time of the hydrogels was evaluated by the time of irradiation under 365 nm UV light to turn the gel precursor solution into a gel, and the gelling time of PAAM/DA-SA/GMA-GEL and PDGA hydrogels was about 20 s. As shown in Figure 3A. The UV irradiation time was safe for biological tissues and was favorable for *in vitro* applications (Xu et al., 2022).

During the wound healing process, tissue fluid may persist in exuding. Hydrogel dressings possessing excellent swelling capabilities can efficiently absorb these exudates and create a moist microenvironment for the wound. This moist microenvironment facilitates cell proliferation and differentiation, thereby expediting the wound healing process. Therefore, the swelling properties of these hydrogels were tested. As shown in Figure 3B. The ideal dressing needs to have excellent swelling properties, but PAAM does not have this property. By incorporating DA-SA and GMA-GEL, on one hand, the introduction of additional hydrophilic groups, such as hydroxyl and amino functionalities, facilitates the formation of interactions with water molecules, including hydrogen bonding, thereby enhancing the water absorption capacity and swelling behavior of the hydrogel. On the other hand, the integration of PAAM, DA-SA, and GMA-GEL results in the formation of double

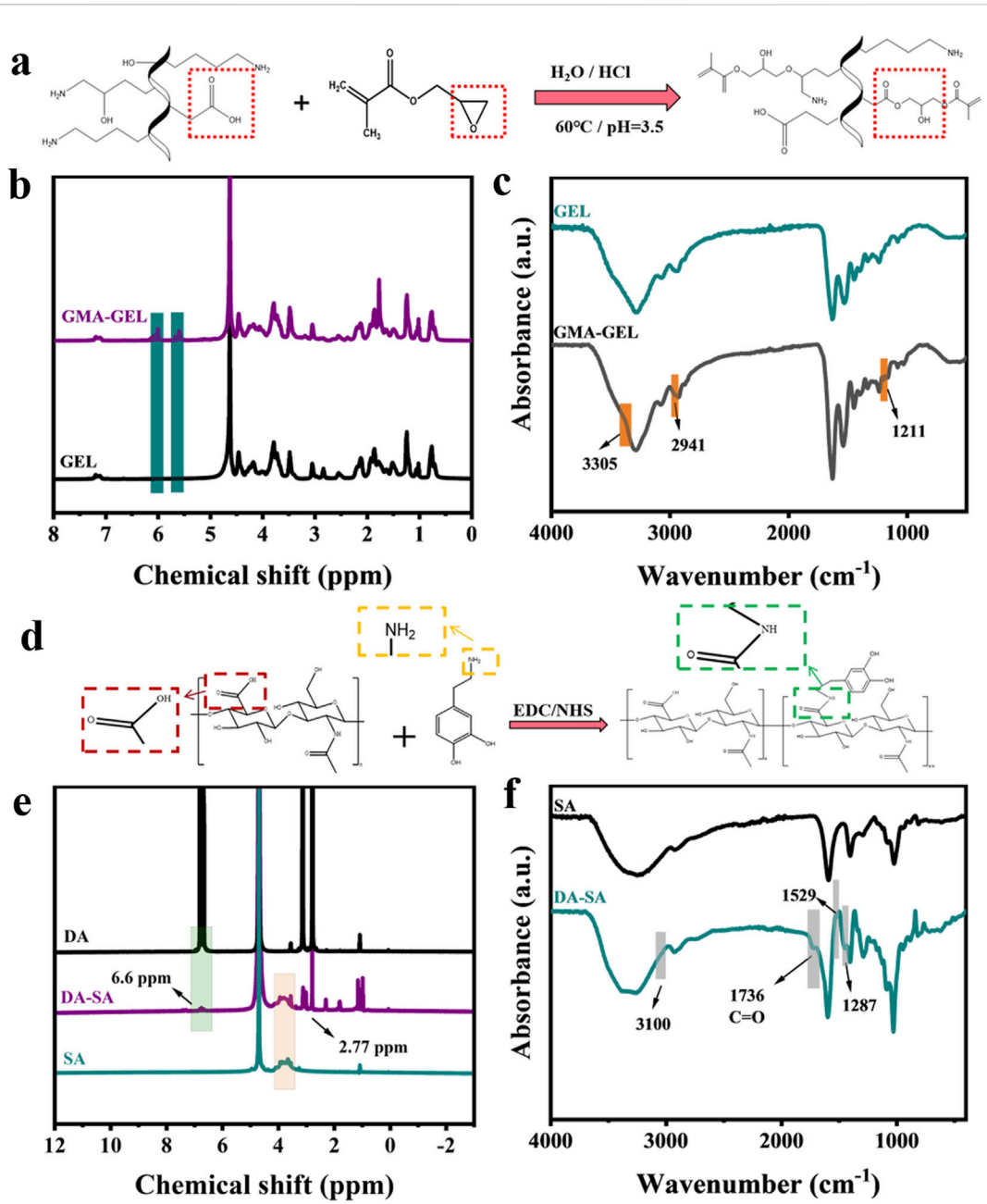


FIGURE 2
(a) Principles of GMA and GEL reactions; **(b)** 1H NMR spectra of gelatin before and after grafting of GMA; **(c)** FT-IR spectra of gelatin before and after grafting of GMA; **(d)** Principles of DA and SA reactions; **(e)** 1H NMR spectra of SA before and after grafting of DA; **(f)** FT-IR spectra of SA before and after grafting of DA.

cross-linked structure, enabling more efficient retention of water, thereby further enhancing the swelling characteristics of the hydrogel.

The degradation properties of the hydrogels were investigated by simulating a physiological environment at 37°C PBS buffer for evaluating the degradation properties of the hydrogels After 3 days of hydrogel immersion in PBS, the residual weight ratio of the PAAM hydrogel was 62% of the initial weight, whereas that of the PAAM/DA-SA, PAAM/DA-SA/GMA-GEL and PAAM/GMA-GEL hydrogels was about 30% of the initial weight. Residual ratio was about 30% of the initial weight. After the PAAM hydrogels reached the degradation equilibrium at day 9, the weight remaining was maintained at about 20%, while the PAAM/DA-SA, PAAM/DA-SA/GMA-GEL and PAAM/GMA-GEL hydrogels reached the degradation equilibrium at day 6, indicating that the PAAM/DA-SA/GMA-GEL hydrogels had a tunable degradation ratio by the introduction of DA-SA and GMA-GEL. hydrogels with adjustable degradation rates by the introduction of DA-SA and GMA-GEL.

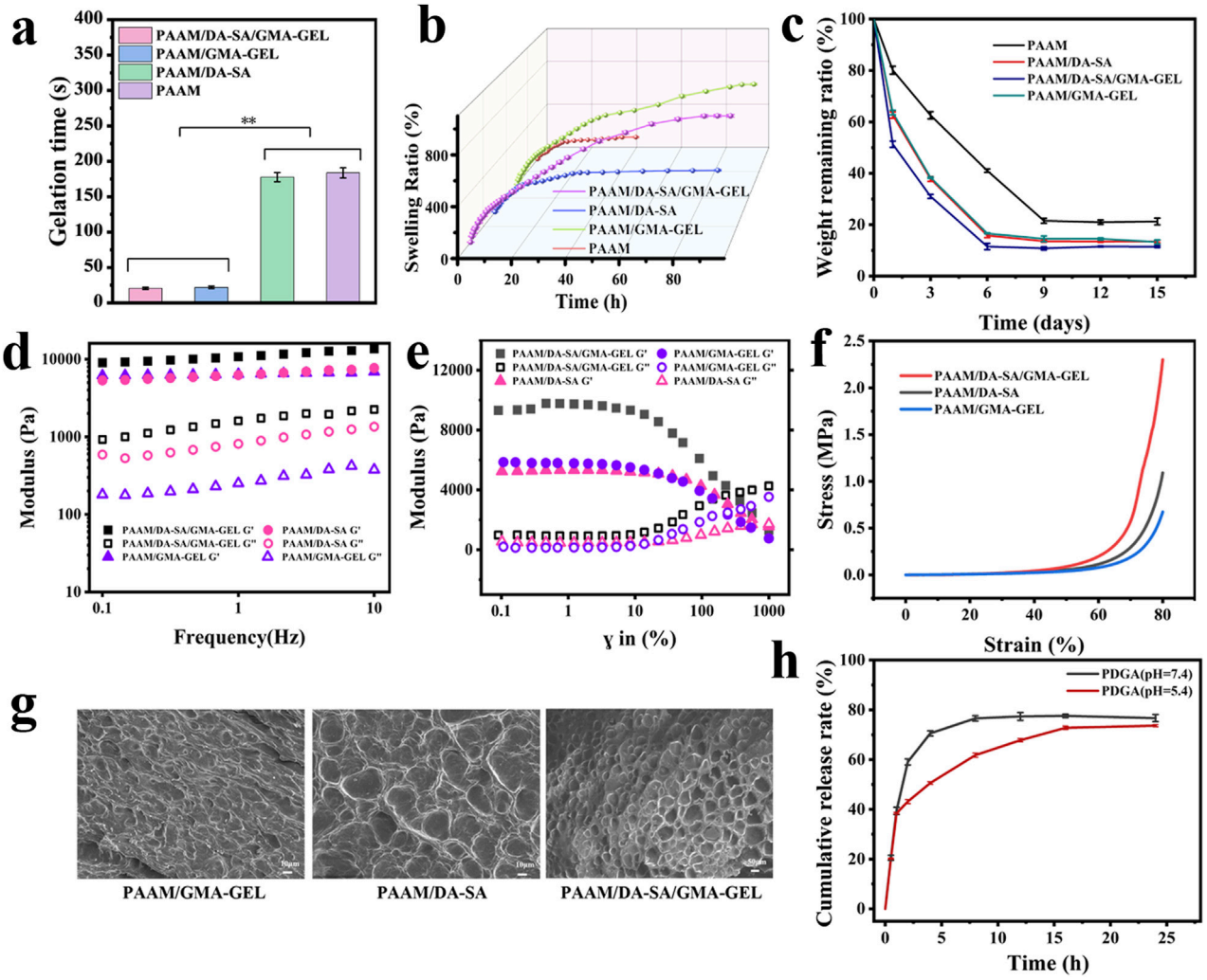


FIGURE 3
(a) Gelation times; **(b)** Swelling performance curves for hydrogels with various compositions; **(c)** Degradation performance curve of different component gels; **(d)** Rheological characteristics of hydrogels at angular frequencies ranging from 0 to 10 rad/s; **(e)** Rheological behavior of hydrogels under varying strains; **(f)** Compressive properties of hydrogels with diverse compositions; **(g)** SEM of hydrogels; **(h)** Rate of drug release at different pH.

The rheological properties of the hydrogels were assessed, with the temperature set at 37°C to mimic the body temperature of human skin (Fares et al., 2024). The storage modulus (G′) and loss modulus (G") of different hydrogels were tested at a fixed frequency of 10 rad s^{-1}. It was found that the storage modulus (G′) was higher than the loss modulus (G") for all hydrogels, implying that they were stable (Figure 3D). As shown in Figure 3E, no significant difference in fracture strain of hydrogels.

The compression properties of the different component hydrogels are shown in Figure 3F. Compared to the PAAM/GMA-GEL group and the PAAM/DA-SA group, the addition of DA-SA and GMA-GEL to the hydrogels resulted in an increase in compressive strength. The high molecular mass of DA-SA and the presence of more polar hydroxyl groups enhanced the entanglement between polymer chains through hydrogen bonding. This resulted in a denser structure of the hydrogel, subsequently increasing its compressive strength. The incorporation of GMA-GEL via photo-crosslinking and chemical crosslinking contributed to a denser gel structure. Collectively, these results suggested that PAAM/DA-SA/GMA-GEL hydrogels exhibited good energy dissipation capacity under external forces, owing to their non-covalent cross-linking network.

During the synthesis process of PAAM/DA-SA/GMA-GEL hydrogels, the polymer chains undergo both chemical and photocross-linking to establish a dual cross-linked network architecture. The resultant uniform morphology and interconnected pore structure empower the hydrogel to preserve its structural robustness and coherence under external stress (Figure 3G).

The PDGA (pH = 7.4) hydrogel had reached drug release equilibrium at 8 h with a drug release rate of 76.68%, whereas the PDGA (pH = 5.4) hydrogel effectively reduced the drug release efficiency and reached drug release equilibrium at 24 h with a release rate of 73.65%. The PDGA hydrogel at pH = 5.4 helped in the slow release of the drug (Figure 3H).

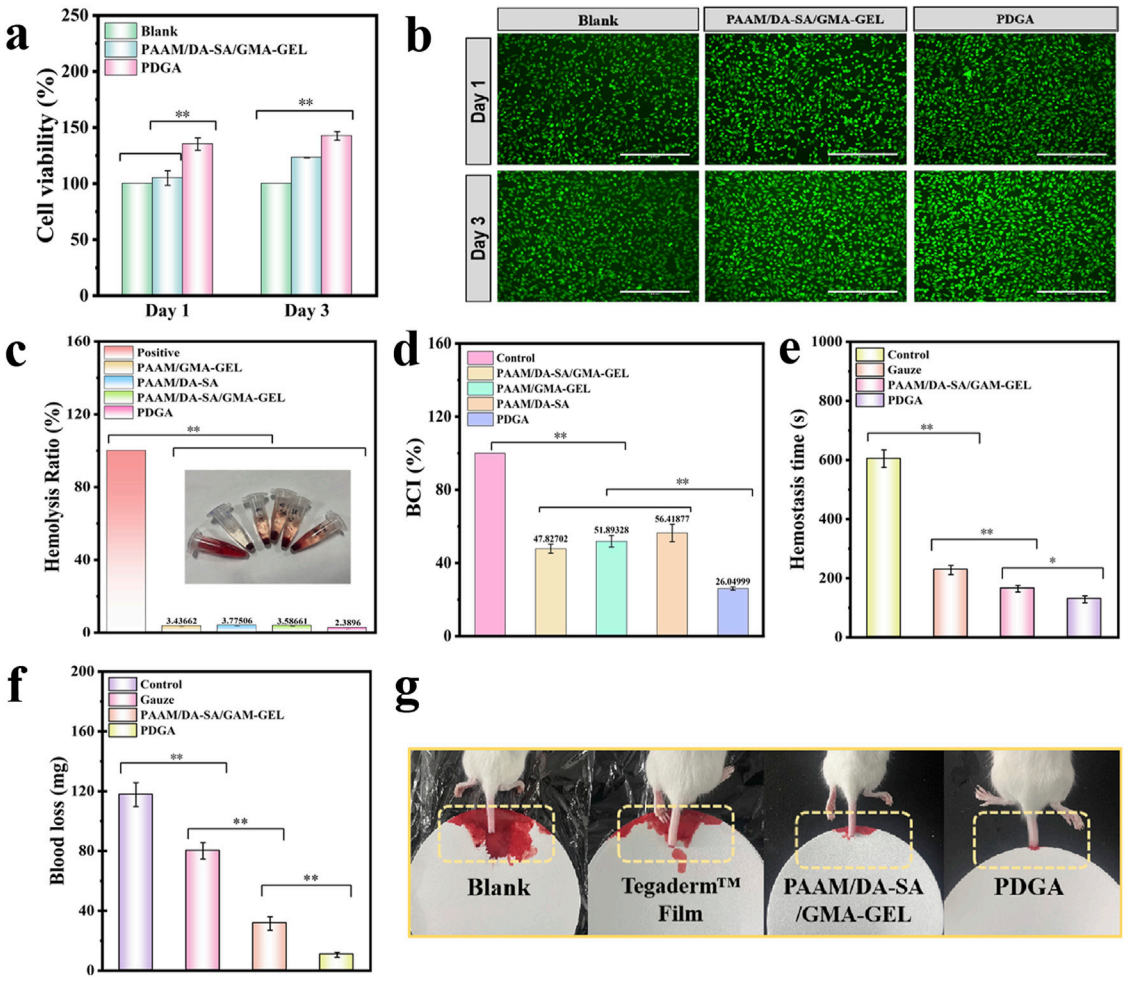


FIGURE 4
(a) Cell compatibility assessment of the PDGA and PAAM/DA-SA/GMA-GEL hydrogel; **(b)** LIVE/DEAD staining of L929 cells after contacted with the hydrogels for 1 d and 3d; Scale bar: 400 μm; **(c)** Hemolysis rate (%) of various hydrogels; **(d)** Whole blood clotting time assay; **(e)** Blood loss time in the mouse-tail amputation model; **(f)** Quantitative results of blood loss in the mouse-tail amputation model (n = 3); **(g)** Schematic diagram of the mouse-tail amputation model. Statistical significance *P < 0.05, **P < 0.01.

3.3 Evaluation of hydrogel biocompatibility

The cytocompatibility of PAAM/DA-SA/GMA-GEL and PDGA hydrogels was assessed using the cell viability of L929 cells. Cytotoxicity of the aforementioned hydrogels was determined using the leachate method. A significant increase in cell viability was observed within 3 days, suggesting robust cell growth during the experimental period (Figure 4A). On the day 3, the cell viability of PDGA hydrogel was significantly higher than that of PAAM/DA-SA/GMA-GEL and the control group ($P < 0.01$). In addition, almost all L929 cells showed a pike-shaped morphology and were stained green (live cells), and only a few red (dead cells) cells were observed in live/dead viability staining, suggesting good cytocompatibility of the immersed hydrogel (Figure 4B). The results demonstrate that the hydrogel exhibits good cytocompatibility with no apparent cytotoxicity, indicating its potential as an alternative material for clinical dressings.

Good blood compatibility is crucial for the application of biomaterials. An *in vitro* hemolysis assessment was conducted to evaluate the blood compatibility of PDGA hydrogels. After a 1-h incubation in a simulated physiological environment *in vitro*, qualitative observations were made on the visual appearance of the four hydrogel groups, along with the positive control group, as shown in Figure 4C. The hydrogels exhibited a Quantitative analysis revealed that the hemolysis rates for all hydrogels were below 5%. These results indicate good blood compatibility for these hydrogels.

The human skin and tissues are densely populated with blood vessels. Upon injury or trauma caused by external forces, these blood vessels may rupture, resulting in blood loss. Therefore, achieving hemostasis is a crucial initial step in the wound healing process. An *in vitro* whole-blood coagulation assessment is a widely used method to evaluate the coagulation efficacy of hemostatic hydrogels (Bao et al., 2022). A lower Blood Coagulation Index (BCI) signifies higher coagulation efficiency. Medical gauze was selected as the control material for comparison with the hydrogels. Following incubation of various hydrogels with blood at 37 °C for 10 min, the results revealed that the BCI values for all hydrogel groups were significantly lower than that of the gauze control ($P < 0.05$) (Figure 4D).

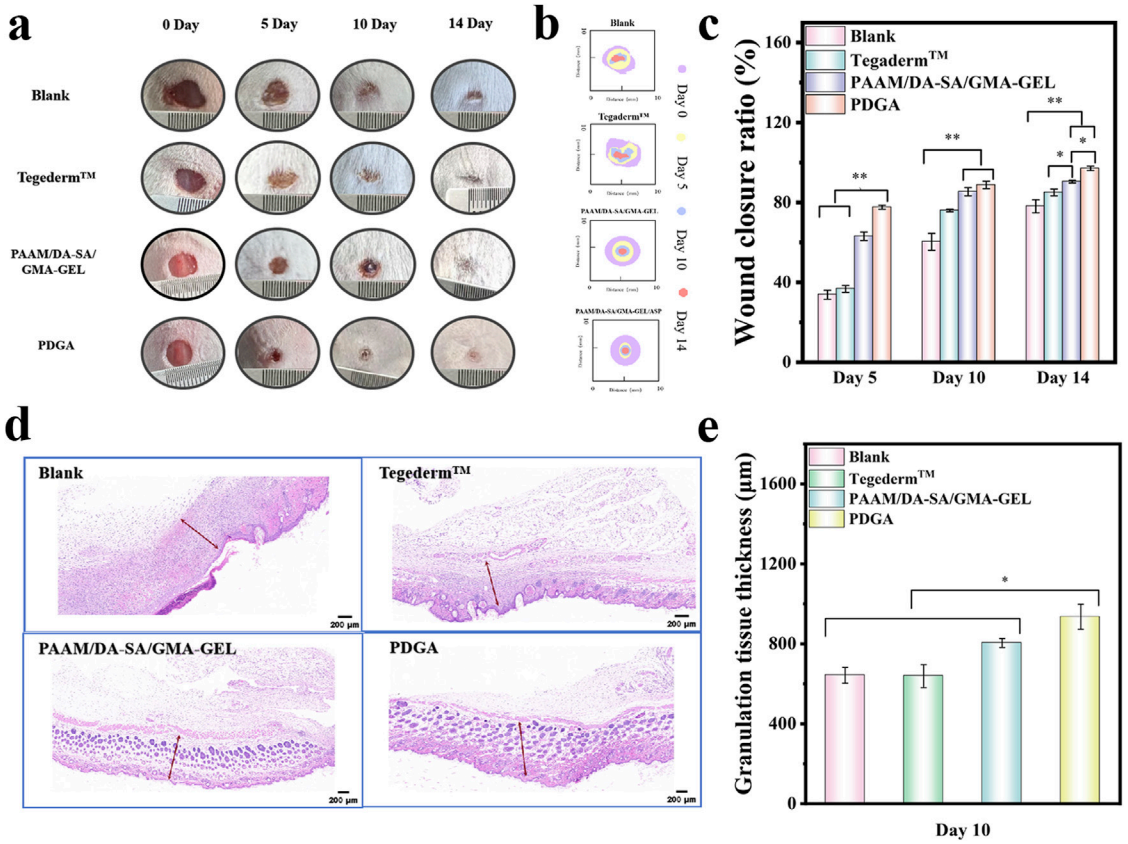


FIGURE 5
(a) Photographs of the wound healing site captured on the 5th, 10th, and 14th days; **(b)** Schematic illustration of the wound healing process on days 5, 10, and 14; **(c)** Statistical analysis of wound closure ratio (n = 3); **(d)** Micrographs of regenerating granulation tissue on the 10th day (granulation tissue indicated by red arrows), scale bar: 200 μm; **(e)** Thickness measurements of the regenerated granulation tissue on the 10th day (n = 3). Statistical significance *P < 0.05, **P < 0.01.

Due to the good blood compatibility and blood-clotting index of PDGA hydrogel, its hemostatic performance was further evaluated using a mouse-tail amputation model (Figures 4E–G). The hemostatic performance of the PDGA hydrogel was tested in the mouse-tail amputation model, resulting in a significant reduction in blood loss ($P < 0.01$) and bleeding time. Compared to the control group, rat tails treated with PDGA hydrogel exhibited a 91.4% reduction in blood loss and a 78.8% decrease in bleeding time. The *in vivo* hemostatic effect of the PDGA hydrogel was primarily attributed to the angelica polysaccharides within the hydrogel interacted with integrins on the platelet surface, leading to increased platelet adhesion, activation, and aggregation, thereby enhancing hemostasis.

3.4 *In vivo* wound healing in full-thickness skin defect model

To assess the efficacy of these hydrogels as wound dressings, a mouse model of dorsal skin defect was established. Two control groups were established using Blank and Tegaderm™ films. The wound area in all four groups exhibited a gradual decrease over the course of 5, 10, and 14 days (Figures 5A–C). Following 5 days of treatment, the wound areas in the PAAM/DA-SA/GMA-GEL and PDGA hydrogel groups were significantly smaller compared to those in the commercial Membrane and Blank groups (Figure 5C). The wound closure ratio of the PDGA hydrogel group was approximately 44% higher than that of the Blank group ($P < 0.01$), indicating the most effective wound healing. The wound closure ratios of the PAAM/DA-SA/GMA-GEL and PDGA hydrogel groups were comparable and significantly higher than those of the Blank and Tegaderm™ Film groups. After 10 days of treatment, the wound closure ratios of the PAAM/DA-SA/GMA-GEL and PDGA hydrogel groups were 85% and 88%, respectively. These results suggest that the wound healing efficacy of these hydrogels exceeded that of both the Tegaderm™ Film and Blank groups. Furthermore, the wound area recovery of the PAAM/DA-SA/GMA-GEL and PDGA hydrogel groups was significantly greater than that of the Tegaderm™ Film and Blank groups ($P < 0.01$). On day 14, the wound in the PDGA group achieved near-complete healing, with a wound area recovery exceeding 97%.

Granulation tissue is a newly formed, capillary-rich fibrous connective tissue that plays a key role in the healing process after tissue injury (Clark, 1985). Therefore, the stage of wound healing was assessed by measuring the thickness of the granulation tissue. As shown in Figures 5D, E, after 10 days of healing, the Blank and Tegaderm™ Film groups exhibited a thinner granulation tissue thickness (642.8 μm and 638.5 μm, respectively). The granulation

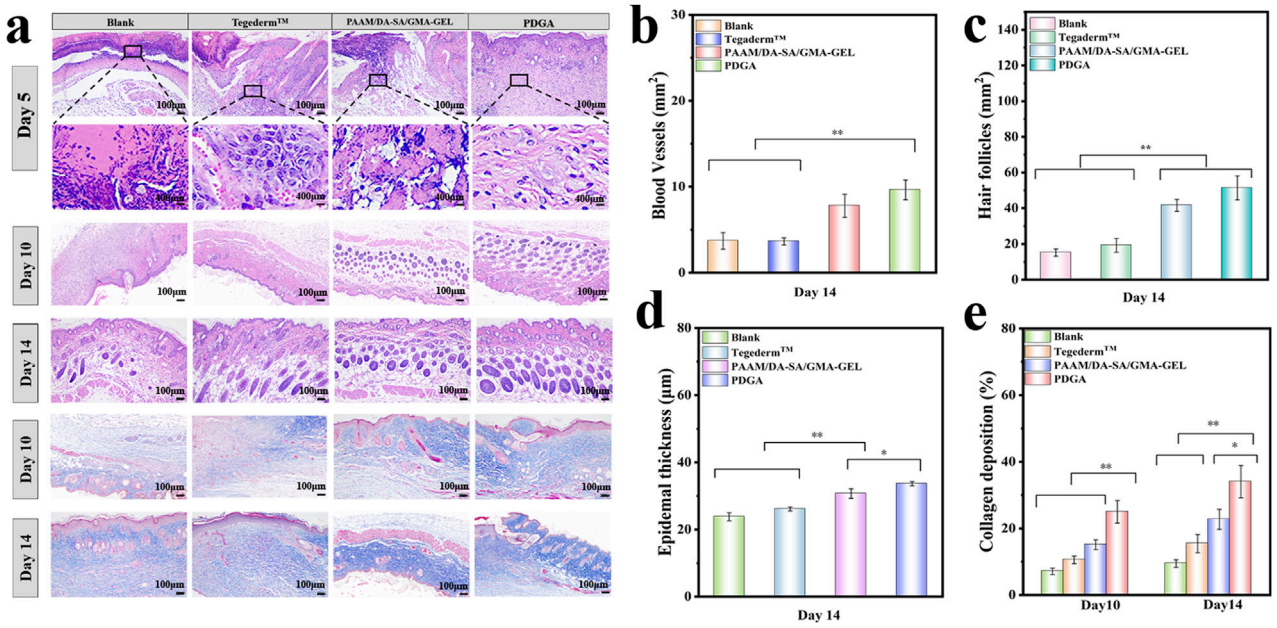


FIGURE 6
(a) Morphological results of the wound healing site after treatment for 5, 10, and 14 days, with Masson's trichrome staining at the wound site on the 10th and 14th days; **(b)** Regeneration of blood vessels on the 14th day post-treatment; **(c)** Newly formed hair follicles on the 14th day post-treatment; **(d)** Epidermal thickness for different groups on the 14th day post-treatment; **(e)** Collagen deposition. Statistical significance *P < 0.05, **P < 0.01.

tissue thickness of the PAAM/DA-SA/GMA-GEL and PDGA hydrogels were 804.4 μm and 935 μm, respectively. The latter was significantly thicker than that of the other groups ($P < 0.05$). These results indicate that the PDGA hydrogel has a more favorable effect on wound repair.

3.5 Histomorphological evaluation

Wound healing is a continuous process that encompasses wound contraction, granulation tissue formation, and regeneration of the epidermis and other tissues (Wang et al., 2023). Hematoxylin and eosin-stained sections (H&E staining) were used to assess the wound healing effect on days 5, 10, and 14 (Shamloo et al., 2018). On the fifth day of wound healing, HE staining revealed no significant inflammatory reaction in any of the groups. However, compared to the two hydrogel groups, more inflammatory cells were observed at the wound site in the blank and Tegaderm™ groups (Figure 6A). Furthermore, the PDGA hydrogel group exhibited relatively fewer inflammatory cells and a higher presence of fibroblasts compared to the PAAM/DA-SA/GMA-GEL hydrogel group. These results indicate that the PDGA hydrogels did not elicit an increased foreign body response. Neovascularization is crucial for repairing the blood microcirculatory system of subcutaneous damaged tissues, thereby providing essential nutrients. As shown in Figure 6B, both the PAAM/DA-SA/GMA-GEL and PDGA hydrogel groups displayed a greater number of blood vessels compared to the blank and Tegaderm™ groups ($P < 0.05$). Additionally, some hair follicles formed in the PDGA group (Figure 6C). On day 14, although relatively intact skin had grown in the blank and Tegaderm™ Film groups, few hair follicles were observed (Figure 6A). In contrast, the wounds treated with hydrogels were covered with epithelial tissues that more closely resembled normal skin. The increased number of skin follicles and blood vessels in the PAAM/DA-SA/GMA-GEL and PDGA hydrogel groups was also significantly different from that in the blank and Tegaderm™ groups ($P < 0.05$). Notably, both the PAAM/DA-SA/GMA-GEL group and the PDGA group exhibited nearly intact epidermis recovery (Figure 6D). These results indicate that the hydrogel was beneficial to ECM remodeling and tissue regeneration. In addition, ASP can significantly stimulate the proliferation of hematopoietic stem cells and promote the synthesis of hemoglobin and red blood cells (Bai et al., 2018; Zhang et al., 2019; Chi et al., 2022; Guo et al., 2024).

Collagen deposition plays a critical role in tissue remodeling during wound healing. As shown in Figure 6E, the amount of collagen deposition in the PDGA hydrogel group was significantly higher than in the PAAM/DA-SA/GMA-GEL hydrogel group on the 10th day ($P < 0.01$). On the 14th day, the collagen volume ratio of the PDGA hydrogel group was still significantly higher than that in the Tegaderm™ group and Blank group ($P < 0.01$). The collagen volume ratio at the wound site continued to increase over the 14 days of treatment. The hydrogel group exhibited a better collagen volume ratio throughout the repair process compared to the Tegaderm™ and blank groups. Masson trichrome staining of tissue sections was performed on days 10 and 14 to qualitatively observe and quantitatively analyze collagen deposition (Figure 6A). Collagen during wound recovery was stained blue. The PDGA group showed the best collagen regeneration compared to the other hydrogel groups, as well as the Tegaderm™ membrane and blank groups.

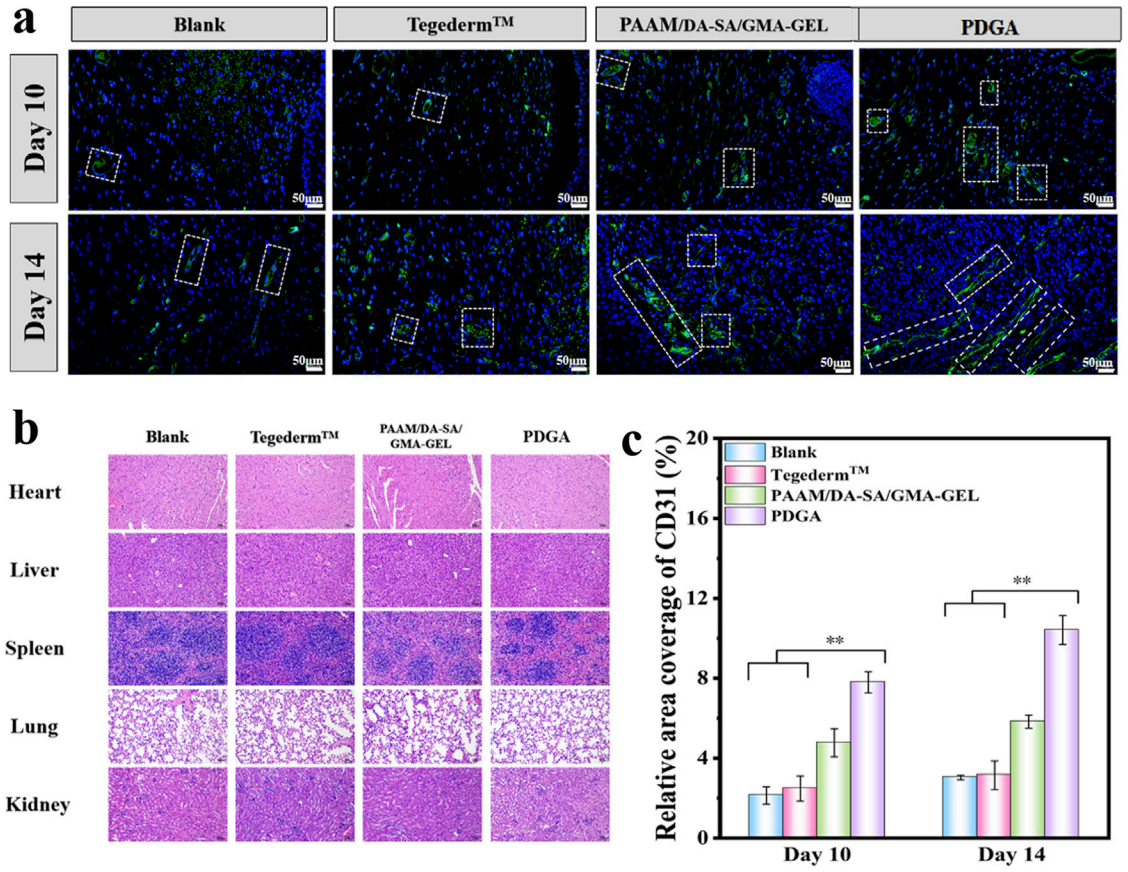


FIGURE 7
(a) Expression of CD31 on 10 and 14 days; White line indicate the expression of CD31; **(b)** HE staining results of liver, spleen, lungs, and kidneys in each group 14 days after surgery; **(c)** With n = 3, the CD31 relative area ratio was calculated. Statistical significance *P < 0.05, **P < 0.01.

Thus, these results demonstrate that PDGA hydrogel can effectively promote collagen deposition.

3.6 The expression of CD31 during wound healing

CD31 is a member of the vascular endothelial cell markers and is mainly expressed on the surface of endothelial cells, B-lymphocytes, platelets, granulocytes, and certain T cells (Yang et al., 2020; Guo et al., 2022; Liu et al., 2024). Consequently, we selected CD31 as an indicator for evaluating wound dressings to promote angiogenesis during wound healing. The immunofluorescence staining of CD31 and quantitative results were shown in Figures 7A, C. Compared with Blank, Tegaderm™ Film, and PAAM/DA-SA/GMA-GEL, the wound site treated with the PDGA hydrogel showed more CD31 expression ($P < 0.01$) on the 10th day. In addition, on the 14th day, the expression levels of CD31 in the PDGA group were significantly higher than those of other groups ($P < 0.01$). In conclusion, the PDGA hydrogel significantly promotes wound healing by enhancing CD31 expression, collagen deposition, angiogenesis, and hair follicle generation. Compared to the blank group and Tegaderm™, the PDGA hydrogel demonstrates superior repair efficacy.

Pathological examination was conducted on the hearts, liver, spleen, lungs, and kidneys of mice in the blank group, Tegaderm™ group, PAAM/DA-SA/GMA-GEL group, and PDGA group 14 days postsurgery. No significant abnormalities were found, thus indicating that PDGA hydrogel did not cause damage to any organ tissues.

4 Discussion

PDGA hydrogel benefits from the rapid response of the photocross-linking process, achieving rapid curing, which is particularly important for emergency hemostasis scenarios and bleeding situations can be rapidly control. At the same time, its low initial crosslinking degree gives the material good shape adaptability, enabling PDGA hydrogel to closely fit the surface of various complex wounds, effectively forming a protective barrier, blocking the invasion of bacteria and microorganisms, and reducing the risk of infection. Over time, the chemical cross-linking mechanism is gradually activated and strengthened, enhancing the mechanical strength and adhesion properties of the PDGA hydrogel, ensuring the durable and stable attachment of the hydrogel at the wound site, and providing a more reliable support for the wound healing.

5 Conclusion

A hydrogel dressing (PDGA) with *in situ* formation properties which has been applied for rapid hemostasis, wound healing and repair was developed. The dual-crosslinked structure of PDGA hydrogels was constructed through the combined action of chemical crosslinking initiated by PAAM radical polymerization and photocrosslinking mediated by GMA-GEL radical polymerization. The hydrogel facilitates the sustained release of ASP. PDGA hydrogel can significantly improve the speed and quality of wound healing by promoting cell proliferation, platelet adhesion and aggregation, collagen deposition, vascularization and folliculogenesis. The *in situ* tissue engineering of the PDGA hydrogel allows the material to have good shape adaptability to closely fit the surface of a variety of complex wounds, effectively forming a protective barrier that stops the invasion of bacteria and microorganisms and reduces the risk of infection while also allowing for rapid control of bleeding situations. This is particularly important in emergency hemostasis scenarios, where there is a strong need for fast, effective and safe wound treatment strategies in the operating room environment. We anticipate that this study will provide a scientific basis for the application of hydrogels in wound healing and provide new ideas for the development of novel wound treatment strategies.

Data availability statement

The original contributions presented in the study are included in the article/Supplementary Material, further inquiries can be directed to the corresponding author.

Ethics statement

The animal study was approved by Changchun University of Chinese Medicine. The study was conducted in accordance with the local legislation and institutional requirements.

Author contributions

YL: Data curation, Formal Analysis, Validation, Writing–original draft. YZ: Writing–review and editing. QJ: Writing–original draft. XL: Writing–original draft. KX: Funding acquisition, Project administration, Resources, Writing–review and editing.

Funding

The author(s) declare that financial support was received for the research and/or publication of this article. This research was funded by The Science and Technology Research Project of the Education Department of Jilin Provincial, grant number "JJKH20241093KJ" The Science and Technology Research Project of Jilin Provincial Administration of Traditional Chinese Medicine, grant number "2024078".

Conflict of interest

The authors declare that the research was conducted in the absence of any commercial or financial relationships that could be construed as a potential conflict of interest.

Generative AI statement

The author(s) declare that no Generative AI was used in the creation of this manuscript.

Publisher's note

All claims expressed in this article are solely those of the authors and do not necessarily represent those of their affiliated organizations, or those of the publisher, the editors and the reviewers. Any product that may be evaluated in this article, or claim that may be made by its manufacturer, is not guaranteed or endorsed by the publisher.

Supplementary material

The Supplementary Material for this article can be found online at: https://www.frontiersin.org/articles/10.3389/fphar.2025.1562264/full#supplementary-material

References

Agarwal, R., Niezgoda, J., Niezgoda, J., Madetipati, N., and Gopalakrishnan, S. (2022). Advances in hemostatic wound dressings: clinical implications and insight. *Adv. Skin. Wound Care* 35 (2), 113–121. doi:10.1097/01.ASW.0000790488.72494.57

Bai, Z., Dan, W., Yu, G., Wang, Y., Chen, Y., Huang, Y., et al. (2018). Tough and tissue-adhesive polyacrylamide/collagen hydrogel with dopamine-grafted oxidized sodium alginate as crosslinker for cutaneous wound healing. *RSC Adv.* 8 (73), 42123–42132. doi:10.1039/c8ra07697a

Bao, L., Li, C., Tang, M., Chen, L., and Hong, F. F. (2022). Potential of a composite conduit with bacterial nanocellulose and fish gelatin for application as small-diameter artificial blood vessel. *Polym. (Basel)* 14 (20), 4367. doi:10.3390/polym14204367

Bi, S.-J., Fu, R.-J., Li, J.-J., Chen, Y.-Y., and Tang, Y.-P. (2021). The bioactivities and potential clinical values of angelica sinensis polysaccharides. *Nat. Product. Commun.* 16 (3). doi:10.1177/1934578x21997321

Brumberg, V., Astrelina, T., Malivanova, T., and Samoilov, A. (2021). Modern wound dressings: hydrogel dressings. *Biomedicines* 9 (9), 1235. doi:10.3390/biomedicines9091235

Chen, S., Wang, Y., Lai, J., Tan, S., and Wang, M. (2023). Structure and properties of gelatin methacryloyl (GelMA) synthesized in different reaction systems. *Biomacromolecules* 24 (6), 2928–2941. doi:10.1021/acs.biomac.3c00302

Chi, J., Li, A., Zou, M., Wang, S., Liu, C., Hu, R., et al. (2022). Novel dopamine-modified oxidized sodium alginate hydrogels promote angiogenesis and accelerate healing of chronic diabetic wounds. *Int. J. Biol. Macromol.* 203, 492–504. doi:10.1016/j.ijbiomac.2022.01.153

Chou, P. Y., Chen, S. H., Chen, C. H., Chen, S. H., Fong, Y. T., and Chen, J. P. (2017). Thermo-responsive *in-situ* forming hydrogels as barriers to prevent post-operative peritendinous adhesion. *Acta Biomater.* 63, 85–95. doi:10.1016/j.actbio.2017.09.010

Ciolacu, D. E., Nicu, R., Suflet, D. M., Rusu, D., Darie-Nita, R. N., Simionescu, N., et al. (2023). Multifunctional hydrogels based on cellulose and modified lignin for advanced wounds management. *Pharmaceutics* 15 (11), 2588. doi:10.3390/pharmaceutics15112588

Clark, R. A. (1985). Cutaneous tissue repair: basic biologic considerations. *I. J. Am. Acad. Dermatol* 13 (5 Pt 1), 701–725. doi:10.1016/s0190-9622(85)70213-7

Del Giudice, F. (2020). Simultaneous measurement of rheological properties in a microfluidic rheometer. *Phys. Fluids* 32 (5). doi:10.1063/5.0006060

Ding, L., He, L., Wang, Y., Zhao, X., Ma, H., Luo, Y., et al. (2023). Research progress and challenges of composite wound dressings containing plant extracts. *Cellulose* 30 (18), 11297–11322. doi:10.1007/s10570-023-05602-0

Fang, J., Li, H., Wang, J., Yang, M., Zong, Z., and Zhang, Y. (2019). Compression and stress relaxation characteristics of alfalfa during rotary compression. *BioResources* 14 (2), 3860–3872. doi:10.15376/biores.14.2.3860-3872

Fares, M. M., Radaydeh, S. K., and Jabani, Z. H. (2024). IPN based hydrogels for *in-vivo* wound dressings; catalytic wound healing dynamics and isothermal adsorption models. *J. Photochem Photobiol. B* 254, 112901. doi:10.1016/j.jphotobiol.2024.112901

Feng, F., Zhao, Z., Li, J., Huang, Y., and Chen, W. (2024). Multifunctional dressings for wound exudate management. *Prog. Mater. Sci.* 146, 101328. doi:10.1016/j.pmatsci.2024.101328

Feng, Y., Qin, S., Li, H., Yang, Y., Zheng, Y., Liu, H., et al. (2023). Composite hydrogel dressings with enhanced mechanical properties and anti-inflammatory ability for effectively promoting wound repair. *Int. J. Nanomedicine* 18, 5183–5195. doi:10.2147/IJN.S411478

Francesko, A., Petkova, P., and Tzanov, T. (2018). Hydrogel dressings for advanced wound management. *Curr. Med. Chem.* 25 (41), 5782–5797. doi:10.2174/0929867324666170920161246

Guo, J., Wang, T., Yan, Z., Ji, D., Li, J., and Pan, H. (2022). Preparation and evaluation of dual drug-loaded nanofiber membranes based on coaxial electrostatic spinning technology. *Int. J. Pharm.* 629, 122410. doi:10.1016/j.ijpharm.2022.122410

Guo, Y., Shao, Z., Wang, W., Liu, H., Zhao, W., Wang, L., et al. (2024). Periodontium-mimicking, multifunctional biomass-based hydrogel promotes full-course socket healing. *Biomacromolecules* 25 (2), 1246–1261. doi:10.1021/acs.biomac.3c01221

Hasani-Sadrabadi, M. M., Sarrion, P., Pouraghaei, S., Chau, Y., Ansari, S., Li, S., et al. (2020). An engineered cell-laden adhesive hydrogel promotes craniofacial bone tissue regeneration in rats. *Sci. Transl. Med.* 12 (534), eaay6853. doi:10.1126/scitranslmed.aay6853

Jones, J., and Hampton, S. (2021). Use of a superabsorbent dressing in the management of exudate in hard-to-heal wounds. *Br. J. Community Nurs.* 26 (Suppl. 3), S20–S29. doi:10.12968/bjcn.2021.26.Sup3.S20

Kamoun, E. A., Kenawy, E. S., and Chen, X. (2017). A review on polymeric hydrogel membranes for wound dressing applications: PVA-based hydrogel dressings. *J. Adv. Res.* 8 (3), 217–233. doi:10.1016/j.jare.2017.01.005

Klabukov, I., Shestakova, V., Krasilnikova, O., Smirnova, A., Abramova, O., Baranovskii, D., et al. (2023). Refinement of animal experiments: replacing traumatic methods of laboratory animal marking with non-invasive alternatives. *Anim. (Basel)* 13 (22), 3452. doi:10.3390/ani13223452

Kowalski, G., Witczak, M., and Kuterasinski, L. (2024). Structure effects on swelling properties of hydrogels based on sodium alginate and acrylic polymers. *Molecules* 29 (9), 1937. doi:10.3390/molecules29091937

Krasilnikova, O. A., Baranovskii, D. S., Yakimova, A. O., Arguchinskaya, N., Kisel, A., Sosin, D., et al. (2022). Intraoperative creation of tissue-engineered grafts with minimally manipulated cells: new concept of bone tissue engineering *in situ*. *Bioeng. (Basel)* 9 (11), 704. doi:10.3390/bioengineering9110704

Li, J., Shen, J., Zhuang, B., Wei, M., Liu, Y., Liu, D., et al. (2022). Light-triggered on-site rapid formation of antibacterial hydrogel dressings for accelerated healing of infected wounds. *Biomater. Adv.* 136, 212784. doi:10.1016/j.bioadv.2022.212784

Liu, F., Xu, X., and Sun, T. (2024). Vascular endothelial growth factor accelerates healing of foot ulcers in diabetic rats via promoting M2 macrophage polarization. *Diabet. Med.* 41 (9), e15388. doi:10.1111/dme.15388

Nai, J., Zhang, C., Shao, H., Li, B., Li, H., Gao, L., et al. (2021). Extraction, structure, pharmacological activities and drug carrier applications of Angelica sinensis polysaccharide. *Int. J. Biol. Macromol.* 183, 2337–2353. doi:10.1016/j.ijbiomac.2021.05.213

Reinhards-Hervás, C., Cano, A. J., Rico, A., Salazar, A., and Rodríguez, J. (2024). Fracture resistance of polyacrylamide-alginate hydrogels. *Eng. Fract. Mech.* 295, 109812. doi:10.1016/j.engfracmech.2023.109812

Shamloo, A., Sarmadi, M., Aghababaie, Z., and Vossoughi, M. (2018). Accelerated full-thickness wound healing via sustained bFGF delivery based on a PVA/chitosan/gelatin hydrogel incorporating PCL microspheres. *Int. J. Pharm.* 537 (1-2), 278–289. doi:10.1016/j.ijpharm.2017.12.045

Sk, M. M., Das, P., Panwar, A., and Tan, L. P. (2021). Synthesis and characterization of site selective photo-crosslinkable glycidyl methacrylate functionalized gelatin-based 3D hydrogel scaffold for liver tissue engineering. *Mater Sci. Eng. C Mater Biol. Appl.* 123, 111694. doi:10.1016/j.msec.2020.111694

Tavakoli, S., and Klar, A. S. (2020). Advanced hydrogels as wound dressings. *Biomolecules* 10 (8), 1169. doi:10.3390/biom10081169

Tavakoli, S., and Klar, A. S. (2021). Bioengineered skin substitutes: advances and future trends. *Appl. Sci.* 11 (4), 1493. doi:10.3390/app11041493

Tian, Y., Shen, X., Hu, T., Liang, Z., Ding, Y., Dai, H., et al. (2024). Structural analysis and blood-enriching effects comparison based on biological potency of Angelica sinensis polysaccharides. *Front. Pharmacol.* 15, 1405342. doi:10.3389/fphar.2024.1405342

Tirey, T. N., Singh, A., Arango, J. C., and Claridge, S. A. (2024). Nanoscale surface chemical patterning of soft polyacrylamide with elastic modulus similar to soft tissue. *Chem. Mater.* 36 (17), 8264–8273. doi:10.1021/acs.chemmater.4c01106

Tottoli, E. M., Dorati, R., Genta, I., Chiesa, E., Pisani, S., and Conti, B. (2020). Skin wound healing process and new emerging technologies for skin wound Care and regeneration. *Pharmaceutics* 12 (8), 735. doi:10.3390/pharmaceutics12080735

Villa, C., Cuna, F., Grignani, E., Perteghella, S., Panzeri, D., Caviglia, D., et al. (2024). Evaluation of the biological activity of manna exudate, from fraxinus ornus L., and its potential use as hydrogel formulation in dermatology and cosmetology. *Gels* 10 (6), 351. doi:10.3390/gels10060351

Wang, J., Lian, P., Yu, Q., Wei, J., and Kang, W. Y. (2017). Purification, characterization and procoagulant activity of polysaccharides from Angelica dahurice roots. *Chem. Cent. J.* 11, 17. doi:10.1186/s13065-017-0243-y

Wang, L., Zhou, M., Xu, T., and Zhang, X. (2022a). Multifunctional hydrogel as wound dressing for intelligent wound monitoring. *Chem. Eng. J.* 433, 134625. doi:10.1016/j.cej.2022.134625

Wang, Y., Feng, Y., Yan, J., Han, X., Song, P., Wu, Y., et al. (2023). Spiky surface topography of heterostructured nanoparticles for programmable acceleration of multistage wound healing. *Mater. Today Nano* 23, 100351. doi:10.1016/j.mtnano.2023.100351

Wang, Y., Xiao, D., Quan, L., Chai, H., Sui, X., Wang, B., et al. (2022b). Mussel-inspired adhesive gelatin-polyacrylamide hydrogel wound dressing loaded with tetracycline hydrochloride to enhance complete skin regeneration. *Soft Matter* 18 (3), 662–674. doi:10.1039/d1sm01373d

Xu, Y., Chen, H., Fang, Y., and Wu, J. (2022). Hydrogel combined with phototherapy in wound healing. *Adv. Healthc. Mater* 11 (16), e2200494. doi:10.1002/adhm.202200494

Yang, M., Li, C. J., Xiao, Y., Guo, Q., Huang, Y., Su, T., et al. (2020). Ophiopogonin D promotes bone regeneration by stimulating CD31(hi) EMCN(hi) vessel formation. *Cell Prolif.* 53 (3), e12784. doi:10.1111/cpr.12784

Zangeneh, M. M., Saneei, S., Zangeneh, A., Toushmalani, R., Haddadi, A., Almasi, M., et al. (2019). Preparation, characterization, and evaluation of cytotoxicity, antioxidant, cutaneous wound healing, antibacterial, and antifungal effects of gold nanoparticles using the aqueous extract of *Falcaria vulgaris* leaves. *Appl. Organomet. Chem.* 33 (11). doi:10.1002/aoc.5216

Zhang, H. Y., Wang, K. T., Zhang, Y., Cui, Y. L., and Wang, Q. (2023). A self-healing hydrogel wound dressing based on oxidized Bletilla striata polysaccharide and cationic gelatin for skin trauma treatment. *Int. J. Biol. Macromol.* 253 (Pt 6), 127189. doi:10.1016/j.ijbiomac.2023.127189

Zhang, J., Zhang, S., Liu, C., Lu, Z., Li, M., Hurren, C., et al. (2024). Photopolymerized multifunctional sodium alginate-based hydrogel for antibacterial and coagulation dressings. *Int. J. Biol. Macromol.* 260 (Pt 2), 129428. doi:10.1016/j.ijbiomac.2024.129428

Zhang, W., Zhu, J. H., Xu, H., Huang, X. P., Liu, X. D., and Deng, C. Q. (2019). Five active components compatibility of astragali radix and angelicae sinensis radix protect hematopoietic function against cyclophosphamide-induced injury in mice and t-BHP-induced injury in HSCs. *Front. Pharmacol.* 10, 936. doi:10.3389/fphar.2019.00936

Zhao, P., Guo, Z., Wang, H., Zhou, B., Huang, F., Dong, S., et al. (2023). A multi-crosslinking strategy of organic and inorganic compound bio-adhesive polysaccharide-based hydrogel for wound hemostasis. *Biomater. Adv.* 152, 213481. doi:10.1016/j.bioadv.2023.213481

frontiers | Frontiers in Pharmacology

TYPE Original Research
PUBLISHED 25 March 2025
DOI 10.3389/fphar.2025.1567762

Check for updates

OPEN ACCESS

EDITED BY
Yizhou Zhan,
Dongguan University of Technology, China

REVIEWED BY
Kaikai Xue,
Wenzhou Medical University, China
Renhao Jiang,
Second Affiliated Hospital and Yuying Children's Hospital of Wenzhou Medical University, China

*CORRESPONDENCE
Jun He,
tianwanqd@126.com

†These authors have contributed equally to this work

RECEIVED 28 January 2025
ACCEPTED 10 March 2025
PUBLISHED 25 March 2025

CITATION
Yang J, Zhang H, Ni L and He J (2025) Thymoquinone alleviates the accumulation of ROS and pyroptosis and promotes perforator skin flap survival through SIRT1/NF-κB pathway. *Front. Pharmacol.* 16:1567762. doi: 10.3389/fphar.2025.1567762

COPYRIGHT
© 2025 Yang, Zhang, Ni and He. This is an open-access article distributed under the terms of the Creative Commons Attribution License (CC BY). The use, distribution or reproduction in other forums is permitted, provided the original author(s) and the copyright owner(s) are credited and that the original publication in this journal is cited, in accordance with accepted academic practice. No use, distribution or reproduction is permitted which does not comply with these terms.

Thymoquinone alleviates the accumulation of ROS and pyroptosis and promotes perforator skin flap survival through SIRT1/NF-κB pathway

Jianxin Yang[1†], Haojie Zhang[2†], Libin Ni[1] and Jun He[1*]

[1]Department of Orthopaedics, Zhejiang Hospital, Hangzhou, Zhejiang, China, [2]Department of Spine Surgery, The Third Affiliated Hospital, Sun Yat-Sen University, Guangzhou, China

Perforator flap transplantation is an important technique in flap reconstructive surgery, but flap necrosis limits its clinical effectiveness. Thymoquinone (TQ), a natural bioactive plant quinone found in black seed, exhibits anti-inflammatory, angiogenic, and antimicrobial properties. This study investigates the therapeutic effects of TQ in a perforator flap model through *in vivo* and *in vitro* experiments. Human umbilical vein endothelial cells (HUVECs) were treated with Tert-butyl Hydroperoxide (TBHP) to simulate an *in vitro* flap model and were then treated with TQ. *In vivo* experiments used a rat perforator flap model, and vascularization was assessed using Doppler ultrasound on days 3 and 7 after flap creation. On day 7 post-surgery, flap samples were collected to evaluate vascularity, reactive oxygen species, apoptosis and pyroptosis. Network pharmacology analysis was conducted to identify relevant signaling pathways, and molecular docking techniques were used to predict potential target binding sites. *In vitro* results showed that both TQ treatment and NLRP3 inhibitors reduced the expression of pyroptosis-related proteins. *In vivo* results indicated that the TQ-treated group had increased flap survival area, blood flow intensity, and microvascular density, while oxidative stress, apoptosis, and pyroptosis levels were reduced. Angiogenesis was enhanced, and expression of the SIRT1 protein was increased, while the p-P65/NF-κB/NLRP3 pathway was downregulated. After treatment with a SIRT1 inhibitor, flap survival rate and angiogenesis were reduced. These findings suggest that TQ improves perforator flap survival by inhibiting the NF-κB/NLRP3 pathway and promoting angiogenesis.

KEYWORDS

perforator flap, thymoquinone, pyroptosis, SIRT1, NF-κB/NLRP3 signaling pathway

Introduction

For a considerable length of time, multi-regional perforator flaps have been widely utilized in clinical settings for the treatment of dermatological conditions, including congenital abnormalities, traumatic injuries, tumor ablations, and skin ulcers resulting from diabetes (Cheng et al., 2017). However, due to the limited blood supply range of skin arteries, insufficient blood perfusion often occurs in the flap area during the early stages, leading to ischemic injury in the distal portion of the flap (Peng et al., 2022). With neovascularization and vasodilation, reperfusion injury may further occur in the distal part

of the flap (Liu et al., 2019a). Therefore, ischemia-reperfusion (I/R) injury is one of the primary factors contributing to distal flap necrosis, which limits its clinical application. I/R injury leads to the accumulation of reactive oxygen species (ROS), ultimately resulting in cell death. Both ROS and apoptosis can accumulate due to I/R injury, ultimately leading to cellular demise (Xie et al., 2023). Previous studies have demonstrated that inhibiting oxidative stress, apoptosis can reduce the risk of ischemia-reperfusion injury and distal necrosis in flaps (Jiang et al., 2022; Chen et al., 2022).

Sirtuin 1 (SIRT1), an NAD+-dependent deacetylase, is involved in regulating angiogenesis, inflammation, oxidative stress, and apoptosis, including the inhibition of NLRP3 inflammasomes (Chen et al., 2013). To date, SIRT1 has been found to attenuate damage resulting from cerebral I/R in rats (Mei et al., 2022). Furthermore, under injury conditions, SIRT1 can enhance cardiac and neuroprotective activities (Hu et al., 2022; Xu et al., 2021). Recent studies have also indicated that SIRT1 can aid in the survival of random-pattern flaps (Jiang et al., 2022). However, uncertainties remain regarding the mechanisms controlling SIRT1 in the survival of multi-regional perforator flaps.

Cell pyroptosis, a recently discovered form of programmed cell death accompanied by inflammation, is regulated by numerous signaling pathways, including the most frequently studied NLRP3-Caspase-1-GSDMD pathway (He et al., 2015). The NLRP3 inflammasome detects endogenous and microbial danger signals and initiates innate immune responses. Upon activation, cytosolic NLRP3 oligomerizes with other inflammasome complex proteins, particularly ASC and pro-caspase-1. Pro-caspase-1 is then activated, leading to the cleavage of GSDMD (Man and Kanneganti, 2016). Following activation, the N-terminal portion of GSDMD oligomerizes and generates membrane pores, causing cell swelling, plasma membrane rupture, and release of cytosolic contents (Wang et al., 2019). Previous studies have shown that pyroptosis is a crucial pathological event in various diseases (Wan et al., 2020; Zhaolin et al., 2019), especially in vascular diseases (Zhou et al., 2018). Tissue ischemia-reperfusion injury and the development of microvascular diseases are significant factors contributing to flap necrosis (Odake et al., 2021). Recent research has highlighted the role of pyroptosis in maintaining vascular homeostasis and cardiovascular diseases, with NLRP3 inflammasome-induced pyroptosis playing a key role in vascular endothelial dysfunction (Bergsbaken et al., 2009). As a specific inhibitor of NLRP3, MCC950 has recently been found to effectively inhibit pyroptosis in various diseases, such as inflammatory bowel disease, diabetic cardiomyopathy, kidney injury (Wang et al., 2024; Ba et al., 2025; Luo et al., 2025). Therefore, tailored modulation of pyroptosis may represent a novel approach to improving the survival of multi-regional perforator flaps, as pyroptosis may play a pivotal role in inflammation associated with ischemia-reperfusion injury.

Thymoquinone (TQ), a pharmacologically active plant quinone found in the seeds of black cumin, is used in folk medicine worldwide for the treatment and prevention of various diseases and disorders (Ahmad et al., 2016). Notably, TQ has been reported to possess a wide range of biological activities, including anti-inflammatory (Wang et al., 2015; Chen et al., 2016), antioxidant (Lu et al., 2018), anti-tumor (Darakhshan et al., 2015), and immunomodulatory effects (Salem, 2005). Additionally, TQ can promote burn wound healing by reducing inflammation and oxidative stress (Selçuk et al., 2013). Recently, several studies have demonstrated the protective effects of TQ on cardiac injury, such as reperfusion injury in the context of ischemic damage and acute abdominal aortic ischemia, mediated through the pyroptosis pathway (Liu et al., 2019b). Currently, there are few studies exploring whether TQ has the potential to inhibit pyroptosis and promote angiogenesis in perforator flap models. Therefore, we aim to investigate the effects of TQ on flap survival and explore the biological mechanisms in multi-regional perforator flaps.

Materials and methods

Animal details

Healthy male Sprague Dawley rats (250–300 g), aged 6–8 weeks, were provided by the Experimental Animal Center of Wenzhou Medical University (license no. SCXK [ZJ] 2015-0001). The animal research procedures adhered to the ethical standards established by the National Institutes of Health for animal experiments. The use of these rats in the current investigation was approved by the Animal Research Committee of Wenzhou Medical University (wydw2023-0003). The rats were housed in a sanitary environment with a controlled 12-h light/dark cycle at a temperature of 25°C and had access to food and water *ad libitum*. The rats were randomly assigned to one of three experimental groups: the control group (n = 25), the TQ (TQ) group (n = 25), and the TQ+EX527 group (n = 15).

Reagents and antibodies

TQ (TQ; purity 99.48%) and MCC950 (purity 99.62%) are provided by MedChemExpress LLC (USA). EX527 is purchased from meilunbio (China). Sodium pentobarbital, hematoxylin and eosin staining kits, lead oxide-gelatin, and diaminobenzidine (DAB) are procured from Solarbio Life Science (China). Anti-cadherin 5 is provided by Wuhan Boster Biological Technology, Ltd. Primary antibodies against GAPDH, HO1, SOD1, Bax, Bcl-2, GSDMD-N, and VEGF are sourced from The Proteintech Group (Chicago, USA). Antibodies against caspase-3, NLRP3, IL-18, IL-1β, SIRT1, p-P65, P65, and IkB-α are obtained from Cell Signaling Technologies (Beverly, Massachusetts). The goat anti-rabbit IgG secondary antibody is provided by Santa Cruz Biotechnology Inc. (Dallas, Texas, USA). The ECL Plus Reagent kits and BCA Kits are obtained from PerkinElmer Life Sciences and Beyotime Biotechnology, respectively.

Flap animal model

Rats are anesthetized using isoflurane. Subsequently, back hair is removed using an electric razor and depilatory cream. The remainder of the surgical procedure is performed in a sterile environment. The anatomical landmarks of the rats influence the size of the skin flaps. The longitudinal axis of the spine serves as the basis for the medial edge (posterior midline) of the skin flap. The lateral boundary is positioned 2.5 cm away from the medial

boundary. The lateral and medial edges converge at the anterior iliac spine, forming the caudal edge, which acts as an external barrier. As previously mentioned, the skin flap measures approximately 2.5 × 11 cm. Once the skin flap is fully elevated from the underlying fascia, hemostasis is achieved satisfactorily. The flap model comprises three vascular territories: the anatomic territory, represented by the deep circumflex iliac (DCI) vascular plexus, the dynamic territory, represented by the intercostal (IC) vascular plexus, and the potential territory, represented by the thoracodorsal (TD) vascular plexus. The DCI vascular plexus is preserved, while the other two vascular plexuses are ligated. The skin flap is then sutured in place using 4–0 silk. On postoperative day 7, all rats are euthanized, and the skin flap tissues are collected for further investigation.

Cell culture

As previously reported in studies aiming to simulate apoptosis and oxidative stress injury *in vitro* experiments involving skin flaps, Human Umbilical Vein Endothelial Cells (HUVECs) were selected (Lu et al., 2024). HUVECs were obtained from the American Type Culture Collection (ATCC; Manassas, VA) and cultured in Dulbecco's Modified Eagle Medium (DMEM; Gibco, Carlsbad, USA), supplemented with 10% Fetal Bovine Serum (FBS; Gibco, Carlsbad, USA) and 1% Penicillin-Streptomycin (Gibco, Carlsbad, USA). The cells were maintained in a humidified incubator at 37°C with 5% CO2. Upon reaching 70%–80% confluence, HUVECs were subjected to the corresponding treatments and utilized for subsequent experimental procedures.

Drug treatment

For *in vitro* experiments: The Tert-butyl Hydroperoxide (TBHP) group was incubated with 100 μM TBHP for 24 h, the selection of concentrations is referenced to previous literature (Chen et al., 2022). The TBHP + TQ (TQ) group was simultaneously incubated with 100 μM TBHP and 10 μM TQ for 24 h. The TBHP + MCC950 group was pretreated with 10 μM MCC950 for 30 min prior to the addition of 100 μM TBHP and then incubated for 24 h. For *in vivo* experiments, the TQ group received daily gavage of 2 mg/kg TQ for 7 days post-surgery, while the control group received an equal volume of dimethyl sulfoxide (DMSO). The TQ + EX527 group received an intraperitoneal injection of EX527 (10 mg/kg/day) 30 min prior to TQ administration.

Measurement of perforator flap survival area

Within 7 days after establishing the perforator flap model, the appearance of the flaps was observed. On postoperative days 3 and 7, five rats from each group were randomly selected and anesthetized. High-resolution photographs of the dorsal flaps were taken using a digital camera to measure the percentage of survival area as follows: (survival flap area/total flap area) × 100%.

Doppler blood flow measurement

Doppler blood flow measurement was used to detect blood flow in the flaps of live rats. On postoperative days 3 and 7, five rats from each group were randomly selected and anesthetized. The flaps were scanned using a Doppler instrument in a stable state. To assess blood flow in the flaps, the images were imported into moorLDI Review software for quantitative analysis. Each rat was tested three times, and the average values were calculated for statistical analysis.

Hematoxylin and eosin staining

On the seventh postoperative day (POD), three tissue samples (0.5 cm × 0.5 cm) were collected from the middle of the surgical critical zone in each group for histopathological analysis. After perfusing with phosphate-buffered saline (PBS) solution to remove blood cells, the specimens were fixed in 4% paraformaldehyde for 24 h and subsequently embedded in paraffin. The paraffin-embedded samples were then sectioned transversely into 4-μm-thick slices. These slices were stained with hematoxylin and eosin (H&E) according to standard histological protocols provided by Solarbio Science and Technology (Beijing, China; Catalog No. G1120). Six randomly selected regions in three random sections from each sample were observed under a light microscope (Olympus Corp, Tokyo, Japan). Additionally, to assess the microcirculation level, the number of microvessels per unit area (per square millimeter) in a random visual field was counted as a measure of microvascular density (MVD). This provided a quantitative evaluation of the microvasculature within the tissue samples.

Immunohistochemical

The slides were first deparaffinized and rehydrated through a series of graded alcohols. After blocking endogenous peroxidase activity, the slides were incubated with primary antibodies against CD34 (1:100), cleaved caspase-3 (C-CASP3; 1:200), and superoxide dismutase 1 (SOD1; 1:100) overnight at 4°C. Following three washes, the slides were incubated with a secondary antibody for 1 h at 37°C. Images were then captured under an optical microscope and analyzed using Image Pro-plus software. The next day, the sections were soaked in PBS solution at room temperature for 5 min, with this step repeated three times. The sections were then incubated with horseradish peroxidase-labeled secondary antibody at 37°C for 30 min. In a darkroom, DAB (3,3′-diaminobenzidine) chromogenic solution was added dropwise to the tissues and observed under a microscope for 1–2 min, followed by rinsing with PBS solution. The nuclei were then stained with hematoxylin for 1 min and rinsed under slow running water to restore the blue color. Subsequently, the sections underwent gradient alcohol dehydration, xylene permeabilization, and were mounted with gum. Observations and recordings were made under a 200x optical microscope. In the later stage, specialized software was utilized to automatically analyze the absorbance of CD34, C-CASP3, and SOD1, as well as to count the number of blood vessels with

positive expression of CD34. This provided a quantitative assessment of the immunohistochemical staining results.

Immunofluorescence staining

For *In Vitro* Studies: HUVECs are seeded onto glass dishes and treated with the corresponding designated reagents. After fixation, the cells are permeabilized with Triton X-100 for 10 min at room temperature. Subsequently, the cells are blocked with goat serum for 1 h and incubated with primary antibodies against GSDMD-N (1:200), Caspase-1 (1:200), and NLRP3 (1:200) overnight at 4°C. Secondary antibodies are then added and incubated at 37°C for 1 h. The cell nuclei are stained with DAPI solution. Images are captured using a fluorescence microscope, and the integrated optical density is analyzed using software. For *In Vivo* Studies: Following immunohistochemical procedures, six samples undergo dewaxing and rehydration. After antigen retrieval and blocking, primary antibodies diluted in 10% goat serum in PBS (GSDMD-N 1:100, SIRT1 1:100, VEGF 1:100) are applied and incubated overnight at 4°C. Subsequently, FITC-labeled goat anti-rabbit IgG secondary antibody (1:200) is incubated at room temperature for 1 h. The sections are soaked in PBS for 5 min, repeated three times. An appropriate amount of DAPI solution is added to the slides for 5 min, and observations are made under a 200x fluorescence microscope. Later, software is used to count the number of GSDMD-N, SIRT1, and VEGF positive cells.

Western blotting

Protein extracts from animal samples and total cellular proteins isolated from HUVECs were obtained using RIPA lysis buffer supplemented with 1 mM PMSF. Subsequently, protein concentrations were determined using a BCA kit sourced from Beyotime Biotechnology in China. The proteins were then subjected to electrophoresis and transferred onto PVDF membranes manufactured by Millipore, located in Bedford, MA, USA. Following blocking with NcmBlot blocking buffer, provided by New Cells and Molecular Biotech in China, the membranes were incubated with their respective antibodies overnight at a temperature of 4°C. Afterward, the membranes were further incubated with secondary antibodies for a duration of 2 h. Finally, the grayscale values of the blots were quantitated and analyzed using Image Lab 3.0 software, developed by Bio-Rad in California, United States.

Collection of targets for ischemia reperfusion injury and prediction of thymoquinone targets

To identify disease targets related to the perforator flap, we conducted a database search using keywords such as 'ischemia reperfusion injury' and found relevant targets in GeneCards. Additionally, we obtained targets for TQ using SwissTargetPrediction with a canonical SMILE downloaded from PubChem. These target genes were then intersected for further KEGG analysis.

KEGG enrichment analysis

We utilized Metascape (version 3.5.20230101) to perform KEGG enrichment analysis on the intersection target genes. Metascape employs the hypergeometric test and Benjamini–Hochberg p-value correction algorithm to identify ontology terms with a statistically significant number of genes in common with the input list. KEGG serves as a comprehensive knowledge base for analyzing gene functions and related pathways.

Molecular docking

The SIRT1 protein's three-dimensional model was constructed using the SWISS-MODEL online tool with a template PDB ID of 5BTR, revealing a 98.44% homology between the target protein and its template. The TQ ligand's molecular structure was downloaded from PubChem. PyMOL 2.3.0 was used to remove water molecules and original ligands from the downloaded target protein, while Chem3D software (version 2020) optimized the molecular mechanics of the preferred conformation of the small molecule. AutoDock Tools 1.5.6 prepared the pdbqt files for docking simulations, which were conducted using AutoDock Vina v.1.2.0 with the Lamarckian Genetic Algorithm and semi-flexible docking. The exhaustiveness parameter was set to 8, and the maximum number of output conformations was set to 9. PyMOL 2.3.0 was used for 3D visualization, while Discovery Studio was employed for 2D visualization of the docking complex.

Statistical analysis

All experiments were executed in a randomized and double - blinded manner by investigators who were masked to the experimental groups. The results are presented as mean ± SEM, with the group size (n) indicated for each experimental group/condition, representing independent values rather than replicates. To minimize unwanted variability, the entire dataset was normalized. Statistical analysis was performed using SPSS version 19 (Chicago, IL, United States). Independent-sample t tests were employed to determine remarkably significant differences between two groups. Statistical analysis between multiple groups was performed by one-way ANOVA or Tukey's multiple comparison test. Significance was determined at $p < 0.05$. Additionally, KEGG pathway analysis results with a p value <0.05 were considered statistically significant.

Results

TQ enhanced the survival rate and angiogenesis in rat perforator flaps following ischemia-reperfusion injury

After establishing the perforator flap model, the survival and necrosis of the flaps in rats were observed and recorded. Over time, the boundary between survival and necrosis progressed from the distal end of the flap towards the pedicle, stabilizing by the seventh

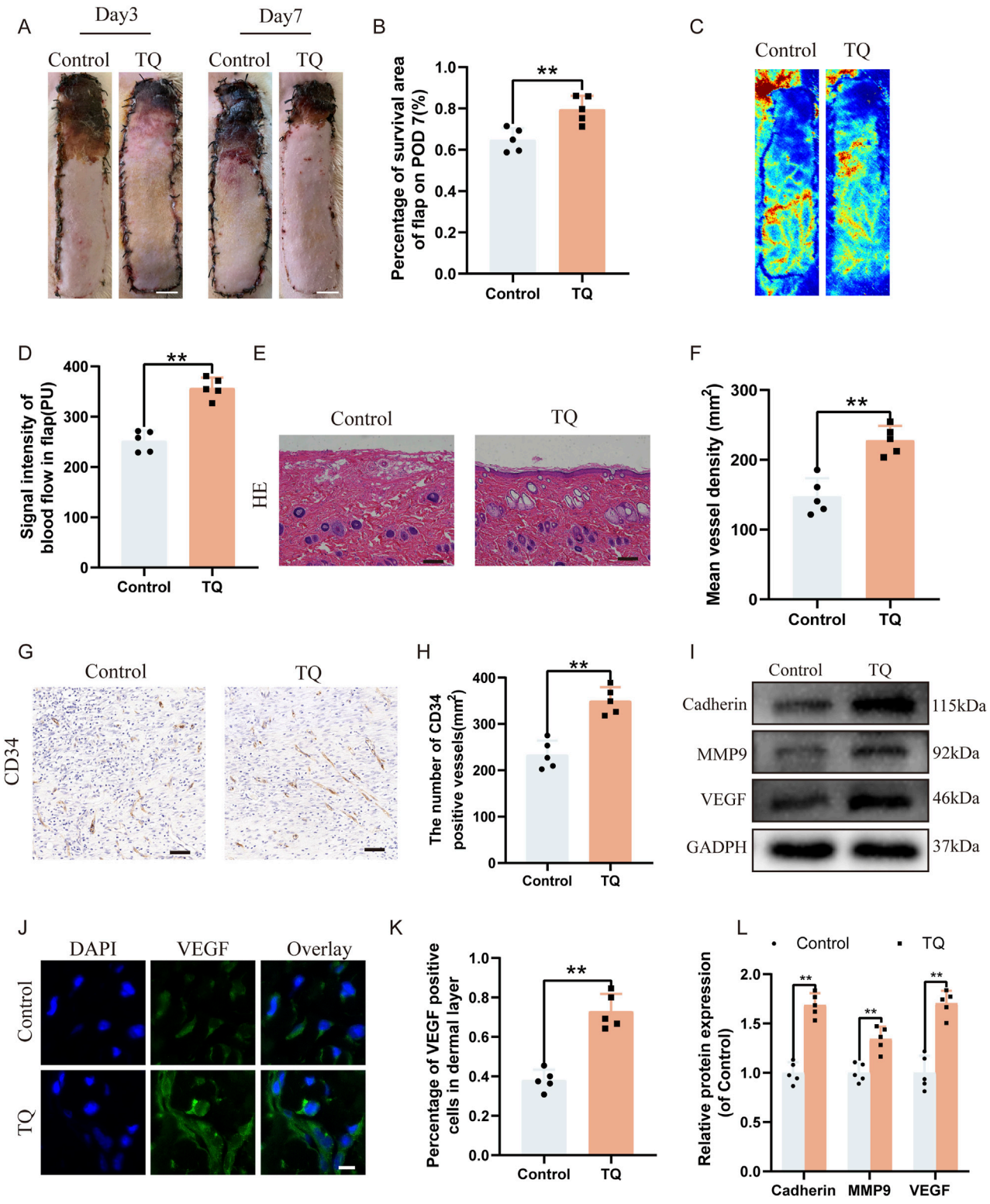


FIGURE 1
TQ enhances the survival rate and angiogenesis of multi-regional perforator flaps. **(A)** Gross images of dorsal flaps in the control and TQ groups on postoperative days 3 and 7. (scale bar: 1 cm) **(B)** Histogram showing the percentage of flap survival area in each group on postoperative day 7. **(C)** Doppler imaging of blood supply in perforator flaps of the control and TQ groups. **(D)** Quantitative assessment of blood flow intensity in flaps of the control and TQ groups. **(E)** H&E staining of flap tissues in the control and TQ groups (scale bar, 50 μm). **(F)** Quantitative assessment of microvascular density (MVD) in the control and TQ groups. **(G)** Immunohistochemical staining images of CD34 in the control and TQ groups (scale bar, 50 μm). **(H)** Quantitative assessment of CD34-positive vessel counts in the control and TQ groups. **(I)** Western blotting to detect the expression of angiogenesis-related proteins:
(*Continued*)

FIGURE 1 (Continued)
Cadherin-5, MMP9, and VEGF in flap tissues of the control and TQ groups. **(J)** VEGF protein expression levels in flap tissues of rats in the control and TQ groups measured by immunofluorescence (scale bar: 20 μm). **(K)** Fluorescence intensity of VEGF expression analyzed using Image J. **(L)** Quantitative analysis of angiogenesis-related protein blots. Significance: *$p < 0.05$ and **$p < 0.01$. Data are presented as mean ± SEM, with five rats per group.

postoperative day in rats, with the distal areas of the flaps turning black, dry, and stiff (Figure 1A). Furthermore, we found that compared to the experimental control group, TQ significantly increased the survival area of the rat flaps (Figure 1B). Laser Doppler imaging revealed better blood perfusion in the TQ group, with significantly higher blood flow signal intensity in this group as well (Figures 1C, D). H&E staining showed a greater microvessel density in the TQ group (Figures 1E, F). Immunohistochemical staining data indicated an increase in CD34-positive vessel counts in the TQ group (Figures 1G, H). Based on these findings, we concluded that TQ improved the survival rate of rat perforator flaps following ischemia-reperfusion injury. Adequate blood flow and angiogenesis are among the most critical factors for perforator flap survival. To further determine whether TQ promotes angiogenesis after ischemia-reperfusion injury in perforator flaps, we used immunofluorescence and Western blot analysis to detect the expression of angiogenesis markers. Angiogenesis-related markers, including Cadherin-5, VEGF, and MMP9, were detected. Western blot results demonstrated that TQ treatment increased the levels of Cadherin-5, MMP9, and VEGF (Figures 1I, L). Additionally, immunofluorescence staining data showed a significant increase in VEGF-positive cell rates in the treatment group compared to the control group (Figures 1J, K). These results collectively indicate that TQ effectively promoted angiogenesis in perforator flaps, improving flap survival rates.

TQ inhibits pyroptosis after ischemia-reperfusion injury in rat perforator flaps

To determine which pathways are involved in the angiogenic effects of TQ, we searched for downstream targets of TQ and ischemia-reperfusion injury-related genes using SwissTargetPrediction and GeneCards. We took the intersection of these results, and a Venn diagram showed that 48 genes might be related to the therapeutic effects of TQ in ischemia-reperfusion injury (Figure 2A). Next, we selected these 48 genes for KEGG analysis, which revealed that the top 20 pathways were involved in the therapeutic effects of TQ, such as regulating inflammatory responses, oxidative stress, and apoptosis (Figure 2B). Inflammasome assembly of inflammatory mediators is an important manifestation of pyroptosis (Newton et al., 2024). It has been reported that pyroptosis is crucial for the development of ischemia-reperfusion injury, and inhibiting pyroptosis can effectively alleviate the progression of ischemia-reperfusion diseases (Qu et al., 2024; Chen et al., 2024). Based on the results of the KEGG enriched pathways, we speculated that the positive effects of TQ partly depend on the inhibition of pyroptosis. Using immunofluorescence staining, we assessed the levels of pyroptosis-related markers GSDMD-N and Caspase-1 to determine whether TQ leads to a reduction in pyroptosis in rat perforator flaps (Figures 2C–F). The analysis results indicated that TQ significantly decreased the percentage of GSDMD-N-positive and Caspase-1-positive cells in the dermis. Furthermore, Western blot analysis of pyroptosis-related proteins NLRP3, GSDMD-N, Caspase-1, IL-1β, IL-18, and ASC showed lower expression levels of these proteins in the TQ group compared to the control group (Figures 2G, H). To further explore the effects of TQ on pyroptosis, we conducted *in vitro* experiments using HUVECs. According to the immunofluorescence results, the expression levels of pyroptosis-related proteins GSDMD-N and Caspase-1 were significantly increased under TBHP stimulation but decreased under the action of TQ (Supplementary Figures S1A–D). Additionally, Western blot analysis showed that TBHP significantly increased the protein expression levels of NLRP3, GSDMD-N, Caspase-1, IL-1β, IL-18, and ASC, while TQ decreased their expression levels (Supplementary Figures S1E, F). To confirm our hypothesis, we conducted experiments using an NLRP3 inhibitor (Babuta et al., 2024). According to the immunofluorescence results, the expression level of NLRP3 was significantly decreased under the action of MCC950 (Supplementary Figures S1G, H). Moreover, Western blot analysis showed that the levels of pyroptosis-related proteins in the MCC950 group were also significantly inhibited (Supplementary Figures S1I, J). This indicates that MCC950 treatment significantly inhibited TBHP-induced pyroptosis. In summary, our results suggest that TQ inhibits pyroptosis in rat perforator flaps following ischemia-reperfusion injury.

TQ ameliorates oxidative stress and apoptosis following ischemia-reperfusion injury in rat perforator flaps

Oxidative stress is also crucial for the survival of perforator flaps. Immunohistochemical staining was employed to detect the expression of SOD1, an essential endogenous antioxidant enzyme (Nam et al., 2024), to further assess whether TQ can reduce oxidative stress following ischemia-reperfusion injury in rat perforator flaps. Immunohistochemical staining revealed that the SOD1 absorbance in the TQ group was higher than that in the control group (Figures 3A, B). Additionally, Western blot analysis was used to detect the expression levels of angiogenesis-related proteins, including eNOS, HO1, and SOD1, in multi-regional perforator flaps (Figures 3C, D). TQ treatment promoted the expression of these angiogenesis-related proteins. Collectively, these results suggest that TQ can ameliorate oxidative stress following ischemia-reperfusion injury in rat perforator flaps, which contributes to flap survival.

To investigate how TQ prevents necrosis in perforator flaps, the effects of apoptosis-related proteins on perforator flaps were assessed. According to immunohistochemical staining results, the C-CASP3 absorbance in the TQ group was lower compared to the

10.3389/fphar.2025.1567762

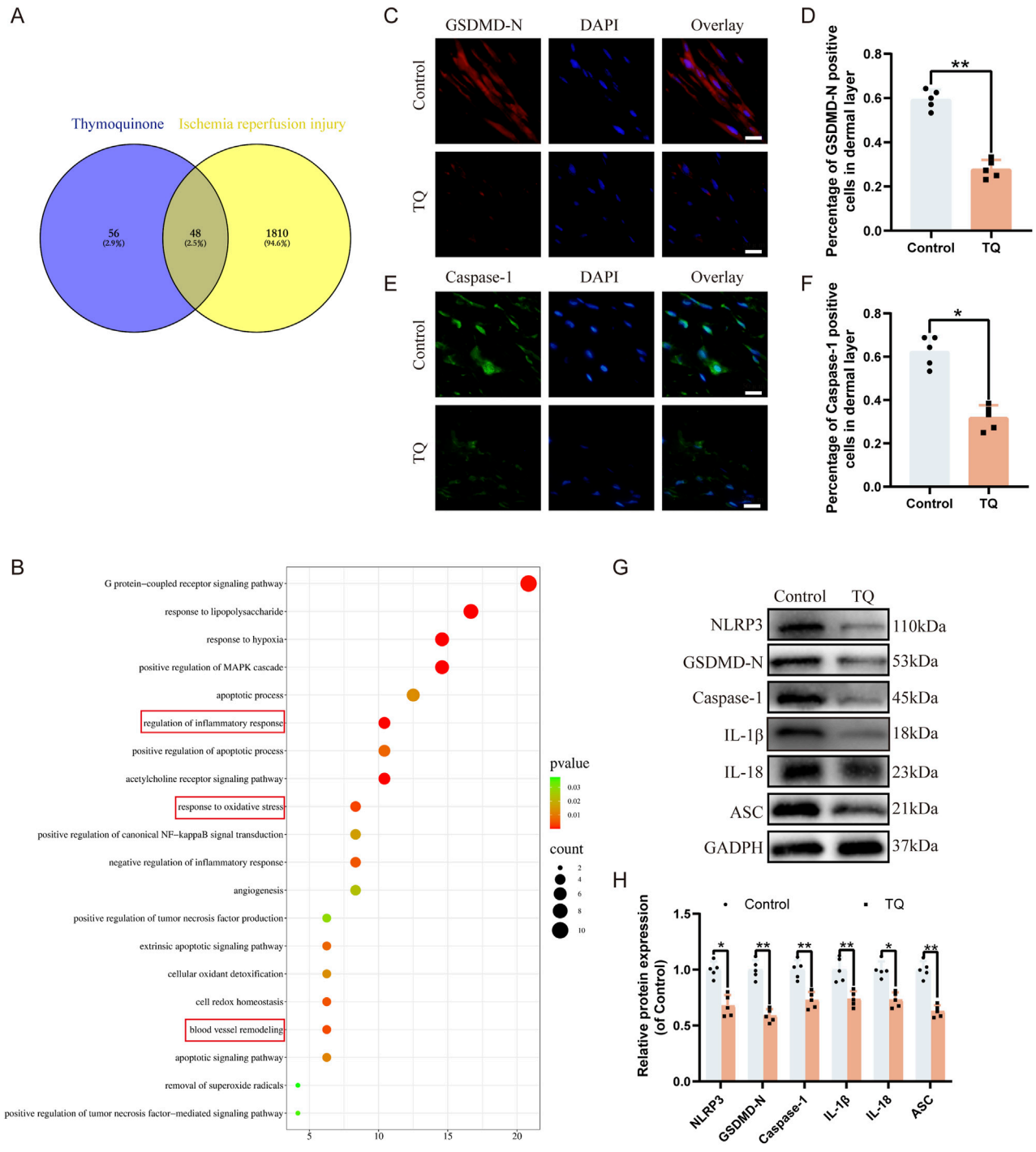


FIGURE 2
TQ inhibits pyroptosis in rat perforator flaps after ischemia-reperfusion injury. **(A)** Venn diagram showing overlapping targets of ischemia-reperfusion-related genes from GeneCards and predicted targets of TQ. **(B)** Top 15 enriched KEGG pathways for overlapping genes in **(A)**. **(C)** GSDMD-N protein expression levels in flap tissues of rats in the control and TQ groups measured by immunofluorescence (scale bar: 20 μm). **(D)** Fluorescence intensity of GSDMD-N expression analyzed using Image J. **(E)** Caspase-1 protein expression levels in flap tissues of rats in the control and TQ groups measured by immunofluorescence (scale bar: 20 μm). **(F)** Fluorescence intensity of Caspase-1 expression analyzed using Image J. **(G)** Western blotting to detect the expression of pyroptosis-related proteins: NLRP3, GSDMD-N, Caspase-1, IL-1β, IL-18, and ASC in flap tissues of the control and TQ groups. **(H)** Quantitative analysis of pyroptosis-related protein blots. Significance: *$p < 0.05$ and **$p < 0.01$. Data are presented as mean ± SEM, with five rats per group.

control group (Figures 3E, F). Western blot results were consistent with immunohistochemical findings in terms of the expression of apoptosis-related proteins Bax and C-CASP3. The protein expression levels of Bax and C-CASP3 were significantly reduced, while the Bcl-2 protein expression level was significantly increased (Figures 3G, H). In summary, these findings indicate that a portion

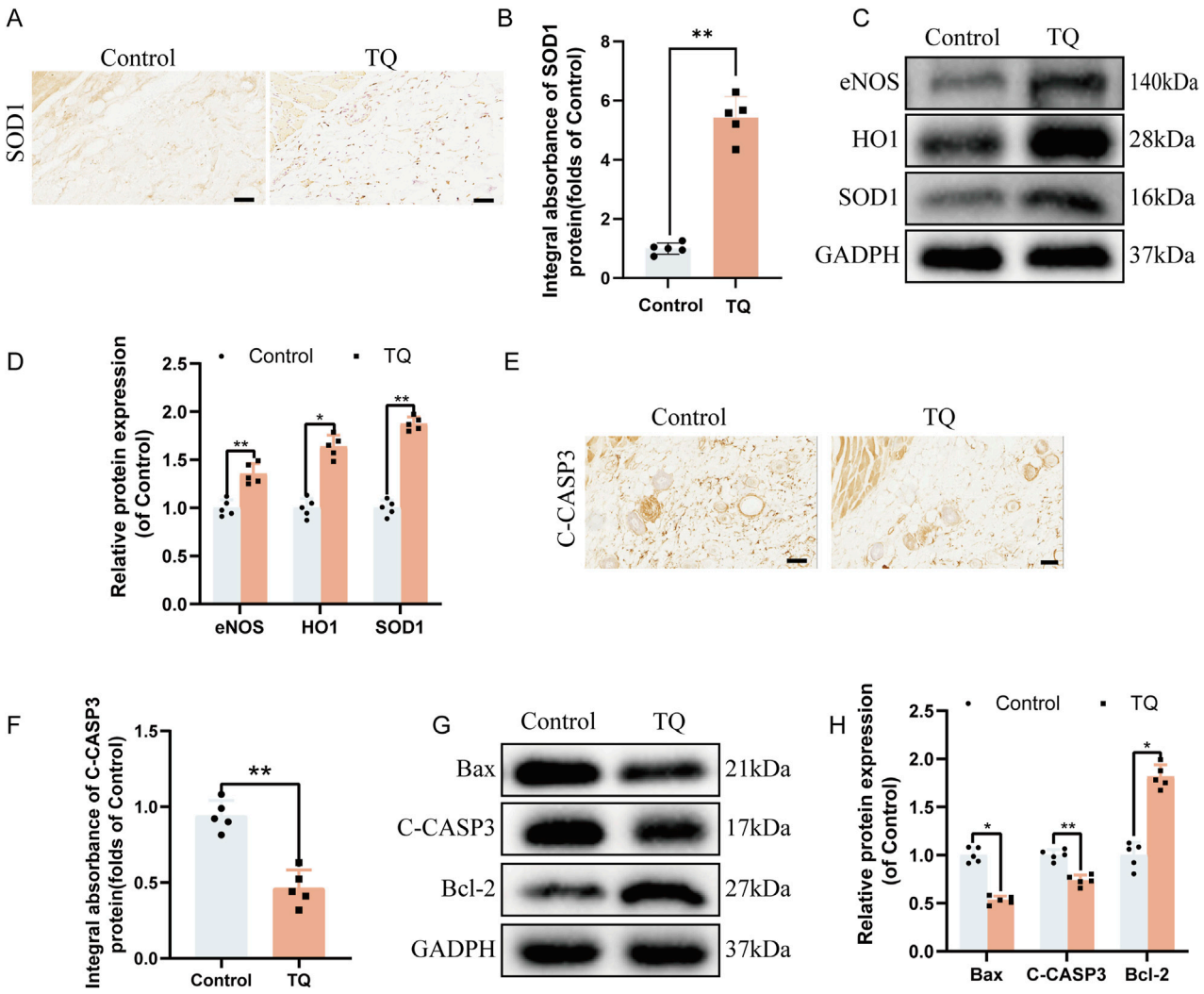


FIGURE 3
TQ Ameliorates Oxidative Stress and Apoptosis in Rat Perforator Flaps After Ischemia-Reperfusion Injury. **(A)** Immunohistochemical staining images of SOD1 in the control and TQ groups (scale bar, 50 μm). **(B)** Quantitative analysis of SOD1 absorbance in the control and TQ groups. **(C)** Western blotting to detect the expression of oxidative stress-related proteins: eNOS, HO1, and SOD1 in flap tissues of the control and TQ groups. **(D)** Quantitative analysis of oxidative stress-related protein blots. **(E)** Immunohistochemical staining images of C-CASP3 in the control and TQ groups (scale bar, 50 μm). **(F)** Quantitative analysis of C-CASP3 absorbance in the control and TQ groups. **(G)** Western blotting to detect the expression of apoptosis-related proteins: Bax, C-CASP3, and Bcl-2 in flap tissues of the control and TQ groups. **(H)** Quantitative analysis of apoptosis-related protein blots. Significance: *$p < 0.05$ and **$p < 0.01$. Data are presented as mean ± SEM, with five rats per group.

of the beneficial effects of TQ on the survival of rat perforator flaps following ischemia-reperfusion injury is attributed to the inhibition of apoptosis.

The regulation of flap survival by TQ is related to the expression of SIRT1

Recent studies have also shown that SIRT1 can aid in the survival of random flaps (Jiang et al., 2022). We hypothesize that TQ may limit pyroptosis in rat perforator flaps through SIRT1 regulation, thereby reducing flap necrosis. We employed molecular docking analysis to explore the protective effects of TQ on flaps via the SIRT1/p65 pathway. As shown in Supplementary Table S1A, the binding affinity between the small molecule TQ and the target protein SIRT1 is −6.3 kcal/mol. Generally, ligands and receptor proteins can bind spontaneously if the binding energy is less than 0 kcal/mol, and they can bind stably if the binding energy is less than −4 kcal/mol[36]. A binding energy of less than −6 kcal/mol indicates a strong binding interaction. Therefore, a strong binding exists between TQ and SIRT1 protein.

As illustrated in Figure 4C, the small ligand molecule binds to the "aromatic cage" of the target protein, with the interacting amino acids all being aromatic. These amino acids bind to phenylalanine (PHE) amino acids at positions 81, 105, and 22 of the receptor protein through strong hydrophobic interactions at distances of 3.5, 3.6, 3.6, 3.8, and 3.6 Å, respectively. Additionally, the ligand TQ binds to histidine (HIS) amino acid at position 171 of the receptor protein through a hydrogen bond with a distance of 3.4 Å. Simultaneously, HIS-171 also forms a π-cation interaction with the ligand. Furthermore, the two-dimensional interaction

10.3389/fphar.2025.1567762

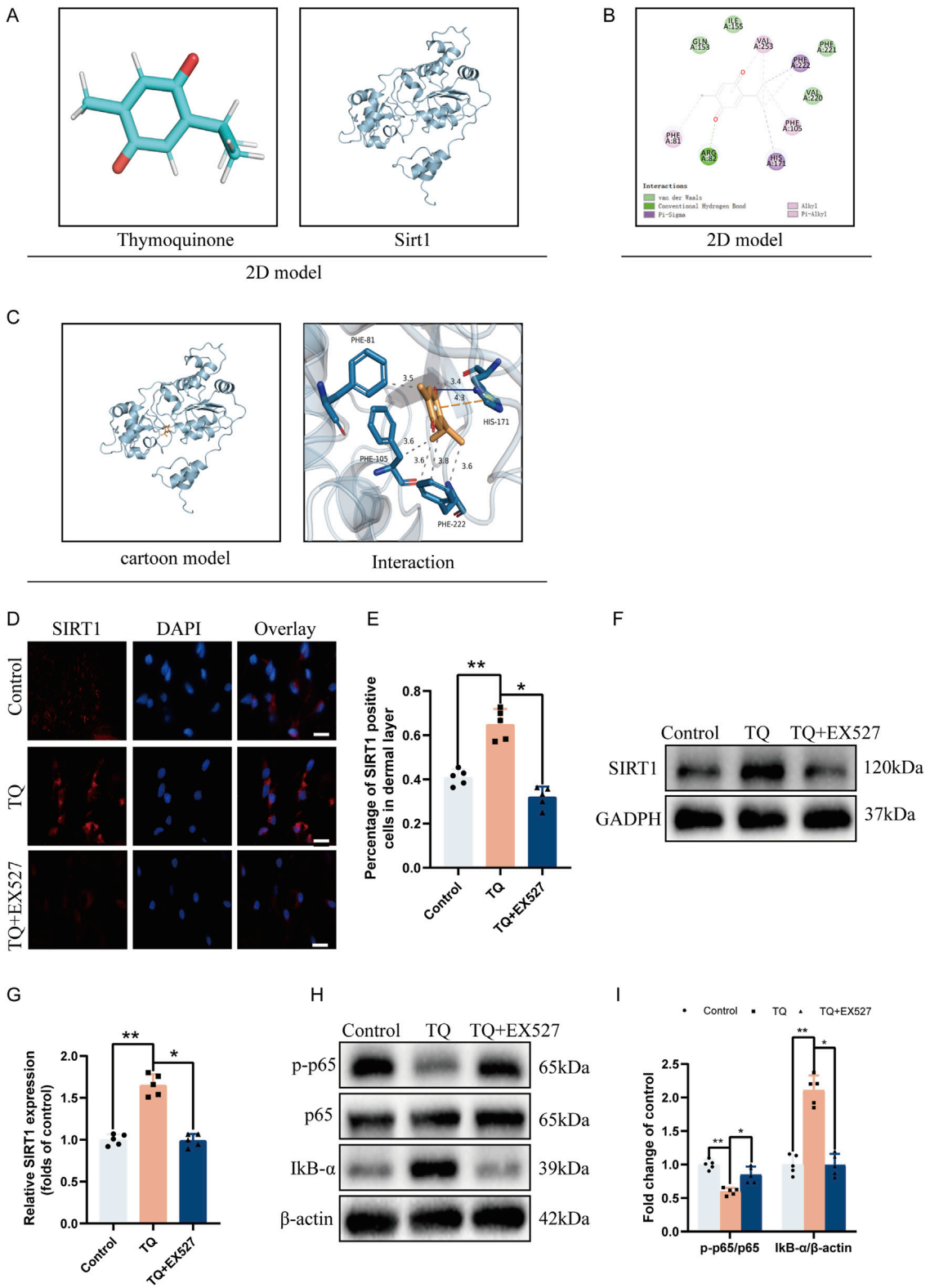


FIGURE 4
TQ Ameliorates Apoptosis in Rat Perforator Flaps After Ischemia-Reperfusion Injury by Targeting SIRT1. **(A)** Two-dimensional structural diagrams of TQ and SIRT1 protein. **(B)** Two-dimensional interaction diagram of the target protein with the ligand. **(C)** Overall view of TQ in the SIRT1 domain based on space-filling and ribbon models. **(D)** SIRT1 protein expression levels in flap tissues of rats in the control, TQ, and TQ+EX527 groups measured by immunofluorescence (scale bar: 20 μm). **(E)** Fluorescence intensity of SIRT1 expression in each group analyzed using Image J. **(F)** Western blotting to detect SIRT1 target protein expression in flap tissues of the control, TQ, and TQ+EX527 groups. **(G)** Quantitative analysis of SIRT1 protein blots. **(H)** Western blotting to detect the expression levels of NF-κB signaling pathway-related proteins in flap tissues of the control, TQ, and TQ+EX527 groups. **(I)** Quantitative analysis of NF-κB signaling pathway-related protein blots. Significance: *$p < 0.05$ and **$p < 0.01$. Data are presented as mean ± SEM, with five rats per group.

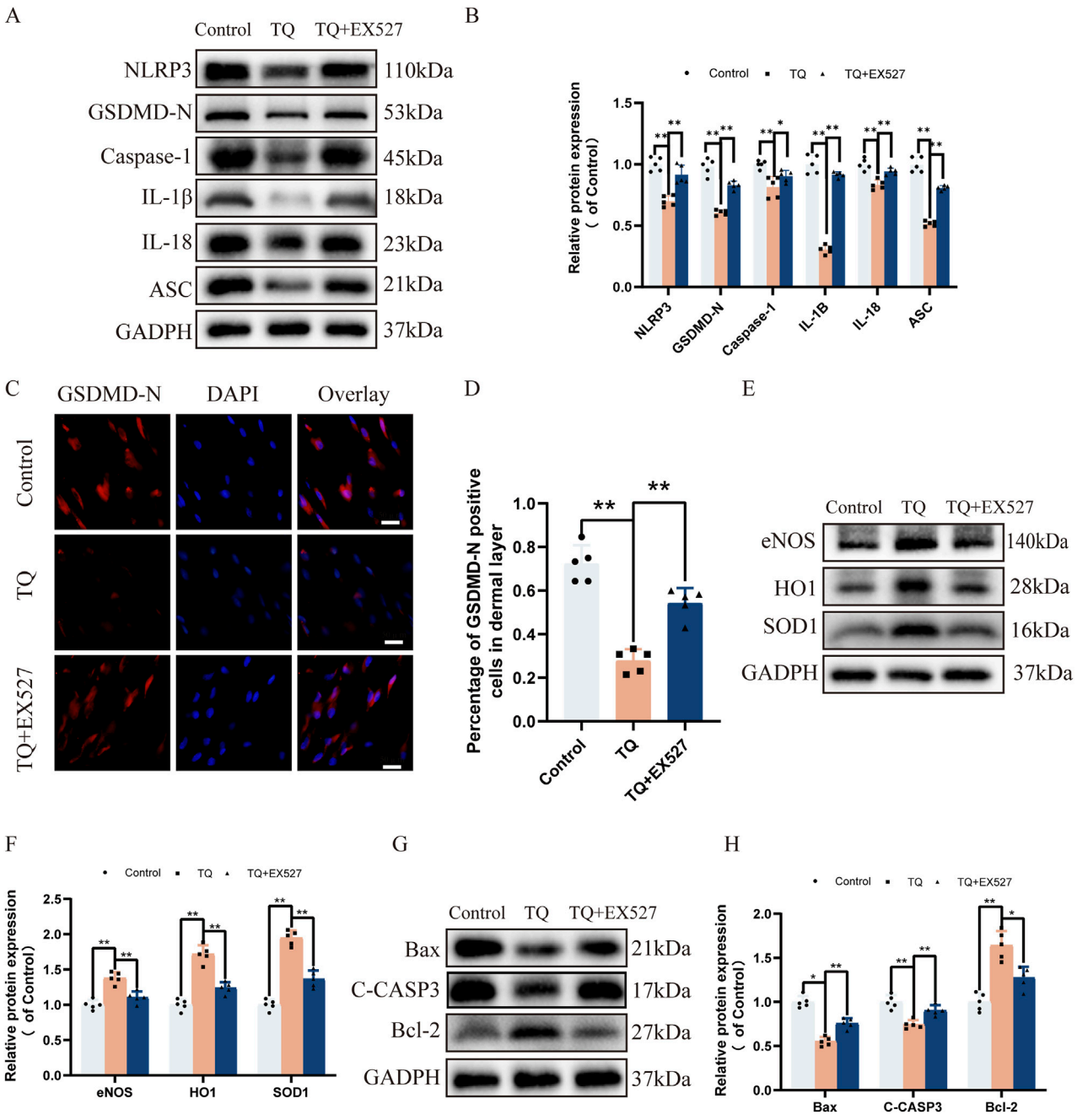


FIGURE 5
EX527 Reverses the Inhibitory Effects of TQ on Pyroptosis, Oxidative Stress, and Apoptosis in Rat Perforator Flaps After Ischemia-Reperfusion Injury. **(A)** Western blotting to detect the expression of pyroptosis-related proteins: NLRP3, GSDMD-N, Caspase-1, IL-1β, IL-18, and ASC in flap tissues of the control, TQ, and TQ+EX527 groups. **(B)** Quantitative analysis of pyroptosis-related protein blots. **(C)** GSDMD-N protein expression levels in flap tissues of rats in the control, TQ, and TQ+EX527 groups measured by immunofluorescence (scale bar: 20 μm). **(D)** Fluorescence intensity of GSDMD-N expression in each group analyzed using Image J. **(E)** Western blotting to detect the expression of oxidative stress-related proteins: eNOS, HO1, and SOD1 in flap tissues of the control, TQ, and TQ+EX527 groups. **(F)** Quantitative analysis of oxidative stress-related protein blots. **(G)** Western blotting to detect the expression of apoptosis-related proteins: Bax, C-CASP3, and Bcl-2 in flap tissues of the control, TQ, and TQ+EX527 groups. **(H)** Quantitative analysis of apoptosis-related protein blots. Significance: *$p < 0.05$ and **$p < 0.01$. Data are presented as mean ± SEM, with five rats per group.

diagram (Figures 4A, B) analysis shows that, besides results similar to the three-dimensional interaction diagram (Figure 4C), there are van der Waals forces between the ligand molecule and multiple amino acids of the receptor protein. Due to the existence of these forces, the ligand small molecule can stably bind to the receptor protein. This indicates that the binding site between the ligand and the receptor protein has excellent binding free energy and good affinity. Therefore, the binding of TQ to SIRT1 protein is likely to exert the corresponding pharmacological effect.

To further confirm the binding of TQ to SIRT1 protein, we used the SIRT1 inhibitor EX527 (Li et al., 2023) before treating rat flaps with TQ. According to immunofluorescence, the number of SIRT1-positive cell

expressions increased in the perforator flaps after TQ treatment (Figures 4D, E), while EX527 reversed the upregulation effect of TQ on SIRT1. Similarly, Western blot analysis revealed that TQ administration restored SIRT1 expression levels (Figures 4F, G), while EX527 attenuated the upregulation effect of TQ on SIRT1. Compared with the control group, the phosphorylated NF-κB p65 subunit decreased and IκB-α increased in the TQ group (Figures 4H, I), while EX527 reversed the dephosphorylation effect of TQ on p65 protein. These results suggest that TQ increases the expression of SIRT1 and decreases the expression level of phosphorylated NF-κB p65 after ischemia-reperfusion injury in rat perforator flaps.

EX527 reverses the inhibitory effects of TQ on pyroptosis, oxidative stress, and apoptosis in rat perforator flaps following ischemia-reperfusion injury

Previous research has shown that the activation of SIRT1 target protein can inhibit NLRP3 inflammasome activation and subsequent caspase-1 cleavage and IL-1β secretion (Li et al., 2017). To investigate the impact of SIRT1 target protein on rat perforator flaps after ischemia-reperfusion injury, we used SIRT1 inhibitor EX527 prior to TQ treatment. Western blot analysis revealed that SIRT1 protein expression increased after TQ treatment, while the use of SIRT1 inhibitor EX527 increased the protein expression levels of NLRP3, GSDMD-N, Caspase-1, IL-1β, IL-18, and ASC (Figures 5A, B). Furthermore, for the pyroptosis marker protein GSDMD-N, its expression was inhibited after TQ treatment but increased after SIRT1 inhibitor treatment (Figures 5C, D). These findings suggest that SIRT1 inhibitor diminishes the ability of TQ to inhibit pyroptosis. We also investigated whether SIRT1 inhibitor could suppress the beneficial effects of TQ on oxidative stress and apoptosis in rat perforator flaps. Compared to the TQ group, SIRT1 inhibitor EX527 treatment significantly decreased the expression of eNOS, HO1, and SOD1 (Figures 5E, F). SIRT1 inhibitor EX527 treatment increased the expression of Bax and C-CASP3 and inhibited the expression of Bcl-2 (Figures 5G, H). Overall, these results indicate that the effects of TQ on pyroptosis, oxidative stress, and apoptosis in perforator flaps after ischemia-reperfusion injury may be associated with SIRT1.

EX527 reverses the promotional effects of TQ on angiogenesis and survival of rat perforator flaps post ischemia-reperfusion injury

To further confirm whether the promotional effects of TQ on angiogenesis and survival of rat perforator flaps subjected to ischemia-reperfusion injury are SIRT1-mediated, SIRT1 inhibitor EX527 was administered prior to TQ treatment. Compared with the TQ-treated group, the survival area of flaps decreased in the TQ + EX527 group (Figures 6 A, B). Moreover, Doppler imaging revealed a decrease in blood flow intensity in the flaps of the TQ + EX527 group relative to the TQ-treated group (Figures 6 C, D). Histological analysis using HE staining showed a significant reduction in microvasculature in the TQ + EX527 group compared to the TQ-treated group (Figures 6 E, F). Additionally, WB assays demonstrated a significant downregulation of angiogenesis-related markers in the TQ + EX527 group (Figures 6 G, H). In summary, these findings indicate that the protective effects of TQ on flap survival are at least partially mediated through the SIRT1/NF-κB/NLRP3 pathway.

Discussion

Perforator flaps are increasingly being utilized in clinical settings, yet local necrosis of perforator flaps has emerged as a significant issue caused by multiple factors. Angiogenesis is crucial for flap survival. In our study, we observed that TQ significantly increased microvascular density and CD34-positive endothelial cells in the flaps, thereby enhancing blood supply to rat perforator flaps. Furthermore, our results indicate that TQ upregulated the expression of cadherin-5, VEGF, and MMP9, raising the possibility that TQ promotes angiogenesis in rat perforator flaps and enhances flap survival by elevating these angiogenesis-related proteins. These findings suggest that TQ can improve the survival rate of perforator flaps after ischemia-reperfusion injury by facilitating angiogenesis.

Ischemia-reperfusion injury, characterized by the accumulation of ROS in ischemic tissues upon reperfusion and the subsequent induction of oxidative stress, is another factor contributing to flap necrosis (Kim and Hong, 2007). Superoxide dismutase (SOD) is a vital component of the cellular response to ROS-induced oxidative stres (Miao and St Clair, 2009). Similarly, the antioxidant effects of eNOS and HO1 are also present (Wang et al., 2013). In our study, we found that TQ treatment increased the protein expression levels of SOD1, HO1, and eNOS in rat perforator flap tissues, thereby conferring resistance to oxidative stress. Apoptosis, a normal form of programmed cell death, occurs in flap necrosis. Several studies have shown that TQ exerts anti-apoptotic effects by altering various cellular pathways (Bimonte et al., 2019). Our results demonstrate that TQ can prevent apoptosis in rat perforator flaps after ischemia-reperfusion, as indicated by the apoptosis-related proteins Bax, Bcl-2, and C-CASP3 mentioned above. In summary, our findings indicate that TQ protects perforator flaps from necrosis by reducing oxidative stress and apoptosis.

Pyroptosis, an emerging type of cell death, regulates critical physiological processes such as cell development, tissue homeostasis, stress responses, and inflammatory reactions (Robinson et al., 2019). Pyroptosis is often accompanied by ROS production and organelle damage (Pétrilli et al., 2007). Additionally, ROS upregulate the NF-κB signaling axis, which activates the NLRP3 inflammasome and ultimately triggers pyroptosis (Jia et al., 2019). Previous reports have shown that inhibiting pyroptosis can improve the viability of random flaps (Li et al., 2021a; Li et al., 2021b; Zhu et al., 2021). Prior studies have demonstrated that TQ can alleviate cardiac injury by inhibiting pyroptosis (Wang et al., 2022). To investigate the mechanisms underlying the role of TQ in rat perforator flap survival, we assessed its modulation of pyroptosis in rat perforator flaps after ischemia-reperfusion. In our current experiments, we found that TQ reduced the expression of NLRP3, GSDMD-N, Caspase-1, IL-1β, IL-18, and ASC proteins both *in vivo* and *in vitro*. Furthermore, the positive effects of TQ were inhibited when the SIRT1 inhibitor EX527 enhanced pyroptosis. All these findings suggest the potential

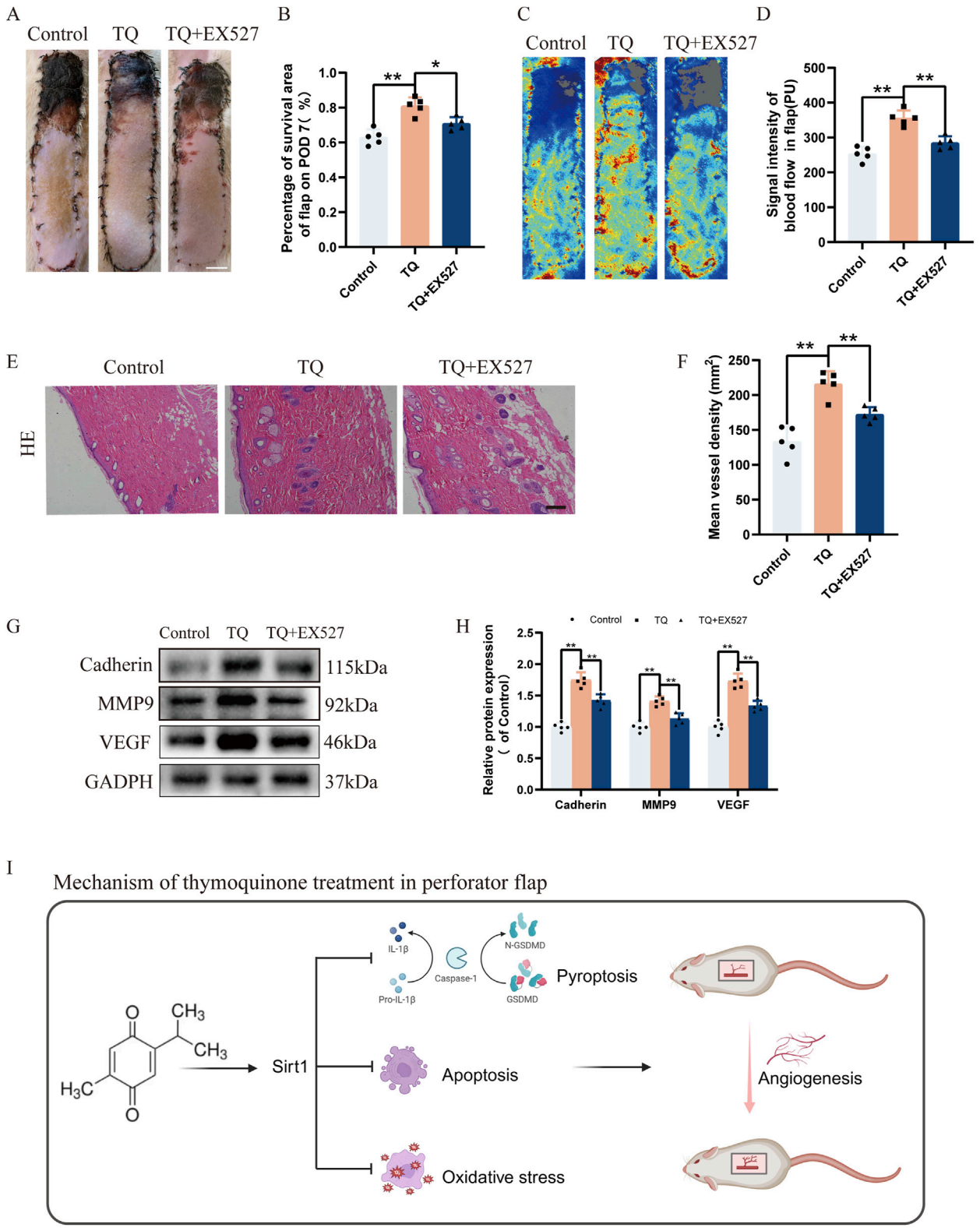


FIGURE 6
EX527 Reverses the Promoting Effects of TQ on Angiogenesis and Flap Survival in Rat Perforator Flaps After Ischemia-Reperfusion Injury. **(A)** Gross images of the dorsal flaps on the seventh postoperative day in the control, TQ, and TQ+EX527 groups. (scale bar, 1 cm) **(B)** A histogram showing the percentage of flap survival area on the seventh day for each group. **(C)** Doppler imaging of the blood supply in the perforator flaps of the control, TQ, and TQ+EX527 groups. **(D)** Quantitative examination of blood flow intensity in the flaps of each group. **(E)** H&E staining of flap tissues in the control, TQ, and TQ+EX527 groups (scale bar, 50 μm). **(F)** Quantitative examination of microvascular density (MVD) in each group. **(G)** Western blotting to detect the expression of angiogenesis-related proteins: Cadherin-5, MMP9, and VEGF in flap tissues of the control, TQ, and TQ+EX527 groups. **(H)** Quantitative
(*Continued*)

FIGURE 6 (Continued)
analysis of angiogenesis-related protein blots. **(I)** Schematic diagram illustrating the protective effects of TQ on rat perforator flaps after ischemia-reperfusion injury. Significance: *p < 0.05 and **p < 0.01. Data are presented as mean ± SEM, with five rats per group.

role of TQ in improving flap survival by inhibiting the activation of pyroptosis.

Considering the pivotal roles SIRT1 plays in numerous diseases, stimulating SIRT1 may emerge as a therapeutic option to enhance the survival rate of skin flaps. Prior studies have demonstrated that SIRT1 is positively regulated in various conditions, including hypoxic-ischemic brain injury (Li et al., 2022), acute kidney injury (Lin et al., 2022), and acute lung injury (Fu et al., 2019). In this investigation, skin flap tissues treated with TQ exhibited a significant increase in SIRT1 protein expression. When SIRT1-specific inhibitor EX527 was utilized, the activating effect of TQ on SIRT1 protein was attenuated, leading to increased levels of pyroptosis, decreased angiogenesis, elevated oxidative stress and apoptosis, and ultimately, increased necrosis area in the skin flaps. Collectively, we hypothesize that TQ may limit pyroptosis in rat perforator flaps through SIRT1 modulation, thereby reducing flap necrosis.

Regarding inflammation, NF-κB serves as a major transcriptional regulator of inflammation-related genes (Leslie et al., 2013). Current research on random skin flap ischemia-reperfusion models confirms the significance of NF-κB in the pathophysiology of flap ischemia-reperfusion injury (Fan et al., 2021). In this study, TQ inhibited the phosphorylation of NF-κB following ischemia-reperfusion injury in rat perforator flaps, indicating its ability to suppress the NF-κB signaling pathway. It has been reported that SIRT1 inhibits the NF-κB pathway by directly deacetylating p65 at lysine 310 (Yeung et al., 2004). Notably, our study also suggests that the beneficial effects of TQ are partially mediated by SIRT1, as demonstrated by the effects of the SIRT1 inhibitor EX-527 mentioned above. With SIRT1 expression suppressed by EX-527, NF-κB phosphorylation and NLRP3-mediated pyroptosis-related proteins were significantly elevated. Typically, NF-κB is bound in the cytoplasm by its inhibitor IκB. Upon stimulation, IκB is degraded, allowing NF-κB to translocate to the nucleus and stimulate the expression of inflammatory genes. In this study, the SIRT1 inhibitor increased NF-κBp65 phosphorylation, indicating that NF-κB p65 acts as a downstream target of SIRT1. The acetylation of p65 represents a potential mechanism for the pro-inflammatory effects of SIRT1 inhibitors (Schug et al., 2010). Ultimately, our research indicates that TQ treatment can inhibit pyroptosis in perforator flaps through the SIRT1/NF-κB/NLRP3 signaling pathway, an effect that was reversed by the SIRT1 inhibitor EX-527.

Summary

Our research demonstrates that TQ positively influences the survival of multi-regional perforator flaps primarily by inhibiting pyroptosis, promoting angiogenesis, and reducing apoptosis and oxidative stress accumulation. Additionally, *in vitro* experiments have shown that TQ can inhibit pyroptosis. Furthermore, we have discovered that SIRT1 plays a crucial role in mediating these processes within perforator flaps, suggesting it may serve as a potential therapeutic target for enhancing flap survival. By utilizing SIRT1 inhibitor EX527 and NLRP3 inhibitor MCC950, we have validated that the SIRT1/NF-κB/NLRP3 pathway may partially contribute to the beneficial effects of TQ on perforator flaps (Figure 6I).

Data availability statement

The datasets presented in this study can be found in online repositories. The names of the repository/repositories and accession number(s) can be found in the article/Supplementary Material.

Ethics statement

The animal study was approved by Guangzhou Shuiyuntian Laboratory Animal Welfare and Ethics Committee. The study was conducted in accordance with the local legislation and institutional requirements.

Author contributions

JY: Data curation, Investigation, Methodology, Writing–original draft, Writing–review and editing. HZ: Data curation, Formal Analysis, Writing–original draft, Writing–review and editing. LN: Data curation, Formal Analysis, Validation, Visualization, Writing–original draft. JH: Project administration, Supervision, Validation, Writing–review and editing.

Funding

The author(s) declare that financial support was received for the research and/or publication of this article. This study was supported by Zhejiang Province Traditional Chinese Medicine Science and Technology Project (2022ZQ007).

Conflict of interest

The authors declare that the research was conducted in the absence of any commercial or financial relationships that could be construed as a potential conflict of interest.

Generative AI statement

The author(s) declare that no Generative AI was used in the creation of this manuscript.

Publisher's note

All claims expressed in this article are solely those of the authors and do not necessarily represent those of their affiliated organizations, or those of the publisher, the editors and the reviewers. Any product that may be evaluated in this article, or claim that may be made by its manufacturer, is not guaranteed or endorsed by the publisher.

Supplementary material

The Supplementary Material for this article can be found online at: https://www.frontiersin.org/articles/10.3389/fphar.2025.1567762/full#supplementary-material

References

Ahmad, N., Ahmad, R., Alam, M. A., Samim, M., Iqbal, Z., and Ahmad, F. J. (2016). Quantification and evaluation of thymoquinone loaded mucoadhesive nanoemulsion for treatment of cerebral ischemia. *Int. J. Biol. Macromol.* 88, 320–332. doi:10.1016/j.ijbiomac.2016.03.019

Ba, X., Ye, T., He, Y., Tong, Y., Shang, H., Wu, J., et al. (2025). Engineered macrophage membrane-coated nanoparticles attenuate calcium oxalate nephrocalcinosis-induced kidney injury by reducing oxidative stress and pyroptosis. *Acta biomater*. doi:10.1016/j.actbio.2025.02.021

Babuta, M., Morel, C., de Carvalho Ribeiro, M., Calenda, C., Ortega-Ribera, M., Thevkar Nagesh, P., et al. (2024). Neutrophil extracellular traps activate hepatic stellate cells and monocytes via NLRP3 sensing in alcohol-induced acceleration of MASH fibrosis. *Gut* 73 (11), 1854–1869. doi:10.1136/gutjnl-2023-331447

Bergsbaken, T., Fink, S. L., and Cookson, B. T. (2009). Pyroptosis: host cell death and inflammation. *Nat. Rev. Microbiol.* 7 (2), 99–109. doi:10.1038/nrmicro2070

Bimonte, S., Albino, V., Barbieri, A., Tamma, M. L., Nasto, A., Palaia, R., et al. (2019). Dissecting the roles of thymoquinone on the prevention and the treatment of hepatocellular carcinoma: an overview on the current state of knowledge. *Infect. agents cancer* 14, 10. doi:10.1186/s13027-019-0226-9

Chen, J., Michan, S., Juan, A. M., Hurst, C. G., Hatton, C. J., Pei, D. T., et al. (2013). Neuronal sirtuin1 mediates retinal vascular regeneration in oxygen-induced ischemic retinopathy. *Angiogenesis* 16 (4), 985–992. doi:10.1007/s10456-013-9374-5

Chen, L., Li, B., Chen, B., Shao, Y., Luo, Q., Shi, X., et al. (2016). Thymoquinone alleviates the experimental diabetic peripheral neuropathy by modulation of inflammation. *Sci. Rep.* 6, 31656. doi:10.1038/srep31656

Chen, S., Hao, P., Liang, Y., Cao, Y., Han, W., and Sun, S. (2024). Electroacupuncture protects against cerebral ischemia-reperfusion injury: reducing inflammatory response and cell pyroptosis by inhibiting P2X7/NLRP3/GSDMD pathway. *Neuropsychiatric Dis. Treat.* 20, 2335–2346. doi:10.2147/NDT.S485884

Chen, Z., Wu, H., Yang, J., Li, B., Ding, J., Cheng, S., et al. (2022). Activating Parkin-dependent mitophagy alleviates oxidative stress, apoptosis, and promotes random-pattern skin flaps survival. *Commun. Biol.* 5 (1), 616. doi:10.1038/s42003-022-03556-w

Cheng, L., Yang, X., Chen, T., and Li, Z. (2017). Peroneal artery perforator flap for the treatment of chronic lower extremity wounds. *J. Orthop. Surg. Res.* 12 (1), 170. doi:10.1186/s13018-017-0675-z

Darakhshan, S., Bidmeshki Pour, A., Hosseinzadeh Colagar, A., and Sisakhtnezhad, S. (2015). Thymoquinone and its therapeutic potentials. *Pharmacol. Res.* 95-96, 138–158. doi:10.1016/j.phrs.2015.03.011

Fan, W., Liu, Z., Chen, J., Liu, S., Chen, T., Li, Z., et al. (2021). Effect of memantine on the survival of an ischemic random skin flap and the underlying mechanism. *Biomed. and Pharmacother. = Biomedecine and Pharmacother.* 143, 112163. doi:10.1016/j.biopha.2021.112163

Fu, C., Hao, S., Xu, X., Zhou, J., Liu, Z., Lu, H., et al. (2019). Activation of SIRT1 ameliorates LPS-induced lung injury in mice via decreasing endothelial tight junction permeability. *Acta Pharmacol. Sin.* 40 (5), 630–641. doi:10.1038/s41401-018-0045-3

He, W. T., Wan, H., Hu, L., Chen, P., Wang, X., Huang, Z., et al. (2015). Gasdermin D is an executor of pyroptosis and required for interleukin-1β secretion. *Cell Res.* 25 (12), 1285–1298. doi:10.1038/cr.2015.139

Hu, C., Zhang, S., Chen, Q., and Wang, R. (2022). Ovatodiolide protects ischemia-reperfusion-induced neuronal injury via microglial neuroinflammation via mediating SIRT1/NF-κB pathway. *Brain Res. Bull.* 180, 97–107. doi:10.1016/j.brainresbull.2021.12.010

Jia, C., Chen, H., Zhang, J., Zhou, K., Zhuge, Y., Niu, C., et al. (2019). Role of pyroptosis in cardiovascular diseases. *Int. Immunopharmacol.* 67, 311–318. doi:10.1016/j.intimp.2018.12.028

Jiang, R. H., Dong, C. J., Chen, Z. L., Cheng, S., Yang, J. X., and Gao, W. Y. (2022). Catalpol enhances random-pattern skin flap survival by activating SIRT1-mediated enhancement of autophagy. *Oxidative Med. Cell. Longev.* 2022, 5668226. doi:10.1155/2022/5668226

Kim, E. K., and Hong, J. P. (2007). The effect of recombinant human erythropoietin on ischemia-reperfusion injury: an experimental study in a rat TRAM flap model. *Plastic Reconstr. Surg.* 120 (7), 1774–1781. doi:10.1097/01.prs.0000287131.53488.c4

Leslie, K. L., Song, G. J., Barrick, S., Wehbi, V. L., Vilardaga, J. P., Bauer, P. M., et al. (2013). Ezrin-radixin-moesin-binding phosphoprotein 50 (EBP50) and nuclear factor-κB (NF-κB): a feed-forward loop for systemic and vascular inflammation. *J. Biol. Chem.* 288 (51), 36426–36436. doi:10.1074/jbc.M113.483339

Li, C., Wu, Z., Xue, H., Gao, Q., Zhang, Y., Wang, C., et al. (2022). Ferroptosis contributes to hypoxic-ischemic brain injury in neonatal rats: role of the SIRT1/Nrf2/GPx4 signaling pathway. *CNS Neurosci. and Ther.* 28 (12), 2268–2280. doi:10.1111/cns.13973

Li, J., Chen, H., Lou, J., Bao, G., Wu, C., Lou, Z., et al. (2021b). Exenatide improves random-pattern skin flap survival via TFE3 mediated autophagy augment. *J. Cell. physiology* 236 (5), 3641–3659. doi:10.1002/jcp.30102

Li, J., Lou, J., Yu, G., Chen, Y., Chen, R., Chen, Z., et al. (2021a). Targeting TFE3 protects against lysosomal malfunction-induced pyroptosis in random skin flaps via ROS elimination. *Front. cell Dev. Biol.* 9, 643996. doi:10.3389/fcell.2021.643996

Li, Y., Yang, X., He, Y., Wang, W., Zhang, J., Zhang, W., et al. (2017). Negative regulation of NLRP3 inflammasome by SIRT1 in vascular endothelial cells. *Immunobiology* 222 (3), 552–561. doi:10.1016/j.imbio.2016.11.002

Li, Y., Zhu, Y., Hu, F., Liu, L., Shen, G., and Tu, Q. (2023). Procyanidin B2 regulates the Sirt1/Nrf2 signaling pathway to improve random-pattern skin flap survival. *Phytotherapy Res. PTR* 37 (9), 3913–3925. doi:10.1002/ptr.7847

Lin, W. H., Jiang, W. P., Chen, C. C., Lee, L. Y., Tsai, Y. S., Chien, L. H., et al. (2022). Renoprotective effect of pediococcus acidilactici GKA4 on cisplatin-induced acute kidney injury by mitigating inflammation and oxidative stress and regulating the MAPK, AMPK/SIRT1/NF-κB, and PI3K/AKT pathways. *Nutrients* 14 (14), 2877. doi:10.3390/nu14142877

Liu, H., Sun, Y., Zhang, Y., Yang, G., Guo, L., Zhao, Y., et al. (2019b). Role of thymoquinone in cardiac damage caused by sepsis from BALB/c mice. *Inflammation* 42 (2), 516–525. doi:10.1007/s10753-018-0909-1

Liu, H., Wang, L., Weng, X., Chen, H., Du, Y., Diao, C., et al. (2019a). Inhibition of Brd4 alleviates renal ischemia/reperfusion injury-induced apoptosis and endoplasmic reticulum stress by blocking FoxO4-mediated oxidative stress. *Redox Biol.* 24, 101195. doi:10.1016/j.redox.2019.101195

Lu, H., Zeng, H., Wei, W., Chen, Y., Zhou, Z., Ning, X., et al. (2024). A fluorogenic ROS-triggered hydrogen sulfide donor for alleviating cerebral ischemia-reperfusion injury. *Theranostics* 14 (19), 7589–7603. doi:10.7150/thno.100930

Lu, Y., Feng, Y., Liu, D., Zhang, Z., Gao, K., Zhang, W., et al. (2018). Thymoquinone attenuates myocardial ischemia/reperfusion injury through activation of SIRT1 signaling. *Cell. physiology Biochem. Int. J. Exp. Cell. physiology, Biochem. Pharmacol.* 47 (3), 1193–1206. doi:10.1159/000490216

Luo, L., Wu, Q., Xiao, Q., Chen, Y., Deng, Z., Cen, C., et al. (2025). Lipotoxicity-induced upregulation of FIS1 exacerbates mitochondrial fragmentation and promotes NLRP3-dependent pyroptosis in diabetic cardiomyopathy. *Free Radic. Biol. and Med.* 228, 183–196. doi:10.1016/j.freeradbiomed.2024.12.049

Man, S. M., and Kanneganti, T. D. (2016). Converging roles of caspases in inflammasome activation, cell death and innate immunity. *Nat. Rev. Immunol.* 16 (1), 7–21. doi:10.1038/nri.2015.7

Mei, Z., Du, L., Liu, X., Chen, X., Tian, H., Deng, Y., et al. (2022). Diosmetin alleviated cerebral ischemia/reperfusion injury *in vivo* and *in vitro* by inhibiting oxidative stress

via the SIRT1/Nrf2 signaling pathway. *Food and Funct.* 13 (1), 198–212. doi:10.1039/d1fo02579a

Miao, L., and St Clair, D. K. (2009). Regulation of superoxide dismutase genes: implications in disease. *Free Radic. Biol. and Med.* 47 (4), 344–356. doi:10.1016/j.freeradbiomed.2009.05.018

Nam, Y. E., Kim, H. J., and Kwon, O. (2024). Acute and prolonged effects of Bacillus amyloliquefaciens GF424-derived SOD on antioxidant defense in healthy individuals challenged with intense aerobic exercise. *Free Radic. Biol. and Med.* 224, 484–493. doi:10.1016/j.freeradbiomed.2024.09.015

Newton, K., Strasser, A., Kayagaki, N., and Dixit, V. M. (2024). Cell death. *Cell* 187 (2), 235–256. doi:10.1016/j.cell.2023.11.044

Odake, K., Tsujii, M., Iino, T., Chiba, K., Kataoka, T., and Sudo, A. (2021). Febuxostat treatment attenuates oxidative stress and inflammation due to ischemia-reperfusion injury through the necrotic pathway in skin flap of animal model. *Free Radic. Biol. and Med.* 177, 238–246. doi:10.1016/j.freeradbiomed.2021.10.033

Peng, P., Dong, Z., Wei, J., and Luo, Z. (2022). Distal arterialized venous supercharging improves perfusion and survival in an extended dorsal three-perforasome perforator flap rat model. *Plastic Reconstr. Surg.* 150 (4), 921e–2e. doi:10.1097/PRS.0000000000009505

Pétrilli, V., Dostert, C., Muruve, D. A., and Tschopp, J. (2007). The inflammasome: a danger sensing complex triggering innate immunity. *Curr. Opin. Immunol.* 19 (6), 615–622. doi:10.1016/j.coi.2007.09.002

Qu, X., Xu, D., Yang, T., Tian, Y., King, C. T., Wang, X., et al. (2024). Macrophage Dvl2 deficiency promotes NOD1-Driven pyroptosis and exacerbates inflammatory liver injury. *Redox Biol.* 79, 103455. doi:10.1016/j.redox.2024.103455

Robinson, N., Ganesan, R., Hegedűs, C., Kovács, K., Kufer, T. A., and Virág, L. (2019). Programmed necrotic cell death of macrophages: focus on pyroptosis, necroptosis, and parthanatos. *Redox Biol.* 26, 101239. doi:10.1016/j.redox.2019.101239

Salem, M. L. (2005). Immunomodulatory and therapeutic properties of the Nigella sativa L. seed. *Int. Immunopharmacol.* 5 (13-14), 1749–1770. doi:10.1016/j.intimp.2005.06.008

Schug, T. T., Xu, Q., Gao, H., Peres-da-Silva, A., Draper, D. W., Fessler, M. B., et al. (2010). Myeloid deletion of SIRT1 induces inflammatory signaling in response to environmental stress. *Mol. Cell. Biol.* 30 (19), 4712–4721. doi:10.1128/MCB.00657-10

Selçuk, C. T., Durgun, M., Tekin, R., Yolbas, L., Bozkurt, M., Akçay, C., et al. (2013). Evaluation of the effect of thymoquinone treatment on wound healing in a rat burn model. *J. burn care and Res. official Publ. Am. Burn Assoc.* 34 (5), e274–e281. doi:10.1097/BCR.0b013e31827a2be1

Wan, P., Su, W., Zhang, Y., Li, Z., Deng, C., Li, J., et al. (2020). LncRNA H19 initiates microglial pyroptosis and neuronal death in retinal ischemia/reperfusion injury. *Cell death Differ.* 27 (1), 176–191. doi:10.1038/s41418-019-0351-4

Wang, D., Qiao, J., Zhao, X., Chen, T., and Guan, D. (2015). Thymoquinone inhibits IL-1β-induced inflammation in human osteoarthritis chondrocytes by suppressing NF-κB and MAPKs signaling pathway. *Inflammation* 38 (6), 2235–2241. doi:10.1007/s10753-015-0206-1

Wang, H., Zhou, X., Li, C., Yan, S., Feng, C., He, J., et al. (2022). The emerging role of pyroptosis in pediatric cancers: from mechanism to therapy. *J. Hematol. and Oncol.* 15 (1), 140. doi:10.1186/s13045-022-01365-6

Wang, R., Tu, J., Zhang, Q., Zhang, X., Zhu, Y., Ma, W., et al. (2013). Genistein attenuates ischemic oxidative damage and behavioral deficits via eNOS/Nrf2/HO-1 signaling. *Hippocampus* 23 (7), 634–647. doi:10.1002/hipo.22126

Wang, Y., Shi, P., Chen, Q., Huang, Z., Zou, D., Zhang, J., et al. (2019). Mitochondrial ROS promote macrophage pyroptosis by inducing GSDMD oxidation. *J. Mol. cell Biol.* 11 (12), 1069–1082. doi:10.1093/jmcb/mjz020

Wang, Y., Wang, J., Chen, Y., Li, X., and Jiang, Z. (2024). Decursinol angelate relieves inflammatory bowel disease by inhibiting the ROS/TXNIP/NLRP3 pathway and pyroptosis. *Front. Pharmacol.* 15, 1520040. doi:10.3389/fphar.2024.1520040

Xie, X., Cao, Y., Dai, L., and Zhou, D. (2023). Bone marrow mesenchymal stem cell-derived exosomal lncRNA KLF3-AS1 stabilizes Sirt1 protein to improve cerebral ischemia/reperfusion injury via miR-206/USP22 axis. *Mol. Med. Camb. Mass* 29 (1), 3. doi:10.1186/s10020-022-00595-1

Xu, J. J., Cui, J., Lin, Q., Chen, X. Y., Zhang, J., Gao, E. H., et al. (2021). Protection of the enhanced Nrf2 deacetylation and its downstream transcriptional activity by SIRT1 in myocardial ischemia/reperfusion injury. *Int. J. Cardiol.* 342, 82–93. doi:10.1016/j.ijcard.2021.08.007

Yeung, F., Hoberg, J. E., Ramsey, C. S., Keller, M. D., Jones, D. R., Frye, R. A., et al. (2004). Modulation of NF-kappaB-dependent transcription and cell survival by the SIRT1 deacetylase. *EMBO J.* 23 (12), 2369–2380. doi:10.1038/sj.emboj.7600244

Zhaolin, Z., Jiaojiao, C., Peng, W., Yami, L., Tingting, Z., Jun, T., et al. (2019). OxLDL induces vascular endothelial cell pyroptosis through miR-125a-5p/TET2 pathway. *J. Cell. physiology* 234 (5), 7475–7491. doi:10.1002/jcp.27509

Zhou, W., Chen, C., Chen, Z., Liu, L., Jiang, J., Wu, Z., et al. (2018). NLRP3: a novel mediator in cardiovascular disease. *J. Immunol. Res.* 2018, 5702103. doi:10.1155/2018/5702103

Zhu, X., Hu, X., Lou, J., Li, J., Xu, Y., Yu, G., et al. (2021). Liraglutide, a TFEB-mediated autophagy agonist, promotes the viability of random-pattern skin flaps. *Oxidative Med. Cell. Longev.* 2021, 6610603. doi:10.1155/2021/6610603

frontiers | Frontiers in Pharmacology

TYPE Original Research
PUBLISHED 27 March 2025
DOI 10.3389/fphar.2025.1552174

Check for updates

OPEN ACCESS

EDITED BY
Yizhou Zhan,
Dongguan University of Technology, China

REVIEWED BY
Ilya D. Klabukov,
National Medical Research Radiological Center, Russia
Zihua Xu,
Northern Theater Command General Hospital, China

*CORRESPONDENCE
Ping Zhao,
zhaop@swu.edu.cn
Hong Chen,
nazhagunlun@163.com

RECEIVED 27 December 2024
ACCEPTED 26 February 2025
PUBLISHED 27 March 2025

CITATION
Tian Z, Shen Z, Chen H and Zhao P (2025) Silk fibroin–collagen hydrogel loaded with IGF1-CESCs attenuates intervertebral disk degeneration by accelerating annulus fibrosus healing in rats.
Front. Pharmacol. 16:1552174.
doi: 10.3389/fphar.2025.1552174

COPYRIGHT
© 2025 Tian, Shen, Chen and Zhao. This is an open-access article distributed under the terms of the Creative Commons Attribution License (CC BY). The use, distribution or reproduction in other forums is permitted, provided the original author(s) and the copyright owner(s) are credited and that the original publication in this journal is cited, in accordance with accepted academic practice. No use, distribution or reproduction is permitted which does not comply with these terms.

Silk fibroin–collagen hydrogel loaded with IGF1-CESCs attenuates intervertebral disk degeneration by accelerating annulus fibrosus healing in rats

Zhiqiang Tian[1], Zigang Shen[2], Hong Chen[3]* and Ping Zhao[1]*

[1]Biological Science Research Center, Integrative Science Center of Germplasm Creation in Western China (CHONGQING) Science City, Southwest University, Chongqing, China, [2]Sericulture Science and Technology Research Institute of Chongqing, Chongqing, China, [3]Department of Orthopedics, 903 Hospital of Joint Logistic Support Force of The People's Liberation Army, Hangzhou, China

Introduction: The self-healing capacity of a damaged annulus fibrosus (AF) leads to intervertebral disk (IVD) degeneration. AF wound treatment is challenging. The combination of biomaterials and stem cell-derived exosomes is a promising wound treatment strategy with significant clinical value.

Methods: We isolate primary nucleus pulposus cells (NPCs) and primary annulus fibrosus cells (AFCs) from rats as the target cells of rat insulin-like growth factor 1(IGF1), and verify the proliferation and migration; constructed cartilage endplate stem cells (CESCs) engineered cells that release exosomes containing high concentrations of IGF1by lentiviral infection, and used the IGF1-CESCs combined with combined silk fibroin (SF) and a collagen-mixed hydrogel for the treatment of AF wounds in rat.

Results: We found that both IGF1 and IGF1-rich exosomes (IGF1 Exo) promoted the proliferation and migration of AFCs. SF and collagen mixed hydrogels have excellent compressive mechanical properties and are suitable for use in IVD therapy. After the IGF1-CESCs@SF-collagen hydrogel was filled in the damaged area of the AF in rat, the wound healing was accelerated, nucleus pulposus overflow was inhibited, the IVD height was maintained, and degeneration was reduced.

Discussion: The IGF1-CESCs@SF-collagen hydrogel can efficiently treat AF wounds and inhibit degeneration of IVD, and has potential for clinical treatment.

KEYWORDS

annulus fibrosus, wound treatment, IGF1, exosome, intervertebral disc

1 Introduction

Lower back pain (LBP) seriously affects the life of patients, leads to a large loss of labor, and increases the medical burden on the society (Freemont, 2009). The annulus fibrosus (AF) and nucleus pulposus (NP) are important tissues that support the height of the intervertebral disk (IVD) and enable the spine to bend. Long-term failure to heal after damage induces IVD degeneration, eventually resulting in LBP. Particularly, rapid AF repair after damage is crucial for maintaining IVD homeostasis (Sloan et al., 2020). The timely supply of trophic factors is essential

for the wound treatment of the damaged IVD. Insulin-like growth factor-1 (IGF1) is a cytokine closely related to bone growth (Zhang et al., 2020) and can regulate angiogenesis and bone regeneration. IGF1 inhibits the apoptosis of nucleus pulposus cells (NPCs) and activates the Akt pathway to release the extracellular matrix (ECM) such as aggrecan and collagen II (Xiao et al., 2021; Chen et al., 2020); it is also considered crucial in wound healing of the damaged AF (Elmasry et al., 2016).

Stem cells have been widely studied in regenerative medicine, but their senescence, tumorigenicity, and low efficiency in directed differentiation limit their clinical applications. Exosomes derived from stem cells not only retain the excellent characteristics of stem cells but also avoid the limitations of stem cells, and they have a wider range of clinical application prospects (Tan et al., 2024). Combinations of stem cells and exosomes are widely used for wound treatment (Rani and Ritter, 2016) and have attracted considerable attention for their use in repair after the damage of IVD (Luo et al., 2022). In contrast to exogenous stem cells (mesenchymal stem cells, skeletal stem cells, and adipose-derived stem cells), cartilage endplate stem cells (CESCs) are derived from the cartilage endplate (CEP) tissue of the IVD itself and have considerable potential for bone repair, IVD wound treatment, and other applications. We found that CESCs could release exosomes to induce NPC differentiation, thus repairing the NP (Luo et al., 2021a). We induced CESCs to stably express *Sphk2* and release Sphk2 protein-rich exosomes and then combined them with the costal chondrocyte extracellular matrix and collagen hydrogel to form an injectable Sphk2-CESC-exosome hydrogel, which effectively attenuated IVD degeneration (Luo et al., 2022). Although loose collagen hydrogels are beneficial for the growth of CESCs, because of their low mechanical pressure-bearing capacity, they cannot resist pressure from the spine, which limits their potential for clinical application. Silk fibroin (SF) has advantages such as good biocompatibility, adjustable degradability, and low toxicity, and it has been widely used as a dressing and pharmaceutical ingredient in wound treatment research (Farokhi et al., 2018). SF is also considered the best natural biomaterial for treating and reconstructing AF wounds (Wang et al., 2022; Bhattacharjee et al., 2012). In recent years, biomaterials such as collagen I/II, glycosaminoglycans, and pentosan polysulfate combined with stem cells have been widely favored for treating IVD. SF is highly favored in the medical field owing to its low immunogenicity and good biocompatibility. However, relatively few studies have examined the combination of silk fibroin and CESCs as biomaterials for IVD diseases.

In this study, we re-examined the relationship between IGF1 in AF wound treatment and IVD degeneration and verified its effects on the proliferation and migration of NPCs and annulus fibrosus cells. We constructed CESCs that stably transcribed the rat *igf1* gene, released exosomes rich in rIGF1 protein, and transformed them into a rIGF1-CESCs@SF-collagen hydrogel. This injectable hydrogel exhibited excellent mechanical properties and a strong ability to repair damaged AF, which can thus be an effective treatment strategy to attenuate IVD degeneration.

2 Materials and methods

2.1 Reagents and antibodies

Antibodies to glyceraldehyde 3-phosphate dehydrogenase (GAPDH) (cat. 60004-1-Ig), Cytl1, HSP70, Alix, and cleaved caspase-3 were purchased from Proteintech (Wuhan, China). Antibodies to IGF1 and KRT19 were purchased from BOSTER. DAPI nucleic acid dye (cat. C1006) and crystal violet staining solution (cat. C0121) were purchased from Beyotime Biotechnology (Shanghai China). Anti-TSG101 was obtained from ABclonal (cat. no. A1692, Wuhan, China). Goat anti-rabbit IgG (cat. ab150080, Alexa Fluor® 594) and Goat anti-rabbit IgG (cat. ab150077, Alexa Fluor® 488) were obtained from Abcam (Cambridge, MA, USA). The EdU Cell Proliferation Kit with Alexa Fluor 594 (cat. C0078S) was obtained from Beyotime Biotechnology (Shanghai, China). Type 2 (cat. A004174-0001) and type 4 collagenase (cat. A004186-0100) were purchased from Sangon Biotech (Shanghai, China).

2.2 Patient tissues and histological analysis

Clinical specimens were obtained from 15 patients undergoing surgery at the Department of Orthopedics of 903 Hospital of Joint Logistic Support Force of The People's Liberation Army. The severity assessment of IVD degeneration follows the modified Pfirrmann magnetic resonance imaging (MRI) method. Those with grades 1 and 2 were classified as having mild degeneration, whereas those with grades above 2 were considered as having severe degeneration. They were divided into several parts. Some of the tissues were frozen in liquid nitrogen for immunofluorescence and RT-qPCR analysis; others were fixed in 4% formalin buffer, decalcified with 10% ethylenediaminetetraacetic acid, embedded in paraffin after dehydration, and then used to perform tissue sectioning. The tissue slices were soaked in citrate buffer (0.01 M) at 110°C for 15 min, in 3% hydrogen peroxide for 15 min, and in 5% bovine serum albumin (BSA) for 40 min. The tissue sections were incubated with the IGF1 primary antibody (1: 200) for 6 h at 4°C, and they were incubated with the secondary antibody (horseradish peroxidase-conjugated) for 1 h at 37°C. They were detected via 3,3′diaminobenzidine tetrahydrochloride (DAB) staining. This study was approved by the Medical Ethics Committee of 903 Hospital of Joint Logistic Support Force of The People's Liberation Army (NO. 20241229/49/01/003), and all included patients provided informed consent.

2.3 Immunofluorescence

Immunofluorescence detection follows the method we previously used (Luo et al., 2022), which is briefly described as follows: the tissue sections were incubated in 10% hydrogen peroxide/formaldehyde buffer for 35 min at 37°C. They were then treated with 0.2% Triton for 5 min, blocked with 5% (w/v) BSA, and incubated with the primary antibody (IGF1, 1:00; cleaved caspase 3, 1:50) for 6 h. They were then incubated with a fluorescent secondary antibody and stained with 4′,6-diamidino-2-phenylindole. Images were captured using a fluorescence microscope (Olympus, Tokyo, Japan).

2.4 Animal experiments

Twenty-four 1-month-old Sprague–Dawley rats were purchased from the Experimental Animal Center of the Army Military Medical

University and divided into four experimental groups: a healthy control group (n = 6), acupuncture group (n = 6), rIGF1-CESCs@SF-collagen hydrogel group (n = 6), and CESCs@SF-collagen hydrogel treatment group (n = 6). The injury was induced, as described by Han et al. (2008). The rats were anesthetized with Delivector™ Avertin (10–20 μL/g). The AFs were damaged using a 21-gage needle. The needle was inserted into the AF, but no damage was caused to the NP tissue. After the induction of the injury was completed, in the rIGF1-CESCs@SF-collagen hydrogel group and the CESCs@SF-collagen hydrogel treatment group, 10 μL of rIGF1-CESCs@SF-collagen hydrogel and CESCs@SF-collagen hydrogel were injected into the damaged sites, respectively. The rats were sacrificed at weeks 1 and 6, respectively. IVD tissues were isolated for immunofluorescence and hematoxylin and eosin (HE) staining. Images were captured and analyzed (Olympus, Tokyo, Japan). The handling of rats complies with the requirements of the Guidelines for the Care and Use of Laboratory Animals of the National Institutes of Health, and the approval number from the Animal Ethics Committee of Army Medical University is AMUWEC20230455.

2.5 Separation of AFCs and NPCs

The cells were derived from the IVD of 2-week-old male rats. First, the isolated rat tail IVD was washed with 0.1 M sterile phosphate-buffered saline (PBS). NP and AF tissues were peeled off from the IVD tissue and cut into fragments by mechanical cutting. The tissues were digested with collagenase II (0.2%) for 3.5 h at 37°C. A filter was used to remove undigested clumps, and the clumps were washed with PBS. They were centrifuged at 1,000 rcf for 10 min. The isolated cells were cultured with the medium containing 10% fetal bovine serum and 1% penicillin–streptomycin in 5% CO_2 at 37°C. The medium was changed every 2 days. Cells were passed to the second generation for subsequent experiments. CESCs come from our laboratory's previous preservation (Luo et al., 2022).

2.6 Gene Ontology enrichment analysis

The analysis data are obtained from our previous research (Luo et al., 2021a). The overview is as follows: exosomes are extracted from CESCs cultured *in vitro*, and proteins are extracted from exosomes for protein mass spectrometry analysis. The top 200 proteins with the most abundant expression are selected, Gene Ontology (GO) enrichment analysis is performed by WeChat online (https://www.bioinformatics.com.cn/?keywords=pathway), and GO enrichment analysis graphs are created using GraphPad prism 10.3.

2.7 Wound healing and transwell assay

AFCs or NPCs (5×10^5/well) were inoculated into a 6-well plate. When the confluence reached 80%, a pipette tip was used to create a straight scratch. They were washed with PBS containing 10% fetal bovine serum. Scratches were photographed under an optical microscope at 0, 24, and 48 h. For the cell migration analysis, an appropriate amount of complete medium was added to a 24-well plate, the transwell chamber was placed in the 24-well plate, and the cell suspension was added. After 24 h, the chamber was removed and stained with crystal violet to determine the number of cells that passed through the membrane.

2.8 Lentivirus transfection

Lentiviruses to overexpress *rIGF1* were obtained from Honglian (Chongqing, China). When the CESCs reached 60% confluence, the *rIGF1*-lentivirus was added to the culturing cell, referring to the method (Luo et al., 2023) we previously used for screening positive cells. We analyzed the transfection efficiency by RT-qPCR and Western blotting.

2.9 Quantitative reverse transcription polymerase chain reaction (RT-qPCR) analysis

Total RNA was extracted from tissue or cells using TRIzol and was reverse-transcribed into cDNA using an RT kit (Takara, Japan). Three independent qPCR detections were performed using a Bio-Rad CFX96 qPCR machine (Bio-Rad Laboratories, Hercules, CA, USA), with GAPDH as the control to assess the gene expression. The primer sequence is as follows: *h(human)Igf1-F*: 5′-TGA AGG GAG GTG GTG GGT AT-3′, R:5′-CTC TGA ATC TTG GCT GCT GG-3'; *hGapdh*-F: 5′-TGG AAG ATG GTG ATG GGA TT-3′, R:5′-CTC TGA TTT GGT CGT ATT GGG-3'; *r(rat)Igf1*-F: 5′-TAA GAA AGG GCA GGG CTA AT-3′, R:5′-TTT ATA GGT GGT TGA TGA ATG G-3'; *rCytl1-F*: 5′-TGT GAC AGG GTA CTG CCC AC-3′, R: 5′-TCC CAT GAT GCA ATC GTT GA-3'; *rCol1α1*-F: 5′-GAT TGG GAT GGA GGG AGT TTA-3′, R:5′-TAC AGC ACG CTT GTG GAT GG-3'; *rKrt19*-F: 5′-AAG TCG CAC TGG TAG CAA GG-3′, R:5′-ATC AAG TCG AGG CTG GAG CA-3'; *rSox9*-F: 5′-CAA CAG ATG ACC ATA CCC TTT-3′, R:5′-TCA CCT GTA CCT CCC TGA ATA-3'; *rGapdh*-F: 5′-CGC CAG TAG ACT CCA CGA CAT-3′, R:5′-CGG CAA GTT CAA CGG CAC AG-3'.

2.10 Western blotting

Tissue or collected cells were lysed in RIPA buffer containing phenylmethylsulfonyl fluoride and extracted. The protein concentration of the supernatant was determined using a spectrophotometer (Beckman, Fullerton, CA, USA). Proteins were separated by polyacrylamide gel electrophoresis, and they were transferred to a polyvinylidene fluoride (PVDF) membrane by electroblotting. The PVDF membrane was placed in a closed solution containing 5% (w/v) skim milk for 1 h, incubated with antibodies (1:1000–2000) for 6 h at 4°C, and then washed thrice with PBS and incubated with secondary antibodies (horseradish peroxidase-conjugated) for 1 h at 37°C. The PVDF membrane was soaked in an ECL working solution (Millipore, MO, USA) for color development. Finally, the proteins were detected, and images were captured using the chemiluminescence system (Bio-Rad Laboratories).

2.11 Preparation of the SF–collagen hydrogel

Rats were anesthetized and sacrificed by cervical dislocation. The skin on the tail was incised, and the tail tendons were removed and washed with normal saline. The tail tendons were chopped and placed in 150-mL acetic acid solution (0.5%). They were then placed on a shaker and dissolved at 4°C for 48 h. Next, the mixture was centrifuged at 12,000 rcf for 15 min. The supernatant was aspirated and added to a 10% NaCl solution to precipitate the collagen. An appropriate amount of hydrochloric acid (0.2 mM) was added to dissolve the supernatant, and the collagen concentration was adjusted to 10 mg/mL. The collagen solution was stored at 4°C for later use.

Two grams of silkworm cocoons was weighed, placed into 1 L of a 0.5%–1% Na_2CO_3 solution, and boiled in water for 60 min to remove the sericin. The silk fibroin fibers were washed three times with 100 mL of double-distilled water, placed in an oven, and baked at 60°C for 30–50 min. A ternary solution was prepared by mixing 30.43 mL dd H_2O, 19.57 mL ethanol, and 24 g calcium chloride. The silk fibroin was placed in the ternary solution and dissolved at 60°C for 1–2 h. Centrifugation was performed at 4,000 rcf for 15 min, and the supernatant with the silk fibroin was collected. The silk fibroin solution was then transferred into a dialysis bag with a molecular weight cutoff of 8,000–14,000 D for 48 h. Centrifugation was performed at 4,000 rcf for 10 min, and the supernatant was collected to detect the concentration of the SF solution. The SF solution was concentrated with 15% polyvinyl alcohol 20000 to obtain a protein concentration of 8%–15%. Finally, collagen and SF solution were mixed at a ratio of 4:1 (the higher concentration of SF is not conducive to cell survival) to prepare the hydrogel.

2.12 Transmission electron microscope (TEM)

Extracellular vesicles (Luo et al., 2022) were collected and fixed with glutaraldehyde (3%) for 10 h. Osmium acid (1%) was fixed for 1.5 h. Gradient dehydration, embedding, sectioning (70–90 nm), and staining were performed. The sample was observed by using a TEM (Philips, Amsterdam, Netherlands).

2.13 Scanning electron microscope (SEM)

SF and collagen were mixed into a hydrogel, cooled at 20°C for 30 min, installed on a fixed frame and cooled at −70°C for 2 h, and then placed in a freeze dryer for 12 h; after gold plating and slicing for detection, images were captured using the SU3500 SEM (Hitachi, Tokyo, Japan).

2.14 Statistical analysis

The results were presented as the mean ± standard deviation. GraphPad Prism 7.0 (GraphPad Software, Inc., CA, United States) was used for statistical analyses. One-way analysis of variance or Student's t-test was used to compare the means between groups. A *p*-value of less than 0.05 was statistically significant.

3 Results

3.1 IGF1 expression in human and rat IVDs

We isolated CESC-derived exosomes from rats in previous research (Luo et al., 2021a). Through proteomic mass spectrometry detection and GO enrichment analysis, we found that the degree of activation of proteins related to the IGF pathway was abnormally high (Figure 1A). IGF is an important regulatory factor for bone growth and the main stimulatory factor for ECM synthesis. We speculate that CESCs release IGF-containing exosomes to maintain IVD homeostasis.

We collected tissues from patients who underwent IVD removal and performed pathological examinations. Immunohistochemical analysis showed that IGF1 in IVD tissues with mild degeneration was significantly higher than that in tissues severe degeneration (Figure 1B). The immunofluorescence and qRT-PCR results were similar to those of immunohistochemistry (Figures 1C,D), and there are significant differences in the number of IGF1-positive cells between patient tissues with mild and severe degeneration (Figure C). We induced degeneration of the rat tail IVD using a puncture method. At the 6th week, we used tissue immunofluorescence to detect the expression and localization of IGF1 in the rat tail IVD and found that it mainly existed in the CEP and NP regions of healthy IVD. The healthy IVD group had a higher expression of IGF1 protein than the degenerated IVD group (Figure 1E). These results indicate that IGF1 is crucial for maintaining the homeostasis of IVD.

3.2 Isolation and identification of rat AFCs and NPCs

To verify the influence of IGF1 on the physiological activities of these cells within the IVD, we isolated NP and AF tissues from rat tail IVD (Figure 2A). The tissues were digested with collagenase to obtain single NPCs and AFCs and then cultured for *in vitro* cell experiments (Figure 2B). We identified differences in the expression of AF-specific markers (*cytl1* and *col1*) (Fernandes et al., 2020; van den Akker et al., 2016) in rat AF tissues and AFCs using RT-qPCR and Western blotting (Figures 2C,D). The expression of NP-specific markers (*krt19* (Rutges et al., 2010), *sox9*, and *col2a1*) in NP tissues and NPCs was determined in a similar manner (Figures 2E,F). These results showed that the characteristics of AFCs and NPCs isolated *in vitro* were highly similar to those of AF and NP tissues, respectively. The AFCs and NPCs that were separated can represent AF and NP tissues, respectively, for *in vitro* experiments.

3.3 Effects of IGF1 on the proliferation and migration of AFCs and NPCs

IGF1 contributes to osteocyte proliferation and is involved in the homeostasis of bone tissues (Xian et al., 2012). IGF1 must bind to the

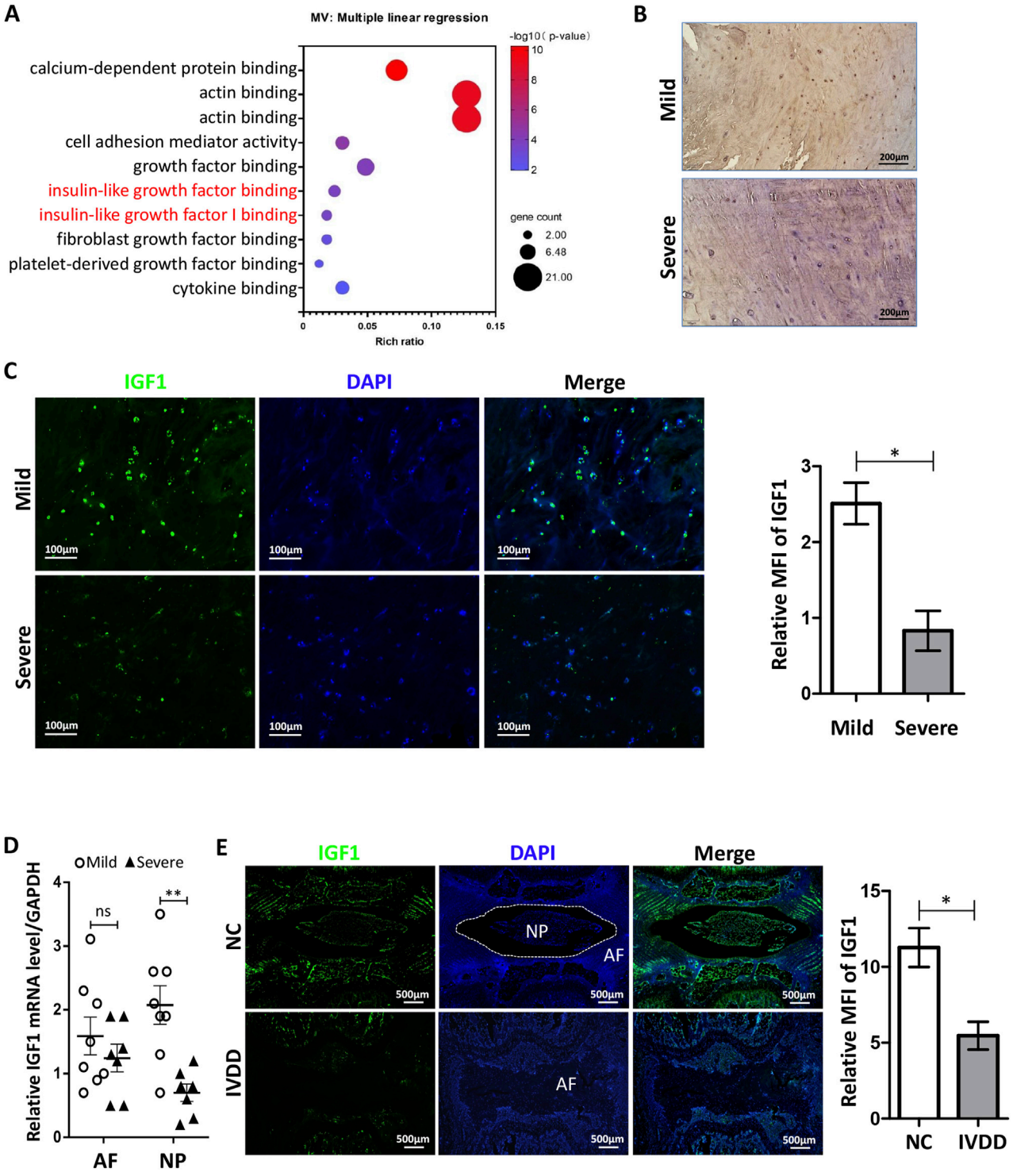


FIGURE 1
Expression of IGF1 in human and rat IVDs. **(A)** Enrichment analysis of CESCs-Exo carrier proteins in healthy rats using GO enrichment analysis (Luo et al., 2021a). **(B)** Immunohistochemistry was performed to detect IGF1 (green) expression in degenerated IVD tissues in patients. **(C)** Expression of IGF1 in patients degenerative IVD tissues was detected by immunofluorescence. **(D)** RT-qPCR was used to detect the expression of *Igf1* in the NP and AF in patients degenerative IVD tissues (mild, n = 8; severe, n = 7). **(E)** Punctures induced degeneration in the rat tail IVD, and after 6 weeks, the protein expression and tissue localization of IGF1 (green) in the tail IVD of healthy and degenerated rat tissues were detected by tissue immunofluorescence. Data in **(C–E)** are presented as the mean ± SD,*$p < 0.05$, **$p < 0.01$, ns: not significant by two-tailed Student's t-test.

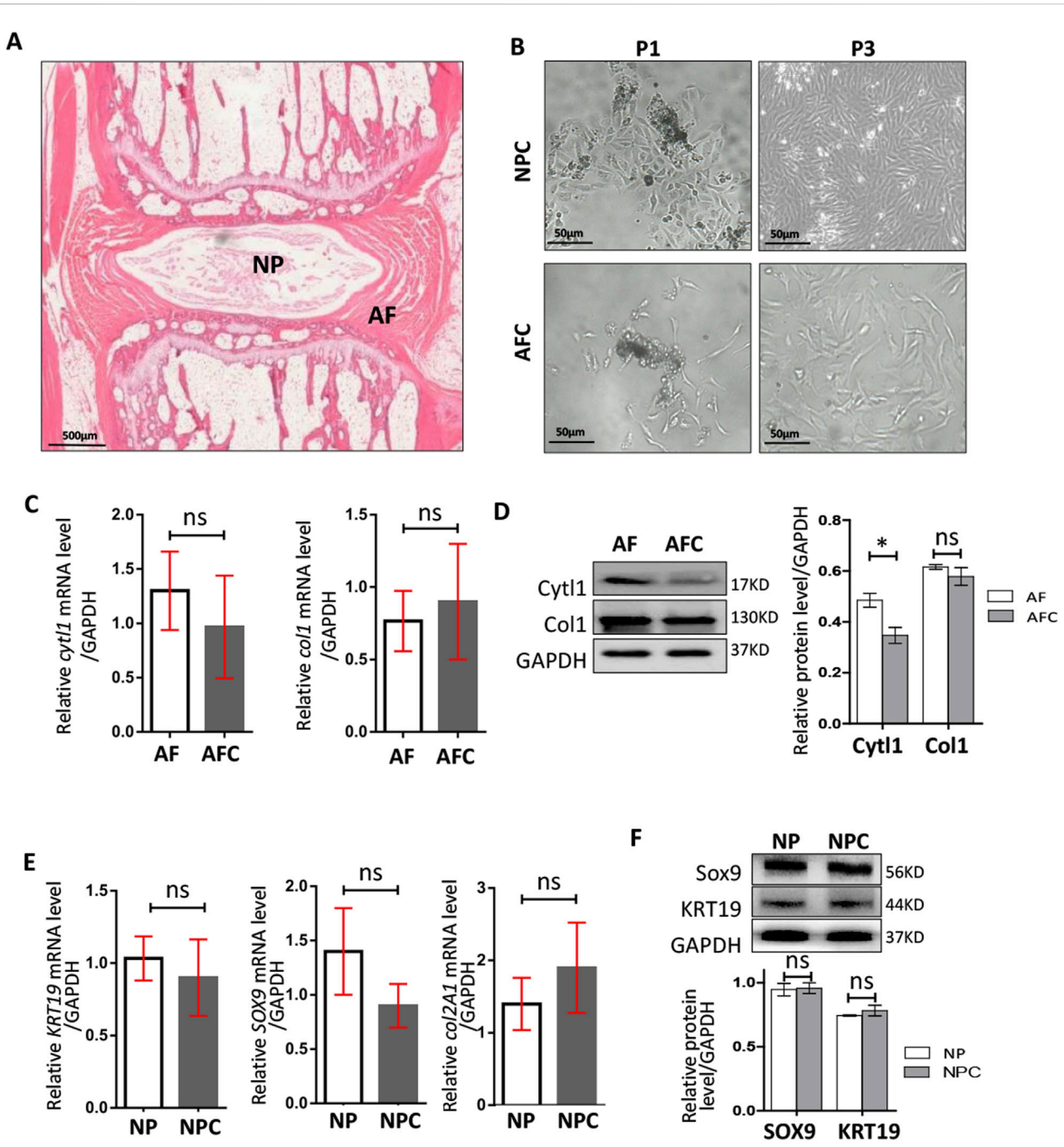


FIGURE 2
Isolation and identification of rat AFCs and NPCs. **(A)** Morphological map of rat tail IVD using hematoxylin–eosin staining, AF: annulus fibrosus, NP: nucleus pulposus. **(B)** Annulus fibrosus cells (AFCs) and nucleus pulposus cells (NPCs) cultured after tissue dissociation and collagenase digestion, P1: the first generation, P3: the third generation. **(C)** Expressions of *cytl1* and *col1* genes in AF tissue and AFCs were detected by RT-qPCR. **(D)** Western blotting was used to detect the differences in the expressions of Cytl1 and Col1 in AF tissues and AFCs. **(E)** Expression levels of *Sox9*, *krt19*, *and col2a1* genes in the NP and NPCs were detected by RT-qPCR. **(F)** Western blotting was used to detect the differences in the expression levels of Sox9 and KRT19 in the NP and NPCs. Data are presented as the mean ± SD in **(D, F)**, $*p < 0.05$, ns: not significant by two-tailed Student's t-test.

IGF receptor (IGFR) of target cells to activate intracellular signaling pathways and perform its functions.

To determine the influence of IGF1 on the proliferation of AFCs and NPCs, we measured the expression of IGFR in rat AF and NP tissues. Immunohistochemistry was performed to detect IGFR in healthy rat tail IVD tissues and those with degeneration. We found that IGFR was expressed in both AF and NP tissues, and its expression showed no significant differences between healthy and degenerated tissues (Figure 3A). Western blotting showed that IGFR expression in AF tissues remained relatively stable, with no differences in IGFR expression between healthy and degenerated AF tissues (Figures 3B,C), aligning with results from previous

10.3389/fphar.2025.1552174

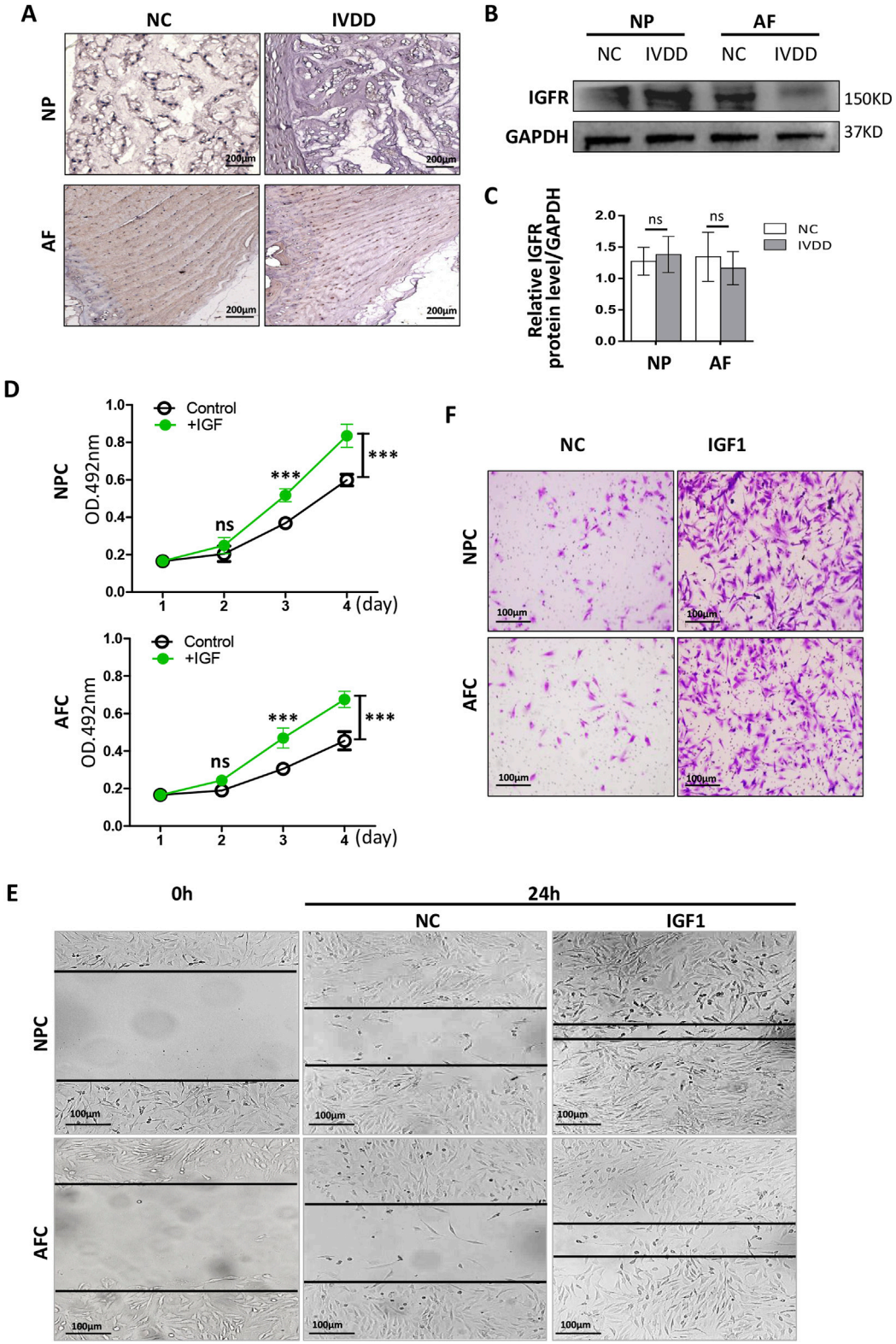


FIGURE 3
Effects of IGF1 on the proliferation and migration of NPCs and AFCs. **(A)** Immunohistochemical detection of IGFR expression in rat IVD tissue by staining with 3′- diaminobenzidine (NP, healthy; IVDD, degeneration). **(B)** Western blotting was used to detect the differences in the expression levels of IGFR in the AF/NP tissue between NP and IVDD. **(C)** Grayscale analysis of relative expression levels of IGFR protein. **(D)** Recombinant rat IGF1 was added to the AFC and NFC culture medium, and the cells were cultured *in vitro* for 4 days; the cell proliferation was detected by MTT. **(E)** Wound healing and transwell assay **(F)** were used to detect the migration of recombinant rIGF1 on AFCs and NPCs (crystal violet staining solution for cell nuclei). Data are presented as mean ± SD in **(C, D)**, ***$p < 0.001$, ns: not significant by two-tailed Student's t-test.

10.3389/fphar.2025.1552174

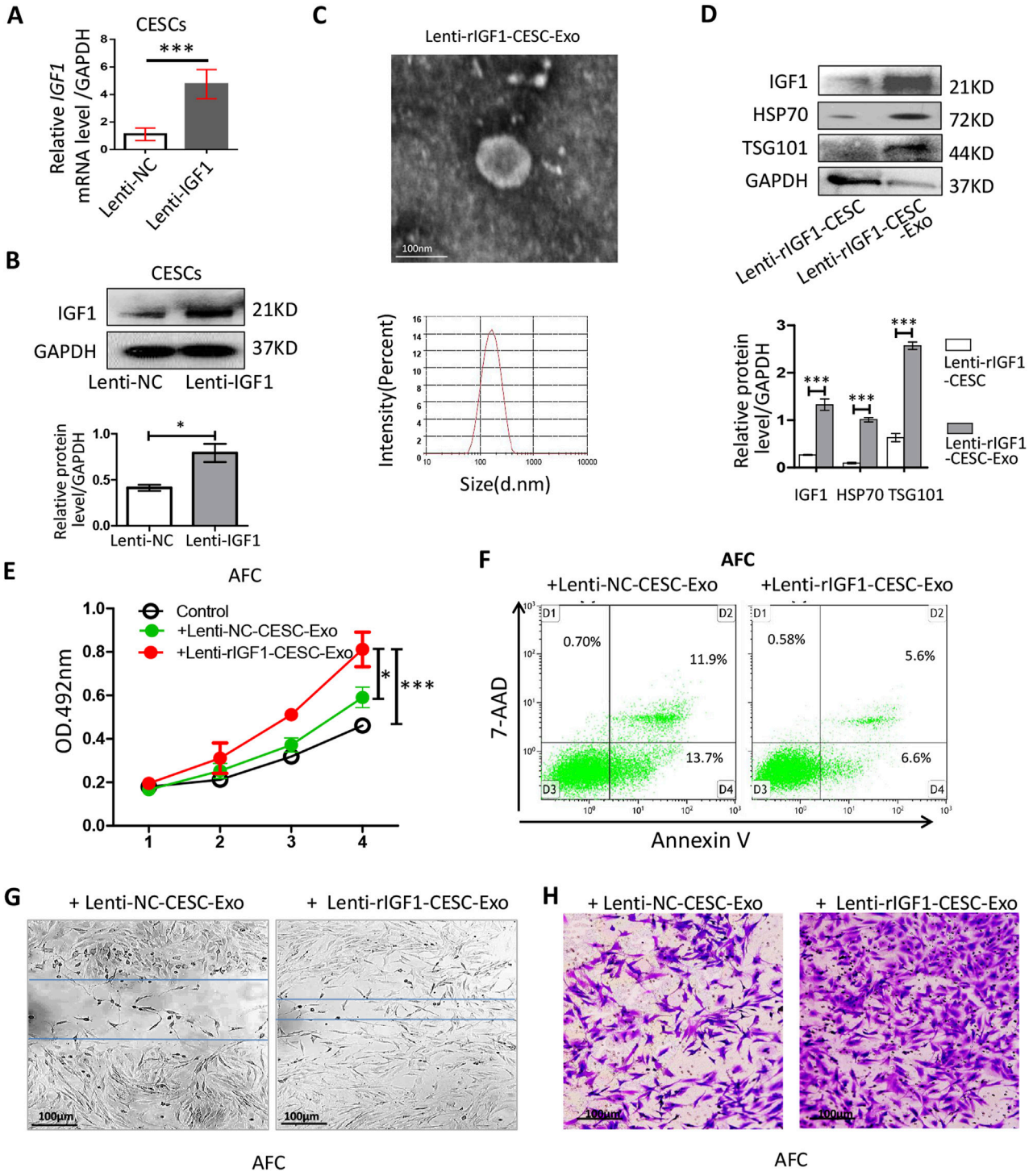


FIGURE 4
Identification of the activity of lent-*rIGF1*-CESC exosomes on AFCs. **(A)** RT-qPCR was used to detect the level of *rIgf1* mRNA in CESCs transfected with the lentiviral *rIgf1* gene or empty vector (NC). **(B)** Western blotting was used to detect the differences in the expression of IGF1 protein. **(C)** Morphology of lent-*rIGF1*-CESCs-Exo was observed by TEM, and particle size was detected through a particle size analyzer. **(D)** Western blotting was used to detect the expressions of lent-*rIGF1*-CESCs-Exo-specific markers (HSP70 and TSG101) and rIGF1 protein. **(E)** Lent-I *rIGF1*-CESCs-Exo was added to the culture medium of AFCs, which were cultured *in vitro* for 4 days, and the cell proliferation was detected by MTT. **(F)** The AnnexinV/7-AAD kit was used to stain the cultured AFCs, and flow cytometry was used to detect apoptosis. **(G)** The migration of lent-*rIGF1*-CESCs-Exo to AFC cells was detected by wound healing and **(H)** transwell assays (crystal violet staining solution for cell nuclei). Data are presented as the mean ± SD in **(B, D)** by two-tailed Student's t-test or in **(E)** by one-way ANOVA. *$p < 0.05$, ***$p < 0.001$.

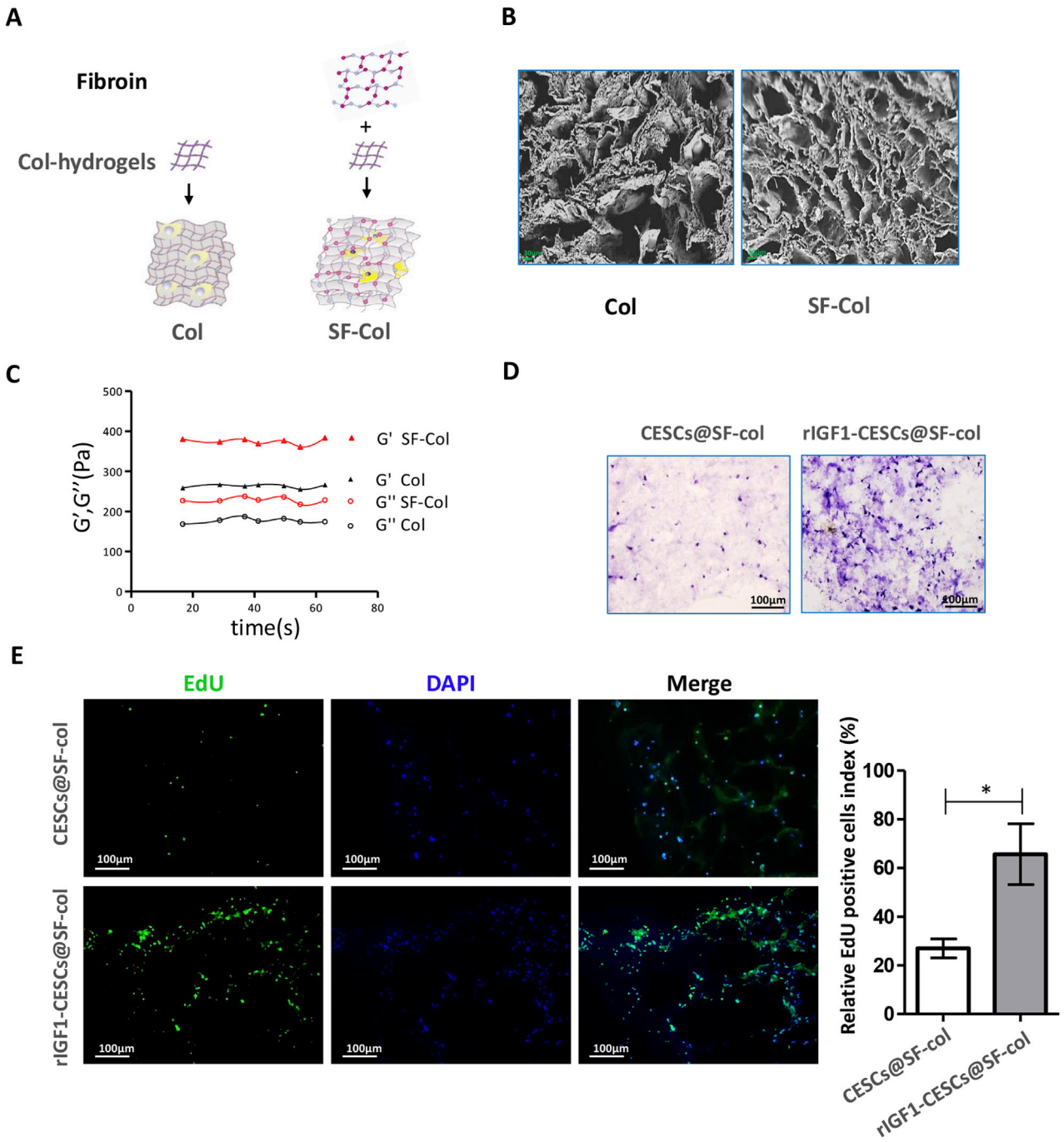


FIGURE 5
SF hydrogel is beneficial for the proliferation of CESCs. **(A)** SF–collagen and collagen hydrogel preparation diagram. **(B)** SEM was used to observe the SF–collagen hydrogel (silk fibroin: 2.5 mg/mL, collagen: 10 mg/mL) and collagen hydrogel (collagen: 10 mg/mL). **(C)** Analysis of storage modulus and loss modulus of SF–collagen hydrogel and collagen hydrogel. **(D)** Hematoxylin/eosin and EdU staining **(E)** to detect the growth of CESCs with or without IGF1 expression in the SF–collagen hydrogel. CESCs are encapsulated in SF–collagen hydrogels and cultured in the medium containing 10% fetal bovine serum for 72 h. Data are presented as the mean ± SD in **(E)**, $*p < 0.05$ by two-tailed Student's t-test.

studies (Le Maitre et al., 2005). There was also no significant difference in the expression of IGFR between healthy NP and degenerated NP (Figures 3B, C).

Recombinant rat IGF1 (rIGF1) (100 ng/mL) was added to the culture media of AFCs and NPCs, and the cells were continuously cultured for 4 days. Subsequently, the MTT assay was used to detect cell proliferation. The rIGF1 effectively promoted the proliferation of AFCs and NPCs (Figure 3D). Wound healing and transwell assays confirmed that IGF1 promoted the migration of AFCs and NPCs (Figures 3E, F). These results suggest that IGF1 can regulate physiological IVD homeostasis by exerting an influence on AF and NP.

3.4 Effects of rIGF1-CESC exosomes on NPCs

We aimed to develop a treatment strategy that could allow rapid healing after AF damage. Increasing the concentration of IGF1 in exosomes enhanced their ability to activate AFCs. We transfected the rat *IGF1* gene into CESCs to construct CESCs-exosomes with a high expression of rIGF1 (IGF1-CESCs-Exo). The *rigf1* gene was transfected into CESCs using a lentivirus. Identification by qRT-PCR and Western blotting showed that lenti-rIGF1-CESCs expressed higher levels of *rigf1* mRNA (Figure 4A) and IGF1 protein (Figure 4B) than the controls. The exosomes were isolated, and their particle size was determined using TEM and particle size analyzer (Figure 4C). The expressions of exosome-specific markers and IGF1 (Figure 4D) were detected by Western blotting, and the results showed that rIGF1-CESCs-Exo was rich in rIGF1 protein.

Exosomes were extracted and added to the AFC culture medium. The MTT assay was used to detect cell proliferation, and rIGF1-CESCs-Exo could increase the growth rate of AFCs (Figure 4E). Flow cytometry was used to detect the apoptosis rate, and the results showed that the ability of rIGF1-CESCs-Exo to inhibit the apoptosis of AFCs was slightly improved compared with that of the control group (Figure 4F). Moreover, wound healing and transwell assays confirmed that rIGF1-CESCs-Exo significantly enhanced the migration ability of AFCs (Figures 4G,H).

These results indicate that promoting the activation and proliferation of AFCs by releasing rIGF1-rich exosomes from rIGF1-CESCs is a potential strategy for repairing damaged AF.

3.5 Preparation and identification of SF hydrogel biomaterials

To obtain exosomes of rIGF1-CESC engineered cells, we further prepared materials that could carry cells within the IVD to enable them to proliferate stably and continuously release exosomes containing the IGF1 protein, thereby enhancing the potential for wound treatment.

SF exhibits excellent biocompatibility and is used to treat damaged AF [10]. The SF solution was combined with a collagen hydrogel to form an SF–collagen hydrogel (with a silk fibroin concentration of 2.5 mg/mL and a collagen concentration of 10 mg/mL) (Figure 5A). SEM revealed that the pore size of the SF–collagen hydrogel was slightly smaller than that of the pure collagen hydrogel (Figure 5B). Moreover, both the storage modulus (G′) and the loss modulus (G″) of the SF–collagen hydrogel were higher than those of the pure collagen hydrogel, indicating that its mechanical strength was superior to that of the pure collagen hydrogel material (Figure 5C), which gave it an advantage in terms of the compressive capacity in the IVD.

To examine the impact of the material on cell activity, we placed composites of CESCs and SF–collagen hydrogels in the culture medium for continuous culture. After 72 h, HE staining was performed, and microscopic observations showed that the number of rIGF1-CESC cells in the SF–collagen hydrogel was significantly greater than the number of CESC cells in SF–collagen hydrogel (Figure 5D). 5-Ethynyl-2′-deoxyuridine (EdU) staining also confirmed that rIGF1-CESC had also gained better proliferation and survival ability (Figure 5E), which enables it to continuously release a large amount of exosomes containing rIGF1, thereby promoting the proliferation of surrounding AFCs and accelerating AF repair.

3.6 rIGF1-CESCs@SF-collagen hydrogel attenuated IVD degeneration in rats

To verify the effects of the rIGF1–CESCs@SF–collagen hydrogel on the treatment of AF wounds, rats were divided into the following groups: the healthy control group, puncture group, the CESCs @SF-collagen hydrogel group, and the rIGF1-CESCs@SF-collagen hydrogel treatment group. A puncture was used to induce damage to the AF of the rat tail IVD. CESCs@ SF-collagen hydrogel or rIGF1-CESCs@SF-collagen hydrogel was then injected into the AF damage site. One week later, IVDs were isolated, and immunofluorescence was used to detect the protein expression and localization of cleaved caspase-3 and IGF1. After puncture, the expression of cleaved caspase-3 in the IVD tissues of each experimental group increased, and the concentration of IGF1 in the rIGF1-CESCs@SF-collagen hydrogel experimental group significantly increased (Figure 6). The elevation of IGF1 to some extent inhibits the expression of cleaved caspase-3. Six weeks later, MRI detection of tail IVD and acquisition of images (Figures 7A,B) and Safranin O-fast green staining of the isolated IVDs (Figure 7C) were carried out. The above results showed that the rIGF1–CESCs@SF–collagen hydrogel effectively repaired the damaged AF, maintained the integrity of the NP by preventing the loss and death of NPCs, maintained the height of the IVD, and significantly attenuated IVD degeneration.

4 Discussion

The CEP is a crucial hub connecting the IVD to the vertebrae and is an essential pathway for the nutrition and metabolism of the IVD. CESCs are derived from CEP tissues and play an important role in maintaining normal physiological functions of the entire IVD and CEP. Multiple studies have confirmed that CESCs secrete various factors (Shang et al., 2015) and extracellular vesicles (Luo et al., 2021a; Luo et al., 2021b) to regulate IVD function. In the treatment of IVD diseases using stem cells (such as mesenchymal stem cells and adipose-derived stem cells), the ECM is generated by inducing stem cell differentiation into NPCs or AFCs to induce repair in the IVD. CESCs are derived from the IVD and thus have higher compatibility than mesenchymal stem cells and adipose-derived stem cells. Based on our extensive research experience with CESCs (Luo et al., 2022; Luo et al., 2021a; Luo et al., 2021b) and SF (Luo et al., 2023; Wang et al., 2023), we performed IVD treatment experiments using these two materials.

Through proteomic mass spectrometry, we found that CESC-exosomes (CESC-Exos) were rich in rIGF1. IGF is crucial for the growth and development of bone tissues (McCarthy et al., 1989) and directly inhibits IVD degeneration (Liu et al., 2015). It has been speculated that CESCs could maintain the physiological balance of IVDs by releasing IGF1 via extracellular vesicles. Through mRNA

10.3389/fphar.2025.1552174

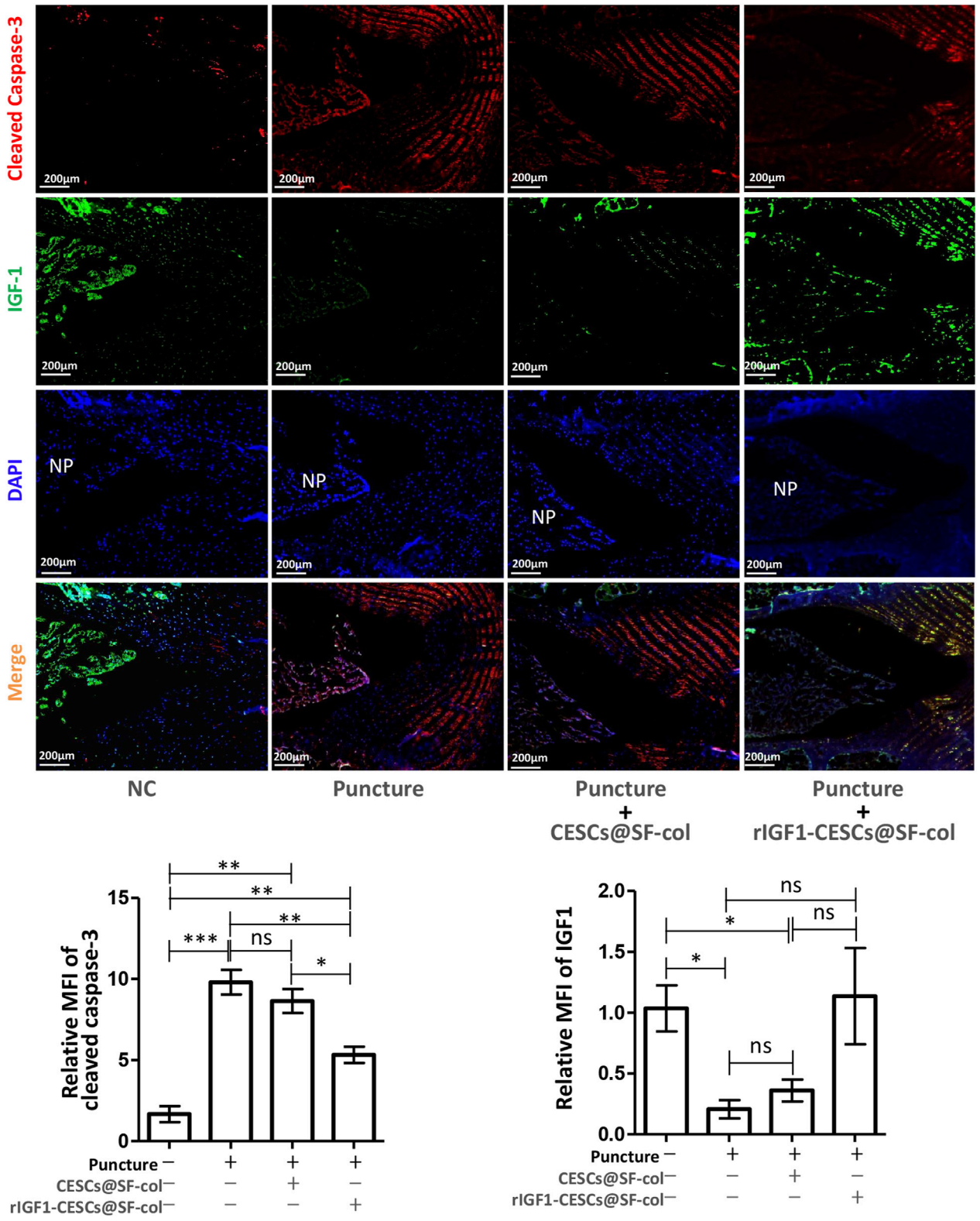


FIGURE 6
rIGF1-CESCs@SF–collagen hydrogel releases IGF1 and inhibits apoptosis of cells within IVD. Design grouping: healthy control group, puncture group, the CESCs@SF-collagen hydrogel treatment group, and rIGF1-CESCs@SF-collagen hydrogel group. A puncture damage in AF tissue and injection of hydrogel for wound treatment; 1 week later, three rats in each group were taken, the tail IVDs of rats were separated, and the cleaved caspase-3 (red) and IGF1 (green) were detected by immunofluorescence. Data are presented as the mean ± SD; *$p < 0.05$, **$p < 0.01$, and ***$p < 0.001$. ns: not significant by one-way ANOVA.

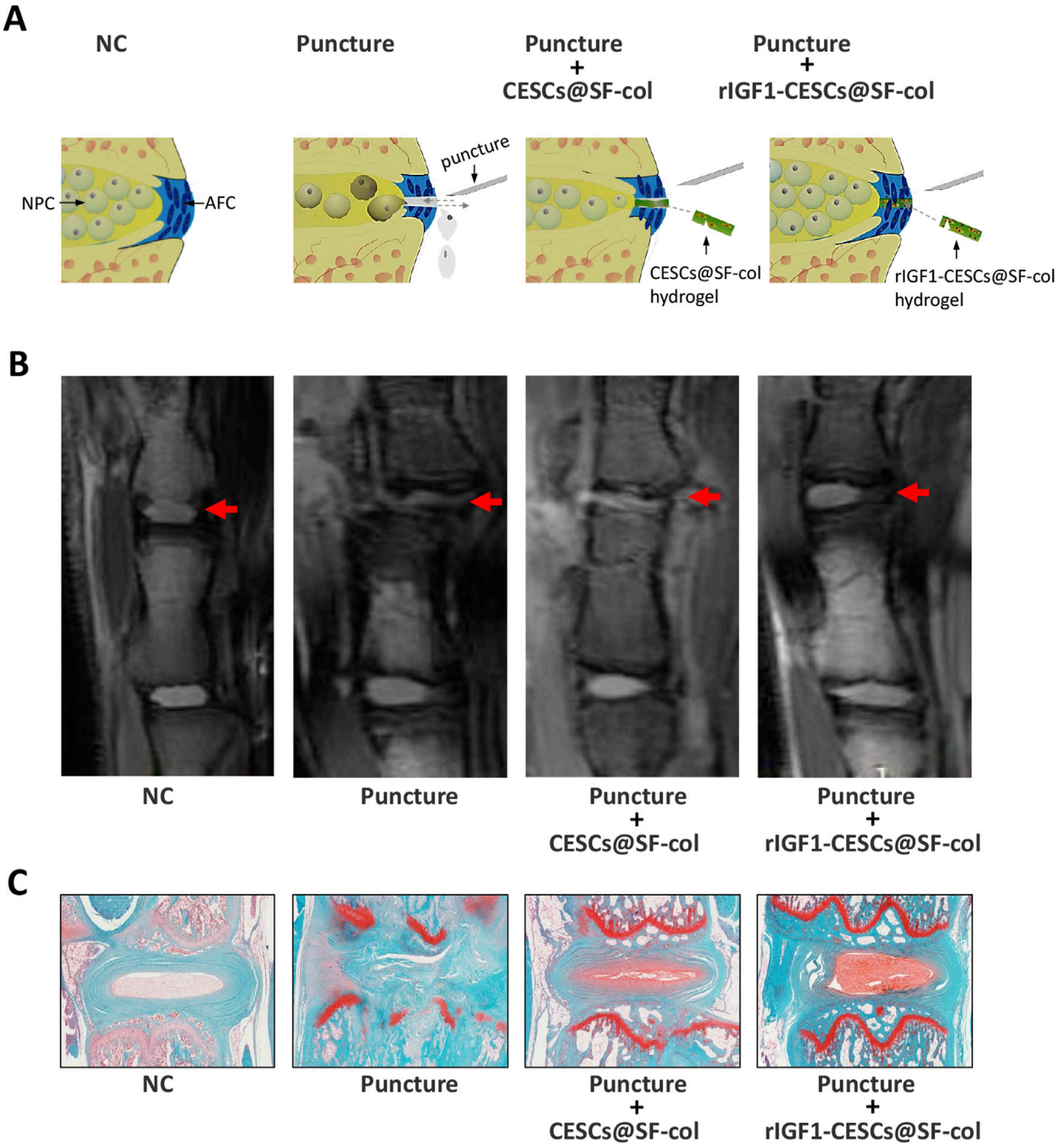


FIGURE 7
rIGF1-CESCs@SF-collagen hydrogel attenuates the degeneration of IVD in rats. **(A)** Graphic description of treatment for AF wounds with rIGF1-CESCs@SF-collagen hydrogel. **(B)** In the sixth week after AF tissues were punctured, the IVD was detected using MRI, and then they were separated. Safranin O-fast green staining **(C)**, microscopic observation, and imaging were performed. n = 3.

and protein detection, we observed that IGF1 was abundantly present in mildly degenerated human CEP regions of IVD tissues, whereas it was expressed at low levels in severely degenerated tissues. The results of the rat experiments were similar to those in humans, with IGF1 being highly expressed in the CEP and NP regions of healthy rats. We isolated and cultured rat NPCs and AFCs *in vitro* and determined the effects of IGF1 on these two cell types. Because IGF1 needs to bind to the IGFR of target cells and activate multiple intracellular signaling pathways to perform its functions, we examined the expression of IGFR in these two cell types. Western blotting revealed IGFR expressions in both AF and NP tissues, with no significant differences in IGFR expression between healthy and degenerated tissues. Recombinant rIGF1 was added to AFCs and NPCs cultured *in vitro*. The MTT assay confirmed that rIGF1 effectively promoted the proliferation of AFCs and NPCs. Wound healing and transwell assays confirmed

that IGF1 contributed to the migration of AFCs and NPCs. This indicates that the IGF1/IGFR pathway could activate AFCs within the IVD. Furthermore, rIGF1 was overexpressed in CESCs, and exosomes were extracted. When the latter was added to the culture medium of AFCs *in vitro*, AFC activity was enhanced. This confirms that CESCs promote the proliferation and migration of cells by activating the IGF1/IGFR signaling network of AFCs through the release of IGF1-exosomes. This provided an engineered cellular exosome that could rapidly repair damaged AF.

Furthermore, we searched for materials that could support the growth of CESCs within the IVD. SF has been widely used in studies on repair and degeneration after IVD damage (Lin et al., 2023). SF–collagen hydrogels were prepared using silk fibroin and collagen. SEM and strength tests confirmed that it had a loose and porous structure and relatively high compressive capacity, making it suitable for treating IVD tissues. EdU staining confirmed that it promotes CESC growth. To further verify the effect of the rIGF1-CESCs@SF-collagen hydrogel on the treatment of AF wounds, puncture was used to induce damage to the AF in rat IVD. Meanwhile, the rIGF1-CESCs@SF-collagen hydrogel was injected at the wound site. Immunofluorescence was used to detect the expressions of cleaved caspase-3 and IGF1. After puncture, the expression of cleaved caspase-3 in the IVD tissues of each experimental group increased, whereas the expression of IGF1 in the rIGF1-CESCs@SF-collagen hydrogel experimental group increased. The concentration of IGF1 is negatively correlated with the expression of cleaved caspase-3, and IGF1 inhibited the expression of cleaved caspase-3, suggesting that IGF1 may promote wound healing in AF tissue by inhibiting AFC cell apoptosis and promoting proliferation. MRI detection and Safranin O-fast green staining of the IVDs at 6 weeks showed that the rIGF1-CESCs@SF-collagen hydrogel significantly inhibited IVD degeneration, and it is effective for wound treatment of AF.

This indicates that the rIGF1-CESCs@SF-collagen hydrogel can accelerate the healing of AF wound tissues and prevent the loss of NP tissues. This is an ideal strategy for the treatment of IVD injury and degeneration and provides meaningful references for basic and clinical research in this field. There is a significant difference between real-world AF injury and induced injury in rat AF, which will bring unpredictable difficulties to wound treatment. However, many drawbacks of stem cells still exist, such as uncontrolled expansion and cell aging. In addition, the function of exosomes released by uncontrolled or aging stem cells is also affected, leading to uncontrollable consequences for treatment. Therefore, further exploration of CESCs to maintain the stability of their stem cells and sustain the release of functional exosomes *in vivo* is crucial (Meng et al., 2020). In addition, the immunologic responses to the activated SF–collagen hydrogel are still in the shadows. Although SF and hydrogel are generally considered medical materials with low immunogenicity, they can still induce inflammatory reaction to a certain extent, and the difference in the processing technology of SF will also have different effects on the resistance of the mammalian immune system (Majumder et al., 2024). Therefore, a large number of *in vivo* and *in vitro* experiments are still needed before the clinical application of the rIGF1-CESCs@SF-collagen hydrogel.

Data availability statement

The original contributions presented in the study are included in the article/supplementary material; further inquiries can be directed to the corresponding authors.

Ethics statement

The studies involving humans were approved by the Medical Ethics Committee of 903 Hospital of Joint Logistic Support Force of The People's Liberation Army. The studies were conducted in accordance with the local legislation and institutional requirements. The participants provided their written informed consent to participate in this study. The animal study was approved by the Animal Ethics Committee of Army Medical University. The study was conducted in accordance with the local legislation and institutional requirements.

Author contributions

ZT: conceptualization, data curation, investigation, and writing–original draft. ZS: data curation, investigation, and writing–review and editing. HC: funding acquisition and writing–review and editing. PZ: funding acquisition, supervision, validation, and writing–review and editing.

Funding

The author(s) declare that financial support was received for the research and/or publication of this article. The National Natural Science Foundation of China (No. 32172798) and the Medical and Health Science and Technology Program of Zhejiang (2025KY1192) provided support for this work.

Acknowledgments

The authors would like to thank Editage (www.editage.cn) for English language editing.

Conflict of interest

The authors declare that the research was conducted in the absence of any commercial or financial relationships that could be construed as a potential conflict of interest.

Generative AI statement

The authors declare that no generative AI was used in the creation of this manuscript.

Publisher's note

All claims expressed in this article are solely those of the authors and do not necessarily represent those of their affiliated organizations, or those of the publisher, the editors and the reviewers. Any product that may be evaluated in this article, or claim that may be made by its manufacturer, is not guaranteed or endorsed by the publisher.

References

Bhattacharjee, M., Miot, S., Gorecka, A., Singha, K., Loparic, M., Dickinson, S., et al. (2012). Oriented lamellar silk fibrous scaffolds to drive cartilage matrix orientation: towards annulus fibrosus tissue engineering. *Acta Biomater.* 8 (9), 3313–3325. doi:10.1016/j.actbio.2012.05.023

Chen, R. S., Zhang, X. B., Zhu, X. T., and Wang, C. S. (2020). The crosstalk between IGF-1R and ER-α in the proliferation and anti-inflammation of nucleus pulposus cells. *Eur. Rev. Med. Pharmacol. Sci.* 24 (11), 5886–5894. doi:10.26355/eurrev_202006_21481

Elmasry, S., Asfour, S., de Rivero Vaccari, J. P., and Travascio, F. (2016). A computational model for investigating the effects of changes in bioavailability of insulin-like growth factor-1 on the homeostasis of the intervertebral disc. *Comput. Biol. Med.* 78, 126–137. doi:10.1016/j.compbiomed.2016.09.016

Farokhi, M., Mottaghitalab, F., Fatahi, Y., Khademhosseini, A., and Kaplan, D. L. (2018). Overview of silk fibroin use in wound dressings. *Trends Biotechnol.* 36 (9), 907–922. doi:10.1016/j.tibtech.2018.04.004

Fernandes, L. M., Khan, N. M., Trochez, C. M., Duan, M., Diaz-Hernandez, M. E., Presciutti, S. M., et al. (2020). Single-cell RNA-seq identifies unique transcriptional landscapes of human nucleus pulposus and annulus fibrosus cells. *Sci. Rep.* 10 (1), 15263. doi:10.1038/s41598-020-72261-7

Freemont, A. J. (2009). The cellular pathobiology of the degenerate intervertebral disc and discogenic back pain. *Rheumatol. Oxf.* 48 (1), 5–10. doi:10.1093/rheumatology/ken396

Le Maitre, C. L., Richardson, S. M., Baird, P., Freemont, A. J., and Hoyland, J. A. (2005). Expression of receptors for putative anabolic growth factors in human intervertebral disc: implications for repair and regeneration of the disc. *J. Pathol.* 207 (4), 445–452. doi:10.1002/path.1862

Lin, M., Hu, Y., An, H., Guo, T., Gao, Y., Peng, K., et al. (2023). Silk fibroin-based biomaterials for disc tissue engineering. *Biomater. Sci.* 11 (3), 749–776. doi:10.1039/d2bm01343f

Liu, Z., Zhou, K., Fu, W., and Zhang, H. (2015). Insulin-like growth factor 1 activates PI3k/akt signaling to antagonize lumbar disc degeneration. *Cell. Physiol. Biochem.* 37 (1), 225–232. doi:10.1159/000430347

Luo, L., Gong, J., Wang, Z., Liu, Y., Cao, J., Qin, J., et al. (2022). Injectable cartilage matrix hydrogel loaded with cartilage endplate stem cells engineered to release exosomes for non-invasive treatment of intervertebral disc degeneration. *Bioact. Mater* 15, 29–43. doi:10.1016/j.bioactmat.2021.12.007

Luo, L., Gong, J., Zhang, H., Qin, J., Li, C., Zhang, J., et al. (2021b). Cartilage endplate stem cells transdifferentiate into nucleus pulposus cells via autocrine exosomes. *Front. Cell. Dev. Biol.* 9, 648201. doi:10.3389/fcell.2021.648201

Luo, L., Jian, X., Sun, H., Qin, J., Wang, Y., Zhang, J., et al. (2021a). Cartilage endplate stem cells inhibit intervertebral disc degeneration by releasing exosomes to nucleus pulposus cells to activate Akt/autophagy. *Stem Cells* 39 (4), 467–481. doi:10.1002/stem.3322

Luo, L., Zhang, H., Zhang, S., Luo, C., Kan, X., Lv, J., et al. (2023). Extracellular vesicle-derived silk fibroin nanoparticles loaded with MFGE8 accelerate skin ulcer healing by targeting the vascular endothelial cells. *J. Nanobiotechnology* 21 (1), 455. doi:10.1186/s12951-023-02185-7

Majumder, N., Bhattacharjee, M., Spagnoli, G. C., and Ghosh, S. (2024). Immune response profiles induced by silk-based biomaterials: a journey from 'immunogenicity' towards 'immuno-compatibility. *J. Mater Chem. B* 12 (38), 9508–9523. doi:10.1039/d4tb01231c

McCarthy, T. L., Centrella, M., and Canalis, E. (1989). Insulin-like growth factor (IGF) and bone. *Connect. Tissue Res.* 20 (1-4), 277–282. doi:10.3109/03008208909023897

Meng, Q. S., Liu, J., Wei, L., Fan, H. M., Zhou, X. H., and Liang, X. T. (2020). Senescent mesenchymal stem/stromal cells and restoring their cellular functions. *World J. Stem Cells* 12 (9), 966–985. doi:10.4252/wjsc.v12.i9.966

Rani, S., and Ritter, T. (2016). The exosome - a naturally secreted nanoparticle and its application to wound healing. *Adv. Mater* 28 (27), 5542–5552. doi:10.1002/adma.201504009

Rutges, J., Creemers, L. B., Dhert, W., Milz, S., Sakai, D., Mochida, J., et al. (2010). Variations in gene and protein expression in human nucleus pulposus in comparison with annulus fibrosus and cartilage cells: potential associations with aging and degeneration. *Osteoarthr. Cartil.* 18 (3), 416–423. doi:10.1016/j.joca.2009.09.009

Shang, J., Fan, X., Shangguan, L., Liu, H., and Zhou, Y. (2015). Global gene expression profiling and alternative splicing events during the chondrogenic differentiation of human cartilage endplate-derived stem cells. *Biomed. Res. Int*, doi:10.1155/2015/604972

Sloan, S. R., Jr., Wipplinger, C., Kirnaz, S., Navarro-Ramirez, R., Schmidt, F., McCloskey, D., et al. (2020). Combined nucleus pulposus augmentation and annulus fibrosus repair prevents acute intervertebral disc degeneration after discectomy. *Sci. Transl. Med.* 12 (534), eaay2380. doi:10.1126/scitranslmed.aay2380

Tan, F., Xu, M. X., Li, X. R., Wang, Z., Li, J. J., and Shahzad, K. A. (2024). Biomaterial-facilitated local delivery of stem cell-derived small extracellular vesicles: perspectives in surgical therapy. *Adv. Ther.* 7 (4). doi:10.1002/adtp.202300387

van den Akker, G. G., Surtel, D. A., Cremers, A., Richardson, S. M., Hoyland, J. A., van Rhijn, L. W., et al. (2016). Novel immortal cell lines support cellular heterogeneity in the human annulus fibrosus. *PLoS One* 11 (1), e0144497. doi:10.1371/journal.pone.0144497

Wang, H., Wang, D., Luo, B., Wang, D., Jia, H., Peng, P., et al. (2022). Decoding the annulus fibrosus cell atlas by scRNA-seq to develop an inducible composite hydrogel: a novel strategy for disc reconstruction. *Bioact. Mater* 14, 350–363. doi:10.1016/j.bioactmat.2022.01.040

Wang, R., Wang, Y., Song, J., Tian, C., Jing, X., Zhao, P., et al. (2023). A novel method for silkworm cocoons self-degumming and its effect on silk fibers. *J. Adv. Res.* 53, 87–98. doi:10.1016/j.jare.2022.12.005

Xian, L., Wu, X., Pang, L., Lou, M., Rosen, C. J., Qiu, T., et al. (2012). Matrix IGF-1 maintains bone mass by activation of mTOR in mesenchymal stem cells. *Nat. Med.* 18 (7), 1095–1101. doi:10.1038/nm.2793

Xiao, Q., Teng, Y., Xu, C., Pan, W., Yang, H., Zhao, J., et al. (2021). Role of PI3K/AKT signaling pathway in nucleus pulposus cells. *Biomed. Res. Int.*, doi:10.1155/2021/9941253

Zhang, X., Xing, H., Qi, F., Liu, H., Gao, L., and Wang, X. (2020). Local delivery of insulin/IGF-1 for bone regeneration: carriers, strategies, and effects. *Nanotheranostics* 4 (4), 242–255. doi:10.7150/ntno.46408

frontiers | Frontiers in Pharmacology

TYPE Original Research
PUBLISHED 23 April 2025
DOI 10.3389/fphar.2025.1587351

Check for updates

OPEN ACCESS

EDITED BY
Yapei Zhang,
Michigan State University, United States

REVIEWED BY
Ilya D. Klabukov,
National Medical Research Radiological Center, Russia
Arihant Kumar Singh,
Michigan State University, United States

*CORRESPONDENCE
Dongxu Zhang,
zhangdxwy@163.com
Jitao Wu,
wjturology@163.com

†These authors have contributed equally to this work

RECEIVED 04 March 2025
ACCEPTED 08 April 2025
PUBLISHED 23 April 2025

CITATION
Yang Y, Wu G, Wang Y, Mao Q, Zhang D and Wu J (2025) LL37 promotes angiogenesis: a potential therapeutic strategy for lower limb ischemic diseases.
Front. Pharmacol. 16:1587351.
doi: 10.3389/fphar.2025.1587351

COPYRIGHT
© 2025 Yang, Wu, Wang, Mao, Zhang and Wu. This is an open-access article distributed under the terms of the Creative Commons Attribution License (CC BY). The use, distribution or reproduction in other forums is permitted, provided the original author(s) and the copyright owner(s) are credited and that the original publication in this journal is cited, in accordance with accepted academic practice. No use, distribution or reproduction is permitted which does not comply with these terms.

LL37 promotes angiogenesis: a potential therapeutic strategy for lower limb ischemic diseases

Yingying Yang, Gang Wu, Yini Wang, Qiancheng Mao, Dongxu Zhang*† and Jitao Wu*†

Yantai Yuhuangding Hospital, Yantai, China

Purpose: To study the angiogenic capacity of antimicrobial peptide LL37 (cathelicidin antimicrobial peptide), explore its molecular mechanisms, and provide new ideas for treating lower limb ischemic diseases.

Methods: LL37 was applied exogenously to human umbilical vein endothelial cells (HUVECs), and its effects on cell proliferation, migration, and angiogenesis were assessed using Cell Counting Kit-8 (CCK-8), plate cloning, scratch, and angiogenesis assays. A mouse lower limb ischemia model was established, with LL37 injected intramuscularly on days 0, 4, and 8. Blood flow recovery was evaluated by laser Doppler flowmetry. Immunofluorescence staining detected cluster of differentiation 31 (CD31) and cluster of differentiation 34 (CD34) expression, while Hematoxylin and Eosin (H&E) staining assessed muscle cell morphology. Quantitative real-time polymerase chain reaction (qRT-PCR) and Western blotting analyzed gene and protein expression changes in HUVECs.

Results: LL37 enhanced the proliferative, migratory, and pro-angiogenic abilities of HUVECs. It significantly improved blood flow recovery in ischemic limbs, with higher CD31/CD34 expression and more intact muscle morphology. qRT-PCR analysis demonstrated elevated expression of angiogenesis-related genes in LL37-treated HUVECs. Western blotting revealed increased vascular endothelial growth factor A (VEGFA) expression and enhanced phosphorylation levels of the phosphatidylinositol 3-kinase (PI3K)/protein kinase B (AKT)/mammalian target of rapamycin (mTOR) pathway in LL37-treated cells.

Conclusion: LL37 promotes angiogenesis via the VEGFA-PI3K/AKT/mTOR pathway, showing potential for treating lower limb ischemia by improving perfusion.

KEYWORDS

antimicrobial peptide, LL37, VEGFA-PI3K/AKT/mTOR pathway, angiogenesis, lower limb ischemia

1 Introduction

Chronic limb ischemia (CLTI) is the end stage of peripheral arterial disease (PAD). It is a disease characterized by intermittent claudication, ulceration or gangrene of the limbs due to various reasons such as narrowing or occlusion of the arteries and inadequate blood perfusion (Farber, 2018; Beard, 2000). It is a problem with high morbidity and high healthcare costs worldwide. Of these, lower limb ischemic disease is the most common type (Levin et al., 2020). Currently, there is no standardized treatment for CLTI in most

countries, and treatment varies considerably from region to region, resulting in CLTI still being associated with higher rates of amputation. Surgical bypass and endovascular therapy are the main blood supply reconstruction strategies for the treatment of CLTI (Cheng and Farber, 2024; Zeller et al., 2009). However, conservative treatments are more in line with the needs of some patients due to the limitations of operators, patients' arterial disease patterns, surgical risks, available autologous venous bypass access, and patient preferences, placing new demands on the search for appropriate drugs (Desai et al., 2024).

Cathelicidin, a family of antimicrobial peptides (AMPs), is a critical component of the body's innate immune system and is widely expressed across species. These small bioactive polypeptides are induced in response to infection and inflammation (Agier et al., 2015; Zhang Q. et al., 2023). In humans, cathelicidins are primarily represented by two major groups: defensins and the sole cathelicidin-derived peptide, LL37 (Fry, 2018; Izadpanah and Gallo, 2005). The name "LL37" reflects its structure—a 37-amino acid peptide originating from the N-terminal cleavage of the cathelicidin precursor protein, with leucine (L) as its first two residues.

LL37 exhibits broad-spectrum antimicrobial activity against Gram-positive and Gram-negative bacteria, fungi, and viruses (Luo et al., 2019; Rashki et al., 2022). I Beyond its direct microbicidal effects, LL37 plays a multifaceted role in immune regulation, including modulation of inflammatory mediators, immune cell chemotaxis, cytokine release, endotoxin neutralization, and even tumor suppression or promotion depending on the context (Chieosilapatham et al., 2018; Frasca and Lande, 2012).

The formation of new blood vessels is a prerequisite for tissue repair and improvement of ischemic symptoms (Veith et al., 2019). Angiogenesis is caused by various factors, from mechanical stress and hypoxia to the presence of soluble inflammatory mediators, and involves the germination of small capillaries (angiogenesis) and the growth of existing blood vessels (arteriogenesis) (Eelen et al., 2020; Kuwano et al., 2001). Emerging evidence highlights LL37 as a potent modulator of vascular growth. Studies have shown that LL37 promotes endothelial cell migration, tube formation, and VEGF-mediated signaling, accelerating wound healing and ischemic tissue recovery (Khung et al., 2015). For instance, LL37 activates formyl peptide receptor 2 (FPR2) and Epidermal Growth Factor Receptor/Extracellular Signal-Regulated Kinase (EGFR/ERK) pathways, mimicking pro-angiogenic factors like Vascular Endothelial Growth Factor (VEGF) (Tjabringa et al., 2003; Zhang H. et al., 2023). Additionally, LL37 synergizes with hypoxia-inducible factors (HIFs) to enhance perfusion in diabetic and ischemic models (Rodríguez-Martínez et al., 2008).

Despite these advances, the precise mechanisms by which LL37 influences functional angiogenesis and arterial growth remain incompletely understood. In this study, we investigate the role of LL37 in driving therapeutically relevant angiogenesis and evaluate its potential for treating ischemic diseases.

2 Materials and methods

2.1 Cell culture

Human umbilical vein endothelial cells (HUVECs) were purchased from the Shanghai Institute of Cell Biology, Chinese Academy of Sciences. HUVECs were cultured in DMEM medium supplemented with 10% FBS, 1% penicillin/streptomycin, and the cell lines were maintained at 37°C in a humidified 5% CO2 atmosphere. Cells were used between passages three and six to ensure consistent cell behavior, prior to treatment with: LL-37 (MCE, Cat# HY-P1222, ddH_2O); VEGF165 (MCE, Cat#HEK293, 0.1% BSA); Control: phosphate-buffered saline (PBS) (Gibco, Cat# 10010001).

2.2 Cell Counting Kit-8 (CCK8) cell proliferation experiment

HUVECs were seeded in 96-well plates at 4,000 cells per well. LL37 was added to the experimental group to 5 μg/mL, and an equal volume of PBS was added to the control group. 10 μL CCK8 (Beyotime, Cat# C0038) was added to each well at 0, 12, 24, 36, and 48 h, and OD550 absorbance was measured 1 h later (Thermo Fisher Company, United States). Growth curves were plotted based on OD values to analyze the results. The experiment was repeated three times to ensure data reliability.

2.3 Clonogenic assay

HUVECs were seeded in 6-well plates at a density of 1,000 cells per well. LL37 was added to the experimental group to 5 μg/mL, and an equal volume of PBS was added to the control group. The medium was changed every 3 days, and cells were cultured for 12 days. 4% paraformaldehyde was added to each well to fix the cells for 20 min 700 μL of crystal violet (Beyotime, Beijing, China) was added to each well, left for 30 min at room temperature away from light. The number of clones >10 cells was counted by ImageJ. The experiment was repeated three times.

2.4 Angiogenesis test

Matrigel Basement Membrane Matrix (BD Biosciences) was melted overnight in a 4°C refrigerator. 50 μL/well of Matrigel gel was added to a pre-cooled 96-well plate and left at 37°C for 45 min to solidify. HUVECs were seeded at a density of 3×10^4 cells/well onto the Matrigel gel. The experimental group was incubated with complete medium containing LL37 (5 μg/mL) or VEGF165 (20 ng/mL), and the control group was incubated with complete medium only. Photographs were taken at 4, 6, and 10 h, and the number of tubes and branches were quantified using ImageJ software. The experiment was repeated three times.

2.5 Scratching experiment

HUVECs were seeded into six-well plates and cultured until the cell density reached approximately 90%. A 'cross' was drawn in the center of each well with a sterile 1 mL pipette tip. The wells were rinsed with PBS to remove cell debris, and fresh serum-free DMEM medium was added. LL37 (5 μg/mL) was added to the experimental group, while the control group received only fresh serum-free

DMEM medium. Microscopic photographs were taken at 0, 24, and 48 h after the scratch, and the migration distance was measured. The experiment was repeated three times.

2.6 Transwell assay

Transwell assays were performed using Transwell inserts (8 μm pore size, BD Biosciences, United States) inserted into 24-well plates. For invasion assays, the upper chamber was coated with Matrigel (BD Biosciences, United States of America). The upper chamber was then coated with 200 μL of serum-free medium. In the experimental group, LL37 was added to a final concentration of 5 μg/mL, while no LL37 was added to the control group. The upper chamber contained either 2×10^4 cells (for migration assays) or 3×10^4 cells (for invasion assays). The lower chamber contained 700 μL of medium supplemented with 10% fetal bovine serum (FBS). After incubation at 37°C for 24 h, the cells were fixed with methanol, stained with 0.5% crystal violet, and observed and quantified under a light microscope.

2.7 Real-time quantitative RT–PCR (qRT–PCR)

Experimental HUVECs were treated with 5 μg/mL of LL37 for 24 h or 48 h, while control HUVECs were not treated with LL37. Total Ribonucleic Acid (RNA) was extracted from the HUVECs using a total RNA kit (Omega Biotek, Norcross, GA, United States of America) according to the manufacturer's instructions. The RNA concentration was determined by measuring the ratio of absorbance at 260 nm to absorbance at 280 nm. The RNA was then reverse transcribed to cDNA using PrimeScript RT Master Mix (Zhongke Bioengineering Co., Ltd.). Quantitative PCR was performed using TB Green Premix Ex Taq II (Zhongke Bioengineering Co., Ltd.) on a Light Cycler 96 (Roche Group). The expression levels of the relevant genes were normalized to GAPDH, and the fold change was calculated using the comparative threshold cycling (ΔΔCt) method.

2.8 Animal culture

Clean-grade mice (C57BL/6) were purchased from Beijing Viton Lihua Laboratory Animal Technology Co. And housed under standard laboratory conditions (temperature 22°C ± 2°C, humidity 50%–60%, 12-h light/dark cycle). We used a non-invasive fluorescent labeling method to label and characterize the animal model. After shaving the dorsal fur of mice, numbering was performed using a 1% fluorescein sodium solution. Marking clarity was verified daily under UV light. The labeled area was maintained at least 1 cm away from the wound site (Klabukov et al., 2023). The study protocol was reviewed and approved by the Animal Ethics Committee of Yantai Yuhuangding Hospital (Approval Number 2025-YHD-036). This study report adheres to the ARRIVE 2.0 guidelines (Animal Research: Reporting of *In Vivo* Experiments) (Kilkenny et al., 2010).

2.9 Lower limb ischemia model in mice

Twenty-four 8-week-old C57/BL6J mice were randomly divided into three groups: Sham, Model, and LL37. After anesthesia and disinfection, a longitudinal incision was made from the groin to expose the femoral artery. In the Model and LL37 groups, the femoral artery was ligated, while the Sham group remained unligated. Quadriceps muscle injections were given on postoperative days 1, 4, and 8. The LL37 group received 25 μL of 5 μg/mL LL37 at 4 sites, and the Model group received an equal volume of PBS. Laser Doppler flow imaging was performed on days 0, 7, 14, and 21. The images allowed direct comparison of the pseudo-color images of the affected and the healthy side to quickly identify abnormal areas of perfusion. Quantitatively analyzed the perfusion situation by measuring the perfusion values of the injured and healthy limbs and calculating the ratio.

2.10 Hematoxylin-eosin (H&E) staining

Paraffin sections of mouse quadriceps muscle tissue were baked in an oven at 65°C for 45 min. Place in xylene I (15 min), xylene II (15 min), anhydrous ethanol I (10 min), anhydrous ethanol II (10 min), 95% ethanol (10 min), and 85% alcohol (10 min) for gradient dewaxing. Place in hematoxylin for 10 min and rinse with water. Place in 1% aqueous hydrochloric acid solution for a few seconds and rinse with water. Place in 1% ammonia solution for 1 min and rinse with running water. Place in eosin staining solution for a few seconds and rinse with running water. Place in 75% ethanol (2 min), 85% ethanol (2 min), anhydrous ethanol (5 min), anhydrous ethanol (5 min), xylene (5 min) for dehydration. The slices were sealed with neutral gum, dried naturally, and observed under the microscope.

2.11 Immunofluorescence

HUVECs were cultured in 6-well plates. The experimental group was treated with LL37 in complete culture medium for 48 h, while the control group was untreated. Cells were fixed with 4% paraformaldehyde for 20 min at room temperature. Cells were permeabilized with 0.5% Triton X-100 (diluted in PBS) for 20 min at room temperature. Cells were blocked with BSA for 2 h at room temperature. Sufficient primary antibodies were added: Mouse Anti-Human CD31 (Platelet Endothelial Cell Adhesion Molecule-1, PECAM-1) (Abcam, Cat# ab28364) and Rabbit Anti-Human CD34 (Hematopoietic Progenitor Cell Antigen CD34) monoclonal antibody (Abcam, Cat# ab81289). Incubated overnight at 4°C in a humidified chamber. After washing with PBS buffer 3 times, sufficient secondary antibodies were added: HRP-Sheep Anti-Rabbit Secondary Antibody (Abcam, Cat# ab7090) and HRP-Sheep Anti-Mouse Secondary Antibody (Abcam, Cat# ab47827). Incubated for 1 h at 37°C in the dark. After washing with PBS buffer 3 times, DAPI (Affinity Biosciences, United States) was added and incubated for 10 min in the dark. After washing with PBS buffer 3 times, the cells were observed and analyzed under a fluorescence inverted microscope.

2.12 Western blot assay

Cells were collected after trypsin digestion and centrifugation. Lysate was prepared by mixing RIPA lysate, protease inhibitor PMSF and phosphatase inhibitor NaF (NCM Biotech). Ensure that the final concentration of PMSF is 1 mM and the final concentration of NAF is 10 mM. collect the cells and add the lysate, 20–30 min on ice. After centrifuging and sonicating the supernatant, use the BCA technique (Beijing Tiangen Biotechnology Co., Ltd.) to determine the protein content. The protein was transferred to a PVDF membrane (Millipore, Bedford, MA, United States) after SDS-PAGE separation. Use β-actin and β-tublin as the loading control. After leaving it overnight in the primary antibody, let it sit in the secondary antibody for 2 h. Primary antibodies: VEGF-A (Rabbit monoclonal, Proteintech, Cat# 19003-1-AP, 1:6,000); PI3K (Rabbit polyclonal, Proteintech, Cat# 21739-1-AP, 1:5,000); Phospho-PI3K (Tyr458) (Rabbit monoclonal, Abmart, Cat# P42338, 1:1,000); AKT (Rabbit monoclonal, Cell Signaling Technology, Cat# 9272S, 1:1,000); Phospho-AKT (Ser473) (Rabbit polyclonal, Abcam, Cat# ab38449, 1:1,000); mTOR (Rabbit monoclonal, Cell Signaling Technology, Cat# 2972, 1:1,000); Phospho-mTOR (Ser2448)** (Rabbit monoclonal, Cell Signaling Technology, Cat# 2971, 1:1,000); β-Actin (Mouse monoclonal, Proteintech, Cat# 66009-1-Ig, 1:10,000); β-tubulin (Rabbit monoclonal, Cell Signaling Technology, Cat# 2146, 1:1,000); Secondary antibodies: Goat Anti-Mouse IgG-HRP (Abmart, Cat# M21001, 1:5,000); Goat Anti-Rabbit IgG-HRP (Abmart, Cat# M21002, 1:5,000). Using Image Quant LAS4000 (General Electric, Boston, Massachusetts, United States of America), protein bands were found, and ImageJ software was used to quantify them.

2.13 Statistical analysis

GraphPad Prism 8 software was used to analyze and graph the statistical results, and ImageJ software was used to count and calculate the relevant experimental results. All data were expressed as mean ± standard deviation (x ± s). Independent samples t-test was used for comparison of two independent groups (data verified for normality and chi-square); one-way/two-factor ANOVA supplemented by Tukey or Sidak *post hoc* tests was used for comparison of three and more groups. $p < 0.05$ was considered statistically significant. *$P < 0.05$, **$P < 0.01$, ***$P < 0.001$.

3 Results

3.1 Exogenous application of LL37 to HUVEC

HUVEC is sensitive to a variety of growth factors and can be used to assess the promotion of angiogenesis by LL37. The proliferative capacity of the cells was detected by the CCK-8 assay and plate cloning assay. The results showed that the OD value (450 nm) of HUVEC treated with LL37 for 48 h was significantly higher than Control group ($P < 0.05$) (Figure 1a). The number of plate clones of HUVEC treated with LL37 was significantly higher than Control group ($P < 0.05$) (Figure 1b).

After LL37 (5 μg/mL) was added to HUVECs, the angiogenesis results showed that both control and LL37 groups formed tubular structures after 4 h. The number of lumens formed in the LL37 group was higher, and statistical differences were found between the two groups by counting the number of branches and cumulative tube length ($P < 0.05$). After 6 h, the number of branches and cumulative tube length were significantly higher in the LL37 group compared with the control group ($P < 0.01$). After 10 h, part of the luminal structures in the control group disappeared, and the wall was defective and ruptured, while the luminal structures in the LL37 group remained intact, similar to the condition at 6 h. The number of branches ($P < 0.01$) and cumulative tube length ($P < 0.05$) were statistically significant between the two groups (Figure 1c), which indicated that LL37 could promote the angiogenic ability of HUVECs.

The results of the scratch assay showed that the average distance of cell migration was significantly greater in the HUVECs group with the addition of LL37 at both 24 h and 48 h ($P < 0.01$) (Figure 1d), suggesting that LL37 promotes the migratory ability of HUVECs. The results of the Transwell migration assay showed that the number of membrane-penetrating cells in the LL37-treated group was significantly higher than that in the control group ($P < 0.05$). This indicated that LL37 could enhance the migration ability of HUVEC. The Transwell invasion assay better simulated the environment that cells encounter the basement membrane and extracellular matrix during the invasion process *in vivo*. The results showed that the number of invaded cells in the LL37-treated group was significantly increased compared with that in the control group ($P < 0.05$), indicating that LL37 could promote the invasion ability of HUVEC (Figure 1e).

3.2 Endogenous application of LL37 to the mouse ischemia model

The laser speckle blood flow imaging results showed that the blood flow in the lower limbs of the Sham surgery group mice remained normal. The blood flow in the lower limbs of the model group and LL37 group mice was normal before surgery, with no signs of hypoperfusion. On the second day after surgery, the blood flow perfusion in the lower limbs of mice in the model group and LL37 group decreased significantly compared to before surgery, and the blood flow in the affected limb accounted for only about 20% of the blood flow in the healthy side, indicating successful experimental modeling. On the seventh day after surgery, the LL37 group mice showed a recovery in lower limb blood flow perfusion, while the model group mice remained in a low blood flow perfusion state, but the difference between the two groups was not statistically significant ($P > 0.05$). On the 14th day after surgery, compared with the model group, the blood flow perfusion of ischemic limbs in the LL37 group mice was significantly improved, while the ischemic limbs in the model group mice were still in a state of low blood flow perfusion ($P < 0.05$). On the 21st day after surgery, the difference between the LL37 group mice and the model group was more significant ($P < 0.05$) (Figure 2a).

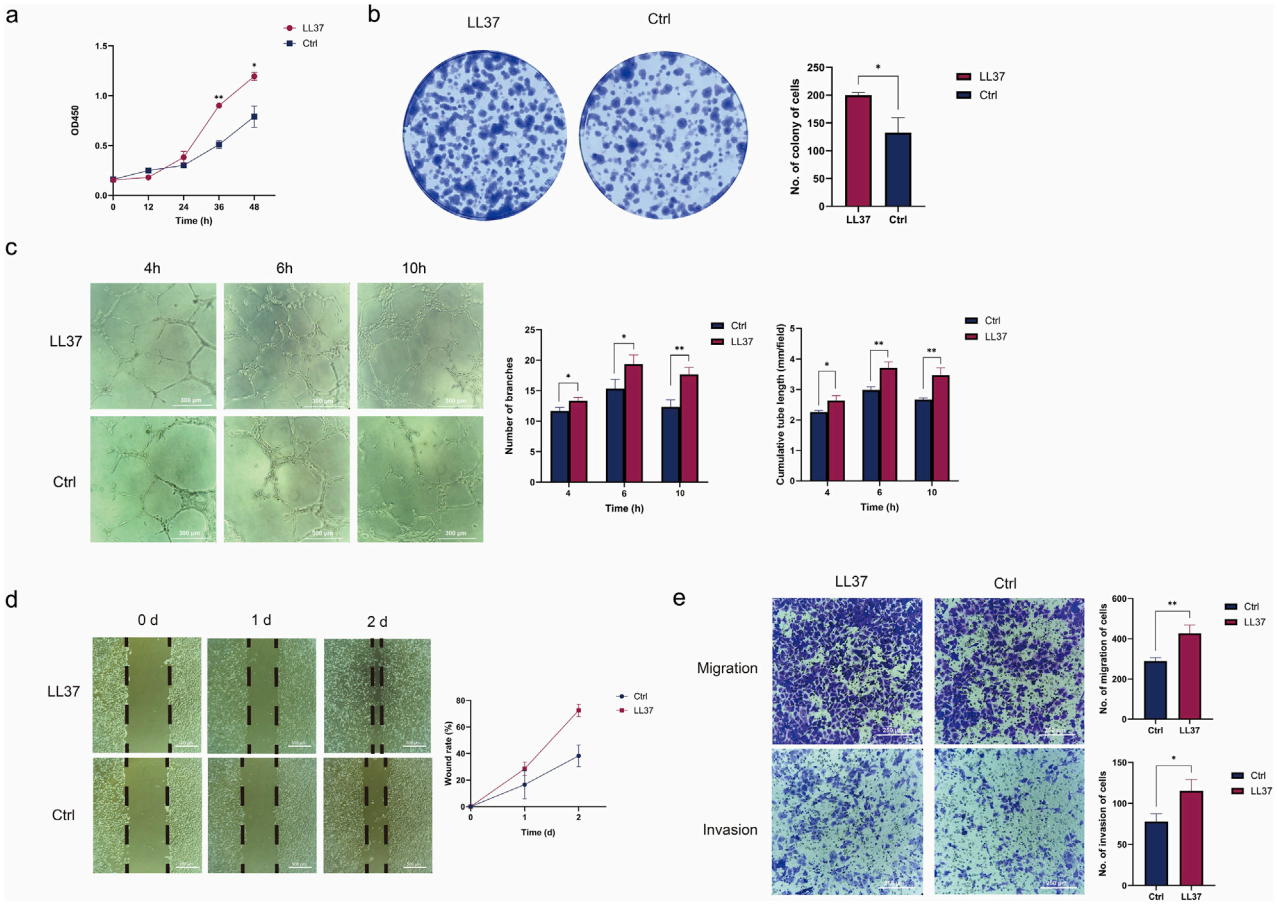


FIGURE 1
(a) The CCK8 assay examined the growth curves of control cells and LL37-treated HUVECs. **(b)** The plate cloning assay examined the proliferation of control cells and LL37-treated HUVECs. **(c)** The angiogenesis assay examined the angiogenesis of control cells and LL37-treated HUVECs. **(d)** The migration ability of control cells and LL37-treated HUVECs was detected by wound healing assay. **(e)** The capacity for migration and invasion of control cells and LL37-treated HUVECs was detected by transwell assay. Note: All experiments were independently repeated at least three times. *P < 0.05, **P < 0.01, ***P < 0.001, and ****P < 0.0001 indicate statistical significance.

On the 14th and 21st postoperative days, frozen sections of the quadriceps muscle were prepared respectively using mice from the model group and the LL37 group. Immunofluorescence experiments showed that the expression of CD31 and CD34 in the muscle cells of the LL37 group was significantly stronger than that of the model group (Figure 2b).

We performed H&E staining on the quadriceps muscle of the ischemic lower limbs of mice in each group on the 21st postoperative day. The results showed that the muscle cell morphology in the quadriceps muscle of the Sham operation group was plump, and the cell outline was clear, with nearly no atrophic or apoptotic cells observed. The quadriceps muscle in the model group showed extensive atrophy and apoptosis. The diameter and size of muscle fibers were unevenly distributed, and most of the muscle fibers were morphologically atrophied with incomplete cell outlines. In contrast, only part of the muscle cells of the quadriceps in the LL37 group showed atrophy and apoptosis. The muscle morphology was more complete (Figure 2c). The experimental results indicated that LL37 could reduce the adverse effects of ischemia on muscle cells, maintain the basic morphology of the cells, and protect the muscle cells. The protective effect of LL37 on the cells is likely to be relevant for its improvement of blood perfusion, ensuring that muscle cells receive sufficient oxygen and nutrients to maintain normal metabolism and function.

3.3 LL37 might be involved in the VEGFA-pi3K/AKT/mTOR-signaling pathway

After adding LL37 (5 μg/mL) into HUVECs culture medium, the expression levels of angiogenesis related genes in HUVECs were detected by qRT-PCR at 24 and 48 h, respectively. The results showed that after 24 h of LL37 treatment, the expression levels of Vascular Endothelial Growth Factor (VEGF), TGF- β (Transforming Growth Factor-β), bFGF (Basic Fibroblast Growth Factor), PDGF-A (Platelet-Derived Growth Factor Alpha Polypeptide and Platelet-Derived Growth Factor Subunit B (PDGF-B) were higher than those of the control group ($P < 0.01$); After 48 h, the above genes in the LL37 group were significantly elevated compared to the control group ($P < 0.01$) (Figures 3a,b), which proves that LL37 can promote the expression of angiogenesis related genes in HUVECs. The role of VEGFA on

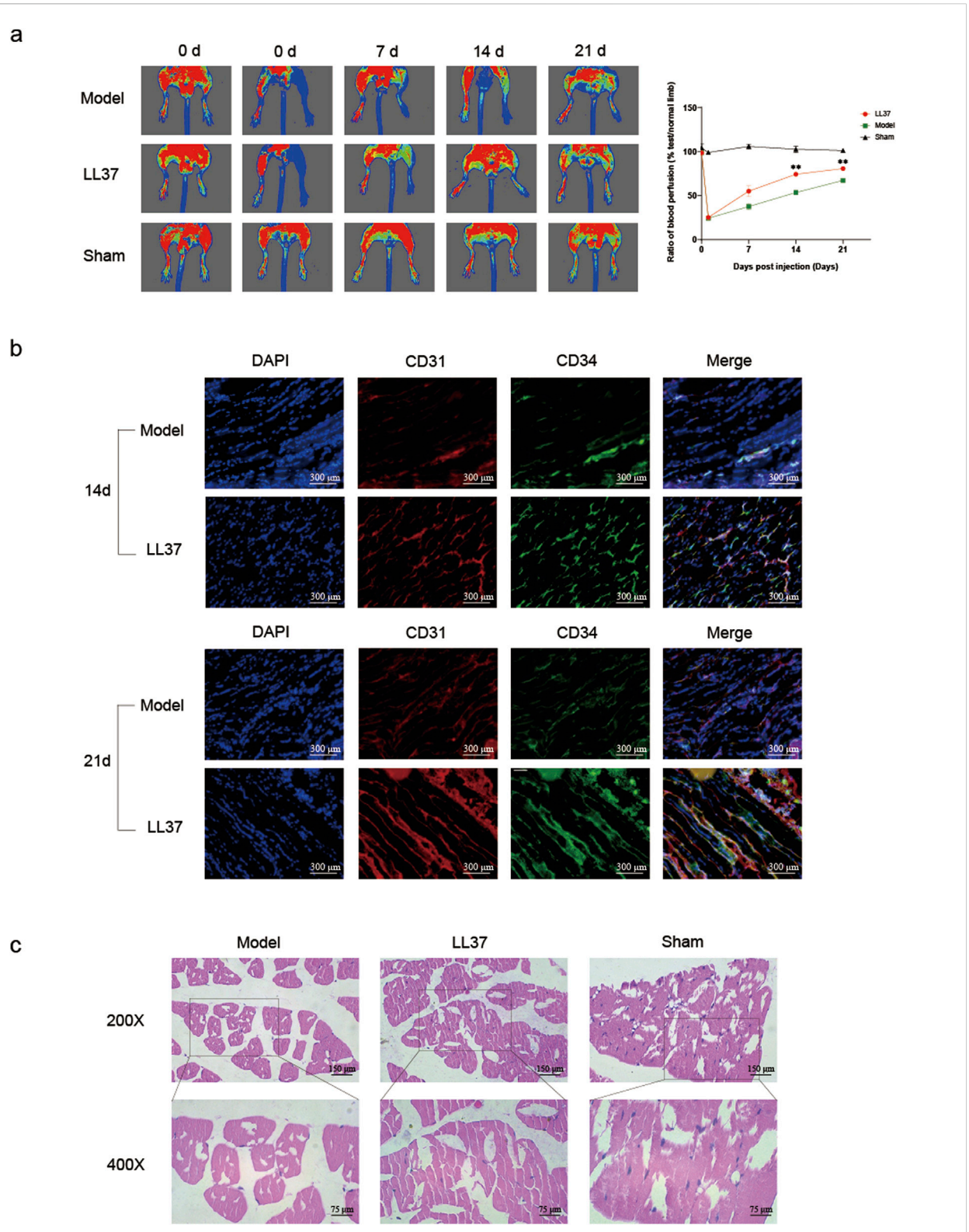


FIGURE 2
(a) Laser Doppler detection of lower limb blood perfusion in mice. Warmer colors (red or yellow) indicate higher perfusion, while cooler colors (blue) indicate lower perfusion. The perfusion values of the affected and healthy limbs were measured, and the ratio of the two was calculated for quantitative analysis. **(b)** Immunofluorescence detection of the expression of CD31 and CD34 in the lower limb muscles of mice. Blue fluorescence indicates nuclei, red fluorescence represents CD31, and green fluorescence represents CD34 (×200 magnification). **(c)** Observation of the morphology of mouse lower limb muscle cells using H&E staining. Note: *P < 0.05, **P < 0.01, ***P < 0.001, and ****P < 0.0001 indicate statistical significance.

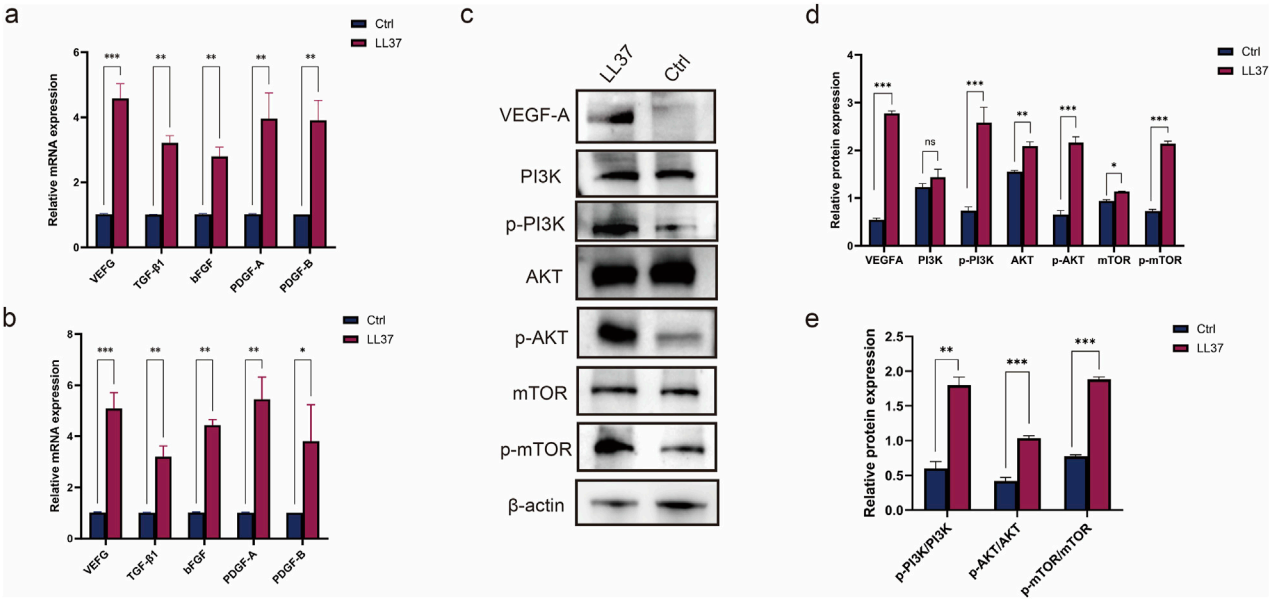


FIGURE 3
(a) qRT-PCR was used to detect the expression of angiogenesis-related genes in HUVECs treated with LL37 for 24 h **(b)** qRT-PCR was used to detect the expression of angiogenesis-related genes in HUVECs treated with LL37 for 48 h. **(c)** The changes in protein levels in HUVECs after treatment with LL37 were detected by Western blot. **(d)** Quantitative analysis of changes in protein expression levels in HUVECs after LL37 treatment. **(e)** Quantitative analysis of changes in protein phosphorylation levels in HUVECs after LL37 treatment.

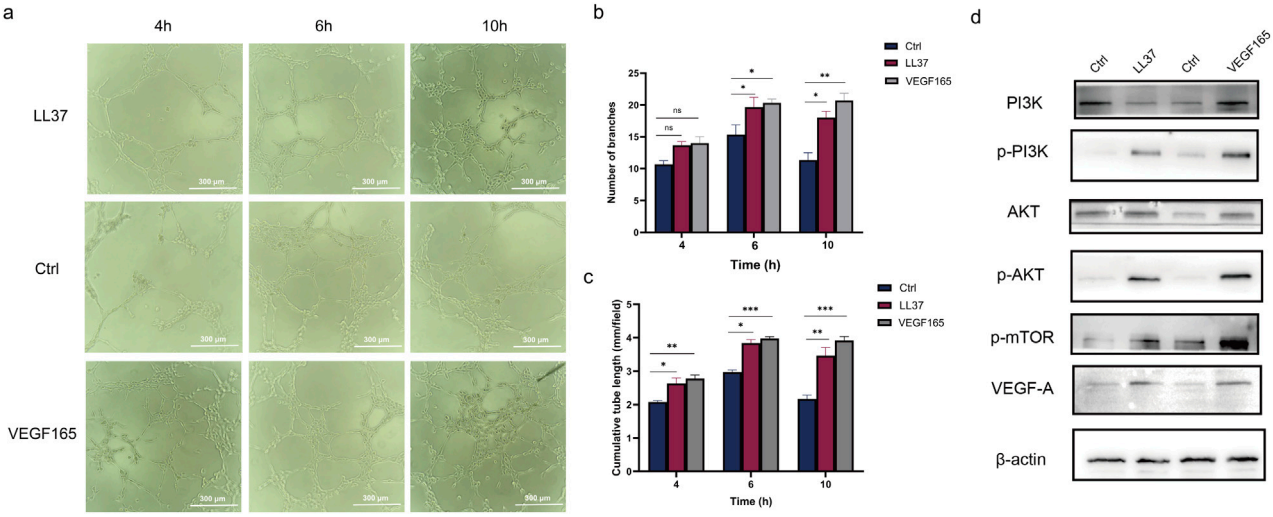


FIGURE 4
(a–c) The angiogenesis assay examined the angiogenesis of control cells and LL37-treated HUVECs. **(d)** The changes in protein levels in HUVECs after treatment with LL37 and VEGF165 were detected by Western blot.

specific pathways was further explored by Western blotting (WB) (Supplementary Data Sheet 1). WB results showed that the application of LL37 was able to activate the PI3K/AKT/mTOR pathway in cells and significantly increase its phosphorylation level (Figure 3c). The expression of each relevant molecule of this pathway (Figure 3d) and its level of phosphorylation (Figure 3e) were quantitatively analyzed using ImageJ.

3.4 LL-37 versus VEGF165 in angiogenesis

By counting the number of branches and cumulative tube length, we found that both LL-37 and VEGF165 significantly enhanced endothelial tube formation compared to controls ($p < 0.05$, Figures 4a–c). Western blot analysis showed that LL-37 and VEGF165 induced comparable levels of phosphorylation of the

VEGFA-PI3K/AKT/mTOR pathway after 1 h of treatment (Figure 4d; Supplementary Data Sheet 2).

4 Discussion

LL37 is a group of 37 amino acids at the N-terminus of the Cathelicidin protein, named after its initial amino acid L-L. As the only antimicrobial peptide present in the human body within the Cathelicidin family, it has been receiving attention for its bactericidal effect. LL-37 may disrupt the arrangement of membrane lipid molecules by interacting with amphiphilic phospholipid molecules at the N-terminus of the polymer, affecting the structure and function of the cell membrane, forming a so-called "carpet like" model that plays a bactericidal role. In addition to having direct antibacterial effects, it has also been found to have functions such as chemotactic immune cells, regulating the secretion of inflammatory promoting/inhibiting factors, coordinating natural and acquired immunity, and exerting immune regulatory effects. Currently, its clinical application is mainly limited to being a new type of antibacterial drug (Rashki et al., 2022; Boge et al., 2017; Geitani et al., 2022; Nagaoka et al., 2020).

Rebert Koczulla et al. first proposed the angiogenic effects of the human peptide antibiotic LL-37/hCAP-18 in 2003, stating that LL-37 may act on vascular endothelial cells and epithelial cells to stimulate angiogenesis (Koczulla et al., 2003). The key to the treatment of lower limb ischemic diseases is to promote angiogenesis to restore blood perfusion to ischemic tissues. Our study focused on the effects of LL37 on vascular endothelial cells to further expand its application in lower limb ischemic diseases (Lukasiewicz, 2016).

Proliferation and migration of vascular endothelial cells is the first step in vascular reconstruction and repair (Yan et al., 2011). CCK8 and plate cloning assay confirmed that LL37 could promote cell proliferation. The scratch assay showed that LL37 could promote the migration of endothelial cells. The HUVEC matrix gel angiogenesis assay more visually demonstrated the promotional effect of LL37 on endothelial cell angiogenesis. Quantify the number of branches and cumulative tube length. Branch number reflects the ability of cells to form complex networks and usually correlates with their ability to migrate and adhere. Cumulative tube length reflects the overall ability of cells to form tubular structures and is an important indicator for assessing angiogenic activity. After treatment with LL37, HUVEC exhibited a higher branching number and longer cumulative tube length, indicating that the cells possessed an enhanced ability to migrate and form tubular structures (Figure 1).

High ligation of the femoral artery with dissection was used to establish a stable lower limb ischemia model. This method was less traumatic to mice, and the ischemic state was obvious, stable, and long-lasting. Laser Doppler flowmetry was performed before and after the operation. The results showed that the mice in the model and experimental groups exhibited a significant decrease in the perfusion of the right lower limb, and a decrease in the intensity of astigmatism without disappearance, indicating that the modeling was successful. This approach was used to simulate the lower limb ischemic disease state. Laser Doppler was used to visualize the lower limb perfusion before, 1 week, 2 weeks and 3 weeks after ischemia, and the comparative results showed that LL37 treatment significantly improved the lower limb perfusion in mice (Figure 2).

CD31 is an adhesion molecule expressed on the surface of a variety of cells including vascular endothelial cells, platelets, and monocytes. It plays an important role in maintaining the normal function of vascular endothelial cells and in angiogenesis (DeLisser et al., 1997; Figueiredo et al., 2019). CD31 is currently the single best marker of endothelial differentiation and is expressed in 90% of hemangiosarcomas, hemangioendotheliomas, hemangiomas, and Kaposi's sarcomas (Handra-Luca, 2019; Venkataramani et al., 2018). CD34 is a highly glycosylated transmembrane glycoprotein expressed mainly on the surface of hematopoietic stem cells and vascular endothelial cells. It plays a key role in vascular development and hematopoiesis and is involved in cell adhesion and signaling (Díaz-Flores et al., 2022). CD34 has a higher sensitivity to smaller, immature micro vessels and therefore may be more accurate in assessing micro vessel density (Mathiou et al., 2023). We respectively assessed the expression of CD31, CD34 at 14 and 21 days postoperatively and found that the expression of both molecules was significantly increased after LL37 treatment compared to the model group. It suggested that LL37 had a potential role in promoting angiogenesis, enhancing endothelial cell function and reducing endothelial function impairment (Figure 2).

The morphology of muscle cells is one of the most visual results of blood perfusion. Obstruction of blood supply to the muscle leads to clinical manifestations such as ischemia, hypoxia, nutritional deficiencies, and metabolic disorders, which in turn cause muscle atrophy, pain, and limitation of movement. If left untreated, it may lead to localized muscle necrosis or even paralysis (Fales et al., 1962). H&E staining was used to observe the morphology of muscle cells in the lower limbs. After adding LL37 treatment, the diameter and size distribution of muscle fibers were more uniform than control group, and atrophy and necrosis were not obvious. It indicated that the addition of LL37 could promote the recovery of muscle morphology and function. This change may be due to the promoting effect of LL37 on angiogenesis, which further increased the blood perfusion of the muscle tissue and improved the nutrient supply and oxygenation status of the muscle (Figure 2).

Angiogenesis is a complex process involving the interaction of multiple molecules and signaling pathways. VEGF is one of the most important regulators of angiogenesis, and the VEGF-A/VEGFR-2 signaling pathway is the most critical signaling pathway in physiological and pathological angiogenesis, which stimulates endothelial cell mitosis, chemotaxis, and morphogenesis, and induces tissue angiogenesis (Melincovici et al., 2018; Wang et al., 2021). TGFB1, bFGF, and PDGF are also important factors in angiogenesis, and are able to stimulate endothelial cell proliferation, migration, and vascular lumen formation, thus participating in the process of angiogenesis and remodeling (He et al., 2024; Lei et al., 2024; Ren et al., 2019; Xie et al., 2014). PCR results showed that HUVEC was treated with LL37, and the expression of VEGF, TGF-β1, bFGF, PDGF-A and PDGF-B were significantly elevated (Figure 3).

VEGF binds through its receptor VEGFR-2, which is an important upstream of the PI3K/AKT/mTOR pathway (Adamičková et al., 2023; Jia et al., 2023; Manjunathan et al., 2021). HUVEC treated with LL37 showed a significant increase in the expression level of VEGF, and furthermore, the

phosphorylation level of the PI3K/AKT/mTOR pathway was found to be significantly elevated in the cells by WB (Figure 3). PI3K/AKT/mTOR pathway plays an important role in cell proliferation, survival, metabolism and angiogenesis. Activation of this pathway promotes endothelial cell proliferation and migration, enhances vascular permeability, and participates in angiogenesis (Ersahin et al., 2015; Karar and Maity, 2011).

Activation of PI3K produces phosphatidylinositol-3,4,5-trisphosphate (PIP3), which in turn activates AKT. activation of AKT promotes cell survival and proliferation, and inhibits apoptosis (Cheng et al., 2022). mTOR is a downstream target of AKT, and is divided into two complexes, mTORC1 and mTORC2. mTORC1 promotes protein synthesis and cell proliferation by phosphorylating S6K1 and 4 E-BP1. mTORC1 is also an active pathway in endothelial cell proliferation, and is involved in angiogenesis. And cell proliferation (Napolitano et al., 2022; Szwed et al., 2021). mTORC2, on the other hand, further enhances AKT activity by phosphorylating the S473 site of AKT (Fu and Hall, 2020; Guri et al., 2017). LL-37 recapitulated the proangiogenic effects and pathway activation characteristics of VEGF165 (Figure 4), suggesting that LL-37 may function as a VEGF mimetic peptide. However, further studies are needed to determine whether LL-37 acts through direct binding to VEGFR2 or through alternative receptors. Notably, the antimicrobial properties of LL-37 may further position it as a dual-function therapeutic candidate for infected wounds requiring concurrent angiogenesis and infection control. Future studies should explore whether LL-37 directly interacts with VEGF receptors or synergizes with endogenous VEGF.

It is noteworthy that LL-37 may indirectly promote angiogenesis through macrophage recruitment/activation (Zhang W. et al., 2023). However, our study has unequivocally demonstrated its direct mechanism of action using purified endothelial models and targeted pathway inhibition experiments. The potential synergistic effects between these direct and indirect mechanisms require further investigation.

5 Conclusion

LL37 can exert its pro-angiogenic effect by increasing the expression of VEGF in cells and enhancing the phosphorylation level of PI3K/AKT/mTOR pathway. We hope that it will play a therapeutic role in lower limb ischemic diseases.

Data availability statement

The original contributions presented in the study are included in the article/Supplementary Material, further inquiries can be directed to the corresponding author.

Ethics statement

The animal study was approved by Approval by Ethics Committee of Yantai Yuhuangding Hospital: 2025-YHD-036. The study was conducted in accordance with the local legislation and institutional requirements.

Author contributions

YY: Formal Analysis, Methodology, Visualization, Writing – original draft. GW: Investigation, Software, Writing – original draft. YW: Data curation, Methodology, Writing – original draft. QM: Project administration, Resources, Visualization, Writing – original draft. DZ: Project administration, Validation, Writing – review and editing. JW: Funding acquisition, Methodology, Supervision, Writing – review and editing.

Funding

The author(s) declare that financial support was received for the research and/or publication of this article. This work was supported by the National Natural Science Foundation of China (No. 82370690); the Natural Science Foundation of Shandong Province (No. ZR2023MH241); and the Taishan Scholars Program of Shandong Province (No. tsqn201909199).

Conflict of interest

The authors declare that the research was conducted in the absence of any commercial or financial relationships that could be construed as a potential conflict of interest.

Generative AI statement

The author(s) declare that no Generative AI was used in the creation of this manuscript.

Publisher's note

All claims expressed in this article are solely those of the authors and do not necessarily represent those of their affiliated organizations, or those of the publisher, the editors and the reviewers. Any product that may be evaluated in this article, or claim that may be made by its manufacturer, is not guaranteed or endorsed by the publisher.

Supplementary material

The Supplementary Material for this article can be found online at: https://www.frontiersin.org/articles/10.3389/fphar.2025.1587351/full#supplementary-material

SUPPLEMENTARY DATA SHEET 1
The changes in protein levels in HUVECs after treatment with LL37 were detected by Western blot.

SUPPLEMENTARY DATA SHEET 2
The changes in protein levels in HUVECs after treatment with LL37 and VEGF165 were detected by Western blot.

References

Adamičková, A., Chomaničová, N., Gažová, A., Maďarič, J., Červenák, Z., Valášková, S., et al. (2023). Effect of atorvastatin on angiogenesis-related genes VEGF-A, HGF and IGF-1 and the modulation of PI3K/AKT/mTOR transcripts in bone-marrow-derived mesenchymal stem cells. *Curr. Issues Mol. Biol.* 45 (3), 2326–2337. doi:10.3390/cimb45030150

Agier, J., Efenberger, M., and Brzezińska-Błaszczyk, E. (2015). Cathelicidin impact on inflammatory cells. *Cent. Eur. J. Immunol.* 40 (2), 225–235. doi:10.5114/ceji.2015.51359

Beard, J. D. (2000). Chronic lower limb ischemia. *West J. Med.* 173 (1), 60–63. doi:10.1136/ewjm.173.1.60

Boge, L., Umerska, A., Matougui, N., Bysell, H., Ringstad, L., Davoudi, M., et al. (2017). Cubosomes post-loaded with antimicrobial peptides: characterization, bactericidal effect and proteolytic stability. *Int. J. Pharm.* 526 (1-2), 400–412. doi:10.1016/j.ijpharm.2017.04.082

Cheng, T. W., and Farber, A. (2024). Surgery or endovascular therapy for chronic limb-threatening ischemia. *Adv. Surg.* 58 (1), 121–133. doi:10.1016/j.yasu.2024.04.008

Cheng, Y., Bai, F., Ren, X., Sun, R., Guo, X., Liu, W., et al. (2022). Phosphoinositide-binding protein TIPE1 promotes alternative activation of macrophages and tumor progression via PIP3/akt/tgfβ Axis. *Cancer Res.* 82 (8), 1603–1616. doi:10.1158/0008-5472.CAN-21-0003

Chieosilapatham, P., Ikeda, S., Ogawa, H., and Niyonsaba, F. (2018). Tissue-specific regulation of innate immune responses by human cathelicidin LL-37. *Curr. Pharm. Des.* 24 (10), 1079–1091. doi:10.2174/1381612824666180327113418

DeLisser, H. M., Christofidou-Solomidou, M., Strieter, R. M., Burdick, M. D., Robinson, C. S., Wexler, R. S., et al. (1997). Involvement of endothelial PECAM-1/CD31 in angiogenesis. *Am. J. Pathol.* 151 (3), 671–677.

Desai, S., Sharma, D., Srinivas, R., Balaji, V., Thakore, V., Bedi, V. S., et al. (2024). Mesenchymal stromal cell therapy (REGENACIP(®)), a promising treatment option in chronic limb threatening ischemia - a narrative review. *Stem Cell Res. Ther.* 15 (1), 352. doi:10.1186/s13287-024-03957-0

Díaz-Flores, L., Gutiérrez, R., García, M. P., González-Gómez, M., Díaz-Flores, L., Jr, Carrasco, J. L., et al. (2022). Comparison of the behavior of perivascular cells (pericytes and CD34+ stromal cell/telocytes) in sprouting and intussusceptive angiogenesis. *Int. J. Mol. Sci.* 23 (16), 9010. doi:10.3390/ijms23169010

Eelen, G., Treps, L., Li, X., and Carmeliet, P. (2020). Basic and therapeutic aspects of angiogenesis updated. *Circ. Res.* 127 (2), 310–329. doi:10.1161/CIRCRESAHA.120.316851

Ersahin, T., Tuncbag, N., and Cetin-Atalay, R. (2015). The PI3K/AKT/mTOR interactive pathway. *Mol. Biosyst.* 11 (7), 1946–1954. doi:10.1039/c5mb00101c

Fales, J. T., Heisey, S. R., and Zierler, K. L. (1962). Blood flow from and oxygen uptake by muscle, during and after partial venous occlusion. *Am. J. Physiol.* 203, 470–474. doi:10.1152/ajplegacy.1962.203.3.470

Farber, A. (2018). Chronic limb-threatening ischemia. *N. Engl. J. Med.* 379 (2), 171–180. doi:10.1056/NEJMcp1709326

Figueiredo, C. C., Pereira, N. B., Pereira, L. X., Oliveira, L. A. M., Campos, P. P., Andrade, S. P., et al. (2019). Double immunofluorescence labeling for CD31 and CD105 as a marker for polyether polyurethane-induced angiogenesis in mice. *Histol. Histopathol.* 34 (3), 257–264. doi:10.14670/HH-18-038

Frasca, L., and Lande, R. (2012). Role of defensins and cathelicidin LL37 in auto-immune and auto-inflammatory diseases. *Curr. Pharm. Biotechnol.* 13 (10), 1882–1897. doi:10.2174/138920112802273155

Fry, D. E. (2018). Antimicrobial peptides. *Surg. Infect. (Larchmt)* 19 (8), 804–811. doi:10.1089/sur.2018.194

Fu, W., and Hall, M. N. (2020). Regulation of mTORC2 signaling. *Genes (Basel)* 11 (9), 1045. doi:10.3390/genes11091045

Geitani, R., Moubareck, C. A., Costes, F., Marti, L., Dupuis, G., Sarkis, D. K., et al. (2022). Bactericidal effects and stability of LL-37 and CAMA in the presence of human lung epithelial cells. *Microbes Infect.* 24 (3), 104928. doi:10.1016/j.micinf.2021.104928

Guri, Y., Colombi, M., Dazert, E., Hindupur, S. K., Roszik, J., Moes, S., et al. (2017). mTORC2 promotes tumorigenesis via lipid synthesis. *Cancer Cell* 32 (6), 807–823. doi:10.1016/j.ccell.2017.11.011

Handra-Luca, A. (2019). CD31 immunohistochemical expression in tumors. *Appl. Immunohistochem. Mol. Morphol.* 27 (10), e98–e99. doi:10.1097/PAI.0000000000000693

He, J., Wu, F., Li, J., Deng, Q., Chen, J., Li, P., et al. (2024). Tumor suppressor CLCA1 inhibits angiogenesis via TGFB1/SMAD/VEGF cascade and sensitizes hepatocellular carcinoma cells to Sorafenib. *Dig. Liver Dis.* 56 (1), 176–186. doi:10.1016/j.dld.2023.05.010

Izadpanah, A., and Gallo, R. L. (2005). Antimicrobial peptides. *J. Am. Acad. Dermatol* 52 (3 Pt 1), 381–390. quiz 391-2. doi:10.1016/j.jaad.2004.08.026

Jia, H., Qi, X., Wu, H., and Wang, J. (2023). Danshensu enhances cerebral angiogenesis in mice by regulating the PI3K/Akt/Mtor/VEGF signaling Axis. *CNS Neurol. Disord. Drug Targets* 22 (4), 607–613. doi:10.2174/1871527321666220329144538

Karar, J., and Maity, A. (2011). PI3K/AKT/mTOR pathway in angiogenesis. *Front. Mol. Neurosci.* 4, 51. doi:10.3389/fnmol.2011.00051

Khung, R., Shiba, H., Kajiya, M., Kittaka, M., Ouhara, K., Takeda, K., et al. (2015). LL37 induces VEGF expression in dental pulp cells through ERK signalling. *Int. Endod. J.* 48 (7), 673–679. doi:10.1111/iej.12365

Kilkenny, C., Browne, W. J., Cuthill, I. C., Emerson, M., and Altman, D. G. (2010). Improving bioscience research reporting: the ARRIVE guidelines for reporting animal research. *PLoS Biol.* 8 (6), e1000412. doi:10.1371/journal.pbio.1000412

Klabukov, I., Shestakova, V., Krasilnikova, O., Smirnova, A., Abramova, O., Baranovskii, D., et al. (2023). Refinement of animal experiments: replacing traumatic methods of laboratory animal marking with non-invasive alternatives. *Anim. (Basel)* 13 (22), 3452. doi:10.3390/ani13223452

Koczulla, R., von Degenfeld, G., Kupatt, C., Krötz, F., Zahler, S., Gloe, T., et al. (2003). An angiogenic role for the human peptide antibiotic LL-37/hCAP-18. *J. Clin. Invest.* 111 (11), 1665–1672. doi:10.1172/JCI17545

Kuwano, M., Fukushi, J., Okamoto, M., Nishie, A., Goto, H., Ishibashi, T., et al. (2001). Angiogenesis factors. *Intern Med.* 40 (7), 565–572. doi:10.2169/internalmedicine.40.565

Lei, X., Li, Z., Huang, M., Huang, L., Huang, Y., Lv, S., et al. (2024). Gli1-mediated tumor cell-derived bFGF promotes tumor angiogenesis and pericyte coverage in non-small cell lung cancer. *J. Exp. Clin. Cancer Res.* 43 (1), 83. doi:10.1186/s13046-024-03003-0

Levin, S. R., Arinze, N., and Siracuse, J. J. (2020). Lower extremity critical limb ischemia: a review of clinical features and management. *Trends Cardiovasc Med.* 30 (3), 125–130. doi:10.1016/j.tcm.2019.04.002

Lukasiewicz, A. (2016). Treatment of acute lower limb ischaemia. *Vasa* 45 (3), 213–221. doi:10.1024/0301-1526/a000527

Luo, X. L., Li, J. X., Huang, H. R., Duan, J. L., Dai, R. X., Tao, R. J., et al. (2019). LL37 inhibits Aspergillus fumigatus infection via directly binding to the fungus and preventing excessive inflammation. *Front. Immunol.* 10, 283. doi:10.3389/fimmu.2019.00283

Manjunathan, R., Devarajan, N., and Ragunathan, M. (2021). Possible mechanism of human recombinant leptin-induced VEGF A synthesis via PI3K/Akt/mTOR/S6 kinase signaling pathway while inducing angiogenesis: an analysis using chicken chorioallantoic membrane model. *J. Vasc. Res.* 58 (6), 343–360. doi:10.1159/000516498

Mathiou, V., Tsiambas, E., Maipas, S., Thymara, I., Peschos, D., Lazaris, A. C., et al. (2023). Impact of CD34-dependent micro vessel density on periapical odontogenic cysts. *Cancer Diagn Progn.* 3 (2), 189–193. doi:10.21873/cdp.10200

Melincovici, C. S., Boşca, A. B., Şuşman, S., Mărginean, M., Mihu, C., Istrate, M., et al. (2018). Vascular endothelial growth factor (VEGF) - key factor in normal and pathological angiogenesis. *Rom. J. Morphol. Embryol.* 59 (2), 455–467.

Nagaoka, I., Tamura, H., and Reich, J. (2020). Therapeutic potential of cathelicidin peptide LL-37, an antimicrobial agent, in a murine sepsis model. *Int. J. Mol. Sci.* 21 (17), 5973. doi:10.3390/ijms21175973

Napolitano, G., Di Malta, C., and Ballabio, A. (2022). Non-canonical mTORC1 signaling at the lysosome. *Trends Cell Biol.* 32 (11), 920–931. doi:10.1016/j.tcb.2022.04.012

Rashki, S., Safardoust-Hojaghan, H., Mirzaei, H., Abdulsahib, W. K., Mahdi, M. A., Salavati-Niasari, M., et al. (2022). Delivery LL37 by chitosan nanoparticles for enhanced antibacterial and antibiofilm efficacy. *Carbohydr. Polym.* 291, 119634. doi:10.1016/j.carbpol.2022.119634

Ren, P., Sun, X., Zhang, C., Wang, L., Xing, B., and Du, X. (2019). Human UTP14a promotes angiogenesis through upregulating PDGFA expression in colorectal cancer. *Biochem. Biophys. Res. Commun.* 512 (4), 871–876. doi:10.1016/j.bbrc.2019.03.142

Rodríguez-Martínez, S., Cancino-Diaz, J. C., Vargas-Zuñiga, L. M., and Cancino-Diaz, M. E. (2008). LL-37 regulates the overexpression of vascular endothelial growth factor (VEGF) and c-IAP-2 in human keratinocytes. *Int. J. Dermatol* 47 (5), 457–462. doi:10.1111/j.1365-4632.2008.03340.x

Szwed, A., Kim, E., and Jacinto, E. (2021). Regulation and metabolic functions of mTORC1 and mTORC2. *Physiol. Rev.* 101 (3), 1371–1426. doi:10.1152/physrev.00026.2020

Tjabringa, G. S., Aarbiou, J., Ninaber, D. K., Drijfhout, J. W., Sørensen, O. E., Borregaard, N., et al. (2003). The antimicrobial peptide LL-37 activates innate immunity at the airway epithelial surface by transactivation of the epidermal growth factor receptor. *J. Immunol.* 171 (12), 6690–6696. doi:10.4049/jimmunol.171.12.6690

Veith, A. P., Henderson, K., Spencer, A., Sligar, A. D., and Baker, A. B. (2019). Therapeutic strategies for enhancing angiogenesis in wound healing. *Adv. Drug Deliv. Rev.* 146, 97–125. doi:10.1016/j.addr.2018.09.010

Venkataramani, V., Küffer, S., Cheung, K. C. P., Jiang, X., Trümper, L., Wulf, G. G., et al. (2018). CD31 expression determines redox status and chemoresistance in human angiosarcomas. *Clin. Cancer Res.* 24 (2), 460–473. doi:10.1158/1078-0432.CCR-17-1778

Wang, H., Chen, L., Wang, S., Tian, X., Zhang, L., Li, H., et al. (2021). Tetrandrine promotes angiogenesis via transcriptional regulation of VEGF-A. *Vasc. Pharmacol.* 141, 106920. doi:10.1016/j.vph.2021.106920

Xie, H., Cui, Z., Wang, L., Xia, Z., Hu, Y., Xian, L., et al. (2014). PDGF-BB secreted by preosteoclasts induces angiogenesis during coupling with osteogenesis. *Nat. Med.* 20 (11), 1270–1278. doi:10.1038/nm.3668

Yan, B. P., Moran, D., Hynes, B. G., Kiernan, T. J., and Yu, C. M. (2011). Advances in endovascular treatment of critical limb ischemia. *Circ. J.* 75 (4), 756–765. doi:10.1253/circj.cj-11-0103

Zeller, T., Sixt, S., and Rastan, A. (2009). New techniques for endovascular treatment of peripheral artery disease with focus on chronic critical limb ischemia. *Vasa* 38 (1), 3–12. doi:10.1024/0301-1526.38.1.3

Zhang, H., Yuan, X., Yang, Y., Wanyan, Y., Tao, L., and Chen, Y. (2023b). Cathelicidin LL-37 promotes EMT, migration and metastasis of hepatocellular carcinoma cells *in vitro* and mouse model. *Cell Adh Migr.* 17 (1), 20–34. doi:10.1080/19336918.2023.2168231

Zhang, Q., Ul Ain, Q., Schulz, C., and Pircher, J. (2023a). Role of antimicrobial peptide cathelicidin in thrombosis and thromboinflammation. *Front. Immunol.* 14, 1151926. doi:10.3389/fimmu.2023.1151926

Zhang, W., Sun, L., Gao, H., and Wang, S. (2023c). Mechanism of the HIF-1α/VEGF/VEGFR-2 pathway in the proliferation and apoptosis of human haemangioma endothelial cells. *Int. J. Exp. Pathol.* 104 (5), 258–268. doi:10.1111/iep.12485

frontiers | Frontiers in Pharmacology

TYPE Original Research
PUBLISHED 30 April 2025
DOI 10.3389/fphar.2025.1587890

Check for updates

OPEN ACCESS

EDITED BY
Yizhou Zhan,
Dongguan University of Technology, China

REVIEWED BY
Xiaoliang Qi,
Wenzhou Medical University, China
Changyong Gao,
Chinese Academy of Sciences (CAS), China

*CORRESPONDENCE
Chuanliang Liu,
Chuanliang_Liu@163.com

RECEIVED 05 March 2025
ACCEPTED 11 April 2025
PUBLISHED 30 April 2025

CITATION
Wang Q, Zhang D, Qi Y, Huang C, Ding D and Liu C (2025) Multifunctional PdH-hydride MOFs for synergistic hydrogen and photothermal antibacterial therapy in accelerated wound healing.
Front. Pharmacol. 16:1587890.
doi: 10.3389/fphar.2025.1587890

COPYRIGHT
© 2025 Wang, Zhang, Qi, Huang, Ding and Liu. This is an open-access article distributed under the terms of the Creative Commons Attribution License (CC BY). The use, distribution or reproduction in other forums is permitted, provided the original author(s) and the copyright owner(s) are credited and that the original publication in this journal is cited, in accordance with accepted academic practice. No use, distribution or reproduction is permitted which does not comply with these terms.

Multifunctional PdH-hydride MOFs for synergistic hydrogen and photothermal antibacterial therapy in accelerated wound healing

Qing Wang[1], Daixing Zhang[1], Yining Qi[1], Changbao Huang[2], Dejun Ding[2] and Chuanliang Liu[1,3]*

[1]School of Clinical Medicine, Shandong Second Medical University, Weifang, Shandong, China, [2]College of Pharmacy, Shandong Second Medical University, Weifang, Shandong, China, [3]Department of Geriatrics, Weifang People's Hospital, Weifang, Shandong, China

Introduction: The growing threat of bacterial infections poses a critical challenge to public health, underscoring the urgent need for innovative antibacterial agents and therapeutic strategies. In response, we have developed a multifunctional nanoplatform based on palladium-hydride metal–organic frameworks (P(H)ZPAg) for synergistic hydrogen and photothermal antibacterial therapy.

Methods: This nanoplatform integrates palladium hydride (PdH) encapsulated within a zeolitic imidazolate framework (ZIF-8), surface modification with polydopamine (PDA), and in situ generation of silver nanoparticles (Ag NPs) to achieve enhanced antibacterial efficacy. Comprehensive characterization was performed to assess hydrogen release kinetics, photothermal performance, and silver-mediated bactericidal activity. The therapeutic potential of P(H)ZPAg was further evaluated in vivo using a *Staphylococcus aureus*-infected rat wound model.

Results: The P(H)ZPAg nanoplatform demonstrated a successful combination of hydrogen release, photothermal conversion, and silver ion-based antibacterial mechanisms. In vitro assays revealed potent synergistic antibacterial effects against both *Escherichia coli* and *Staphylococcus aureus*. In vivo studies showed that treatment with P(H)ZPAg nanoparticles significantly enhanced wound healing and bacterial clearance compared to control groups.

Discussion: These findings highlight the potential of combining hydrogen therapy, photothermal therapy, and silver ion release within a single nanoplatform to markedly improve antibacterial outcomes. This study presents a promising strategy for the development of multifunctional nanotherapeutics, offering a novel and effective approach for managing topical bacterial infections and promoting wound healing.

KEYWORDS

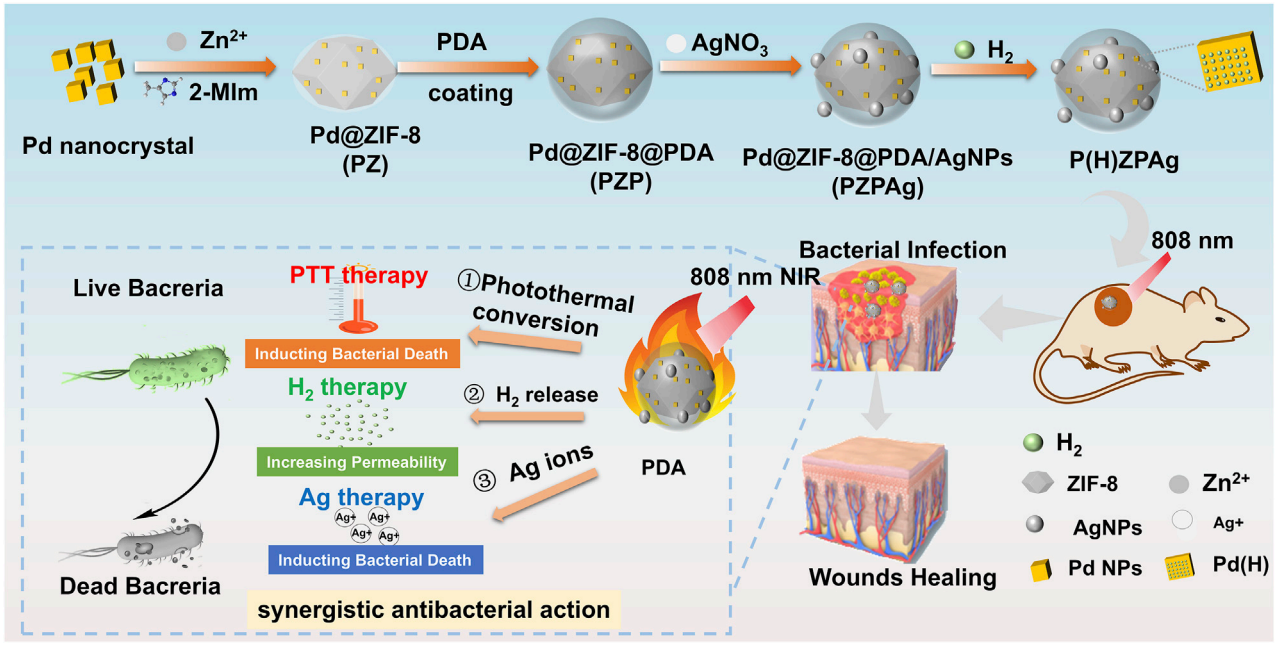
antibacterial therapy, hydrogen therapy, photothermal therapy, wound healing, hydride MOFs

1 Introduction

Skin damage, encompassing both acute and chronic wounds, represents a widespread and significant concern in clinical practice (Falanga et al., 2022; Siddiqui and Bernstein, 2010). Of particular concern are trauma-induced infections caused by pathogenic bacteria, which continue to pose substantial challenges to global public health (Falcone et al., 2021). It is estimated that approximately 15 million people die annually worldwide as a result of bacterial infections (Fongang et al., 2023). These infections can severely impede the wound healing process by inducing chronic inflammation, a hallmark of non-healing wounds. For decades, antibiotics have served as the cornerstone in the treatment of bacterial infections. However, the overuse and misuse of these drugs have inadvertently contributed to the rise of antibiotic-resistant pathogens. This growing resistance undermines the efficacy of current therapeutic options, thereby exacerbating the challenge of managing bacterial infections (MacNair et al., 2024). As such, it is crucial to develop new strategies for combating bacterial infections and promoting wound healing while minimizing reliance on antibiotics.

In recent decades, considerable efforts have been directed toward the development of alternative therapeutic strategies to address antibiotic resistance, including the use of thermal effects (Chen et al., 2020; Huo et al., 2021), reactive oxygen species (ROS) (Lam et al., 2020; Li H. et al., 2021), metal ions (Frei et al., 2023), cationic ions (Cheng et al., 2022) and quaternary ammonium ions (Mohapatra et al., 2023). Among these innovative approaches, gas therapy has emerged as a novel and promising treatment paradigm, garnering significant attention for its potential advantages over traditional therapies (Wang T.-Y. et al., 2023; Wang Z. et al., 2023). Notably, gas therapy offers the ability to circumvent the development of drug resistance, which remains a persistent challenge in infection management. Moreover, gaseous molecules serve as vital endogenous signaling agents, playing crucial roles in various biological processes. Consequently, gas therapy is considered an environmentally friendly ("green") treatment option, providing targeted therapeutic effects with minimal toxicity to healthy tissues. To date, several gaseous molecules, such as nitric oxide (NO) (Andrabi et al., 2023), carbon monoxide (CO) (Cheng and Hu, 2021), hydrogen sulfide (H_2S) (Shi et al., 2024), and hydrogen (H_2) (Yang et al., 2020; Ye et al., 2024), have been extensively studied and shown to be effective against a wide range of bacterial strains, including multidrug-resistant (MDR) bacteria. Notably, hydrogen, the smallest gas with strong reducing properties, is regarded as a highly biocompatible and environmentally friendly gas (Yang et al., 2020). It demonstrates exceptional safety, even at high concentrations, without causing damage to normal cells or tissues. Furthermore, active H_2 has been shown to significantly enhance antibacterial and wound-healing applications by regulating the expression of genes involved in bacterial metabolism (Benoit Stéphane et al., 2020). For instance, Xue et al. (Yu et al., 2019) synthesized Pd nanocubes and incorporated H_2 into their lattice, creating PdH nano-hydrides for antibacterial and wound-healing therapies. More importantly, H_2 molecules can disrupt bacterial membrane permeability, thereby facilitating the entry of antibacterial agents into bacterial cells, promoting the leakage of cellular contents, and ultimately leading to bacterial death (Li et al., 2023). However, hydrogen therapy applied alone is often limited by its low tissue permeability, poor solubility, and suboptimal bioavailability (Jiang et al., 2024). Therefore, combining controlled hydrogen release with other therapeutic modalities can create a synergistic antibacterial effect, significantly enhancing the overall antibacterial performance. Near-infrared (NIR) light-assisted bactericidal strategies, such as photothermal therapy (PTT), have emerged as promising alternatives due to their operability, safety, and controllability (Chen et al., 2020; Huo et al., 2021). Photoconversion agents, including metal nanoparticles (Kadkhoda et al., 2022), metal-organic frameworks (MOFs) (Zheng et al., 2021), and carbon dots (Li B. et al., 2021), can effectively convert light into thermal energy, which can be used to eradicate bacteria. This hyperthermic effect disrupts bacterial cell membranes, denatures proteins, enzymes, and DNA, and induces cell death (Chen et al., 2020). Polydopamine (PDA) nanoparticles, in particular, have recently been utilized in antibacterial studies due to their excellent biocompatibility and efficient photothermal conversion properties (Yang et al., 2021). Qi et al. (2025) proposed an inorganic-organic hybrid system composed of a zeolitic imidazolate framework (ZIF-8) and PDA, which leverages 808 nm near-infrared-induced photothermal effects to enhance catalytic activity for the treatment of bacteria-infected pressure ulcers. Additionally, metal or metal oxide nanocomposites (Pachaiappan et al., 2021), have proven to be powerful antimicrobial agents, exhibiting broad-spectrum activity against both Gram-positive and Gram-negative microorganisms. These composites frequently release metal ions that bind to and interact with bacterial proteins and enzymes, generating ROS that cause structural damage to bacterial cell walls and membranes, thereby leading to membrane permeability alterations, cellular disintegration, and bacterial death (Godoy-Gallardo et al., 2021). Therefore, integrating hydrogen release with silver nanoparticles (AgNPs) and PTT capabilities is expected to synergistically enhance the antibacterial efficacy of these therapies.

In this study, a multifunctional PdH-hydride MOFs-based nanoplatform (PdH@ZIF@PDA/Ag nanoparticles, denoted as P(H)ZPAg NPs) was developed to integrate hydrogen release, PTT, and AgNP therapy for the treatment of bacterial infections associated with wound healing (Scheme 1), achieving a synergistic antibacterial effect that surpasses conventional single-modality treatments. Mechanistically, the released hydrogen was found to compromise the permeability of bacterial cell membranes, thereby facilitating the enhanced entry of Ag^+ ions (Zhang et al., 2022). In addition, PTT contributed to bacterial eradication by generating localized thermal energy that disrupts microbial structures and induces irreversible cellular damage, collectively leading to significantly improved antibacterial efficacy (Yang et al., 2021). ZIF-8 was initially used to encapsulate PdH through a simple covalent growth strategy, preserving the functionality of PdH as a hydrogen-releasing material. Subsequently, PDA was modified onto the surface of PdH@ZIF via mussel-inspired chemistry. In this system, PDA serves as an efficient NIR-absorbing agent with excellent biocompatibility and photothermal stability, facilitating PTT. Furthermore, AgNPs were deposited onto the surface of PDA through coordination forces and *in situ* reduction by the catechol



SCHEME 1
Illustration of the P(H)ZPAg NPs synthesis and its multimode synergistic mechanism for antibacterial and promoting healing process for bacterial infected wounds.

groups of PDA. The resulting P(H)ZPAg NPs exhibit three distinct features: (i) high photothermal performance of PDA, leading to effective photothermal antibacterial therapy; (ii) hydrogen-releasing PdH-Hydride MOFs that demonstrate on-demand, controlled hydrogen release under NIR laser irradiation; and (iii) the release of Ag^+ ions, which further promote bacterial death. *In vitro* antibacterial efficacy and *in vivo* wound disinfection were evaluated using *Escherichia coli* (*E. coli*) and *Staphylococcus aureus* (*S. aureus*) bacteria, as well as bacteria-bearing mouse models. The antibacterial system demonstrated enhanced antibacterial activity, offering a promising strategy in the fight against bacterial infections.

2 Materials and methods

2.1 Materials

Poly (vinyl pyrrolidone) (PVP), L-ascorbic acid, 2-methylimidazolate (2-MIm), dopamine hydrochloride (DA) were purchased from Shanghai Aladdin Biochemical Technology Co. KBr, sodium tetrachloropalladate (Na_2PdCl_4), zinc nitrate hexahydrate ($Zn(NO_3)_2{\cdot}6H_2O$), sodium borohydride ($NaBH_4$), and silver nitrate ($AgNO_3$) were purchased from Shanghai McLean Biochemistry and Technology Co. Methylene blue, 2,5-diphenyltetra-zolium bromide (MTT), 4′,6-diamidino-2-phenylindole (DAPI), were purchased from Shanghai Macklin Biochemical Co., Ltd. Phosphate buffered saline (PBS) and 2,2-diphenyl-1-picrylhydrazyl (DPPH) radical scavenging assay was purchased from Beijing Solaibao Technology Co. LB broth powder and agar powder were purchased from Qingdao Hi-Tech Industrial Park HaiBo Biotechnology Co. Polyformaldehyde tissue fixation solution (4%) was purchased from Biosharp Biological Technology (Anhui, China). Live & Dead Bacterial Staining Kit was provided by Yeasen Biotechnology (Shanghai) Co., Ltd.

2.2 Synthesis of Pd@Zif-8 (PZ) NPs

PZ NPs were obtained referring to reported methods (Zhang et al., 2022). In a typical synthesis of Pd nanocubes, 11 mL of an aqueous solution containing PVP, L-ascorbic acid (60 mg), potassium bromide (KBr, 300 mg), and sodium tetrachloropalladate (Na_2PdCl_4, 57 mg) was heated to 80°C in air under continuous magnetic stirring for 3 h. After the reaction, the solution was allowed to cool to room temperature. The resulting Pd nanocubes were isolated via centrifugation and subsequently washed three times with a water/acetone mixture. The purified Pd nanoparticles were then dispersed in 10 mL of deionized water and stored at 4°C in the dark to maintain stability. These Pd nanoparticles were subsequently encapsulated within a ZIF-8 using a previously reported method (Zhang et al., 2022). Briefly, 200 mg of zinc nitrate hexahydrate ($Zn(NO_3)_2{\cdot}6H_2O$) was completely dissolved in 2.8 mL of deionized water. Next, 2 mL of the synthesized Pd nanocubes solution was added to the zinc nitrate solution, and the mixture was magnetically stirred for 10 min. Next, 2 g of 2-MIm was dissolved in 8 mL of deionized water to form a homogeneous solution, which was then rapidly added to the above Pd nanocubes mixture. The combined solution was stirred continuously for an additional 12 min. The final product was washed three times with a 1:1 ethanol-water solution by centrifugation at 8,000 rpm and subsequently freeze-dried to yield PZ NPs.

2.3 Synthesis Pd@Zif-8@PDA (PZP) and Pd@Zif-8@PDA/Ag (PZPAg) NPs

Firstly, 100 mg of PZ NPs were uniformly redispersed in 20 mL of tris-buffer solution (pH 8.5) using sonication for 10 min to achieve a homogeneous suspension. Subsequently, 50 mg of DA was introduced into the solution, and the mixture was subjected to continuous stirring for 48 h to facilitate the reaction. The resulting product, denoted as PZP NPs, was thoroughly washed three times with ethanol to remove any unreacted species and then redispersed in 20 mL of methanol. Following this, 100 mL of an aqueous silver nitrate ($AgNO_3$) solution (8 mg mL^{-1}) was added dropwise to the suspension at room temperature, and the reaction was allowed to proceed for 1 h. The final product, PZPAg, characterized by its distinct brown coloration, was collected through washing and freeze-drying overnight to yield a stable powder.

2.4 Synthesis P(H)ZPAg NPs

A solution (5 mL) of PZPAg NPs at a concentration of 5 mg/mL, which was subsequently transferred into a 20 mL vial and securely sealed with a rubber stopper. In parallel, 100 mg of sodium borohydride ($NaBH_4$) was measured and placed into a separate vial, which was also sealed with a rubber stopper. The two vials were then interconnected using a capillary tube. To facilitate atmospheric connection, a needle attached to a 1 mL syringe was inserted into the first vial containing the PZPAg NPs. Following this, 2 mL of a sulfuric acid solution with a pH of 5 was injected into the second vial containing $NaBH_4$. The acidic environment induced the generation of hydrogen gas from $NaBH_4$, which subsequently diffused through the capillary into the vial containing the Pd tetrahedrons solution. After a reaction period of 15 min, the needle and capillary were carefully removed. The vial containing the P(H)ZPAg NPs was then sealed and stored in a dark environment to prevent photodegradation, ensuring its stability for subsequent applications.

2.5 Characterization

The morphological characteristics of the samples were examined using a Hitachi HT-7700 transmission electron microscope (Hitachi, Japan). The hydrodynamic diameter and ζ-potential of the nanoparticles were quantitatively assessed using a Zetasizer Nano ZS90 instrument (Malvern Instruments, United Kingdom), providing insights into their colloidal stability and surface charge properties. Chemical composition and elemental analysis were conducted via X-ray photoelectron spectroscopy (XPS) employing an AXIS UltraDLD spectrometer (Kratos Analytical, Japan).

2.6 *In vitro* photothermal performance of PZPAg NPs

The photothermal characteristics of the PZPAg NPs were systematically investigated using an 808 nm fiber optic coupler. Under NIR light irradiation (808 nm, 0.75 W cm^{-2}) for a duration of 6 min, the temperature changes of PZPAg NP dispersions at varying concentrations (0, 50, 100, 150, 200, and 250 μg mL^{-1}) were meticulously monitored. Real-time temperature data and thermal imaging were captured using an infrared thermal camera, providing a comprehensive visualization of the photothermal response. In NIR light absorption density experiment, PZPAg NPs at a fixed concentration of 200 μg/mL were subjected to NIR light irradiation at different power densities (0.35, 0.5, and 0.75 W cm^{-2}) for 6 min to evaluate the influence of power intensity on photothermal performance. Furthermore, the photothermal stability of the PZPAg NPs (200 μg/mL) was assessed over five consecutive irradiation cycles (808 nm, 0.75 W cm^{-2}), demonstrating their robustness under repeated exposure. The photothermal conversion efficiency (η) was calculated in accordance with established methodologies (Cui et al., 2023):

$$\eta = \frac{hA\left(T_{max,sam} - T_{max,water}\right)}{I\left(1 - 10^{-A_{808}}\right)} \quad (1)$$

2.7 Reductive hydrogen release measurement in solution

Prior to conducting the experiment, a standard calibration curve for methylene blue (MB) was established using a UV–vis spectrophotometer. The characteristic absorption peak of MB at 664 nm was measured for aqueous solutions of varying concentrations, and the resulting data were used to construct the calibration curve (Supplementary Figure S1). This curve served as a reference for quantifying the concentration of reductive hydrogen released during the reaction. Additionally, hydrogen-rich water was prepared as a control by saturating deionized water with hydrogen gas generated in the aforementioned reaction apparatus. To evaluate the catalytic activity of the P(H)ZPAg NPs and assess the release of reductive hydrogen from the nanohydride systems, the reduction of MB was employed as a model reaction. For this purpose, 3.4 mL of MB solution (25 μM) was combined with 50 μL of P(H)ZPAg NPs (1 mg mL^{-1}) and 50 μL of deionized water in a sealed 1 cm quartz cuvette. In a parallel experiment, 50 μL of PZPAg NPs (1 mg mL^{-1}) was mixed with 50 μL of hydrogen-rich water and added to an identical MB solution. The reduction process was monitored in real time by tracking the characteristic absorption of MB at 664 nm using the UV–vis spectrophotometer. Measurements were recorded continuously until the absorbance reached a steady state, indicating the completion of the reaction.

2.8 Intracellular reductive hydrogen release

The intracellular release of hydrogen (H_2) from P(H)ZPAg NPs was assessed using a methylene blue-platinum (MB-Pt) probe (Chen et al., 2021). For this analysis, L929 cells were seeded into 6-well plates and incubated for 24 h. Following this, the MB-Pt probe was introduced into the co-culture system and allowed to incubate for 4 h. The culture medium was then replaced with a fresh medium containing P(H)ZPAg NPs nanohydride at a concentration of 50 μg mL^{-1}. Additionally, the mixture was subjected to NIR light irradiation (808 nm, 0.75 W cm^{-2}) for a duration of 6 min, to

evaluate the influence of NIR irradiation. The hydrogen release was monitored at specific time intervals (0, 30, and 60 min). Observations of color changes were conducted using an inverted fluorescence microscope (Olympus, Japan).

2.9 DPPH and hydroxyl radicals scavenging activity

The *in vitro* free radical scavenging efficacy of hydrogels was assessed using two distinct assays: the DPPH radical scavenging assay and the hydroxyl radical scavenging assay. The DPPH radical scavenging activity was evaluated following a modified protocol (Liu et al., 2019). Briefly, 3 mL of a 100 mM DPPH solution prepared in 95% ethanol was introduced into a scintillation vial. Subsequently, NPs samples with concentrations ranging from 0.2 to 1 mg mL^{-1} were added to the solution. The mixture was kept in the dark for 30 min, after which the decrease in absorbance at 517 nm was measured to determine the scavenging activity. The DPPH radical scavenging activity was quantified using the following equation (Liu et al., 2019):

$$\textit{Radical Scavenging Activity}\ (\%) = \left[1 - \frac{(Ai - Aj)}{Ac}\right] \times 100\% \quad (2)$$

where Ac is the absorbance of DPPH solution without particle samples, Ai is the absorbance of the sample particles mixed with DPPH solution, and Aj is the absorbance of the sample particles mixed with 95% ethanol.

The hydroxyl radical scavenging activity was evaluated using a commercially available hydroxyl radical assay kit (Nanjing Jiancheng Bioengineering Institute, Nanjing, China), which operates on the principle of the Fenton reaction (Fu et al., 2023). According to the procedure, NPs samples of varying concentrations were incubated at 37°C for 1 min. Subsequently, Fenton reagent was introduced into each well, and the mixture was allowed to stand for 20 min. The absorbance at 550 nm was then measured using a microplate reader. A control experiment was conducted by substituting H_2O_2 with distilled water. The hydroxyl radical scavenging activity was quantified using the following equation:

$$\textit{Radical Scavenging Activity}\ (\%) = \left[\frac{(A_0 - A_1)}{A_0}\right] \times 100\% \quad (3)$$

where A_0 is the absorbance of the control, and A_1 is the absorbance of the sample.

2.10 *In vitro* antibacterial assay

The antibacterial efficacy of the NPs was investigated against *S. aureus* and *E. coli* using the spread plate method. Luria Broth (LB) medium served as the culture medium for both bacterial strains. The experimental design comprised six groups: (1) Control, (2) P(H)Z NPs, (3) PZP NPs, (4) P(H)ZP NPs, (5) PZPAg, and (6) P(H)ZPAg. To assess the antibacterial efficacy of the nanoparticles (NPs) under photothermal conditions, a standardized bacterial suspension was prepared at a concentration of 10^6 colony-forming units per milliliter (CFU mL^{-1}). A 0.1 mL aliquot of this suspension was mixed with an equal volume (0.1 mL) of the respective NP solution at a concentration of 400 μg mL^{-1}, ensuring uniform interaction between the bacterial cells and the NPs. The mixtures were subjected to NIR laser irradiation at a power density of 0.75 W cm^{-2} for 6 min. Following treatment, all bacterial suspensions were incubated at 37°C for 12 h under optimal growth conditions to allow for potential bacterial recovery or further inhibition. Subsequently, the samples were serially diluted in sterile phosphate-buffered saline (PBS) to achieve appropriate countable colony densities. After an additional 24-h incubation period at 37°C, bacterial colonies were clearly visible, and high-resolution images of the plates were captured for quantitative analysis. Colony enumeration was performed using ImageJ software (National Institutes of Health, United States), employing standardized thresholding and particle-counting algorithms to ensure accuracy. The bacterial inhibition rate (%) was calculated by comparing the colony-forming units (CFUs) of the treated groups against the untreated control, providing a quantitative measure of the NPs' antibacterial efficiency with or without NIR.

To further elucidate the antibacterial mechanisms, a live/dead staining assay was performed. After treatment, 100 μL of the bacterial suspension was transferred to a 96-well plate, and 1 μL of a dual-fluorescence dye mixture (DMAO/EthD-III) was added to each well. The plate was incubated in the dark at room temperature for 15 min. Bacterial viability was assessed using an inverted fluorescence microscope (Leica DMI4000B). Viable cells were stained green by DMAO, while non-viable or membrane-compromised cells were stained red by EthD-III. Fluorescence images were captured to quantify the proportion of live and dead cells.

2.11 Animal model

Five-week-old BALB/c mice (weighing 14–18 g) were procured from Jinan Pengyue Experimental Animal Co., Ltd. The mice were acclimatized for 7 days in standard plastic rodent cages under controlled environmental conditions prior to experimentation. To establish a wound infection model, the mice were anesthetized using pentobarbital sodium, and a circular wound (5 mm in diameter) was created on the disinfected dorsal skin using a sterile annulus. The wound was inoculated with *S. aureus* (100 μL, 10^7 CFU mL^{-1}). The mice were subsequently divided into experimental groups and treated with various formulations, including PBS (control), NIR, PZP, P(H)ZP, P(H)ZPAg, and P(H)ZPAg combined with near-infrared irradiation (0.75 W cm^{-2} for 6 min), to assess their antibacterial efficacy in promoting wound healing. Wound progression was documented using a digital camera on days 0, 3, 7, and 12 post-treatments. After 12 days, the mice were euthanized, and skin tissue surrounding the wound was excised, fixed in 4% paraformaldehyde, and embedded in paraffin for histological analysis. Hematoxylin and eosin (H&E) staining and Masson's trichrome staining were performed to evaluate tissue regeneration and collagen deposition, respectively.

To assess the *in vivo* photothermal performance of the P(H)ZPAg, an 808 nm fiber optic coupler (0.75 W cm^{-2}) was employed in conjunction with a FLIR thermal imaging camera to monitor temperature changes over a 6-min irradiation period. Additionally, to quantify the antibacterial efficacy, wound tissue

samples were collected from each treatment group on the third day. The bacterial solutions were serially diluted, plated onto LB agar plates, and incubated at 37°C for 24 h. Colony-forming units were enumerated using ImageJ software, and the bacterial inhibition rate was calculated.

2.12 Biocompatibility, blood compatibility, and biosafety evaluation

The *in vitro* cytotoxicity of P(H)ZPAg NPs was evaluated using the MTT assay. Initially, L929 cells were seeded into 96-well plates and allowed to adhere for 24 h. Following this, the culture medium was replaced with basal medium containing varying concentrations of P(H)ZPAg NPs (0–400 μg/mL). After incubation, a standard MTT assay was performed to determine cell viability. To further corroborate these findings, a live/dead cell staining assay was conducted under identical treatment conditions. Fluorescence images were acquired using an inverted fluorescence microscope (Leica DMI4000B).

For the hemolysis assay, fresh mouse blood was utilized. Red blood cells (RBCs) were isolated via centrifugation (1,000 rpm, 5 min) and washed six times with phosphate-buffered saline (PBS; 0.01 M, pH 7.4). A 0.5 mL aliquot of RBC suspension in PBS was mixed with 0.5 mL of PZ, PZP, or PZPAg NPs (400 μg/mL). PBS and deionized water served as negative and positive controls, respectively. The mixtures were incubated at 37°C for 4 h, followed by centrifugation to observe the supernatant's color. Hemolysis was quantified by measuring the absorbance of the supernatant using an ultraviolet-visible spectrophotometer.

Biosafety was further assessed through *in vivo* antimicrobial experiments in mice. Body weight changes were monitored throughout the treatment period to evaluate systemic toxicity. Upon completion of the wound healing experiments, the mice were euthanized via cervical dislocation. Major organs, including the heart, liver, spleen, lungs, and kidneys, were excised and fixed in 4% paraformaldehyde. The tissues were paraffin-embedded, sectioned at 5 μm thickness, and subjected to H&E staining for histopathological analysis.

2.13 Statistical analysis

All experiments were conducted in triplicate, and the results are presented as mean values ± standard deviation (SD). Statistical comparisons between two groups were performed using the Student's t-test. The threshold for statistical significance was set at $^{*}p < 0.05$, $^{**}p < 0.01$, and $^{***}p < 0.001$, with $^{*}p < 0.05$ considered marginally significant, $^{**}p < 0.01$ deemed highly significant, and $^{***}p < 0.001$ regarded as extremely significant. Conversely, results with $^{*}p > 0.05$ were considered statistically non-significant (N.S.).

3 Results

3.1 Preparation and characterization of P(H)ZPAg NPs

Palladium (Pd) is widely recognized for its high hydrogen storage capacity and excellent catalytic activity, particularly at the nanoscale (Li et al., 2014). Recent research has highlighted the potential of ZIF-8, a subclass of MOFs, in antibacterial applications due to their ability to combat bacterial infection, favorable biocompatibility, and acid-degradable properties (Yan et al., 2022). The synthesis of the P(H)ZPAg nanoplatform is outlined in Figure 1a. Initially, Pd nanoparticles (Pd NPs) were encapsulated within ZIF-8 through a one-pot reaction, creating a Pd@ZIF-8 (PZ) nanoparticles, which efficiently stores hydrogen. To enhance the functionality, a PDA shell was polymerized around the PZ structure (called Pd@ZIF-8/PDA, PZP NPs) through an *in-situ* polymerization of dopamine (Yang et al., 2021), providing stability and biocompatibility. Ag NPs were then integrated into the PDA layer via a redox reaction (Tong et al., 2020), forming Pd @ ZIF-8@PDA/Ag (PZPAg NPs). This combination endows the nanoplatform with additional antibacterial properties, as Ag^{+} ions are known to disrupt bacterial membranes. The finally P(H)ZPAg was synthesized by introducing hydrogen into PZPAg NPs solution using hydrogen-generation device. With the design, hydrogen-releasing from Pd NPs for *in situ* hydrogen therapy, the PDA shell exhibited photothermal bactericidal ability, and Ag^{+} and Zn^{2+} respectively released from AgNPs and ZIF-8 exhibited chemical antibacterial ability.

Transmission electron microscopy (TEM) images (Figure 1b) confirmed the cubic shape and smooth surface of Pd NPs, with an average diameter of approximately 10 nm. When incorporated into ZIF-8, the diameter of PZ NPs increased in size to 240 ± 16 nm. The successful loading of Pd NPs (blue circles) into ZIF-8 was further validated by TEM. Next, a PDA shell, approximately 10 nm thick, was polymerized around PZ NPs, forming a yolk-shell structure, as seen in Figure 1b. AgNPs were then added to the surface of PZP NPs via *in situ* reduction of Ag^{+} by PDA's catechol groups, resulting in the formation of PZPAg nanohydride. TEM images confirmed the uniform distribution of AgNPs with an average size of 26 ± 3 nm. There was no difference in morphology for P(H)ZPAg after hydrogen loading.

Dynamic light scattering (DLS) measurements showed an increase in particle size following the PDA coating (Supplementary Figure S2), which was accompanied by a shift in zeta potential from +19.9 mV to −22.8 mV (Figure 1c). This suggests that the PDA layer successfully coated the PZ NPs. Additional characterization through X-ray photoelectron spectroscopy (XPS) showed a uniform distribution of elements including zinc (Zn), silver (Ag), palladium (Pd), nitrogen (N), and oxygen (O) throughout the PZPAg NPs (Figure 1d), confirming the successful synthesis of the hydride nanoparticles.

The porosity of the core-shell catalyst was further assessed by nitrogen sorption-desorption isotherms at 77 K. The isotherm exhibited a type IV pattern, with a sharp increase in nitrogen uptake at low relative pressures, indicating microporosity (Figure 1e). The Brunauer–Emmett–Teller (BET) surface area and pore volume were calculated to be 588.4 m^2/g and 0.0.337 cm^3/g, respectively (Supplementary Tables S1). The decrease in both surface area and pore volume can be attributed to PDA and AgNPs on the surface, which contributes significantly to the overall mass of the core-shell structure (Kasemset et al., 2017). The promising porous structural characteristics is beneficial for hydrogen loading.

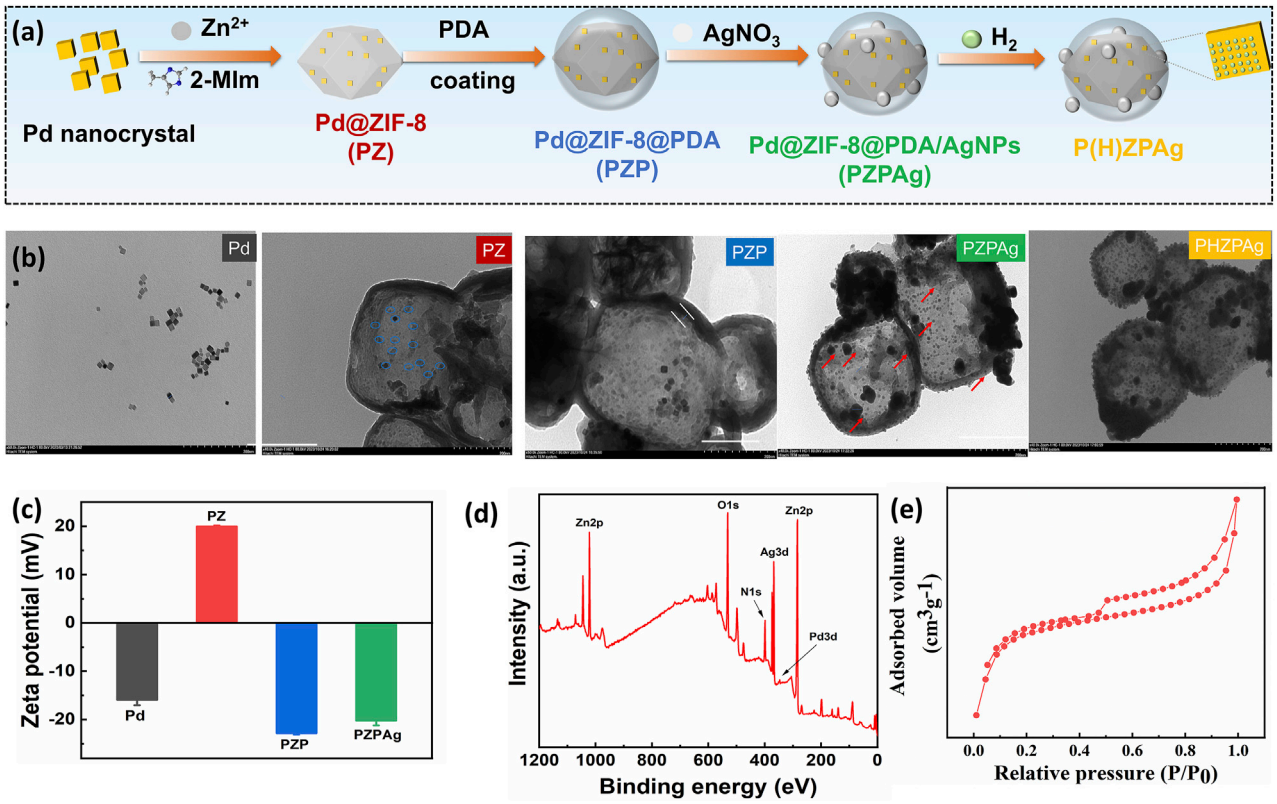


FIGURE 1
Preparation and characterization of PZPAg NPs. **(a)** Schematic illustration depicting the synthesis of P(H)ZPAg NPs. **(b)** TEM images and **(c)** zeta potential of Pd NPs, PZ NPs, PZP NPs and PZPAg NPs. **(d)** XPS spectra and **(e)** N_2 adsorption–desorption isotherms of PZPAg NPs.

3.2 Photothermal conversion efficiency of PZPAg NPs

PDA is known for its broad light absorption spectrum, which allows it to efficiently convert absorbed energy into heat, making it an ideal candidate for photothermal therapy (Yang et al., 2021). The photothermal conversion efficiency of the PZPAg NPs was evaluated under 808 nm NIR laser irradiation. Initially, the temperature response of the PZPAg NPs solution was measured as a function of nanoparticle concentration, with a fixed power density of 0.75 W cm^{-2}. As shown in Figure 2a, the temperature of the PZPAg NPs solution increased significantly upon exposure to 808 nm NIR light. For instance, a 250 μg/mL solution of PZPAg NPs heated from 26.1°C to 61.4°C within 6 min, demonstrating both the strong NIR light absorption and the concentration-dependent photothermal performance of the nanocomposite. The temperature increase was also tested at a fixed concentration of 200 μg/mL under varying NIR laser power densities. As shown in Figure 2b, the photothermal effect of PZPAg NPs intensified with higher laser power. At a power density of 0.75 W cm^{-2}, the solution temperature increased by approximately 35.2°C in just 6 min, indicating the potential of PZPAg to disrupt bacterial membranes. Further real-time infrared thermal imaging (Figure 2c) confirmed that the heat generated by PZPAg NPs was sufficient to effectively kill bacteria.

Additionally, the photostability of PZPAg NPs was assessed by alternating the NIR laser irradiation cycles. As seen in Figure 2d, the temperature of the PZPAg solution increased by around 34.9°C after four irradiation cycles, demonstrating good reversibility and durability for repeated photothermal therapy applications. The photothermal conversion efficiency (η) of PZPAg NPs was calculated (Equation 1) to be 36.9%, based on the heating-cooling curve and the time constant obtained from the cooling period (Figure 2e). These results confirm the effective photothermal properties and stability of PZPAg NPs for potential therapeutic applications.

3.3 Releasing reductive hydrogen and scavenging reactive oxygen species (ROS) capacity of PHZAP NPs

Pd is well-known for its high hydrogen storage capacity, as hydrogen atoms can easily integrate into its crystal lattice, forming PdH nanohydride (Li et al., 2014). This property, coupled with its catalytic activity, makes Pd a valuable material for hydrogenation reactions, especially at the nanoscale. To evaluate the hydrogen release profile of P(H)ZPAg nanohydride, we utilized a methylene blue (MB) probe, a common method for detecting hydrogen release detection and quantification (Li et al., 2023). Typically, MB is combined with platinum (Pt) nanoparticles to enhance its hydrogenation capacity, allowing for rapid detection. The fading of the blue color in the MB solution indicates the reduction of MB,

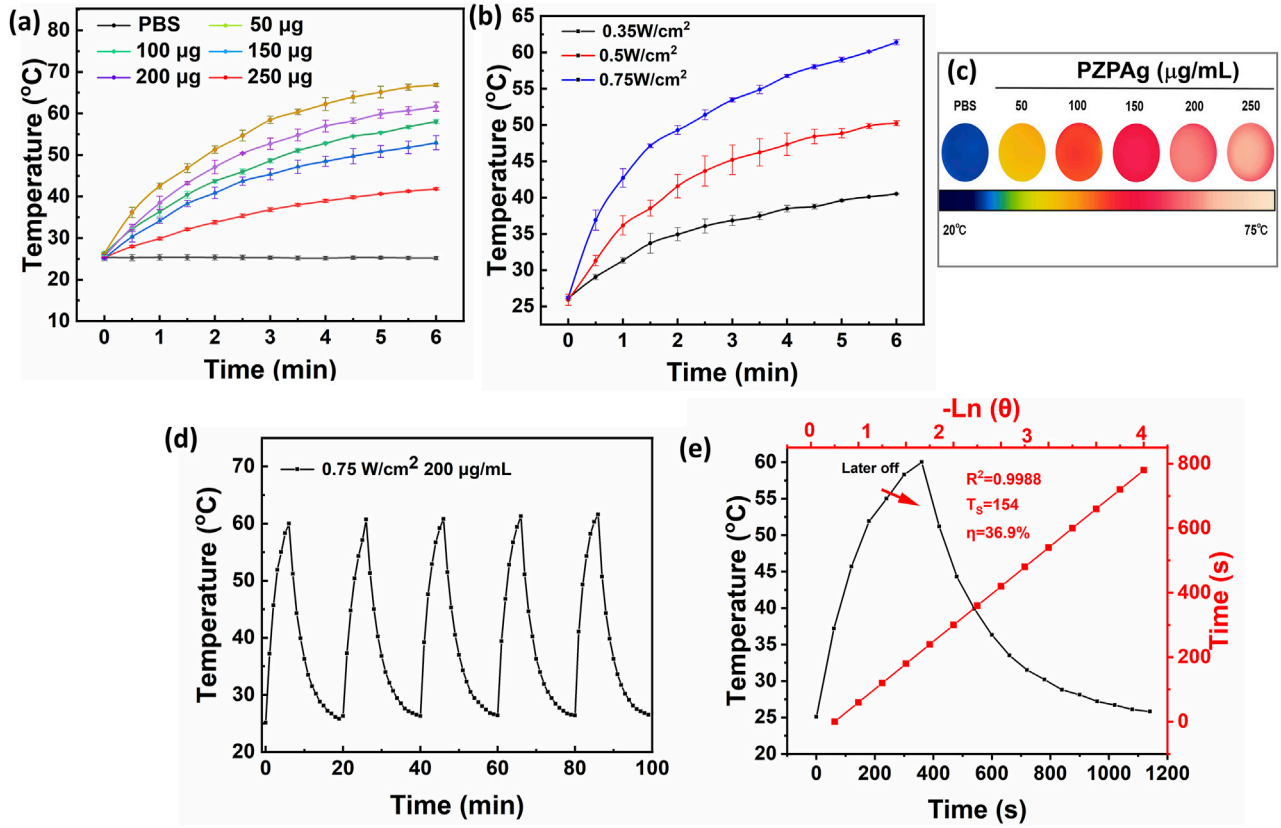


FIGURE 2
The photothermal properties of PZPAg NPs. **(a)** Temperature changes of PZPAg NPs solution with different concentrations (0, 50, 100, 150, 200, and 250 μg mL^{-1}) under 808 nm laser irradiation (0.75 W cm^{-2}) for 6 min. **(b)** Temperature curves of PZPAg NPs solution (200 μg mL^{-1}) under 808 nm laser irradiation with various laser powers (0.35, 0.50 and 0.75 W cm^{-2}). **(c)** Thermal images of PZPAg NPs at different concentrations after 6 min of 0.75 W cm^{-2} NIR irradiation. **(d)** Photothermal stability of PZPAg NPs at a concentration of 200 μg mL^{-1} over five irradiation cycles (808 nm, 0.75 W cm^{-2}). **(e)** Heating–cooling curve and Plot of cooling time versus negative natural logarithm of the temperature driving force.

and the amount of hydrogen released can be quantified by measuring the decrease in absorbance at the characteristic MB peak (664 nm).

As shown in Figure 3a, the absorbance of MB at 664 nm gradually decreased when incubated with P(H)ZPAg nanohydride at 25°C, indicating a continuous release of hydrogen over time. The degree of color fading corresponds to the amount of hydrogen released, which was tracked using UV-Vis absorbance measurements. According to the standard curve (Supplementary Figure S1), the hydrogen release profile of P(H)ZPAg nanohydride was established (Figure 3b). The results demonstrated that hydrogen was released rapidly during the first 5 h, followed by a slower release over the next 19 h, totaling about 5 μM of hydrogen at 25°C. Interestingly, the reductive capacity of hydrogen within P(H)ZPAg was significantly higher than that of hydrogen gas itself (Figure 3b). Furthermore, the hydrogen release rate from P(H)ZPAg nanohydride could be enhanced by applying NIR laser irradiation (Figure 3b). This suggests that on-demand hydrogen release can be precisely controlled by adjusting the NIR laser power density and irradiation time, which is crucial for optimizing hydrogen's therapeutic effects. These findings highlight the potential of P(H)ZPAg nanohydride as a versatile and controllable hydrogen delivery platform for therapeutic applications.

The intracellular hydrogen release from P(H)ZPAg nanohydride was further investigated using methylene blue-platinum (MB-Pt) as a probe (Chen et al., 2021). As illustrated in Figure 3c, following treatment with P(H)ZPAg nanohydride, the blue coloration of the cells progressively diminished over time. This fading indicates a significant increase in hydrogen (H_2) release within the cells, attributed to the reduction of MB by the released H_2 under the catalytic action of platinum (Pt). These observations provide clear evidence of the time-dependent hydrogen generation capability of P(H)ZPAg nanohydride in a cellular environment.

Excessive oxidative stress contributes significantly to tissue damage during bacterial infections, often leading to necrosis and impaired wound healing (Wang G. et al., 2023). Both molecular hydrogen (Jiang et al., 2024) and PDA (Yang et al., 2021) are recognized for their antioxidant properties. To evaluate the antioxidative potential of P(H)ZPAg NPs, we conducted tests using several representative ROS, including DPPH, and hydroxyl radicals (•OH). As shown in Figure 3d, the purple color of the DPPH solution gradually faded with increasing concentrations of PHZAP NPs, and the DPPH scavenging rate (Equation 2) reached 60.4% at 1 mg/mL. This indicates a significant ROS-neutralizing effect. The •OH-scavenging activity of P(H)ZPAg NPs was also examined, revealing a substantial reduction in •OH levels. At a

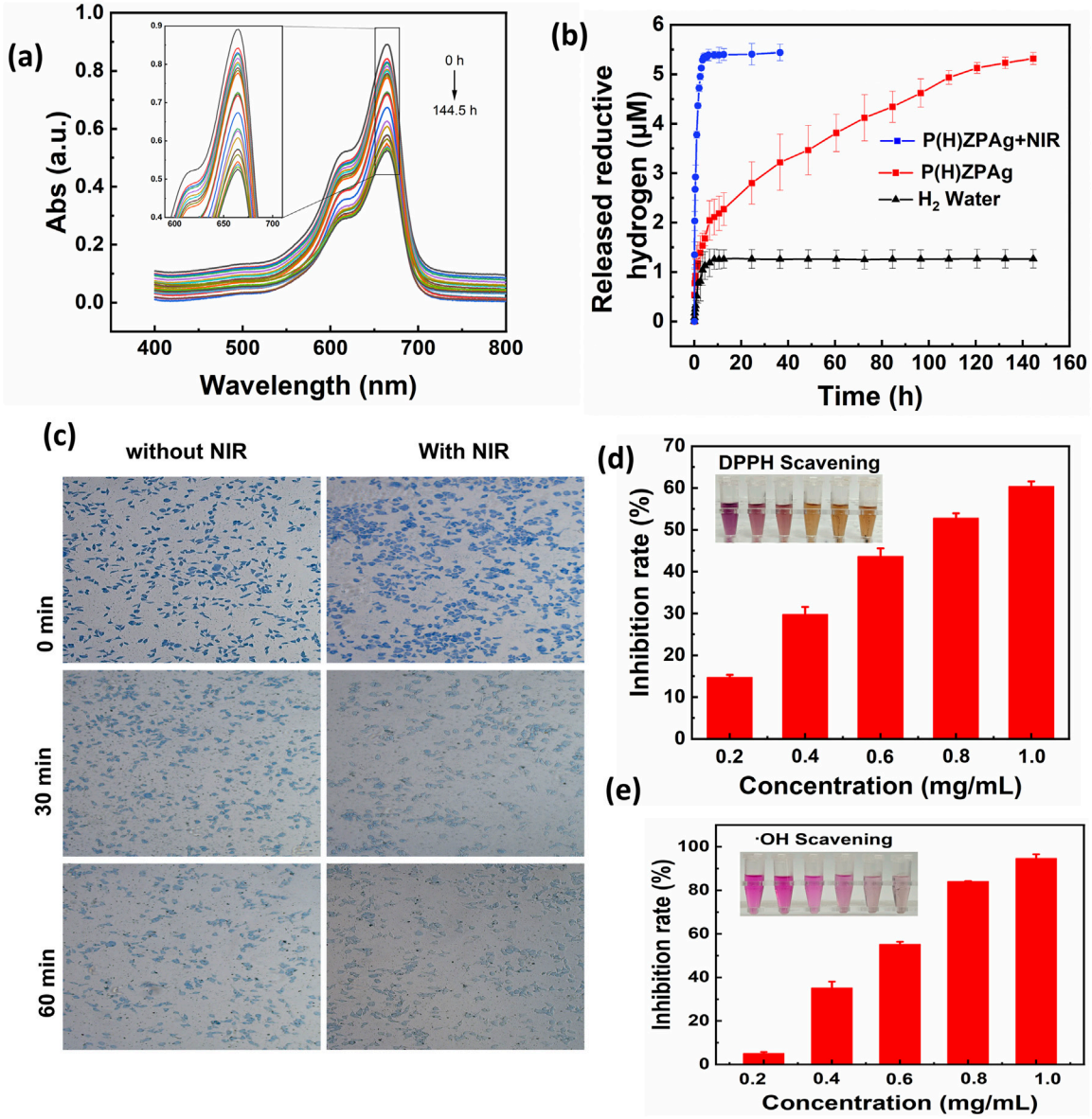


FIGURE 3
H_2 release and antioxidant profile of P(H)ZPAg NPs. **(a)** Changes in UV-Vis spectra of MB incubated with P(H)ZPAg NPs at room temperature. **(b)** H_2 release profile of H_2 water, P(H)ZPAg NPs and P(H)ZPAg NPs with NIR irradiation. **(c)** Hydrogen production experiments of P(H)ZPAg NPs in L929 cells. **(d)** DPPH and **(e)** hydroxyl radicals scavenging activity of P(H)ZPAg NPs.

concentration of 1 mg/mL, the •OH-scavenging rate (Equation 3) reached 94.5%, as evidenced by the visible fading of the solution (Figure 3e). Collectively, these results highlight the broad-spectrum ROS-scavenging capacity of P(H)ZPAg NPs, emphasizing their potential in mitigating oxidative stress-related tissue damage during infection and promoting wound healing.

3.4 Antimicrobial properties of P(H) ZPAg NPs

Chronic wounds are often complicated by bacterial infections, which exacerbate inflammation, promote pus formation, and delay the healing process (Falcone et al., 2021). Given the hydrogen-releasing properties of P(H)ZPAg nanohydride and its ability to convert light into heat, we investigated its antibacterial performance *in vitro*, targeting both Gram-positive *S. aureus* and Gram-negative *E. coli* using a plate counting method. As shown in Figures 4a,b, when tested against *S. aureus*, P(H)Z alone exhibited limited antibacterial activity, with a bacterial survival rate of 85.3%, likely due to the mild effect of the hydrogen released. However, when PDA was added to the P(H)Z structure, the antibacterial activity improved, particularly when exposed to NIR light. This enhancement suggests a synergistic effect between hydrogen release and photothermal PTT. The addition of AgNPs further decreased bacterial survival, likely due to the combined effects of hydrogen release and the antibacterial action of Ag^+ ions. Notably, after 808 nm NIR irradiation, the bacteriostatic effect of P(H)ZPAg

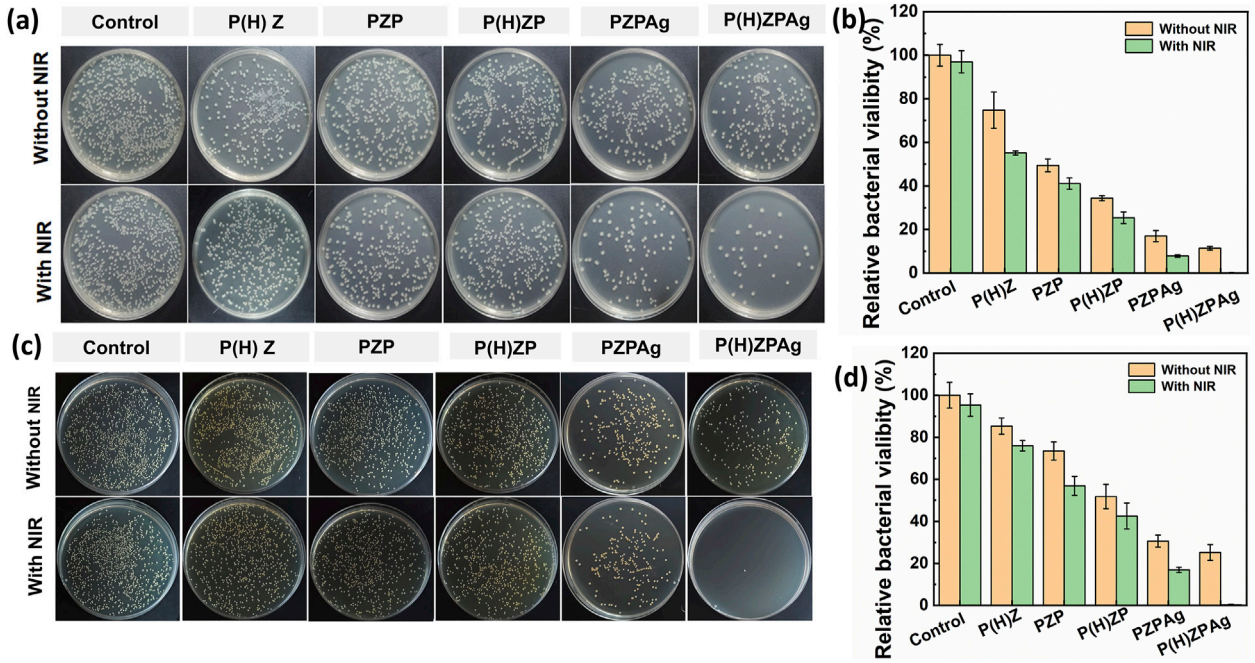


FIGURE 4
Evaluation of the antibacterial activity of P(H)ZPAg NPs. Plate counting assays of *S. aureus* **(a)** and f *E. coli* **(c)** incubation with different treatment. Relative percentages of bacterial remaining on *S. aureus* **(b)** and *E. coli* **(d)** after treatments.

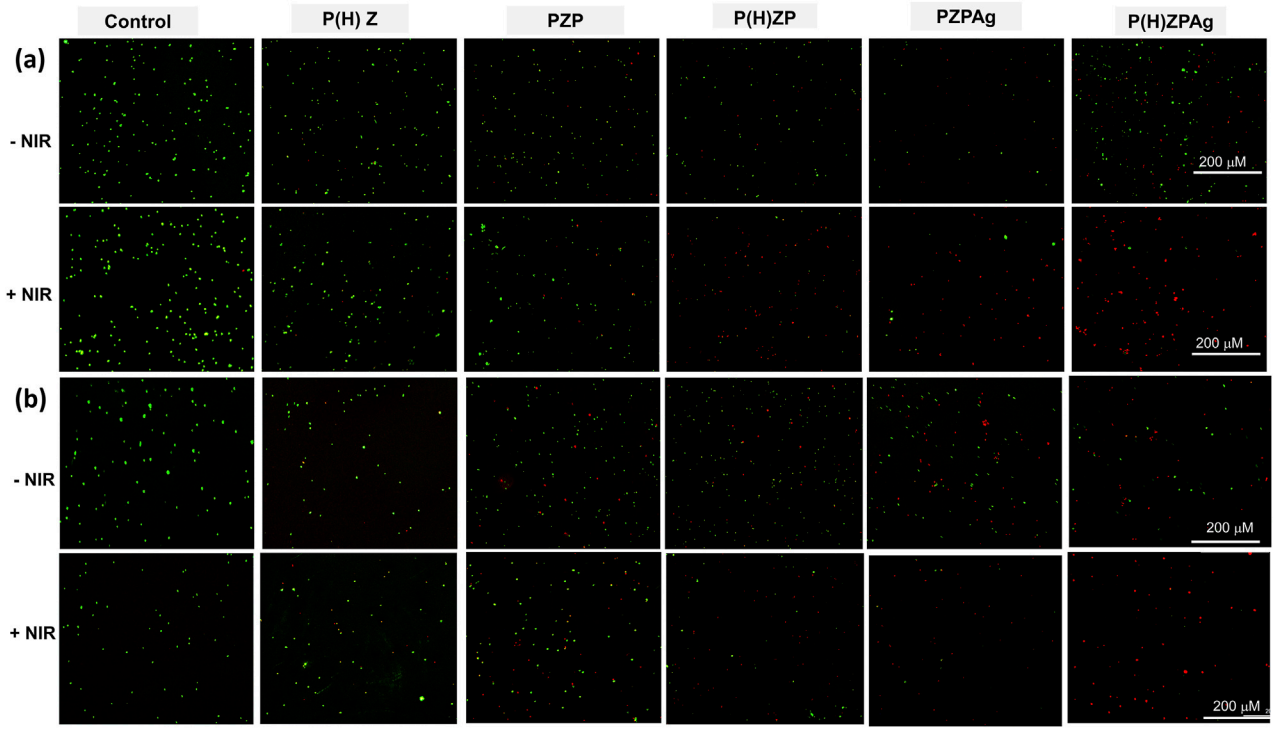


FIGURE 5
Live/dead co-staining of *S. aureus* **(a)** and *E. coli* **(b)** after treatments. Scale bars: 200 μm.

10.3389/fphar.2025.1587890

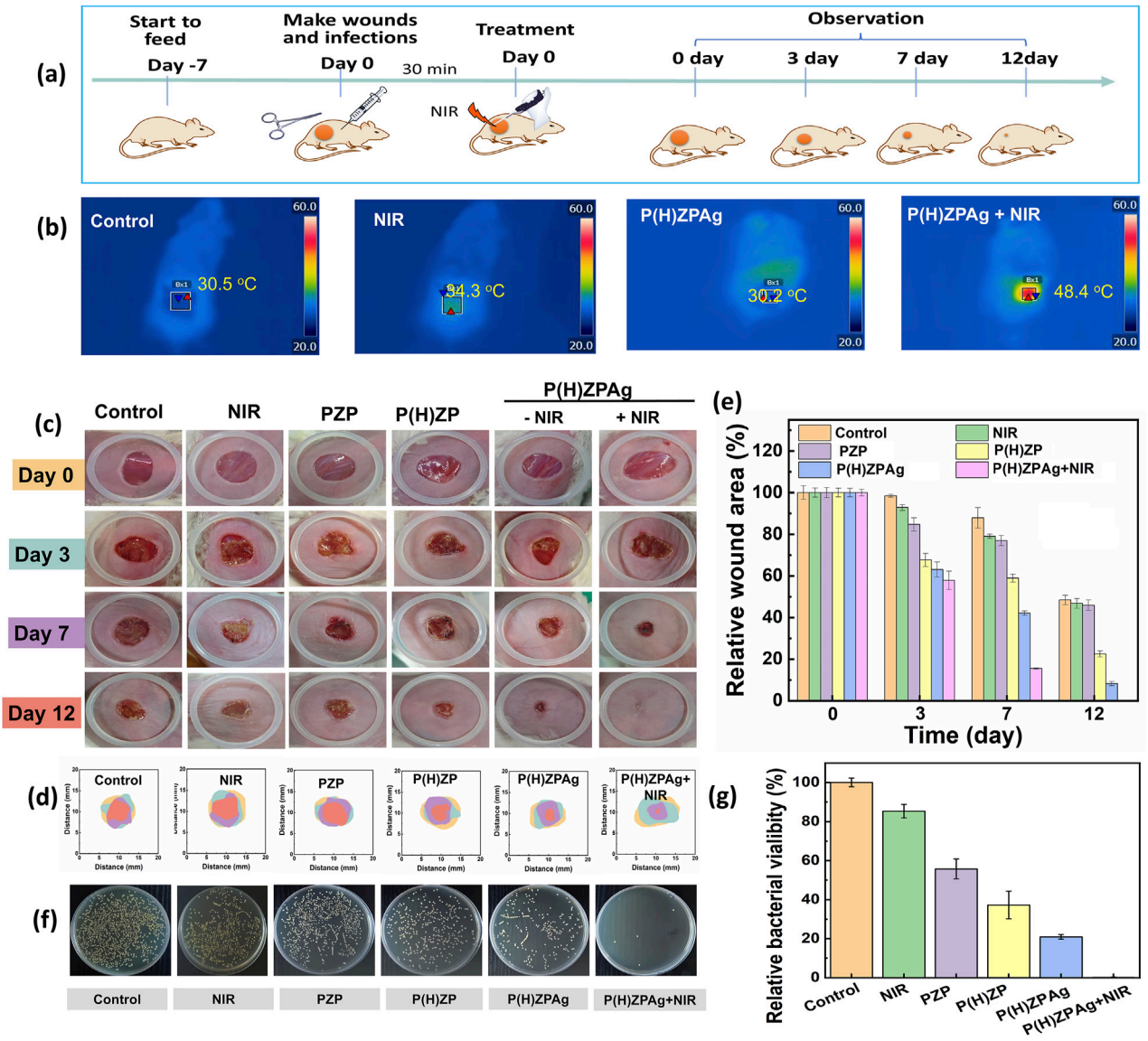


FIGURE 6
In vivo therapeutic efficacy of P(H)ZPAg was evaluated using a *S. aureus*-infected rat wound model. **(a)** Schematic illustration for the establishment of *in vivo* bacterial infections model and subsequent treatment regime. **(b)** Infrared thermograms and recordings of mice under laser irradiation (0.75 W cm^{-2}) for 6 min. **(c)** Digital images and **(d)** physical analog maps, and **(e)** area quantification of area on different days underwent different treatment. **(f)** Photographs of bacterial colonies and **(g)** colony quantification after various treatments.

reached 99.3% In contrast, P(H)ZPAg without hydrogen release showed a less significant reduction in bacterial survival, indicating that hydrogen release enhanced the antibacterial efficacy by increasing bacterial membrane permeability. A similar trend was observed with *E. coli*, where P(H)ZPAg + NIR achieved a sterilization rate of 99.8% (Figures 4c,d). The combined effects of hydrogen and heat from PTT likely disrupted bacterial membranes, facilitating the entry of Ag^+ ions, which contributed to bacterial death.

Further validation through live-dead staining using DMAO/EthD-III demonstrated the effectiveness of P(H)ZPAg + NIR treatment (Figure 5). Bacteria in untreated groups predominantly displayed green fluorescence, indicating live cells, while those treated with P(H)ZPAg + NIR showed mainly red fluorescence, indicative of dead bacteria. These findings confirm that the multimodal approach—combining PTT, hydrogen release, and Ag^+ ions—enhances the antibacterial effect, offering a promising strategy for wound healing.

3.5 *In Vivo* wound healing analysis of P(H)ZPAg NPs

Building upon the promising *in vitro* antibacterial results, the *in vivo* therapeutic efficacy of P(H)ZPAg was evaluated using a *S. aureus*-infected rat wound model. The experimental setup for the *in vivo* studies is depicted in Figure 6a. A 5 mm diameter round wound was created on the back of mice, followed by inoculation of *S. aureus*

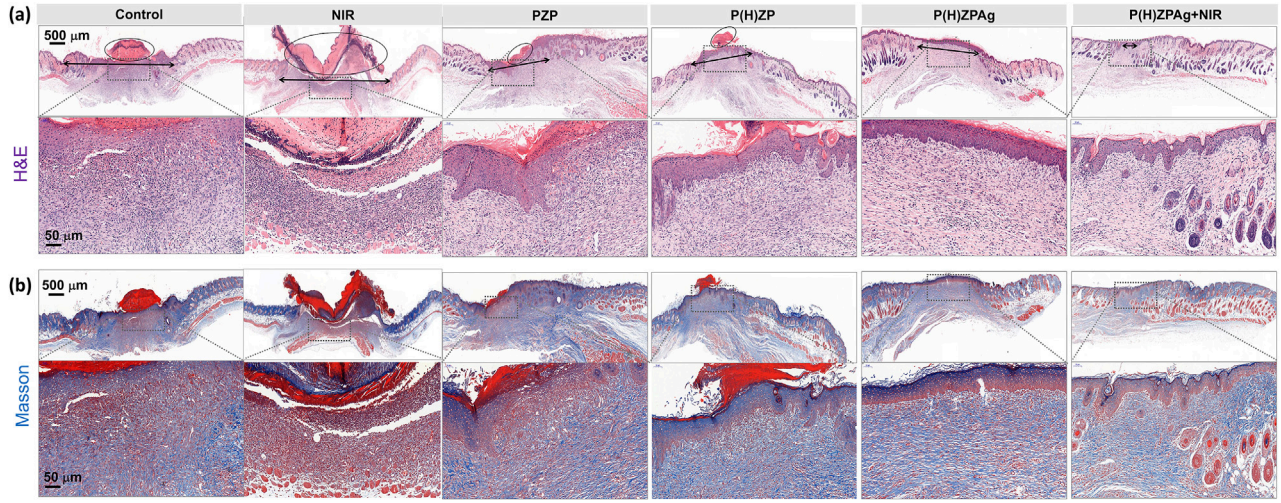


FIGURE 7
In Vivo Histopathological Analysis after various treatments. **(a)** H&E staining and **(b)** Masson's trichrome-stained images of various treated abscess tissues. Scale bars: 500 and 50 μm.

(1×10^7 CFU) into the fresh wounds. After 2 days of incubation, an infected wound model was established. The animals were then treated with different formulations, including PBS, NIR, PZP, P(H)ZP, P(H)ZPAg, and P(H)ZPAg combined with NIR irradiation, to evaluate their antibacterial effects on the open wounds. First, the *in vivo* photothermal effect of P(H)ZPAg was assessed by monitoring the temperature at the wound sites during laser treatment. As shown in Figure 6B, the wound temperature increased sharply from 30.5°C to 48.4°C within 6 min of 808 nm laser irradiation (0.75 W cm^{-2}), whereas the PBS-treated wound temperature only reached 34.3°C. This result supports the hypothesis that P(H)ZPAg, under NIR irradiation, function as a potent photothermal antibacterial agent *in vivo*. Importantly, no significant damage to the surrounding skin tissue was observed during the treatment.

Macroscopic examination of wound healing was performed by capturing images at various time points and measuring the wound closure rates (Figure 6c). On day 3, scars were visible in all treatment groups, except for the PBS and NIR group. Over time, the scars darkened and reduced in size, indicating that bacterial infection was effectively controlled and wound healing was underway. The wound closure in the P(H)ZPAg and P(H)ZPAg groups showed significantly better healing compared to the PBS, PZP and P(H)ZP groups. By day 12, the P(H)ZPAg + NIR group showed complete wound closure, with no visible scar, indicating that the synergistic treatment led to rapid and effective sterilization. Quantitative analysis of wound area was also conducted (Figures 6d.e). After 7 days of treatment, the relative wound areas in the PBS, NIR, PZP, P(H)ZP, P(H)ZPAg, and P(H)ZPAg + NIR groups decreased to 87.8%, 80.1%, 77.1%, 58.9%, 42.1%, and 15.5%, respectively. Remarkably, by day 12, the wound area in the P(H)ZPAg + NIR group reduced to just 0.4% of the initial size, demonstrating the outstanding therapeutic potential of P(H)ZPAg NPs in promoting wound healing through the combined effects of PTT, hydrogen release, and AgNPs under NIR irradiation.

In addition, to assess the antibacterial efficacy *in vivo*, wound tissues were harvested on day 5 and the bacterial load was quantified using the plate counting method. As shown in Figures 6F,G, the lowest bacterial survival (0.1%) was found in the PHZAP + NIR treatment group, significantly lower than in the positive control and PHZAP-only groups. These results suggest that PHZAP NPs, when coupled with NIR irradiation, effectively eradicated *S. aureus* infection *in vivo* through synergistic antibacterial effects, leading to enhanced wound healing. Thus, PHZAP NPs represent a promising candidate for the treatment of infected chronic wounds.

3.6 *In vivo* histopathological analysis

To assess structural changes in the epidermis and collagen deposition during wound healing, histopathological analyses were conducted on wound tissues harvested on day 12 using hematoxylin and eosin (H&E) and Masson's trichrome staining. As depicted in Figure 7a, the control group (I), NIR group (II), the PZP-treated group (III), and the P(H)ZP(IV) displayed substantial areas of unhealed tissue covered by scabs. Notably, large epithelial gaps (marked by black circles) and necrotic foci were observed, indicative of delayed healing and persistent tissue damage. In stark contrast, the P(H)ZPAg + NIR-treated group (VI) exhibited nearly complete epithelial regeneration, characterized by well-formed granulation tissue and the presence of skin appendages, underscoring its exceptional regenerative capacity.

Collagen deposition, a critical factor in wound healing, plays a pivotal role in maintaining structural integrity, facilitating cellular migration, and supporting the formation of a new extracellular matrix. As illustrated in Figure 7b, the P(H)ZPAg + NIR group (VI) demonstrated a more organized and dense collagen arrangement compared to other groups. This enhanced collagen organization is essential for effective extracellular matrix remodeling, thereby promoting robust skin tissue regeneration. Collectively, these findings highlight the superior wound-healing efficacy of the

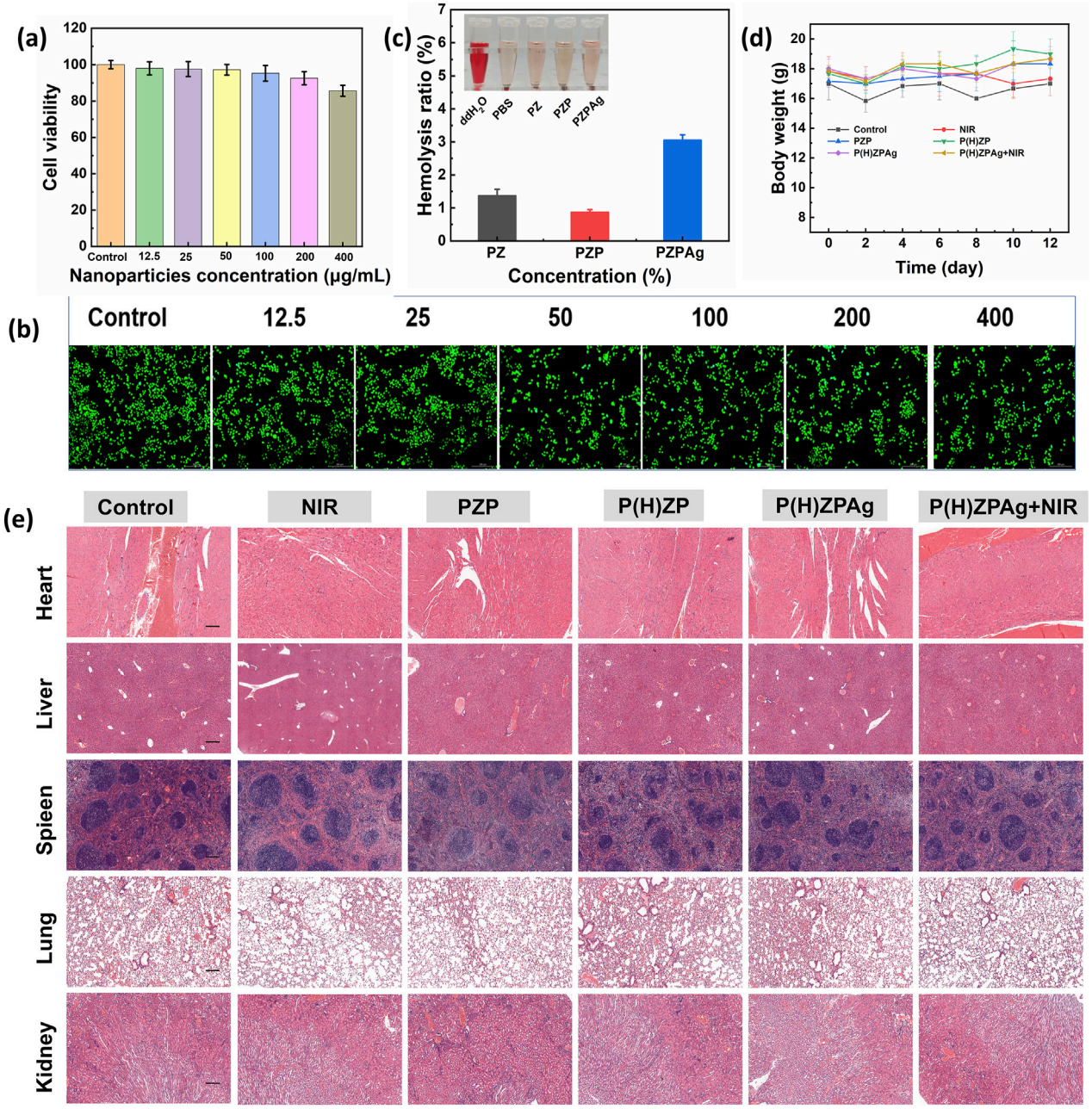


FIGURE 8
Evaluation of biocompatibility of P(H)ZPAg NPs. **(a)** MTT assays and **(b)** LIVE/DEAD viability staining of P(H)ZPAg NPs with different concentrations (μg mL^{-1}). Scale bars: 200 μm. **(c)** Relative Hemolysis ratios of water, PBS, and Noise **(d)** Body weight change curves of mice in different groups as a function of time. **(e)** H&E-stained tissue slices from major organs (heart, liver, spleen, lung and kidney) of different treatment groups. Scale bars: 200 μm.

P(H)ZPAg + NIR treatment, further validating the remarkable potential of this multimodal synergistic therapeutic approach.

3.7 Evaluation of biocompatibility of P(H)ZPAg NPs

Biocompatibility is crucial for the successful *in vivo* application of therapeutic materials (Chandy, 2020). To assess the cellular compatibility of P(H)ZPAg, a series of tests were conducted using fibroblast cells (L929), including MTT assays and LIVE/DEAD viability staining. As shown in Figure 8a, cell viability remained above 85% across a concentration range from 12.5 to 400 μg/mL, indicating that P(H)ZPAg NPs did not exhibit significant cytotoxicity. LIVE/DEAD staining further confirmed this, with green fluorescence marking viable cells and red fluorescence indicating dead cells (Figure 8b). Very few red-stained cells were observed, demonstrating the excellent biocompatibility of P(H)ZPAg NPs.

Additionally, hemolysis assays were performed to evaluate potential toxicity to red blood cells. Unlike the positive control group, which showed complete erythrocyte lysis, the erythrocyte suspension in the P(H)ZPAg NPs group remained clear with only

minimal hemolysis (3.0%), well below the internationally accepted threshold of 5% for hemolytic toxicity (Figure 8c). These results underscore the low hemolytic potential of PHZAP NPs.

In vivo, the safety of PHZAP NPs was further confirmed through body weight monitoring (Figure 8d) and histological analysis of major organs, including the heart, liver, spleen, lungs, and kidneys, after treatment. Hematoxylin and eosin (H&E) staining (Figure 8e) revealed no adverse effects, and blood biochemistry tests indicated that all key blood markers remained within normal ranges (Supplementary Figure S3). Together, these findings validate the excellent biocompatibility and safety profile of P(H)ZPAg NPs, highlighting their potential for antibacterial and wound-healing applications in clinical settings.

4 Discussion

In this study, a multifunctional antibacterial therapy nanoplatform based on PdH-hydride MOFs was developed in the treatment of bacterial infections associated with skin damage. The multifunctional P(H)ZPAg represents a significant integration of hydrogen release, PTT, and silver AgNP therapy, addressing several limitations of conventional treatments. By leveraging the synergistic effects of these three therapeutic modalities, we observed a marked enhancement in antibacterial efficacy, as evidenced by the substantial reduction in bacterial viability both *in vitro* and *in vivo*.

Hydrogen, known for its strong reducing properties and biocompatibility, has been shown to disrupt bacterial membrane permeability, facilitating the entry of antibacterial agents and promoting cellular content leakage (Wang T.-Y. et al., 2023; Wang Z. et al., 2023; Benoit Stéphane et al., 2020; Li et al., 2023). However, the low tissue permeability and poor solubility of hydrogen have historically limited its therapeutic utility (Jiang et al., 2024). By encapsulating PdH within ZIF-8 and utilizing NIR irradiation, we achieved controlled hydrogen release, which significantly enhanced the bactericidal effects of the nanoplatform. PTT is another critical component of the P(H)ZPAg nanoplatform. The use of PDA nanoparticles, which exhibit excellent photothermal conversion properties, allowed for effective heat generation upon NIR irradiation (Yang et al., 2021). This hyperthermia-induced disruption of bacterial cell membranes, protein denaturation, and DNA damage resulted in significant bacterial cell death (Chen et al., 2020). The combination of hydrogen release and PTT further amplified the bactericidal effects, as the elevated temperatures facilitated the diffusion of hydrogen into bacterial cells, thereby enhancing the overall antibacterial performance. AgNPs were also integrated into the P(H)ZPAg nanoplatform to leverage their broad-spectrum antimicrobial activity. AgNPs are known to release metal ions that interact with bacterial proteins and enzymes, generating ROS that cause structural damage to bacterial cell walls and membranes (Tong et al., 2020). The deposition of AgNPs onto the PDA surface through coordination forces and *in situ* reduction by catechol groups of PDA ensured a stable and controlled release of Ag+ ions, further contributing to the enhanced antibacterial efficacy.

The *in vitro* results demonstrated that P(H)ZPAg NPs exhibited antibacterial activity against both Gram-positive and Gram-negative bacteria, including *E. coli* and *S. aureus*. The synergistic effect of hydrogen release, PTT, and Ag + ions led to a significant reduction in bacterial viability. The *in vivo* results further corroborated the efficacy of P(H)ZPAg NPs. In the S. aureus-infected rat model, the PHZAP + NIR treatment group showed rapid and effective wound healing, with complete wound closure observed within 12 days. Histological evaluations confirmed minimal bacterial presence and no signs of tissue damage, underscoring the safety and biocompatibility of the nanoplatform. These results are demonstrating the therapeutic potential of combined therapies in wound healing. These findings highlight the potential of P(H)ZPAg NPs as a promising strategy for treating chronic, infection-induced wounds, offering a highly effective and safe platform for future antibacterial therapies. Looking ahead, several future research directions are essential to advance the clinical translation of the P(H)ZPAg nanoplatform. Comparative studies against current clinical standards, such as antibiotic therapies and commercial silver dressings, are necessary to benchmark its therapeutic advantages. Comprehensive biosafety evaluations, including long-term toxicity and immunogenicity assessments, will be conducted to ensure clinical safety. Mechanistic investigations using molecular profiling techniques will elucidate the pathways underlying the observed synergistic antibacterial effects. Overall, the findings suggest that PHZAP NPs represent a promising strategy for treating chronic, infection-induced wounds, offering a highly effective and safe platform for future antibacterial therapies.

Data availability statement

The original contributions presented in the study are included in the article/Supplementary Material, further inquiries can be directed to the corresponding author.

Ethics statement

The animal studies were approved by Animal Advisory Committee at Shandong Second Medical University. The studies were conducted in accordance with the local legislation and institutional requirements. Written informed consent was obtained from the owners for the participation of their animals in this study.

Author contributions

QW: Data curation, Formal Analysis, Validation, Writing – original draft, Writing – review and editing. DZ: Data curation, Formal Analysis, Visualization, Writing – original draft, Writing – review and editing. YQ: Data curation, Methodology, Writing – review and editing. CH: Data curation, Methodology, Visualization, Writing – review and editing. DD: Conceptualization, Funding acquisition, Supervision, Writing – review and editing. CL: Conceptualization, Project administration, Supervision, Validation, Writing – review and editing.

Funding

The author(s) declare that financial support was received for the research and/or publication of this article. The authors are grateful for the generous financial support from Development Plan for Youth Innovation Technology Project of Higher School in

Shandong Province (2022KJ265), the National Natural Science Foundation of Shandong Province (ZR2020MH400).

Conflict of interest

The authors declare that the research was conducted in the absence of any commercial or financial relationships that could be construed as a potential conflict of interest.

Generative AI statement

The author(s) declare that no Generative AI was used in the creation of this manuscript.

Publisher's note

All claims expressed in this article are solely those of the authors and do not necessarily represent those of their affiliated organizations, or those of the publisher, the editors and the reviewers. Any product that may be evaluated in this article, or claim that may be made by its manufacturer, is not guaranteed or endorsed by the publisher.

Supplementary material

The Supplementary Material for this article can be found online at: https://www.frontiersin.org/articles/10.3389/fphar.2025.1587890/full#supplementary-material

References

Andrabi, S. M., Sharma, N. S., Karan, A., Shahriar, S. M. S., Cordon, B., Ma, B., et al. (2023). Nitric oxide: physiological functions, delivery, and biomedical applications. *Adv. Sci.* 10, 2303259. doi:10.1002/advs.202303259

Benoit Stéphane, L., Maier Robert, J., Sawers, R. G., and Greening, C. (2020). Molecular hydrogen metabolism: a widespread trait of pathogenic bacteria and protists. *Microbiol. Mol. Biol. Rev.* 84, e00092–19. doi:10.1128/mmbr.00092-19

Chandy, T. (2020). "12 - biocompatibility of materials and its relevance to drug delivery and tissue engineering," in *Biointegration of medical implant materials*. Editor C. P. Sharma Second Edition. (Cambridge, MA: Woodhead Publishing), 297–331.

Chen, J., Lin, S., Zhao, D., Guan, L., Hu, Y., Wang, Y., et al. (2021). Palladium nanocrystals-engineered metal–organic frameworks for enhanced tumor inhibition by synergistic hydrogen/photodynamic therapy. *Adv. Funct. Mater.* 31, 2006853. doi:10.1002/adfm.202006853

Chen, Y., Gao, Y., Chen, Y., Liu, L., Mo, A., and Peng, Q. (2020). Nanomaterials-based photothermal therapy and its potentials in antibacterial treatment. *J. Control. Release* 328, 251–262. doi:10.1016/j.jconrel.2020.08.055

Cheng, J., and Hu, J. (2021). Recent advances on carbon monoxide releasing molecules for antibacterial applications. *ChemMedChem* 16, 3628–3634. doi:10.1002/cmdc.202100555

Cheng, S., Wang, H., Pan, X., Zhang, C., Zhang, K., Chen, Z., et al. (2022). Dendritic hydrogels with robust inherent antibacterial properties for promoting bacteria-infected wound healing. *ACS Appl. Mater. and Interfaces* 14 (9), 11144–11155. doi:10.1021/acsami.1c25014

Cui, X., Ruan, Q., Zhuo, X., Xia, X., Hu, J., Fu, R., et al. (2023). Photothermal nanomaterials: a powerful light-to-heat converter. *Chem. Rev.* 123, 6891–6952. doi:10.1021/acs.chemrev.3c00159

Falanga, V., Isseroff, R. R., Soulika, A. M., Romanelli, M., Margolis, D., Kapp, S., et al. (2022). Chronic wounds. *Nat. Rev. Dis. Prim.* 8, 50. doi:10.1038/s41572-022-00377-3

Falcone, M., De Angelis, B., Pea, F., Scalise, A., Stefani, S., Tasinato, R., et al. (2021). Challenges in the management of chronic wound infections. *J. Glob. Antimicrob. Resist.* 26, 140–147. doi:10.1016/j.jgar.2021.05.010

Fongang, H., Mbaveng, A. T., and Kuete, V. (2023). "Chapter One - global burden of bacterial infections and drug resistance," in *Advances in botanical research*. Editor V. Kuete (Cambridge, MA: Academic Press), 1–20.

Frei, A., Verderosa, A. D., Elliott, A. G., Zuegg, J., and Blaskovich, M. A. T. (2023). Metals to combat antimicrobial resistance. *Nat. Rev. Chem.* 7, 202–224. doi:10.1038/s41570-023-00463-4

Fu, Y.-J., Shi, Y.-F., Wang, L.-Y., Zhao, Y.-F., Wang, R.-K., Li, K., et al. (2023). All-natural immunomodulatory bioadhesive hydrogel promotes angiogenesis and diabetic wound healing by regulating macrophage heterogeneity. *Adv. Sci.* 10, 2206771. doi:10.1002/advs.202206771

Godoy-Gallardo, M., Eckhard, U., Delgado, L. M., de Roo Puente, Y. J. D., Hoyos-Nogués, M., Gil, F. J., et al. (2021). Antibacterial approaches in tissue engineering using metal ions and nanoparticles: from mechanisms to applications. *Bioact. Mater.* 6, 4470–4490. doi:10.1016/j.bioactmat.2021.04.033

Huo, J., Jia, Q., Huang, H., Zhang, J., Li, P., Dong, X., et al. (2021). Emerging photothermal-derived multimodal synergistic therapy in combating bacterial infections. *Chem. Soc. Rev.* 50, 8762–8789. doi:10.1039/D1CS00074H

Jiang, Z., Ainiwaer, M., Liu, J., Ying, B., Luo, F., and Sun, X. (2024). Hydrogen therapy: recent advances and emerging materials. *Biomaterials Sci.* 12, 4136–4154. doi:10.1039/D4BM00446A

Kadkhoda, J., Tarighatnia, A., Barar, J., Aghanejad, A., and Davaran, S. (2022). Recent advances and trends in nanoparticles based photothermal and photodynamic therapy. *Photodiagnosis Photodyn. Ther.* 37, 102697. doi:10.1016/j.pdpdt.2021.102697

Kasemset, S., Wang, L., He, Z., Miller, D. J., Kirschner, A., Freeman, B. D., et al. (2017). Influence of polydopamine deposition conditions on hydraulic permeability, sieving coefficients, pore size and pore size distribution for a polysulfone ultrafiltration membrane. *J. Membr. Sci.* 522, 100–115. doi:10.1016/j.memsci.2016.07.016

Lam, P. L., Wong, R. S. M., Lam, K. H., Hung, L. K., Wong, M. M., Yung, L. H., et al. (2020). The role of reactive oxygen species in the biological activity of antimicrobial agents: an updated mini review. *Chemico-Biological Interact.* 320, 109023. doi:10.1016/j.cbi.2020.109023

Li, B., Zhao, S., Huang, L., Wang, Q., Xiao, J., and Lan, M. (2021a). Recent advances and prospects of carbon dots in phototherapy. *Chem. Eng. J.* 408, 127245. doi:10.1016/j.cej.2020.127245

Li, G., Kobayashi, H., Taylor, J. M., Ikeda, R., Kubota, Y., Kato, K., et al. (2014). Hydrogen storage in Pd nanocrystals covered with a metal–organic framework. *Nat. Mater.* 13, 802–806. doi:10.1038/nmat4030

Li, H., Song, X., Liu, W., Zhang, Y., Guan, H., Wu, J., et al. (2023). Revealing the antibacterial power of hydrogen-releasing PdH nanohydride against drug resistant *Staphylococcus aureus*: an in-depth mechanism study. *J. Mater. Chem. B* 11, 1495–1505. doi:10.1039/D2TB02068H

Li, H., Zhou, X., Huang, Y., Liao, B., Cheng, L., and Ren, B. (2021b). Reactive oxygen species in pathogen clearance: the killing mechanisms, the adaption response, and the side effects. *Front. Microbiol.* 11, 622534. doi:10.3389/fmicb.2020.622534

Liu, H., Qu, X., Tan, H., Song, J., Lei, M., Kim, E., et al. (2019). Role of polydopamine's redox-activity on its pro-oxidant, radical-scavenging, and antimicrobial activities. *Acta Biomater.* 88, 181–196. doi:10.1016/j.actbio.2019.02.032

MacNair, C. R., Rutherford, S. T., and Tan, M.-W. (2024). Alternative therapeutic strategies to treat antibiotic-resistant pathogens. *Nat. Rev. Microbiol.* 22, 262–275. doi:10.1038/s41579-023-00993-0

Mohapatra, S., Yutao, L., Goh, S. G., Ng, C., Luhua, Y., Tran, N. H., et al. (2023). Quaternary ammonium compounds of emerging concern: classification, occurrence, fate, toxicity and antimicrobial resistance. *J. Hazard. Mater.* 445, 130393. doi:10.1016/j.jhazmat.2022.130393

Pachaiappan, R., Rajendran, S., Show, P. L., Manavalan, K., and Naushad, M. (2021). Metal/metal oxide nanocomposites for bactericidal effect: a review. *Chemosphere* 272, 128607. doi:10.1016/j.chemosphere.2020.128607

Qi, X., Xiang, Y., Li, Y., Wang, J., Chen, Y., Lan, Y., et al. (2025). An ATP-activated spatiotemporally controlled hydrogel prodrug system for treating multidrug-resistant bacteria-infected pressure ulcers. *Bioact. Mater.* 45, 301–321. doi:10.1016/j.bioactmat.2024.11.029

Shi, X., Li, H., Guo, F., Li, D., and Xu, F. (2024). Novel ray of hope for diabetic wound healing: hydrogen sulfide and its releasing agents. *J. Adv. Res.* 58, 105–115. doi:10.1016/j.jare.2023.05.009

Siddiqui, A. R., and Bernstein, J. M. (2010). Chronic wound infection: facts and controversies. *Clin. Dermatology* 28, 519–526. doi:10.1016/j.clindermatol.2010.03.009

Tong, C., Zhong, X., Yang, Y., Liu, X., Zhong, G., Xiao, C., et al. (2020). PB@PDA@Ag nanosystem for synergistically eradicating MRSA and accelerating diabetic wound healing assisted with laser irradiation. *Biomaterials* 243, 119936. doi:10.1016/j.biomaterials.2020.119936

Wang, G., Yang, F., Zhou, W., Xiao, N., Luo, M., and Tang, Z. (2023a). The initiation of oxidative stress and therapeutic strategies in wound healing. *Biomed. and Pharmacother.* 157, 114004. doi:10.1016/j.biopha.2022.114004

Wang, T.-Y., Zhu, X.-Y., and Wu, F.-G. (2023b). Antibacterial gas therapy: strategies, advances, and prospects. *Bioact. Mater.* 23, 129–155. doi:10.1016/j.bioactmat.2022.10.008

Wang, Z., Rong, F., Li, Z., Li, W., Kaur, K., and Wang, Y. (2023c). Tailoring gas-releasing nanoplatforms for wound treatment: an emerging approach. *Chem. Eng. J.* 452, 139297. doi:10.1016/j.cej.2022.139297

Yan, L., Gopal, A., Kashif, S., Hazelton, P., Lan, M., Zhang, W., et al. (2022). Metal organic frameworks for antibacterial applications. *Chem. Eng. J.* 435, 134975. doi:10.1016/j.cej.2022.134975

Yang, M., Dong, Y., He, Q., Zhu, P., Zhuang, Q., Shen, J., et al. (2020). Hydrogen: a novel option in human disease treatment. *Oxidative Med. Cell. Longev.* 2020, 8384742. doi:10.1155/2020/8384742

Yang, P., Zhu, F., Zhang, Z., Cheng, Y., Wang, Z., and Li, Y. (2021). Stimuli-responsive polydopamine-based smart materials. *Chem. Soc. Rev.* 50, 8319–8343. doi:10.1039/D1CS00374G

Ye, S., Jin, N., Liu, N., Cheng, F., Hu, L., Zhang, G., et al. (2024). Gases and gas-releasing materials for the treatment of chronic diabetic wounds. *Biomaterials Sci.* 12, 3273–3292. doi:10.1039/D4BM00351A

Yu, S., Li, G., Zhao, P., Cheng, Q., He, Q., Ma, D., et al. (2019). NIR-Laser-Controlled hydrogen-releasing PdH nanohydride for synergistic hydrogen-photothermal antibacterial and wound-healing therapies. *Adv. Funct. Mater.* 29, 1905697. doi:10.1002/adfm.201905697

Zhang, W., Zhou, Y., Fan, Y., Cao, R., Xu, Y., Weng, Z., et al. (2022). Metal–organic-framework-based hydrogen-release platform for multieffective Helicobacter pylori targeting therapy and intestinal flora protective capabilities. *Adv. Mater.* 34, 2105738. doi:10.1002/adma.202105738

Zheng, Q., Liu, X., Zheng, Y., Yeung, K. W. K., Cui, Z., Liang, Y., et al. (2021). The recent progress on metal–organic frameworks for phototherapy. *Chem. Soc. Rev.* 50, 5086–5125. doi:10.1039/D1CS00056J

frontiers | Frontiers in Pharmacology

TYPE Original Research
PUBLISHED 04 June 2025
DOI 10.3389/fphar.2025.1580994

Check for updates

OPEN ACCESS

EDITED BY
Jinlong Ma,
Shandong Second Medical University, China

REVIEWED BY
Ilya D. Klabukov,
National Medical Research Radiological Center, Russia
Lingfei Han,
China Pharmaceutical University, China

*CORRESPONDENCE
Jingwei Xue,
xuejingwei11111@163.com
Chunmao Han,
hanchunmao1@126.com
Yilin Zhang,
393342963@qq.com
Zhongtao Zhang,
zhangzhongtao@qdu.edu.cn

†These authors have contributed equally to this work

RECEIVED 21 February 2025
ACCEPTED 26 May 2025
PUBLISHED 04 June 2025

CITATION
Zhang Y, Yu Y, Yu L, Wang F, Yang F, Liang S, Xu W, Ji M, Geng Y, Xue J, Han C, Zhang Z and Zhang Y (2025) BaDuShengJi hydrogel accelerates diabetic wounds healing and regeneration of deep burn injury by anti-bacteria, anti-inflammation and promoting epithelialization.
Front. Pharmacol. 16:1580994.
doi: 10.3389/fphar.2025.1580994

COPYRIGHT
© 2025 Zhang, Yu, Yu, Wang, Yang, Liang, Xu, Ji, Geng, Xue, Han, Zhang and Zhang. This is an open-access article distributed under the terms of the Creative Commons Attribution License (CC BY). The use, distribution or reproduction in other forums is permitted, provided the original author(s) and the copyright owner(s) are credited and that the original publication in this journal is cited, in accordance with accepted academic practice. No use, distribution or reproduction is permitted which does not comply with these terms.

BaDuShengJi hydrogel accelerates diabetic wounds healing and regeneration of deep burn injury by anti-bacteria, anti-inflammation and promoting epithelialization

Yuxiang Zhang[1†], Yuanyuan Yu[2,3†], Lien Yu[1], Fang Wang[2,3], Fuwei Yang[2,3], Shiyu Liang[4], Wen Xu[5], Mengying Ji[5], Yinuo Geng[6], Jingwei Xue[2*], Chunmao Han[1*], Zhongtao Zhang[1,2*] and Yilin Zhang[7,8,9*]

[1]Department of Burns and Wound Care Center, Second Affiliated Hospital, College of Medicine, Zhejiang University, Hangzhou, China, [2]Tumor Precise Intervention and Translational Medicine Laboratory, The Affiliated Taian City Central Hospital of Qingdao University, Taian, China, [3]Shandong Provincial Key Medical and Health Laboratory of Microenvironment-Responsive Biomedical Materials, Taian City Central Hospital, Taian, China, [4]Department of Nursing Division, First Affiliated Hospital, College of Medicine, Zhejiang University, Hangzhou, China, [5]Department of Nursing Division, Second Affiliated Hospital, College of Medicine, Zhejiang University, Hangzhou, China, [6]Department of Nursing, Taishan Vocational College of Nursing, Taian, China, [7]Taishan Academy of Medical Sciences, The Affiliated Taian City Central Hospital of Qingdao University, Taian, China, [8]Postdoctoral Mobile Station, Shandong University of Traditional Chinese Medicine, Jinan, China, [9]Affiliated Hospital of Shandong Institute of Traditional Chinese Medicine, Jinan, China

Bacterial infection, excessive inflammation, and delayed re-epithelialization are the biggest obstacles to diabetic wound healing and burn injuries. As a classic prescription, BaDuShengJi San (BDS) has been proven to accelerate chronic wound healing through anti-bacterial and anti-inflammatory mechanisms. However, there are few reports on its role in preventing the malignant progression of deep burns or accelerating deep burn wound healing. Furthermore, the powder formulation of BDS has limited application scenarios, difficult dosage control, potential environmental pollution, and contradiction with the theory of moist wound healing, which has constrained its scope of application and efficacy to some extent. To address these issues, this study developed a novel hydrogel formulation incorporating BDS using carbomer 940 as the gel matrix, glycerol as a humectant, and triethanolamine as a pH adjuster, through orthogonal design. The results demonstrated that the prepared BDS-loaded gel (BDN) exhibited excellent stability and good biocompatibility, preserving the antibacterial and angiogenesis-promoting properties of BDS while enhancing its anti-inflammatory capabilities. Additionally, BDN significantly accelerated re-epithelialization in diabetic chronic wounds and burn wounds compared to BDS, achieving superior healing quality and mitigating renal damage associated with long-term BDS application. This study provides a comprehensive strategy for accelerating

wound healing in diabetic chronic wounds and deep burn injuries and offers insights into expanding the clinical application of BDS and enhancing its therapeutic effects.

KEYWORDS

BaDuShengJi San, wound healing, diabetic wound, deep burn injury, anti-bacteria, anti-inflammation, promote re-epithelialization

1 Introduction

The prevalence of wounds poses a significant threat to human health, resulting in considerable economic burdens (Freedman et al., 2023). As the population ages and obesity rates rise, the need for effective wound management strategies has become increasingly urgent, particularly for diabetic chronic wounds. Studies have shown that 25% of diabetic patients develop chronic wounds, which are associated with higher rates of amputation and mortality (Sun et al., 2024; Yang et al., 2023; Theodore Hart et al., 2017; Armstrong et al., 2023). This underscores the importance of developing innovative and efficient wound healing treatments.

The standard clinical approach to wound treatment involves surgical debridement followed by hemostasis. The healing process is complex, encompassing inflammation, proliferation, and remodeling phases (Tang et al., 2023). However, delayed re-epithelization, excessive inflammatory reaction, and bacterial infection are the primary factors that hinder wound closure in deep burn injury and diabetic chronic wounds (Zhu S. et al., 2023; Xu et al., 2021; Zhong et al., 2022).

Re-epithelization is crucial for reconstructing the epidermal layer, involving the separation, proliferation, migration, and differentiation of epidermal keratinocytes (Martin and Nunan, 2015; Singer and Clark, 1999). This process is vital for restoring the skin's barrier function, which is essential for maintaining internal stability and defending against external threats. In diabetic patients, hyperglycemia disrupts this process, leading to impaired angiogenesis, re-epithelialization, and collagen deposition (Armstrong et al., 2017). Due to the hyperglycemic effects associated with diabetes, wound healing in diabetic patients is characterized by lack of coordination and spatial disorganization compared to normal healing (Shao et al., 2023). Manifestations include impaired angiogenesis and re-epithelialization, degraded collagen deposition, and epithelial structural disorders (Armstrong et al., 2017). Deep burn wounds, often with extensive skin loss, face difficulties in achieving complete re-epithelization shortly and thus frequently require autologous/allogeneic skin grafting for wound coverage. However, limited skin donor sites and graft availability pose significant challenges (Wang et al., 2018; Jeschke et al., 2020; Derkenne et al., 2019).

The inflammatory phase is indispensable in wound repair, as it clears harmful substances, initiates immune responses, and provides a clean environment for tissue regeneration and wound healing (Singer and Clark, 1999; Pena and Martin, 2024). It also promotes the proliferation and differentiation of wound healing-related cells, such as fibroblasts, by releasing growth factors, creating conditions for subsequent granulation tissue formation and re-epithelization (Singer and Clark, 1999). However, persistent inflammation hinders the transition to the proliferative and tissue remodeling stages, leading to delayed wound healing and, even after healing, uneven wound surfaces and scarring (Martin and Nunan, 2015). Diabetic wounds experience chronic inflammation due to macrophage polarization dysregulation, imbalanced pro-inflammatory/anti-inflammatory cytokine expression, and increased oxidative stress, which exacerbates ischemia and hypoxia in the wound and leads to necrosis (Martin and Nunan, 2015; Chang and Nguyen, 2021; Sharifiaghdam et al., 2022; Huang et al., 2022). Deep second-degree burns, with damage to the deep dermis, often exhibit progressive worsening and require prompt surgical or medical intervention for healing. Studies have found that the post-burn inflammatory cascade leads to excessive release of inflammatory factors, causing tissue edema, ischemia, and progressive wound deepening or even necrosis (Fang et al., 2017). Therefore, controlling excessive inflammation is essential to prevent wound deterioration and accelerate healing.

Due to the loss of skin's protective barrier, blood, exudate, and damaged tissues provide a nutrient basis for rapid bacterial growth. Bacterial infection not only enhances local inflammatory response, disrupts normal wound healing processes, but can also severely induce sepsis, threatening patients' lives (Uberoi et al., 2024). While antibiotics such as tetracycline, neomycin, and quinolones are currently used for wound healing, non-antibiotic antibacterial strategies are gaining attention due to antibiotic restrictions (Sun et al., 2024).

In summary, bacterial infection, wound inflammation, and re-epithelization are interconnected and mutually influential. Preventing wound infection, controlling excessive inflammation, and promoting re-epithelization through appropriate means can accelerate wound healing and restore skin function. Existing treatment strategies, including antibiotics (Chang and Nguyen, 2021; Liu et al., 2024), surgical debridement (Wang et al., 2018), skin grafting (Sun et al., 2014), as well as hyperbaric oxygen (Wunderlich et al., 2000), stem cells (Yu et al., 2023), growth factors (Desmet et al., 2018), have shown limited efficacy and are often costly. Therefore, there is an urgent need to develop a novel strategy for comprehensive wound treatment to accelerate the healing of chronic and burn wounds.

"BaDuShengJi San (BDS)," a traditional Chinese medicine preparation which consists of Red Ochre, Huangdan, Calomel, Calcined Calamine, Calcined Os Draconis, Insect-white Wax, Calcined Plaster, Borneol., has been documented for its detoxifying properties and promotion of tissue regeneration and wound healing in the Qing Dynasty's "Secrets of Injury Treatment" (Cheng et al., 2023). Red Ochre and Huangdan are the monarch drugs, providing both cold and warm properties to aid in toxin expulsion and healing. Calomel acts as minister drug by promoting ulcer healing and removing necrotic tissue. Calcined Calamine absorbs dampness and prevents putrefaction, while Calcined Os

Draconis stops bleeding and aids tissue regeneration. Calcined Plaster clears heat and promotes healing. Together, these ingredients act as guide drugs to reduce toxicity, and support the monarch drugs. Borneol has a pungent, bitter, cool, and clear nature. When used externally, it clears heat, alleviates pain, reduces swelling, and promotes tissue regeneration. Ceresin wax has a sweet, warm, and non-toxic nature, and excels at stopping bleeding and promoting tissue regeneration. When these two assistant drugs are combined, they assist the monarch and minister drugs in astringing wounds and promoting tissue regeneration.

BDS has demonstrated clear efficacy in expediting the healing process of chronic wounds, with numerous studies highlighting its application in the treatment of diabetic foot ulcers (Cui and Hu, 2024; Guo et al., 2018), non-lactational mastitis (Zhang et al., 2025; Xie and Dai, 2021; Cao et al., 2018), postoperative wounds associated with anorectal diseases (Wang, 2024; Xiang, 2021), refractory wounds following calcaneal fracture surgery (Yin, 2019). For example, the use of BDS, either alone or in conjunction with debridement techniques such as gradual debridement, can substantially reduce the treatment duration for diabetic foot ulcers (Cui and Hu, 2024; Guo et al., 2018). The Wnt/β-catenin and Keap1/Nrf2 pathways have been identified as being closely linked to its capacity to enhance the healing of diabetic ulcers (Wang and Li, 2023a; Wang and Li, 2023b). In cases with a high risk of postoperative wound infection and delayed wound healing, such as low perianal abscesses and simple anal fistulas, BDS can significantly decrease the length of hospital stay, mitigate postoperative pain, and markedly enhance patient satisfaction (Xiang, 2021; Chen and Zeng, 2024). Recent research has identified that the application of BDS-impregnated thread for ligation in the treatment of fistulas located in the areola region, associated with non-lactational mastitis, can significantly reduce the time required for fistula opening, expedite the healing process, and decrease both infection and recurrence rates (Zhang et al., 2025). In light of the notable efficacy of BDS in managing chronic wounds, an expert consensus on its clinical application was established in 2023, which aims to standardize the rational use of BDS in clinical practice and to provide guidance for the management of wound-related diseases utilizing BDS (Cheng et al., 2023).

The skin's compromised barrier at the site of a burn or scald significantly elevates the risk of infectious complications. Moreover, the inflammatory cascade activated by such thermal trauma is a principal etiology in the progression of wounds, often culminating in deeper tissue injury and necrosis. Although BDS is currently utilized for various types of chronic refractory wounds, but its applications in preventing and treating acute wounds like deep burns has not been extensively reported. Modern research suggests that BDS can kill bacteria, promote granulation tissue growth, provide a favorable microenvironment for wound healing and epithelial repair, improve local tissue blood circulation, and exhibit anti-inflammatory effects (Cheng et al., 2023). These properties of BDS align with current strategies for preventing early deepening of burn wounds and accelerating their healing (Singh et al., 2007). Therefore, it is speculated that this formulation can alleviate the burn wound progressive deepening and promote the repair of deep second-degree burn wounds.

Despite the evident therapeutic effect of BDS on wounds, its clinical use as a powder formulation encounters several challenges. These include difficulty in reaching deep-seated ulcers, inconvenience in administration, large single-use dosages, the potential for heavy metal poisoning, and environmental pollution due to powder scattering (Liu et al., 2020). Furthermore, the powder formulation does not maintain a moist environment on the wound surface for an extended period, which is essential for wound healing (WINTER, 1962).

In this study, we have successfully reformulated BDS into a hydrogel, denoted as BaiDuShengJi gel (BDN), which introduces an array of advantageous attributes beyond those inherent to BDS. These improvements encompass enhanced mechanical plasticity, heightened adhesiveness, improved moisture retention capabilities, a potent drug depot function, and superior barrier properties. Furthermore, the meticulous preparation of BDN is anticipated to elevate both the safety profile and therapeutic efficacy of BDS in wound healing applications, thereby rendering it an even more viable candidate for clinical adoption (Scheme 1). The research not only broadens the clinical applicability of BDS in managing acute burn wounds and chronic diabetic wounds but also establishes a versatile framework for the modification of powder dosage forms. This approach offers a novel and promising strategy for optimizing therapeutic interventions in the realm of wound healing.

2 Materials and methods

2.1 Preparation and properties of hydrogels

2.1.1 The screening of matrix for preparation of BDN

Various concentrations of carbomer 940, sodium alginate and CMC-Na were prepared using ultrapure water. Centrifugal stability, homogeneity, and fluidity were used to screen the gel matrices. In addition, experiments on the mixing and formation of BDN were conducted in this section. BDS suspensions were prepared using ultrapure water, followed by the preparation of 1% carbomer 940 gel, 10% sodium alginate gel, and 5% CMC-Na gel, each containing 1 mg/mL of the drug. The changes in gel state and the dispersion of the drug within the gel were recorded.

2.1.2 The screening of humectant for preparation of BDN

Moisture retention was used to screen the optimal humectant. Two portions of the preferred BDN were prepared, and the same mass of 5% glycerol and 1,2-propanediol were added to each, respectively. The mixtures were thoroughly stirred and then transferred into Petri dishes with constant weight.

The moisture-retention Rate (%) was calculated as follows:

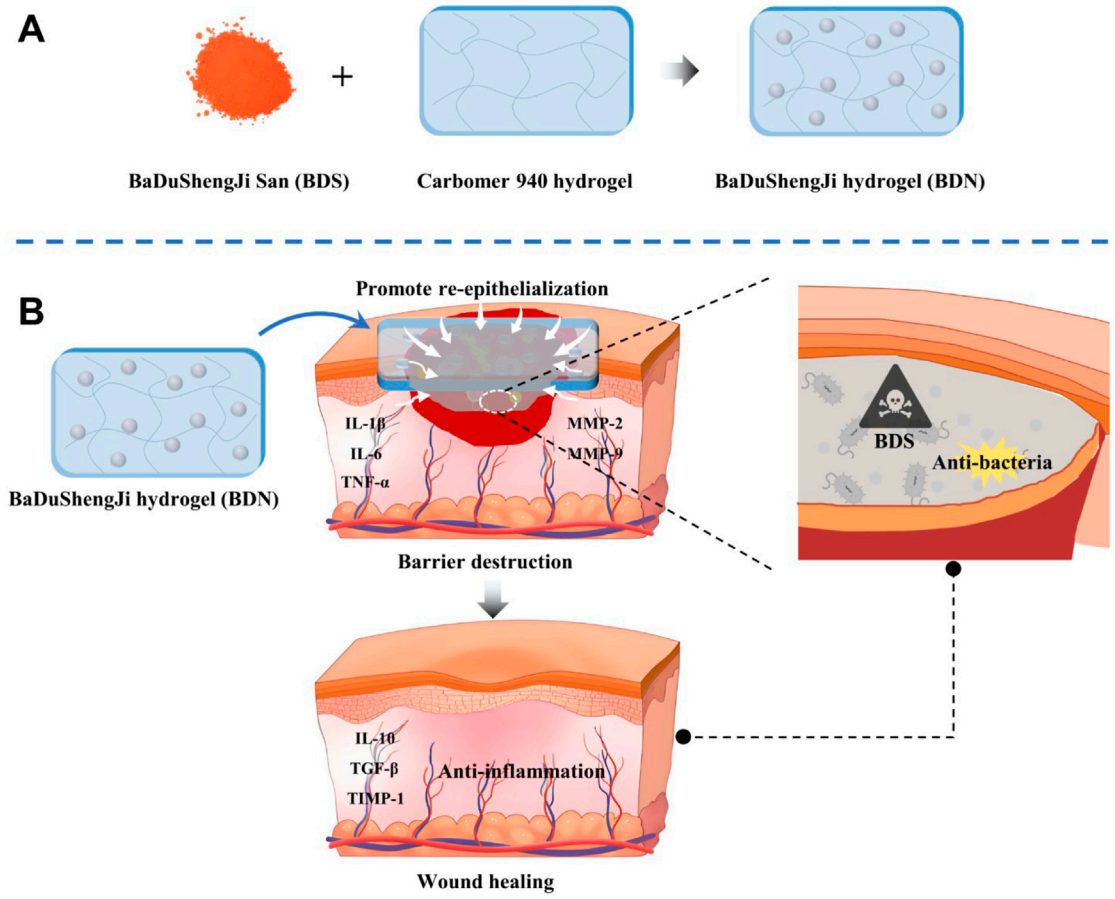
$$S_i = (M_0 - M_i) / M_s \times 100\%;$$

$$\text{Moisture} - \text{retention Rate } (\%) = (1 - S_i) \times 100\%$$

S_i: Water loss rate at the time I, M_0: Total weight before drying, M_i: Total weight at the time i, M_s: Weight of moisturizing agent and water.

2.1.3 The orthogonal experimental design for the preparation of BDN

The content of carbomer 940, the dosage of BDS, pH value, and propylene glycol content in the gel were investigated, and the



SCHEME 1
Schematic illustration for **(A)** the preparation of BaDuShengJi hydrogel and **(B)** the barrier destruction and promoting wound healing mechanisms of BDN. The picture was created by PowerPoint 2019 and Adobe illustrator 2024.

prescription of the gel was optimized by orthogonal design with the comprehensive sensory score as the evaluation criteria.

2.1.4 Characterization of BDN

Use a Scanning Electron Microscope (SEM) (ZEISS ULTRATM 55) to observe the internal morphology and element mapping of various hydrogel samples. An advanced rotational rheometer (ARES G2, TA Instruments, USA) was used to perform oscillatory frequency scans of hydrogel samples at 24°C to analyze the gelation process.

Swelling ratio (%): Immerse lyophilized hydrogel sample (W_0) in 5 mL PBS solution (pH = 7.4). At interval time point, blot excess surface water and weigh the swollen hydrogel (W_t). Three parallel samples are used for each group. The swelling ratio (SR) is calculated by the following formula:

$$SR\ (\%) = (W_t - W_0)/W_0 \times 100\%$$

2.2 *In vitro* antibacterial test

2.2.1 Turbidity and plate count method

The Gram-positive bacteria *Staphylococcus aureus* (*S. aureus,* ATCC 8099) and the Gram-negative bacteria *Escherichia coli* (*E. coli,* ATCC 6538) were used. A total of 1 mL of bacteria (10^6 CFU/mL for *S. aureus* and *E. coli*) were treated with different concentrations of BDN. The *in vitro* antimicrobial activity of BDN against *S. aureus* and *E. coli* was assessed using the turbidity and plate count method, live/dead staining for bacteria.

2.2.2 Anti-biofilms effect of BDN

The anti-biofilm effect of BDN was studied using SEM and crystal violet staining. For biofilm culturing, an *S. aureus* suspension and Mueller-Hinton broth medium were placed in 96-well plates and cultured at 37°C for 24 h. The anti-biofilm effect of different concentrations of BDS and BDN extracts was incubated for 24 h. After treatment, 0.5% crystal violet solution was added to the biofilms, stained for 30 min, and washed 6 times with PBS. Lastly, the crystal violet was dissolved in methanol, and the absorbance at 595 nm was measured using a microplate reader. For SEM observation, glutaraldehyde and osmic acid solutions were used to fix the samples. Dehydrate the samples using an alcohol gradient (30%, 50%, 70%, 90%, 100%) and spray the surface with gold. Examine the anti-biofilm effect using an emission scanning electron microscope (Hitachi SU-8010).

2.3 Evaluation of anti-inflammatory performance of BDN on raw 264.7

RAW 264.7 was incubated in a 6-well plate for 24 h, followed by co-incubation with LPS and various samples for 24 h. Subsequently, RAW 264.7 cells and the supernatant were collected for Elisa experiments.

2.4 Animal models and treatments

All animal experiments were performed according to the guidelines for laboratory animals established by Zhejiang University. During the study, rats were identified solely through labeled cage boxes without any direct markings on the animals themselves. Given the relatively large surgical wounds on the rats, each cage was housed with only one individual to minimize their distress and discomfort, as well as to prevent cross-inflicted wounds from mutual scratching that could exacerbate injuries. This arrangement was implemented to ensure the reliability and stability of experimental data to the greatest extent possible.

2.4.1 Diabetic wound model

To create the type 1 diabetic model, Sprague Dawley rats (male, 6 weeks, 150–200 g) were injected with STZ (40 mg/kg) for 1 week. Rats with a blood glucose concentration of above 16.7 mM were considered as diabetic ones. Subsequently, full-layer skin wounds were established in all diabetic rats (approximately 10 mm in diameter) and grafted with saline, blank carbomer gel (KN), BDS and BDN. The wound dressing was changed every other day, digital images of wounds were acquired at different intervals (day 0, 7, 14, 21) and the wound area was calculated using ImageJ. The pathological status and healing process of wounds were evaluated by H&E staining and Masson's trichrome staining. Keratin 10 expression was using immunohistochemical staining and CD31, α-SMA levels were determined using immunofluorescence staining. Western blot analysis was used to evaluate the anti-inflammatory activity and collagen synthesis of BDN: TNF-α, IL-10, TGF-β, IL-6, IL-1β, MMP-2/9, TIMP-1, β-actin. Skin tissues of rat wounds at day 21 were collected and used for bacterial culture by the standard plate counting assay to value the anti-bacterial activity of BDN.

2.4.2 "Comb" burn model

The "comb" burn model was established following previous reports. (Fang et al., 2017). The burn wound area occupied approximately 4% of the total body surface area (TBSA). During the operation, the breathing and heart rates of the burned rats were carefully monitored to ensure that all of the rats were under anesthesia and pain-free before being allowed to recover from the anesthesia. Twenty animals were randomly assigned to four groups: Saline, KN, BDS and BDN group. The wounds were administered therapeutic agents at a dosage equivalent to 1 mg/cm^2 of BDS. In the KN group, an equivalent volume blank hydrogel of BDN was applied. The wound sites were subsequently dressed with a four-layer petrolatum gauze as the primary (inner) dressing, overlaid with a four-layer cotton gauze as the secondary (outer) dressing. Following this, the wounds were secured using an elastic bandage, which was applied with gentle compression to ensure proper adherence and stabilization. Dressing changes were performed at 2-day intervals to maintain aseptic conditions and promote optimal wound healing dynamics.

The wound area was evaluated and recorded at different intervals (day 0, 4, 8, 14, 21). Skin samples were fixed in 4% paraformaldehyde, embedded in paraffin and sectioned at a thickness of 5 μm using a rotary microtome. The pathological status and healing process of wounds were evaluated followed the detection in the diabetic wound model.

2.5 Safety evaluation

Various concentrations (4, 20, 100 μg/mL) of BDS, and BDN were co-incubated with 2% of rabbit RBC for 1 h at 37°C, water was used as the positive control while saline was used as the negative control. After centrifuging at 3,000 rpm for 10 min, the supernatant was collected and the absolution was measured at 541 nm. The hemolysis ratio (HR) was calculated following the formula:

$$\mathrm{HR}\ (\%) = \left(\mathrm{OD}_{\mathrm{sample}} - \mathrm{OD}_{\mathrm{negative\ control}}\right) \times 100\% \Big/ \left(\mathrm{OD}_{\mathrm{positive}} - \mathrm{OD}_{\mathrm{negative\ control}}\right)$$

The liver and kidney were collected for conducting the histology analysis after the 21 days' treatment was ended.

2.6 Statistical analysis

Data analysis was performed using GraphPad Prism 8.0.2 software to calculate mean ± standard de*via*tion (SD). Student's t-test were used to assess significant differences between two groups, while One-way or Two-way ANOVA were used to assess significant differences when compared with more than two groups, while $^{*}p < 0.05$, $^{**}p < 0.01$, $^{***}p < 0.001$, $^{****}p < 0.0001$ indicating significance, and n s indicating no significance.

3 Results and discussion

3.1 Preparation and characterization of BDN hydrogel

As a macromolecular material, hydrogel can load drugs into a three-dimensional cross-linked network through physical or chemical methods. Compared with other commonly used topical dosage forms such as creams or petroleum jelly-based preparations, hydrogels offer the following advantages:

Firstly, the moist environment of hydrogels aligns better with the "moist wound healing theory" for wounds, demonstrating potential in accelerating granulation formation (Huang et al., 2024). In contrast, while petroleum jelly-based preparations can soften keratin, their poor air permeability may hinder the drainage of exudate, leading to wound maceration and anaerobic bacterial proliferation (Butko et al., 2021). The oil-water mixed system of creams is prone to loss with exudate (the water loss rate of cream bases is 3–5 times faster than that of gels), making it difficult to

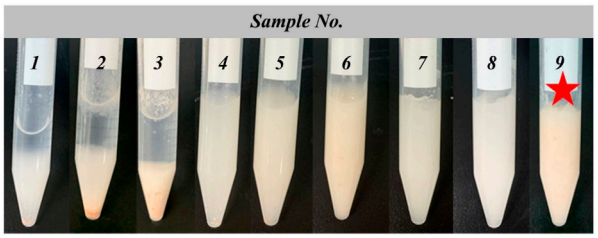


FIGURE 1
Appearances of the BDN hydrogel prepared with different compositions.

maintain a stable moist environment (Miastkowska et al., 2020). Secondly, Hydrogels possess strong swelling properties and the ability to absorb wound exudate (Tian et al., 2025). Although creams can promote drug penetration, their ability to absorb exudate is relatively poor, which may prolong healing time due to retained exudate. Thirdly, Hydrogels have a soft texture and are easy to remove, reducing mechanical damage and pain during dressing changes. Petroleum jelly gauze, on the other hand, tends to adhere to the wound when dry, and forced dressing changes may exacerbate injury (Wen and Shen, 2021). Fourthly, Hydrogels can optimize drug activity by adjusting pH, whereas creams or petroleum jelly-based preparations may limit drug effects due to the properties of their bases (Chen et al., 2023).

Considering the intrinsic properties of hydrogels, in addition to the bioactive drug substance-BDS, the prescription should also include gel base, humectant, preservative, and pH adjuster. Therefore, this study optimized the gel formulation using an orthogonal design to determine the optimal process for the preparation of BDN (Supplementary Table S1). As the preservative content in the gel is merely 0.1%, it has a negligible impact on the gel properties, hence preservative screening was not conducted.

Carbomer 940, sodium carboxymethyl cellulose (CMC-Na), and sodium alginate, as widely utilized gel bases, are recognized for their superior biocompatibility. Therefore, these three gel bases were given priority in the study. The experimental findings revealed that Carbomer 940 possesses superior gel-forming capabilities, enabling the formation of a uniform and refined gel at a 1% (w/v) concentration. This concentration yields a gel with moderate fluidity and viscosity, suitable as the gel base for this study. In contrast, the other gel bases, as depicted in Supplementary Figure S1, even at 10% sodium alginate and 5% CMC-Na, exhibit excessive fluidity, detrimental to drug adherence on wounds.

Humidity agents possess the capacity to adsorb and retain moisture, thereby preventing the evaporation of water from the skin surface, which in turn provides an extended humid environment for the skin or specific areas. In this study, the moisture retention of glycerol and 1,3-propanediol were evaluated. After the samples were incubated in an oven at 37°C for 48 h, the final moisturizing rate was 7.2% for the glycerol group and 5.5% for the 1,3-propanediol group. Additionally, the glycerol-enriched gel matrix was observed to be smoother, more refined, and less aerated. Hence, glycerol was selected as the preferred humectant in the BDN formulation.

To optimize the recipe of BDN, we carried out an orthogonal optimization experiment in which the concentrations of Carbomer 940, BDS, pH value, and propylene glycol as investigation factors and the comprehensive sensory evaluation as an indicator (Supplementary Table S3). An orthogonal analysis was designed to identify factors that have a significant effect on the comprehensive sensory. The orthogonal design is listed in Supplementary Tables S1, S2, and the results revealed that sample 9 achieved the highest score, whereas samples 1–3 received the lowest scores (Figure 1). The range analysis (R) of the orthogonal test results indicated that the content of carbomer 940 had the greatest impact on the gel, followed by the amount of BDS, pH value, and glycerol content. The optimal formulation for BDN, denoted as $A_3B_3C_2D_1$, consisted of 5% carbomer 940, 2% BDS, pH adjusted to 7.40, and 5% glycerol.

Stability assessments demonstrated that the formulated gel maintained its integrity post-centrifugation, with no observable stratification or liquefaction, thereby confirming its favorable centrifugal stability (Supplementary Figure S2). After a 24-h period at both 60°C (Supplementary Figure S3) and −20°C (Supplementary Figure S4), the absence of precipitation, stratification was noted, thereby attesting to the gel's exceptional thermostability across a broad temperature spectrum. The particle size distribution of the gel was analyzed in accordance with the methodology outlined in the Chinese Pharmacopoeia (2020 edition) under General Rule 0,982, First Method. Results showed that the prepared gel was both uniform and delicate, with the majority of particles measuring less than 10 μm, significantly below the Pharmacopoeia's stipulation of less than 180 μm for gels in suspension form (Supplementary Figure S5).

Hydrogels are constituted by hydrophilic polymeric materials soluble in water, which undergo physical or chemical crosslinking to form a three-dimensional network-like structure. Macroscopically, the SEM images of BDN exhibit a more compact and ordered honeycomb-like network compared to the blank gel group. On a microscopic scale, the gel network of the blank gel group appears relatively smooth, whereas the BDN group displays numerous minute particles embedded within or on the surface of the gel network (Figure 2A). Combining the results of elemental mapping (Figure 2A) with prior slide analysis of the BDN gel (Supplementary Figure S5), suggests that these particles are likely to be microscopic granules of the BDS powder encapsulated within the gel. The elemental mapping further reveals a uniform distribution of representative elements from the powder within the hydrogel matrix, indicating a homogeneous dispersion of the powder without significant agglomeration. Further physicochemical characterization reveals that the storage modulus consistently exceeds the loss modulus at low frequencies, confirming the formation of an elastic hydrogel network in the BDN group (Figure 2B). Swelling analysis underscores the remarkable water-absorbing capacity of BDN, capable of absorbing approximately 1200% of its own weight in water (Figure 2C). The thixotropic properties of the hydrogel were analyzed with periodic strain changes (1% or 500% strain), which indicated that the hydrogel could recover its gel phase at 1% strain after gel rupture at 500% strain (Figure 2D). These results indicating that BDN exhibited self-healing property and recover to its original structure after broken. Collectively, these data underscore the exceptional physicochemical

10.3389/fphar.2025.1580994

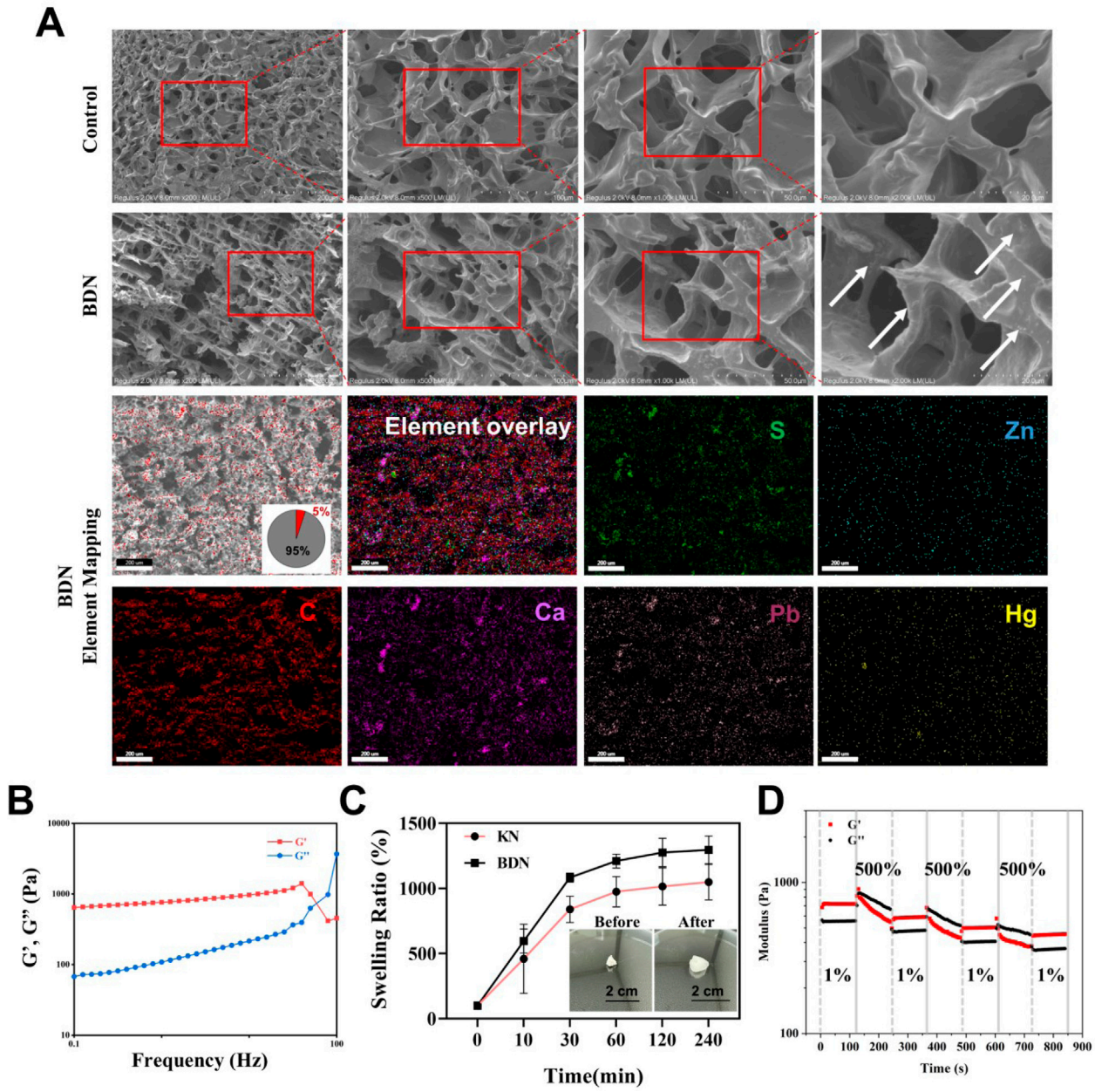


FIGURE 2
Characterization of BDN. **(A)** SEM images and element mapping of KN and BDN. **(B)** Storage modulus (G′) and loss modulus (G″) of BDN against frequency. **(C)** The swelling ratio (%) of BDN after being immersed in water at various times. **(D)** Thixotropic characterization of self-healing hydrogel at alternate strain of 1% and 500%, with angular frequency of 10 rad s^{-1}.

properties of the formulated BDN, rendering it a suitable candidate as a hydrogel dressing for wound care.

3.2 Cell behavior with BDN hydrogel

The wound healing process involves the participation of various cellular activities, such as the proliferation and migration of keratinocytes and fibroblasts, as well as the involvement of endothelial cells in the formation of new blood vessels. In this section, we focused on examining the effects of BDN on several representative cellular activities related to wound healing. The results of the CCK-8 assay (Figures 3A–C) combined with live/dead cell staining (Figure 3D) showed that BDN is highly biocompatible, as over 75% of Hacat and Fb cells remain viable even at concentrations up to 100 μg/mL. Furthermore, it was observed that BDN and BDS exhibit a proliferation-promoting effect on HUVECs, consistent with literature reports that highlight the angiogenic activities of their primary constituents, calcined calamine and calcined plaster (Cheng et al., 2023). Scratch assays indicated that BDS and BDN significantly promoted the migration of the 3 cell lines, suggesting that BDS and BDN may

10.3389/fphar.2025.1580994

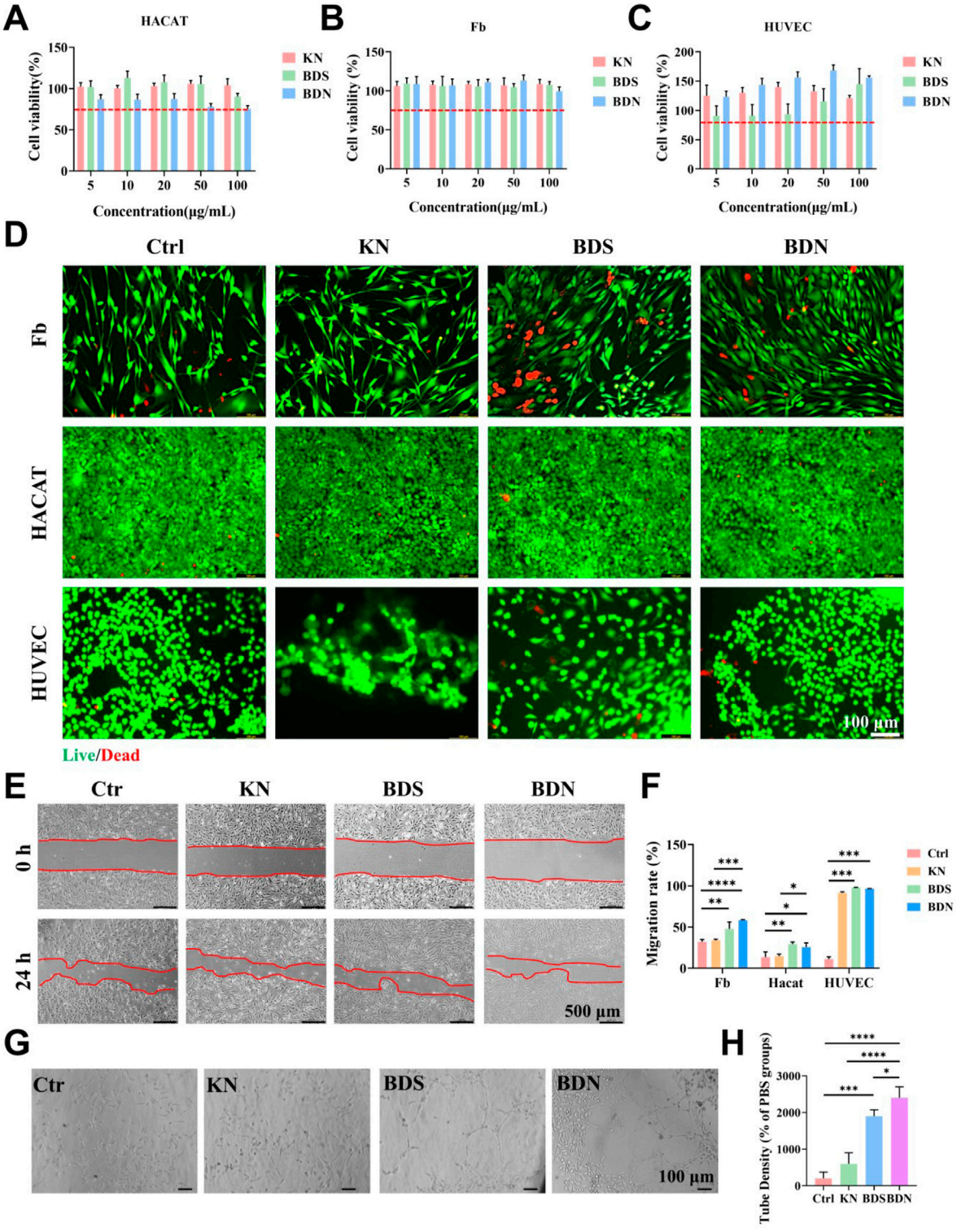


FIGURE 3
Cytotoxicity of KN, BDS and BDN against **(A)** Hacat, **(B)** Human Skin Fibroblasts (Fb) and **(C)** HUVEC cells (n = 6). The red dashed line represents a 75% survival rate. **(D)** Live/dead cell assay for cells treated with various samples. (Scale bar = 100 μm, concentration of hydrogel extract = 100 μg/mL). **(E)** BDN promoted the migration of Fb cells by cell scratch assay and **(F)** the quantity data of migration rate. Concentration of hydrogel extract was 100 μg/mL, n = 3. **(G)** Representative images and **(H)** quantitative analysis of tube formation of HUVECs treated with different groups, scale bar = 100 μm, n = 3. All data are presented as mean ± SD. Data were analyzed using contrast analyses following one-way ANOVA. *$p < 0.05$, **$p < 0.01$, ***$p < 0.001$, ****$p < 0.0001$. ns, No significant difference.

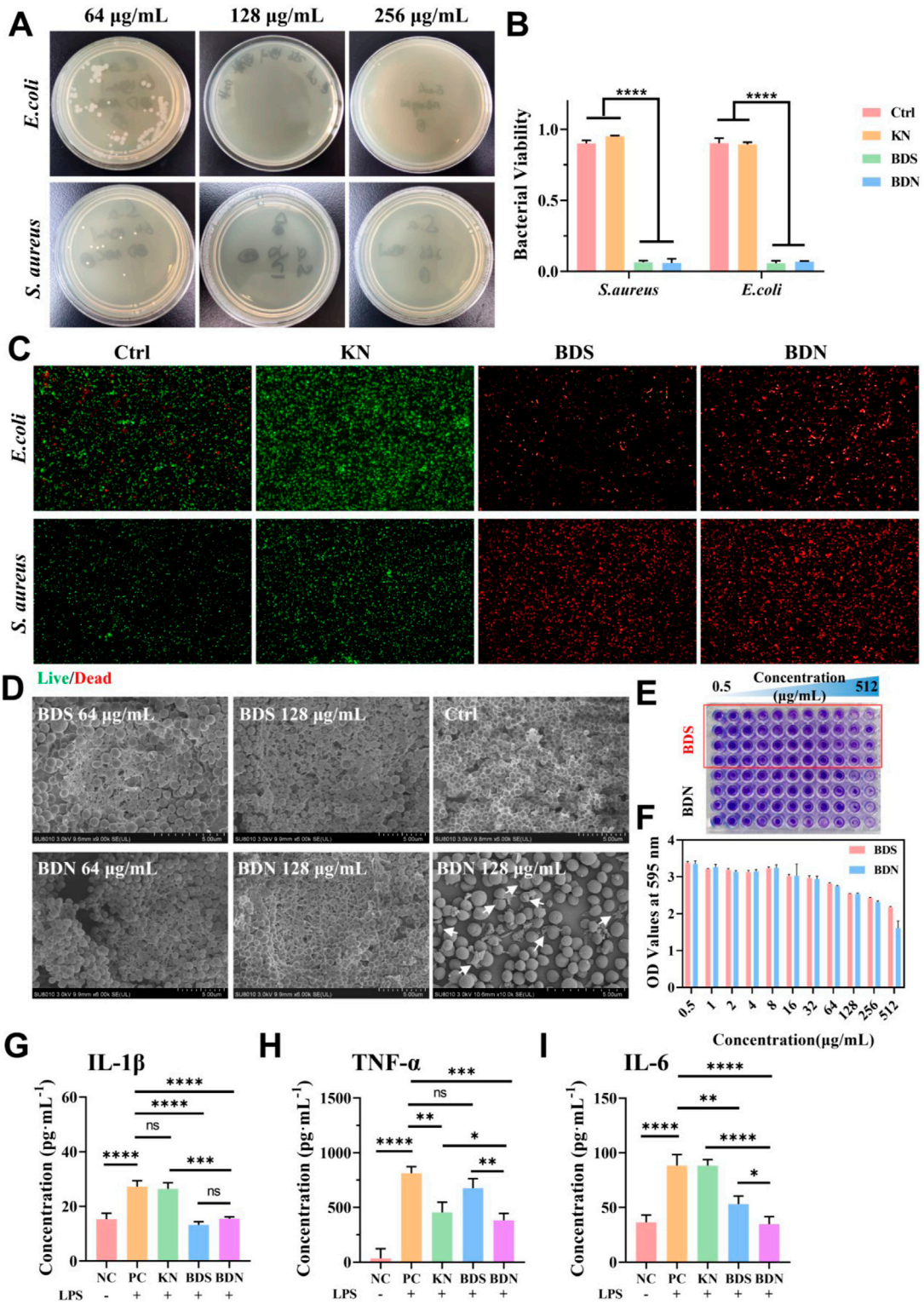


FIGURE 4
Evaluation of the antibacterial effect and antiinflammation of hydrogels. **(A)** Images of survival bacteria clones after the treatment of BDN hydrogels. **(B)** The quantitation data and **(C)** the live/dead staining of bacteria after the treatment of hydrogels, n = 3. (×40). **(D)** The corresponding SEM images of *Staphylococcus aureus* biofilm treated with different substances. Arrows pointed to the damaged bacterial structure. **(E)** The crystal violet staining results of the biofilm after being treated with various substances and **(F)** its OD values at 595 nm (n = 4). Expression levels of **(G)** IL-1β, **(H)** TNF-α, **(I)** IL-6 inflammatory factors in macrophages treated with various substances for 24 h, n = 3. All data are presented as mean ± SD. Data were analyzed using contrast analyses following one-way ANOVA. *$p < 0.05$, **$p < 0.01$, ***$p < 0.001$, ****$p < 0.0001$. ns, No significant difference.

accelerate wound healing by promoting cell migration (Figure 3E, F; Supplementary Figure S6). Tube formation assays showed that BDS and BDN significantly promoted the formation of new blood vessels, with BDN showing a stronger ability to promote angiogenesis than BDS (Figures 3G,H). The phenomenon attributed to the angiogenic potential of the carbomer gel itself, and on the other hand, it may be due to the gel's certain degree of fibrinolytic effect on the red ochre, calcined calamine, calcined plaster contained in BDS (Cheng et al., 2023).

3.3 Antibacterial and anti-inflammation activity *in vitro*

Wound infection is one of the primary causes of delayed wound healing, particularly in diabetic patients where the hyperglycemic microenvironment of chronic wounds favors bacterial growth. Bacterial proliferation releases toxins and damages surrounding tissues, leading to necrosis that deprives nascent tissues of essential nutritional support on one hand, and exacerbating and perpetuating inflammatory responses on the other, thereby disrupting the normal wound healing process and delaying recovery (Yang et al., 2023; Chang and Nguyen, 2021; Uberoi et al., 2024).

The BDS and its components, such as red ochre and calomel, have been proven to possess broad-spectrum antibacterial properties (Cheng et al., 2023). In this section, the minimum inhibitory concentration (MIC) and minimum bactericidal concentration (MBC) of the prepared BDN were further measured by the microbroth dilution method. The results (Supplementary Figure S7) indicated that BDN significantly inhibited the growth of both *S. aureus* and *E. coli*, with an MIC value of 64 μg/mL and an MBC value of 128 μg/mL (Figure 4A). Since the BDS in BDN has poor solubility in water, the extraction of BDN used in this experiment was only co-incubated, diluted, shaken, and centrifuged with the medium. Therefore, considering the solubility factor, the actual MIC and MBC values of BDN should be lower. Live/dead bacterial staining (Figures 4B,C) further confirmed the comparable antibacterial capacity of BDN to BDS, demonstrating significant killing effects against both *S. aureus* and *E. coli*.

Bacterial biofilms are the major contributor to antibiotic resistance and recurrent wound infections. Firstly, biofilms impede the penetration of antibiotics or disinfectants, adsorb and inactivate certain antibiotics, thereby reducing the effective concentration of antibiotics within the biofilm. Simultaneously, the protective barrier of the biofilm allows bacteria time to adapt and develop antibiotic resistance. Furthermore, bacteria deep within biofilms often experience nutrient deprivation, leading to slow growth or even dormancy, enabling them to resist antibiotics targeting metabolic pathways through reduced metabolism. Therefore, disrupting bacterial biofilms is beneficial in reducing bacterial resistance to antimicrobials (Yang et al., 2023).

SEM (Figure 4D) revealed that most of the *S. aureus* cells in the control group were interconnected through a reticulated extracellular matrix (ECM) and forming large clusters, while the bacteria in BDS or BDN group were detached from the biofilm and exposed the ECM. Notably, more detached bacteria can be seen in the BDN group, indicating a stronger biofilm-disrupting ability than BDS. Additionally, SEM demonstrates that BDN significantly damages bacterial cell structures, with visible ruptures and efflux of cellular contents, suggesting that BDN exerts bactericidal effects by disrupting cell wall structures or causing imbalances in osmotic pressure across bacterial membranes. As the drug concentration in BDS and BDN groups decreases to 64 μg/mL, the interlaced filamentous ECM structures transform into a buried-like structure while the bacterial density within the ECM increases significantly, suggesting reduced disruption of the bacterial biofilm structure occurred. The crystal violet staining results (Figures 4E,F) further confirmed that BDS and BDN can significantly disrupt *S. aureus* biofilms at a concentration of no lower than 128 μg/mL.

Chronic inflammation is another significant factor contributing to delayed wound healing. In this study, an *in vitro* inflammatory model was constructed using LPS-induced macrophage polarization, and the anti-inflammatory abilities of BDN and BDS were evaluated by measuring the changes of inflammatory factor levels. The results showed that macrophages pretreated with BDN or BDS significantly alleviated or even reversed the release of various inflammatory factors, such as IL-1β, IL-6, and TNF-α (Figures 4G–I). Furthermore, BDN demonstrated stronger inhibitory effects on IL-6 and TNF-α compared to BDS, which may be partly attributed to the anti-inflammatory properties of carbomer gel itself and the interaction between carbomer and BDS (Cheng et al., 2023).

3.4 Therapeutic effects on the diabetic chronic wound healing

The favorable biocompatibility, remarkable antibacterial, anti-inflammatory, and angiogenesis-promoting properties exhibited by BDN *in vitro* have prompted us to further validate its ability to facilitate diabetic chronic wound healing *in vivo*. In this study, a full-thickness diabetic rat wound model was established (Figure 5A). Our findings revealed that both BDN and BDS significantly accelerated the wound healing process, with BDN demonstrating superior wound healing speed and quality compared to BDS. Gross observation revealed that the wound healing rate in the BDN group approached 40% on day 7 post-treatment, whereas it was approximately 20% in the BDS group. In contrast, the wound sizes in the control and KN groups remained virtually unchanged, and even slightly increased due to infection-induced necrotic, indirectly confirming the antibacterial properties of BDS and BDN (Figures 5B–D). On Day 14, significant inflammatory cell recruitment was observed in the Ctrl and KN groups, correlating with visible bacterial infections (Figure 5E). The occasional erythrocytes in the BDS and BDN groups may result from minor scab dislodgment during wound debridement before sample collection, potentially causing slight bleeding (Figure 5E; Supplementary Figure S8). Additionally, combined with K10 staining (Figure 5G), the results showed that the newly formed epidermis was significantly thicker in the BDS and BDN groups compared to the control and KN groups (Figure 5F), with a tighter attachment to the subcutaneous tissue and a more abundant stratum spinosum in the BDN group, indicating higher healing quality. Masson staining (Figure 5G) showed that both BDN and

10.3389/fphar.2025.1580994

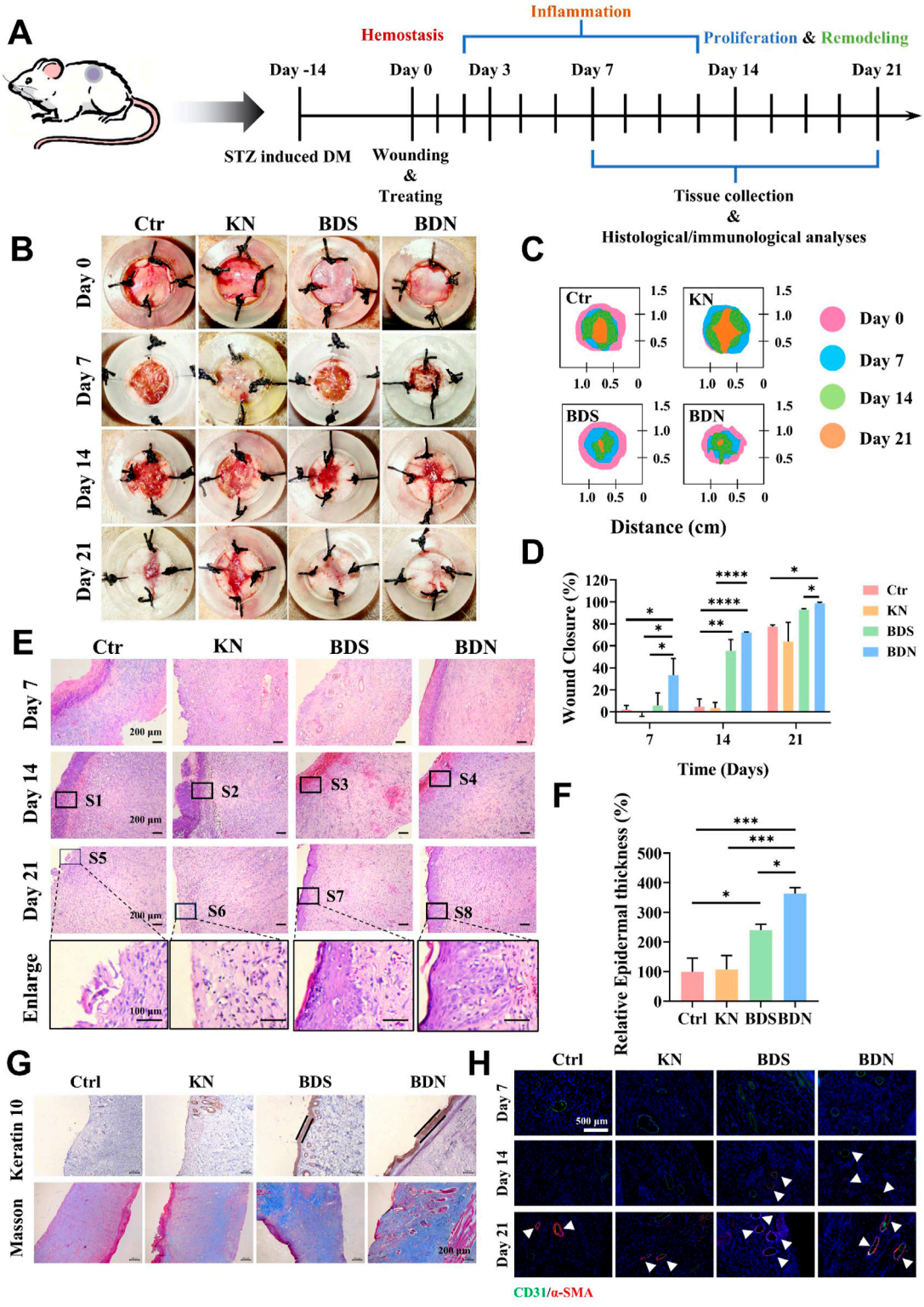


FIGURE 5
The efficiency of the BDN hydrogel on a full-thickness wound healing of diabetic rat. **(A)** Schematic representation of *in vivo* wound healing experiment process. **(B)** Photographs of wounds treated with different samples on day 0, 7, 14, 21. **(C)** Traces of wound closure over 21 days and **(D)** the Quantification of the wound healing rate (n = 3). **(E)** H&E images of wound tissue with varied treatments at different timepoint. **(F)** Quantitative analysis of epidermal thickness. **(G)** Immunohistochemical results of keratin 10 and Masson's trichrome staining of wound tissue with different treatments on day 21, n = 3. **(H)** α-SMA and CD31 immunofluorescence staining for each group at different time. All data are presented as mean ± SD. Data were analyzed using contrast analyses following one-way or two-way ANOVA. *$p < 0.05$, **$p < 0.01$, ***$p < 0.001$, ****$p < 0.0001$. ns, No significant difference.

10.3389/fphar.2025.1580994

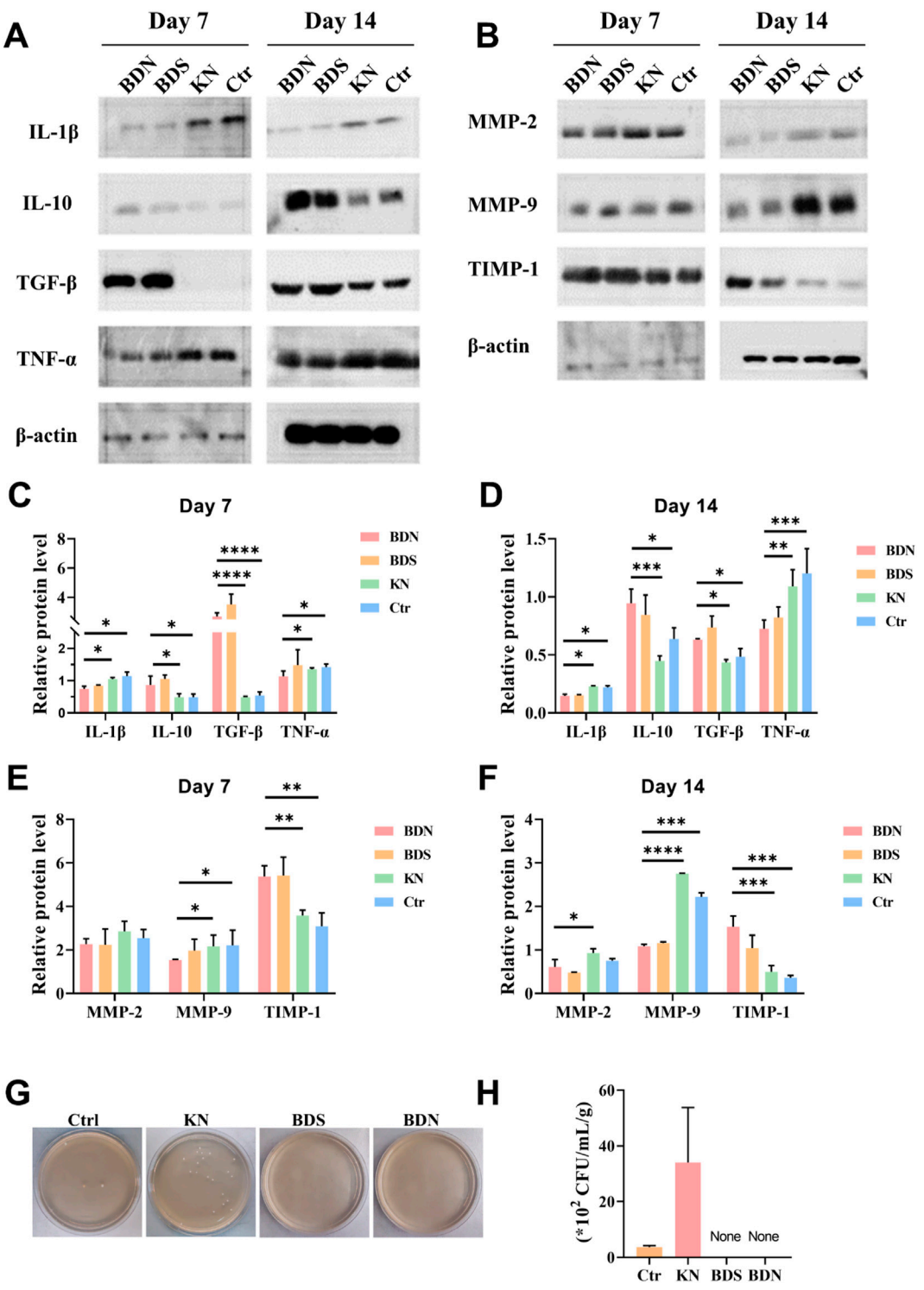


FIGURE 6
The representative protein levels related to inflammation or collagen formation. The Western blot results of **(A)** inflammation factors and **(B)** factors related to collagen formation in wounds. The quantitative results of **(C,D)** inflammation factors and **(E,F)** factors related to collagen formation, n = 3. **(G)** Representative photographs and **(H)** quantitative data of bacterial culture from the skin tissue of rat wounds at day 21 characterized by the standard plate counting assay (n = 3). All data are presented as mean ± SD. Data were analyzed using contrast analyses following one-way or two-way ANOVA. *p < 0.05, **p < 0.01, ***p < 0.001, ****p < 0.0001. ns, No significant difference.

BDS promoted collagen deposition, with BDN exhibiting a more compact and uniform distribution of collagen fibers in a basketweave pattern within the dermis. CD31 and α-SMA were used to label vascular endothelial cells and smooth muscle cells, respectively. The immunofluorescence staining results revealed that the presence of mature vessels in the wounds of the BDS and BDN

groups at an earlier stage (day 14), with a higher proportion of mature vessels in the BDN group. Additionally, on day 21, the density of mature vessels in the BDS and BDN groups was significantly higher than that in the control and KN groups, indicating the angiogenesis-promoting ability of BDS and BDN *in vivo* (Figure 5H; Supplementary Figure S10).

Inflammation and proteolysis are pivotal in the orchestration of tissue regenerS7ation and wound repair. To elucidate the impact of BDS and BDN on these processes, we quantified inflammatory mediators and factors associated with protein breakdown in regenerative tissues using Western blot. Our findings indicate that both BDS and BDN markedly attenuated the expression of pro-inflammatory cytokines, including IL-1β and TNF-α, while concurrently augmenting the levels of anti-inflammatory mediators, IL-10 and TGF-β. This modulation was sustained over a 14-day period, facilitating a seamless progression of the wound healing cascade from the inflammatory to the proliferative and remodeling phases (Figures 6A,C,D).

Matrix metalloproteinases (MMPs) and tissue inhibitors of metalloproteinases (TIMPs) play crucial roles in regulating the metabolic balance between ECM synthesis and degradation, which is closely related to wound healing and tissue remodeling. Comparative analysis with control and KN groups revealed that BDS and BDN significantly curtailed the wound tissue expression levels of MMP-2/9 at multiple time points post-treatment, and concurrently elevated TIMP-1 content. These results suggest a superior capacity of BDS and BDN to enhance tissue protein synthesis compared to the control and KN groups (Figures 6B,E,F).

Finally, bacterial cultures were performed on homogenized wound tissues from each group. The results showed that the bacterial growth was observed in both the control and KN groups, whereas BDS and BDN groups exhibited significant antibacterial effects, consistent with the results of *in vitro* antibacterial experiments (Figures 6B,E). Notably, the KN group exhibited a higher bacterial load and more severe infection in wound tissues compared to the control group, which explained the slowest wound healing rate and higher MMP-2/9 content related to protein degradation in the KN group (Figures 6G,H). These observations underscore the propensity for bacterial proliferation in moist environments and highlight the critical role of effective antibacterial strategies in wound management.

In conclusion, the aforementioned series of results indicate that both BDS and BDN possess the ability to accelerate chronic wound healing. However, BDN exhibits superior healing speed and quality compared to BDS, which may be attributed to the synergistic healing effect between BDS and the moist environment provided by the hydrogel.

3.5 *In vivo* healing performance of the BDN hydrogel in a "comb" burn model

Burns and scalds, frequent occurrences in everyday life, demand swift primary care guided by the quintessential "rinse, remove, soak, cover, and transport" approach. Concurrently, the judicious and timely use of pharmaceuticals is imperative to prevent the escalation of wound severity, avert infection, and preclude critical sequelae such as shock and sepsis. Given the remarkable antibacterial and anti-inflammatory properties of BDS and BDN previously demonstrated in chronic wounds, this section we have utilized a high-temperature brass comb to induce a deep second-degree burn model in rats and following evaluated the wound-healing effects of BDN on deep second-degree burns. A rigorous 21-day monitoring of dynamic wound progression in rats were conducted (Figures 7A,B). As depicted in Supplementary Figure S9, the successful establishment of the deep second-degree burn model was primarily determined by the histological examination. H&E staining indicated full-thickness epidermal necrosis and superficial dermal coagulation necrosis in rats. While some follicular necrosis with cystic cavitation was present, residual skin appendages remained, distinguishing these burns from third-degree burns and aligning with the characteristics of deep second-degree burns. Necrosis emerged on day 4 within the untreated control and BDS groups, while their onset was deferred to day 8 in the KN and BDN groups, implicating that the moist environment provided by the hydrogel could postpone skin tissue necrosis in the early stages of burns. Notably, the majority of the BDN group remained non-necrotic until day 14, underscoring a synergistic effect between the gel matrix and BDS contained in BDN in preventing tissue necrosis. From day 8 to day 14, the dense eschar formed by skin necrosis and coagulation, conspicuously impeded transdermal drug permeation, particularly pronounced in the BDS and control groups. On day 21, pronounced bleeding was observed upon trimming the eschar at the edges of the BDN group's wounds, indicating that BDN could improve wound microcirculation and potentially promote angiogenesis, which was further corroborated by immunofluorescence analysis for neovascularization (Figure 7F). Conversely, significant infection and swelling were observed in the untreated control and KN groups, with the former exhibiting subcutaneous infection. Notably, the wound area in the BDN group was significantly smaller than the other three groups, and no infection occurred, demonstrating that BDN significantly accelerated healing in acute deep second-degree burn wounds (Figure 7C).

H&E staining results showed that the newly formed epidermis in the BDN group was significantly thicker than that in the other groups. Besides, BDS alone also had a certain pro-re-epithelialization effect (Figures 7D,E). Further, K10 immunostaining elucidated that BDN significantly bolstered keratinocyte differentiation and fortified the keratinocyte barrier function, surpassing BDS and KN (Figure 7D). Moreover, BDN prominently facilitated collagen deposition, with BDS also demonstrating a notable contribution in this regard (Figures 7D,G). The results of bacterial culture of wound tissues were consistent with visual observations, with obvious infections in the untreated control and KN groups, while BDS and BDN exhibited significant antibacterial effects (Figures 7H,I).

Collectively, these findings confirmed that BDN accelerates deep second-degree burn wound healing through moisture retention, antibacterial activity, promotion of wound re-epithelialization, angiogenesis, and keratinocyte differentiation.

In clinical practice, it has been observed that deep burn wounds are not usually stable and undergo a dynamic progress that results in the deepening and expansion of the initial burn area, a process defined as burn-wound progression (Fang et al., 2017). This progressive damage can induce the conversion of the burn

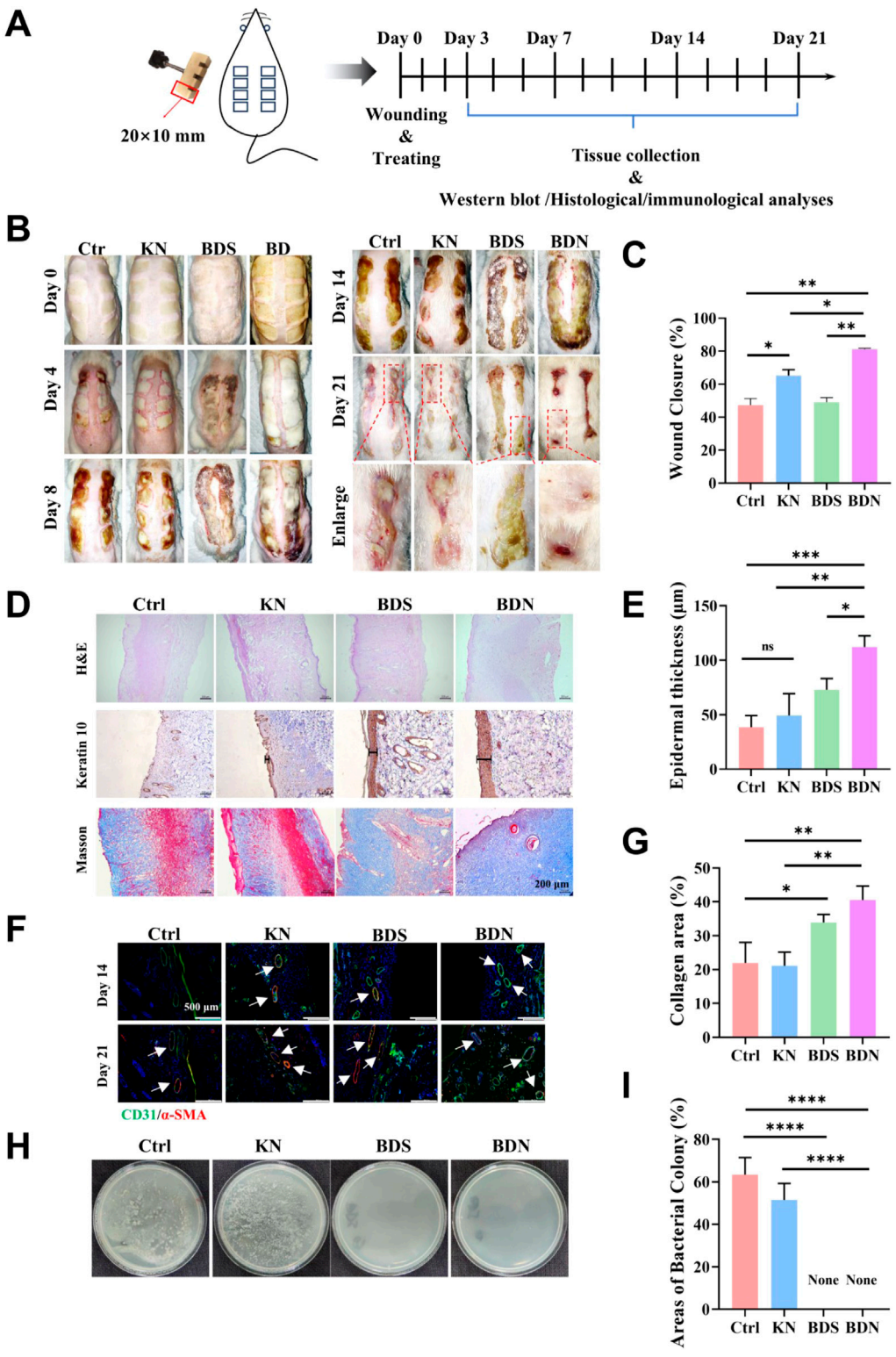


FIGURE 7
In vivo healing performance of the BDN hydrogel in a "comb" burn model. **(A)** Schematic illustration of the experimental procedure for treating deep burn wounds. **(B)** Photographs of wounds on day 0, 4, 8, 14, 21 from the different treatments. **(C)** Wound closure rate measured by ImageJ (n = 3). **(D)** H&E, keratin 10 and masson staining in different treatment groups. The thickness of epidermal **(E)** and **(G)** collagen areas in different treatment groups (n = 3). **(F)** α-SMA and CD31 immunofluorescence staining for each group at different time. **(H)** Representative photographs and **(I)** quantitative data of bacterial culture from the skin tissue of rat wounds at day 21 characterized by the standard plate counting assay (n = 3). All data are presented as mean ± SD. Data were analyzed using contrast analyses following one-way or two-way ANOVA. *$p < 0.05$, **$p < 0.01$, ***$p < 0.001$, ****$p < 0.0001$. ns, No significant difference.

10.3389/fphar.2025.1580994

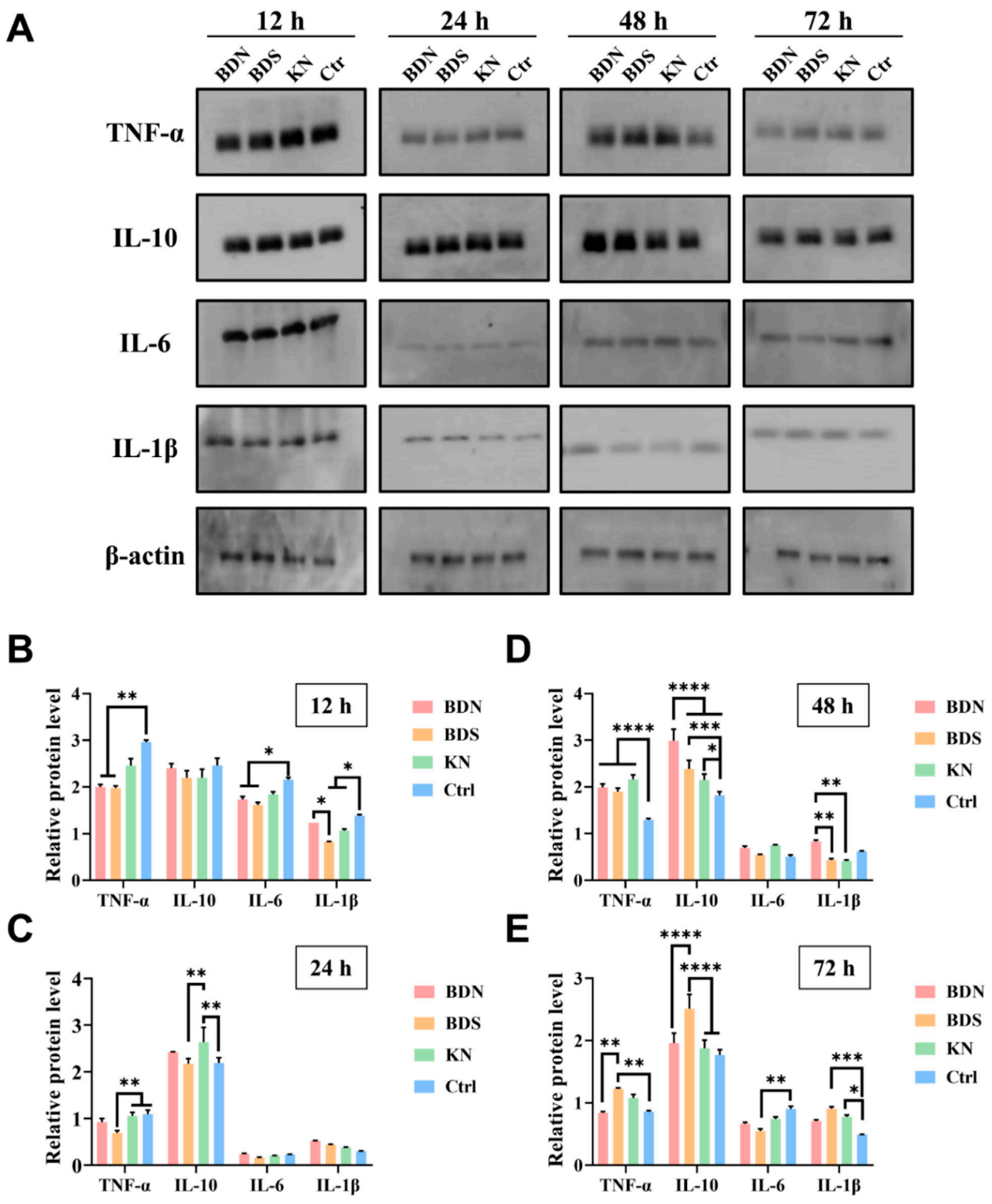


FIGURE 8
The **(A)** Western blot results and relative protein levels of inflammation factors measured from the skin tissue of rat wounds at **(B)** 12 h, **(C)** 24 h, **(D)** 48 h and **(E)** 72 h. All data are presented as mean ± SD. Data were analyzed using contrast analyses following one-way or two-way ANOVA. *$p < 0.05$, **$p < 0.01$, ***$p < 0.001$, ****$p < 0.0001$. ns, No significant difference.

wound from a superficial partial-thickness burn to a deep partial-thickness or full-thickness burn and the development of initially unburned skin into part of the burn wound, which will affect both the appearance and function of the affected area, imposing significant treatment and psychological burdens on patients. Researches have shown that the inflammatory cascade response

following burns results in excessive release of inflammatory factors, triggering tissue edema and ischemia, which may be the primary cause of progressive deepening in burn wounds (Fang et al., 2017). Therefore, controlling the inflammatory cascade response in burn wounds is crucial for preventing their progressive deepening.

Given that progressive wound deepening typically occurs within 72 h and directly correlates with excessive inflammatory cascades at the burn site, hence, we focused on examining the levels of inflammatory factors in various groups after intervention within 72 h post-burn (Figure 8A). Both BDS and BDN exerted rapid anti-inflammatory effects by reducing the levels of TNF-α and IL-6 after 12 h of administration (Figures 8A,B). Notably, BDS, due to its direct contact with the wound, was able to decrease IL-1β levels faster than BDN. Moreover, the use of KN for moisturizing within 48 h post-burn was found to elevate IL-10 levels in the wound, aiding in suppressing the inflammatory storm and preventing wound necrosis and progressive deepening (Figures 8C,D). After 48 h post-burn, compensatory self-regulation occurred in response to the earlier inhibition of TNF-α by BDS, BDN, and KN, leading to an upregulation of TNF-α levels and a significant upregulation of the anti-inflammatory factor IL-10 (Figure 8D). Notably, the IL-10 levels in the BDN group were significantly higher than those in the other three groups. At 72 h, TNF-α, IL-6, IL-1β, and IL-10 levels in the BDN group were the first to decrease and reach a balanced state (Figure 8E). These data indicate that BDN was able to more rapidly and smoothly guide burn wounds through the inflammatory storm, preventing their progressive deepening, which is consistent with the overall wound observations.

During the pathological progression of burns, macrophage polarization status undergoes dynamic evolution, generally manifesting an initial pro-inflammatory M1 phenotype post-burn, which ultimately transitions to an anti-inflammatory M2 phenotype (Zhu Z. et al., 2023). Our results revealed significantly higher M2 macrophage infiltration in the BDN group compared to the other three groups, with the BDS group showing moderate levels, and the KN group marginally higher than control (Supplementary Figure S11). These findings suggest that M2 macrophages in the BDN group exert enhanced anti-inflammatory effects within 72 h, facilitating a rapid transition of the wound environment through the inflammatory storm. This early modulation of inflammation by M2 macrophages in the BDN group also explains the subsequent superior angiogenesis and collagen deposition observed during the wound healing cascade in this cohort.

3.6 Safety evaluation

Safety is one of the most crucial evaluation metrics for drugs used in *in vivo* therapy. The results demonstrate that neither BDS nor BDN poses a risk of hemolysis (Supplementary Figure S12A; Supplementary Figure S12B). Kidney is one of the primary target organs for the mercury toxicity of BDS (Yanli et al., 2012), and H&E staining revealed significant dilation of renal tubules in the BDS group after 4 weeks of use, whereas this symptom was markedly alleviated in the BDN group (Supplementary Figure S12C). The formulation of BDS comprises heavy metals, including lead and mercury, which are considered essential medicinal components and constitute a distinctive characteristic of this prescription (Yanli et al., 2012; Lu et al., 2012). Existing literature indicates that the toxicity of BDS is predominantly associated with its mercury and lead content, with mercury being the principal contributor and lead serving as a secondary factor (Yanli et al., 2012). The primary organ affected by its toxicity is the kidney. Presently, there is a paucity of clinical reports addressing dermatological toxicity or allergic reactions following the administration of BDS. Consequently, this study concentrated on examining its renal toxicity. Notably, within the formulation of BDS, components such as calcined os draconis, calcined gypsum, and calcined calamine exhibit certain detoxifying properties. Specifically, calcined calamine has been shown to mitigate the mercury-induced toxicity of BDS. Zinc ions, as the main component of calcined calamine, play a role in reducing mercury-induced renal toxicity through various mechanisms, such as competitively inhibiting the binding of mercury to plasma proteins, thereby decreasing renal accumulation (Lu et al., 2011; He et al., 2012). In comparison to BDS, the renal toxicity associated with BDN was further alleviated in this study. It is hypothesized that this effect is primarily due to BDN's enhanced dissolution of zinc ions present in BDS, which subsequently amplifies the detoxification efficacy of calcined calamine on mercury ions.

Additionally, no organic damage to the liver was detected in any of the groups (Supplementary Figure S12C). Consequently, the BDN prepared in this study not only exhibits excellent wound healing capabilities but also possesses good biosafety, mitigating renal damage associated with the long-term use of BDS.

4 Conclusion

In this study, we have reformulated and optimized BDS from a powder to BDN. Its efficacy in promoting the healing of diabetic chronic wounds and acute second-degree burn wounds also be investigated. Ultimately, we found that there exists a synergistic effect between carbomer gel and BDS. The prepared BDN not only retains BDS's abilities in promoting cell migration, stimulating angiogenesis, exerting antibacterial and anti-inflammatory effects but also, due to the moisturizing properties of the hydrogel and its potential solubilizing capacity for BDS, further enhances the wound healing speed, quality, and safety. The study not only expands the clinical application scope of BDS, providing a novel tool for clinical acute and chronic wound care but also offers a general approach for the modification of powder dosage forms.

Data availability statement

The original contributions presented in the study are included in the article/Supplementary Material, further inquiries can be directed to the corresponding authors.

Ethics statement

The animal study was approved by The Ethics Committee of The Second Affiliated Hospital Zhejiang University School of Medicine.

The study was conducted in accordance with the local legislation and institutional requirements.

Author contributions

YuZ: Writing – original draft, Data curation, Investigation, Validation. YY: Data curation, Writing – original draft. LY: Formal Analysis, Methodology, Writing – review and editing. FW: Writing – review and editing, Investigation, Supervision. FY: Writing – review and editing, Data curation, Software. SL: Data curation, Writing – review and editing. WX: Project administration, Writing – original draft. MJ: Investigation, Writing – review and editing. YG: Writing – review and editing. JX: Writing – review and editing. CH: Writing – review and editing. ZZ: Writing – review and editing, Conceptualization, Funding acquisition, Project administration, Writing – original draft. YiZ: Data curation, Investigation, Writing – review and editing.

Funding

The author(s) declare that financial support was received for the research and/or publication of this article. This work was financially supported by the National Natural Science Foundation of China (82202451, 82472139), Traditional Chinese Medicine Science and Technology Planning Project of Zhejiang Province (2022ZZ021), Shandong Provincial Natural Science Foundation (ZR2024QH062), National Key Research and Development Program of China (2022YFC2403100), Shandong Postdoctoral Science Foundation (SDCX-ZG-202301012), Taian Science and Technology Innovation Development Project (2022NS316), and National Key Research and Development Projects Intergovernmental Cooperation in Science and Technology of China (2023YFE0109800).

Conflict of interest

The authors declare that the research was conducted in the absence of any commercial or financial relationships that could be construed as a potential conflict of interest.

Generative AI statement

The author(s) declare that no Generative AI was used in the creation of this manuscript.

Publisher's note

All claims expressed in this article are solely those of the authors and do not necessarily represent those of their affiliated organizations, or those of the publisher, the editors and the reviewers. Any product that may be evaluated in this article, or claim that may be made by its manufacturer, is not guaranteed or endorsed by the publisher.

Supplementary material

The Supplementary Material for this article can be found online at: https://www.frontiersin.org/articles/10.3389/fphar.2025.1580994/full#supplementary-material

References

Armstrong, D. G., Boulton, A., and Bus, S. A. (2017). Diabetic foot ulcers and their recurrence. *N. Engl. J. Med.* 376 (24), 2367–2375. doi:10.1056/NEJMra1615439

Armstrong, D. G., Tan, T. W., Boulton, A., and Bus, S. A. (2023). Diabetic foot ulcers: a review. *JAMA* 330 (1), 62–75. doi:10.1001/jama.2023.10578

Butko, Y. O., Tkachova, O., Tishakova, T., Gordienko, A., and Bondariev, Y. (2021). *Wound healing effect of "Prolidoxid" and "Dexpanthenol with ceramides": a comparative study based on the model of chemical burns with expressed alterative skin processes.* ScienceRise Pharmaceutical Science. (Kyiv, Ukraine: National Technical University of Ukraine). doi:10.15587/2519-4852.2021.230031

Cao, S., Tang, T., Shao, X., Wang, C., Feng, Z., Zhu, Z., et al. (2018). Clinical observation on badu shengji powder in the treatment of abscess and sinus of non-lactating mastitis. *World Chin. Med.* 13 (06), 1380–1384. doi:10.3969/j.issn.1673-7202.2023.10.001

Chang, M., and Nguyen, T. T. (2021). Strategy for treatment of infected diabetic foot ulcers. *Acc. Chem. Res.* 54 (5), 1080–1093. doi:10.1021/acs.accounts.0c00864

Chen, J., and Zeng, J. (2024). Clinical observation of Badu Shengji Powder combined with Kangfuxin Liquid on wound healing after simple anal fistula operation. *J. Shanxi Univ. Chin. Med.* 25 (03), 291–295. doi:10.19763/j.cnki.2096-7403.2024.03.09

Chen, Y., Wang, X., Tao, S., Wang, Q., Ma, P. Q., Li, Z. B., et al. (2023). Research advances in smart responsive-hydrogel dressings with potential clinical diabetic wound healing properties. *Mil. Med. Res.* 10 (1), 37. doi:10.1186/s40779-023-00473-9

Cheng, Y., Cao, J., Zhang, D., Niu, S., Chang, J., Fang, Y., et al. (2023). Expert consensus on the clinical application of badu shengji powder. *World Chin. Med.* 18 (10), 1357–1361. doi:10.3969/j.issn.1673-7202.2023.10.001

Cui, Y., and Hu, S. (2024). Application of Badu Shengji Powder combined with nibbling debridement in the treatment of diabetic foot ulcer. *China Mod. Med.* 31 (10), 110–113.

Derkenne, C., Ronchi, L., and Prunet, B. (2019). Management of burns. *N. Engl. J. Med.* 381 (12), 1188. doi:10.1056/NEJMc1909342

Desmet, C. M., Preat, V., and Gallez, B. (2018). Nanomedicines and gene therapy for the delivery of growth factors to improve perfusion and oxygenation in wound healing. *Adv. Drug Deliv. Rev.* 129, 262–284. doi:10.1016/j.addr.2018.02.001

Fang, Q., Guo, S., Zhou, H., Han, R., Wu, P., and Han, C. (2017). Astaxanthin protects against early burn-wound progression in rats by attenuating oxidative stress-induced inflammation and mitochondria-related apoptosis. *Sci. Rep.* 7, 41440. doi:10.1038/srep41440

Freedman, B. R., Hwang, C., Talbot, S., Hibler, B., Matoori, S., and Mooney, D. J. (2023). Breakthrough treatments for accelerated wound healing. *Sci. Adv.* 9 (20), eade7007. doi:10.1126/sciadv.ade7007

Guo, X., Hu, A., and He, C. (2018). Clinical efficacy observation on badu shengji powder in the treatment of diabetic foot ulcer disease. *World Chin. Med.* 13 (06), 1376–1379. doi:10.3969/j.issn.1673-7202.2018.06.016

He, R., Peng, B., Lu, Y., Gao, J., Hui, L., and Li, J. (2012). Observation on effect of Badu Shengji San and its decomposed recipes on morphological changes of injured skin tissues in rats. *China J. Chin. Materia Medica* 37 (6), 715–718. doi:10.4268/cjcmm20120604

Huang, C., Dong, L., Zhao, B., Lu, Y., Huang, S., Yuan, Z., et al. (2022). Anti-inflammatory hydrogel dressings and skin wound healing. *Clin. Transl. Med.* 12 (11), e1094. doi:10.1002/ctm2.1094

Huang, C., Huangfu, C., Bai, Z., Zhu, L., Shen, P., Wang, N., et al. (2024). Multifunctional carbomer based ferulic acid hydrogel promotes wound healing in radiation-induced skin injury by inactivating NLRP3 inflammasome. *J. Nanobiotechnology* 22 (1), 576. doi:10.1186/s12951-024-02789-7

Jeschke, M. G., van Baar, M. E., Choudhry, M. A., Chung, K. K., Gibran, N. S., and Logsetty, S. (2020). Burn injury. *Nat. Rev. Dis. Prim.* 6 (1), 11. doi:10.1038/s41572-020-0145-5

Liu, D., Wu, G., Luo, L., Ou, C., and Zou, Y. (2020). Research progress of badu shengji powder in the treatment of chronic wounds. *World Chin. Med.* 15 (6), 949–952. doi:10.3969/j.issn.1673-7202.2020.06.028

Liu, X., Sun, Y., Wang, J., Kang, Y., Wang, Z., Cao, W., et al. (2024). A tough, antibacterial and antioxidant hydrogel dressing accelerates wound healing and suppresses hypertrophic scar formation in infected wounds. *Bioact. Mater* 34, 269–281. doi:10.1016/j.bioactmat.2023.12.019

Lu, Y., He, R., Peng, B., Gao, J., and Li, J. (2011). Attenuation effects of compatible medicines on arsenical and lead toxicity of Badu Shengji San. *China J. Chin. Materia Medica* 36 (15), 2118–2123. doi:10.4268/cjcmm20111524

Lu, Y., He, R., Peng, B., Xu, Q., Zhang, X., Lin, H., et al. (2012). Comparison of effects of Badu Shengji San on rats with different injured skins. *China J. Chin. Materia Medica* 37 (6), 711–714. doi:10.4268/cjcmm20120603

Martin, P., and Nunan, R. (2015). Cellular and molecular mechanisms of repair in acute and chronic wound healing. *Br. J. Dermatol* 173 (2), 370–378. doi:10.1111/bjd.13954

Miastkowska, M., Kulawik-Pióro, A., and Szczurek, M. (2020). Nanoemulsion gel formulation optimization for burn wounds: analysis of rheological and sensory properties. *Processes* 8 (11), 1416. doi:10.3390/pr8111416

Pena, O. A., and Martin, P. (2024). Cellular and molecular mechanisms of skin wound healing. *Nat. Rev. Mol. Cell Biol.* 25 (8), 599–616. doi:10.1038/s41580-024-00715-1

Shao, Z., Yin, T., Jiang, J., He, Y., Xiang, T., and Zhou, S. (2023). Wound microenvironment self-adaptive hydrogel with efficient angiogenesis for promoting diabetic wound healing. *Bioact. Mater* 20, 561–573. doi:10.1016/j.bioactmat.2022.06.018

Sharifiaghdam, M., Shaabani, E., Faridi-Majidi, R., De Smedt, S. C., Braeckmans, K., and Fraire, J. C. (2022). Macrophages as a therapeutic target to promote diabetic wound healing. *Mol. Ther.* 30 (9), 2891–2908. doi:10.1016/j.ymthe.2022.07.016

Singer, A. J., and Clark, R. A. (1999). Cutaneous wound healing. *N. Engl. J. Med.* 341 (10), 738–746. doi:10.1056/NEJM199909023411006

Singh, V., Devgan, L., Bhat, S., and Milner, S. M. (2007). The pathogenesis of burn wound conversion. *Ann. Plast. Surg.* 59 (1), 109–115. doi:10.1097/01.sap.0000252065.90759.e6

Sun, B. K., Siprashvili, Z., and Khavari, P. A. (2014). Advances in skin grafting and treatment of cutaneous wounds. *Science* 346 (6212), 941–945. doi:10.1126/science.1253836

Sun, J., Jia, W., Qi, H., Huo, J., Liao, X., Xu, Y., et al. (2024). An antioxidative and active shrinkage hydrogel integratedly promotes Re-epithelization and skin constriction for enhancing wound closure. *Adv. Mater* 36 (21), e2312440. doi:10.1002/adma.202312440

Tang, Q., Xue, N., Ding, X., Tsai, K. H. Y., Hew, J. J., Jiang, R., et al. (2023). Role of wound microbiome, strategies of microbiota delivery system and clinical management. *Adv. Drug Deliv. Rev.* 192, 114671. doi:10.1016/j.addr.2022.114671

Theodore Hart, M., Ross Milner, M., and Adam Cifu, M. (2017). Management of a diabetic foot. *JAMA* 318, 1387–1388. doi:10.1001/jama.2017.11700

Tian, X., Wen, Y., Zhang, Z., Zhu, J., Song, X., Phan, T. T., et al. (2025). Recent advances in smart hydrogels derived from polysaccharides and their applications for wound dressing and healing. *Biomaterials* 318, 123134. doi:10.1016/j.biomaterials.2025.123134

Uberoi, A., McCready-Vangi, A., and Grice, E. A. (2024). The wound microbiota: microbial mechanisms of impaired wound healing and infection. *Nat. Rev. Microbiol.* 22 (8), 507–521. doi:10.1038/s41579-024-01035-z

Wang, B. (2024). Clinical observation of badu shengji powder application in postoperative management of low perianal abscess. *J. Pract. Traditional Chin. Med.* 40 (05), 824–826.

Wang, S., and Li, D. (2023a). Study on mechanism of badu shengji powder on regulating keap1/nrf2 pathway to promote skin ulcer healing in diabetes rats. *J. Basic Chin. Med.* 29 (10), 1645–1649. doi:10.19945/j.cnki.issn.1006-3250.2023.10.020

Wang, S., and Li, D. (2023b). Promoting effect of badu shengji powder on skin ulcer healing in diabetic rats based on wnt/β-catenin pathway. *Chin. Archives Traditional Chin.* 41 (02), 115–119. doi:10.13193/j.issn.1673-7717.2023.02.025

Wang, Y., Beekman, J., Hew, J., Jackson, S., Issler-Fisher, A. C., Parungao, R., et al. (2018). Burn injury: challenges and advances in burn wound healing, infection, pain and scarring. *Adv. Drug Deliv. Rev.* 123, 3–17. doi:10.1016/j.addr.2017.09.018

Wen, X., and Shen, J. (2021). Application of nano-silver antibacterial hydrogel dressing combined with recombinant human basic fibroblast growth factor on wound healing after debridement of open ankle fracture. *Chin. J. Tissue Eng. Res.* 25 (29), 6. doi:10.12307/2021.162

Winter, G. D. (1962). Formation of the scab and the rate of epithelization of superficial wounds in the skin of the young domestic pig. *Nature* 193, 293–294. doi:10.1038/193293a0

Wunderlich, R. P., Peters, E. J., and Lavery, L. A. (2000). Systemic hyperbaric oxygen therapy: lower-extremity wound healing and the diabetic foot. *Diabetes Care* 23 (10), 1551–1555. doi:10.2337/diacare.23.10.1551

Xiang, P. (2021). Efficacy study of badu shengji powder combined with yixiao ointment gauze strips in postoperative wound dressing for anal fistula. *Chin. J. Mod. Drug Appl.* 15 (01), 58–59. doi:10.14164/j.cnki.cn11-5581/r.2021.01.024

Xie, M., and Dai, X. (2021). Combined topical application of badu shengji powder and kuiyang oil with oral traditional Chinese medicine (tcm) for non-lactating mastitis: a clinical study. *Shenzhen J. Integr. Traditional Chin. West. Med.* 31 (12), 67–69. doi:10.16458/j.cnki.1007-0893.2021.12.028

Xu, Z., Liang, B., Tian, J., and Wu, J. (2021). Anti-inflammation biomaterial platforms for chronic wound healing. *Biomater. Sci.* 9 (12), 4388–4409. doi:10.1039/d1bm00637a

Yang, L., Zhang, D., Li, W., Lin, H., Ding, C., Liu, Q., et al. (2023). Biofilm microenvironment triggered self-enhancing photodynamic immunomodulatory microneedle for diabetic wound therapy. *Nat. Commun.* 14 (1), 7658. doi:10.1038/s41467-023-43067-8

Yanli, L., Rong, H., Bo, P., Xu, Q., Zhang, X., Lin, H., et al. (2012). Study on mercury accumulation in rats induced by Badu Shengji San. *China J. Chin. Materia Medica* 37 (6), 700–705.

Yin, F. (2019). Clinical investigation of badu shengji powder in managing postoperative wound non-union following calcaneal fracture surgery. *J. Pract. Traditional Chin. Med.* 35 (09), 1156–1157.

Yu, Q., Wang, Q., Zhang, L., Deng, W., Cao, X., Wang, Z., et al. (2023). The applications of 3D printing in wound healing: the external delivery of stem cells and antibiosis. *Adv. Drug Deliv. Rev.* 197, 114823. doi:10.1016/j.addr.2023.114823

Zhang, X., Ren, X., Bian, W., Ying, Y., Xue, J., and Tang, J. (2025). Clinical effect of Qingxiao Formula combined with silk seton therapy by applying Badu Shengji Powder on areola fistula of non-lactating mastitis withliver meridian stagnation heat syndrome. *Chin. J. Clin. Res.* 38 (02), 289–293. doi:10.13429/j.cnki.cjcr.2025.02.026

Zhong, J., Wang, H., Yang, K., Wang, H., Duan, C., Ni, N., et al. (2022). Reversibly immortalized keratinocytes (iKera) facilitate re-epithelization and skin wound healing: potential applications in cell-based skin tissue engineering. *Bioact. Mater* 9, 523–540. doi:10.1016/j.bioactmat.2021.07.022

Zhu, S., Zhao, B., Li, M., Wang, H., Zhu, J., Li, Q., et al. (2023a). Microenvironment responsive nanocomposite hydrogel with NIR photothermal therapy, vascularization and anti-inflammation for diabetic infected wound healing. *Bioact. Mater* 26, 306–320. doi:10.1016/j.bioactmat.2023.03.005

Zhu, Z., He, F., Shao, H., Shao, J., Li, Q., Wang, X., et al. (2023b). Chitosan/alginate nanoparticles with sustained release of esculentoside A for burn wound healing. *ACS Appl. Nano Mater.* 6 (1), 573–587. doi:10.1021/acsanm.2c04714

frontiers | Frontiers in Pharmacology

TYPE Original Research
PUBLISHED 30 June 2025
DOI 10.3389/fphar.2025.1614967

Check for updates

OPEN ACCESS

EDITED BY
Yizhou Zhan,
Dongguan University of Technology, China

REVIEWED BY
Ilya D. Klabukov,
National Medical Research Radiological Center, Russia
Wenqian Zhang,
Huazhong University of Science and Technology, China

*CORRESPONDENCE
Li Lu,
luli@tjh.tjmu.edu.cn

†These authors have contributed equally to this work

RECEIVED 20 April 2025
ACCEPTED 26 May 2025
PUBLISHED 30 June 2025

CITATION
Liu L, Wang H, Zhou J, Lu J, Zhang Y, Liu H and Lu L (2025) Narirutin treatment accelerates the process of diabetic wound repair by regulating phenotype switching of macrophages through affecting metabolic reprogramming.
Front. Pharmacol. 16:1614967.
doi: 10.3389/fphar.2025.1614967

COPYRIGHT
© 2025 Liu, Wang, Zhou, Lu, Zhang, Liu and Lu. This is an open-access article distributed under the terms of the Creative Commons Attribution License (CC BY). The use, distribution or reproduction in other forums is permitted, provided the original author(s) and the copyright owner(s) are credited and that the original publication in this journal is cited, in accordance with accepted academic practice. No use, distribution or reproduction is permitted which does not comply with these terms.

Narirutin treatment accelerates the process of diabetic wound repair by regulating phenotype switching of macrophages through affecting metabolic reprogramming

Liang Liu[1†], Han Wang[2,3†], Juan Zhou[1], Jing Lu[1], Yan Zhang[1], Haiyan Liu[1] and Li Lu[4*]

[1]Department of Cardiology, Hubei Provincial Hospital of Traditional Chinese Medicine, Wuhan, China, [2]Department of Anesthesiology, Peking University People's Hospital, Qingdao, China, [3]Department of Anesthesiology, Women and Children's Hospital, Qingdao University, Qingdao, China, [4]Department of Rehabilitation, Tongji Hospital, Tongji Medical College, Huazhong University of Science and Technology, Wuhan, China

Introduction: Diabetic foot ulcer (DFU) is one of the most common complications of diabetes, with substantial morbidity and mortality. Narirutin (Nar), a bioactive phytochemical derived from citrus peel, has been suggested to possess anti-inflammatory abilities. However, the involvement of Nar in DFU development remains poorly understood.

Methods: The polarization traits of bone marrow derived macrophages (BMDMs) with indicated treatments were determined by flow cytometry, immunofluorescence staining, western blot and qRT-PCR. Levels of lactate and α-ketoglutarate were measured for investigating the metabolic profiles. The cutaneous wounds of diabetic mice were established for evaluating the promotive roles of Nar in wound healing *in vivo*.

Results: We found that high glucose treatment significant elevated the contents of TNF-α and IL-1β and lactate and reduced the levels of TGF-β1 and IL-4 and α-ketoglutarate in BMDMs. Then, Nar intervention effectively induced BMDMs repolarization from M1 to M2 state and the molecular mechanism was ascribed to drug-elicited activation of AMPK, which in turn increased the expression of downstream Mfn2, thereby enhancing the activity of oxidative phosphorylation and GATA3 cascade activation and disrupting the progress of glycolysis and NF-κB axis activation. Subsequently, we discovered that Nar injection effectively enhanced the healing rate of skin wounds in diabetic mice. Histological analysis showed that Nar dose-dependently induced dermis growth and collagen deposition in the wound area. Via activating AMPK/Mfn2 axis, Nar inhibited the activity of glycolysis and enhanced the extent of oxidative phosphorylation, accompanied by inflammation repression and angiogenesis promotion in the damaged tissue

Discussion: Our study discovered that macrophages repolarization to M2 phenotype was required for Nar-induced promotive effects on diabetic

wound repair by regulating reprogramming of glucose metabolism via mediating AMPK/Mfn2 pathway, providing a promising strategy for DFU management.

KEYWORDS

diabetic foot ulcer, narirutin, macrophage, metabolic reprogramming, AMPK, inflammation

1 Introduction

Epidemiological data have established that the global incidence of diabetes is increasing year by year, with nearly 30% of patients developing diabetic foot ulcer (DFU), which is associated with poor prognosis and a high death rate (Armstrong et al., 2023). Approximately one-third of individuals with a DFU will experience a severe infection and even a lower extremity amputation, which puts a huge burden on the social economy and health (Evstratova et al., 2024; Spampina et al., 2020). Due to the limited effects produced by current treatment modalities like surgical debridement, antibacterial dressing, and biomaterial applications, seeking alterative and complementary agents with high efficiency and safety to antagonize DFU is urgent (Li et al., 2023; Petric et al., 2025; Szunerits et al., 2025).

Typically, the healing process of acute skin wounds can be divided into four sequential steps: hemostasis, inflammation, proliferation, and remodeling. It has been shown that macrophages play pivotal roles during the course of wound repair (Mao K. et al., 2025). In the inflammation stage, under the stimulation of pro-inflammatory factors, macrophages are recruited to the damaged area where they phagocytize invaded pathogens and cellular debris and secrete multiple cytokines to augment inflammation responses for accelerating the elimination of exogenous microbes and injured tissues. Then, at the proliferation phase, macrophages are transformed from M1 to the anti-inflammatory M2 phenotype for confining the inflammation extent and releasing diverse growth factors, thereby enhancing the process of tissue repair (Xiong et al., 2023; Li et al., 2021). However, in the diabetic microenvironment, several pathological factors, like hyperglycemia, hypoxia, and pH abnormality, hamper the M2 phenotype repolarization of macrophages, which cause local inflammation exacerbation and pro-proliferative cytokine deficiency, ultimately leading to angiogenesis dysfunction and delayed healing of diabetic wounds (Wu et al., 2022).

It has been shown that metabolites *in vivo* are closely associated with the processes of immune regulation (Zhu et al., 2021). Lactate, as a main product from the glycolytic pathway, is reported to participate in the pro-inflammatory reactions of M1 macrophages (Feng et al., 2022). α-Ketoglutarate (α-KG) is an intermediate metabolite of oxidative phosphorylation (OXPHOS) and acts as a pivotal anti-inflammatory effector in M2 macrophages (Zhou et al., 2022). There is evidence that activity changes in the metabolic pathways like inhibition of glycolysis and enhancement of oxidative phosphorylation, which are termed as metabolic reprogramming, are indicated to be implicated in the inflammation resolution of macrophages (Faas et al., 2021). Previous studies have shown that AMP-activated protein kinase (AMPK) serves as an important intracellular energy sensor responsible for the anabolism and catabolism of glucose and lipid. Mitofusin 2 (Mfn2) locates in the mitochondrial outer membrane and takes part in the regulation of mitochondria fusion and fission to maintain physiological functions of the organelle (Zhang et al., 2021). Isolated from citrus fruits, narirutin (Nar) is found to be a bioactive phytochemical possessing potent anti-inflammatory and anti-oxidative capacities (Luo et al., 2024; Gao et al., 2025). It was uncovered that Nar restrains NLRP3 inflammasome assembly and IL-1β generation of macrophages via abrogating NF-κB, MAPK, and PI3K/Akt cascades (Ri et al., 2023). To date, whether Nar suppresses the inflammation development in macrophages through regulating metabolic reprogramming remains unclear. In this study, we discovered that Nar effectively strengthened oxidative phosphorylation and encumbered glycolysis by activating the AMPK/Mfn2 signaling axis, thereby increasing α-KG levels and reducing lactate, which were accompanied by the alleviation of inflammation in macrophages and enhanced angiogenesis.

2 Materials and methods

2.1 Reagents

Nar (purity >99.8%) was obtained from MedChemExpress (Monmouth Junction, NJ, United States) and was dissolved in dimethyl sulfoxide (DMSO, St. Louis, MO, United States). Cell Counting Kit-8 was purchased from Boster Biological Technology Co., Ltd. (Wuhan, China). The calcein/PI cell viability/cytotoxicity assay kit and the 5-ethynyl-2′-deoxyuridine (EdU) cell proliferation kit were acquired from Beyotime (Shanghai, China). Flow cytometry anti-CD11b (FITC), anti-F4/80 (APC), anti-CD86 (PE), and anti-CD206 (PerCP) were purchased from BioLegend, Inc. (San Diego, CA, United States). Anhydrous D-glucose was obtained from Solarbio Science & Technology Co., Ltd. (Beijing, China). The AMPK inhibitor Compound C was acquired from Selleck (Houston, Texas, United States). The reagent for blood biochemistry was purchased from Nanjing Jiancheng Bioengineering Institute (Nanjing, China). The Lactic Acid Content Assay Kit and the α-KG Content Assay Kit were purchased from Solarbio (Beijing, China). The Lipofectamine 3000 kit was obtained from Life Technologies (Carlsbad, CA, United States). Matrigel Matrix was purchased from Corning, Inc. (NY, United States). Primary antibodies for arginase 1 (Arg-1), inducible nitric oxide synthase (iNOS), TNF-α, TGF-β1, AMPK, p-AMPK, Mfn2, carnitine palmitoyl-transferase 1A (CPT-1A), isocitrate dehydrogenase 3 (IDH3), lactate dehydrogenase (LDH), p65, p-p65, and GATA binding protein 3 (GATA3) were obtained from Cell Signaling Technology (Danvers, MA, United States).

Primary antibodies for CD86, CD206, proliferating cell nuclear antigen (PCNA), p21, matrix metalloproteinase-9 (MMP-9), tissue inhibitor of metal protease 1 (TIMP-1), vascular endothelial growth factor receptor 2 (VEGFR2), PI3K, p-PI3K, Akt, p-Akt, hypoxia-inducible factor-1α (HIF-1α), cytochrome c oxidase subunit 4 (COX IV), and GAPDH were purchased from ABclonal (Wuhan, China). The reverse transcription kit and SYBR-Green PCR Master Mix were purchased from Vazyme Biotech Co., Ltd. (Nanjing, China).

2.2 Cell culture

Bone marrow-derived macrophages (BMDMs) were acquired as previously reported (Li et al., 2019). In brief, the femur and tibia were obtained from healthy male C57BL/6 mice aged 6 weeks. Bone marrow cells were collected by rinsing the marrow cavity, and they were resuspended in RPMI-1640 supplemented with 10% fetal bovine serum and 40 ng/mL murine recombinant M-CSF. After being cultured for 7 days in a 37°C incubator with 5% CO_2, the cells differentiated into BMDMs, which were then used for the following experiments.

Human umbilical vein endothelial cells (HUVECs) were obtained from the American Type Culture Collection (Rockville, MD, United States) and maintained in RPMI-1640 containing 10% fetal bovine serum. The culture medium was renewed every 2 days, and cells at the logarithmic growth stage were collected for *in vitro* experiments.

2.3 CCK-8 assay

The Cell Counting Kit-8 was applied to detect the viability of BMDMs in accordance with the manufacturer's protocols. The BMDMs were seeded into a 96-well plate at a density of approximately 6×10^3 cells per well. Then, they were co-incubated with different concentrations of Nar (0, 50, 100, 200, and 400 μM) for a duration of 24 h. A volume of 10 μL CCK-8 dye solution was added to each well, and the plate was maintained at 37°C for 2–4 h. The absorbance value at a wavelength of 450 nm was measured using a microplate reader.

2.4 Live/dead staining

To further determine the cytotoxicity of Nar on BMDMs, cells were co-cultured with Nar in a 96-well plate for 24 h. Then, the samples were washed with PBS and stained with calcein AM and PI for 30 min at 37°C in the dark. The images were captured using a fluorescence microscope.

2.5 Flow cytometry

BMDMs were distributed into individual wells of a 6-well plate and exposed to varying concentrations of high glucose (HG) (0, 15, 30, and 45 mM) with/without incubation with Nar for 24 h. Subsequently, cells were collected, washed with ice-cold PBS, and treated with an unlabeled anti-CD16/32 antibody to block Fcγ3 peptide. Cells were then stained with CD11b, F4/80, CD86, and CD206 diluted in FACS buffer for 30 min at 4°C. Samples were acquired using the LSRFortessa X-20 cytometer, and data analyses were performed using FlowJo software.

2.6 RNA interference assay

The small interfering RNA (siRNA) sequences targeting Mfn2 were synthesized by GenePharma (Shanghai, China). BMDMs were cultured into a 6-well plate at a concentration of 10^6 per well. Then, Lipofectamine 3000 and opti-minimum essential medium were used for transfection. The Mfn2 siRNA sequences were shown as follows: Mfn2-siRNA Forward (5′–3′) GCGGGUUUAUUGUCUAGAAAUTT, Reverse (5′–3′) AUUUCUAGACAAUAAACCCGCTT.

2.7 The 5-ethynyl-2′-deoxyuridine incorporation assay

HUVECs were seeded into a 24-well plate and co-incubated with BMDMs pretreated with varying dosages of HG. Then, EdU working solution was added to each well for 2 h. The HUVECs were washed with PBS and fixed with 4% paraformaldehyde for 30 min. Subsequently, the nuclei were stained with Hoechst33342 for 30 min. After being washed thrice, the cells were examined under a fluorescence microscope.

2.8 Cell scratch test

HUVECs were cultured into the lower chamber of a 6-well plate and scratched with a sterile 1-mL pipette tip. Then, the cells were exposed to the stimulation of BMDMs pretreated with HG in the upper chamber. After 24 h of incubation, HUVECs were photographed, and the remaining wound area was measured using ImageJ software.

2.9 Transwell migration assay

The 24-well culture plates inserted with 8-μm-pore-sized filters were used to evaluate the cell migratory ability. HUVECs (1×10^4) were suspended in low-serum (5% fetal bovine serum) medium and plated into the upper chamber. BMDMs suspended in complete medium (10% fetal bovine serum) were seeded into the lower chamber. After being cultured for 24 h, HUVECs migrated on the bottom side of the filter were fixed and stained with 0.5% crystal violet, and then they were captured using an optical microscope.

2.10 Tube formation assay

For the tube formation detection, 250 μL of cold Matrigel was added to each well of a 24-well plate and maintained at 37°C for 1 h. Subsequently, HUVECs (2×10^4 per well) were plated on the

Matrigel-coated plate and co-incubated with BMDMs in the upper chamber for 24 h. The tube length and total branch points were observed using an inverted microscope and assessed using ImageJ software.

2.11 Animal experiment

Male C57BL/6 mice aged 6–8 weeks were obtained from Vital River Laboratory Animal Technology Co. Ltd. (Beijing, China). Animals were maintained under specific pathogen-free conditions with a 12-h light–dark cycle, and food and water were provided ad libitum. The mice were fed with a high-fat diet for 4 weeks, accompanied by intraperitoneal administration of streptozotocin (60 mg/kg/day) for 5 days to establish the diabetes model. After the concentration of the random blood glucose exceeded 16.8 mmol/L in two measurements, the mice were selected for the next experiment. Mice were then anesthetized by intraperitoneal injection of pentobarbital sodium (50 mg/kg), and full-thickness excisional skin wounds were made on the dorsum. The animals were randomly allocated and marked with noninvasive skin dying (Klabukov et al., 2023; Sensini et al., 2020) and then received a total of 100 μL PBS, low-dosage Nar (60 mg/kg in 100 μL PBS) or high-dosage Nar (120 mg/kg in 100 μL PBS) injection subcutaneously in four sites adjacent to the wound. After injection, the wounds were covered with transparent dressings (Tegaderm™; 3M™; United States) and photographed at days 0, 3, 7, 10, and 14 post-wounding. The area of wound closure was assessed using ImageJ software. On day 14, mice were sacrificed, and the skin tissues and internal organs were harvested for further analysis. All animal studies were approved by the Institutional Animal Care and Use Committee of the Tongji Medical College, the Huazhong University of Science and Technology (IACUC number: 3936), and studies were performed in accordance with the National Institutes of Health Guide for Care and Use of Laboratory Animals.

2.12 Blood perfusion determination in the wound site

On day 10 post-operation, the laser speckle contrast imaging system was used to measure the local blood flow in the wound region. A near-infrared laser at 785 nm was applied to detect blood perfusion, which was termed as the perfusion unit. The wounds were imaged at a fixed distance, and the mean perfusion unit (MPU) ratio was calculated by comparing the MPU of the wound area with that of the area surrounding the wound.

2.13 Histopathological analysis

On day 14, wound tissue samples were collected, fixed in 4% paraformaldehyde, and then dehydrated and embedded in paraffin. The paraffin samples were cut into 4-μm-thick sections, which were subjected to hematoxylin–eosin (HE)/MASSON staining as previously described. For immunohistochemistry, the skin wound sections were rehydrated and incubated with antibody against CD31. Subsequently, the sections were incubated with secondary antibody and visualized using the DAB substrate under an optical microscope.

2.14 Blood biochemical test

The blood samples of mice were collected on day 14, which were then centrifuged, and the upper serum was obtained. The levels of AST, ALT, and Cr were detected using kits from Nanjing Jiancheng Bioengineering Institute, according to the manufacturer's protocols.

2.15 Immunofluorescence staining

The fixed BMDMs were permeabilized with 0.3% Triton X-100, blocked in 1% BSA, and then incubated overnight with anti-Arg-1 and anti-iNOS at 4°C. The samples were washed with PBS thrice and stained with fluorescence-conjugated secondary antibodies. The nuclei were incubated with DAPI, and the images were captured using a fluorescence microscope.

2.16 Quantitative real-time PCR

Total RNA was extracted from BMDMs, HUVECs, and skin wound tissues using TRIzol reagent. The HiScript III RT Super-Mix was used to reverse-transcribe the RNA into cDNA, following the manufacturer's instructions. Real-time PCR was executed using a Light-Cycler 480 II with 2x SYBR Green qPCR Mix. The $2^{-\Delta\Delta CT}$ method was used to quantify relative mRNA expression, and GAPDH was used to normalize mRNA levels. Primer sequences are listed in Table 1.

2.17 Measurement of metabolite lactate and α-KG

After treatment, BMDMs and wound tissues were collected and used for detecting the quantity of endogenous lactate and α-KG using the Lactic Acid Content Assay Kit and α-Ketoglutaric Acid Content Assay Kit, according to the manufacturer's protocols.

2.18 Western blot

The total proteins and mitochondrial proteins from cells and tissues were extracted using kits from Beyotime, according to the protocols. After quantification, protein samples were separated using 10% SDS-PAGE and then transferred onto polyvinylidene difluoride membranes. Then, membranes were blocked with 5% BSA at room temperature for 1 h, followed by incubation with primary antibodies at 4°C overnight. Subsequently, membranes were washed thrice with Tris-buffered saline–Tween 20 and incubated with corresponding secondary antibodies for 1 h at room temperature. The protein bands were visualized using the

TABLE 1 Primer sequences for qRT-PCR

Gene	Forward	Reverse
Arg-1	AGCCAGGGACTGACTACCTT	TTGGGAGGAGAAGGCGTTTG
iNOS	CTGCCAGGGTCACAACTTTACA	AACAGCTCAGTCCCTTCACC
TNF-α	CCCACGTCGTAGCAAACCAC	GCAGCCTTGTCCCTTGAAGA
IL-1β	TGCCACCTTTTGACAGTGATG	AAGGTCCACGGGAAAGACAC
TGF-β1	ACTGGAGTTGTACGGCAGTG	GGGGCTGATCCCGTTGATTT
IL-4	CCCCCAGCTAGTTGTCATCC	AGGACGTTTGGCACATCCAT
p21	GGAGGAGCATGAATGGAGACA	AAAGTTCCACCGTTCTCGGG
PCNA	AGATGCCGTCGGGTGAATTT	TGTTCCCATTGCCAAGCTCT
HIF-1α	TTCCCCCGTCCACCCATTTC	GACTCTTTGCTTCGCCGAGA
MMP-1	AGAAGTGTGACCCAGCCCTA	GGTCACGGGATGGATGTTCA
MMP-9	ACCTCCAACCTCACGGACA	AGGTTTGGAATCGACCCACG
TIMP-1	AGAAATCAACGAGACCACCTTA	TGATCCGTCCACAAACAGTGA
LDH	CTGTGAGCCTGCTGCATTCG	ACTTGGGTGGTTGGTTCCAT
CPT-1A	CCTACATGGGCCAGGCTTTG	GTAGACGTCCAGCCACAGTC
IDH3	TCGAGTACGCTCGGAACAAC	ACAGTTCTCCGCAACTTCCC
SDH	TACGAGCAACCAAGTGGGAG	AAGAGGTTGAAATCGGGGCA
AMPK	ACACCAATTGACAGGCCATAA	AGGTGCTGCATAATTTGGCG
Mfn2	AGGTTGAGGTGACAGCGTTC	GGACTCGAGGTCTCCTCTGT

electrochemiluminescence kit, and the gray values of the bands were quantified and analyzed using ImageJ software.

2.19 Statistical analysis

The data in this study were presented as the mean ± standard deviation (SD) and were analyzed using GraphPad Prism software (version 8.0.1; San Diego, CA, United States). Statistical analyses of multiple groups were accomplished using one-way ANOVA, followed by Tukey's *post hoc* test. P-values < 0.05 were considered statistically significant.

3 Results

3.1 HG stimulated inflammatory responses and altered the activities of glycolysis and OXPHOS

To observe the effects of the high-glucose microenvironment on regulating the inflammatory responses in macrophages, we treated the BMDMs with HG for 24 h and found that the percentage of the M1 phenotype was increased and the proportion of the M2 phenotype was reduced, as indicated by elevated levels of CD86 and iNOS and decreased levels of CD206 and Arg-1 (Figures 1A–C). Then, we discovered that the pro-inflammatory cytokines TNF-α and IL-1β showed increased concentrations, whereas the anti-inflammatory cytokines TGF-β and IL-4 showed reduced contents in BMDMs under HG stimulation (Figures 1C,D). In addition, the level of metabolite lactate in the glycolysis pathway was decreased, and the content of metabolite α-KG in the OXPHOS was increased in HG-irritated BMDMs in a dose-dependent manner (Figure 1E). These results showed that HG administration significantly induced macrophages to polarize to the M2 status, accompanied by the inflammation response progression.

3.2 Narirutin induced phenotype repolarization of macrophages stimulated by HG

The chemical structure of Nar, which included flavanone naringenin bound to the disaccharide rutinose, is shown in Figure 2A. We evaluated the cytotoxicity of Nar and found that the viability of BMDMs was unchanged after the incubation with varying dosages of Nar (0–400 μM) for 24 h, as indicated by the results of the CCK-8 test and calcein AM/PI staining (Figures 2B,C). To investigate the regulatory roles of Nar in the inflammatory status of macrophage, Nar was administered to BMDMs with simultaneous HG incubation for 24 h. Our findings revealed that different concentrations of Nar promoted M1 macrophage repolarization to the M2 phenotype, as evidenced by the reduced expressions of iNOS, CD86, TNF-α, and IL-1β and increased levels of Arg-1, CD206, TGF-β, and IL-4 (Figures 2D–F). Results of Western blot indicated that HG-triggered elevation in TNF-α and

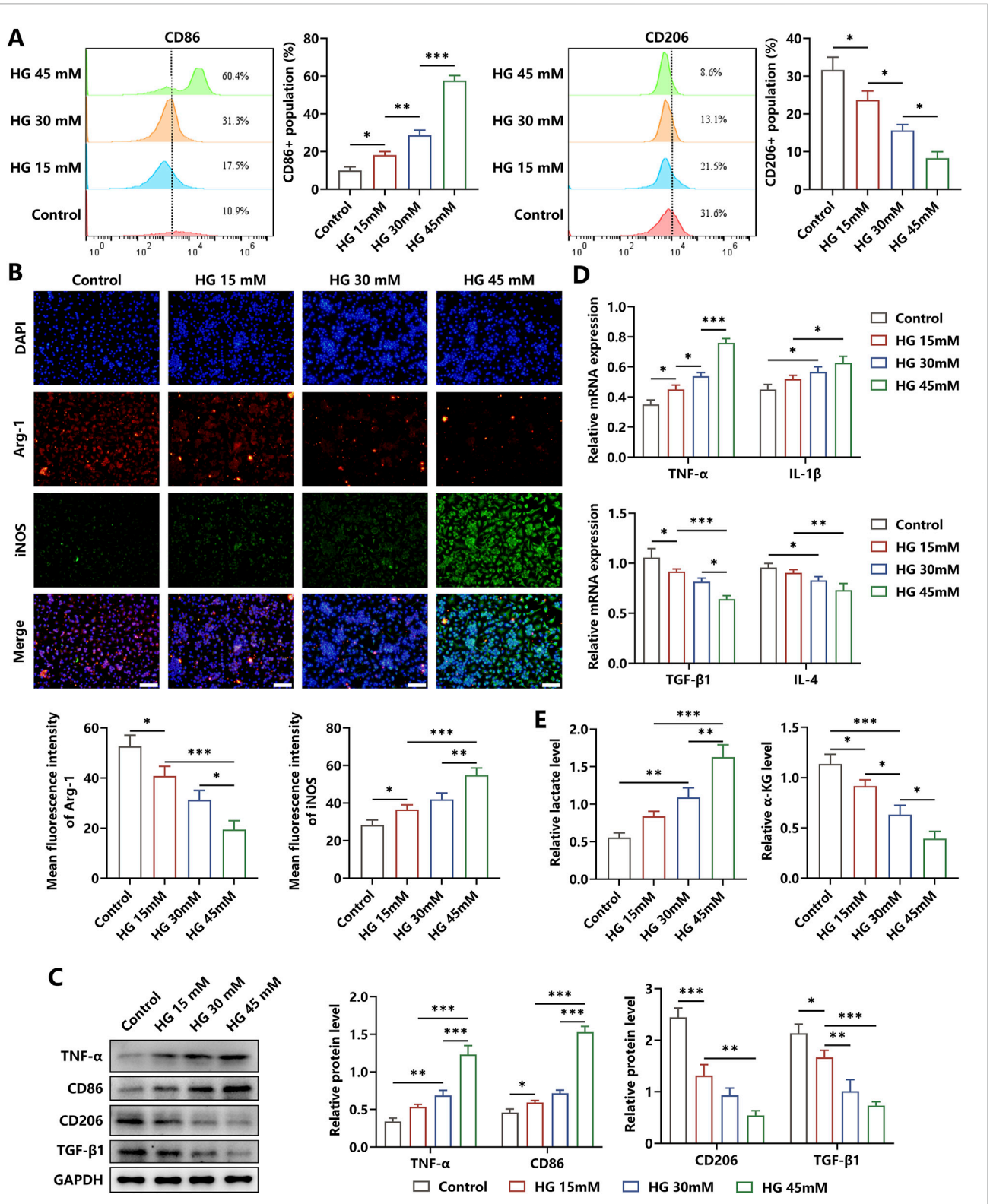


FIGURE 1
Effects of HG on the inflammation responses in macrophages. **(A)** Flow cytometry analysis showed the phenotype profiles of macrophages induced by different dosages of HG. **(B)** The levels of Arg-1 and iNOS in HG-stimulated BMDMs were determined through immunofluorescence staining (scale bar: 200 μm). **(C)** Western blot analysis showed that there was an increase in the levels of TNF-α and CD86 and a reduction in the contents of CD206 and TGF-β in the macrophages triggered by HG in a dose-dependent manner. **(D)** Relative mRNA expressions of pro-inflammatory factors and anti-inflammatory biomarkers. **(E)** HG dose-dependently increased the level of lactate and decreased the level of α-KG in macrophages. The experiments were performed independently thrice. *p < 0.05, **p < 0.01, and ***p < 0.001.

10.3389/fphar.2025.1614967

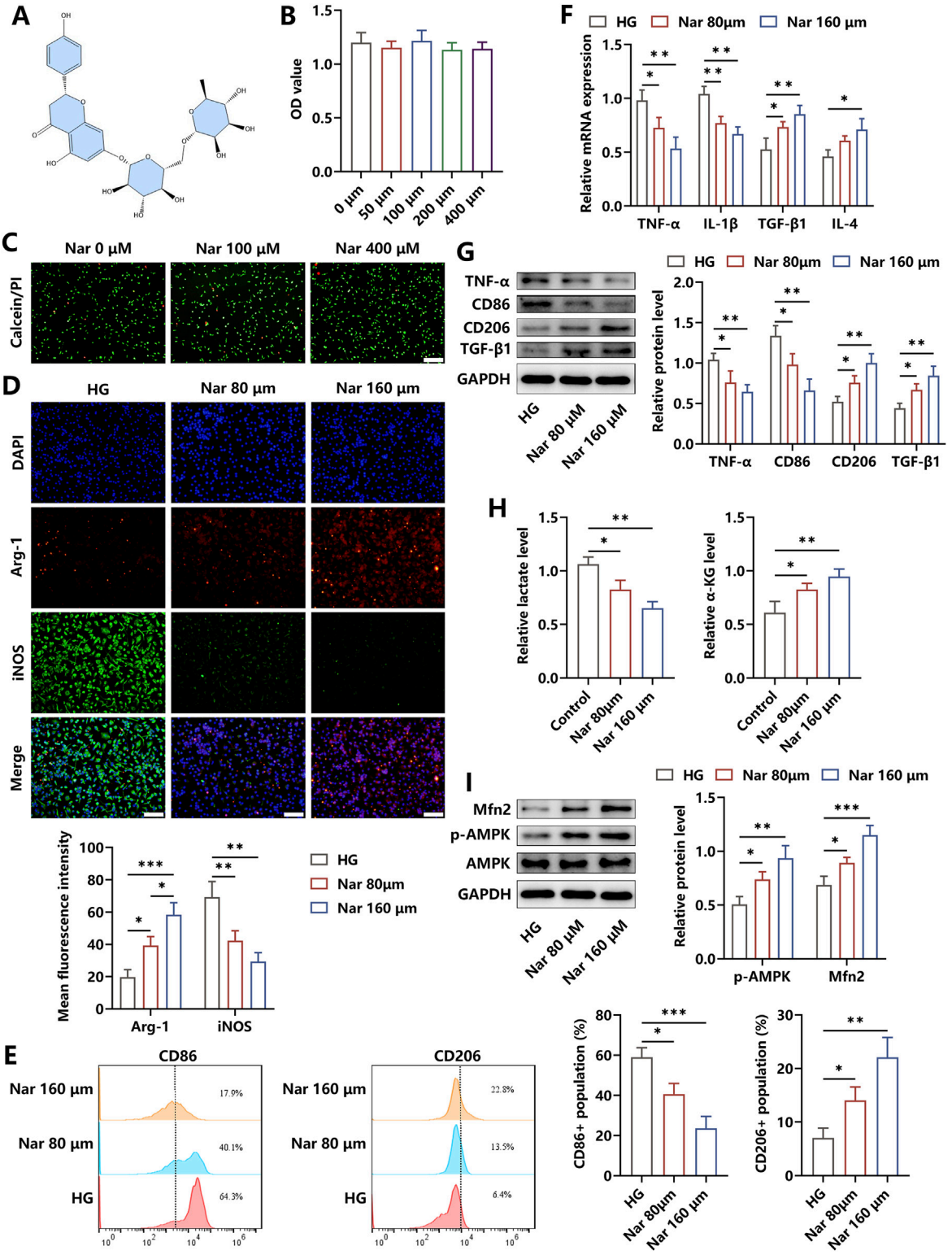


FIGURE 2
Nar treatment effectively attenuated inflammation in HG-stimulated macrophages. **(A)** Chemical structure of Nar. **(B,C)** Effects of Nar on viability of BMDMs were detected using the CCK-8 test and calcein/PI staining (scale bar: 200 μm). **(D)** BMDMs were incubated with HG (45 mM) in the presence of Nar with different doses (0, 80, and 160 μM) for 24 h. The levels of Arg-1 and iNOS in each group were detected through immunofluorescence staining (scale bar: 200 μm). **(E)** Flow cytometry analysis of macrophages with indicated treatments. **(F)** The results of qRT-PCR showed that Nar reduced the mRNA expression of pro-inflammatory factors and elevated the mRNA expression of anti-inflammatory molecules. **(G)** Nar dose-dependently decreased the protein levels of TNF-α and CD86 and elevated the protein contents of CD206 and TGF-β in macrophages. **(H)** The production of lactate and α-KG in BMDMs was reduced and increased separately after Nar treatment in a dose-dependent fashion. **(I)** AMPK phosphorylation and Mfn2 expression were evaluated using Western blot; n = 3; *p < 0.05, **p < 0.01, and ***p < 0.001.

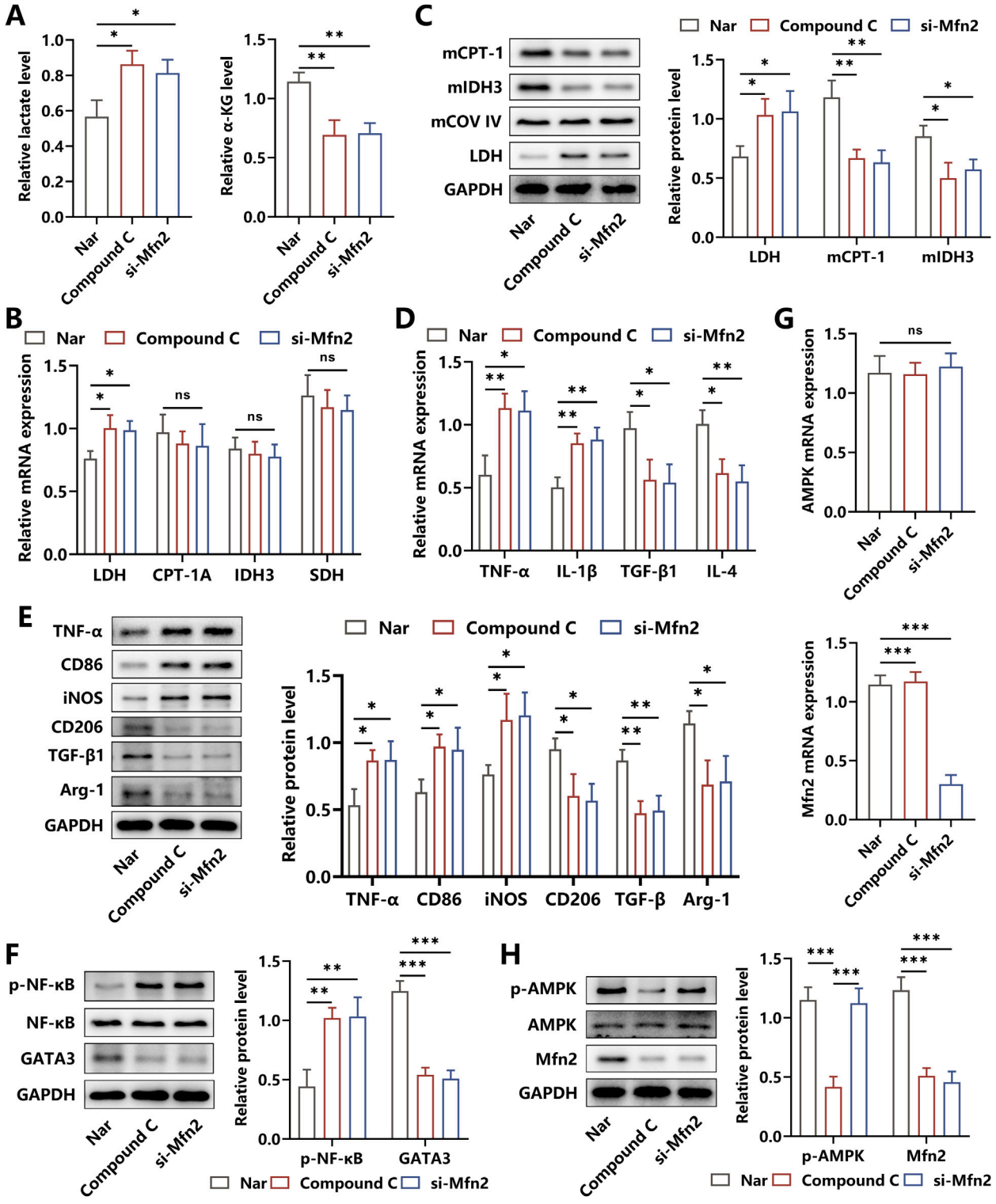


FIGURE 3
Effects of AMPK inhibition and Mfn2 silencing on the glucose metabolism and inflammation response of Nar-treated macrophages. **(A)** Both HG (45 mM) and Nar (160 μM) were incubated with BMDMs in the presence of PBS, Compound C, or si-Mfn2, respectively, for 24 h. Relative levels of lactate and α-ketoglutaric acid in each group. **(B)** The mRNA expressions of LDH, CPT-1A, IDH3, and SDH were determined using qRT-PCR. **(C)** The protein levels of LDH, mitochondrial CPT-1A, and mitochondrial IDH3 were detected using Western blot. **(D)** Results from qRT-PCR showed that Compound C or si-Mfn2 intervention reversed Nar-induced suppression of TNF-α and IL-1β levels and inhibited Nar-triggered elevation of TGF-β and IL-4 levels in macrophages. **(E)** Western blot analysis showed that the protein levels of M1-related biomarkers and M2-related molecules were increased and reduced separately in BMDMs after Compound C or si-Mfn2 administration. **(F)** The activities of NF-κB and GATA3 expressions were measured using Western blot. **(G,H)** The expressions of AMPK and Mfn2 at the transcriptional and translational levels were detected using qRT-PCR and Western blot, respectively; n = 3; *p < 0.05, **p < 0.01, and ***p < 0.001.

CD86 levels and reduction in TGF-β and CD206 contents were reversed by Nar intervention in a dose-dependent way in BMDMs (Figure 2G). Then, we observed that Nar significantly alleviated HG-induced increase in lactate content and decrease in α-KG content (Figure 2H). Moreover, AMPK participating in glucose metabolism was observed to possess increased activity in the presence of Nar treatment. The decreased expression of Mfn2, which was involved in mitochondrial homeostasis in HG-primed macrophages, was enhanced by Nar administration (Figure 2I). Our results suggested that Nar treatment effectively weakened inflammation responses and affected glucose metabolism pathways in macrophages.

3.3 Nar induced metabolic reprogramming to trigger inflammation amelioration

It was illustrated that Mfn2 displayed crucial roles in maintaining the biological functions of mitochondrion, and AMPK was reported to be an upstream regulator of Mfn2, participating in multiple pathophysiological processes (Zhang et al., 2021). Herein, to assess whether Nar altered the glucose metabolism pathway by regulating the AMPK/Mfn2 signal cascade, the BMDMs were co-incubated with Nar and HG simultaneously in the absence/presence of Compound C or si-Mfn2 for 24 h. We discovered that both Compound C and si-Mfn2 administration abolished Nar-induced reduction in lactate levels and elevation of α-KG content in macrophages (Figure 3A). Then, LDH responsible for the glycolysis process was found to be upregulated after the intervention of Compound C or si-Mfn2. Of note, the expressions of mitochondrial CPT-1A, IDH3, and succinate dehydrogenase (SDH) acting as rate-limiting enzymes of the OXPHOS process were observed to be unchanged in Nar-induced macrophages supplemented with Compound C or si-Mfn2 treatment at the transcriptional level but were significantly suppressed at the translational level (Figures 3B,C).

Considering that glycolysis and OXPHOS dominate the glucose metabolic pathway in M1 and M2 phenotypes of macrophages, respectively, strategies targeting metabolic reprogramming had been proven to be efficient in regulating inflammation responses in macrophage (Faas et al., 2021). Then, to probe the effects of the AMPK/Mfn2 axis-related alteration in metabolic pathways on Nar-evoked inflammation relief in macrophages, the key cytokines and inflammatory signaling cascades were detected. As shown in Figures 3D,E, after the administration of Compound C or si-Mfn2, the contents of TNF-α and IL-1β were increased and the levels of TGF-β and IL-4 were decreased, accompanied by the elevated expressions of M1 biomarkers CD86 and iNOS and reduced expressions of M2 biomarkers CD206 and Arg-1. Additionally, our results indicated that the increased activity of the pro-inflammatory signal factor NF-κB and decreased expression of the anti-inflammatory signal molecule GATA3 were observed in Compound C- or si-Mfn2-treated BMDMs (Figure 3F). We further determined the interaction between AMPK and Mfn2 and discovered that Compound C intervention suppressed the expression of Mfn2 at both the transcriptional and translational levels, whereas si-Mfn2 failed to alter the expression and the activity of AMPK, indicating the upstream regulatory roles of AMPK in Mfn2 expression (Figures 3G,H). Considering the abovementioned results, we had reasons to believe that the mechanisms underlying Nar-elicited anti-inflammatory effects were to some extent attributed to the metabolic reprogramming induced by the AMPK/Mfn2 signal cascade.

3.4 Nar-induced anti-inflammatory effects improved the pro-angiogenic abilities of HUVECs

It has been demonstrated that inflammation acts as a pivotal pathogenic factor antagonizing the development of angiogenesis. To verify whether Nar alleviated the inhibitory angiogenic functions of HUVECs induced by HG-triggered macrophages, HUVECs were co-incubated for 24 h with BMDMs pretreated with indicated administrations. Our findings revealed that the proportion of EdU + cells was increased after the addition of Nar to the HG niche, whereas a remarkable decrement under the treatment of Compound C was observed (Figure 4A). Meanwhile, the results from the wound scratch and transwell migration assay indicated that Nar administration markedly accelerated the rate of cell scratch closure and enhanced HUVEC mobilization to the lower chamber when compared to the HG stimulation alone, but these effects were inhibited by Compound C intervention (Figures 4B,C). In addition, there was an enhancement in the tube formation ability of HUVECs in the Nar group, which then was restrained in the Compound C group, as indicated by the number change in tube branch points (Figure 4D). In terms of the bioactive molecules involved in angiogenesis, we found that Compound C dramatically abolished the Nar-evoked expression elevation of PCNA, HIF-1α, MMP-1, and MMP-9, which acted as positive regulators of angiogenesis. The expressions of anti-angiogenic factors p21 and TIMP-1 were prohibited by Nar intervention but were obviously enhanced by Compound C (Figures 4E–G). To further investigate the molecular mechanisms required for angiogenesis in HUVECs, we observed that Nar administration markedly increased the expression of VEGFR2, followed by the activation of the PI3K/Akt axis and then the elevation of the HIF-1α level, yet this pathway was inhibited after Compound C intervention (Figure 4H). Our results suggested that Nar was likely to exhibit pro-angiogenic effects by switching the M1-related inflammatory niche to the M2-related regenerative microenvironment formed by macrophages.

3.5 Nar abated local inflammation and promoted diabetic wound repair *in vivo*

A diabetic skin wound model was established to determine the therapeutic roles of Nar in inflammation elimination and damaged tissue healing. In this study, the diabetic mice were divided into three groups: PBS, low dose of Nar (60 mg/kg), and high dose of Nar (120 mg/kg) injection. The regenerative process of skin wound was recorded for 14 days, and we observed that Nar dose-dependently enhanced the rate of wound closure (Figure 5A). The histopathological detection showed that Nar treatment significantly promoted dermis regeneration in the

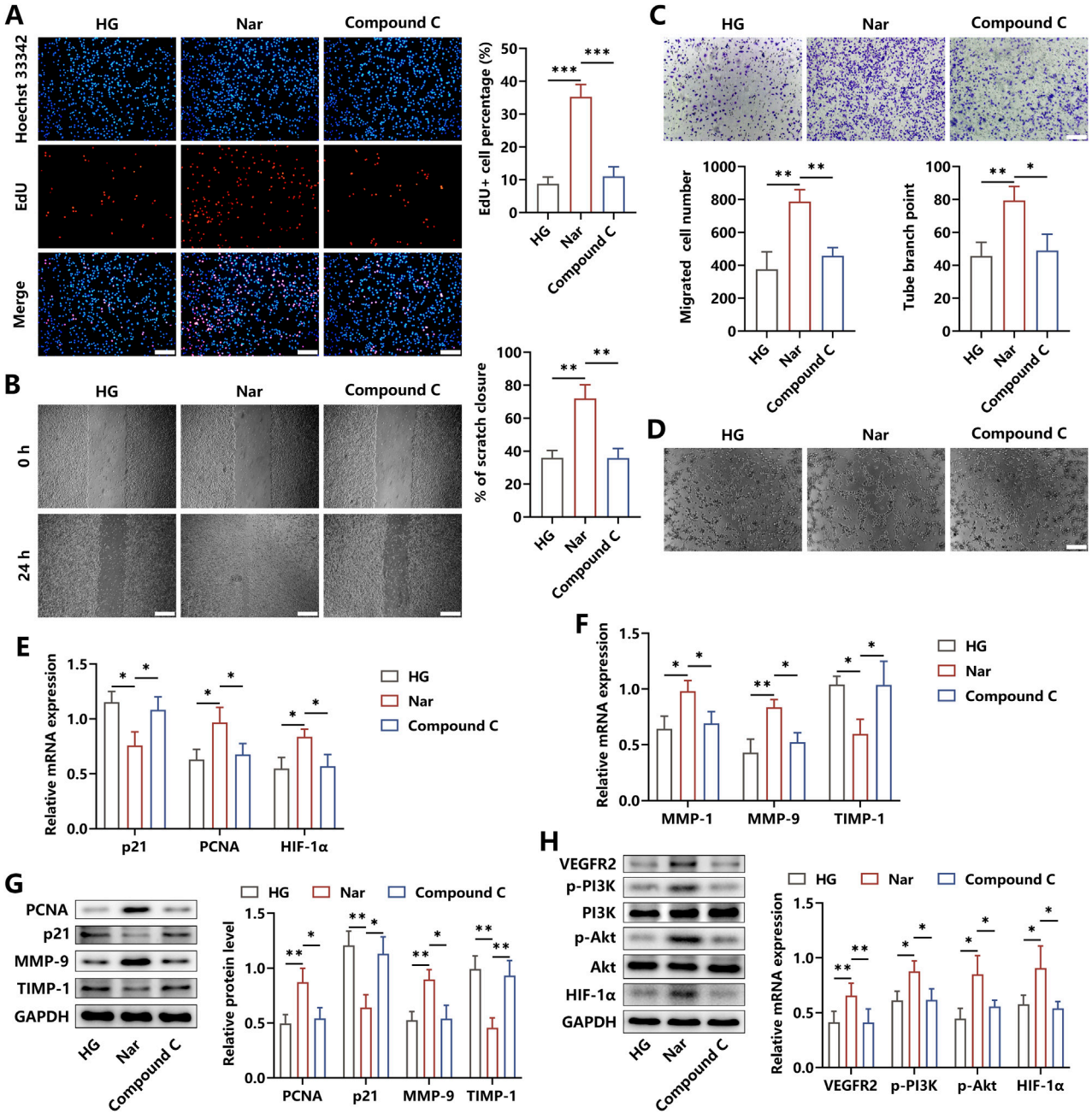


FIGURE 4
AMPK signaling affected the roles of macrophage-produced micro-niche in regulating angiogenic abilities of HUVECs. **(A)** BMDMs were incubated with HG, HG + Nar, or HG + Nar + Compound C for 24 h. Afterward, the cells were seeded in the upper chamber, and HUVECs were seeded in the lower chamber for 24 h. Edu staining showed that Compound C reversed Nar-induced proliferation enhancement of HUVECs (scale bar: 200 μm). **(B, C)** Results of cell scratch and transwell migration assay indicated that the increased migration of HUVECs induced by Nar was repressed by Compound C (scale bar: 500 μm **(B)** and 200 μm **(C)**). **(D)** Nar treatment enhanced the tube formation ability of HUVECs, which were inhibited by Compound C (scale bar: 200 μm). **(E, F)** The mRNA expression of angiogenesis-related genes was detected using qRT-PCR. **(G)** The protein levels of PCNA, p21, MMP-9, and TIMP-1 were measured using Western blot. **(H)** Molecular expression of the VEGFR2/PI3K/Akt/HIF-1α axis was determined using Western blot; n = 3; *p < 0.05, **p < 0.01, and ***p < 0.001.

wound area, and the extent of collagen deposition was strengthened after Nar administration in a dose-dependent manner (Figures 5B,C). Local injection of Nar suppressed the mRNA expressions of TNF-α, IL-1β, iNOS, and CD86 and facilitated the mRNA expressions of TGF-β1, IL-4, Arg-1, and CD206 in the HG microenvironment (Figures 5D–F). Meanwhile, the lactate level and NF-κB activity were decreased and the contents of α-KG and GATA3 were increased separately after Nar intervention in the wound tissue (Figures 5F,G). Moreover, the Western blot analysis suggested that Nar administration obviously induced AMPK activation and downstream Mfn2 expression, accompanied by metabolic reprogramming, as evidenced by LDH

10.3389/fphar.2025.1614967

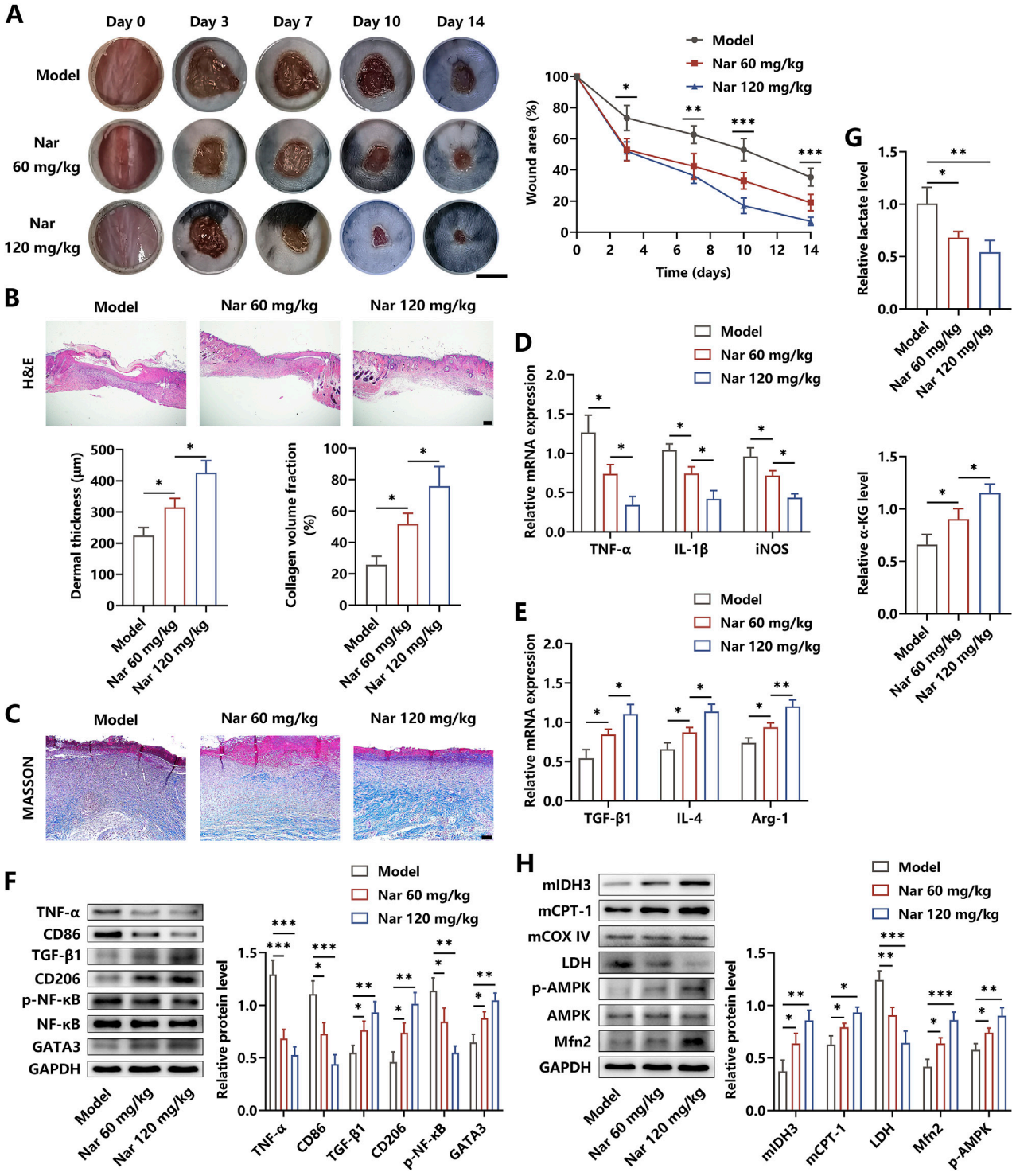


FIGURE 5
Nar treatment accelerated the healing processes of diabetic wound. **(A)** After the diabetic wound model was established, PBS, Nar at 60 mg/kg, or Nar at 120 mg/kg was locally injected for 14 days. The healing curve of each group is displayed (scale bar: 500 mm). **(B, C)** H&E and MASSON staining of the wound tissue in each group (scale bar: 200 μm **(B)** and 100 μm **(C)**). **(D, E)** The mRNA expression of inflammation-related molecules was measured using qRT-PCR. **(F)** The protein expression of inflammation-related molecules was measured using Western blot. **(G)** Nar dose-dependently decreased the level of lactate and increased the level of α-KG in the wound tissue. **(H)** The AMPK/Mfn2 pathway and expressions of LDH, mitochondrial CPT-1A, and mitochondrial IDH3 were detected using Western blot; n = 4; *p < 0.05, **p < 0.01, and ***p < 0.001.

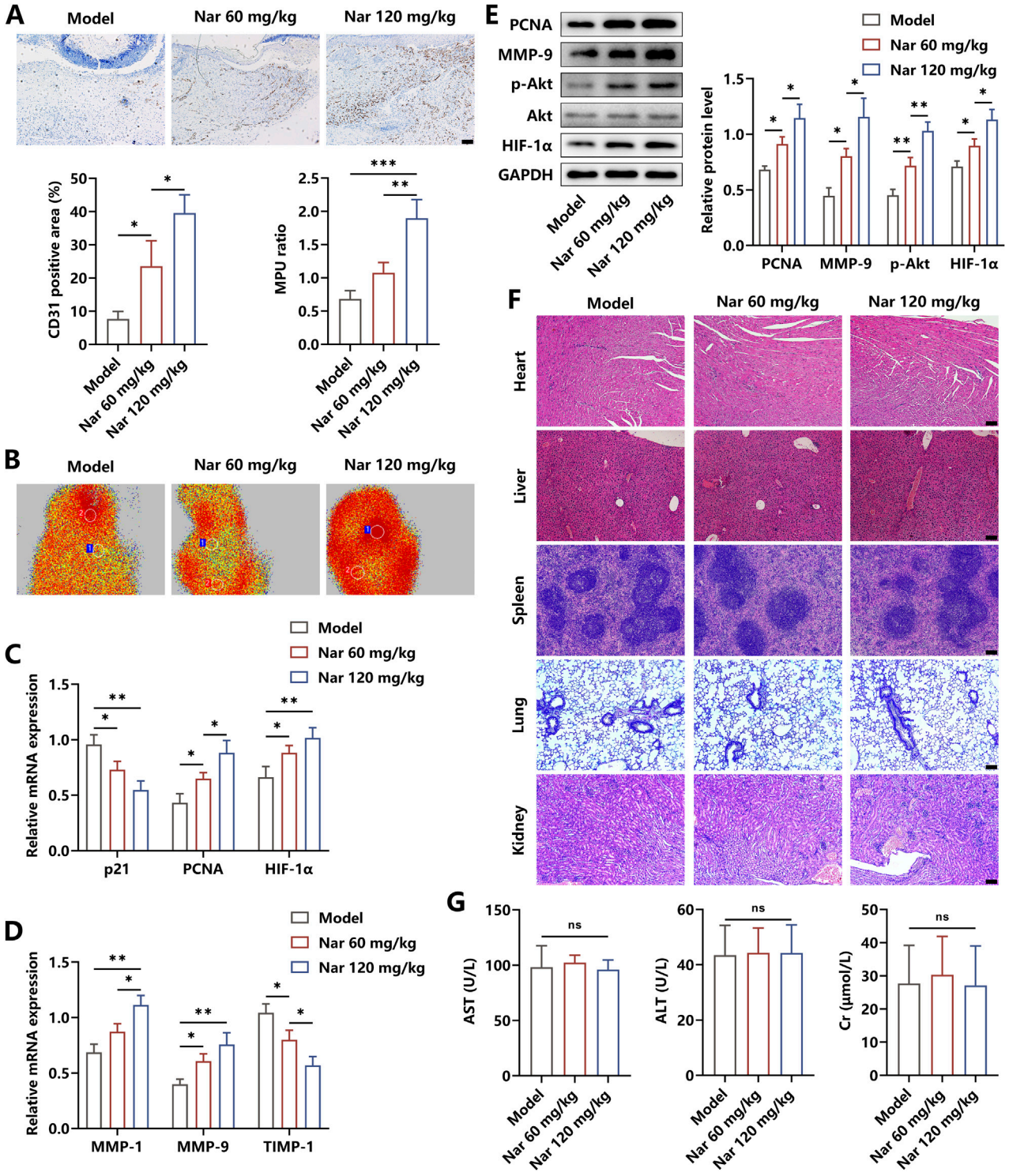


FIGURE 6
Effects of Nar on the angiogenesis and toxicity *in vivo*. **(A, B)** Immunohistochemical staining of CD31 and MPU ratios reflecting the blood flow in each group (scale bar: 100 μm). **(C–E)** The mRNA and protein expression of angiogenesis-related molecules were measured using qRT-PCR and Western blot. **(F,G)** The H&E staining of the heart, liver, spleen, lung, and kidney, along with blood levels of AST, ALT, and CK, in each group (scale bar: 100 μm); n = 4; *p < 0.05, **p < 0.01, and ***p < 0.001.

level reduction and mitochondrial IDH3 and CPT-1 content elevation (Figure 5H).

To further explore the effects of Nar on angiogenesis in the wound area, immunohistochemical detection was performed. As shown in Figure 6A, Nar dose-dependently increased the expression of CD31, which is an important biomarker of vessel tissues. The value of the MPU ratio, reflecting blood flow, was increased with the dose increment of Nar (Figure 6B). We found that Nar treatment

enhanced the activity of the pro-angiogenic pathway and facilitated the expression of targeting effector molecules, as indicated by the results from qRT-PCR and Western blot (Figures 6C–E). Then, with the histopathological examination, we discovered that Nar treatment had no toxicity on the main organs *in vivo* (Figure 6F). Furthermore, findings from the blood biochemical test showed that Nar failed to alter the levels of AST, ALT, and Cr of mice (Figure 6G). Collectively, our results suggested that Nar exerted beneficial roles in promoting diabetic wound healing via attenuating local inflammation responses and subsequently favoring angiogenesis.

4 Discussion

There is evidence in the literature indicating that multiple pathogenic factors, particularly inflammation responses, exert detrimental effects on regulating the process of wound healing (Peña and Martin, 2024). Repressing the normal functions of endothelial cells, including proliferation and migration, inflammatory stimuli restrain the development of angiogenesis in the damaged tissue, thereby triggering the supply shortage of nutrients and oxygen, and finally leading to the delayed healing of diabetic wounds (Mao J. et al., 2025). Cumulative studies have depicted that the therapeutic effects of Nar are attributed to anti-inflammation, anti-oxidation, autophagy regulation, lipid metabolism, and more (Ri et al., 2023; Fang et al., 2023; Park et al., 2023; Wong et al., 2021). In this study, we discovered that Nar diminished HG-induced inflammation progression via regulating AMPK/Mfn2 axis-dependent metabolic reprogramming in macrophages, which in turn enhanced the angiogenic abilities of HUVECs and then facilitated the process of diabetic wound repair.

It is known that moderate inflammation response is beneficial for immunocytes to eliminate the invading bacterium and phagocytose cellular debris when exposed to tissue injury. Once the etiological factors persist in the local microenvironment, such as HG in the diabetic niche, the irritated immune cells continuously release pro-inflammatory cytokines and then induce inflammation extension, which result in cell death aggravation and tissue healing retardation, among which macrophages are considered the representative (Li et al., 2021; Sharifiaghdam et al., 2022). In the damaged tissue area, macrophages fail to switch from the M1 state to the M2 phenotype under the stimulation of diverse irritants, thereby inducing the amplification of M1 pro-inflammatory effects and diminution of M2 pro-regenerative effects, which contribute to the slow closure of diabetic wounds (Lu et al., 2024). As expected, our results manifested that HG significantly triggered macrophage polarization to the M1 phenotype, followed by the generation of inflammation cytokines, including TNF-α and IL-1β, which further activate inflammatory signaling cascades, verifying the pivotal pathogenic roles of HG in DFU development.

Traditional herbal medicines have been used for treating diseases and improving health for thousands of years, and the phytochemicals isolated from them are documented to possess therapeutic roles to some extent (Puri et al., 2023). Evidence from basic experiments has clarified that the bioactive agent Nar exhibits potent anti-inflammatory roles in abolishing aliment progression. Ri et al. reported that administration of Nar effectively inhibited NLRP3/IL-1β-related pyroptosis in LPS-primed macrophages through suppressing the inflammation signaling molecules NF-κB, MAPK, and PI3K/Akt (Ri et al., 2023). Likewise, Ha et al. revealed that the inflammatory proteins, including iNOS, COX-2, IL-1β, and TNF-α, in LPS-stimulated macrophages developed reduced expression after Nar intervention, which were partly attributed to drug-induced prohibition of NF-κB and MAPK pathways (Ha et al., 2012). Another study showed that Nar treatment restrained the expression of thioredoxin-interacting protein, followed by activation repression of NLRP3 inflammasome and alleviation of oxygen–glucose deprivation/reperfusion-induced damage (Luo et al., 2024). In this study, we observed that Nar markedly promoted macrophage repolarization from M1 to M2 status and enhanced the production of anti-inflammatory molecules TGF-β and IL-4, confirming the efficient effects of Nar on antagonizing inflammation development.

Considerable documentations have clarified that metabolic reprogramming frequently occur in tissue-resident macrophages, which affect the dynamic balance between local inflammatory effects and anti-inflammatory actions and determine the outcome of several diseases, including cancer, atherosclerosis, cardiomyopathy, and diabetes (Chen et al., 2022; Liu et al., 2023; Xiao et al., 2023; Russo et al., 2021). Glycolysis is defined as a glucose catabolism pathway that occurs in the cytoplasm for energy acquisition under hypoxic conditions, which is the main glucose metabolic mode in M1 macrophages. LDH, the rate-limiting enzyme of glycolysis, is responsible for the generation of lactate, which is the primary end product. It has been affirmed that under an aerobic situation, OXPHOS located in the mitochondria is regarded as the principal glucose degradation way for energy capture, and the key enzymes including CPT-1, IDH3, and SDH are involved in the mechanism. With respect to M2 macrophages, OXPHOS is the dominant intracellular glucose metabolic pathway, and several metabolites comprising α-KG, itaconate, and succinate are required for the pro-regenerative functions of the M2 phenotype (Liu et al., 2023; Wculek et al., 2023). Approaches aimed at inducing OXPHOS enhancement and glycolysis repression are demonstrated to be excellent in promoting anti-inflammation-related macrophage repolarization (Li et al., 2025; Bi et al., 2025). Here, we observed that Nar administration remarkably reduced the level of lactate and increased the content of α-KG *in vitro* and *in vivo*. Of note, in the Nar-treated groups, the expression of LDH was decreased, while there was an elevation in the protein content of mitochondrial CPT-1 and IDH3 without altering their transcriptional levels, suggesting that Nar probably affected mitochondrial homeostasis to regulate the location of rate-limiting enzymes and then mediate the progress of OXPHOS.

An ever-growing wealth of evidence illustrates that AMPK is believed to be a hub of metabolic control, which perceive falling cellular energy status by direct interactions with ATP, ADP, and AMP, elucidating the crucial roles of AMPK in the management of metabolic disorders like obesity, dyslipidemia, and diabetes (Herzig and Shaw, 2018; Lin and Hardie, 2018; Trefts and Shaw, 2021). Mfn2m located on the outer membrane of mitochondrionm is necessary to control the fusion and fission of the mitochondrial membrane, which is a prerequisite for proper functioning of the mitochondria. There were studies indicating that Mfn2 was capable of shortening the distance between mitochondria and sarco/endoplasmic reticulum and then

enhancing their crosstalk, thereby contributing to optimize $CD8^+$ T cell function and attenuate oxidative stress-induced endothelial cell injury (Yepuri et al., 2023; Yang et al., 2023). Recently, an intracellular signal cascade comprising AMPK and downstream Mfn2 was discovered to exert various pharmacological effects, including inflammation relief, reactive oxygen species elimination, autophagy mediation, and apoptosis inhibition (Zhang et al., 2021; Yu et al., 2021; Ashraf and Kumar, 2022; Hu et al., 2021). Our results revealed that Nar treatment increased the activity of the AMPK/Mfn2 axis, accompanied by OXPHOS enhancement and glycolysis diminution. Given that the AMPK/Mfn2 pathway was deeply implicated in the improvement of mitochondrial health (Trefts and Shaw, 2021), the underlying mechanism of Nar-triggered metabolic reprogramming was possibly that upregulation of Mfn2 maintained membrane homeostasis, reinforcing the stability of the inner mitochondrial microenvironment, which restored the activities of key enzymes in the tricarboxylic acid (TCA) cycle and then indirectly suppressed the initiation of glycolysis. In addition, we observed that Nar-induced inflammatory macrophage repolarization to M2 status was reversed by the inactivation of the AMPK/Mfn2 signal axis. An increase in NF-κB activity and its target gene expression and a decrease in anti-inflammatory GATA3 and cytokine expression were observed after Compound C or si-Mfn2 application. Considering that lactate was reported to be associated with NF-κB activation and metabolic intermediates in the TCA cycle were unveiled to be the upstream regulators for GATA3 expression (Faas et al., 2021; Arora et al., 2022), we inferred that Nar-related activation of the AMPK/Mfn2 cascade triggered the alteration of metabolite profiles, which then resulted in the priority of inhibitory signals in the inflammation regulation network in macrophages.

Evidence from laboratory statistics has established that the angiogenic abilities in the wound area play vital roles in determining the tissue repair speed (Guan et al., 2021; Chen et al., 2023). In the diabetic micro-niche, vascular endothelial cells, as the main executor of angiogenesis, develop diverse behaviors like early apoptosis, poor proliferation, and slow migration, which are detrimental to the angiogenic processes when exposed to harmful stimuli, especially inflammation (Wang et al., 2023). A large number of studies indicate that bioactive molecules like phytochemicals and small non-coding RNAs weakening local inflammation responses are advantageous to facilitate the angiogenic abilities of endothelial cells (Li et al., 2022; Wang G. et al., 2021). Here, our findings manifested that Nar obviously enhanced the proliferation and migration of HUVECs under the microenvironment of HG-evoked macrophages, which was repressed by AMPK inhibition. Moreover, the activity of the VEGFR2/PI3K/Akt/HIF-1α pathway, a growth-promoting signal axis (Wang Z. et al., 2021), was found to be increased after Nar administration but suppressed by AMPK inhibitor incubation. In view of the pro-inflammatory property of M1 and pro-regenerative capacity of M2 macrophages, Nar was likely to exert dual actions in favoring angiogenesis by abolishing M1-related inflammation cascades and enhancing M2-related proliferative pathways.

5 Conclusion

Taken together, we, for the first time, discovered that Nar promoted diabetic wound repair by inhibiting inflammation and facilitating angiogenesis. Through activating the AMPK/Mfn2 signal pathway, Nar effectively enhanced the extent of OXPHOS and repressed the activity of glycolysis, thereby contributing to macrophage repolarization from the M1 to M2 phenotype and then inducing the generation of pro-regenerative micro-niche-favoring angiogenesis. This study provided a scientific basis for the potential application of Nar in the management of DFU.

Data availability statement

The original contributions presented in the study are included in the article/supplementary material; further inquiries can be directed to the corresponding author.

Ethics statement

Ethical approval was not required for the studies on humans in accordance with the local legislation and institutional requirements because only commercially available established cell lines were used. The animal study was approved by the Institutional Animal Care and Use Committee of the Tongji Medical College, Huazhong University of Science and Technology. The study was conducted in accordance with the local legislation and institutional requirements.

Author contributions

LLi: project administration and writing – original draft. HW: visualization and writing – review and editing. JZ: software, writing – original draft, and validation. JL: resources, writing – original draft, and methodology. YZ: formal analysis, writing – review and editing, and investigation. HL: data curation and writing – review and editing. LLu: writing – review and editing, conceptualization, supervision, and funding acquisition.

Funding

The author(s) declare that financial support was received for the research and/or publication of this article. This study was supported by the China Postdoctoral Science Foundation (2023M731217).

Conflict of interest

The authors declare that the research was conducted in the absence of any commercial or financial relationships that could be construed as a potential conflict of interest.

Generative AI statement

The author(s) declare that no Generative AI was used in the creation of this manuscript.

Publisher's note

All claims expressed in this article are solely those of the authors and do not necessarily represent those of their affiliated organizations, or those of the publisher, the editors and the reviewers. Any product that may be evaluated in this article, or claim that may be made by its manufacturer, is not guaranteed or endorsed by the publisher.

References

Armstrong, D. G., Tan, T. W., Boulton, A. J. M., and Bus, S. A. (2023). Diabetic foot ulcers: a review. *JAMA* 330, 62–75. doi:10.1001/jama.2023.10578

Arora, S., Singh, P., Tabassum, G., Dohare, R., and Syed, M. A. (2022). miR-16-5p regulates aerobic glycolysis and tumorigenesis of NSCLC cells via LDH-A/lactate/NF-κB signaling. *Life Sci.* 304, 120722. doi:10.1016/j.lfs.2022.120722

Ashraf, R., and Kumar, S. (2022). Mfn2-mediated mitochondrial fusion promotes autophagy and suppresses ovarian cancer progression by reducing ROS through AMPK/mTOR/ERK signaling. *Cell Mol. Life Sci.* 79, 573. doi:10.1007/s00018-022-04595-6

Bi, X., Mao, Z., Zhang, Y., Ren, Z., Yang, K., Yu, C., et al. (2025). Endogenous dual-responsive and self-adaptive silk fibroin-based scaffold with enhancement of immunomodulation for skull regeneration. *Biomaterials* 320, 123261. doi:10.1016/j.biomaterials.2025.123261

Chen, Y., Wang, X., Tao, S., Wang, Q., Ma, P. Q., Li, Z. B., et al. (2023). Research advances in smart responsive-hydrogel dressings with potential clinical diabetic wound healing properties. *Mil. Med. Res.* 10, 37. doi:10.1186/s40779-023-00473-9

Chen, Y., Wu, G., Li, M., Hesse, M., Ma, Y., Chen, W., et al. (2022). LDHA-mediated metabolic reprogramming promoted cardiomyocyte proliferation by alleviating ROS and inducing M2 macrophage polarization. *Redox Biol.* 56, 102446. doi:10.1016/j.redox.2022.102446

Evstratova, E., Yatsenko, E., Baranovskii, D., and Klabukov, I. (2024). Effectiveness of stem cell therapy for diabetic foot ulcers: cell therapy alone is not enough for effective management of chronic wounds. *Int. J. Low. Extrem Wounds*, 15347346241295306. doi:10.1177/15347346241295306

Faas, M., Ipseiz, N., Ackermann, J., Culemann, S., Gruneboom, A., Schroder, F., et al. (2021). IL-33-induced metabolic reprogramming controls the differentiation of alternatively activated macrophages and the resolution of inflammation. *Immunity* 54, 2531–2546 e5. doi:10.1016/j.immuni.2021.09.010

Fang, Z., Xu, Y., Liu, G., Shao, Q., Niu, X., Tai, W., et al. (2023). Narirutin activates TFEB (transcription factor EB) to protect against Acetaminophen-induced liver injury by targeting PPP3/calcineurin. *Autophagy* 19, 2240–2256. doi:10.1080/15548627.2023.2179781

Feng, T., Zhao, X., Gu, P., Yang, W., Wang, C., Guo, Q., et al. (2022). Adipocyte-derived lactate is a signalling metabolite that potentiates adipose macrophage inflammation via targeting PHD2. *Nat. Commun.* 13, 5208. doi:10.1038/s41467-022-32871-3

Gao, Y., Liu, W., Shi, L., Yang, P., Yang, L., Zhao, M., et al. (2025). Narirutin reduces microglia-mediated neuroinflammation by inhibiting the JAK2/STAT3 pathway in MPP+/MPTP-induced Parkinson's disease models. *Exp. Neurol.* 389, 115232. doi:10.1016/j.expneurol.2025.115232

Guan, Y., Niu, H., Liu, Z., Dang, Y., Shen, J., Zayed, M., et al. (2021). Sustained oxygenation accelerates diabetic wound healing by promoting epithelialization and angiogenesis and decreasing inflammation. *Sci. Adv.* 7, eabj0153. doi:10.1126/sciadv.abj0153

Ha, S. K., Park, H. Y., Eom, H., Kim, Y., and Choi, I. (2012). Narirutin fraction from citrus peels attenuates LPS-stimulated inflammatory response through inhibition of NF-κB and MAPKs activation. *Food Chem. Toxicol.* 50, 3498–3504. doi:10.1016/j.fct.2012.07.007

Herzig, S., and Shaw, R. J. (2018). AMPK: guardian of metabolism and mitochondrial homeostasis. *Nat. Rev. Mol. Cell Biol.* 19, 121–135. doi:10.1038/nrm.2017.95

Hu, Y., Chen, H., Zhang, L., Lin, X., Li, X., Zhuang, H., et al. (2021). The AMPK-MFN2 axis regulates MAM dynamics and autophagy induced by energy stresses. *Autophagy* 17, 1142–1156. doi:10.1080/15548627.2020.1749490

Klabukov, I., Shestakova, V., Krasilnikova, O., Smirnova, A., Abramova, O., Baranovskii, D., et al. (2023). Refinement of animal experiments: replacing traumatic methods of laboratory animal marking with non-invasive alternatives. *Anim. (Basel)* 13, 3452. doi:10.3390/ani13223452

Li, J., Li, R., Wu, X., Zheng, C., Shiu, P. H., Rangsinth, P., et al. (2022). An update on the potential application of herbal medicine in promoting angiogenesis. *Front. Pharmacol.* 13, 928817. doi:10.3389/fphar.2022.928817

Li, M., Hou, Q., Zhong, L., Zhao, Y., and Fu, X. (2021). Macrophage related chronic inflammation in non-healing wounds. *Front. Immunol.* 12, 681710. doi:10.3389/fimmu.2021.681710

Li, M. Y., Zhang, Z. H., Wang, Z., Zuo, H. X., Wang, J. Y., Xing, Y., et al. (2019). Convallatoxin protects against dextran sulfate sodium-induced experimental colitis in mice by inhibiting NF-κB signaling through activation of PPARγ. *Pharmacol. Res.* 147, 104355. doi:10.1016/j.phrs.2019.104355

Li, S., Yuan, H., Yang, X., Xu, X., Yu, W., Wu, Y., et al. (2025). Synergistic antitumor immunotherapy via mitochondria regulation in macrophages and tumor cells by an iridium photosensitizer. *ACS Cent. Sci.* 11, 441–451. doi:10.1021/acscentsci.4c02156

Li, X., Jing, X., Yu, Z., and Huang, Y. (2023). Diverse antibacterial treatments beyond antibiotics for diabetic foot ulcer therapy. *Adv. Healthc. Mater* 12, e2300375. doi:10.1002/adhm.202300375

Lin, S. C., and Hardie, D. G. (2018). AMPK: sensing glucose as well as cellular energy status. *Cell Metab.* 27, 299–313. doi:10.1016/j.cmet.2017.10.009

Liu, P. S., Chen, Y. T., Li, X., Hsueh, P. C., Tzeng, S. F., Chen, H., et al. (2023). CD40 signal rewires fatty acid and glutamine metabolism for stimulating macrophage anti-tumorigenic functions. *Nat. Immunol.* 24, 452–462. doi:10.1038/s41590-023-01430-3

Lu, Y. Z., Nayer, B., Singh, S. K., Alshoubaki, Y. K., Yuan, E., Park, A. J., et al. (2024). CGRP sensory neurons promote tissue healing via neutrophils and macrophages. *Nature* 628, 604–611. doi:10.1038/s41586-024-07237-y

Luo, L., Wang, S., Liu, W., Zhang, Z., Zhao, M., and Liu, A. (2024). Narirutin attenuates cerebral ischemia-reperfusion injury by suppressing the TXNIP/NLRP3 pathway. *Neurochem. Res.* 49, 692–705. doi:10.1007/s11064-023-04062-z

Mao, J., Xia, W., Wu, Y., Li, M., Zhao, Y., Zhai, P., et al. (2025). Biosynthesis of lysosomally escaped apoptotic bodies inhibits inflammasome synthesis in macrophages. *Research* 8, 0581. doi:10.34133/research.0581

Mao, K., Yue, M., Ma, H., Li, Z. B., and Liu, Y. (2025). Electro- and magneto-active biomaterials for diabetic tissue repair: advantages and applications. *Adv. Mater* 37, e2501817. doi:10.1002/adma.202501817

Park, K. H., Makki, H. M. M., Kim, S. H., Chung, H. J., and Jung, J. (2023). Narirutin ameliorates alcohol-induced liver injury by targeting MAPK14 in zebrafish larvae. *Biomed. Pharmacother.* 166, 115350. doi:10.1016/j.biopha.2023.115350

Peña, O. A., and Martin, P. (2024). Cellular and molecular mechanisms of skin wound healing. *Nat. Rev. Mol. Cell Biol.* 25, 599–616. doi:10.1038/s41580-024-00715-1

Petric, J. K., Johnson, M. J., Jeans, K., Fortenberry, A. R. G., Wang, J., Tulchin-Francis, K., et al. (2025). Comparison of energy expenditure with level of amputation in patients with diabetes mellitus. *Wound Repair Regen.* 33, e70007. doi:10.1111/wrr.70007

Puri, A., Mohite, P., Maitra, S., Subramaniyan, V., Kumarasamy, V., Uti, D. E., et al. (2023). From nature to nanotechnology: the interplay of traditional medicine, green chemistry, and biogenic metallic phytonanoparticles in modern healthcare innovation and sustainability. *Biomed. Pharmacother.* 170, 116083. doi:10.1016/j.biopha.2023.116083

Ri, M. H., Li, M. Y., Xing, Y., Zuo, H. X., Li, G., Li, C., et al. (2023). Narirutin exerts anti-inflammatory activity by inhibiting NLRP3 inflammasome activation in macrophages. *Phytother. Res.* 37, 1293–1308. doi:10.1002/ptr.7686

Russo, S., Kwiatkowski, M., Govorukhina, N., Bischoff, R., and Melgert, B. N. (2021). Meta-inflammation and metabolic reprogramming of macrophages in diabetes and obesity: the importance of metabolites. *Front. Immunol.* 12, 746151. doi:10.3389/fimmu.2021.746151

Sensini, F., Inta, D., Palme, R., Brandwein, C., Pfeiffer, N., Riva, M. A., et al. (2020). The impact of handling technique and handling frequency on laboratory mouse welfare is sex-specific. *Sci. Rep.* 10, 17281. doi:10.1038/s41598-020-74279-3

Sharifiaghdam, M., Shaabani, E., Faridi-Majidi, R., De Smedt, S. C., Braeckmans, K., and Fraire, J. C. (2022). Macrophages as a therapeutic target to promote diabetic wound healing. *Mol. Ther.* 30, 2891–2908. doi:10.1016/j.ymthe.2022.07.016

Spampinato, S. F., Caruso, G. I., De Pasquale, R., Sortino, M. A., and Merlo, S. (2020). The treatment of impaired wound healing in diabetes: looking among old drugs. *Pharm. (Basel)* 13, 60. doi:10.3390/ph13040060

Szunerits, S., Chuang, E., Yang, J., Boukherroub, R., and Burnouf, T. (2025). Platelet extracellular vesicles-loaded hydrogel bandages for personalized wound care. *Trends Biotechnol.* S0167-7799 (24), 00393–00397. doi:10.1016/j.tibtech.2024.12.010

Trefts, E., and Shaw, R. J. (2021). AMPK: restoring metabolic homeostasis over space and time. *Mol. Cell* 81, 3677–3690. doi:10.1016/j.molcel.2021.08.015

Wang G., G., Lin, F., Wan, Q., Wu, J., and Luo, M. (2021). Mechanisms of action of metformin and its regulatory effect on microRNAs related to angiogenesis. *Pharmacol. Res.* 164, 105390. doi:10.1016/j.phrs.2020.105390

Wang, X., Li, R., and Zhao, H. (2023). Enhancing angiogenesis: innovative drug delivery systems to facilitate diabetic wound healing. *Biomed. Pharmacother.* 170, 116035. doi:10.1016/j.biopha.2023.116035

Wang Z, Z., Jiang, L., Wang, J., Chai, Z., and Xiong, W. (2021). Morphine promotes angiogenesis by activating PI3K/Akt/HIF-1α pathway and upregulating VEGF in hepatocellular carcinoma. *J. Gastrointest. Oncol.* 12, 1761–1772. doi:10.21037/jgo-20-394

Wculek, S. K., Heras-Murillo, I., Mastrangelo, A., Mananes, D., Galan, M., Miguel, V., et al. (2023). Oxidative phosphorylation selectively orchestrates tissue macrophage homeostasis. *Immunity* 56, 516–530 e9. doi:10.1016/j.immuni.2023.01.011

Wong, E. S., Li, R. W., Li, J., Li, R., Seto, S. W., Lee, S. M., et al. (2021). Relaxation effect of narirutin on rat mesenteric arteries via nitric oxide release and activation of voltage-gated potassium channels. *Eur. J. Pharmacol.* 905, 174190. doi:10.1016/j.ejphar.2021.174190

Wu, X., He, W., Mu, X., Liu, Y., Deng, J., Liu, Y., et al. (2022). Macrophage polarization in diabetic wound healing. *Burns Trauma* 10, tkac051. doi:10.1093/burnst/tkac051

Xiao, Q., Hou, R., Xie, L., Niu, M., Pan, X., and Zhu, X. (2023). Macrophage metabolic reprogramming and atherosclerotic plaque microenvironment: fostering each other? *Clin. Transl. Med.* 13, e1257. doi:10.1002/ctm2.1257

Xiong, Y., Lin, Z., Bu, P., Yu, T., Endo, Y., Zhou, W., et al. (2023). A whole-course-repair system based on neurogenesis-angiogenesis crosstalk and macrophage reprogramming promotes diabetic wound healing. *Adv. Mater.* 35, e2212300. doi:10.1002/adma.202212300

Yang, J., Xing, X., Luo, L., Zhou, X., Feng, J., Huang, K., et al. (2023). Mitochondria-ER contact mediated by MFN2-SERCA2 interaction supports CD8+ T cell metabolic fitness and function in tumors. *Sci. Immunol.* 8, eabq2424. doi:10.1126/sciimmunol.abq2424

Yepuri, G., Ramirez, L. M., Theophall, G. G., Reverdatto, S. V., Quadri, N., Hasan, S. N., et al. (2023). DIAPH1-MFN2 interaction regulates mitochondria-SR/ER contact and modulates ischemic/hypoxic stress. *Nat. Commun.* 14, 6900. doi:10.1038/s41467-023-42521-x

Yu, H., Hong, X., Liu, L., Wu, Y., Xie, X., Fang, G., et al. (2021). Cordycepin decreases ischemia/reperfusion injury in diabetic hearts via upregulating AMPK/Mfn2-dependent mitochondrial fusion. *Front. Pharmacol.* 12, 754005. doi:10.3389/fphar.2021.754005

Zhang, X., Qin, Y., Ruan, W., Wan, X., Lv, C., He, L., et al. (2021). Targeting inflammation-associated AMPK//Mfn-2/MAPKs signaling pathways by baicalein exerts anti-atherosclerotic action. *Phytother. Res.* 35, 4442–4455. doi:10.1002/ptr.7149

Zhou, W., Hu, G., He, J., Wang, T., Zuo, Y., Cao, Y., et al. (2022). SENP1-Sirt3 signaling promotes α-ketoglutarate production during M2 macrophage polarization. *Cell Rep.* 39, 110660. doi:10.1016/j.celrep.2022.110660

Zhu, L., Luo, X., Fu, N., and Chen, L. (2021). Mitochondrial unfolded protein response: a novel pathway in metabolism and immunity. *Pharmacol. Res.* 168, 105603. doi:10.1016/j.phrs.2021.105603

Frontiers in Pharmacology

Explores the interactions between chemicals and living beings

The most cited journal in its field, which advances access to pharmacological discoveries to prevent and treat human disease.

Discover the latest Research Topics

See more →



Frontiers

Avenue du Tribunal-Fédéral 34
1005 Lausanne, Switzerland
frontiersin.org

Contact us

+41 (0)21 510 17 00
frontiersin.org/about/contact